WASTE HEAT RECOVERY USING FLUID BOTTOMING CYCLES FOR HEAVY DUTY DIESEL ENGINES

ANGAD SINGH PANESAR

PHD 2015

WASTE HEAT RECOVERY USING FLUID BOTTOMING CYCLES FOR HEAVY DUTY DIESEL ENGINES

ANGAD SINGH PANESAR

A thesis submitted in partial fulfilment of the
requirements of the University of Brighton
for the degree of Doctor of Philosophy

April 2015

Abstract

A typical long-haul heavy duty Diesel engine currently rejects up to 50% of the total fuel energy in the form of heat. Due to increasing CO_2 emissions and fuel costs, there is a growing interest in techniques that can even partially utilise this wasted resource to improve the overall system efficiency. Fluid Bottoming Cycles (FBC) including Rankine and organic Rankine cycles offer one means towards converting waste heat into usable power. This thesis investigates the potential of FBCs to improve the net power of two computationally modelled (Ricardo WAVE V8.1) 10 litre engine platforms operating at Euro 6 emission levels.

The heat to power conversion potential of a FBC largely depends on the selected working fluid, its associated cycle operating mode and the system architecture. Firstly, a detailed systematic methodology for the selection and evaluation of pure working fluids was developed and applied using an advanced chemical process modelling tool (Aspen HYSYS V7.3). Using cycle and fluid fundamentals, screening criteria, and ranking indices, the methodology identified ethyl iodide, methanol, R30, acetone, R152 and E152a as the most suitable fluids amongst the 1800 synthetic, organic and inorganic fluids.

Secondly, by varying the expansion inlet parameters, simulations were conducted using 10 pure, dry, isentropic and wet working fluids. The aim was to reduce cycle irreversibilities, highlight the significant sensitivity and performance results, provide directions for practical implementation, and offer new opportunities in energy conversion. For the low, medium and high thermal boundary conditions respectively, liquid expansion (E152a), low pressure limited superheat expansion (methanol, R30, acetone) or dry supercritical expansion (R152), and high pressure limited superheat expansion (using the high temperature organic fluids) were identified as techno-economic optimum. These optimal ORC operating modes achieved efficiencies 65-77% of the theoretical cycle limits.

Finally, 13 combinations of thermal and sub-system architectures were methodically analysed and classified in terms of their level of complexity, average system power and relative size. To provide tailored solutions, the pure working fluid methodology was additionally adapted to examine over 750 water blends and 700 organic blends. Aqueous blends of 3-Methyl-1-Butanol and 1-propanol were found to be best suited to the dual pressure and the dual cycle systems. Furthermore, the ethanol-toluene blend was preferred for the high temperature recuperated cycle. The dual cycle system (aqueous blend and E152a combination) showed the maximum potential and produced an average of 7.5% of additional engine crankshaft power.

Contents

Abstract i
Contents ii
List of Figures x
List of Tables xvii
Declaration xviii
Nomenclature xix
1 Introduction 1
1.1 Heavy duty Diesel truck engines 1
1.2 Waste heat to power conversion 2
1.2.1 Fluid bottoming cycles 4
1.2.2 Long-haul trucks and fluid bottoming cycles 5
2 Literature Review 7
2.1 Introduction 7
2.2 Technology classification 7
2.3 Mechanical turbocompounding 10
2.3.1 Mechanical turbocompounding: Summary 11
2.4 Electric turbocompounding 12
2.4.1 Electric turbocompounding: Summary 14
2.5 Thermoelectric generators 14
2.5.1 Thermoelectric generators: Summary 17
2.6 Fluid bottoming cycles 18
2.7 Organic Rankine cycle (refrigerants) 20
2.7.1 Internal combustion engines 20
2.7.2 Hybrid electric vehicles 24
2.7.3 Organic Rankine cycle (refrigerants): Summary 26
2.8 Rankine cycle (water) 27
2.8.1 Internal combustion engines 27
2.8.2 Hybrid electric vehicles 28
2.8.3 Open loop Rankine cycle for internal combustion engines 30
2.8.4 Rankine cycle (water): Summary 31
2.9 Organic Rankine cycle (alcohols) 32
2.9.1 Internal combustion engines 32
2.9.2 Organic Rankine cycle (alcohols): Summary 35
2.10 Organic Rankine cycle combined with other technologies 36
2.11 Other waste heat recovery technologies 38
2.12 Chapter 2: Summary 39
2.12.1 Rational and justification for selecting fluid bottoming cycles 40

2.13 Research objectives and contributions 42
3 Engine Platform and Waste Heat 46
3.1 Introduction 46
3.2 HDDE emissions platform 46
3.3 Fuel penalty to reach Euro 6 emissions 49
3.4 EGR only platform with waste heat recovery 55
3.5 EGR focused and EGR only engine strategies 55
3.6 2L and 10L engine models 57
3.7 Heat source selection 64
3.7.1 Exhaust gas recirculation and post-turbine exhaust 65
3.7.2 Charge air cooler 67
3.7.3 Engine coolant 68
3.7.4 Stream qualities and quantities used 68
3.8 Heat sink selection 69
3.9 Chapter 3: Summary and study overview 72
4 Working Fluid 74
4.1 Introduction 74
4.2 Ideal cycle and its working fluid (Phase 0) 75
4.2.1 Theoretical parametric analysis 80
4.3 ORC process and control 82
4.4 Fluid selection and evaluation methodology 89
4.5 Fluid screening (Phase 1) 92
4.5.1 Thermo-physical properties 92
4.5.2 Legal criteria 94
4.5.3 Molecular properties 94
4.5.3.1 Saturation vapour curve 99
4.5.4 Fluid screening result 101
4.6 Optimised power recovery under extreme cases (Phase 3) 103
4.6.1 Optimisation Case A 105
4.6.2 Optimisation Case B 105
4.6.3 Optimisation Case C 105
4.6.4 Optimisation Case D 106
4.7 Results and discussion (Phase 4) 106
4.7.1 Ethyl iodide and methanol compared to water 107
4.7.1.1 Case 1 (Appendix 4.6 for tabulated results) 107
4.7.1.2 Case 2 (Appendix 4.7 for tabulated results) 112
4.7.1.3 Suitable source temperatures for organic fluids and water 113
4.7.2 R30 compared to ethanol 114

4.7.2.1 Case 1 (Appendix 4.6 for tabulated results) 115
4.7.2.2 Case 2 (Appendix 4.7 for tabulated results) 117
4.7.3 Acetone compared to R245fa 117
4.7.3.1 Case 1 (Appendix 4.6 for tabulated results) 118
4.7.3.2 Case 2 (Appendix 4.7 for tabulated results) 120
4.7.3.4 Rationality of fluid pairing 120
4.7.4 R152 and E152a compared to R245fa 121
4.7.4.1 Case 3 (Appendix 4.11 for tabulated results) 121
4.7.4.2 Additional possible working fluids 122
4.8 Performance and system index (Phase 5) 122
4.8.1 Case 1 and 2 125
4.8.2 Case 3 126
4.8.3 Importance of appropriate performance and system index 127
4.8.4 Sensitivity to the developed performance and system index 129
4.9 Heat exchanger implications 129
4.9.1 Minimum approach temperature difference 129
4.9.2 Sub-cooling level 130
4.9.3 Heat exchanger irreversibilities 131
4.9.3.1 Condensing irreversibilities 132
4.10 Chapter 4: Summary 133
5 Cycle Operation 135
5.1 Introduction 135
5.2 Expansion machines 136
5.2.1 Positive displacement expanders 137
5.2.2 Dynamic turbines 138
5.2.3 Expansion machine: Summary 140
5.3 Cycle operating modes 142
5.3.1 Cycle boundary conditions 144
5.4 Limited superheat expansion (Cases 4 and 5) 145
5.4.1 Simulation overview 145
5.4.2 Case 4 145
5.4.3 Case 5 148
5.4.4 Process control: Organic fluids vs. water 150
5.5 Large superheat expansion (Cases 4 and 5) 152
5.5.1 Rational and simulation overview 152
5.5.2 Performance: Wet vs. dry fluids 153
5.5.3 Large superheat: Discussion and findings 156
5.6 Cycles with internal heat exchange (Cases 4 and 5) 158

5.6.1 Rational and simulation overview....158
5.6.2 Performance....160
5.6.3 Internal heat exchange: Wet vs. dry fluids....161
5.6.4 Superheated recuperated vs. superheated non-recuperated cycles....163
5.6.5 Cycles with internal heat exchange: Discussion and findings....163
5.7 Supercritical cycles (Cases 4 and 5)....165
5.7.1 Rational and simulation overview....165
5.7.2 Performance....166
5.7.3 Supercritical cycle: Discussion and findings (Case 4)....168
5.7.4 Supercritical cycle: Discussion and findings (Case 5)....169
5.8 Two-phase expansion (Case 4)....170
5.8.1 Rational and simulation overview....170
5.8.2 Performance....171
5.8.3 Two-phase expansion: Discussion and findings....173
5.9 Liquid expansion (Case 3)....174
5.9.1 Rational....174
5.9.2 Simulation overview....175
5.9.3 Performance....175
5.3.4 Liquid expansion: Discussion and findings....177
5.10 Additional inorganic cycles....178
5.10.1 Carbon dioxide....179
5.10.2 Ammonia....180
5.10.3 Ammonia-water....181
5.10.3.1 Rational and simulation overview....181
5.10.3.2 Performance....182
5.10.3.3 Ammonia-water cycle: Discussion and findings....184
5.11 Chapter 5: Summary....185
6 Process Integration....189
6.1 Introduction....189
6.2 Base engine cooling module....191
6.2.1 Impact of exhaust heat recovery and modified engine cooling module....193
6.3 Justification for the use of cruise and full load conditions....194
6.4 Theme 1 - High temperature heat recovery with single stage expansion....195
6.4.1 Process integration 1: EXH then EGR series (baseline)....196
6.4.1.1 System architecture, cycle operation and process optimisation....196
6.4.1.2 Results and discussion....198
6.4.2 Process integration 2: EGR then EXH series....199

6.4.2.1 Problem definition, system architecture, cycle operation and process optimisation....199
6.4.2.2 Results and discussion....201
6.4.3 Process integration 3: EGR + EXH parallel....202
6.4.3.1 Problem definition, system architecture, cycle operation and process optimisation....202
6.4.3.2 Results and discussion....204
6.4.3.3 High load challenges and solutions....205
6.4.4 Process integration 3a: High latent heat solution....206
6.4.4.1 Problem definition, system architecture and cycle operation....206
6.4.4.2 Results and discussion....207
6.4.5 Summary: High temperature heat recovery with single expansion stage....209
6.5 Theme 2 - High and low temperature heat recovery with single expansion stage....209
6.5.1 Process integration 4: EGR + EXH parallel with coolant preheat (baseline)....210
6.5.1.1 System architecture and cycle operation....210
6.5.1.2 Results and discussion....211
6.5.2 Process integration 4a: Modified coolant exergy (baseline)....212
6.5.2.1 Problem definition and process optimisation....212
6.5.2.2 Results and discussion....214
6.5.3 Process integration 5: EGR + CAC-EXH parallel....215
6.5.3.1 Problem definition, system architecture, cycle operation and process optimisation....215
6.5.3.2 Results and discussion....217
6.5.3.3 Low load challenges and solutions: option 1....218
6.5.3.4 Low load challenges and solutions: option 2....219
6.5.4 Summary: High and low temperature heat recovery with single expansion stage....220
6.6 Theme 3 - High temperature thermally stable solutions using water....220
6.6.1 Process integration 6: Cascade (baseline)....222
6.6.1.1 System architecture, cycle operation and process optimisation....222
6.6.1.2 Results and discussion....226
6.6.2 Process integration 7: Two-phase cascade (baseline)....227
6.6.2.1 Problem definition, system architecture and cycle operation....227
6.6.2.2 Results and discussion....229
6.6.3 Process integration 8: Two-phase reheat....230
6.6.3.1 Problem definition, system architecture, cycle operation and process optimisation....230
6.6.3.2 Results and discussion....232
6.7 Theme 4 - Improved thermal stability solutions using water blends....234
6.7.1 Overview of the water blend study....235

6.7.1.1 Zeotropic and azeotropic blends 236
6.7.1.2 Performance and sizing results....238
6.7.1.3 Heat transfer irreversibilities....239
6.7.1.4 Molecular weight 241
6.7.1.5 Freezing and decomposition 242
6.7.1.6 Zeotrope challenges 242
6.7.1.7 Summary: Water blends....243
6.7.2 Process integration 9: Dual pressure system....244
6.7.2.1 Problem definition, system architecture, cycle operation and process optimisation....244
6.7.2.2 Results and discussion 247
6.7.3 Process integration 10: Dual cycle system....250
6.7.3.1 Problem definition and baseline solution....250
6.7.3.2 System architecture, cycle operation and process optimisation....252
6.7.3.3 Results and discussion 255
6.8 Theme 5 - Improved thermal stability solutions using organic fluids 258
6.8.1 Higher thermal stability organic fluids 258
6.8.2 Overview of the organic blend study 259
6.8.2.1 Organic blend results and discussion 261
6.8.3 Process integration 11 and 12: High temperature heat recovery with an IHE ..263
6.8.3.1 System architecture, cycle operation and process optimisation....263
6.8.3.2 Results and discussion 265
6.9 Expansion machine type and efficiency....266
6.10 Chapter 6: Summary 268
6.10.1 System complexity....268
6.10.2 System performance....269
6.10.3 System size....272
6.10.4 Secondary objective functions 274
7 Conclusion 276
7.1 Working fluid....276
7.2 Cycle operation 276
7.3 Process integration 278
7.4 EGR only and EGR focused platforms 279
7.5 Recommendations and future works....279
Reference....281
Appendices....294
Chapter 1 Appendix 294
Appendix 1.1 - List of publications 294

Chapter 2 Appendices 295
Appendix 2.1 - Supplement MTC information 295
Appendix 2.2 - Supplement ETC information 296
Appendix 2.3 - Supplement TEG information 297
Appendix 2.4 - Supplement FBC information 297
Appendix 2.5 - Supplement open loop Rankine cycle information 298
Appendix 2.6 - Supplement information on other WHR concepts 298
Appendix 2.7 - Boundary conditions and assumptions in cited literature 299
Chapter 3 Appendices 301
Appendix 3.1 - Supplement after-treatment information 301
Appendix 3.2 - Relationship between the selected ESC test points and ETC 303
Appendix 3.3 - Test bed dimension 304
Appendix 3.4 - HDDE energy balance 306
Appendix 3.5 - HDDE heat quality and quantity 307
Chapter 4 Appendices 308
Appendix 4.1 - Carcinogenic risk category 308
Appendix 4.2 - ASHRAE 34 classification 308
Appendix 4.3 - NFPA 704 classification 309
Appendix 4.4 - Fluids under consideration in this study 310
Appendix 4.5 - Pure fluid screening 312
Appendix 4.6 - Case 1 simulation results 319
Appendix 4.7 - Case 2 simulation results 320
Appendix 4.8 - Accurate overall UA and LMTD 321
Appendix 4.9 - Varying dT/dS slope 321
Appendix 4.10 - Fluid pairing 322
Appendix 4.11 - Case 3 simulation results 323
Appendix 4.12 - PSI weight factor sensitivity in Case 1 324
Appendix 4.13 - PSI weight factor sensitivity in Case 2 325
Appendix 4.14 - PSI weight factor sensitivity in Case 3 326
Chapter 6 Appendices 327
Appendix 6.1 - Results for process integration 1 327
Appendix 6.2 - Results for process integration 2 328
Appendix 6.3 - Results for process integration 3 329
Appendix 6.4 - Results for process integration 3a 330
Appendix 6.5 - Results for process integration 4 330
Appendix 6.6 - Results for process integration 3 (with R245fa) 331
Appendix 6.7 - Results for process integration 4a (case study) 331
Appendix 6.8 - Results for process integration 5 332

Appendix 6.9 - Results for process integration 5a 333
Appendix 6.10 - Results for process integration 6 334
Appendix 6.11 - Results for process integration 7 335
Appendix 6.12 - Results for process integration 8 335
Appendix 6.13 - Blend constituents under consideration in this study 336
Appendix 6.14- Aqueous blend screening 337
Appendix 6.15 - Results for process integration 9 342
Appendix 6.16 - Results for process integration 10 343
Appendix 6.17- Thermal oil loop 343
Appendix 6.18- High temperature stability organic fluids 345
Appendix 6.19- Organic blend screening 345
Appendix 6.20 - Results for process integration 11 and 12 346
Appendix 6.21 - Secondary objective functions 347

List of Figures

Figure 1.1 HD CO_2 and fuel consumption reduction timeline in EU, US and Japan (Zink, 2011) 2

Figure 1.2 Energy balance for a typical on-highway engine with sources of waste heat and typical temperature levels (adapted from the 10L model, Chapter 3)....3

Figure 1.3 Engine and powertrain technology roadmap for long-haul HDDE showing the need of multiple technologies to address an aggressive GHG scenario (Stanton, 2013)....4

Figure 1.4 A typical long-haul HDDE drive cycle (Cooper et al., 2009) 6

Figure 2.1 Technology classification and schematic representation of the widely proposed WHR technologies 8

Figure 2.2 (a) BSFC variation vs. power turbine pressure ratio (b) Engine power vs. power turbine pressure ratio, at 1700 rpm for various engine loads (Hountalas and Mavropoulos, 2010) 11

Figure 2.3 ETC simulation results using high efficiency components (Kruiswyk et al., 2009, 2008) 13

Figure 2.4 TEG performance under highway driving condition (LaGrandeur et al., 2011, 2010, 2009) 15

Figure 2.5 Proposed 1st generation ORC and HDDE integration schematic for the superheated recuperated cycle using combined EGR and exhaust (Nelson et al., 2009) 21

Figure 2.6 Series exhaust then EGR (a) heat recovery architecture (b) cycle T-S diagram (Edwards et al., 2010) 22

Figure 2.7 Cascade ORC system (a) schematic of the arrangement (b) T-S plot of the HT and LT cycle (Wang et al., 2012)....23

Figure 2.8 ORC with performance enhancement coolant and residual exhaust heat recovery (a) system architecture (b) P-H diagram (c) cycle averaged backpressure during EPA highway drive cycle with and without exhaust recovery (Hussain and Brigham, 2010).....25

Figure 2.9 R245fa as the favoured refrigerant with the associated cycle operation and heat recovery architecture in literature 26

Figure 2.10 (a) BSFC improvement as a function of engine load at 1700 rpm when recuperating heat either from exhaust or both exhaust and EGR (b) T-S diagram of series exhaust then EGR at cruise condition (Katsanos et al., 2010) 28

Figure 2.11 Maximum energy recovery from cooling system and exhaust gas (a) architecture (b) T-S diagram (Arias et al., 2006)....29

Figure 2.12 Water as the favoured working fluid with the associated cycle operation and heat recovery architecture in literature....31

Figure 2.13 Comparison of T-S diagram for (a) R245fa (b) ethanol, superheated recuperated subcritical cycle (Teng and Regner, 2009)....33

Figure 2.14 Ratio of power output of the waste heat recovery system to engine power (Seher et al., 2012) 34

Figure 2.15 Ethanol as the favoured hydrocarbon derivative with the associated cycle operation and heat recovery architecture in literature....35

Figure 2.16 System schematic for combined high and low temperature heat recovery (a) TEG-ORC system (Shu et al., 2012b) (b) ORC-Kalina system (He et al., 2011) 37

Figure 2.17 Relative challenges-benefit trade-off for different WHR technologies applied to HDDEs 42

Figure 2.18 Method overview for evaluation of FBC research themes 43

Figure 3.1 HDDE emissions reduction platform with combined in-cylinder and after-treatment techniques, also shown are the emission standards in EU, US and Japan ..47

Figure 3.2 Paths to reach Euro 6 - engine and platform architecture.....49

Figure 3.3 Schematic layout of the 2L engine test bed with P,T positions.....50

Figure 3.4 Impact of increasing EGR on BSFC at B50 with 2500 bar injection pressure...52

Figure 3.5 Paths to reach Euro 6 - fuel economy impact for the 4 platforms 53

Figure 3.6 European stationary cycle with percentage of time duration (selected points for WHR represented by black markers) 57

Figure 3.7 2L WAVE engine model with intake, exhaust and EGR system 58

Figure 3.8 10L WAVE engine model with two-stage turbocharging and EGR system 59

Figure 3.9 2L engine, 2L model and 10L model quality match (a) intake manifold (b) exhaust manifold 60

Figure 3.10 2L engine, 2L model and 10L model quantity match (a) EGR fraction (b) AFR 61

Figure 3.11 2L engine, 2L model and 10L model normalised performance match (a) power (b) torque.....62

Figure 3.12 (a) reduced tailpipe exhaust quality due to the use of turbochargers (b) negligible reduction in exhaust manifold temperatures due to the use of the high EGR rate strategy 63

Figure 3.13 Relative (a) energy and (b) exergy content of the heat sources.....66

Figure 3.14 Two stage cooling module for the 10L model.....70

Figure 3.15 Engine cooling module with an additional high temperature condenser, showing radiator (condenser) outlet temperature as a function of air temperature, pinch point and temperature rise through the module 71

Figure 3.16 Method overview for evaluation of engine-FBC research avenues.....73

Figure 4.1 Brief overview of the novel fluid selection and evaluation methodology.....74

Figure 4.2 T-S diagram evolution from infinite source and sink to finite source and non-ambient condensing (a) Carnot cycle (b) trilateral cycle (c) quadlateral cycle (d) real quadlateral cycle.....75

Figure 4.3 T-Q diagram for ideal trilateral, ideal quadlateral and real quadlateral cycles using EGR stream 78

Figure 4.4 Working fluid T-S sketch for (a) infinite (b) finite heat source 79

Figure 4.5 Sensitivity analysis to source temperature, condensing temperature and expansion efficiency using real quadlateral cycle.....81

Figure 4.6 Need of high exhaust backpressures in direct WHR methods for increasing overall conversion efficiency 82

Figure 4.7 Detailed T-S sketch and brief T-Q sketch of a subcritical ORC process description.....83

Figure 4.8 A simple ORC layout with instrumentation 83

Figure 4.9 Overview of the novel fluid selection and evaluation methodology 91

Figure 4.10 Working fluid evolution with international protocols 94

Figure 4.11 Molecular and structural trade-offs with (a) chlorine, fluorine and hydrogen content (b) fluorine content (c) oxygen content (d) carbon content (e) complexity between isomers 96

Figure 4.12 Shape of the saturated vapour curve (a) extremely wet fluid (b) marginally wet fluid (c) marginally dry fluid (d) extremely dry fluid, as a function of number of atoms in a molecule 100

Figure 4.13 Shortlisted fluids under consideration in this study and their chemical classes (shown in bold) 102

Figure 4.14 Optimisation cases, point of (a) overall conversion efficiency with R245fa in Case 3 (b) low design intensity overall conversion efficiency with R143 in Case 3 (c) pressure limited overall conversion efficiency with ethanol in Case 1 (d) temperature limited overall conversion efficiency with acetonitrile in Case 1 104

Figure 4.15 Molecular weight correlation to (a) latent heat (b) entropy change (c) pumping power consumption (d) expansion enthalpy drop (e) speed of sound (f) expansion inlet density, in Case 4 109

Figure 4.16 Influence of latent heat on the area formed by the cycle 110

Figure 4.17 T-Q diagram for (a) water Case 1(b) ethyl iodide Case 1 (c) water Case 2 (d) methanol Case 2 112

Figure 4.18 Source temperature sensitivity analysis for organic fluids and water 114

Figure 4.19 T-Q diagram for (a) ethanol Case 1 (b) R30 Case 1 (c) ethanol Case 2 (d) R30 Case 2 116

Figure 4.20 T-Q diagram for (a) R245fa Case 1(b) Acetone Case 1 (c) R245fa Case 2 (d) Acetone Case 2 119

Figure 4.21 Proportionality in exergy destruction in the heat exchanger and the LMTD for equal heat input in Case 1 119

Figure 4.22 Performance and System Index values for (a) Case 1 (b) Case 2, showing suitability of R30, ethyl iodide, methanol and acetone 126

Figure 4.23 Performance and System Index values for Case 3 showing suitability of R152 and E152a 127

Figure 4.24 Influence on the PSI value in Case 1 by (a) ignoring component size per unit net power (b) partial selection of the PSI parameters 128

Figure 4.25 Impact of pinch point and condensing temperature on heat exchanger and condenser UA/W value 130

Figure 4.26 Percentage change in net power and condenser UA value due to increased sub-cooling (a) Case 1 with ethanol (b) Case 3 with R245fa 131

Figure 4.27 Averaged relative component irreversibilities using the alternative organic fluids 132

Figure 4.28 Irreversibilities in the condenser as a function of the de-superheating load and the pressure loss in Case 1 133

Figure 5.1 Method overview for the assessment of cycle operating modes 135

Figure 5.2 Positive displacement and dynamic machine options (<30 kW) preferred in automotive application (mentioned in bold) with typical single stage pressure ratios, volume flow ratios and rotational speeds 137

Figure 5.3 12 cycle operating modes using pure fluids for single stage expansion (a) subcritical operating modes (b) supercritical operating modes (c) subcritical operating

modes specific to dry and isentropic fluids (d) supercritical operating modes specific to dry and isentropic fluids 143

Figure 5.4 Effect of increasing cycle pressure on (a) thermal efficiency (b) heat transfer irreversibilities for organic fluids (c) heat recovery (d) heat exchanger LMTD for organic fluids (e) expansion enthalpy drop (f) net power, in Case 4 for limited superheat expansion 146

Figure 5.5 Effect of (a) pressure ratio on net power (b) volume flow ratio on net power (c) cycle pressure on UA/W value, in Case 4 for limited superheat expansion 147

Figure 5.6 Effect of increasing cycle pressure on (a) thermal efficiency (b) heat recovery (c) heat transfer irreversibilities (d) net power, in Case 5 for limited superheat expansion 148

Figure 5.7 Effect of (a) pressure ratio on net power (b) volume flow ratio on net power (c) cycle pressure on UA/W value, in Case 5 for limited superheat expansion 149

Figure 5.8 (a) working fluid mass flow rate variation (b) working fluid absolute mass flow rate (c) application specific mass flow control challenge for water, in Case 4 for limited superheat expansion 151

Figure 5.9 Effect of large superheat on reduced EGR cooler irreversibilities in Case 4 for ethanol 153

Figure 5.10 Effect of superheating at fixed evaporator pressure on (a,b) thermal efficiency (c,d) net power, in Case 4 (left side) and Case 5(right side) 154

Figure 5.11 Wet vs. dry fluids (a,b) isobars in superheated region (c,d) expansion and pumping power change (e,f) heat transfer percentage load in vapour form, in Case 4 (left side using ethanol) and Case 5 (right side using R245fa) 155

Figure 5.12 Advantages of superheating (a) performance (b) volume flow ratio; Disadvantages of superheating (c) de-superheater inlet densities (d) heat transfer load in vapour form; (e) paths to achieve similar net power by comparing limited superheat using higher pressures and large superheat using lower pressures, in Case 4 157

Figure 5.13 Superheated recuperated cycle (a) configuration (b) T-S sketch (c) T-S sketch as a function of cycle pressure for a fixed maximum temperature (d) T-S sketch as a function of cycle temperature for a fixed maximum pressure 159

Figure 5.14 (a,b) effect of pressure on fixed superheat cycle with an IHE (c,d) effect of superheat on fixed pressure cycle with an IHE, in Case 4 (left side using ethanol) and Case 5 (right side using R245fa) 161

Figure 5.15 Wet vs. dry fluids (a,b) T-Q diagram for the optimised superheated cycle with an IHE (c,d) irreversibilities in the internal heat exchange process for equal load, in Case 4 (left side using ethanol) and Case 5 (right side using R245fa) 162

Figure 5.16 Performance change benchmark using superheated recuperated cycle in (a) Case 4 ethanol (b) Case 5 R245fa 164

Figure 5.17 (a) heat transfer irreversibilities when comparing supercritical and subcritical operating modes (b) densely packed isobars near and above critical point conditions 165

Figure 5.18 Thermal efficiency and net power variation with reference to (a,b) relative critical pressure (c,d) absolute cycle pressure (e,f) expansion pressure ratio, in Case 4 (left side) and Case 5 (right side) 167

Figure 5.19 (a) small scale ORC component cost distribution (b) shell and tube heat exchanger pressure vs. cost relationship 168

Figure 5.20 23 bar limited superheat water expansion (a) T-S (b) T-Q diagram; 171

Figure 5.21 Effect of expansion vapour inlet fraction for 30 bar cycle pressure on (a,b) thermal efficiency, heat recovery and net power (c,d) expansion volume flow ratio, UA/W value and density, in Case 4 for water (left side) and ethyl iodide (right side).....172

Figure 5.22 (a,b) T-Q diagram for the optimised cycle (c,d) thermal efficiency, heat recovery and net power variation with cycle pressure, for limited superheat (left side) and liquid expansion (right side) in Case 3 for E152a.....176

Figure 5.23 (a,b) effect of pressure ratio and volume flow ratio on net power (c,d) effect of cycle pressure on UA/W value, for limited superheat (left side) and liquid expansion (right side) in Case 3 for E152a and R245fa.....178

Figure 5.24 T-S diagram (a) carbon dioxide (b) ammonia 180

Figure 5.25 Net power comparison for E152a and ammonia with reference to (a) expansion pressure ratio (b) maximum cycle pressure, in Case 3 for limited superheat expansion ...181

Figure 5.26 Basic Kalina cycle configuration.....182

Figure 5.27 (a,b) effect of cycle pressure on net power (c,d) T-Q diagram of the optimised ammonia-water cycle (e,f) effect of pressure ratio on net power, in Case 3 (left side) and Case 5 (right side) for ammonia-water cycle and ORCs 183

Figure 5.28 Key results and sensitivity of the different cycle operating modes by varying the three expansion inlet parameters 188

Figure 6.1 Division of process integrations based on 5 themes of approach 190

Figure 6.2 Common heat loads on the engine cooling module across all EGR engine platforms 191

Figure 6.3 Maximum heat rejection capacity of the low and medium-temperature radiators for (a) EGR focused engine (b) EGR only engine 192

Figure 6.4 Modified cooling capacity at the medium-temperature radiator level for (a) EGR focused engine (b) EGR only engine, used in the simulations 193

Figure 6.5 Two themes of approach using single stage expansion 196

Figure 6.6 EXH then EGR series (a) system architecture (b) T-S diagram using water (c) T-S diagram using R245fa.....197

Figure 6.7 PI-1 maximum cycle pressure effect on (a,b) heat recovery and thermal efficiency (c,d) net power and beta value, for water (left side) and R245fa (right side) at E5-B50 198

Figure 6.8 EGR then EXH series (a) heat recovery architecture (b) T-S diagram using methanol.....200

Figure 6.9 PI-2 maximum cycle pressure effect on (a) heat recovery and thermal efficiency (b) net power and beta value, for methanol at E6-B50 200

Figure 6.10 PI-2 guideline and system power/beta value change over PI-1 201

Figure 6.11 EGR + EXH parallel (a) system architecture (b) T-S diagram using ethanol (c) T-S diagram using water 203

Figure 6.12 PI-3 maximum cycle pressure effect on (a) heat recovery and thermal efficiency (b) net power and beta value, for ethanol at E5-C100 204

Figure 6.13 PI-3 guideline and system power/beta value change over PI-2.....205

Figure 6.14 EGR and EXH (series+parallel) heat recovery loop as exhaust heat limitation and high power generation strategy 206

Figure 6.15 High latent heat solution (a) system architecture (b) T-S diagram using water 207

Figure 6.16 Comparison of heat recovery and net power for single-stage expansion process integrations using water with varying maximum cycle pressure at E6-C100 208

Figure 6.17 PI-3a guideline and system power/beta value change over PI-2 208

Figure 6.18 EGR + EXH parallel with coolant preheat (a) system architecture (b) T-S diagram using water (c) T-S diagram using R245fa 210

Figure 6.19 PI-4 guideline and system power/beta value change over PI-3 212

Figure 6.20 Effect of engine block heat recovery on (a,b) EGR, EXH heat recovery and coolant temperature (c,d) net power and thermal efficiency, using water (left side) and R245fa (right side) at E6-B50 213

Figure 6.21 T-S diagram for modified coolant exergy corresponding complete engine block heat recovery using (a) water (b) R245fa, at E6-B50 214

Figure 6.22 EGR + CAC-EXH parallel (a) system architecture (b) T-S diagram using acetone (c) T-S diagram using methanol 216

Figure 6.23 (a) PI-5 maximum cycle pressure effect on heat recovery, thermal efficiency and net power (b) baseline net power and beta value comparison 217

Figure 6.24 PI-5 guideline and system power/beta value change over PI-4 218

Figure 6.25 EGR + EXH parallel (optional CAC) heat recovery loop as exhaust heat limitation with highest power generation strategy 219

Figure 6.26 EGR + CAC-EXH parallel operating under supercritical mode with R152 as an alternative process integration for relatively lower source quality 219

Figure 6.27 Three additional themes of approach coupling fluid selection and system architecture to offer thermally stable or improved stability process integrations 222

Figure 6.28 Cascade system (a) system architecture (b) T-S diagram using water-R245fa combination 224

Figure 6.29 PI-6 maximum high-temperature cycle pressure effect on (a) heat recovery and net power (b) thermal efficiency 226

Figure 6.30 PI-6 guideline and system power/beta value change over PI-3a 227

Figure 6.31 Two-phase cascade system (a) system architecture (b) T-S diagram using water-R245fa combination 228

Figure 6.32 PI-7 guideline and system power/beta value change over PI-6 230

Figure 6.33 Two-phase reheat cycle (a) system architecture (b) T-S diagram using water 231

Figure 6.34 Effect on heat recovery, net power and thermal efficiency by varying (a) PI-8 maximum cycle pressure (b) PI-7 maximum high-temperature cycle pressure 232

Figure 6.35 PI-8 guideline and system power/beta value change over PI-7 233

Figure 6.36 Conventional reheat cycle T-S diagram using water 234

Figure 6.37 Screening method overview of the aqueous blend selection study 236

Figure 6.38 Temperature vs. concentration and key attributes of (a) zeotropic ammonia and water blend (b) azeotropic 3Methyl-1Butanol and water blend 238

Figure 6.39 Net power, UA/W value and heat transfer irreversibilities in Case 4 for (a,b,c) low (d,e,f) medium (g,h,i) high, water content blends 240

Figure 6.40 (a) effect of water content and molecular weight of the organic fluid on the blend expansion enthalpy drop and mass flow rate in Case 4 (b) freezing and flash point of ethanol-water blend with varying water content 241

Figure 6.41 Source temperature sensitivity analysis on 3M-1B53% and water 244

Figure 6.42 Dual pressure system (a) system architecture (b) T-S diagram using 3M-1B53% 246

Figure 6.43 (a) PI-9 high-pressure expansion pressure ratio effect on heat recovery thermal efficiency and net power (b) baseline net power and beta value comparison 247

Figure 6.44 PI-9 guideline and system power/beta value change over PI-7 248

Figure 6.45 AVL solution (a) system architecture (b) T-S diagram using ethanol 251

Figure 6.46 AVL solution maximum cycle pressure effect on (a) heat recovery (b) thermal efficiency and net power 252

Figure 6.47 Dual cycle system (a) system architecture (b,c) T-S diagram using 3M-1B53%(HT)-E152a(LT) 254

Figure 6.48 PI-10 maximum low-temperature cycle pressure effect on (a) thermal efficiency (b) net power (c) heat recovery 255

Figure 6.49 Baseline performance benefit and cooling impact comparison 257

Figure 6.50 PI-10 application guideline and system power/beta value benefits 257

Figure 6.51 Effect of expansion pressure ratio on net power in Case 4 for high thermal stability organic fluids 258

Figure 6.52 Screening method overview of the improved thermal stability organic blend study 259

Figure 6.53 Comparative T-S sketches for 3 types of binary blends 260

Figure 6.54 (a) performance comparison between ET65/35, m-Xylene and ethanol (b) IHE pressure drop sensitivity comparison between ET65/35 and m-Xylene, in Case 4 261

Figure 6.55 T-S diagram comparison between (a) m-Xylene and (b) ET65/35, in Case 4 262

Figure 6.56 System architecture and T-S diagram using ET65/35 (a,b) PI-11, EGR + EXH parallel with IHE preheat (c,d) PI-12, EGR + IHE-EXH parallel 264

Figure 6.57 PI-11 maximum cycle pressure effect on heat recovery, thermal efficiency and net power 264

Figure 6.58 PI-12 application guideline and system power/beta value change over PI-4 .266

Figure 6.59 Piston expander and radial turbine (selection and efficiency) chart for the application of the similarity concept with (a) literature fluids (b) alternative fluids 267

Figure 6.60 Complexity ratings and performance results for different process integrations across (a) EGR only (b) EGR focused platform 270

Figure 6.61 UA/W and beta value results for different process integrations across (a) EGR only (b) EGR focused platform 273

Figure 6.62 Baseline volume flow ratio per unit power output comparison 274

List of Tables

Table 2.1 Results of TEG in an escape HEV using mid-term materials and processes (LaGrandeur et al., 2011, 2010, 2009) 16

Table 3.1 2L engine and test bed specifications 51

Table 3.2 Steady-state NOx strategies derived experimentally from the 2L engine 56

Table 3.3 EGR, exhaust and CAC temperatures and heat loads for the fluid selection study 69

Table 4.1 Carnot, ideal trilateral, ideal quadlateral, real quadlateral efficiencies and real quadlateral power for the 5 cases considered 79

Table 4.2 Phase 2 boundary conditions (left) and performance assumptions (right) used in the simulations 92

Table 4.3 Justification and influence of the 6 parameters used in calculating the PSI value 124

Table 5.1 Maximum working fluid pressure and temperature boundary conditions 144

Table 6.1 Maximum available heat loads at mid-speed mid-load and high-speed full-load used in the simulations 192

Table 6.2 Boundary conditions (left) and performance assumptions (right) used in simulations 195

Table 6.3 Relative comparison of key properties for potential replacement of engine coolant 249

Table 6.4 Detailed breakdown of the complexity rating for process integrations discussed in detail in this chapter 269

Declaration

I declare that the research contained in this thesis, unless otherwise formally indicated within the text, is the original work of the author. The thesis has not been previously submitted to this or any other university for a degree, and does not incorporate any material already submitted for a degree.

Signed:

Date:

Nomenclature

Abbreviations

AFR	Air-to-Fuel Ratio
ATM	Atmospheric lifetime (years)
BiTe	Bismuth telluride
BMEP	Brake Mean Effective Pressure (bar)
BTE	Brake Thermal Efficiency
BSFC	Break Specific Fuel Consumption (g/kWh)
CAC	Charge Air Cooler
CFC	Chlorofluorocarbon
CHP	Combined Heat and Power
DOE	Department of Energy
DOC	Diesel Oxidation Catalyst
DPF	Diesel Particulate Filter
E5	EGR focused platform
E6	EGR only platform
ETC	Electrical Turbocompounding
EPA	Environmental Protection Agency
ESC	European Stationary Cycle
ETC	European Transient Cycle
EU	European Union
EGR	Exhaust Gas Recirculation
FSN	Filter Smoke Number
FBC	Fluid Bottoming Cycle
GWP	Global Warming Potential
GHG	Greenhouse gas
HH	Half Heusler
HEX	Heat exchanger
HD	Heavy Duty
HDDE	Heavy Duty Diesel Engine
HT	High Temperature
C100	High-speed full-load
HPA	Homogeneous Positive Azeotrope
HEV	Hybrid Electric Vehicle
HCC	Hydrochlorocarbon
HCFC	Hydrochlorofluorocarbon
HFC	hydrofluorocarbon
HFE	Hydrofluoroether
HFO	Hydrofluoroolefin
I/C	Inter-Cooler
ICE	Internal Combustion Engine
IHE	Internal Heat Exchanger
LD	Light Duty
LDDE	Light Duty Diesel Engine
LMTD	Log Mean Temperature Difference (°C)
LT	Low Temperature

MTC	Mechanical Turbocompounding
MT	Medium Temperature
MSU	Michigan State University
B50	Mid-speed mid-load
MAC	Mobile Air Conditioning
NFPA	National Fire Protection Association
NTUA	National Technical University of Athens
NEDC	New European Drive Cycle
NESCCAF	Northeast States Center for a Clean Air Future
ORNL	Oak Ridge National Laboratory
ORC	Organic Rankine Cycle
OEM	Original Equipment Manufacturer
ODP	Ozone Depletion Potential
PSI	Performance and System Index
PDE	Positive Displacement Expander
EXH	Post-turbine exhaust gas
PR	Pressure Ratio
P-H	Pressure-Enthalpy
PI	Process Integration
QSS-TB	Quasi-Static Simulation Toolbox
R&D	Research and Development
E4	SCR focused platform
E0	SCR only platform
SCR	Selective Catalytic Reduction
T-S	Temperature-Entropy
T-Q	Temperature-Thermal duty
TEG	Thermoelectric Generator
US	United States
UTRC	United Technologies Research Center
VGT	Variable Geometry Turbocharger
VVA	Variable Valve Actuation
VSLS	Very Short Lived Substance
VFR	Volume Flow Ratio
WHR	Waste Heat Recovery

Symbols

β	Assessment and sensitivity of exhaust heat recovery
A	Heat transfer area (m^2)
D	Diameter
Δ	Differential
ρ	Density (kg/m^3)
η	Efficiency
h	Enthalpy (kJ/kg)
s	Entropy (kJ/kgK)
E	Exergy (kW)
ξ	Exergy of power production
R	Gas constant (J/molK)

Q	Heat (kW)
I	Irreversibility (kW)
H_{vap}	Latent heat of vaporisation (kJ/kg)
L	Litre
m	Mass flow rate (kg/s)
M_{wt}	Molecular weight (g/mol)
N	Speed (rpm)
U	Overall heat transfer coefficient (W/m^2°C)
W	Power (kW)
c_p	Specific heat at constant temperature (kJ/kgK)
γ	Specific heat ratio
λ	Thermal conductivity (W/mK)
X	Vapour fraction
μ	Viscosity (cP)
V	Volume flow (m^3/s)

Subscripts

air,face	Air temperature at the face of the condenser
air,rise	Air temperature rise through the condenser
ign	Auto ignition
avg	Average
BP	Back Pressure
boil	Boiling
c	Cold junction
cond	Condensing or condenser
crit	Critical
exp	Expansion or Expander
I	First law
freez	Freezing
recovery	Heat recovery
h	Hot junction
inc. LOAD	Increased heat load
liq	Liquid
LHV	Lower Heating Value
pp	Pinch Point (minimum temperature difference)
conversion	Overall conversion
quad	Quadlateral cycle
II	Second law
s	Specific
TE	Thermoelectric
tot	Total heat load
trans	Transmission
tri	Trilateral cycle
vap	Vapour heat load
wf	Working fluid

Substance number or formula

Cl	Chlorine
CO	Carbon monoxide
E152a	Difluoromethyl-Methyl-Ether
E245cb1	Pentafluoroethyl-Methyl-Ether
E245fa1	2-Difluoromethoxy-1,1,1-Trifluroethane
F	Fluorine
H	Hydrogen
HC	Hydrocarbon
N	Nitrogen
NH_3	Ammonia
Novec 649	1,1,1,2,2,4,5,5,5-nonafluoro-4-trifluoromethyl-3-pentanone
NOx	Nitrogen oxides
PM	Particulate matter
R11	Trichlorofluoromethane
R113	1,1,2-Trichloro-1,2,2-Trifluoroethane
R123	2,2-Dichloro-1,1,1-trifluoroethane
R1234yf	2,3,3,3-Tetrafluoropropene
R1234ze	1,3,3,3-tetrafluoropropene
R134a	1,1,1,2-Tetrafluoroethane
R141b	1,1-Dichloro-1-fluoroethane
R143	1,1,2-Trifluoroethane
R150	1,2-Dichloroethane
R150a	1,1-Dichloroethane
R152	1,2-Difluoroethane
R152a	1,1-Difluoroethane
R245ca	1,1,2,2,3-Pentafluoropropane
R245fa	1,1,1,3,3-Pentafluoropropane
R30	Dichloromethane

1 Introduction

1.1 Heavy duty Diesel truck engines

The last decade has seen incremental improvements in Heavy Duty Diesel Engine (HDDE) efficiency whilst complying with the exhaust emissions that has been the focus for engine developments. These improvements have been made using various methods and components such as: optimisation of the combustion process, efficient after-treatment devices, high efficiency turbochargers, advanced fuel injection equipment, as well as the use of sophisticated control algorithms (US NAS, 2010). As a result of these advancements, current HDDEs used in long-haul truck application can now achieve a Brake Thermal Efficiency (BTE) of 42-44% at their optimum operating point. The limiting factors in approaching higher BTE include: irreversibilities in the combustion process, structural limits that constrain peak pressures, limits imposed by heat losses during combustion/expansion, untapped exhaust energy, mechanical friction etc. (US DOE, 2011).

The crucial present issue is the need for further Break Specific Fuel Consumption (BSFC) improvements to reduce the impact of greenhouse gases (GHG), anticipated CO_2 emission regulations (fuel consumption regulations), increasing fuel costs and diminishing fossil fuel supplies. In the past decade, emission standards have been used to dictate limits for conventional pollutants such as: hydrocarbons (HC), carbon monoxide (CO), nitrogen oxides (NOx) and Particulate Matter (PM). Future regulations will emphasise more on CO_2 emissions, which will be a significant factor in the development of new HDDEs. Another reason for reducing fuel consumption in the trucking industry is the economic necessity to maintain a competitive operational advantage as the fuel costs represent ≈30% of the total life cycle cost of the truck (second only to wages) (Johnson, 2010).

CO_2 emission regulations are already being implemented for Light Duty (LD) vehicles. For example, the European Union (EU) fuel consumption regulations have been enacted to limit CO_2 emissions to an average of 95 g/km by 2021 from 132.2 g/km in 2012 for new car fleets (European Commission, 2014a). Also, in the United States (US) the corporate average fuel economy standards require small passenger vehicle fleets to meet 23.2 km/l by 2025 from 11.7 km/l in 2010 (US EPA, 2014a).

CO_2 emission regulations for the Heavy Duty (HD) vehicles are less evolved than the LD vehicles (Fig. 1.1). Japan was the first to introduce the HD vehicle fuel economy standards in 2006, which calls for nominally 12% increase in fuel economy (km/l) from a 2002

baseline by 2015 (Johnson, 2010). In the US, the Environmental Protection Agency (EPA) joint fuel consumption and GHG emission regulations are expected to be in effect by 2020. Phase 1 and 2 of the standards to expedite the rule ranges from 3% improvement in 2014 to 9% in 2017 over a 2010 industry baseline (Stanton, 2013). Also, in 2009 California finalised the HD tractor-trailer GHG regulations, with phase-in that began in 2010 and will proceed through 2017 (Johnson, 2010). The reductions to meet the Japanese (until 2015) and US (Phase 1) limits are expected to come from improvements in the present engine platforms themselves (Stanton, 2013). In Europe, the need to address CO_2 emissions from the HD vehicle sector has been recognised by the European Commission (2014b) in its strategy on clean and energy efficient vehicles. The opinions are well formed with CO_2 regulations expected during 2017.

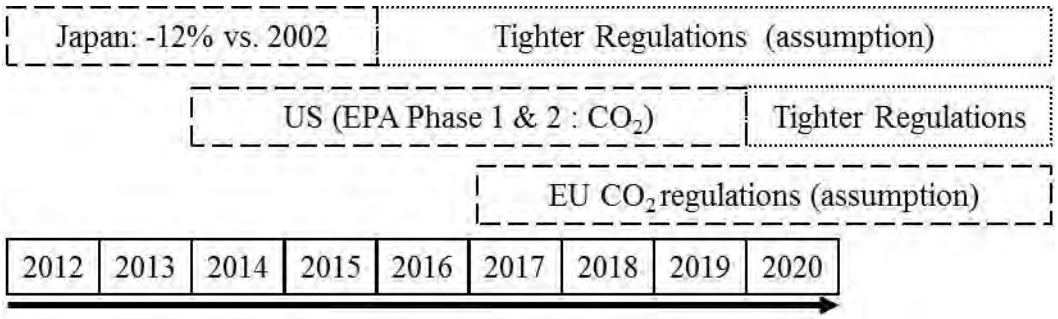

Figure 1.1 HD CO_2 and fuel consumption reduction timeline in EU, US and Japan (Zink, 2011)

1.2 Waste heat to power conversion

The present BTE limit of HDDEs will be insufficient to comply with an aggressive GHG legislation without the implementation of new technologies. Key directions proposed by researchers and engine manufacturers to develop low carbon vehicles include: powertrain efficiency enhancements (e.g. waste heat recovery), advanced thermodynamic cycles (e.g. cryogenic split-cycle) and use of alternative fuels (e.g. biodiesel) (Ricardo, 2013, Fu et al., 2013, Baker et al., 2010). To better utilise the chemical exergy of the fuel, two pathways have emerged. The first utilises the exhaust exergy for waste heat to power conversions, to obtain improvements in thermal efficiency of the prime mover. The second focuses on minimising exergy destruction in the combustion process. Additionally, if biomass is produced sustainably, i.e. the replantation removes the carbon dioxide from the atmosphere during photosynthesis and stores it back in the trees and plants then, a carbon neutral fuel source exists.

The HDDE is still the primary power source for long-haul trucks and this is expected to continue for some decades because of its competitive efficiency, high power density, outstanding durability and drivability. However, it is obvious that despite the efforts to directly increase the BTE of present HDDEs, a significant amount of energy is still lost in the form of heat (Fig. 1.2). The majority of the remaining 56-58% of the supplied fuel energy is rejected to the ambient via coolant, post-turbine exhaust gas (EXH), Charge Air Cooler (CAC), Exhaust Gas Recirculation (EGR) cooler, heat conduction, convection and radiation from engine block, hot surfaces and other heat sinks.

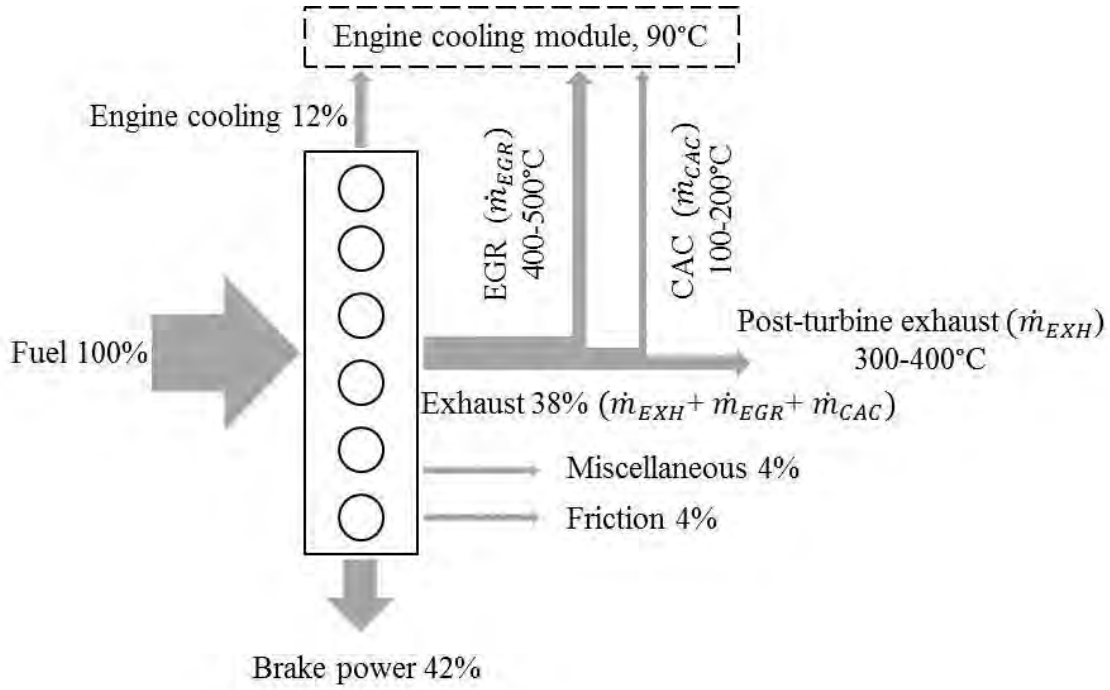

Figure 1.2 Energy balance for a typical on-highway engine with sources of waste heat and typical temperature levels (adapted from the 10L model, Chapter 3)

More effective thermal management of engines has already been implemented by waste heat utilisation. Examples include utilising waste heat for improved performance of after-treatment devices, passenger cabin heating, fast warm-up and optimised cylinder head temperatures (Bennion et al., 2008). A valuable alternative approach is the use of technologies known collectively as Waste Heat Recovery (WHR). These utilise technologies beyond the conventional uses mentioned above to provide additional power from waste heat. The resultant mechanical or electrical power can be used either to supplement engine crankshaft power or power accessories.

With much lower technical maturity compared to the conventional HDDEs and many current technical obstacles in the short term, alternative thermodynamic cycles are not

expected to make a high penetration into the HD vehicle sector in the coming two decades (US DOE, 2011, US NAS, 2010). As the HDDE sector continues its efforts to improve energy efficiency and develop alternative powertrains, WHR systems provide a good starting point and attractive opportunity for enhancements both in energy efficiency and emissions reduction whilst using a wasted resource.

1.2.1 Fluid bottoming cycles

The last decade has seen renewed interest in WHR for reducing overall engine BSFC, with leading engine manufacturers, developers, research centres and Original Equipment Manufacturers (OEM) announcing Research and Development (R&D) on WHR technologies. The R&D efforts are now being further driven by the upcoming CO_2 legislations. This is resulting in a paradigm shift. Wherein WHR technologies historically rejected based on factors like increased cost, complexity, controls and loss in power to weight ratio are now being re-evaluated due to technological innovations, increased fuel cost and necessity. Although some waste heat losses from HDDEs are inevitable, various techniques have been proposed to convert the portion of the unused heat into mechanical or electrical power. Most of these techniques have undergone demonstration stage but are still at the prototype phase. Nonetheless, it has been shown that WHR technologies can play a noticeable part in achieving future BTE goals for long-haul trucks (Fig. 1.3).

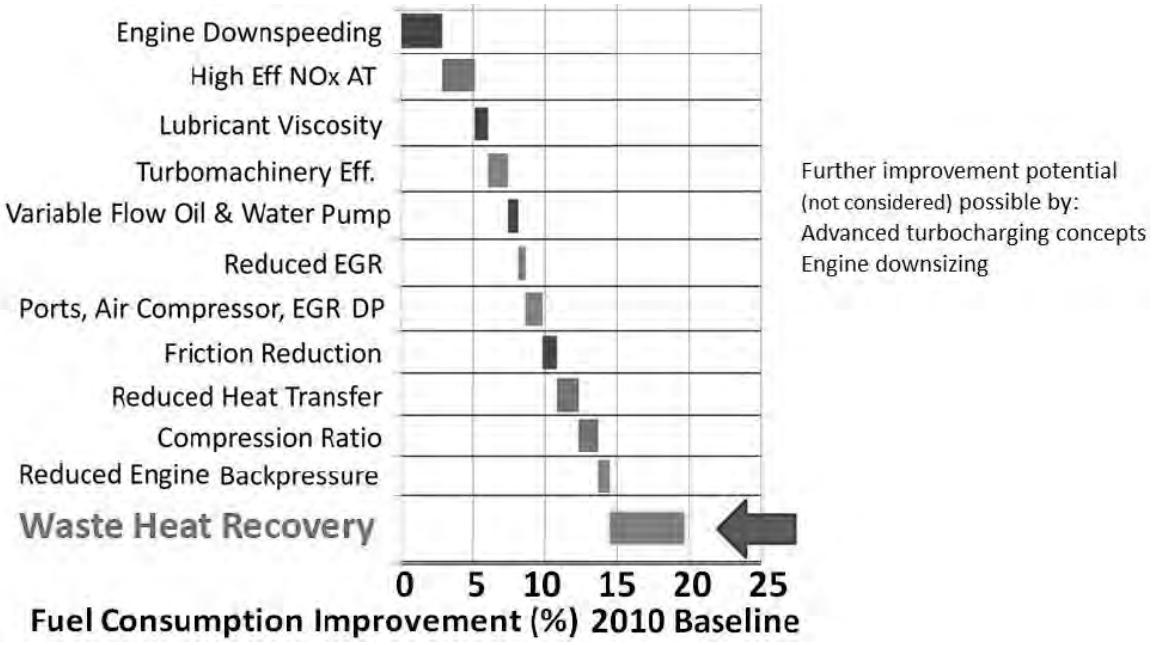

Figure 1.3 Engine and powertrain technology roadmap for long-haul HDDE showing the need of multiple technologies to address an aggressive GHG scenario (Stanton, 2013)

Among the proposed solutions, one suitable method for long-haul truck application is the use of closed loop Fluid Bottoming Cycles (FBC) like Rankine and Organic Rankine Cycles (ORC). These systems, in their simplest form, require five main mechanical components: a pump, a boiler, an expansion machine, a condenser and a tank. Since a FBC coupled to HDDE results in a combined system that generates additional power without requiring extra fuel, it reduces the specific fuel consumption and specific emissions. An alternative combined system strategy would be to downsize the engine or run at a slightly lower output so that the combined engine and WHR output matches the base engine performance. As the first approach requires fewer changes to input variables and the engine, it is widely reported in the literature and also employed in this thesis (Stanton, 2013, Schreier et al., 2014).

The WHR resurgence is favouring FBCs due to the ability to tailor the system for different heat levels and high efficiency than current alternatives. EGR and exhaust streams, due to high energy and exergy contents, are particularly being targeted to justify implementation of FBCs. Experiments have shown that FBCs have the potential to improve the fuel economy of HDDEs by up to 7.2% over a drive cycle (Nelson et al., 2009). In recent years, there has been an increased emphasis on FBCs for LD vehicles as well. FBCs and components are being developed and demonstrated for HD and LD vehicles by Cummins, Oak Ridge National Laboratory (ORNL), United Technologies Research Center (UTRC), Behr, AVL, Bosch, Volvo, Honda, BMW etc.

1.2.2 Long-haul trucks and fluid bottoming cycles

The potential fuel consumption reduction of a specific WHR technology is dependent at least on duty cycle (start-stop vs. steady-state) and application (pick-up vs. tractor-trailer). Although FBCs can be applied to numerous on-road vehicles, the highest benefit will be achieved in long-haul trucking which involves extended time of running at steady cruise speeds (mid or high engine load) on highways. Limited time is spent in the loading docks to the highway, congested traffic, urban or suburban driving which involves frequent stops and speed variations (Fig. 1.4). Highway drive cycles result in higher quality and quantity of heat sources favouring economies of scale, system design and optimisation, as FBCs reach their highest efficiency when operated steadily with high exergy content.

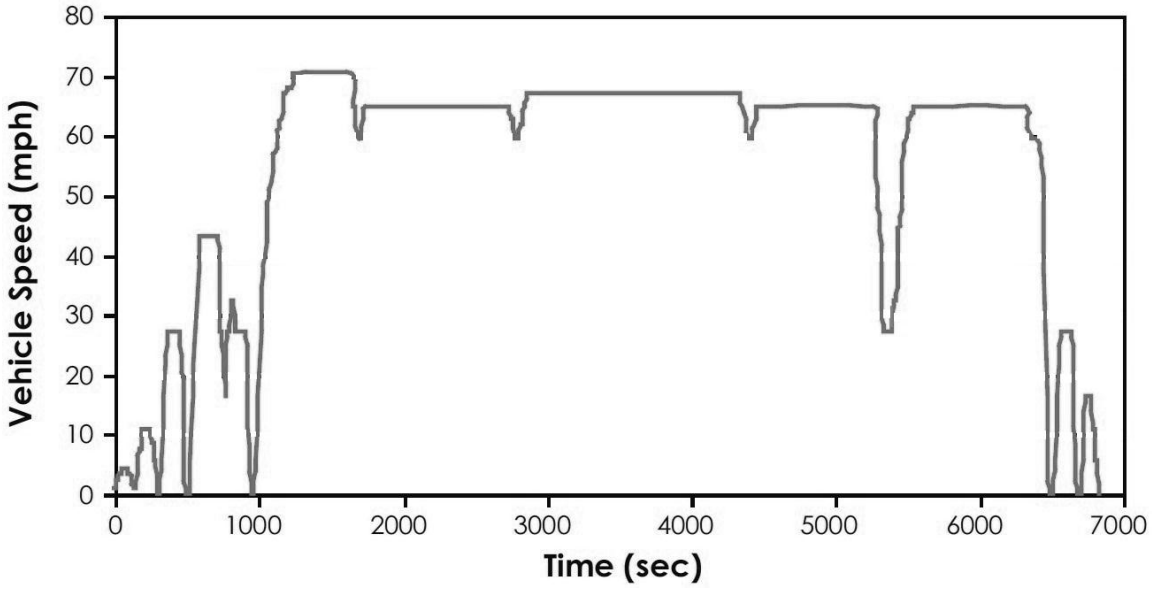

Figure 1.4 A typical long-haul HDDE drive cycle (Cooper et al., 2009)

Long-haul trucks further have higher absolute fuel consumption, accumulating almost 160,000 km/year and show lower sensitivity to fuel economy with increased mass. Across the EU, ≈40% of the total tonne km can be thought of as long-haul (i.e. >500 km) and in the US nearly half of all the combination truck vehicle miles are travelled on interstate distances (Hill et al., 2011, US DOT, 2009). Hence, fuel savings from FBCs can be sufficient for the return on investment to be realised in a relatively shorter time period.

Emissions of CO_2 from HD vehicle fleets in the EU and US currently account for a significant proportion of the total road transport emissions. These emissions are further expected to rise mainly due to increasing road freight traffic. HD vehicles represent about a quarter of the EU road transport CO_2 emissions. Long-haul trucking has further significance as it is estimated to account for ≈37% of all HD vehicle emissions and ≈44% of total truck emissions in the EU (Hill et al., 2011). Similar trends are also seen in the US where long-haul trucks consume ≈45% of the total Class 8 fuel annually (Cooper et al., 2009). Hence, it is appropriate to examine the potential benefits of introducing WHR technologies on long-haul trucks for energy saving and climate change mitigation in the road freight sector.

2 Literature Review

2.1 Introduction

FBCs represent one, but by no means the only technique for WHR in Internal Combustion Engines (ICE). Prior to the selection of FBCs, a background study on existing and state of the art small scale (<30 kW) WHR technologies was carried out. This chapter summarises the relevant literature and analysis that aided the decision. Firstly, a brief discussion on some of the common alternative WHR techniques is presented. Secondly, a detailed technical assessment of FBCs is discussed, which also aided in identifying the research priorities in working fluid selection, optimisation of cycle operation and heat recovery architecture.

2.2 Technology classification

Automotive WHR is a well-funded and emerging sector where numerous technologies with variations and combinations have been proposed. Few engine manufacturers have also upgraded their engine platforms by installing such technologies. Based on how the thermal energy of the heat source (e.g. exhaust gas) is recovered and converted into power, WHR can be divided into direct and indirect methods (Fig. 2.1). Direct methods are associated with the direct use of heat source for power (e.g. turbocompounding, gas expansion cycle). In indirect methods, the thermal energy of the source is transferred for use via a heat exchanger (e.g. ORC, fluid compression and vapour expansion cycle).

Mechanical Turbocompounding (MTC) can be considered a base WHR technology, where the reduction in exhaust gas temperature and pressure is the consequence of a power turbine located downstream of the turbocharger turbine generating additional power (Fig. 2.1a). The power turbine is mechanically coupled to the engine crankshaft via a gear train. This technology has been available in the HDDE sector for over a decade (Baker et al., 2010, Greszler, 2008).

Electrical Turbocompounding (ETC) is an approach similar to MTC, except that ETC can also recuperate part of the exhaust energy directly from the turbocharger unit using an electric generator (Fig. 2.1b). When the turbine produces surplus power than that required to drive the compressor, it is converted to electric power using the high speed generator incorporated into the turbochargers shaft. The electric power is used to run a motor connected to the engine crankshaft. When the exhaust flow is insufficient, the electric motor can also be used to drive the compressor operating like a supercharger.

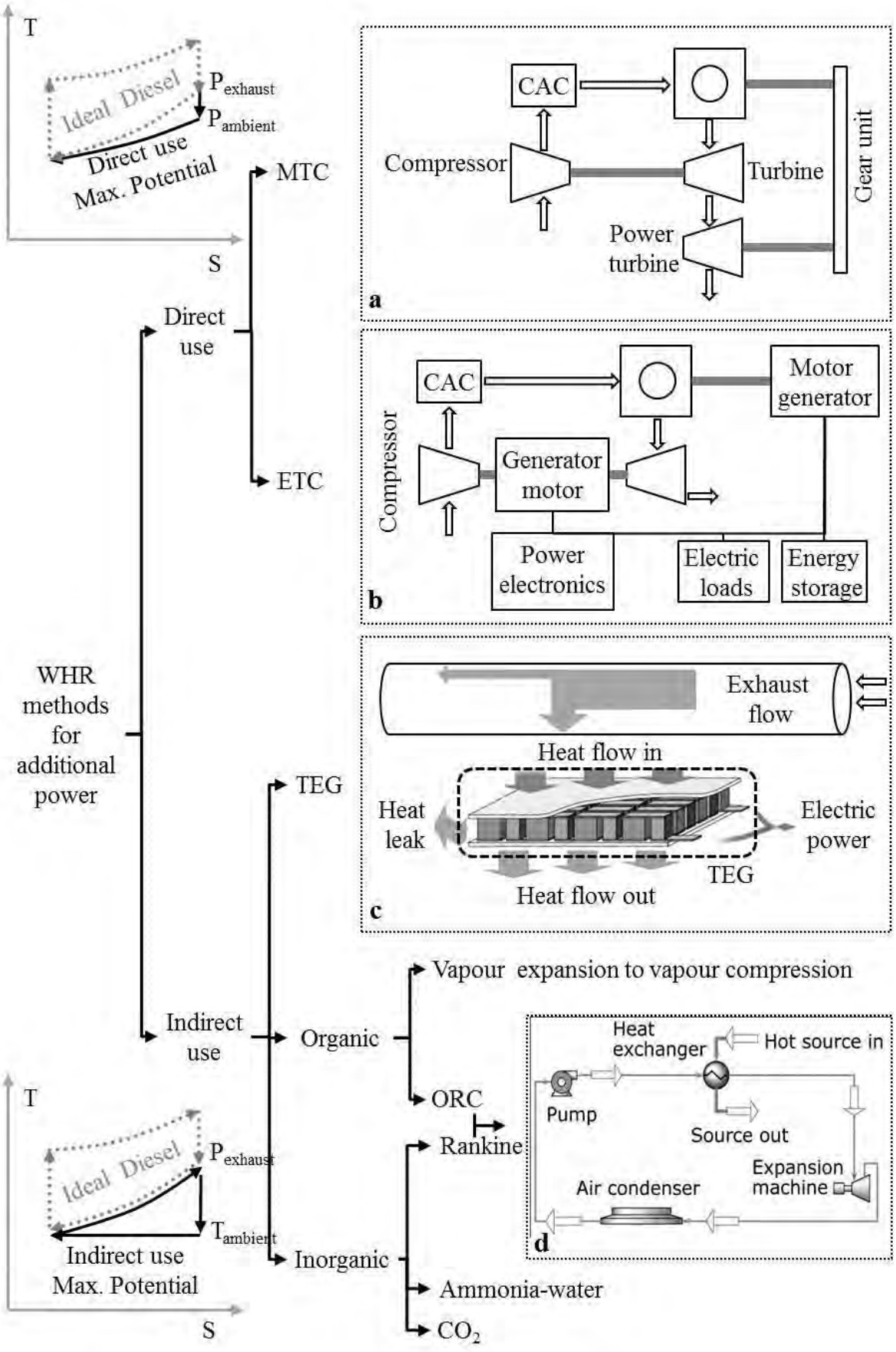

Figure 2.1 Technology classification and schematic representation of the widely proposed WHR technologies

While MTC and ETC can only use pressure gradients and kinetic energy of the exhaust gas, other technologies like thermoelectric generators (TEG) and FBCs can tap into much larger amounts of heat. The overall conversion efficiency of TEGs and FBCs depends on the combined effectiveness of the heat utilisation (heat recovery efficiency, $\eta_{recovery}$) and the power cycle (thermal efficiency, η_I).

Although Rankine cycle, the traditional indirect FBC uses heat to create mechanical energy and eventually electrical energy, TEGs can generate electricity directly from heat (Fig. 2.1c). A practical automotive TEG system consists of an exhaust gas system, a heat exchanger, a thermoelectric system, a power conditioning system and a battery pack. Thermoelectric materials are semiconductor solids composed of a p-type and n-type semiconductors that convert thermal energy into electrical energy via a temperature gradient. Thermoelectric materials can also be used for heating or cooling by applying electricity to dissimilar semiconductors. Efficiencies of thermoelectric conversion (η_{TE}) depend on hot (T_h) and cold (T_c) junction temperatures and characteristic of used materials. The relationship is shown in the equation below:

$$\eta_{TE} = \frac{T_h - T_c}{T_h} \frac{\sqrt{1+ZT}-1}{\sqrt{1+ZT}+\frac{T_c}{T_h}} \ldots (2.1)$$

With known conventional solids, a limit to ZT (figure of merit) is quickly obtained. However, new materials recently developed such as filled skutterudite show progress in performance over previous materials (LaGrandeur et al., 2011, 2010, 2009).

The vapour expansion cycles like ORC (Fig. 2.1d), uses conventional processes (liquid compression, vapour expansion, heat transfer at essentially constant pressure) and unconventional fluids (refrigerants, mixtures etc.). Rankine cycle and ORCs take advantage of the relatively low power needed in pressurising the liquid, rather high enthalpy gained during fluid boiling and relatively large amount of work produced at expansion in the gaseous phase. Applications for ORCs can also be found in combination with the Hybrid Electric Vehicles (HEV) where the particular relevance comes through the architectural advantages. ORCs can also be used to drive directly the turbocharger compressor or power the refrigeration system.

2.3 Mechanical turbocompounding

MTC engines have been investigated for long-haul application since the 1980s. Wilson (1986) described the concept, design and initial performance test of an 11.3 Litre (L), 6 cylinder non-insulated MTC engine. The MTC engine achieved a 5% improvement in BSFC at the same engine rating as the base engine.

DD15 engines introduced by Detroit Diesel claimed a 5% improvement in vehicle fuel economy due to addition of MTC and other engine changes (Millikin, 2007). 3% improvements were associated to the MTC which reached a rotation speed of more than 40,000 rpm at the rated engine speed.

National Technical University of Athens (NTUA) conducted a parametric analysis of MTC considering a variation of power turbine Pressure Ratio (PR) using a 6 cylinder HD turbocharged truck engine (Hountalas and Mavropoulos, 2010, Hountalas et al., 2007). Fig. 2.2a shows the effect of power turbine PR which was varied in the range of 1.5-2.2 on the overall engine BSFC improvement as load increased from 25 to 100% at 1700 rpm. The optimum expansion PR of the power turbine increased with engine load. However, after a certain value in the optimal range of 1.7-1.9 additional improvement was minimal or negative. The potential of BSFC decrease was negligible (0.5%) at 25% load and increased to approximately 4% at 100% load. An important issue was the negative impact of the increased exhaust backpressure on the base engines power output. Fig. 2.2b shows the base engines power decreasing with increasing the power turbine PR. The base engine power decreased from 352 to 325 kW at full engine load linearly with power turbine PR, the slope being roughly the same for all engine loads. At full load the power produced by the power turbine was 62 kW, but the net gain was only 35 kW, due to a 27 kW reduction in engine power in the optimum PR range of 1.7-1.9. The same phenomenon was also seen at low loads and was more profound.

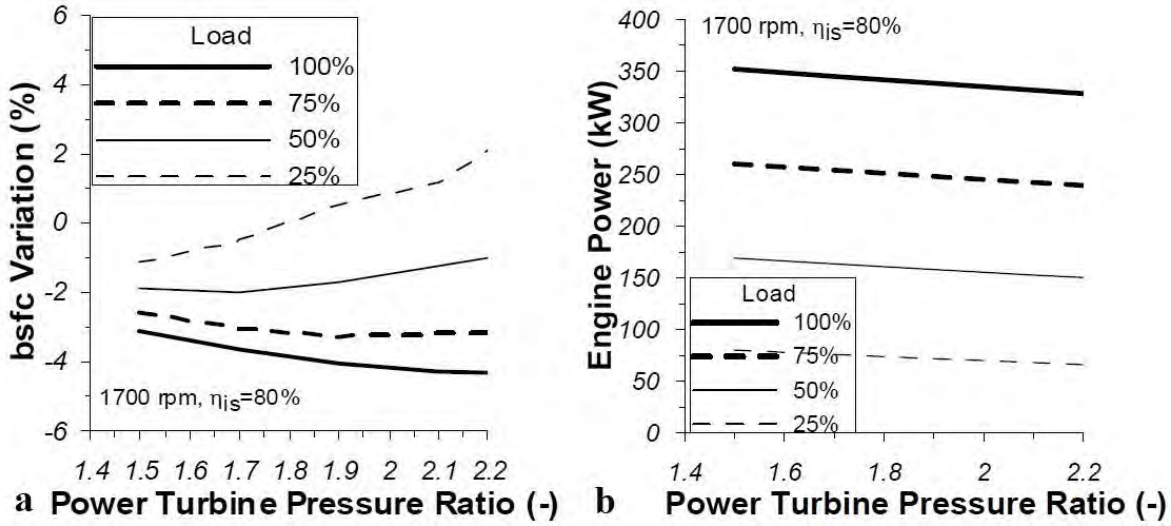

Figure 2.2 (a) BSFC variation vs. power turbine pressure ratio (b) Engine power vs. power turbine pressure ratio, at 1700 rpm for various engine loads (Hountalas and Mavropoulos, 2010)

Volvo carried out detailed MTC simulations on the D13 engine using high efficiency turbochargers, narrow range engine operation, optimised combustion and valve timings (Tai et al., 2010, 2009, Greszler, 2008). Results of simulation of a narrow speed MTC engine operating on a long-haul European cycle showed a BSFC reduction of 5-6 g/kWh.

Northeast States Center for a Clean Air Future (NESCCAF) also used Volvo D13 engine model (GT-POWER) to investigate MTC benefits on a typical long-haul drive cycle (Cooper et al., 2009). Variable Valve Actuation (VVA) was added to help provide more exhaust energy to the power turbine within the constraints of maintaining the efficiency of the base engine. When MTC was applied to the 36,300 kg baseline vehicle, the reduction in fuel consumption was 2.4%.

2.3.1 Mechanical turbocompounding: Summary

MTC engines reacted more positively to improved turbocharger efficiency than a conventional turbocharged engine (Habibzadeh et al., 2007). The backpressure created by the power turbine also allowed the use of a very efficient fixed geometry turbocharger turbine rather than Variable Geometry Turbocharger (VGT) turbine, while still providing the ΔP required to drive the high pressure EGR loop (Cooper et al., 2009). Typically, a MTC system included a fluid coupling (to allow for speed variation and to protect the power turbine from engine crankshaft torsional vibration) and a gear train (for speed reduction to match power turbine speed to crankshaft speed).

The turbocharger turbine wastegate that drove the power turbine usually only happened in a narrow region of very high speed and high load (Xu et al., 2013). With the wastegate mass flow rate usually below 20% of the total mass flow, a relatively small power turbine flow capacity had to be selected in order to improve performance under part load conditions. There was also the challenge of configuring the power turbine PR to give maximum net gain in power for minimal increase in pumping losses and thus fuel consumption. Furthermore, less exhaust energy was available for the power turbine with engines using high rates of cooled EGR and excessive cooling of exhaust reduced the effectiveness of the after-treatment devices. The performance of MTC was extremely sensitive to engine load, highest (4%) BSFC improvement was seen at full load and insignificant (0.5%) or even zero at low load. To improve part and low load performance VVA had to be employed to provide more exhaust energy to the power turbine. BSFC reduction over a typical drive cycle and in production engines was limited to 2.4-3%. (For supplementary information on the cited MTC literature, refer Appendix 2.1).

2.4 Electric turbocompounding

Caterpillar conducted detailed ETC engine simulations (turbocharger unit configuration) on a C15 on highway HD truck engine with turbo machinery efficiencies representative of technologies under development in the project (Kruiswyk et al., 2009, 2008). With backpressure levels representative of the US 2010 after-treatment, a 4% improvement in engine thermal efficiency was predicted at the design point (Fig. 2.3). The concept design of this ETC was capable of providing 25 kW of compound power at design point conditions, with acceptable rotor dynamics, structural integrity and thermal management. The fuel consumption reduction was in the order of 3-5% over the drive cycle. Similar results (4.1% fuel savings) were also presented by NESCCAF using the same engine as in the previous section but including electrification of accessories (additional downstream turbine configuration) (Cooper et al., 2009).

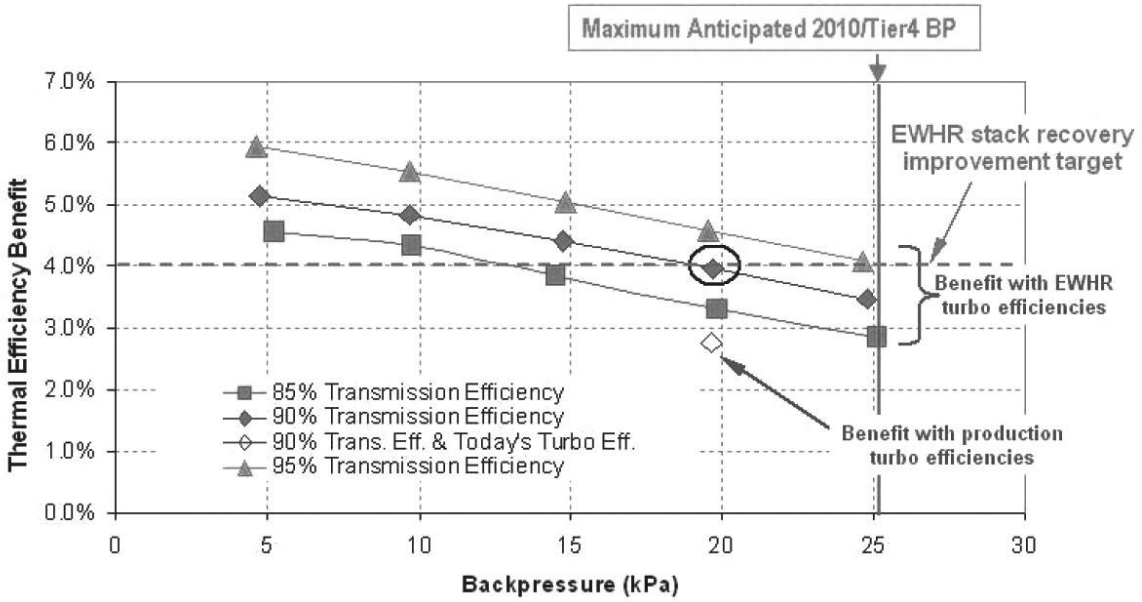

Figure 2.3 ETC simulation results using high efficiency components (Kruiswyk et al., 2009, 2008)

John Deere selected a 9L (275 kW, Tier 3) engine as a demonstration platform for ETC (additional downstream turbine configuration) since this engine was in a power class that fitted both large agricultural tractors and on-highway HD trucks (Vuk et al., 2007, 2006). System efficiencies of over 95% in the key operating areas for off-highway equipment were demonstrated. The ETC added 50 kW at the rated condition and provided a 3-8% BSFC improvement over the typical operating speed range. They stated that the next generation hardware is expected to employ the same system architecture, but the turbocharger will be a series system rather than a single stage high PR machine. This was because the surge margin of the single stage machine proved limited. The turbo generator is expected to evolve to a smaller and higher speed machine.

NTUA parametrically examined the benefits of ETC (turbocharger unit configuration) with varying turbocharger efficiency and increasing exhaust pressure before the turbine (Hountalas and Mavropoulos, 2010, Hountalas et al., 2007). For the 6 cylinder HD ETC truck engine model, the exhaust pressure was increased by 1 bar above the base engine. The results showed that ETC can be very beneficial when used with highly efficient turbochargers. The total overall BSFC improvement due to both ETC and increased turbocharger efficiency was 6.5% at 100% load compared to 2% when using standard turbocharger and ETC. The maximum BSFC reduction of 3.3-6.5% was experienced from 25-100% load at 1700 rpm using a highly efficient ETC and 1 bar exhaust pressure increase.

Apart from MTC and ETC as exhaust gas expansion systems, TIGERS (Turbo generator Integrated Gas Energy Recovery System), which is a water cooled switched reluctance generator was also proposed (CPT, 2013). It was claimed that the system was capable of operating at high exhaust temperatures up to 850°C, at speeds up to 60,000 rpm, delivering a shaft power of 4 kW.

2.4.1 Electric turbocompounding: Summary

Both MTC and ETC increased the engine backpressure and showed relatively low improvements at low and part engine loads. ETC was attractive over MTC only if it was accompanied by a highly efficient turbocharger. The ETC system provided control flexibility in that the amount of power extracted could be varied, thus varying Air-to-Fuel Ratio (AFR). ETC could provide up to 4% fuel economy improvement over a long-haul drive cycle with increased power density. With a maximum of 8% benefit at high loads, it was best suited to off-highway applications like ploughing tractor which runs for a long time at maximum power (Baker et al., 2010).

Most of the difference in performance between MTC and ETC was due to the conversion of accessories from mechanical to electric drive (Cooper et al., 2009). Another factor which slightly improved the efficiency was the independent control of engine speed and turbine speed. Achieving the complete benefit of ETC required the electrification of vehicle accessories, the addition of an electric motor (to apply turbocompound energy to supplement engine output) and an electric storage system (i.e. battery) to store any energy from the power turbine that was not immediately required. Making all of these changes to the vehicle posed significant development and cost challenges. Hence, ETC seemed highly synergistic with a hybrid electric powertrain for long-haul applications where regenerative braking opportunities were limited. (For supplementary information on the cited ETC literature, refer Appendix 2.2).

2.5 Thermoelectric generators

Amerigon and project partners Ford, BMW and Faurecia are developing TEGs for passenger vehicles (Crane et al., 2011, LaGrandeur et al., 2011, 2010, 2009). Two high temperature prototypes cylindrical TEGs comprising Half Heusler (HH) and bismuth telluride (BiTe) were designed, built and tested. Exhaust gas first passed through the segmented HH/BiTe elements. In the cooler exhaust gas portion of the TEG, BiTe was used singularly. Testing performed using electric heaters as the thermal power source

(620°C inlet exhaust gas temperature, 450°C material surface temperature) and a liquid circuit for heat rejection (25°C) produced over 700 W of electric power. The TEG subsystem included an internal exhaust bypass valve to limit backpressure and avoided exposing the thermoelectric materials to potentially harmful temperatures.

Following bench tests at Amerigon, the TEGs were installed in Ford (Lincoln MKT) and BMW (X6) exhaust systems for vehicle level evaluation. Results from Ford's testing showed that, for the highway driving conditions, over 250 W were produced over the majority of the cycle (Fig. 2.4). For city driving, the power produced was between 25 and 150 W. The TEG installed onto X6 with exhaust lines thermally insulated upstream from the TEG produced over 600 W at 125 km/h in road testing. Power produced during vehicle operation was lower than in bench tests due to a warmer cold side circuit. BMW also integrated the TEG in the EGR system and customer testing showed that 250 W could be generated corresponding to a 2% fuel consumption reduction (Millikin, 2011a).

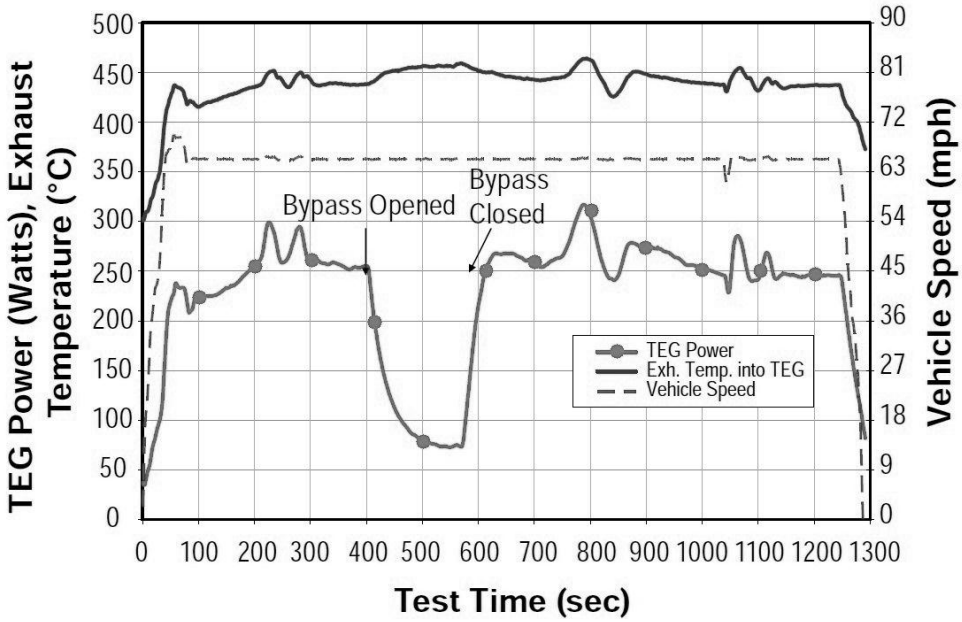

Figure 2.4 TEG performance under highway driving condition (LaGrandeur et al., 2011, 2010, 2009)

One of the highest efficiencies reported by Amerigon was 10% for a 20 W fractional thermoelectric material inclusive of all electrical and thermal parasitic losses (LaGrandeur et al., 2008, 2007). To predict the amount of improvement in fuel economy achievable in the 2015-2017 time-lines, the results of such studies were extrapolated assuming continuing technical and commercial progress (Table 2.1). Key parameters included increased ZT to 1.7 (75% improvement), 3 times improvement in interfacial resistance and

a significant reduction in heat transfer losses due to thermal bypass. With these improvements, the power produced was estimated to increase to 240 W for the city cycle and 1 kW for the highway cycle, with fuel economy improvements in the range of 5-7%.

Table 2.1 Results of TEG in an escape HEV using mid-term materials and processes (LaGrandeur et al., 2011, 2010, 2009)

	2015-2017 Design
Material Performance (ZT)	1.7
Heat Transfer Losses	20% $T_{hot,\ junction}$ = 350 – 420°C
TE Mass	1.1 kg
Interfacial Resistance	0.5 μΩ-cm²
% Conversion Efficiency	14.4 % T_h: 385°C, T_c: 90°C
Power Generated – M/H EPA Cycle (Watts)	240 / 1000
Fuel Economy Improvement	5%-7% (est.)

General Motors and its external R&D partners also tested a prototype TEG for passenger vehicles (Meisner, 2011, Ashley, 2011). Results on a Chevy Suburban SUV showed a fuel consumption improvement of 3%. Using skutterudites (cobalt-antimony-based compounds) which have high ZTs at the elevated temperatures, an average ZT of 1.2 was reported.

Michigan State University (MSU) and project partners set out to determine the viability of using TEGs for exhaust heat recovery in long-haul trucks (Schock et al., 2010, 2009). They fabricated a batch of skutterudite unicouples (1 W), the unicouples were used to build modules (5 W) and the modules were used to construct and test the TEG (50, 100 W). Recent improvements made to the n-type skutterudite showed that the ZT value increased to 1.2. At a maximum inlet temperature of 716°C and a ΔT of 550°C between hot and cold sides, they demonstrated a 50W TEG. For new systems with hot and cold sides at 527°C and 27°C respectively, the thermal efficiency was estimated to be 14%. For more realistic temperatures (370°C hot side, 65°C cold side), a module efficiency of 9.1% was estimated (Schock et al., 2008, 2006, 2005). Assuming similar energy recovery, they concluded that adding modules in the EGR and exhaust line would result in a 4.9% BSFC improvement on an ISX Cummins engine operating at B62. (For architecture, refer Appendix 2.3).

UTRC also calculated similar fuel economy improvement on a Caterpillar C15 engine (4.4%, including fan and pump power) using a TEG system with a dedicated cooling loop (Willigan et al., 2006, 2005). This was based on lower heat recovery and much higher TEG

thermal efficiency (18%). However, this project was terminated as high ZT performance of quantum well films on Kapton at the size required for 5% thermal efficiency went unfulfilled.

More recently, Renault also explored the use of TEGs on a HD 11L truck. They selected the EGR cooler as the heat source (400°C, 0.07 kg/s) (Aixala, 2012). Simulation results showed an additional 400-800 W at cruise. To keep the target system cost below 1.3 $/W they intend to use Silicide (Mg_2Si n-type and MnSi p-type). The maximum demonstrated ZT value in the Ø50 mm material was 0.7.

2.5.1 Thermoelectric generators: Summary

TEGs can directly generate electric energy from waste heat, without using mechanically rotating parts, and providing some advantages such as completely solid state, no noise and no vibration. TEGs are in fact on a path to commercialisation by several manufacturers in the EU and US primarily for LD luxury vehicles by the end of the decade (US DOE, 2011). Projects on TEGs intend to increase the fuel economy of passenger vehicles by 5% by 2017. The use of thermoelectric devices for vehicle occupant comfort heating/cooling is also being pursued as a more fuel efficient alternative to the conventional Mobile Air Conditioning (MAC) systems (US DOE, 2011). It is estimated that thermoelectrics can maintain single occupant comfort with about one-sixth (630 W) of the energy used by conventional systems (3.5-4 kW). This technology is particularly relevant for hybrid electric and all electric vehicles that have insufficient or no engine heat.

The thermal efficiency of TEGs is influenced by the temperature difference between the source and sink (similar to FBCs). In TEGs, this necessitated a cooling circuit, which was associated with parasitic power. Present day thermoelectric systems have seen limited use due to low efficiencies. Segmented couples demonstrated efficiencies of up to 14%, but the high temperature gradient (700°C hot side, 25°C cold side) under which these materials were tested were not available in the exhaust and cooling system of most vehicles (Schock et al., 2008, 2006, 2005). Current automotive thermoelectrics were around 8-10% efficient. When combined with the necessary heat exchangers and pumps, complete system efficiencies were perhaps half of that. With net system efficiencies around 4-5% it was apparent that complete accessory electrification was infeasible for all vehicle platforms (Ashley, 2011).

For given hot and cold side temperatures, the thermoelectric material efficiency depended on the ZT. Commercially available bismuth telluride TEGs from Marlow Industries offer ZT = 0.73. It is believed that the best thermoelectric materials can currently offer ZT = 1.4 (Ashley, 2011). However, to meet the goal of a 10% improvement in fuel economy for HD long-haul trucks as requested by US Department of Energy (DOE) the ZT value needs to be close to 3. There also exist significant system design challenges in achieving the performance goals. These include a reduction in the cost of thermoelectrics, scaling them up into practical devices (e.g. larger sample have more thermal/electrical losses and typical power output is <1 kW), development of high volume production methods and making them durable enough for vehicle applications (e.g. heat resistance). A further significant issue is determining the configuration of the heat exchanger and obtaining high heat transfer rates that offer sufficient energy recovery to justify the weight, volume and cost.

2.6 Fluid bottoming cycles

Concerted efforts to improve the engine efficiency of long-haul trucks by applying Rankine and ORCs were first investigated during the fuel crisis in 1970s. Patel and Doyle (1976) designed and built a prototype of ORC operating on the exhaust of a Mack 676 truck engine. They used Fluorinol-50 as the working fluid operating between 343°C at the turbine inlet and 70°C at the condenser exit. The prototype used a vapour generator as part of the exhaust stack, a condenser combined with the existing trucks radiator and a three-stage axial flow turbine with speed reduction gearbox. Subjecting the ORC equipped truck to a national air pollution control administration route demonstrated a 15% improvement in fuel economy. During the following years, similar research programs with on highway truck fuel economy tests were also carried out by DiBella et al. (1983). Using trifluoroethanol, they demonstrated a 12.5% improvement in fuel consumption.

Other earlier studies, which provided a thermodynamic insight, and examined the improvements in fuel economy for a broad spectrum of engines and WHR concepts include Leising et al. (1978) and Chen and Lin (1983). Leising et al. showed that by turbocharging, turbocompounding and Rankine cycle, drive cycle power could be increased by up to 20% for a Diesel truck engine. They also revealed that Rankine cycle could provide about 3 times as much improvement in fuel economy compared to turbocompounding. Chen and Lin reviewed many methods incorporated by various investigators. They proposed a cascade system with the 1st stage operating on water followed by a 2nd stage operating on trichlorofluoromethane (R11), to recover high and low

temperature exhaust heat, respectively. They predicted a 15% improvement in engine efficiency through the proposed system.

These studies from the early 70s to the early 80s helped to show that Rankine and ORCs were suitable FBCs for WHR from exhaust of trucks. The subsequent drop in fuel costs in the mid-80s reduced the urgency of large increases in fuel economy and none of the FBC approaches were commercialised. Nonetheless, R&D efforts on stationary ORCs continued over the decades (Tchanche et al., 2011, Gaia, 2011, Stine and Geyer, 2001, Crook, 1994). Directives including the industrial emissions directive and the Combined Heat and Power (CHP) directive that require reductions of industrial emissions and promote the use of cogeneration, respectively, have further increased the interest in ORCs (European Parliament, 2010, European Parliament, 2004).

ORCs now play an important role in energy savings by converting waste heat to power for stationary applications. ORCs have seen application in biomass, CHP, solar desalination, geothermal, industries, stationary ICE, gas turbine, solar power (with possibility of storage systems) etc. (Tchanche et al., 2011, BCS Incorporated, 2008). ORC modules are now commercially available in the power range of 5 kW - 1 MW. Some of the manufacturers include: Infinity Turbine, Ormat, Pratt & Whitney, ElectraTherm, Cryostar, Barber-Nichols, Turboden, Tri-O-Gen, Adoratec, Freepower, EnergetixGenlec, Eneftech etc. The heating, ventilation and air conditioning derivative ORC units are on the market for $1300/kW (Dickey, 2007). A review of the stationary applications revealed the most widely used working fluids as butane, 1,1,1,2-Tetrafluoroethane (R134a), 1,1,1,3,3-Pentafluoropropane (R245fa), n-pentane, toluene and silicon oils (Witchger and Lawrence, 2009, Quoilin and Lemort, 2009).

Increasing fuel costs and pressure on CO_2 emissions have once again tipped the trade-off in favour of Rankine and ORCs for long-haul truck applications. Systems being demonstrated today are taking advantage of the advancements in expansion machines and the broader choice of organic working fluids. Vehicle manufacturers have integrated prototypes into LD and HD vehicles addressing issues like packaging and complexity. The following sections provide a comprehensive review of FBC projects and publications. The below review is divided by the type of working fluid used (e.g. refrigerant, water etc.). High emphasis is also placed on the FBC operating condition (e.g. superheated, supercritical etc.) and the system architecture (heat recovery, sub-system etc.).

2.7 Organic Rankine cycle (refrigerants)

2.7.1 Internal combustion engines

Cummins initially conducted an analytical study for maximising HDDE waste heat to power conversion by extracting heat from the coolant, CAC, EGR and exhaust stream (Nelson, 2006). At the peak engine torque conditions (278 kW, 1200 rpm) they showed an additional 42.5 kW produced by the ORC. For the 1st generation laboratory hardware testing, Cummins selected the 15L ISX engine platform with US 2010 EGR level (Nelson et al., 2009). In this work, energy recovery was performed on the EGR and exhaust using a superheated recuperated cycle using R245fa. The proposed schematic of the system architecture and vehicle integration is shown in Fig. 2.5.

The results showed a 7.4% fuel efficiency improvement across the HD corporate composite operating cycle with combined EGR and exhaust as heat sources. The demonstrated benefit was slightly below the 8% predicted through model-based analysis. This was due to greater than anticipated flow restrictions within the ORC system plumbing and additional parasitic losses (windage) in the systems generator. As this engine employed high EGR rates, the EGR only system still provided 70% of the fuel efficiency improvement (5.2%) compared to the combined EGR and exhaust system. For the 1st generation, they also demonstrated a turbine and generator efficiencies of 75 and 90%, respectively. In their latest work, they packaged an ORC system on a long-haul truck using low rates of EGR and high efficiency Selective Catalytic Reduction (SCR) system (Stanton, 2013). The system delivered 4.5-6% fuel efficiency improvements. The architecture included two changes over Fig. 2.5, the output power was mechanical to the crankshaft through a gearbox. Also, the ORC condenser was a direct air condenser at the front of the engine cooling module.

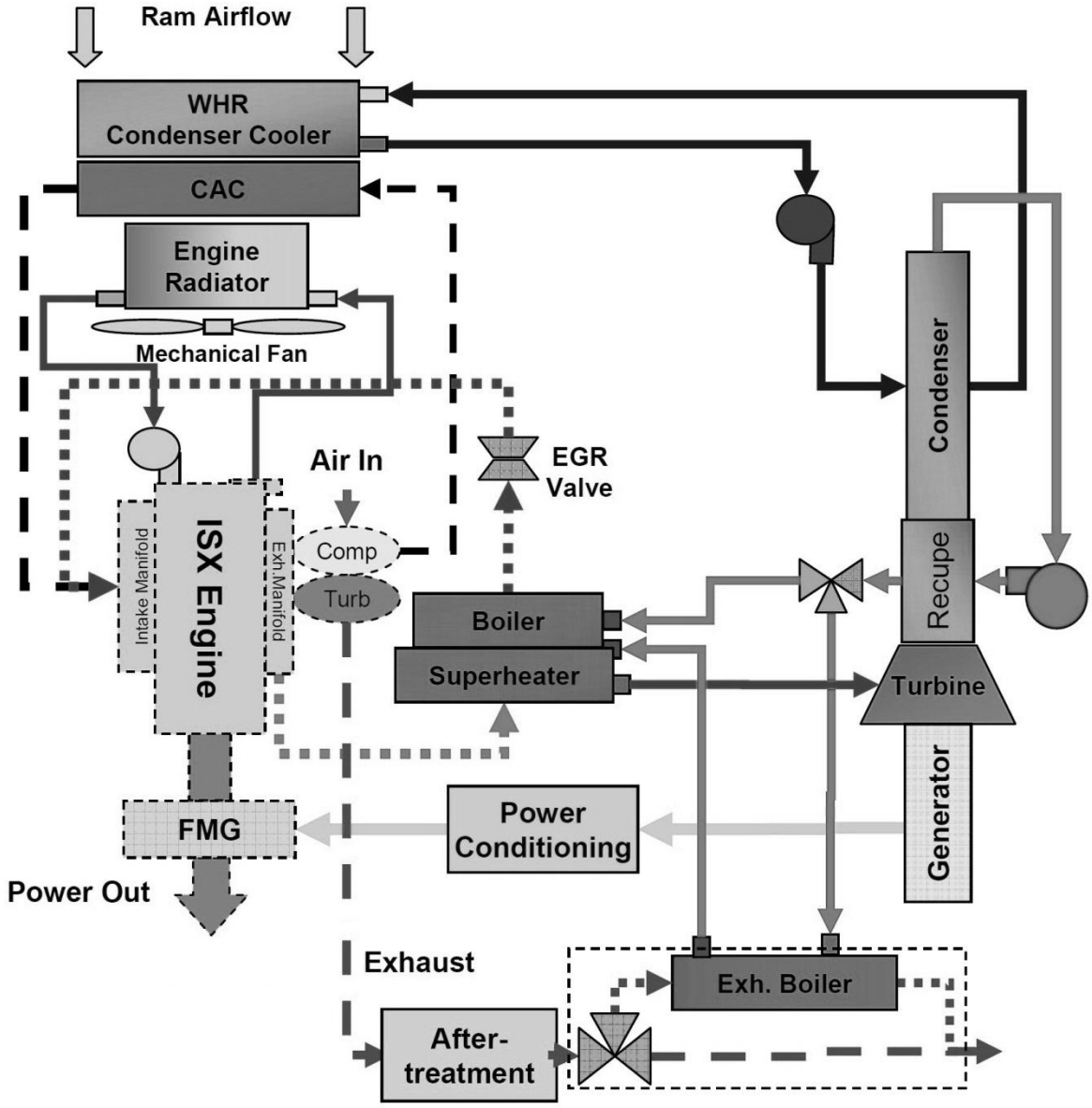

Figure 2.5 Proposed 1st generation ORC and HDDE integration schematic for the superheated recuperated cycle using combined EGR and exhaust (Nelson et al., 2009)

ORNL investigated the potential of ORC on Light Duty Diesel Engine (LDDE) efficiency improvements through laboratory demonstrations and simulations (Valentino et al., 2013, Edwards et al., 2010, Briggs et al., 2010a, Briggs et al., 2010b). The experiments were performed on a 1.9L engine at Euro 4 calibrations. Industrial grade components were used whenever possible as packaging was not a design consideration since the system was only intended for laboratory evaluation. The cycle operation was similar to Cummins, i.e. superheated recuperated cycle using R245fa. The base engine's peak BTE was 42.6% (2250 rpm, 18 bar BMEP). At this operating point, the EGR valve was closed, hence the exhaust was the only chosen heat source. At this single operating condition, the combined base engine and ORC system achieved a BTE of 45%. The net ORC power was 4 kW. The heat input into the ORC was 31.4 kW which gave a thermal efficiency of 12.7%. The

condenser was cooled with 10°C chilled water by ORNL and 13°C ambient air by Cummins, both certainly much colder than what can be achieved in a typical engine cooling module. For a road-load operating point (1500 rpm, 2 bar BMEP), ORNL performed simulations (GT-POWER) to recover EGR and exhaust heat. Fig. 2.6a and b shows the heat recovery architecture and the Temperature-Entropy (T-S) diagram for the cycle. As can be seen from Fig. 2.6a, ORNL opted for a series exhaust then EGR arrangement over Cummins parallel EGR and exhaust arrangement (Fig. 2.5). Results indicated that the ORC could generate 0.4 kW of net electrical power. This electrical output corresponded to an increase in BTE of 2.1% point at this condition, from 24.4% to 26.5%. The model was also used to investigate the transient performance, resulting in a 5% improvement in fuel economy over a warm urban dynamometer driving schedule test.

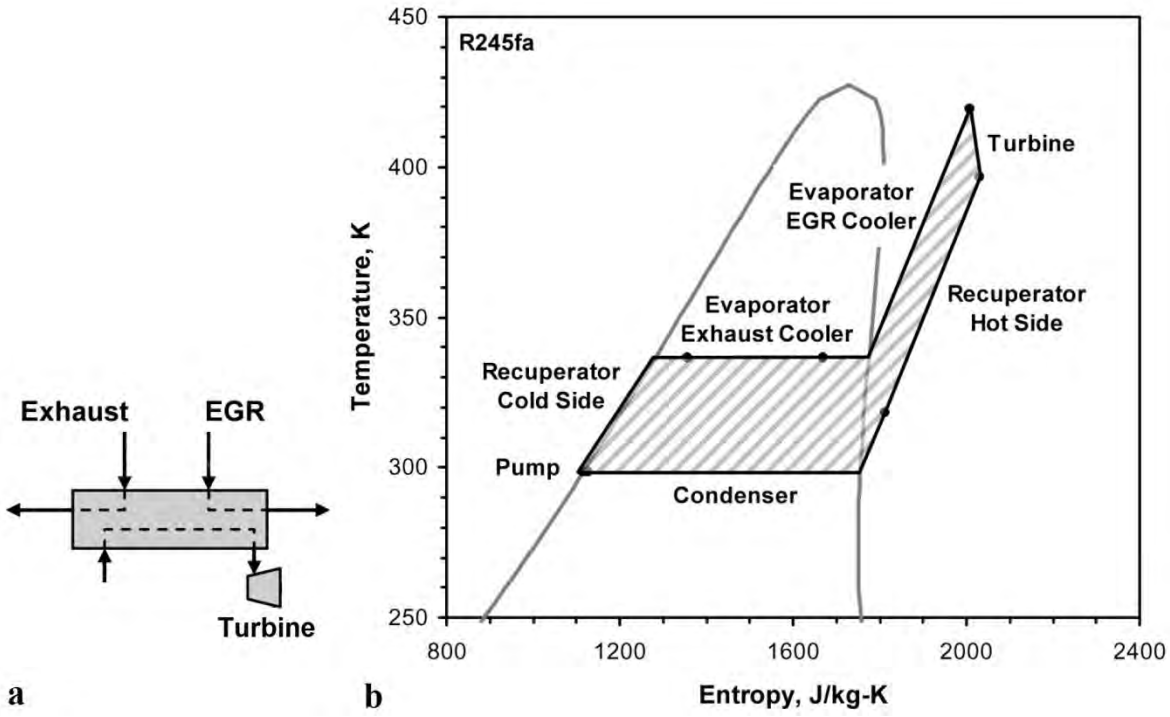

Figure 2.6 Series exhaust then EGR (a) heat recovery architecture (b) cycle T-S diagram (Edwards et al., 2010)

The above two projects by Cummins and ORNL have opted for R245fa as a working fluid, but they did not document detailed thermodynamic comparisons with other organic fluids. Wang et al. (2011a) conducted a simulation study on organic working fluid selection to generate a fixed output of 10 kW. Results from their 9 selected fluids showed that R11, 1,1-Dichloro-1-fluoroethane (R141b), 1,1,2-Trichloro-1,2,2-Trifluoroethane (R113) and 2,2-Dichloro-1,1,1-trifluoroethane (R123) manifest slightly higher thermodynamic performance. However, after the thermodynamic performance evaluation they also evaluated fluids on environmental impact level, using Ozone Depletion Potential (ODP)

and Global Warming Potential (GWP) as indicators. The outcomes indicated that R245fa and 1,1,2,2,3-Pentafluoropropane (R245ca) were the best suited fluids. The selection of R245fa as a suitable working fluid was also pointed out in simulations by Tian et al. (2012) on a commercial diesel generator set. From the considered 20 organic working fluids, they selected R141b, R123 and R245fa on techno-economical merits.

Despite the negative environmental impact of R113, Zhang et al. (2011) used it in their ORC experimental setup as it was a widely used historic refrigerant. They used electric heaters to simulate the exhaust power of a Toyota 1.34L gasoline engine. At the single point test, the experimental ORC system showed a thermal efficiency of 14% (0.7 kW).

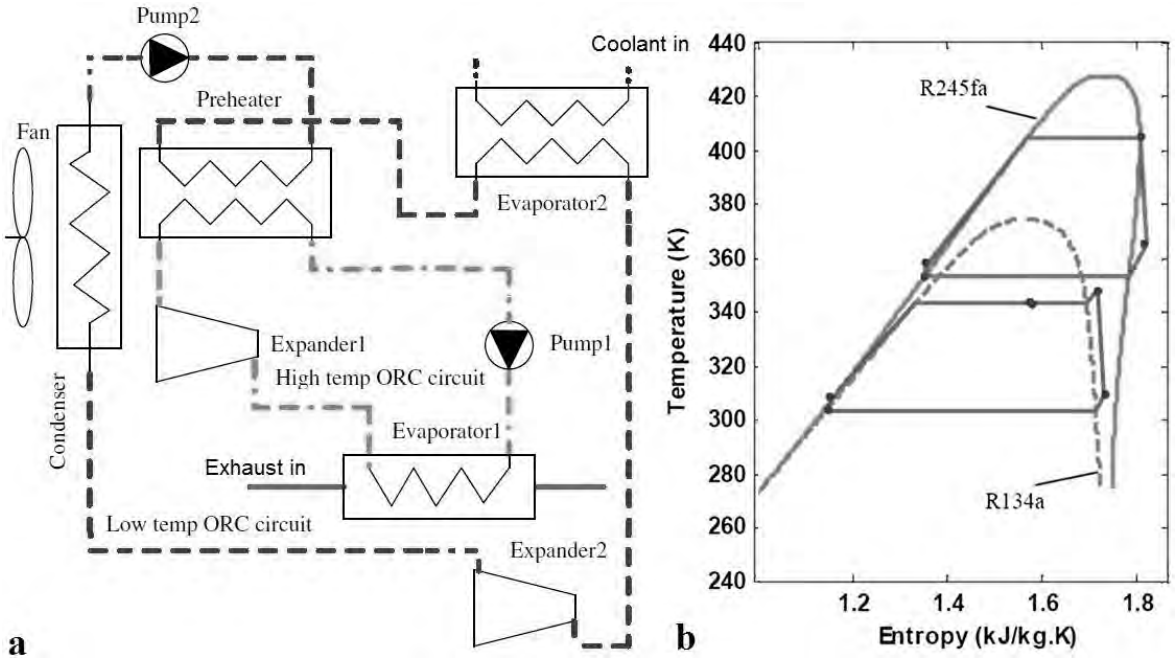

Figure 2.7 Cascade ORC system (a) schematic of the arrangement (b) T-S plot of the HT and LT cycle (Wang et al., 2012)

More recently Wang et al. (2012) proposed a cascade ORC with a gasoline engine. The High Temperature (HT) cycle and a Low Temperature (LT) cycle were simulated to recover heat from the exhaust and the coolant, respectively (Fig. 2.7a). Waste heat from a 1.8L engine was recovered using R245fa and R134a as the working fluids for the high and the low temperature cycles, respectively (Fig. 2.7b). The net power output was shown to improve by 27% relative to the base engine at the rated condition and the BTE increased by 3-6% point throughout the engine's operating region. However, the thermal efficiency of the cascade ORC system was only about 7%, which was mainly due to the low temperature coolant heat recovery.

2.7.2 Hybrid electric vehicles

FBCs generating electric power have an architectural advantage with HEVs. The electric output from the generator can be used for supplementing the engine power, battery charging or covering the on-board electrical power demand (Aneja et al., 2011). The FBC in a series HEV further has the advantage of operating at steady state for most of the time because the engine and drivetrain are decoupled.

El Chammas and Clodic (2005) examined the potential of coolant and exhaust heat recovery from a 1.4L spark ignition engine within an HEV. They examined 8 working fluids (water, isopentane, R123, R245ca, R245fa, butane, isobutane, R152a), with boundary conditions limited by the available heat exchanger and expander technologies. Water, isopentane and R245ca were found to be the most suitable working fluids. Despite the selected higher condensing temperature of water (100°C) compared to the organic fluids (55°C), the simulation results showed that when recovering exhaust only, Rankine cycle offers up to 18% fuel economy improvement. However, ORCs (isopentane, R245ca) were more beneficial since both low temperature coolant and high temperature exhaust heat was recovered delivering a 17-32% fuel economy improvement.

More recently, Ford also conducted ORC simulations on a hybrid LD vehicle (Millikin, 2011b, Hussain and Brigham, 2011, Hussain and Brigham, 2010). To overcome the inherently lower available waste heat in an Atkinson engine in the HEV a performance enhancement strategy was employed. In this strategy, coolant heat and the residual exhaust heat coming out of the evaporator were used to preheat R245fa (Fig. 2.8a). The effects of these two changes over exhaust only heat recovery are shown in the Pressure-Enthalpy (P-H) diagram in Fig. 2.8b. Point 2 moved right to 2a and further to 2b by the addition of the coolant heat and a pre-heater. This reduced the sensible heating and for the same amount of available thermal energy, more vapour was generated driving up the power output. Transient EPA highway drive cycle power output from the ORC was 98% of the electrical accessory load on the vehicle. However, the power generated during EPA city drive cycle could only provide 32% of the accessory load requirement due to the frequent engine off conditions. It was also pointed out that due to excessive cooling of the exhaust in the evaporator and a well-designed ORC system the net backpressure on the engine was actually lowered by around 40% (Fig. 2.8c).

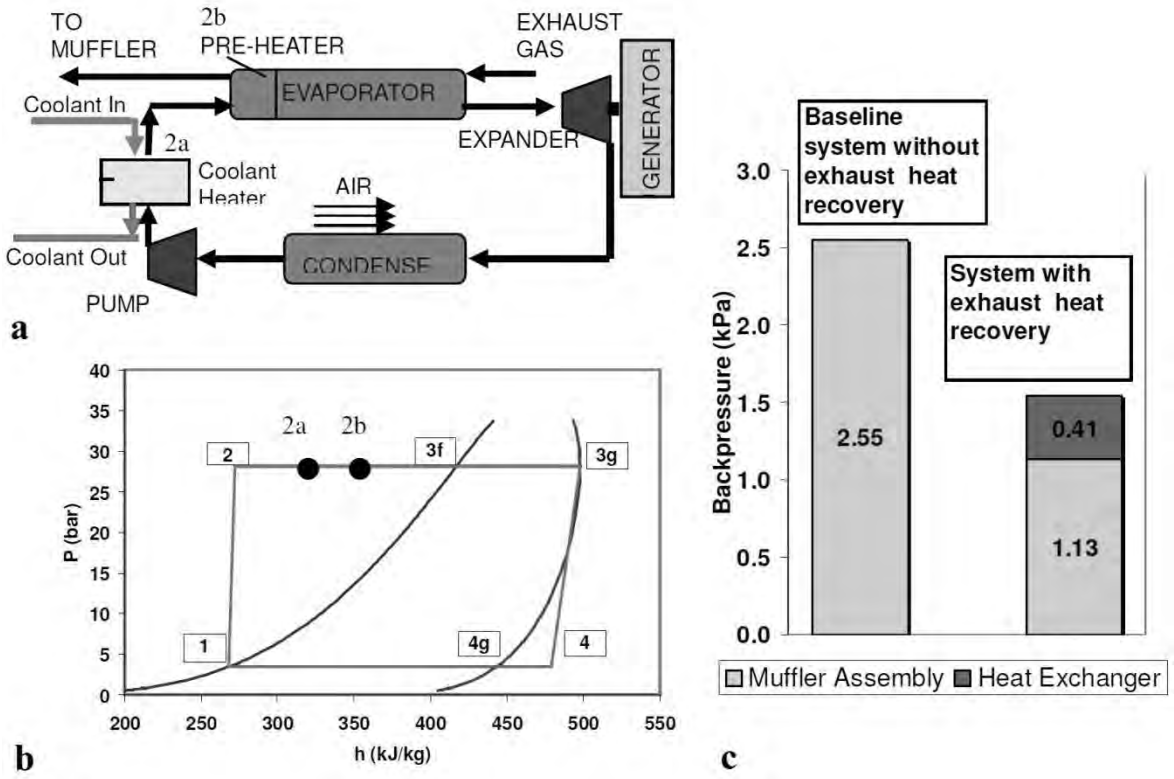

Figure 2.8 ORC with performance enhancement coolant and residual exhaust heat recovery (a) system architecture (b) P-H diagram (c) cycle averaged backpressure during EPA highway drive cycle with and without exhaust recovery (Hussain and Brigham, 2010)

Contrary conclusions to Ford, and El Chammas and Clodic results could be drawn from the work of Vaja and Gambarotta (2010) on a 12 cylinder supercharged stationary natural gas engine. This work analysed exhaust only and series coolant then exhaust architecture. Benzene was selected as the working fluid and the results were only based on thermodynamic attributes. They showed the exhaust only architecture gave an improvement only 9.5% lower than the series coolant then exhaust architecture (11.4 vs. 12.6%). As a result, slight drop in efficiency for a reduction in initial cost and complexity favoured the relatively simpler scheme of exhaust only architecture.

ORCs for buses are also seen as a potentially important step forward in public transport technology. Simulation results from Ricardo showed potential fuel savings of 3-4% for single and double decker conventional buses using either EGR or exhaust as heat source (Atkins et al., 2013). Ricardo and project partners Wrightbus, Revolve and Queen's University Belfast are aiming to have a production ready system for hybrid buses by 2017 to reduce fuel consumption by 10% while also reducing the average power consumption of MAC systems by half (Lopes et al., 2012). More recently, Jung et al. (2013) studied the application of ORC to series type hybrid electric intracity bus which used a compressed natural gas engine. Water and R245fa were used for comparison of improvement in fuel

economy using simulations. For the fixed condensing temperature of 50°C the system with R245fa achieved a specific fuel consumption improvement of 9-13% compared to 2-9% for water.

2.7.3 Organic Rankine cycle (refrigerants): Summary

For refrigerant as a working fluid in the ORC, the majority of publications have selected R245fa (Fig. 2.9). R245fa is a non-toxic, non-flammable and non-ozone depleting refrigerant. Selected publications have also opted for a highly superheated state at expansion inlet (Fig. 2.9). As a result, recuperation of the available energy exiting the expansion machine results in the departure from the simple Rankine cycle arrangement due to the presence of an Internal Heat Exchanger (IHE). When considering heat recovery architecture, if EGR was available, then both EGR and exhaust were considered for recovery, nevertheless recovery of CAC was rarely considered. For engines with no EGR, refrigerants were not only proposed using exhaust but also using series coolant then exhaust heat recovery architecture (Fig. 2.9). However, the use of combined series coolant and exhaust heat recovery with varying working fluids as a suitable architecture was inconclusive.

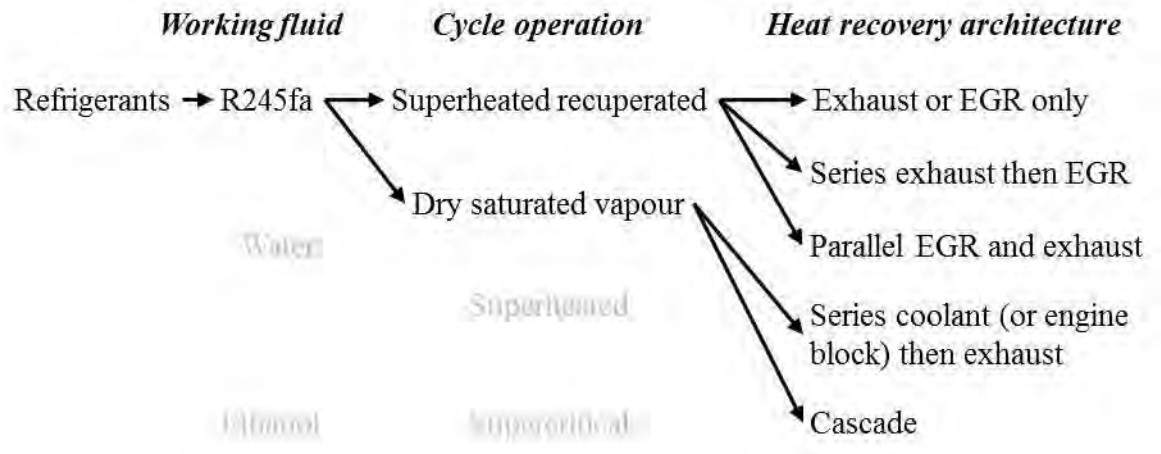

Figure 2.9 R245fa as the favoured refrigerant with the associated cycle operation and heat recovery architecture in literature

R245fa reportedly has the drawback of a high GWP of 1030 years, and efforts are underway to develop more environmentally friendly refrigerants (Calm and Hourahan, 2011). Cummins have recently indicated that they are working on a new low GWP refrigerant (Stanton, 2013). A project by UTRC has explored the use of 1,1,1,2,2,4,5,5,5-nonafluoro-4-(trifluoromethyl)-3-pentanone (Novec 649) (Cogswell et al., 2011). This is a non-flammable per-fluorinated ketone with a GWP of 1 year. Using Novec 649 a 5 kW

supercritical recuperated ORC was proposed for the exhaust of a 60 kW tactical quiet generator.

2.8 Rankine cycle (water)

2.8.1 Internal combustion engines

Yamaguchi et al. (2013) compared Rankine and ORCs for exhaust heat recovery from a 2L Diesel engine. Simulations were conducted for equivalent heat input into the cycle, and fixed expander and pump efficiencies. The BSFC improved by 2.6-3% when using water, methanol, toluene or R123, compared to 1.6-2.1% when using R134a and R245fa. Water showed a 13% lower average power than R123, nonetheless, this was an improvement of 20% over R245fa. Water was regarded as the most suitable working fluid because of safety and environmental friendliness. Thermodynamic analysis performed by Domingues et al. (2013) also favoured the use of water over R245fa for the fixed heat into the cycle using a spark ignition engine.

NTUA examined two different architectures (exhaust only, series exhaust then EGR) for heat recovery from a 6 cylinder, two-stage turbocharged HDDE using Rankine cycle (Katsanos et al., 2010). Fig. 2.10a shows the variation of BSFC improvement as a function of engine load for the two architectures at 1700 rpm. The improvement in BSFC ranged from 6-7.5% for the series exhaust then EGR arrangement and 3.5-5.1% for exhaust only arrangement. Fig. 2.10b shows the T-S diagram for the series exhaust then EGR heat recovery arrangement at B50 (EGR ≈30%). The results showed that the majority of the heat needed for evaporation came from exhaust and the superheating was covered by EGR. NESCCAF also showed that series exhaust then EGR arrangement provided a significant improvement in fuel consumption (8%) and the sensitivity to engine load and speed was low (≈6% improvement in fuel consumption at A20) (Cooper et al., 2009).

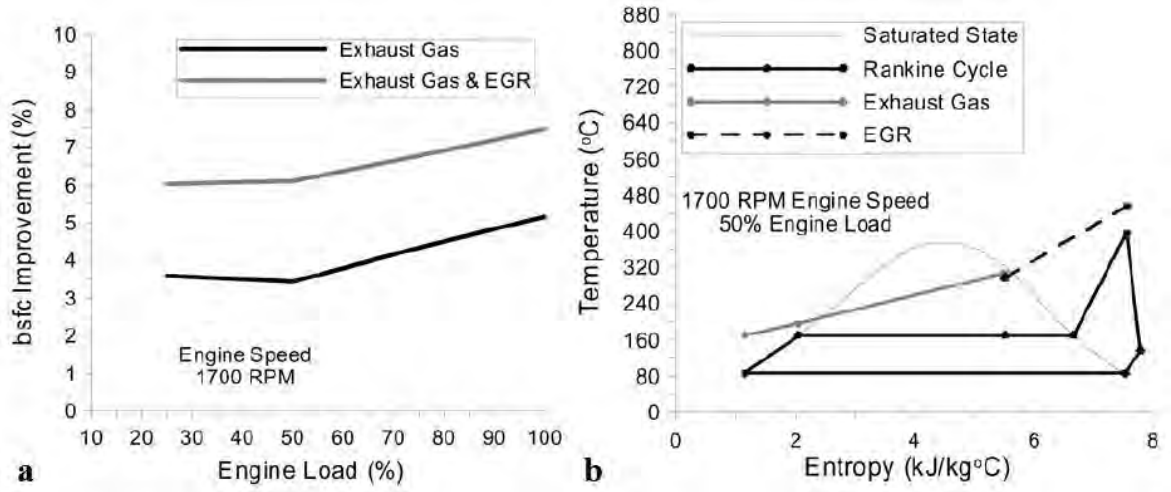

Figure 2.10 (a) BSFC improvement as a function of engine load at 1700 rpm when recuperating heat either from exhaust or both exhaust and EGR (b) T-S diagram of series exhaust then EGR at cruise condition (Katsanos et al., 2010)

A study by Behr also considered different architectures for long-haul trucks at B50 (EGR ≈30%) (Edwards, 2010). The largest fuel consumption improvement (6.9%) was shown by series exhaust then EGR. This was inclusive of the effects of the increased fan power requirement and the exhaust backpressure on engine BSFC. Contrary to NTUA, Behr also compared the series exhaust then EGR, with EGR only heat recovery. The EGR only system offered fuel consumption improvement of 4.8% (70% of series exhaust then EGR), while offering reduced complexity, reduced fan power requirement and no effect on engine backpressure. With similar EGR rates (≈30%) but at C75, Arunachalam et al. (2012) theoretically evaluated five different Rankine cycle architectures, even combining CAC heat recovery from a Volvo D13 engine. They showed that the power produced from EGR only heat recovery was 72% of the combined dual loop Rankine cycle which recovered all three sources (EGR, exhaust and CAC). They favoured EGR only Rankine cycle delivering 4% of engine crankshaft power due to simplicity and economics.

2.8.2 Hybrid electric vehicles

Arias et al. (2006) theoretically analysed a Rankine cycle coupled to the experimental data of a 2004 Toyota Prius hybrid vehicle. Three heat recovery architectures were considered: exhaust only, series engine coolant then exhaust, and series engine block then exhaust. They were not so optimistic on the series engine coolant then exhaust architecture for the Rankine cycle due to the constraint imposed on the temperature of the engine coolant, resulting in very similar performance to exhaust only architecture. The models indicated that using the engine block for preheating and partial evaporation and exhaust for complete evaporation and superheating was the most efficient architecture (Fig. 2.11a). However,

the drawbacks of the proposed system included high pressure (86 bar) and temperature (300°C) in the engine block passages and the evaporator, and a 400°C superheat imposed in the evaporator (Fig. 2.11b).

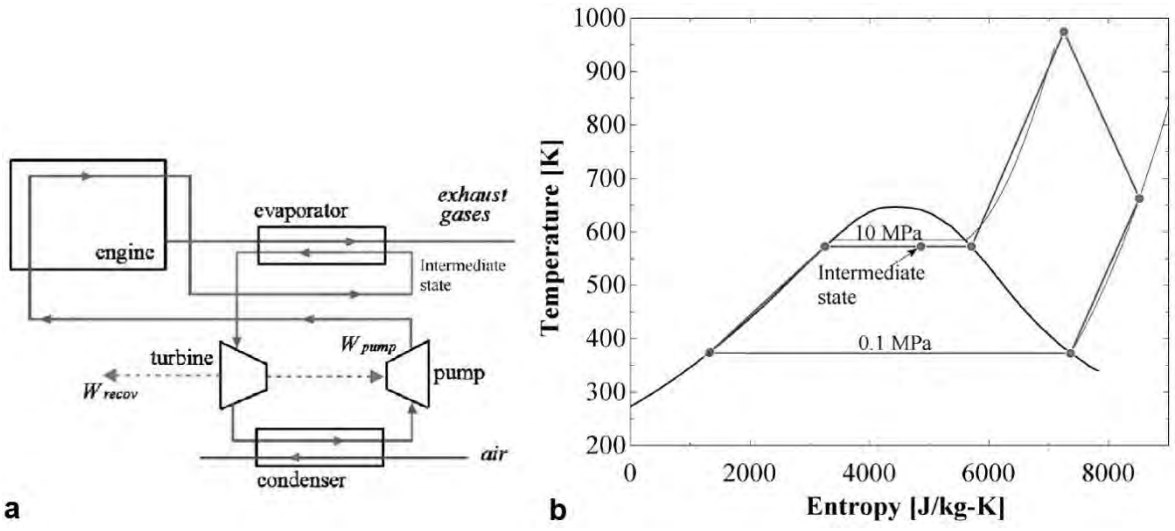

Figure 2.11 Maximum energy recovery from cooling system and exhaust gas (a) architecture (b) T-S diagram (Arias et al., 2006)

Like Arias et al., Honda also made design changes to the base engine (cylinder head, cooling passages) in order to maximise energy recovery from engine cooling and exhaust (Endo et al., 2007). The developed prototype Rankine cycle system was integrated with a 2L Honda Stream gasoline engine. The system used an innovative catalysed evaporation device and insulated exhaust port to increase heat recovery (e.g. from 57% to 95% at engine output of 15 kW). This enabled the generation of high temperature and high pressure steam in the target range (400-500°C, 70-90 bar), depending upon the load on the engine. In addition, the changes to the cooling system produced high temperature water (189°C) without causing any detrimental effect on combustion. The system generated power from a volumetric swash plate axial piston type expander coupled to a generator. Feed-forward control of the steam flow rate was used to control and optimise the expander inlet conditions in transient driving. At 100 km/h (engine output 19.2 kW, air conditioning operating) the expander generated 2.5 kW, increasing BTE from 28.9 to 32.7% (Rankine thermal η = 13%). Furthermore, the reduction in the density of exhaust due to the temperature decrease, and the increased cross-sectional area of gas passages due to the oblong structure, resulted in a reduction of the flow speed of the gas, lowering the backpressure by 1 kPa.

A series of combined studies done by Loughborough University and the University of Sussex have also modelled and investigated the controllability of the Rankine cycle (using exhaust only) (Hounsham et al., 2008a, Stobart et al., 2007). For a base vehicle in Quasi-Static Simulation Toolbox (QSS-TB) the researchers used a 1.6L Volkswagen Golf, and for the Powertrain System Analysis Toolbox they used a 1.8L Honda Civic. Both vehicle models were run against the New European Drive Cycle (NEDC), the US FTP-75 (urban) Drive Cycle and the US06 (highway) Drive Cycle. Simulations showed that there were significant, potential, fuel economy improvements, between 6.3% (1.8L Honda Civic, US06) and 31% (1.8L Honda Civic, US FTP-75). The QSS-TB was also used for a Caterpillar C3126B truck engine (Weerasinghe et al., 2010, Hounsham et al., 2008b). Fuel consumption improvement of 22% was shown using a Rankine cycle in a transient highway drive cycle with practical operating pressures. The higher fuel consumption improvement values reported in these studies were due to a steam storage reservoir between the evaporator and the expander. This provided an energy buffer through periods of varying engine operation.

2.8.3 Open loop Rankine cycle for internal combustion engines

Water is the most environmentally friendly fluid, and hence, has also been proposed for open loop Rankine cycles (i.e. cycles without condenser). Yamada and Mohamad (2010), and Fu et al. (2012) proposed such systems, where the low pressure vapour after the expansion is released to the atmosphere. Yamada and Mohamad proposed an open Rankine cycle on a hydrogen internal combustion engine where two potentially valuable products of combustion (exhaust heat and water vapour in exhaust) were exploited at the same time. The open Rankine cycle subsystem consisted of five main components: water separator, tank, pump, evaporator and expander. The exhaust was separated into liquid, pumped to the evaporator to be superheated, and was then expanded. They proposed two options, sub-system RS-I without a condenser and the sub-system RS-II with a condenser and electric fan. RS-I was claimed to be a better choice in terms of cost effectiveness and smaller system design showing a BTE improvement of 2.9-3.7% point. This system was only applicable for hydrogen engines, and the challenges included the packaging of the separator and the requirement of contaminate free exhaust.

Fu et al. proposed the open Rankine cycle for a conventional ICE, recovering series coolant then exhaust heat. For the selected 4 cylinder engine, 3 cylinders were taken as ignition cylinder and the last one was used as the superheated steam expansion cylinder. Under part load (3000 rpm, 5 bar BMEP), the BTE was shown to increase by 5.3% point.

Compared to the conventional Rankine cycle, this system was easier to realise since the initial system cost was low. However, contrary to the hydrogen engine open Rankine cycle concept, this system required regular replenishment of water. In fact, the water consumption in the hydrogen engine open Rankine cycle concept also exceeded the amount produced by the water separator at an assumed separator efficiency of 50%. (For open Rankine cycle architectures, refer Appendix 2.5).

2.8.4 Rankine cycle (water): Summary

Compared to organic fluids, water has no toxicological effects on the human health and environmental concerns. Water exhibits the highest latent heat (2258 kJ/kg at 100°C) of any known FBC fluid. Hence, for a given ΔT of source, water gave the highest thermal efficiency. The drawbacks of water include the freezing point of 0°C and the requirement of large superheat to reduce moisture at expansion exit when using conventional machines (Fig. 2.12).

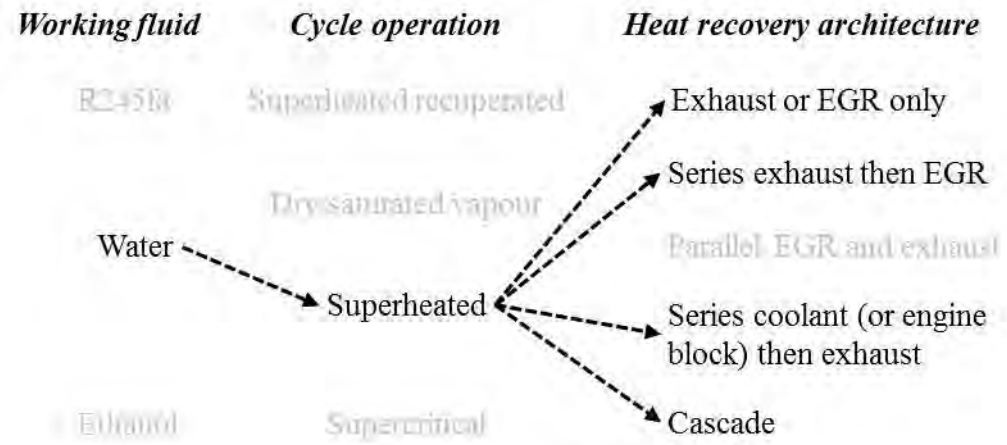

Figure 2.12 Water as the favoured working fluid with the associated cycle operation and heat recovery architecture in literature

Rankine cycle was stated to be effective only for high temperature heat recovery, usually greater than 400°C (Arunachalam et al., 2012). With HDDE long-haul trucks operating around 50% load most of the time and offering lower exhaust temperatures than gasoline engines, EGR only or series exhaust then EGR were the two widely proposed architectures (Fig. 2.12). For LD engines without EGR the architecture widely proposed includes high temperature preheating carried in the engine block followed by exhaust heat recovery. As such Honda showed a Rankine cycle prototype offering a 13% thermal efficiency and 13.2% improvement in BTE (Endo et al., 2007).

With water favouring high temperature heat recovery and refrigerants offering the ability to even recover low temperature coolant heat, the combination of these two different classes of fluids were also proposed in water-organic cascade arrangements. Both, Bae et al. (2013) and Kim and Yu (2011) proposed such system architectures for LD vehicles. In their proposed arrangement the high temperature cycle recovered waste heat only from the exhaust using water, and the low temperature cycle recovered heat dissipated from the high temperature cycle and waste heat from the engine coolant using 2,3,3,3-Tetrafluoropropene (R1234yf). These publications mainly dealt with component developments for the low temperature cycle and the net engine efficiency improvements due to the cascade system were not calculated. (For supplementary FBC architectures, refer Appendix 2.4).

2.9 Organic Rankine cycle (alcohols)

2.9.1 Internal combustion engines

Like Cummins, AVL also undertook an R&D project to demonstrate the feasibility of ORCs on HDDEs (Teng et al., 2006). Their initial work included an analytical study for maximising waste heat to power conversion but only using gaseous sources (EGR, exhaust and CAC) (Teng et al., 2007). Using a supercritical ORC, the case study showed that up to 20% increase in the engine power could be achieved at the rated condition for a condensing temperature of 50°C.

AVL then conducted a working fluid comparisons study between R245fa and ethanol (Teng and Regner, 2009). With EGR as the heat source, the evaporation temperature (120°C), the maximum temperature (350°C) and the thermal efficiency (≈18%) were targeted to be the same for both the fluids (Fig. 2.13). The R245fa cycle was considered inferior as it required higher maximum cycle pressure (19.3 vs. 4.3 bar) and also required a cooler condenser (45 vs. 68°C) compared to ethanol. The fluid comparison under supercritical operation (excluding the IHE) also favoured ethanol.

More recently AVL designed and built a laboratory demonstration recuperated ORC (ethanol) for evaluation on a 10.8L Cummins engine (Park et al., 2011, Teng, 2010). Since the EGR flow was low (<10%), for optimal performance the system was configured to utilise exhaust only as the source. The target maximum, evaporation and condensation temperatures were set to 350°C, 120°C and 70°C, respectively. The experimental results demonstrated a 3.4-4.2% fuel saving at the 4 tested points (B50, B75, B100 and C100). They also conducted a simulation study on a high EGR rate (35-45%) engine, with similar

temperature limits as above, producing 4-4.5% fuel saving at the 4 tested points (using EGR only) (Teng et al., 2011).

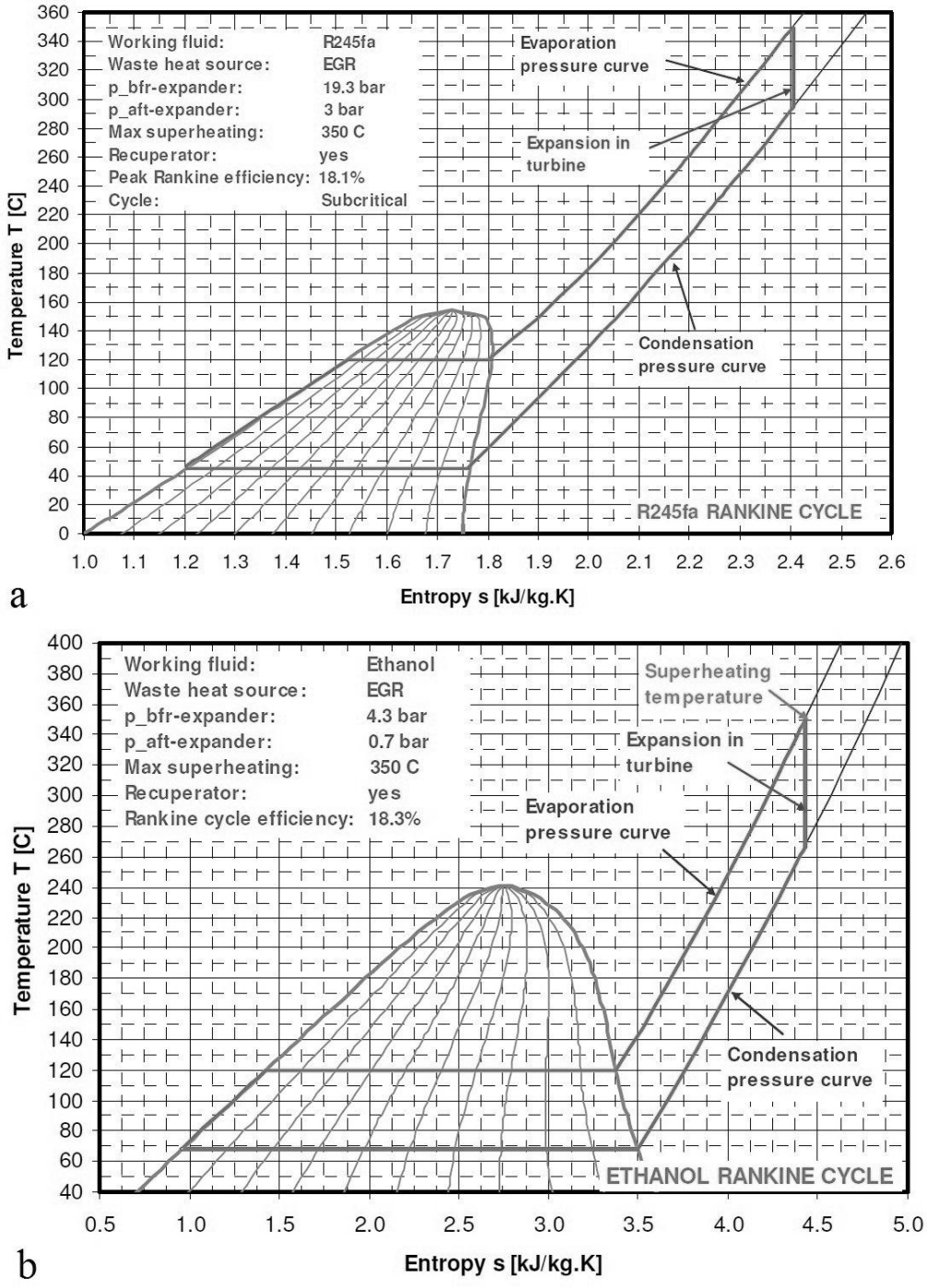

Figure 2.13 Comparison of T-S diagram for (a) R245fa (b) ethanol, superheated recuperated subcritical cycle (Teng and Regner, 2009)

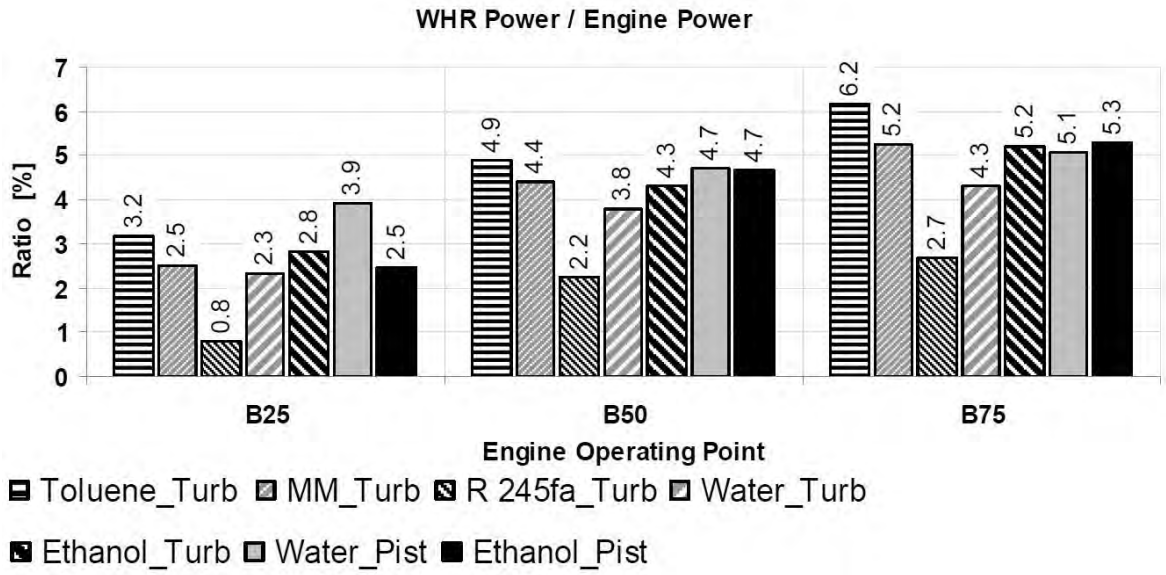

Figure 2.14 Ratio of power output of the waste heat recovery system to engine power (Seher et al., 2012)

Using simulations, Bosch compared 5 working fluids using a piston expander and/or a turbine model (Seher et al., 2012). Fig. 2.14 depicts the ratio of cycle power output (for the parallel EGR and exhaust architecture) to the power of the 12L HDDE at the testing points. With an assumed condensation temperature of 100°C, they showed that R245fa produced the lowest performance benefit. The best performance benefit was obtained using toluene with a turbine at B50 or at higher loads. In a piston machine water and ethanol showed similar performance at B50 or at higher loads. However, ethanol was considered as a suitable working fluid as it provided high performance benefit (88-96% of toluene at B50) using either piston expander or turbine.

Compared to Behr's earlier work on water (Edwards, 2010), their recent work now also include ethanol ORC for HDDEs (Edwards et al., 2012). They investigated architectures which used either EGR or exhaust as the source or a combination of both (parallel architecture). The controlled use of both heat sources was shown to have the greatest simulated net likely fuel consumption improvement (4.3%) over the long-haul cycle. The heat sink of the configuration was a condenser integrated into the high temperature coolant loop of the vehicle cooling system and all configurations investigated used the same piston type expansion machine map.

2.9.2 Organic Rankine cycle (alcohols): Summary

A number of HDDE studies selected to use alcohols as the organic working fluid despite the toxicological and flammability drawbacks compared to R245fa (Fig. 2.15). The main reason for this was the superior thermodynamic performance of ethanol, and the lower evaporation and condensing pressures for given temperatures, allowing the use of lighter and lower cost heat exchangers. Studies also indicated that piston expanders were suitable alternatives to turbines for ethanol as the working fluid.

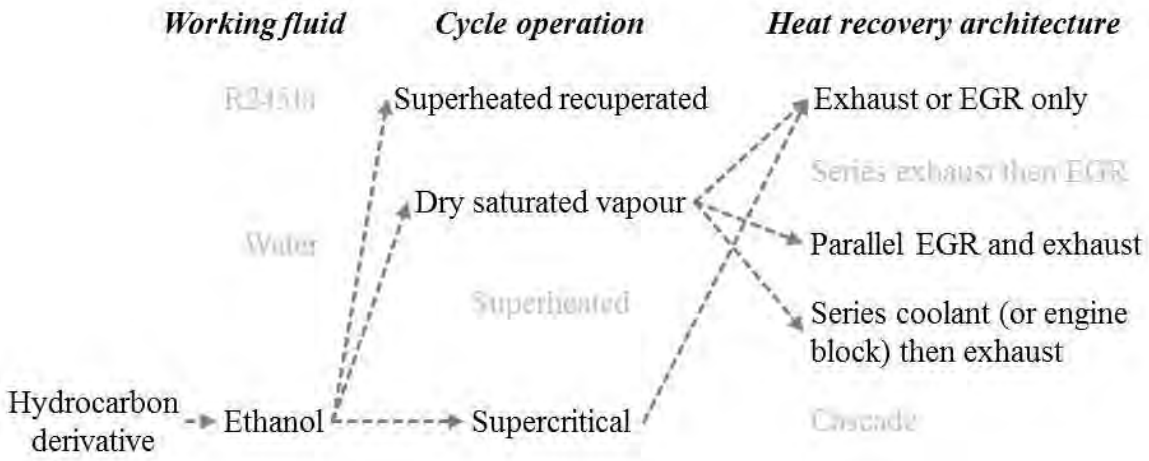

Figure 2.15 Ethanol as the favoured hydrocarbon derivative with the associated cycle operation and heat recovery architecture in literature

Ethanol has been proposed mainly for high temperature heat recovery (Fig. 2.15), however the suitability of ethanol also for low temperature heat recovery was shown by BMW (Ringler et al., 2009). They considered heat recovery using two single loop configurations, A: exhaust only and B: series coolant then exhaust architectures for a 2L stoichiometric gasoline engine. The temperature level of the coolant was raised to ≈115°C to increase the source exergy. No negative effects on the engine efficiency were observed. Water was preferred for system A, which provided high temperatures. However, for system B, which used a low temperature coolant, ethanol was shown to be the right choice. Dymola simulations showed system B was more favourable than system A for typical highway cruising speeds (45-70 mph), for this reason the test bench data focused on this configuration. System B produced an additional net power of 0.7-2 kW, accounting a 10% increase in engine power.

A recent theme of research that emerged to address the drawbacks of alcohols is the investigation of alcohol-water blends. A combined study by Ricardo and Volvo employed ethanol and ethanol-water blends in a parallel EGR and exhaust architecture predicting

additional 9.9 kW at the B50 (≈7% of engine power) and 24.5 kW at the C100 (≈8.5% of engine power) through simulations (Howell et al., 2011, Amar et al., 2011, Tai et al., 2010, 2009). Latz et al. (2012) opted for 20% methanol and 80% water in their theoretical study over ethanol-water blends due to higher first and second law efficiencies. For a 12.8L HDDE, relative power output of the parallel EGR and exhaust architecture, and the series exhaust then EGR architecture were nearly similar at 3.6-3.7% of the engine power output at high waste heat rates (Latz et al., 2013).

2.10 Organic Rankine cycle combined with other technologies

The adaptability of ORCs for different heat sources lead to the proposition of ORCs combined with TEGs and other FBCs (e.g. Kalina cycle). Shu et al. (2012a) theoretically analysed a combined TEG and ORC system recovering exhaust only, and combined coolant and exhaust. In the combined coolant and exhaust arrangement (Fig. 2.16a), the hot side of TEG module exchanged heat directly with the high temperature exhaust, while the cold side of TEG further preheated the working fluid. The low temperature exhaust exiting the TEG was used to fully evaporate the ORC working fluid. The system also used an IHE and coolant heat to raise the temperature of the working fluid. The proposed TEG used tellurium, antimony, germanium and silver as p-type and lead telluride as n-type whereas the ORC used R123. Under the rated condition, the combined TEG-ORC system operated most effectively at supercritical pressures, increasing the BTE from 40.3 to 45%.

Considering the difference in the qualities of exhaust, cooling water and lubricant, He et al. (2011) proposed a combined ORC and Kalina cycle system. Fig. 2.16b shows the ORC (A) for recovering the waste heat of lubricant and high temperature exhaust, and the Kalina cycle (B) for recovering the waste heat of low temperature cooling water. The ammonia-water solution of the Kalina cycle absorbed the heat released by the working fluid of the ORC. Then, the solution was split into two streams with the same ammonia content. One stream flowed into the cooling water heat exchanger and the other stream into the IHE to exchange heat with the stream of water-rich solution flowing from the separator. The two streams were then combined to flow into the separator in which it was split into two streams with different ammonia content and the ammonia rich vapour flowed into the expansion machine. The entire efficiency of the combined system was shown to be highest with ORC using cyclopentane. Compared with standard ORC configurations, both TEG-ORC and ORC-Kalina systems recovered more waste heat. However, irrespective of the high BTE gains by both systems and security of organic fluid from decomposition in

TEG-ORC system, the high complexity, cost and packaging was seen as a significant factor in their application for mobile heat recovery.

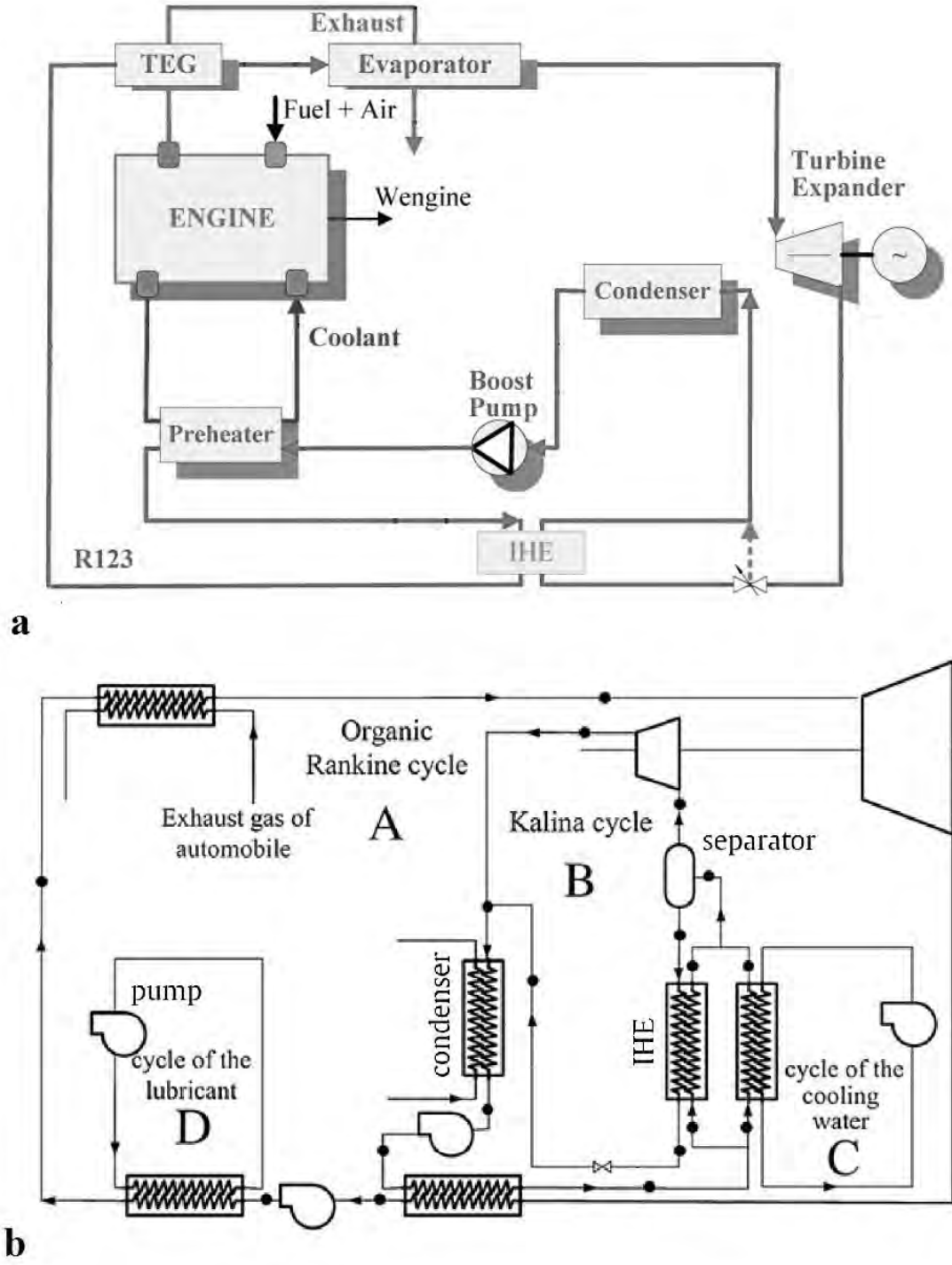

Figure 2.16 System schematic for combined high and low temperature heat recovery (a) TEG-ORC system (Shu et al., 2012b) (b) ORC-Kalina system (He et al., 2011)

ORCs were also proposed in combination with a vapour compression cycle for heat activated cooling by Wang et al. (2011b) and Tian et al. (2013) for stationary and mobile engines. Wang et al. presented a 5 kW cooling capacity prototype under laboratory conditions using R245fa for ORC (superheated recuperated) and R134 for vapour

compression cycle. Whereas Tian et al. simulated the system and its variants using supercritical CO_2 for both cycles with high pressures (86-88 bar) and low ORC condensing temperature (20°C). As in the heat activated cooling system, ORC expander drove the compressor instead of an electrical motor, the primary investigation for high system efficiencies still resided in the high overall conversion efficiency of the ORC.

2.11 Other waste heat recovery technologies

Apart from MTC, ETC, TEG and FBCs other WHR concepts like the heat2power and methanol engines with ORC were also proposed. In the heat2power concept, thermal energy was extracted from the exhaust by means of compressed air in a gas-gas heat exchanger operating at high temperatures (heat2power, 2014, Toom, 2008). This compressed air stream was then expanded in a cylinder, usually proposed as an add-on module (connected to the engine by means of a gear set or a belt drive). After the expansion stroke, the air was released at low temperatures (250-300°C instead of 600-950°C). Simulations showed that adding the system onto a gasoline engine reduced fuel consumption on NEDC by around 12-15%. The challenges with this system included a large sized gas-gas heat exchanger and ≈30% increase in the net cost of the combined system compared to a base turbocharged gasoline engine. The former was because at 100°C, specific heat, density and thermal conductivity of air are $1/4^{th}$, $1/1000^{th}$ and $1/20^{th}$ of water, respectively. The volume flow rates required were large and the heat transfer coefficient was small.

Fu et al. (2013) proposed an open ORC (methanol) to recover exhaust heat from a methanol dissociation ICE. The improvement to the ICE global BTE came from recovering exhaust energy and improving ICE fuel heating value (improving in-cylinder efficiency). As a result, simulations showed the ICE global BTE could improve by 5.3-6.8% points under full load conditions over the liquid methanol ICE. Moreover, the goal of on-board production of hydrogen could be realised. Drawbacks included that the maximum temperature of the dissociated methanol gas was limited by the ICE exhaust temperature and the mass flow rate of the ORC was determined by the ICE operating condition. Furthermore, the mass flow rate of the ORC was low to recover all the exhaust energy and part of the exhaust energy was still wasted, which was proposed to be used by a low temperature ORC. (For architecture of the above two concepts, refer Appendix 2.6).

2.12 Chapter 2: Summary

Waste heat to power conversion from LD and HD vehicles is now a well-funded field with initial technology deployment expected in 2020-2025 timeframe. The simulation and experimental studies reviewed demonstrated the viability of MTC, ETC, TEG and FBC systems. From the published literature, individual WHR technologies were found to produce a broad range of projected fuel savings. The interpretation of results for comparison not only for different WHR technologies but also for the same WHR technology is not straight forward. This is because different studies have used different engine platforms, EGR rates, load/speed points, heat sources, qualities, quantities, boundary conditions and assumptions (refer Appendix 2.7 for a summary), giving different overall conversion efficiencies. Furthermore, the rebound effect was acknowledged in very few of the reviewed studies (i.e. fuel improvements encourage the consumption of other energy forms where part of the gain will be offset by the increase in fuel consumption). A suitable example for this is the condensing process in ORCs and Rankine cycle. Wang et al. (2012) and Hossain and Bari (2013) proposed a cascade ORC and a Rankine cycle, respectively. These simulation studies presented 23.7-27% of additional crankshaft power. However, the condensing temperature (28-30°C) was much lower than that seen in the typical engine cooling module and the effects due to the increased fan power requirement were not considered. The above discussion highlights that, the selection of a long-haul HDDE platform representative of the current production, and identification of realistic boundary conditions/assumptions for WHR analysis, was the starting point.

The efficiency of all the WHR technologies mentioned is limited by the flow rate and temperature levels (also pressure levels in case of MTC, ETC) of the heat streams. WHR might not always be economical or even possible with low quality and/or transient thermal flows. The application of mobile WHR technologies faces numerous barriers that impact the economy and effectiveness of the technology, and impede their wider adoption and installation. The common interrelated barriers include: payback periods, temperature limits of recovery equipment, thermal cycling, weight, size, complexity, durability, reliability, maintenance and performance. They will also include advanced controls to minimise the disadvantage linked to the varied driving conditions. As a result, some technologies may struggle to achieve commercialisation despite the fuel saving benefits.

Despite their success in stationary application, FBCs face some technology specific barriers. These include: economies of scale, heat exchanger material limits, corrosion/fouling, working fluid toxicity and flammability, potential of exhaust and

working fluid mixing, crash safety, heat rejection, variable air flow through the condenser and variable turbine/expander speed. However, the successful operation of secondary fluid cycles like MACs systems as an integral part of the HDDE bodes well for FBCs.

2.12.1 Rational and justification for selecting fluid bottoming cycles

Both MTC and ETC are good solutions for engines that stay in a high load narrow rpm range but show inadequate improvements at part load. MTC in production vehicles have delivered only 3% improvement in fuel economy with the advantages of no impact of vehicle safety, lower cost and complexity (Millikin, 2007). The costs of an MTC for a Volvo D12 engine with simulated fuel consumption improvement of 2.4% over the long-haul drive cycle is estimated to be about £1590 by NESCCAF (Cooper et al., 2009). ETC can offer up-to twice the improvement over the MTC but also introduces the added complexity due to electric motor/generator, associated power electronics and electric accessories. For fuel consumption improvements of 4.1% and 3% for HDDEs, the estimated ETC cost by NESCCAF and Ricardo is £3990 and £5950, respectively (Cooper et al., 2009, Hill et al., 2011). The weight of an ETC on HDDE is in the order of 80 kg (Weerasinghe et al., 2010). ETC can be considered a suitable option when combined with a hybrid platform.

With fewer components needed than FBCs, TEGs have lesser packaging and weight constraints and will play a vital role for LD vehicles in the coming decade. Current thermoelectric materials are delivering a thermal efficiency of 8-10% and fuel consumption improvements of 4-5%. For an assumed 10% efficient TEG for long-haul trucking, MSU has estimated a price of £10,020 for a 5 kW unit (i.e. £2004/kW) (Schock et al., 2010). This is much higher than the expected £300/kW that TEGs have to demonstrate to be commercially viable (Ashley, 2011). For an indication on weight of TEGs, guidelines can be drawn from the works of Amerigon (Crane et al., 2011). Their 500 W TEG (600°C, 0.04 kg/s gas flow), weighs ≈10.5 kg. However, several TEG specialists agree a successful system would weigh less than 10 kg while generating 1 kW.

While no single WHR technology is superior for every engine platform, Rankine and ORCs appear to be the most promising solutions for long-haul HDDE based on thermodynamic merits. The thermal efficiencies of Rankine and ORCs are currently higher than TEGs and are characterised as the only demonstrated technology that are usually used in the range of 10-30 kW. The use of Rankine and ORCs show thermal efficiencies of 10-15% and can result in a significant BSFC reduction, in the range of 5-8% on the entire

engine operating range depending on the system configuration. Favourable results are also seen with LD vehicles. Transient simulations performed by Honda showed a BTE improvement of 6.1% from 29.5 to 31.3% over the Japanese 10-15 mode (Kadota and Yamamoto, 2008).

Rankine and ORCs also have other advantages like low pumping losses on the base engine compared to MTC and ETC, and higher level of technology readiness compared to TEGs. Rankine and ORCs systems being developed for automotive application have achieved rapid evolution in the past 5 years. This is due to the combined result of technical advancements in a series of critical system components, stationary ORC experience, CO_2 regulations, carryover from refrigeration applications and increased fuel prices.

The cost estimation by NESCCAF, Ricardo and AVL, for Rankine and ORCs for HDDEs is £9000, £9835 and £5100 for an assumed fuel consumption improvement of 8%, 5% and 3.5%, respectively (Cooper et al., 2009, Hill et al., 2011, Park et al., 2011). The FBC is regarded as having a high technical risk and initially for the first few years of introduction the technology is expected to cost ≈£740/kW. Standardisation and technology improvements are expected to have a positive effect on the costs of ORCs leading to ≈£300/kW within 5 years of introduction. Rankine and ORCs weight estimations by UTRC, NESCCAF, Behr and the University of Sussex range from 87 kg for a 5 kW unit to 109 kg for a 30 kW unit (Cogswell et al., 2011, Cooper et al., 2009, Christoffel, 2012, Weerasinghe et al., 2010). Although additional weight is undesirable, relative to a 30-40 tonne long-haul truck, the FBC weight will have a low effect on fuel economy. For example, in long-haul trucks the weight reduction benefits ranges from 0.15% to 0.4% per 100 kg over level terrain and uphill climbing routes, respectively (US NPC, 2012).

Using references cited in this section, Fig. 2.17 is plotted normalising the axes to compare the different WHR technologies. Note that the complexity rating (based on a similar approach shown later in Table 6.4) is proportional to the cost and size of the system. Also, note that the variability among engines due to thermal management and regulated emissions treatment could cause a $\Delta 0.5$ variation. With the exception of some overlap, WHR technologies vary significantly in the challenges-benefit evaluation for long-haul HDDEs. ETC, TEGs and FBCs require higher fuel prices and aggressive GHG regulations to justify their application. Despite this, the most favourable technology appears to be Rankine and ORCs for long-haul HDDEs, and hence, the research on FBCs was continued. Similar conclusions have also been drawn by BMW for LD vehicles (Ringler et al., 2009).

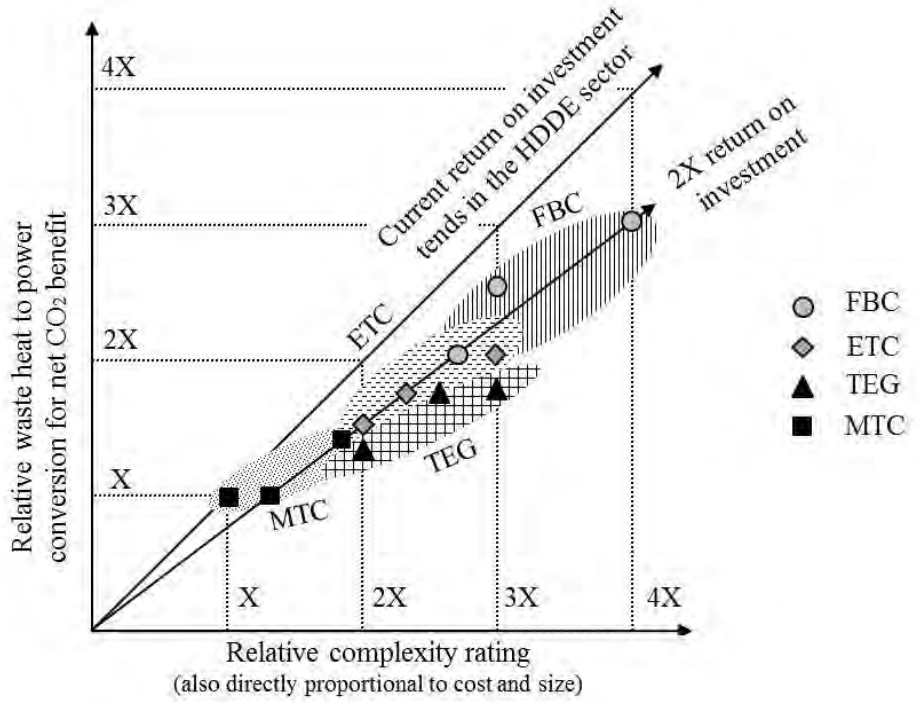

Figure 2.17 Relative challenges-benefit trade-off for different WHR technologies applied to HDDEs

2.13 Research objectives and contributions

Despite the suggested fuel savings by FBCs for transport applications, the experimental setups are not reaching the fuel savings for production maturity within the expected costs. The key consideration in the R&D effort for FBCs is therefore to investigate and identify technical paths that may improve the practicality of such a concept. For this, three research themes were identified for investigation following the detailed review of the current state of knowledge. Prior to the investigation of the research themes, a long-haul HDDE platform selection for FBC analysis was performed (Chapter 3). The three research themes are not entirely independent and the complex overlaps between them will become evident in the later chapters. Nonetheless, the sequential examination as presented in this thesis is desired as each theme utilises the findings from the previous theme to extend the analysis. For a comprehensive view, the performance aspects were based on the energy and exergy equations in all the specific points of the cycle. Fig. 2.18 summarises the step-by-step method overview of these three themes. The associated research objectives and resultant research contribution are summarised below.

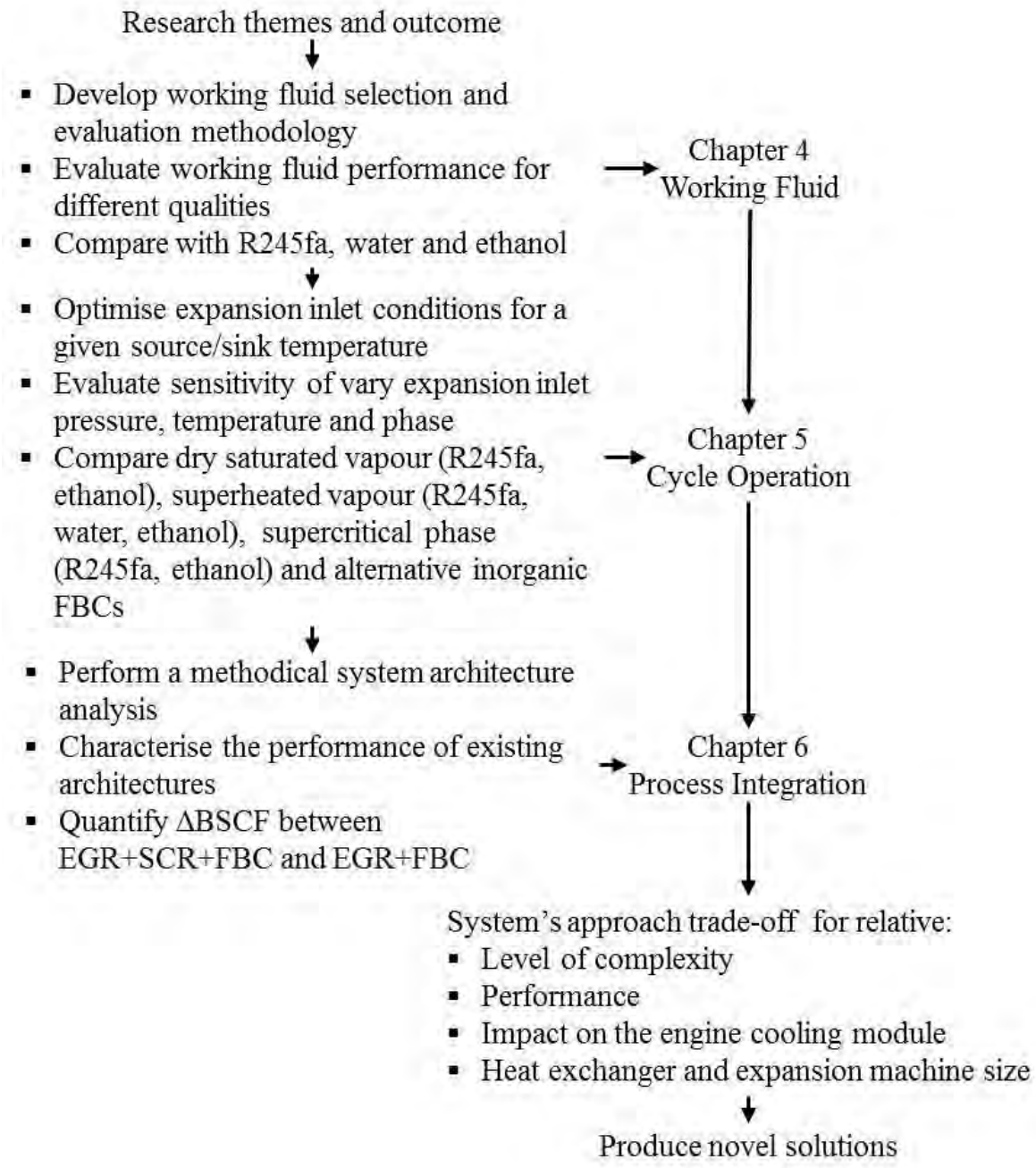

Figure 2.18 Method overview for evaluation of FBC research themes

Working fluid (Chapter 4): So far, there is no consensus on how to select a suitable working fluid in the literature. As a result, three very different types of working fluids, i.e. refrigerant (R245fa), water and alcohol (ethanol) are widely proposed. The first theme of investigation was the selection of suitable working fluids. For this, a novel pure working fluid selection and evaluation methodology was developed. This methodology established a link between the desired process requirements and the fundamental properties of a working fluid, in particular, normal boiling point, reduced temperature, chemical groups and atoms, molecular weight, structure and complexity. The methodology additionally utilised a robust performance and system index parameter for the identification of fluids that maximise the overall conversion efficiency and minimise the system size/cost. This

methodology was finally applied to answer if other fluids exist that may be more favourable over the above three literature fluids.

Cycle operation (Chapter 5): There exists little analysis and comparison in the literature regarding the various expansion inlet conditions (and fluid combinations). Furthermore, contrary recommendations appear for expansion inlet conditions for a given fluid, e.g. dry saturated vapour, superheated vapour and supercritical phase, for ethanol. The second theme of inquiry was to vary the expansion inlet conditions (and fluid combinations) for a given source/sink temperature in order to reduce the cycle irreversibilities. Simulation results for the numerous conventional and variations of the conventional closed loop cycles using pure fluids quantified the relative benefits of the various cycle operating modes, and also highlighted the significant sensitivity and performance results. This provided directions for practical implementation and offered new opportunities in energy conversion.

Process integration (Chapter 6): The preferred FBC architectures in the literature include series exhaust then EGR, parallel EGR and exhaust, series coolant then exhaust, and cascade systems. Furthermore, conflicting conclusions exists for heat recovery architectures, e.g. exhaust heat with/without coolant as preheat. The final theme of inquiry was to optimise energy conversion by plant optimisation (i.e. process integration). The plant optimisation was a function of the working fluid, the cycle operation, the thermal/subsystem architecture and the effects on interconnected processes/utilities. For this, a methodical system architecture analysis was performed with a principal objective of sustainable development for automotive HDDEs. Simple architectures were initially evaluated, problem definitions and universal application guidelines derived from their analysis provided the directions for the design of efficient complex architectures. The problem definitions also led to the adaptation of the pure working fluid methodology to provide tailored solutions using water-organic and organic-organic blends. This methodical analysis resulted in the development of novel process integrations that can overcome the shortcomings of the published process integrations for comparable design complexity. This approach also established explicit links between process integrations and the engine platform/speed/load to give a particular range of system performance.

The investigation of the above three themes leading to identification of novel fluids and/or cycle operation and/or system architecture which will be more suited over the present literature solutions was defined as the aim of the thesis. As a comparison with the absolute

results in the published literature can be misleading, for each research theme, the conclusions from the published literature were re-simulated and more emphasis was placed on the relative results. A comprehensive conclusion of key research outputs and future research recommendations are outlined in Chapter 7. Publications resulting from the research presented in this thesis are mentioned in Appendix 1.1.

3 Engine Platform and Waste Heat

3.1 Introduction

The architecture of current HDDE platforms is highly influenced by emission standards that have been enforced for over two decades. Only few of the WHR studies reviewed in Chapter 2 have explicitly mentioned the emission standard achieved by their engine platform. Hence, the combination of current emission standards and potential CO_2 emission reduction cannot be decoupled, and has to be addressed for the same engine platform.

This chapter firstly introduces the regulated emission technologies for HDDEs, particularly for NOx reduction. This is since the current techniques in NOx reduction have a high impact on engine BSFC and the available waste heat. Secondly, fuel consumption penalty across 4 different engine platforms is analysed for Euro 6 standards. As a result, two engine platforms were selected for FBC analysis. The first platform was similar to the current industry approach, while the second was a systems approach research platform. Finally, calibrated scaled-up 10L engine model for the two platforms were used to provide waste heat qualities and quantities for FBC analysis.

3.2 HDDE emissions platform

Diesel exhaust typically contains N_2, CO_2, H_2O, O_2, sulphur dioxide (SO_2), HC, CO, NOx and PM. The last 5 species combined accounting for less than 1% of the exhaust composition. However, the last 4 species are well established regulated emissions. HDDE and truck manufacturers have faced enormous challenges to find fuel efficient solutions to meet the ever stringent emission targets. This has led to the widespread deployment of various emission reduction technologies, primarily to address criteria emissions rather than increasing fuel economy.

To meet the Euro 6, US 2010 and Japanese 2009 emission regulations, essentially all HDDE platforms are being equipped with a 3-way after-treatment system (Fig. 3.1) (Weissler, 2012, Hill et al., 2011, US DOE, 2008). Diesel Oxidation Catalyst (DOC), Diesel Particulate Filter (DPF) and SCR are being used to treat CO and HC, PM, and NOx, respectively. With a total NOx reduction efficiency requirement of 95% in the full range of engine operations, the engines also use an in-cylinder technique for NOx reduction, i.e. cooled EGR (Fig. 3.1) (Pantow, 2010).

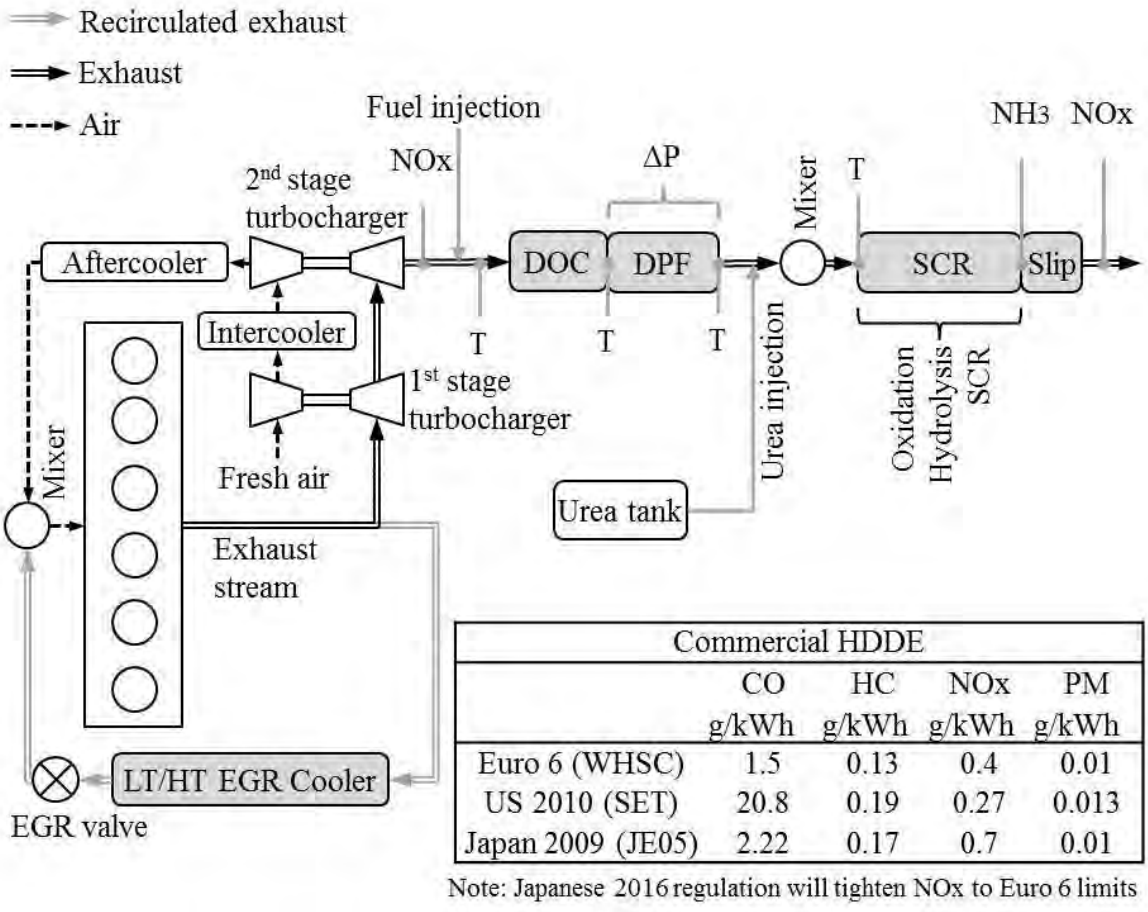

Commercial HDDE	CO g/kWh	HC g/kWh	NOx g/kWh	PM g/kWh
Euro 6 (WHSC)	1.5	0.13	0.4	0.01
US 2010 (SET)	20.8	0.19	0.27	0.013
Japan 2009 (JE05)	2.22	0.17	0.7	0.01

Note: Japanese 2016 regulation will tighten NOx to Euro 6 limits

Figure 3.1 HDDE emissions reduction platform with combined in-cylinder and after-treatment techniques, also shown are the emission standards in EU, US and Japan

DPF, SCR and EGR all incur a varying level of direct or indirect fuel penalty. DPF and SCR use additional fuel/reductant and both raise the exhaust backpressure, while EGR reduces the combustion efficiency. As such, HDDEs have only seen a modest improvement in BSFC over the last decade. The on-board diagnostic requirements for HDDE platforms require the deployment of multiple sensor technologies to provide both alarms and closed loop controls for emissions control (Fig. 3.1) (Stanton, 2013, MECA, 2007). The majority of HDDE platforms also have two-stage turbocharges (inter-cooled and after-cooled, Fig. 3.1) and high pressure, common rail, flexible fuel injection (>2000 bar) (US NAS, 2010).

DPF require active regenerations where a small mist of fuel is injected to raise temperatures to the level required (>600°C) to combust the trapped PM into CO_2 (this CO_2 is usually <0.1% emitted by the engine) (Zhang, 2009). As a result, PM emissions can be reduced by more than 95% at a cost of ≈£4200 for a typical HDDE (US NAS, 2010, US DOE, 2008).

In a SCR system, a small quantity of an aqueous urea solution is sprayed into the exhaust stream where it decomposes to form ammonia (NH_3) and CO_2. NH_3 then reacts with NOx across the SCR catalyst to be reduced into N_2 and H_2O (Arney et al., 2011). The efficiency for SCR catalysts depends on the various fuels, gas constituents, catalyst geometry and NO_2/NOx ratio, but is capable of reducing NOx emissions from 85-95% (Johnson, 2009, MECA, 2007). Higher efficiency SCR system allows higher engine out NOx level, and hence, improved combustion efficiency and a better fuel economy. However, gram for gram, the use of urea has about 2-3 times more CO_2 contribution than Diesel fuel (Johnson, 2009).

An attractive solution in reducing NOx emissions will be to alter the combustion process such that engine-out emissions are at levels which remove or reduce the requirement for NOx after-treatment with a low impact on engine efficiency. The cooling and recirculation of a fraction of the exhaust gas back into the engine intake is a well-established means for NOx reduction (Moore, 2003). Typical Diesel exhaust contains higher levels of CO_2 (10 vs. 4%) and the mixture has higher specific heat (1.15 vs. 1 kJ/kgK, mainly due to higher CO_2 and H_2O levels) compared to atmospheric air. Recirculated exhaust gas lowers the amount of O_2 available for combustion (lowers the effective AFR) and increases the specific heat of the intake mixture. As a consequence, this has the effect of lowering the average combustion temperature. Since NOx formation occurs due to the presence of N_2 and O_2 combined with high temperature (>1800°C), the reduction of temperature in the combustion chamber lowers the amount of NOx produced (Dec, 2009, Zheng et al., 2004). However, the lower O_2 concentration, the lower average combustion temperature and the slower rate of combustion leads to increased fuel consumption and increased PM emissions (Schnitzler, 2007). The reduced rate of PM oxidation/re-burning results in increased carbon deposits and wear of the various vital engine parts along with a more frequent DPF active regenerations (Agarwal et al., 2011). Nevertheless, with high levels of EGR (35-45%), NOx emissions can be reduced by up to 85-95%.

To achieve the 0.4 g/kWh Euro 6 NOx limit, the technology package shown in Fig. 3.1 can be used with different calibrations and after-treatment efficiencies. These are termed as EGR focused platform, where a smaller SCR unit is used with higher EGR rates (typically at Euro 5 level), and SCR focused platform, where a larger SCR unit is used with lower rates of EGR (typically at Euro 4 level). It is also possible to achieve the 0.4 g/kWh using only EGR or SCR. Fig. 3.2 summarises the 4 possible platforms to meet Euro 6 emission targets for HDDEs. The major challenges across all 4 platforms are similar: durability,

weight, powertrain cost (i.e. engine + NOx technology), operational cost of the NOx technology and fuel penalty. As the EGR only platform requires Euro 6 EGR rates, it was abbreviated as E6. Similarly, EGR focused, SCR focused and SCR only platforms were abbreviated as E5, E4, and E0, respectively based on the EGR rates. (For supplementary information on after-treatment, refer Appendix 3.1).

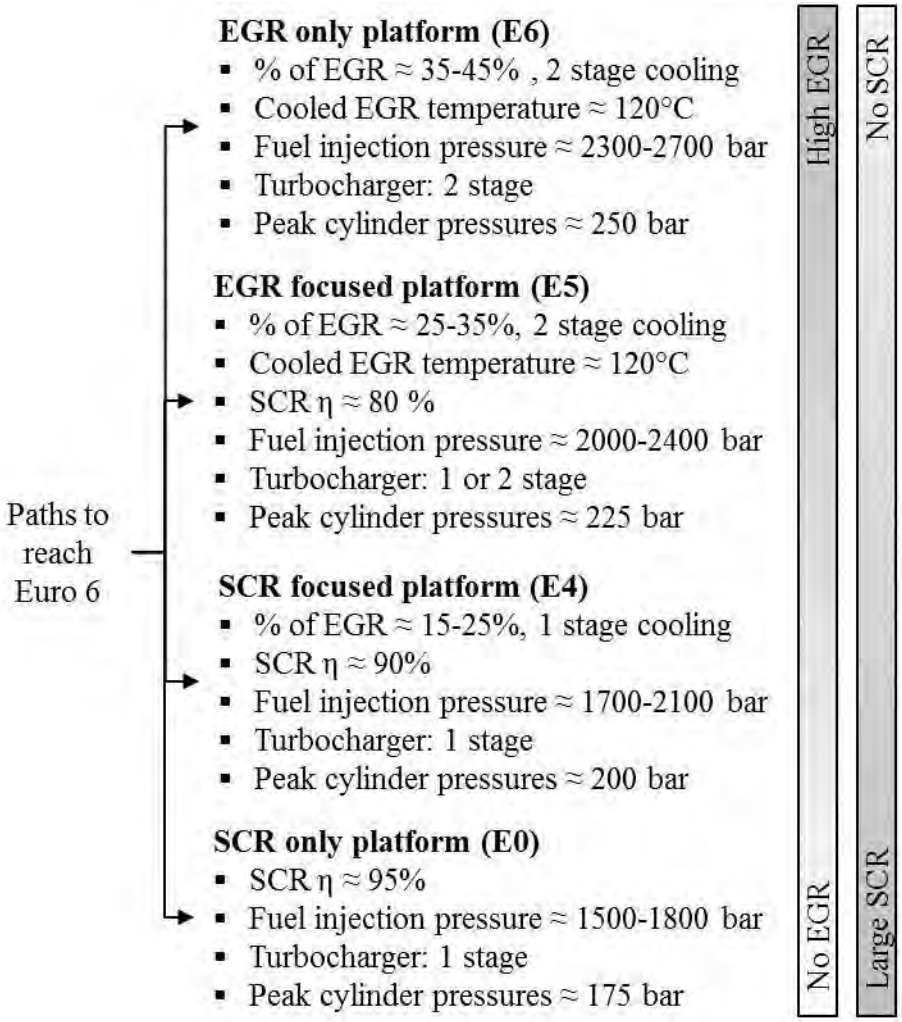

Figure 3.2 Paths to reach Euro 6 - engine and platform architecture

3.3 Fuel penalty to reach Euro 6 emissions

To quantify the impact on fuel consumption for the 4 platforms (Fig. 3.2), published literature and available steady-state data from a 2.02L single cylinder research engine (referred as 2L engine) installed at the University of Brighton were used. This 2L engine was representative of cylinder specifications for a truck application. The goals of the project on this 2L engine were to investigate the potential trade-off between BTE and regulated emissions using variable rates of EGR (SHRL, 2010a, SHRL, 2010b). High pressure (>2000 bar), common rail, fuel injection equipment was used to partly compensate for the increase in PM emissions due to the increased EGR rates. The test bed

schematic and instrumentation is presented in Fig. 3.3, whereas the 2L engine and test bed specifications are given in Table 3.1.

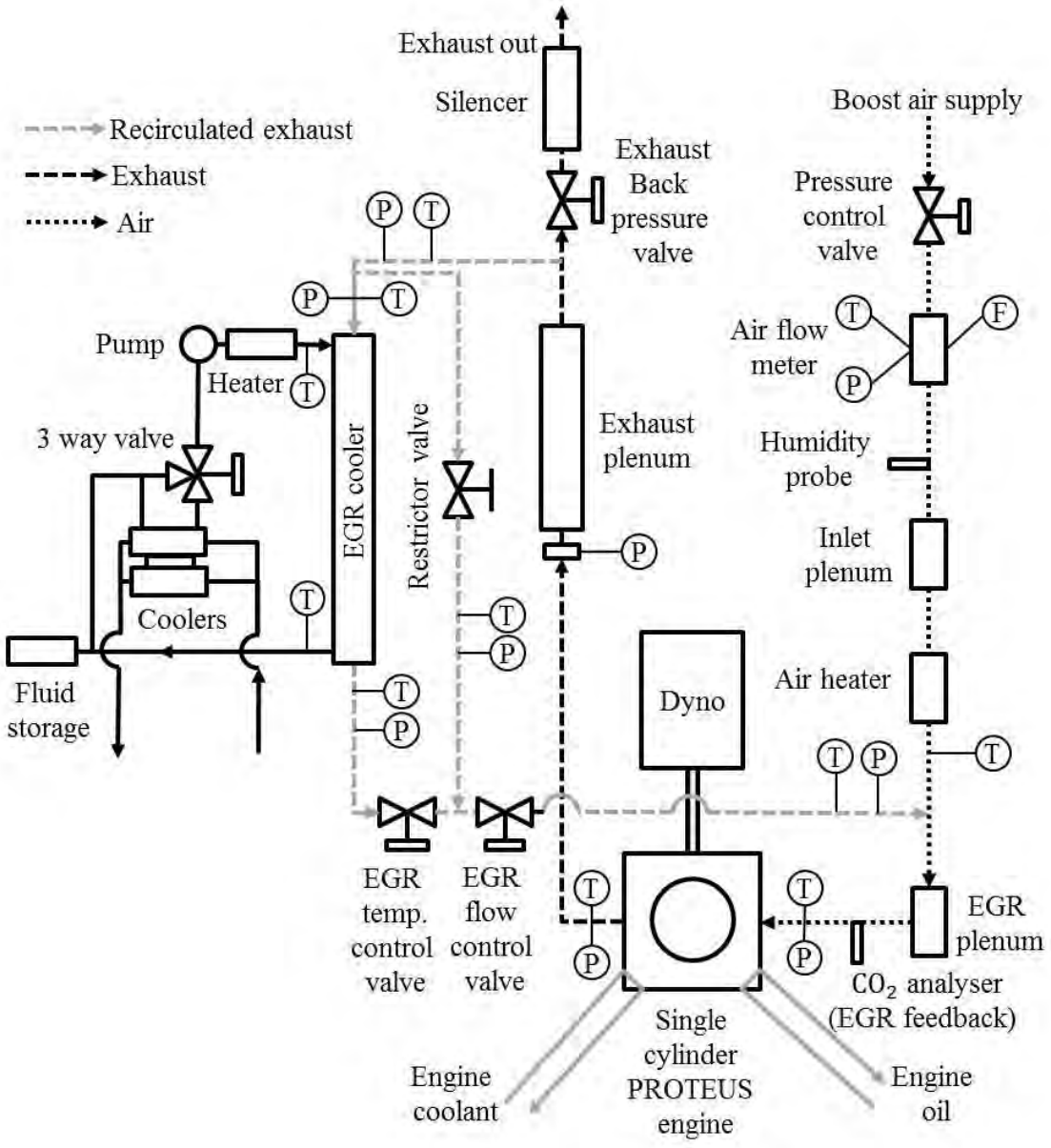

Figure 3.3 Schematic layout of the 2L engine test bed with P,T positions

Table 3.1 2L engine and test bed specifications

Cylinder/Valves	1/4
Bore/Stroke	131/150 mm
Displacement	2.02L
Compression ratio	15.77:1
Max torque	400 Nm @ 1100-1300 rpm
Max power	60 kW @ 1800 rpm
Max in-cylinder pressure	250 bar
Intake valve	Opening (45° BTDC); diameter (40 mm); lift (12.68 mm); duration (245°)
Exhaust valve	Opening (5° BBDC); diameter (40 mm); lift (11.61 mm); duration (240°)
Max inlet pressure	5 bar
Inlet boost air system	Stand-alone compressor
Temperatures measurements	k-type thermocouples
Pressure transducers	Druck PMP 317
Inlet air mass flow rate	Viscous flow air meter Cussons 113 H; Differential pressure indicator Meriam 1500-DN0020
Fuel injection system	Direct injection Delphi F2 ultra high pressure (up to 3000 bar) common rail; Fuel rail oil cooling 70-80°C; Multiple injections up to 3; NOTE: Results presented in this work are bases on single injection
Fuel flow	AVL fuel meter 733
EGR	Control: Exhaust backpressure valve (Apex 4000 pneumatic positioner); Measurement: Intake CO_2 measurement was used to calculate the EGR %; Coolant: Water; Exhaust gas heat exchanger: BOWMAN
Achievable NOx limit using EGR	Euro 6 (0.4 g/kWh)
Dynamometer	Mawdsley 335N DC motor/generator
Emissions measurment	AVL smoke meter 415 (presented as the Filter Smoke Number, FSN); Horiba MEXA 7170 (NOx, HC, CO, CO_2)
In-cylinder pressure	Kistler 6041, AVL QC34C
Combustion data logger	Indiset 620
Controller and data acquisition	Controller: Schenk 3000; Data acquisition: Schenk T2000
High speed data logger	AVL Indiset with AVL optical encoder
Oil	Mobil XOM 15w/40
Engine coolant	50% antifreeze/50% deionised water; Temperature at engine inlet 85°C
Fuel	ULSD
Piston bowl	Low swirl head
Averaged signals	200 cycles of data was collected and the data was averaged for each crank angle degree

Fig. 3.4 presents the BSFC results from the 2L engine at mid-speed mid-load (B50). Point 1 represents Euro 4 NOx limit (3.5 g/kWh), which was achieved using ≈20% EGR rate. Increasing the EGR rate to ≈30% to meet the Euro 5 NOx limit (2 g/kWh, point 2), a 2% BSFC penalty was experienced. Finally, with EGR rates of ≈40%, Euro 6 NOx limit (0.4 g/kWh, point 3) was achieved with a total of 6% BSFC penalty. EGR only platform (with advanced injection timing) inherit the drawback of increasing BSFC, and without compensating measures offset the realisation of CO_2 emission targets. Fig. 3.4 also shows the measured Filter Smoke Number (FSN), which increased sharply from near zero value at Euro 5 limit to 2.5 at Euro 6 limit even when using injection pressures of 2500 bar.

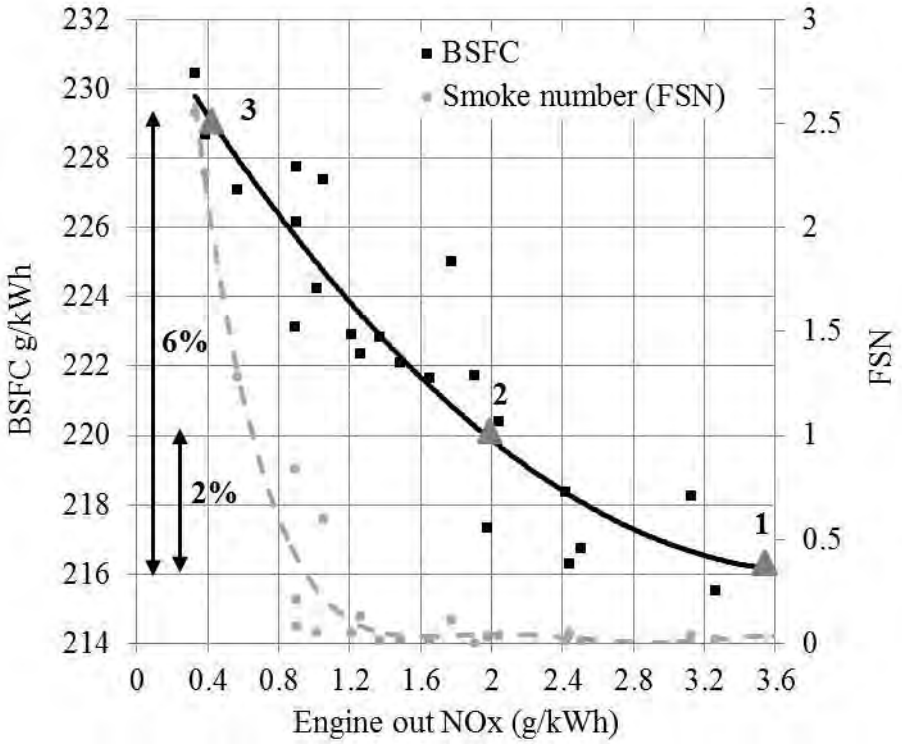

Figure 3.4 Impact of increasing EGR on BSFC at B50 with 2500 bar injection pressure

Fig. 3.5 depicts the final difference in fuel economy for the 4 platforms at Euro 6 NOx limit (Fig. 3.2) using an engine with low rates of EGR (15-25%) meeting the Euro 4 NOx limit as the baseline (point A). The SCR focused platform builds up on the low EGR baseline engine using a highly efficient SCR (≈90%). The use of urea, which depends on vehicle operation, duty cycle, geography, load rating etc. must be accounted for in the calculations of net fuel consumption in engines using SCR. For a SCR focused platform, a urea consumption rate of 3.5% was estimated (A→B) (Assumption, Urea : Diesel cost = 1 : 0.75) (Hill et al., 2011). The cost and weight for the high efficiency larger SCR unit was projected to be around £5760 and 150 kg, respectively (US NAS, 2010).

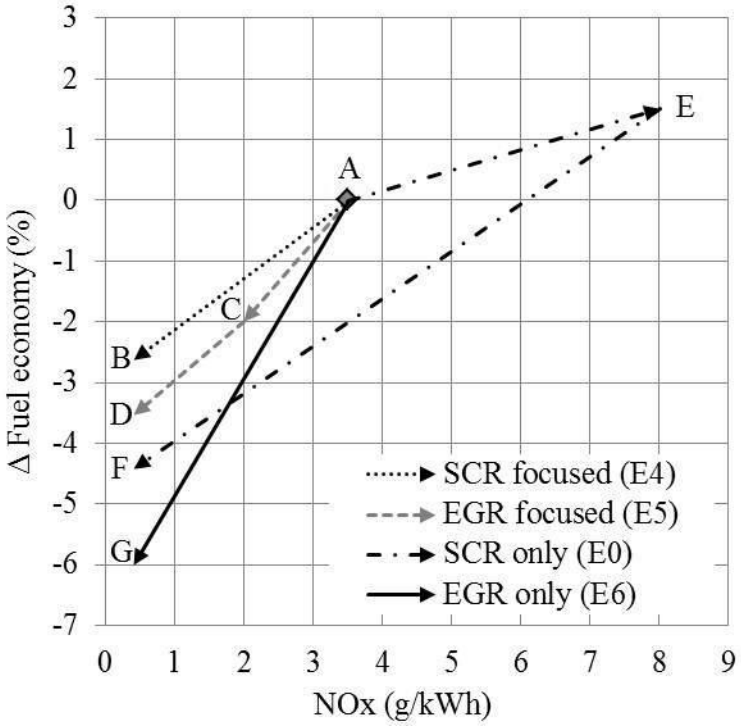

Figure 3.5 Paths to reach Euro 6 - fuel economy impact for the 4 platforms

The EGR focused platform builds up on the baseline engine by switching the EGR rates to higher levels (25-35%) and using a lower efficiency SCR (≈80%). The use of higher EGR rates resulted in a 2% penalty (A→C). Urea penalty for the smaller lower efficiency SCR unit was estimated to be 2% (C→D) (Hill et al., 2011). The cost of the SCR unit delivering the 80% conversion efficiency was expected to be ≈£2800 (Teng and Regner, 2009).

TNO automotive have proposed a full body corrugated vanadium close-coupled SCR only concept (Cloudt et al., 2009a, Cloudt et al., 2009b). This relied on the addition of a small SCR catalyst that benefited from rapid heat up and high temperatures through placement close to the turbocharger turbine outlet. A second larger SCR catalyst that reduced larger part of the NOx emissions followed this. Downstream the larger SCR catalyst was the DOC+DPF and urea was only dosed at a single point upstream of the small SCR catalyst. The SCR only platform allowed the in-cylinder engine efficiency to improve by ≈1.5% (A→E). The recalibrated engine with no EGR however resulted in high engine out NOx emissions (≈8 g/kWh). To reach the Euro 6 and US 2010 NOx requirements, the combined SCR unit has to deliver 95% and 97% conversion efficiencies, respectively. The high conversion efficiencies of the unit required over different operating conditions and the lifetime of the catalyst are ambitious. The fuel penalty due to increased urea consumption and higher backpressures was ≈8% (E→F), potentially cancelling the fuel saving targeted by opting for a SCR only platform. This base engine enabled greater power density, however the weight of the SCR unit was expected to be highest (>180 kg).

The EGR only platform, which utilises a two-stage low temperature EGR cooler, incorporates a highly efficient DOC+DPF downstream of the turbocharger turbine. To accomplish the Euro 6 NOx limit, EGR rates of 35-45% are needed, and an even higher upper limit of 50% is required for the US 2010 limit. A study by Behr on a 10.5L engine showed that a two-stage low temperature EGR cooling only engine gave similar fuel economy to a SCR only engine (urea consumption included) for NOx levels up to 1.7 g/kWh (Krüger et al., 2008). The required cooling performance in this work was achieved via optimisation of the cooling system without an increase in the fan power requirement. However, as can be seen in Fig. 3.4, there is a sharp increase in the engine BSFC moving from Euro 5 limit (point 2) to Euro 6 limit (point 3) using EGR. Incurring a 6% fuel economy penalty from the base engine, the EGR only engine performance resulted at point G (Fig. 3.5). Apart from the higher BSFC, the three biggest drawbacks of the EGR only platform are the highest DPF fuel penalty, the highest load on the engine cooling module and the need of ultra-high fuel injection pressures (>2300 bar). Despite these drawbacks, EGR only platforms are stated to offer advantages like lower vehicle weight, lesser maintenance and lower operating cost (US DOE, 2011). The estimated cost and weight of the additional low temperature EGR cooler that cools the stream from ≈165°C to ≈105°C was only £450 and 18 kg, respectively (Cooper et al., 2009). Furthermore, the adoption of a multiple injection strategy at Euro 6 engine out NOx limit have shown to reduce PM emissions by as much as 40% compared to single injection (Banks et al., 2010).

From the fuel economy analysis presented in Fig. 3.5, it can be concluded that an effective strategy for balancing fuel economy and NOx reduction appears to be the use of combined EGR and SCR. Although the SCR focused platform offered the best fuel economy at Euro 6 limit, the EGR focused platform was selected. This was since, for the stringent US 2010 NOx limit, the SCR focused platform required a much higher efficiency SCR (92 vs. 87%). Whereas, the EGR focused platform with 25-35% EGR rates and 80-87% efficient SCR proficiently complied with Euro 6 and US 2010 emissions over the full range of engine operations. Hence, being universal, the EGR focused platform was selected for FBC analysis. Furthermore, the EGR only and the SCR only platforms may be least suited to the tighter US 2010 NOx limit.

3.4 EGR only platform with waste heat recovery

Future HDDE platforms with FBCs will have a significant effect on thermal management requirements. FBCs delivering overall conversion efficiencies of 10-15% would mean that 85-90% of the heat recovered from the tailpipe exhaust has to be rejected by the engine cooling module. For this, larger and more efficient radiators and condensers along with more powerful fans are necessary.

Data from Fig. 3.5 indicates that an EGR only platform by itself conflicts with the market requirements for improved fuel consumption. However, the application of FBCs to high rates of EGR, the source of highest quality and large quantity heat source will not only generate additional power but will also reduce the load on the engine cooling module. As such, the drawback of one cycle will become a benefit when combined with an appropriate second cycle. Furthermore, WHR systems are predominantly viewed as a separate add-on technology for increasing net power. However, an EGR only platform with WHR may incorporate the FBC as an integral part of the overall platform. An EGR only platform with FBC then offers a systems approach in meeting conflicting requirements of simultaneously in-cylinder NOx reduction and increasing net power.

HDDE vehicles are increasing in cost primarily due to emissions after-treatment equipment (DPF and SCR), which cost ≈£10,200, roughly equivalent to the cost of a long-haul engine (US NAS, 2010). Assuming equal levels of complexity, cost and weight penalty by the FBC system across all 4 different platforms, the EGR only + FBC platform may then result in the least complex and lowest cost solution. Hence, the EGR only platform was the second platform selected for FBC investigations in this thesis.

Another challenge with the SCR platforms is the high reactivity of ammonia with copper (Cole-Parmer, accessed on 10.10.2014). Therefore, exhaust heat exchanger placed downstream of the SCR system have to be constructed with non-ammonia reactive materials.

3.5 EGR focused and EGR only engine strategies

In order to run a truck engine model with the in-cylinder NOx reduction rates of the 2 platforms selected, data from the above mentioned 2L engine were used. Table 3.2 shows the experimentally derived steady-state NOx strategies from the 2L engine leading to engine out NOx levels for the EGR focused (<2 g/kWh) and EGR only (<0.4 g/kWh)

platforms at 4 engine operating points. For all the test points, FSN was kept below 0.3 and 3 for EGR focused and EGR only platforms, respectively.

The 4 operating speed/load points were selected because they would allow the assessment of FBC performance under varying heat quality/quantity conditions. These points covered varying levels of weighting factors in the European Stationary Cycle (ESC, Fig. 3.6) (DieselNet, 2000a) and also represented typical HDDE engine operating conditions. The A50 and B50 points were particularly relevant regarding fuel consumption, as it represented motorway cruise conditions. These two points could also provide an initial insight for the rural and motorway segments of the European Transient Cycle (ETC, Appendix 3.2) (DieselNet, 2000b). However, for accurate results under real world driving conditions, a detailed transient WHR analysis under ETC is needed. In addition, a point representing the high-speed and full-load condition (C100) was selected to investigate the influence of increased heat quality/quantity on process integration.

Table 3.2 Steady-state NOx strategies derived experimentally from the 2L engine

	Inlet temperature (°C)	Inlet pressure (bar)	EGR (%)	AFR	Fuel rail pressure (bar)	Start of injection (°ATDC)	Injection duration (°CA)
E5 (EGR focused)							
A50	58	2.5	32	22.4	2016	-2	9
A70	70	4	35	24.3	2014	-2	13
B50	58	2.7	33	27.1	2522	-3	8
C100	55	4	25	28.1	2200	-10	28
E6 (EGR only)							
A50	68	2.7	43	18.7	3034	-2	8
A70	70	4	43	21.1	2013	-2	13
B50	66	2.7	42	22.1	2523	-3	8
C100	69	4.8	35	24.6	2270	-5	31
A = 1300 rpm (low speed), B =1500 (medium speed), C = 1800 (high speed) 50 = mid load, 70 = high load, 100 = full load NOTE: A70 is approximated as A75 in ESC and SET							

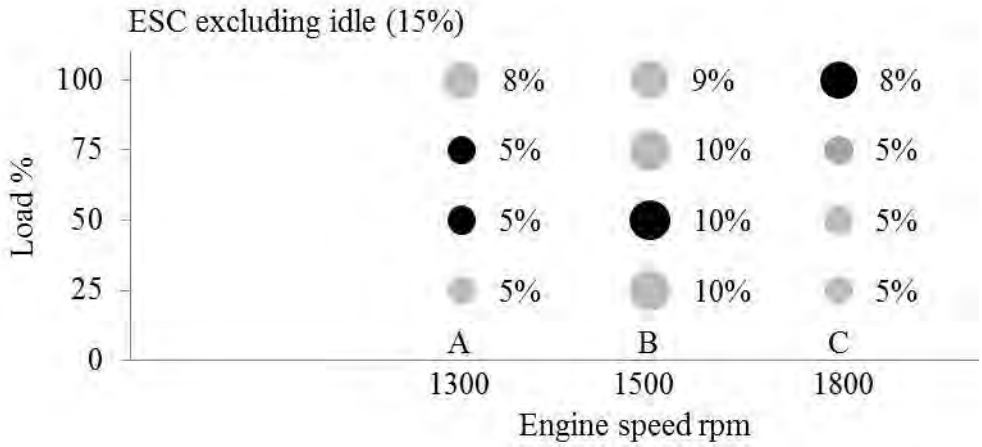

Figure 3.6 European stationary cycle with percentage of time duration (selected points for WHR represented by black markers)

3.6 2L and 10L engine models

To construct a truck engine model, the 2L engine was reproduced as a 2L model, and then the 2L model was scaled up to produce a 10L model. The 2L and 10L engine modelling was done using the 1D engine and gas dynamics simulation software package, Ricardo WAVE V8.1 (Ricardo Software, 2008b). To ensure the 2L model shown in Fig. 3.7 was an appropriate representation of the 2L engine test-bed, the model was constructed acquiring detailed engine, intake, exhaust and EGR system geometries (Appendix 3.3). The 2L and 10L engine models used multi-component Wiebe combustion, Chen-Flynn friction and Woschni heat transfer sub-models, all of which varied with engine speed (Ricardo Software, 2008a). The combustion sub-model used the 10, 50 and 90% fuel mass burned vs. crank angle locations derived from the 2L engines data logger.

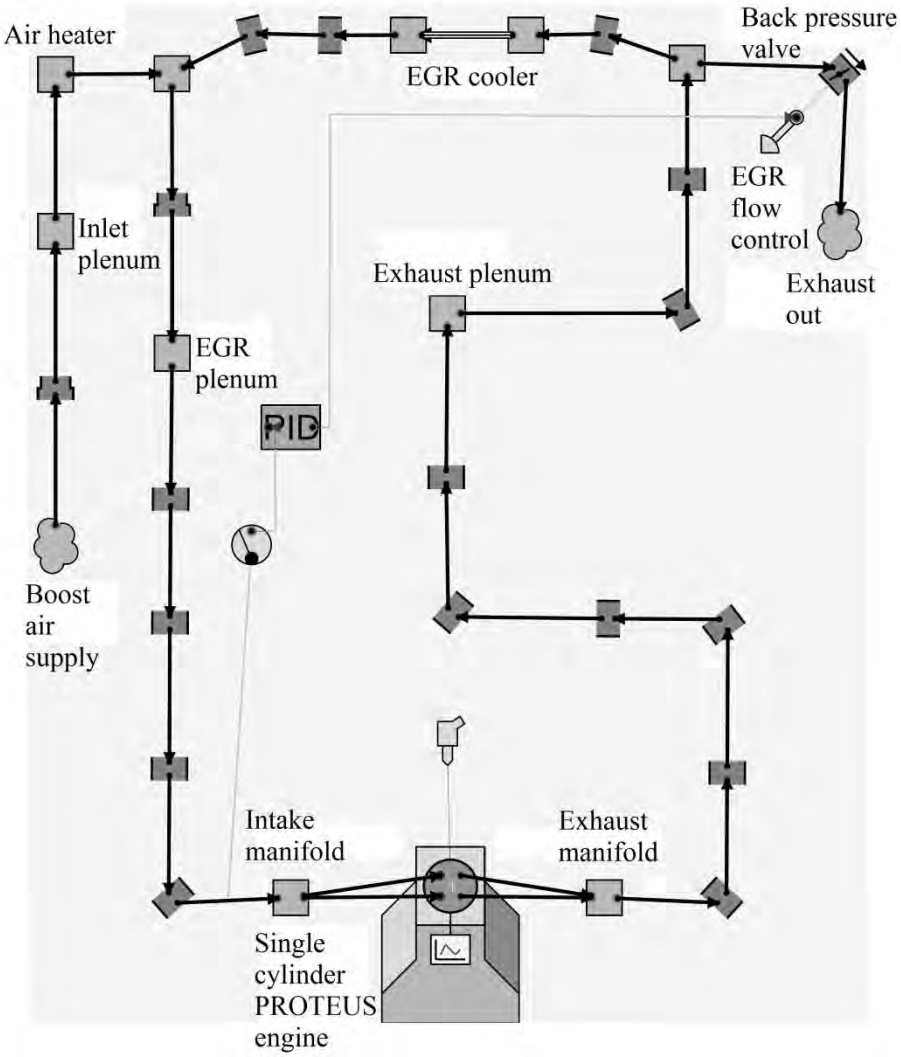

Figure 3.7 2L WAVE engine model with intake, exhaust and EGR system

To generate waste heat qualities and quantities representative of a truck engine the scaled up 10L model was produced (Fig. 3.8). The model included the addition of a two-stage turbocharging system and modifications to the manifolds and engine friction to make the platform more representative of a production vehicle. Both the EGR focused 10L platform and EGR only 10L platform looked similar in the virtual environment (excluding SCR), however, they differed in the compressor and turbine sizing, size and flow rates of the EGR cooler, and fuel injection pressures. To find the appropriate size of compressors and turbines, turbomatching was done for both the platforms. This was predominantly done at low-speed high-load conditions since this was where the charging became problematic because of low compressor speeds and higher mass flow requirements. The desired EGR flow was controlled using a VGT (2^{nd} stage unit) and the boost pressure was regulated by the wastegate of the fixed geometry turbine (1^{st} stage unit). At B50 due to low inlet pressure requirement the 2^{nd} stage unit was bypassed, whereas at C100 both units operated in series. Steady-state turbocharger maps within the WAVE package constructed using rotational speed, pressure ratio, mass flow rate and efficiency were used. In Fig. 3.8 an

optional exhaust heat exchanger is also shown, this was used to recover the large tail pipe waste heat.

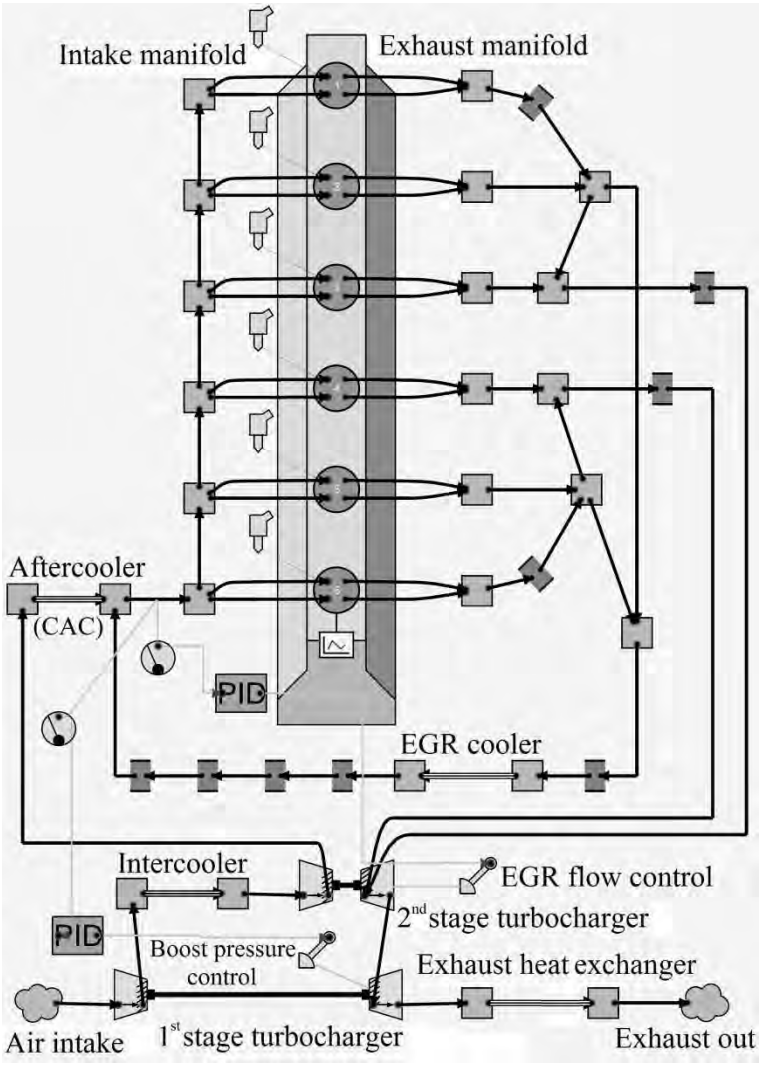

Figure 3.8 10L WAVE engine model with two-stage turbocharging and EGR system

After the construction of the engine models, a detailed validation process was conducted to judge their accuracy and reliability for WHR analysis. The main results of the validation process were intake/exhaust qualities/quantities and normalised engine performance. The simulation results were therefore compared with the experimental results from the 2L engine over the selected 8 points.

Fig. 3.9a and b shows the match with engine intake and exhaust qualities, respectively. The left side of the graph represents the EGR focused values whereas the right side of the graph represents the EGR only values. The intake temperature values obtained from the models and the 2L engine appeared to correlate rather well (within ±3°C, Fig. 3.9a). Engine inlet temperatures were controlled using the heat exchanger sub-models (inter-, after-, EGR) using prescribed heat exchanger performances. The exhaust temperature predicted by the

simulation was found to be within ±15°C for 6 out of the 8 points and within ±30°C for all the 8 points (Fig. 3.9b). EGR inlet temperatures were not calibrated due to a profoundly different EGR loop length and geometry for the 2L engine and the 10L model. The 10L model also used the WAVE structural conduction and heat transfer (Colburn analogy) sub-models for engine and manifold cooling, respectively (Ricardo Software, 2008a). As a guide, the 10L EGR inlet temperatures were up to 50°C cooler than the exhaust manifold temperatures with the non-insulated exhaust ports, exhaust runners and the EGR system employed in this thesis.

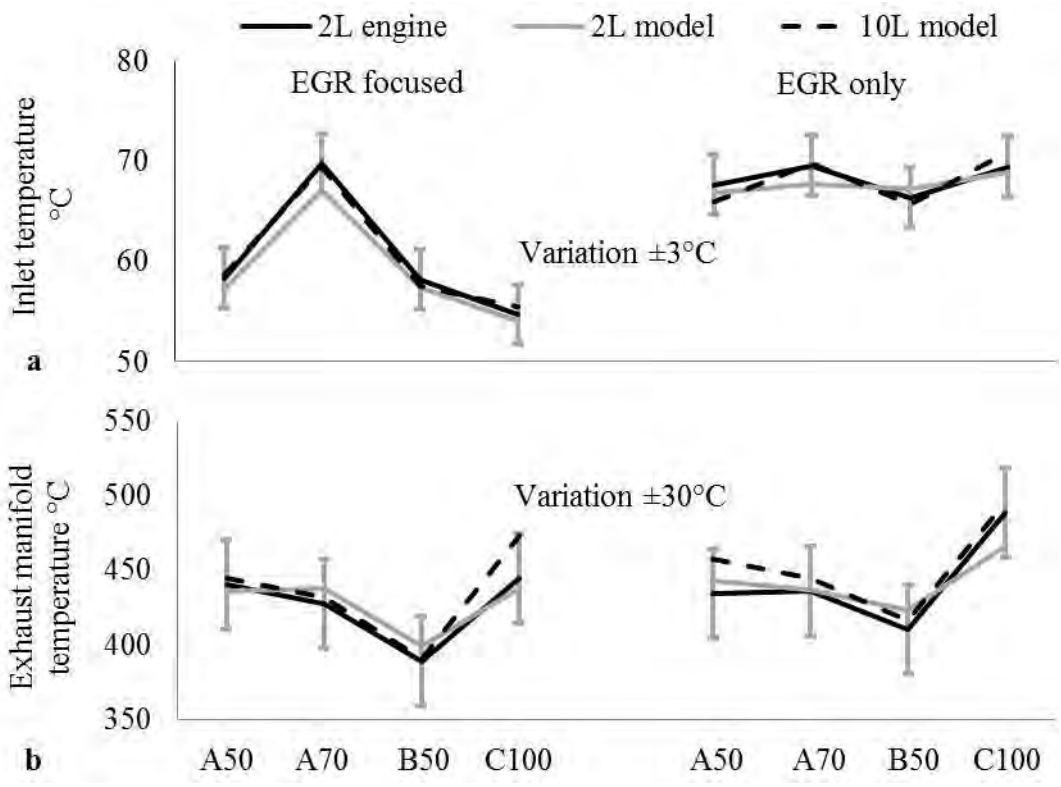

Figure 3.9 2L engine, 2L model and 10L model quality match (a) intake manifold (b) exhaust manifold

For waste heat quantities, the EGR fraction (Fig. 3.10a) and the relative exhaust and air flow (Fig. 3.10b) showed extremely high accuracy control using PID controllers. As 1D models are limited when modelling the exhaust gas chemical composition (especially NOx), matching the EGR rate is vital as the NOx characteristics of the model will then be closer to those of the engine (Fröjd et al., 2011).

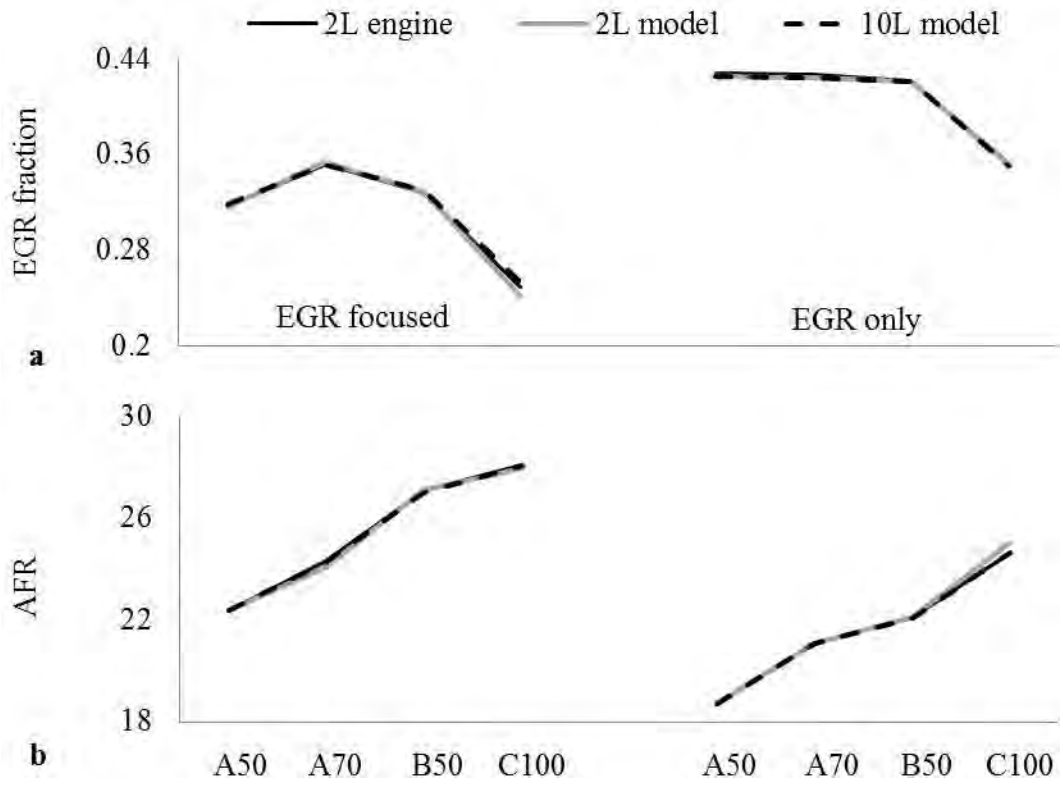

Figure 3.10 2L engine, 2L model and 10L model quantity match (a) EGR fraction (b) AFR

Fig. 3.11a and b shows the comparison of simulation results to measured normalised power and torque, respectively. The 2L model showed only ±5% discrepancy in the results with the 2L engine for both curves. The 10L model which used a different friction sub-model, offered overall lower friction per cylinder, and hence, slightly improved power and torque results (up to 7%). The good agreement between the 2L engine and the 10L model suggested that the 10L model results could be used with high confidence to explore FBCs.

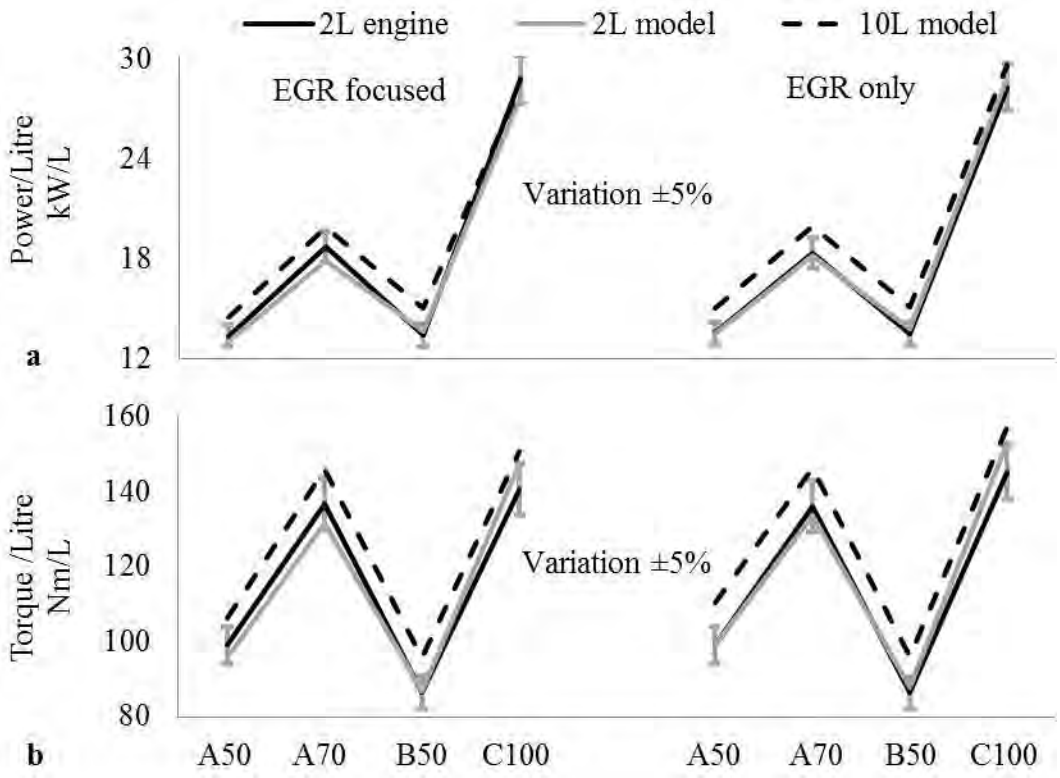

Figure 3.11 2L engine, 2L model and 10L model normalised performance match (a) power (b) torque

Two points relating to the waste heat qualities worth mentioning here are the effect of the two-stage turbochargers and the high rates of EGR. A number of WHR studies used an independent boost system (as was the case for the 2L engine) to provide high inlet pressures. This then resulted in higher than practical post-aftertreatment exhaust temperatures of actual vehicles, and should not be directly used for WHR analysis. As the power needed for boost pressure was extracted from the exhaust, the use of the two-stage turbochargers showed a 100°C decrease in the post-turbine exhaust gas quality on average (Fig. 3.12a). This reduced quality also had an effect on the SCR efficiency for the EGR focused platform. As such, assuming an average 300°C exhaust temperature at the SCR entrance, a 22L catalyst volume was required to provide the 80% NOx conversion efficiency for a NO_2/NOx window of 0.2 to 0.62 (Cloudt et al., 2009b). Hence, the reduced and much more realistic tail pipe temperatures were employed in this thesis.

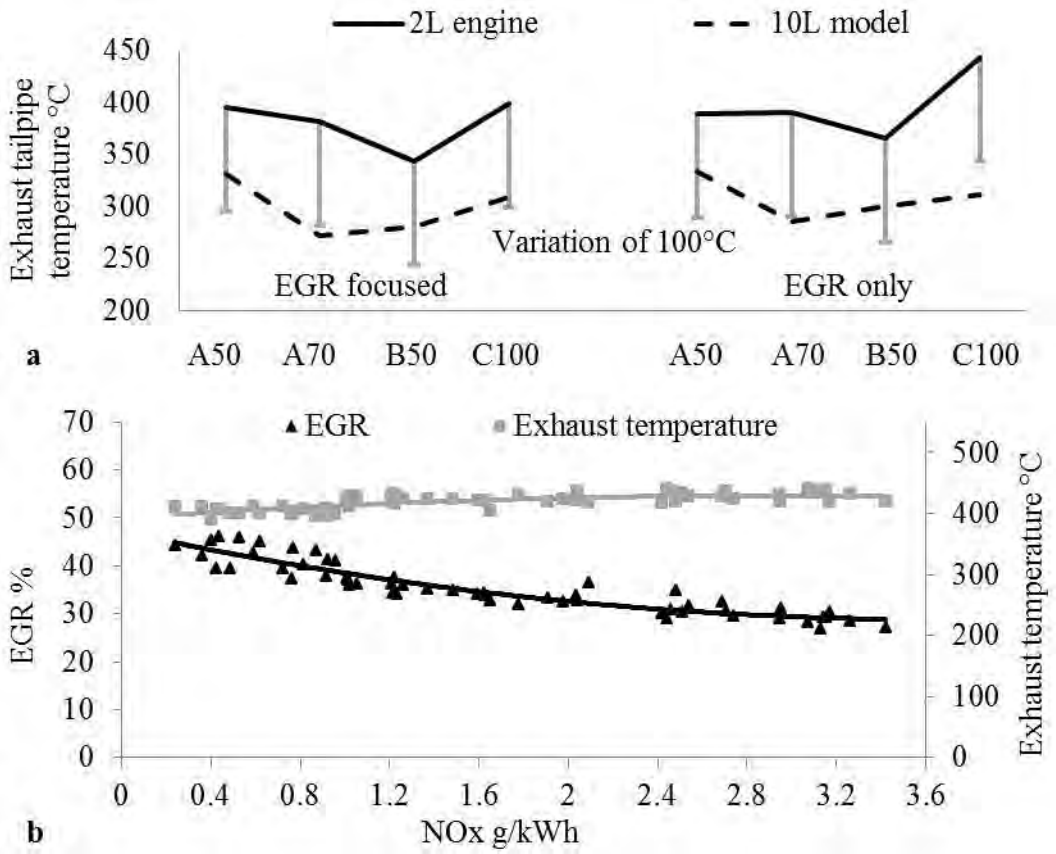

Figure 3.12 (a) reduced tailpipe exhaust quality due to the use of turbochargers (b) negligible reduction in exhaust manifold temperatures due to the use of the high EGR rate strategy

Regarding the use of EGR, it was pointed out that a high EGR rate engine should not be coupled with systems that extract exhaust energy (US NAS, 2010). This is because low temperature combustion reduces the temperature of the exhaust exiting the cylinder. However, high rates of EGR are also accompanied with advanced injection timing delaying the combustion and heat release. As such, results from the 2L engine at B50 showed an exhaust temperature reduction of no greater than 25°C when increasing the EGR rates from 25 to 45% (Fig. 3.12b). Hence, the effect of the high EGR strategy used in this work on exhaust quality was minimal and was used in parallel with WHR techniques. In fact, high EGR rate studies by AVL showed a net increase in exhaust temperatures (Teng et al., 2006).

3.7 Heat source selection

The knowledge of the temperature levels of the various HDDE sources and sinks are essential for WHR analysis. For potential heat sources, EGR, exhaust, CAC (i.e. after-cooler), inter-cooler and engine coolant streams were investigated in terms of energy and exergy content. The stream assessment was also based on:

- Composition
- Engine speed/load
- Impact on engine cooling module
- Minimum allowed temperature
- Emission calibrations
- Barriers and other logistics

Equation 3.1 describes the fuel combustion process according to the conservation of energy.

$$\dot{m}_{fuel}H_{LHV} + \dot{m}_{air}h_{air} = \dot{W}_{brake} + \dot{W}_{friction} + \dot{Q}_{EGR} + \dot{Q}_{exhaust} + \dot{Q}_{CAC} + \dot{Q}_{\mathrm{I/C}} + \dot{Q}_{coolant} + \dot{Q}_{other} \quad \ldots (3.1)$$

Where, H_{LHV} is the lower heating value of the fuel (kJ/kg, reference state 20°C and 1 bar), h is the inlet enthalpy (kJ/kg), $\dot{m}$ is the mass flow rate, $\dot{W}$ is the power produced or lost (kW) and $\dot{Q}$ is the heat rejected (kW). Using results of the 10L engine simulations, Appendix 3.4 provides the energy balance of the two selected engine platforms at the 4 test points. Furthermore, Appendix 3.5 details the waste heat qualities and quantities in the different heat exchanger streams along with the engine performance data.

The energy content ($\dot{Q}_{source,}kW$) of a stream is a function of mass flow rate ($\dot{m}_{source,}kg/s$), specific heat at constant temperature ($c_{p,source,}kJ/kgK$) and temperature entering and leaving the device (ΔT). As the exhaust gas chemical composition determines the specific heat of the EGR and exhaust streams, the exhaust gas composition derived from the 2L engine was used directly. The mean composition of the exhaust gas based on mass fraction used to evaluate the gas properties were: N_2 71%, CO_2 16%, H_2O 7% and O_2 6% ($c_p = 1.17kJ/kgK$). Other minor components contained in the exhaust gas were ignored for WHR analysis. The percent point variation of composition across different speed/load points were N_2 ±2, CO_2 ±2, H_2O ±1.5 and O_2 ±1.5, resulting in a specific heat variation of only ±2%.

The higher CO_2 and H_2O content in the exhaust gases of the selected platforms offered the advantage of higher thermal conductivity ($\lambda, W/mK$) and specific heat values, but also made the cooled EGR and exhaust streams more susceptible to condensation (corrosion and fouling). This then affects the heat recovery process, heat exchanger design, material selection and cost. With the stream condensation starting in a range of 91-93°C, the heat

recovery was limited to maintain a minimum EGR and exhaust temperature of at least 95°C. To provide a 30°C safety margin prior to condensation, EGR and exhaust stream cooling up to only 125°C was also considered.

Apart from the quantity of waste heat, the maximum work potential analysis in order to account for variations in waste heat temperatures was also conducted. The maximum work potential represents the maximum possible reversible work that can be extracted from a heat engine operating between the source and sink temperatures. Ignoring changes in the kinetic, potential and chemical exergy, equation 3.2 describes the physical exergy (E) which is the maximum useful work that can be obtained from a system at a given state (x) in a specified environment (0).

$$E_x = (h_x - h_0) - T_0 (s_x - s_0) \ldots (3.2)$$

Where, h and s are the enthalpy (kJ/kg) and entropy (kJ/kgK), respectively. According to the calculation of the exergy of heat available at a given temperature, the exergy content to classify the energy quality of the stream is then expressed as equation 3.3 (Wang et al., 2012).

$$\dot{E}_{source} = \dot{Q}_{source} \left[1 - \frac{T_0}{T_{max}} \right] \ldots (3.3)$$

Where, T_{max} is the maximum source temperature and $\dot{Q}_{source}$ is the heat quantity. The reference temperature at the dead state (0) was set at 20°C. Note that the concept of physical exergy (as represented in equation 3.2), will be further extended in Section 4.3 due to its usefulness in analysing system losses in a FBC.

3.7.1 Exhaust gas recirculation and post-turbine exhaust

Fig. 3.13a and b represents the relative energy and exergy content of the heat sources, respectively. It is evident that the EGR and post-turbine exhaust were ideal choices for both the EGR focused and EGR only platform offering high energy and exergy contents at 7 out of the 8 test points each. The exhaust temperatures were in the range of 272-335°C and were on average 100°C lower than the EGR temperatures (Appendix 3.5). As the performance of SCR systems decreased sharply below 200-250°C (Edwards et al., 2010), the integration of exhaust heat exchanger was considered downstream of the after-treatment devices. Placement of the exhaust heat exchanger downstream of the DPF reduces the heat exchanger fouling and could also mitigate some of the fuel penalty if a portion of the heat energy released during periodic regeneration events could be recovered. Higher exhaust temperatures that could be greater than 600°C due to regenerations were

not considered in this thesis. Such high temperatures also present control challenges in avoiding organic working fluid decomposition, however, the exhaust heat exchanger still has to be made with special materials meeting the temperature requirements. In this layout, CO_2 emissions dropped in proportion to fuel consumption, with marginal effects on emissions during engine warm up (Sprouse III and Depcik, 2013b). It was assumed that the post-turbine exhaust temperature decreased by a fixed 10°C over the after-treatment devices in all cases. This value was similar to those reported based on test experience by Southwest Research Institute (Cooper et al., 2009).

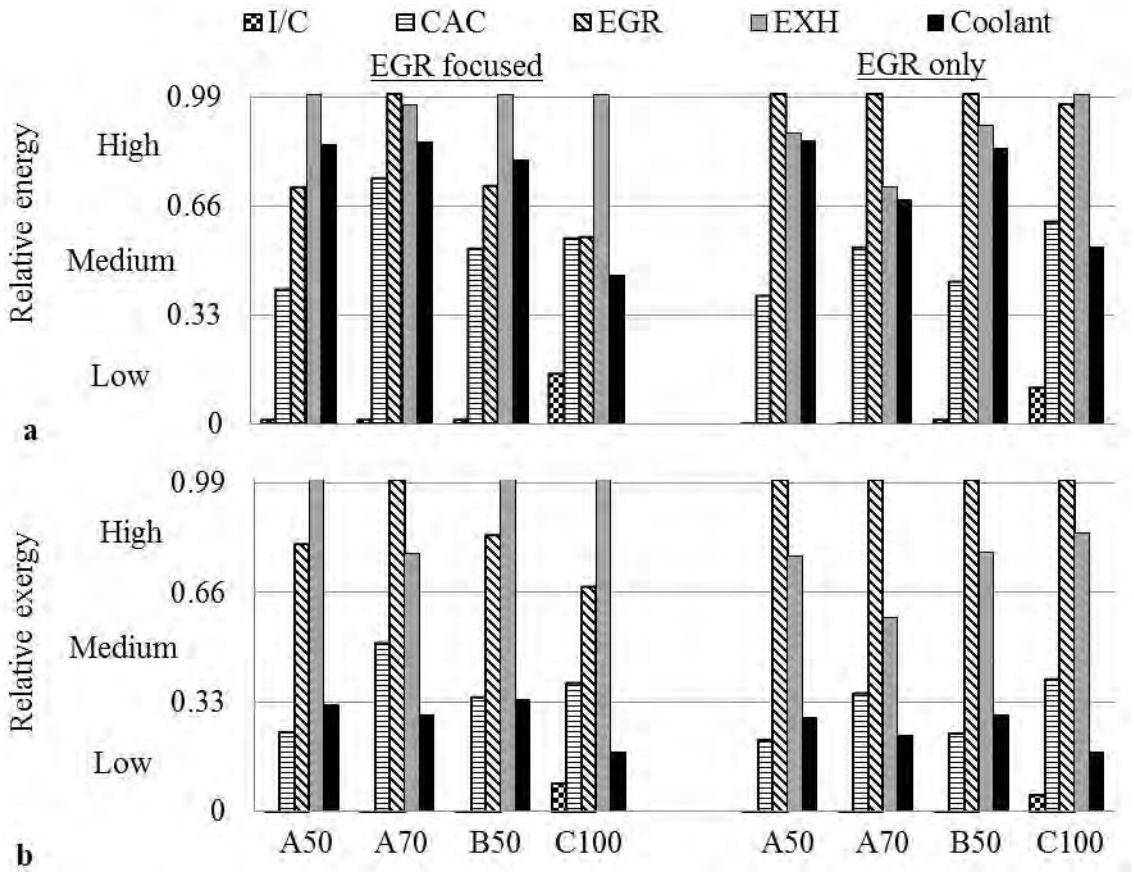

Figure 3.13 Relative (a) energy and (b) exergy content of the heat sources

As the exhaust heat exchanger also impacted the backpressure on the base engine, it was therefore necessary to analyse the change in engine performance. Literature results on whether the exhaust heat exchanger was a limiting factor in increasing the combined engine + FBC performance was contradictory. For LD vehicles, Ford simulations showed the 0.025 bar ΔP in the muffler assembly of the base engine reducing to 0.015 bar in the engine with ORC (Hussain and Brigham, 2010). Whereas, ORNL demonstrated a 0.14 bar increase in backpressure, due to which the base engines BTE reduced from 42.6 to 42.4% (Briggs et al., 2010a). For HD vehicles, NTUA simulations reported a negligible increase in the exhaust backpressure, with a maximum value of 0.022 bar (Katsanos et al., 2010).

However, Behr simulations included a fuel consumption increase of around 1% (Edwards, 2010). Whether the backpressure increased or decreased was dependent on the heat exchanger design. The net reduction in the exhaust line backpressure, despite the marginal increase in the backpressure due to heat exchanger was attributed to the cooling of exhaust stream, and was predominantly mentioned in simulation studies. Nonetheless, more realistic cases where off-the-shelf components were used with the lower exhaust gas quality of HDDEs, a net increase in the backpressure was more likely.

To examine the effect of the exhaust heat exchanger on the 10L model, a maximum pressure drop of 0.1 bar was induced at C100 using friction multipliers in the heat exchanger. The amount of backpressure in the exhaust heat exchanger varied with engine speed and load because the friction and pressure drop across the heat exchanger was flow dependent (Ricardo Software, 2008a). A net reduction of 1.3% at C100 (300 vs. 296 kW) and 0.7% at B50 (152 vs. 151 kW) in engine crankshaft power was calculated. The effect on engine performance was low at cruise conditions and the loss in power was likely to be compensated by the FBC. However, the exhaust heat exchanger was a potential source of inefficiency at higher loads and had to be considered in detail during the process integration phase. These values were higher than those reported by Hossain and Bari (2013), where a loss of ≈0.5% of engine power was shown experimentally at different loads. In order to use off-the-shelf heat exchanger and allow lower development cost for the FBC, combined evaporator-catalyst device as demonstrated by Honda were not considered (Endo et al., 2007).

3.7.2 Charge air cooler

As the exhaust quality of Diesel engines is lower than that of gasoline engines, continued investigation into other heat sources is essential. Since the air cooling in the 10L model was performed in two stages, by by-passing the inter-cooler when only marginal cooling was needed, higher quality and quantity heat loads were made available in CAC. For air temperature exiting 1st stage compressor below 75°C, the inter-cooler was by-passed and the 2nd stage compressor was able to provide the required boost pressure. The high temperature at 2nd stage compressor in engine simulations was limited below 210°C, resulting in hot CAC temperatures between 146-204°C. The required 2nd stage isentropic compressor efficiency was between 75-84%. The selected HDDE platforms used high boost pressures at high loads (4-4.8 bar, Table 3.2), and thus offered medium thermal loads in the CAC (Fig. 3.13a). CAC may be a promising source at higher engine loads, since it was still able to offer medium exergy content (Fig. 3.13b).

Like EGR, CAC is a load on the engine cooling module. Therefore, process integrations that can effectively recover this heat are vital. For FBCs the conventional CAC and EGR coolers will have to be replaced with more suitable higher pressure heat exchangers. If the pressure drop of the charge air and EGR stream can be maintained, then recovering the heat from these two heat sources will not affect the boost pressure or the engine backpressure.

Due to the low boost pressure requirements at typical cruise conditions, the 1st stage compressor was by-passed. As such, the inter-cooler was excluded as a potential source since heat was available only at higher loads (>75%), furthermore with insignificant exergy content (Fig. 3.13).

3.7.3 Engine coolant

The importance of using exergy analysis was most noticeable when considering coolant as a heat source. From an energy perspective, losses through the coolant were substantial, offering medium or high values at 6 out of the 8 test points (Fig. 3.13a). However due to a low temperature of ≈90°C, coolant resulted in low exergy content at all of the 8 test points (Fig. 3.13b). As the coolant temperature difference was typically 10°C across the radiator, large heat exchanger surface area was required to recover this heat. With performance, size and economics favouring higher quality heat recovery, coolant was not considered a suitable source. This also suggested that more focus should be given to architectures that recover heat directly from the engine block where higher temperatures could be achieved.

3.7.4 Stream qualities and quantities used

The performance of FBCs depends on the working fluid entropy changes as well as on the source/sink conditions. For vastly different combinations of temperature levels, there will likely be different optimal working fluids. To identify optimum working fluids, three different waste heat qualities and quantities were considered. Table 3.3 represents the selected EGR, exhaust and CAC temperatures and heat loads. The values presented in the table were averaged over the B50 and C100 operating point for the EGR only platform from Appendix 3.5. With EGR focused platforms source qualities within ±18°C, the conclusion from the fluid selection study will also hold true for this platform.

Table 3.3 EGR, exhaust and CAC temperatures and heat loads for the fluid selection study

Heat source	T_{in} °C	T_{out} °C	$\dot{m}$ kg/s	Heat kW
EGR	427	95	0.19	70
Exhaust	296	95	0.32	70
CAC	176	85	0.435	40

The waste heat qualities and quantities were exported to Aspen HYSYS V7.3 (Aspen Technology, 2011) for detailed FBC analysis. HYSYS is a process modelling software widely used in the chemical and process industries. By interconnecting the unit operations using material, work/heat streams, a complete process flowsheet can be constructed (Aspen HYSYS V 7.3, 2011b). HYSYS also contains physical, chemical and thermodynamic data for a wide variety of chemical compounds, as well as a selection of thermodynamic models required for accurate simulation of a given system (Aspen HYSYS V 7.3, 2011a).

3.8 Heat sink selection

The heat dissipation system is of great importance for FBCs applied to HDDEs because of the relatively lower heat qualities compared to gasoline engines and high sensitivity to temperature variations of the heat sink. Evaluating the practicality of mobile FBCs requires characterising the temperature levels at which the heat can be rejected. To realise synergies between current HDDE cooling modules and FBCs, existing vehicle infrastructures should therefore be considered first.

Fig. 3.14 shows the arrangement of the cooling system for the 10L model. The cooling system comprised of two indirect cooling circuits. The low temperature cooling circuit cooled the LT EGR cooler and the CAC. Such low temperature circuits demonstrated several advantages for indirect CAC, and provided lower EGR and CAC temperatures (Eickels and Müller, 2010, Teng et al., 2007). The Medium Temperature (MT) cooling circuit dissipated heat from the HT EGR cooler, Inter-Cooler (I/C) and engine coolant. As shown in Fig. 3.14, the CAC was divided into two stages, the first was integrated into low temperature circuit and the second covered the remaining cooling process by employing direct air cooling (LT air-air CAC). The coolant (glycol-water) in the low and medium temperature radiators was cooled down to 65 and 90°C, respectively.

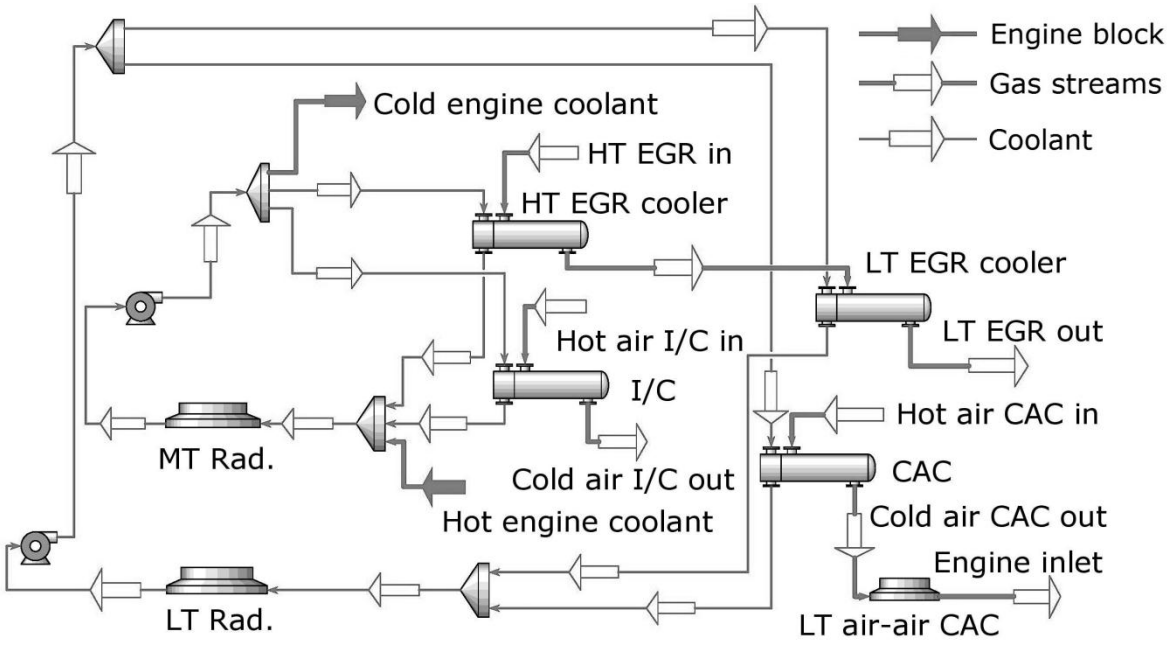

Figure 3.14 Two stage cooling module for the 10L model

From a thermodynamic perspective, the higher the ΔT between source and sink, the higher is the thermodynamic performance of the heat engine. As such, studies using low condensing temperatures (e.g. 28°C) for exhaust heat recovery demonstrated up to 20% BSFC improvement (Hossain and Bari, 2013). Such air cooled condensers, which will be positioned in front of the existing low temperature radiator to recover exhaust heat, may result in insufficient CAC and EGR cooling. To avoid this, the operation of the FBC has to be stopped either when the fan is engaged or when the fan air flow requirement increases significantly.

In reality, when considering BSFC improvement, condenser size and cooling fan power requirements, a trade-off has to be made so as the FBC installation does not lose its feasibility. When recovering CAC and EGR heat by either replacing the current radiators with FBC condensers (direct air-cooled) or adding additional cooling elements (indirect liquid-cooled) to the two radiators a more practical system can be proposed. The indirect liquid-cooled condenser introduces additional heat exchanger and a secondary temperature difference, resulting in a higher system heat exchanger footprint per unit net power. The direct air-cooled condenser requires larger quantities of working fluid. However, it also shows higher potential and was employed in this thesis. Therefore, FBCs using all the three streams (EGR, exhaust, CAC) were considered for a minimum condensing temperature of 65°C.

Achieving the 65°C condensing temperature can be demanding, especially when considering high exhaust heat recovery. However, this situation was a function of vehicle speed/load and ambient conditions. Exhaust heat recovery could be limited by providing an exhaust bypass loop and the cooling load may then be within the engines cooling module capacity. This should also reduce the impact on the engine backpressure. An alternative solution to deal with the additional heat rejection load while recovering exhaust heat was to use an auxiliary high temperature condenser after the medium temperature radiator. Fig. 3.15 schematically represents this engine cooling module. The ambient air was considered at 20°C and air temperature rise through each condenser was limited to 15°C. Therefore, the high temperature condenser was cooled using a heated air stream of 50°C. Using the specified condenser performance, the upper limit for condensing temperature of 105°C was also considered for EGR and exhaust as heat sources. Note that all the condensing temperature levels operated with a 45 or 55°C maximum temperature differential with respect to the cooling air stream.

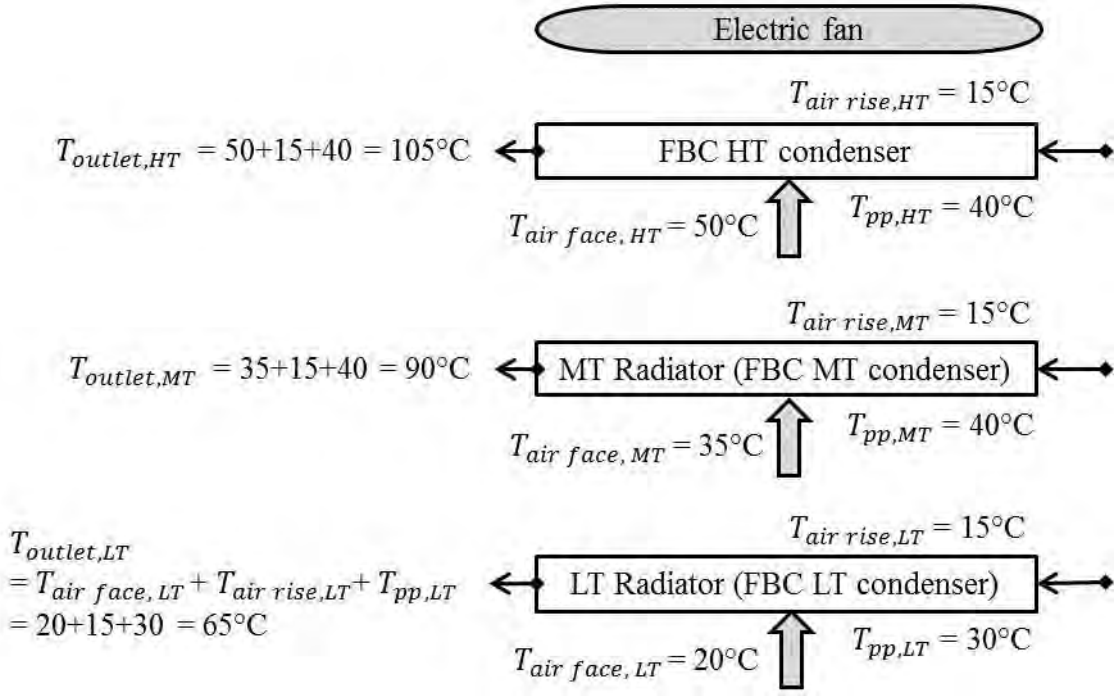

Figure 3.15 Engine cooling module with an additional high temperature condenser, showing radiator (condenser) outlet temperature as a function of air temperature, pinch point and temperature rise through the module

3.9 Chapter 3: Summary and study overview

The fuel economy analysis resulted in the selection of a combined in-cylinder and after-treatment NOx reduction platform for FBC analysis. For research purpose, an alternative route, a systems approach platform with in-cylinder NOx reduction only and FBC was also considered. The EGR focused and EGR only platforms differed in terms of their waste heat quantities. By considering both, it was intended to obtain a wider perspective on FBC process integration and quantify the net BSFC difference between the two combined engine + FBC platforms. Having identified the research themes in Chapter 2, Fig. 3.16 summarises the step-by-step method overview of the thesis. Combining industry specific simulation tools like WAVE for engine modelling and HYSYS for FBC analysis then enabled a wider and more precise simulation of the desired processes.

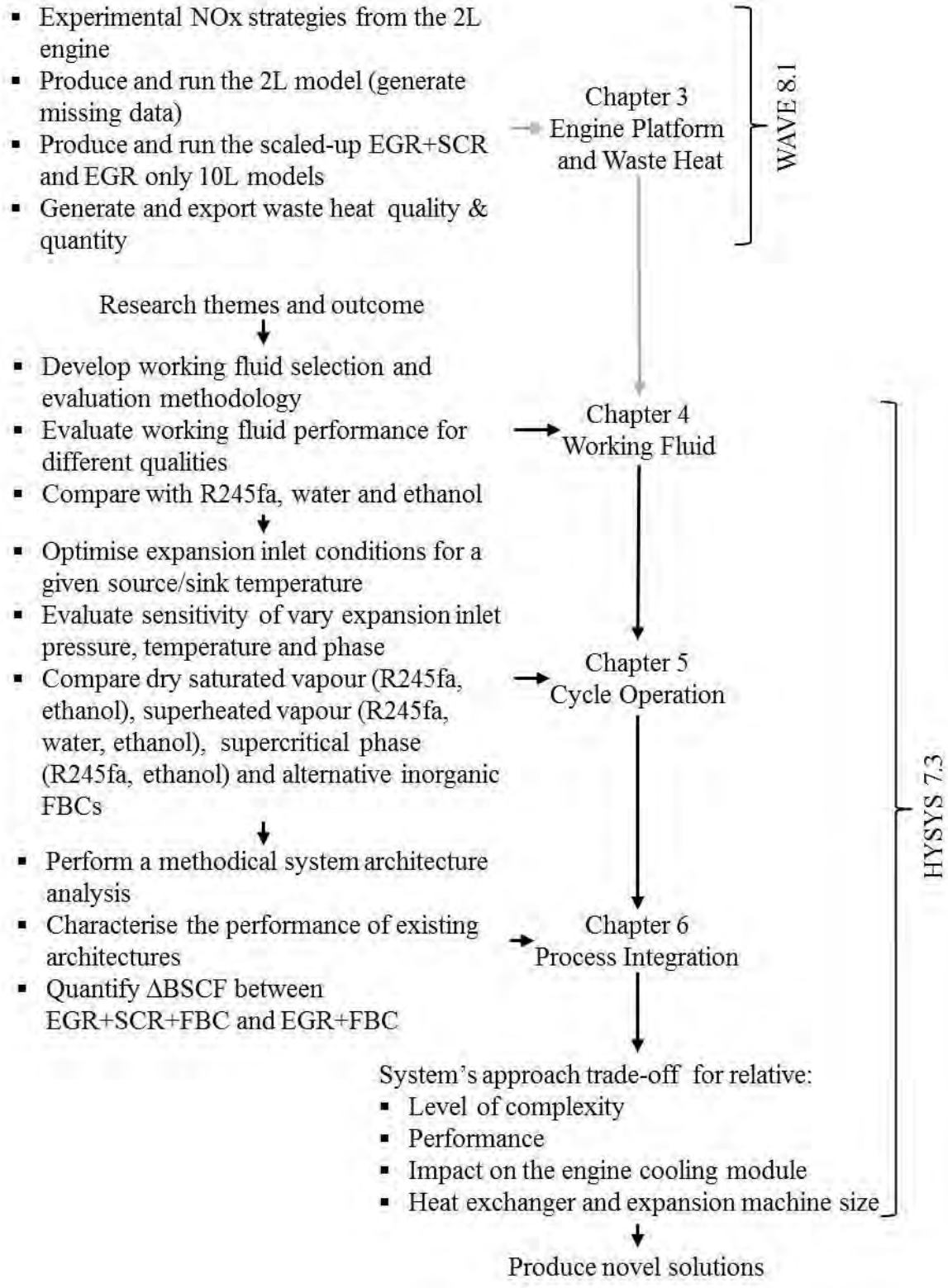

Figure 3.16 Method overview for evaluation of engine-FBC research avenues

4 Working Fluid

4.1 Introduction

The selection of a suitable working fluid for a FBC is the first and the most important step in maximising the system performance, and minimising the system size and cost. Although analytical tools and methodologies that can predict Rankine cycle performance for a given source and sink conditions exist, the equivalent for ORCs is challenged by the large choice of possible working fluids. Furthermore, the published literature reviewed in Chapter 2 regarding methodologies on fluid selection and evaluation is incomplete for automotive HDDEs, and does not show how to appropriately select a fluid suitable to the varying levels of available heat.

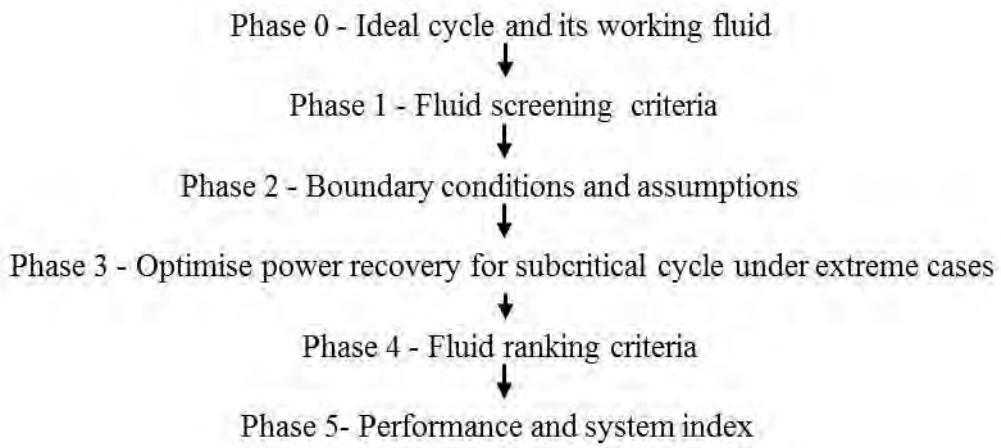

Figure 4.1 Brief overview of the novel fluid selection and evaluation methodology

A detailed study was undertaken to identify adequate working fluids for ORCs using a novel systematic methodology (Fig. 4.1). Following a theoretical overview of the FBC (Phase 0), the fluid screening (Phase 1), which was a function of the thermo-physical, molecular, environmental and safety characteristics was performed based on the fundamental understanding. Using the common boundary conditions and equipment performance assumptions (Phase 2), the ORCs were optimised for maximum overall conversion efficiency (Phase 3). Identifying suitable working fluids based on the developed fluid ranking criteria (Phase 4) involved accounting multiple design and operational features for an objective assessment for different source and sink conditions. Finally, an index was developed (Phase 5) to highlight the favourable working fluids, with the value of this index being a close relation to the practicality of the system.

4.2 Ideal cycle and its working fluid (Phase 0)

A Carnot cycle involves four reversible processes with all the heat exchange taking place at the source (T_{source}) and sink (T_{sink}) temperatures and represents the maximum first law efficiency (η_{carnot}) possible as shown in the T-S diagram in Fig. 4.2a. However, a WHR system as considered in this study utilises finite thermal sources and involves a variable temperature heat addition process. To benchmark a FBC performance against the theoretical maximum, more appropriate limits than those derived from Carnot efficiency are then needed.

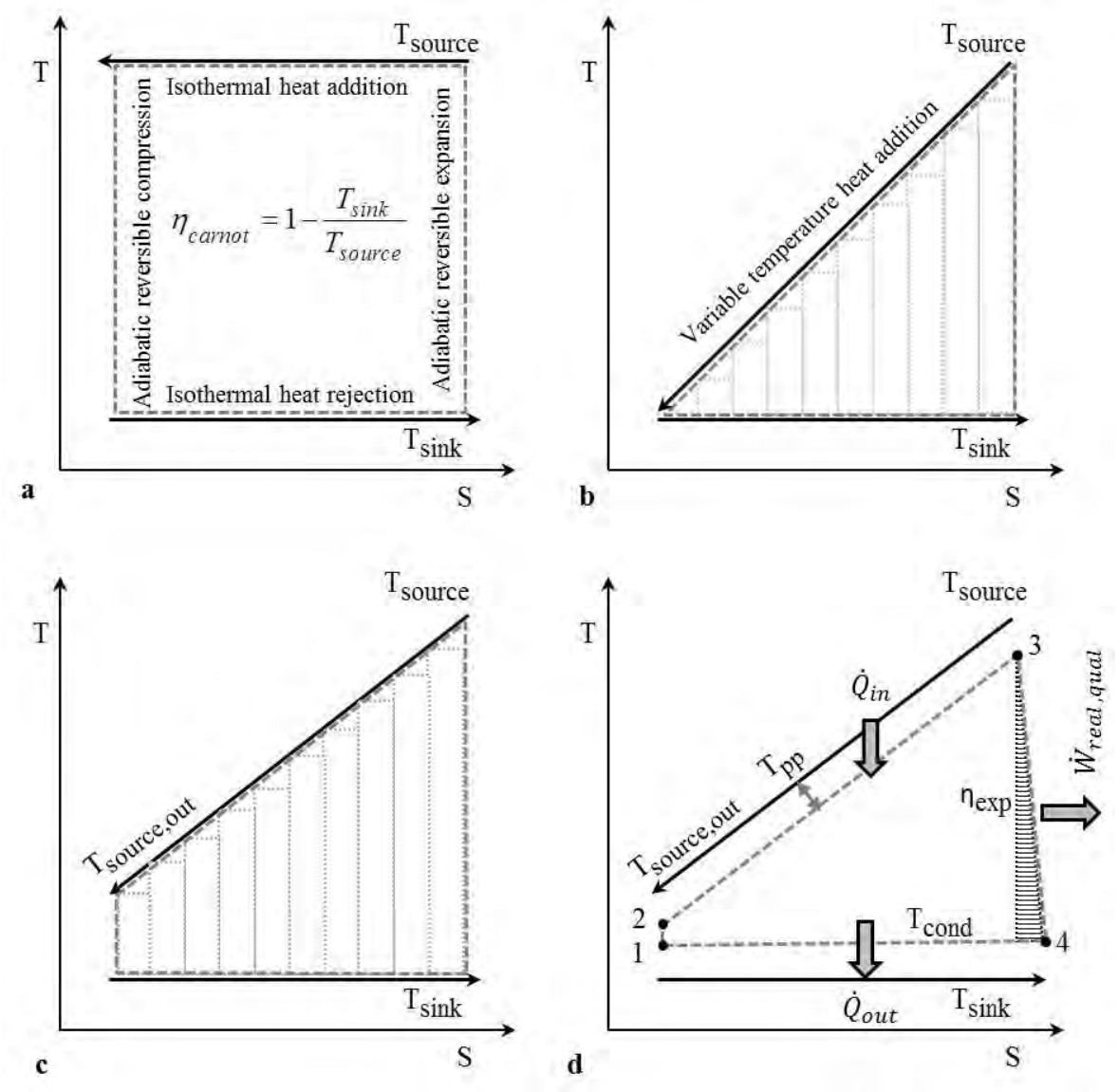

Figure 4.2 T-S diagram evolution from infinite source and sink to finite source and non-ambient condensing (a) Carnot cycle (b) trilateral cycle (c) quadlateral cycle (d) real quadlateral cycle

An ideal system for power recovery under finite source conditions is shown to be equivalent to a succession of infinitesimal Carnot cycles, each operating with a decreasing source temperature (Smith, 1992). These are described as ideal trilateral (Fig. 4.2b) or ideal

quadlateral (Fig. 4.2c), depending on whether the source stream is cooled to the sink or an intermediate temperature ($T_{source,out}$). The ideal trilateral cycle recovers all the available heat by allowing the heat source to be cooled down to the sink temperature. Then, according to Carnot's principle, higher thermal efficiency will be achieved by the ideal quadlateral cycle, whereas the maximum power produced will be by the ideal trilateral cycle.

For ideal trilateral cycle, the thermal efficiency (η_{tri}) is given as:

$$\eta_{tri} = \frac{w_{max}}{q_{max}} \quad \ldots (4.1)$$

Where,

$$w_{max} = \left(h_{source} - h_{sink}\right) - T_{sink}\left(s_{source} - s_{sink}\right) \quad \ldots (4.2)$$

Here, $s_{source} - s_{sink}$ can be integrated to give $c_p \ln\left(T_{source}/T_{sink}\right)$. Since constant heat capacity is assumed, enthalpy differences may be replaced by temperature differences, i.e. $h_{source} - h_{sink}$ can be written as $c_p\left(T_{source} - T_{sink}\right)$.

Hence,

$$w_{max} = c_p\left[\left(T_{source} - T_{sink}\right) - T_{sink}\ln\left(\frac{T_{source}}{T_{sink}}\right)\right] \quad \ldots (4.3)$$

Substituting equation 4.3 and $q_{max} = c_p\left(T_{source} - T_{sink}\right)$ in equation 4.1.

$$\eta_{tri} = 1 - \frac{T_{sink}\ln\left(\frac{T_{source}}{T_{sink}}\right)}{T_{source} - T_{sink}} \quad \ldots (4.4)$$

and maximum work ($\dot{W}_{tri}$) possible is given as:

$$\dot{W}_{tri} = \dot{m}_{source} w_{max} \quad \ldots (4.5)$$

Similarly for quadlateral cycle, work done ($\dot{W}_{quad}$) and thermal efficiency (η_{quad}) are given as:

$$\dot{W}_{quad} = \dot{m}_{source} w_{quad} = \dot{m}_{source} c_p \left[\left(T_{source} - T_{source,out}\right) - T_{sink}\ln\left(\frac{T_{source}}{T_{source,out}}\right)\right] \quad \ldots (4.6)$$

$$\eta_{quad} = 1 - \frac{T_{sink}\ln\left(\frac{T_{source}}{T_{source,out}}\right)}{T_{source} - T_{source,out}} \quad \ldots (4.7)$$

Note for quadlateral cycle, $q_{in} = c_p\left(T_{source} - T_{source,out}\right)$.

A quadlateral cycle that receives heat energy at a high temperature, converts portion of this energy into work, and rejects the remaining heat at a lower temperature is more representative of heat recovery processes in EGR, exhaust and CAC. However, even the ideal quadlateral cycle as shown in Fig. 4.2c cannot be used to establish an upper limit for power and cycle efficiency. This is because the ideal quadlateral cycle performs heat rejection at the sink temperature (i.e. not the condensing temperature T_{cond}), assumes ideal expansion (100% isentropic efficiency η_{exp}) and has a perfect heat transfer (0°C minimum temperature difference, pinch point T_{pp}). However, a real quadlateral cycle includes a condensing temperature higher than sink temperature, heat transfer losses and a non-reversible expansion process with increased entropy as shown in Fig. 4.2d. Neglecting the pumping work the real quadlateral power ($\dot{W}_{real,quad}$) and efficiency ($\eta_{real,quad}$) are then given as:

$$\dot{W}_{real,quad} = \eta_{exp}\dot{m}_{source}c_p\left[\left(\left(T_{source}-T_{pp}\right)-\left(T_{source,out}-T_{pp}\right)\right)-T_{cond}\ln\left(\frac{T_{source}-T_{pp}}{T_{source,out}-T_{pp}}\right)\right] \quad \ldots(4.8)$$

$$\eta_{real,quad} = \frac{\dot{W}_{real,quad}}{\dot{Q}_{in}} \quad \ldots(4.9)$$

Assuming the EGR temperature drop from 427 to 95°C with 30°C overall pinch point, ambient and condensing temperatures of 20 and 65°C respectively, and a 70% efficient expansion, Fig. 4.3 shows the ideal trilateral, ideal quadlateral and real quadlateral cycles in a temperature-thermal duty (T-Q) diagram. This thesis utilises T-Q diagrams in parallel with T-S diagrams to provide additional insight into the ORC processes. In particular, due to the usefulness of the absolute representation of the heat input, heat output and expansion power all on the same axis (Fig. 4.3 vs. Fig. 4.2d). The more realistic T-S and T-Q diagrams of the ORC are introduced later in Section 4.3. Real quadlateral cycle can be used for any source and sink temperatures, with assumed condensing temperature, pinch point in heat exchangers and expansion efficiency (Note $T_{cond} \leq T_{source,out} - T_{pp}$ in equation 4.8).

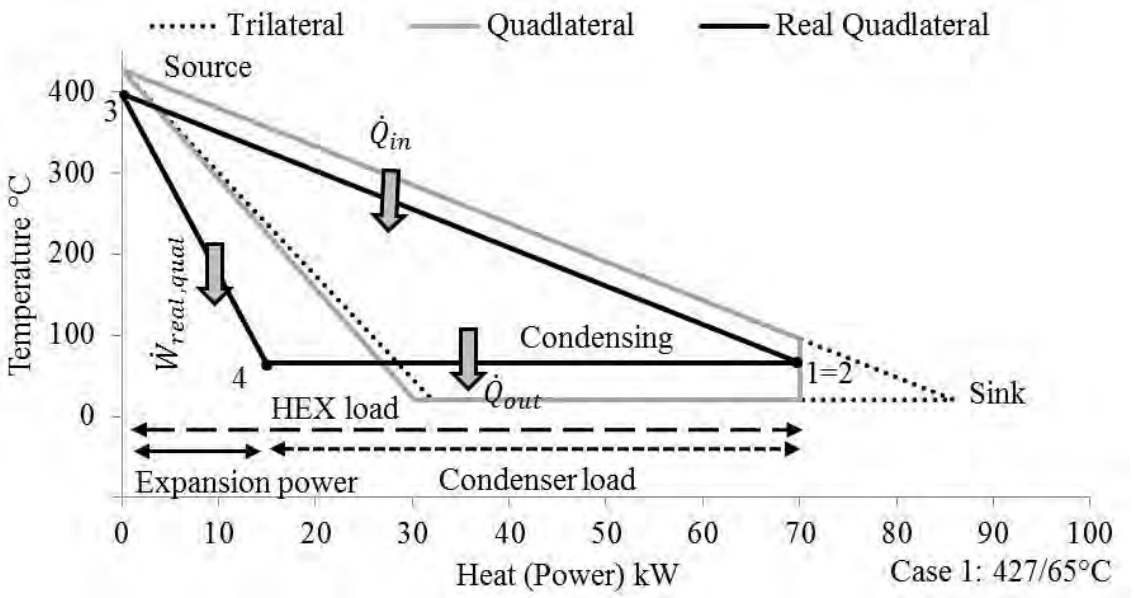

Figure 4.3 T-Q diagram for ideal trilateral, ideal quadlateral and real quadlateral cycles using EGR stream

For higher temperature, i.e. EGR at 427°C and exhaust at 296°C (Table 3.3), the two extreme condensing limits of 65 and 105°C existed (Fig. 3.15). Whereas, for low temperature, i.e. CAC at 176°C a condensing limit of 65°C was preferred. As a result, the 5 cases for the different source and condensing temperature limits that are used in this thesis are given in Table 4.1. Table 4.1 also shows the calculated Carnot, ideal trilateral, ideal quadlateral, real quadlateral efficiencies and real quadlateral power for the 5 cases. (Assumptions: T_{sink}=20°C and η_{exp}=70%). The efficiencies calculated from the real quadlateral cycle were 1/4th to 1/3rd of those derived from Carnot cycle. In the T-S diagram, the thermal efficiency is viewed proportional to the cycle area between the source and sink temperatures. The $\dot{W}_{real,quad}$ values represent a more real upper limit for WHR systems to convert EGR, exhaust and CAC heat into work. The concept of trilateral and quadlateral cycles applies to all indirect WHR cycles. Yet, they have rarely been cited as an upper thermodynamic limit for performance comparison in automotive HDDEs.

Table 4.1 Carnot, ideal trilateral, ideal quadlateral, real quadlateral efficiencies and real quadlateral power for the 5 cases considered

Case		T_{source}/ T_{cond} °C	T_{pp} °C	η_{carnot} %	η_{tri} %	η_{quad} %	$\eta_{real,quad}$ %	$\dot{W}_{real,quad}$ kW
1	EGR	427/65	30	58.1	37.3	43.3	21.2	14.9
2	Exhaust	296/105	20	48.5	29.5	38.8	12.3	7.4
3	CAC	176/65	20	34.7	19.8	27.1	8	3.3
4	EGR	427/105	20	58.1	37.3	45.2	18.6	11.8
5	Exhaust	296/65	30	48.5	29.5	36.5	15.1	10.8

Finally, some characteristics of a working fluid used in a finite heat source can be drawn for a subcritical cycle. Fig. 4.4a and b show an approximation of the working fluid T-S sketch for the Carnot and the real quadlateral cycle. Two noticeable differences are observed, firstly, the relationship between the highest source temperature and the working fluid critical point conditions, and secondly, the ratio between sensible heat and latent heat.

Consider Fig. 4.4b, where the enthalpy of vaporisation for the fluid reduces with increasing evaporating temperature. Beyond the critical point conditions, the liquid and vapour phases no longer co-exist. In order to achieve the trilateral or quadlateral shape the fluid evaporation has to take place near critical point conditions. Therefore, the working fluid necessitates a heat source temperature value higher than the critical temperature. This is contrary to Fig 4.4a, where the change in enthalpy of vaporisation is not a function of temperature, and the critical point can then be higher than the highest heat source temperature.

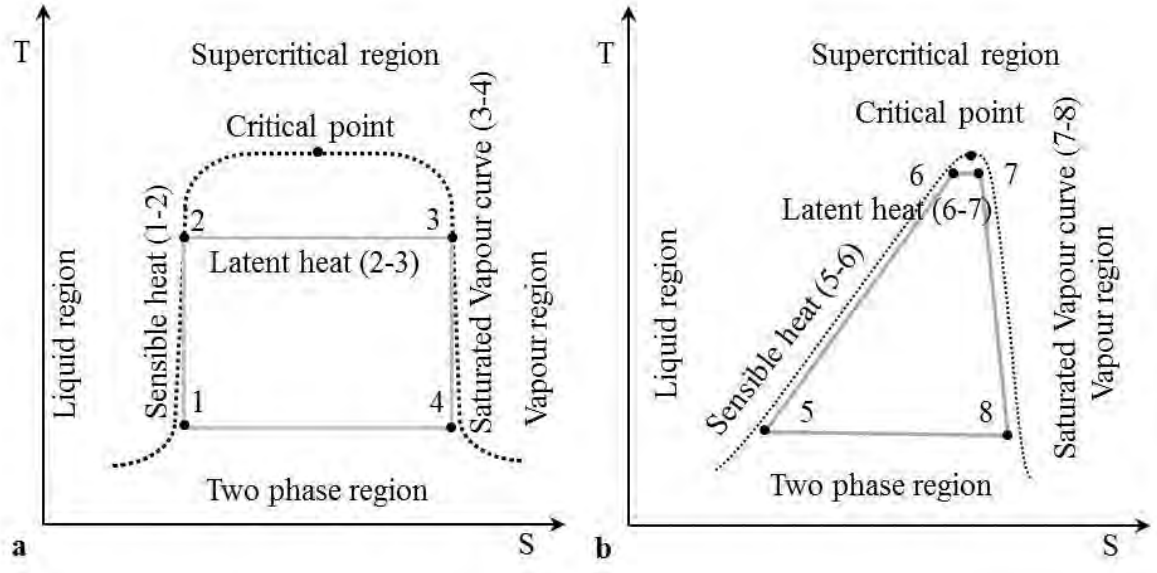

Figure 4.4 Working fluid T-S sketch for (a) infinite (b) finite heat source

The finite heat source then leads to the fundamental difference that is the ratio of sensible heat to latent heat of the working fluid. When considering the fraction of heat transferred in the preheating and evaporating phases, a higher value will result in increased heat recovery efficiency. In other words, the working fluid for a finite heat source has a high sensible heat (5-6) but a low latent heat (6-7), the second characteristic that is different to Fig. 4.4a which requires a value of ≈0.

The common feature that appears in both the cycles is the nearly vertical saturated vapour curve at expansion (3-4, 7-8), the advantages of which will be highlighted later. Therefore, matching a cycle to a finite heat source leads to alternative limits for performance comparison and provides a valuable insight into the required fluid properties at an early stage.

4.2.1 Theoretical parametric analysis

Using the real quadlateral cycle (equation 4.9), the two statements made earlier can be validated and quantified. These being, the exhaust temperature reduction of 25°C when increasing the EGR rates from 25 to 45% has a marginal effect on WHR efficiency, and that the heat dissipation system shows high sensitivity to sink temperatures.

Consider Fig. 4.5, where Pt. 1 refers to the overall conversion efficiency of the real quadlateral cycle using EGR (Case 1: 427/65°C) as calculated in Table 4.1. Keeping all the parameters constant and increasing the EGR temperature by 25°C (Pt. 2) improved the overall conversion efficiency from 21.2 to only 22% (3.5% increase). When this is compared to the equivalent reduction in the condensing temperature (Pt. 3), the overall conversion efficiency improved from 21.2 to 24.8% (14.5% increase). Hence, the power output is 4 times more sensitive to the sink conditions than to the source conditions.

A further parameter variation shown in Fig. 4.5 is the effect of increasing the expansion efficiency. This also serves to stress the importance of realistic design parameters in simulation studies. This thesis uses a fixed isentropic expansion efficiency of 70%, which is much closer to values that a wide variety of dynamic and positive displacement machines can provide up to ±25% of their design condition. Comparing this to a high isentropic expansion efficiency of 85% (Pt. 4) as employed in NTUA simulations (Katsanos et al., 2010), then increased the overall conversion efficiency from 21.2 to 25.7% (17.5% increase). However, components with such high efficiency levels are rare

for the low flow rate, high pressure ratio, less than 30 kW power output conditions, as encountered in the present application.

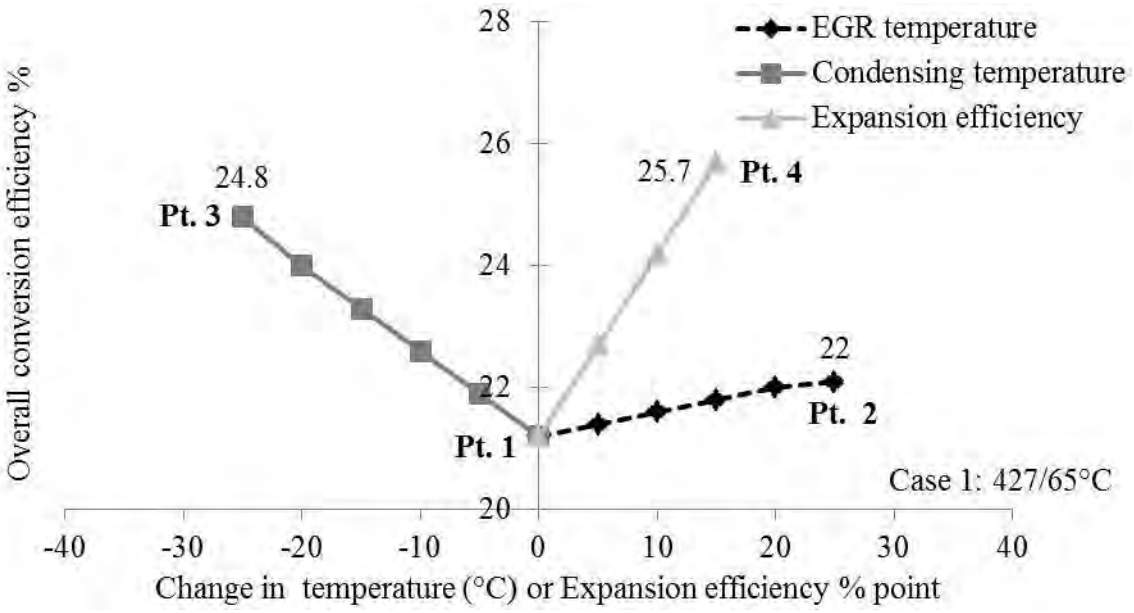

Figure 4.5 Sensitivity analysis to source temperature, condensing temperature and expansion efficiency using real quadlateral cycle

Having identified a more suitable real upper limit for indirect WHR concepts, their theoretical advantage over the direct WHR concepts can further be analysed. Consider the post-turbine exhaust stream which has the characteristics of high temperature (296°C, Table 4.1) and low pressure (1.1 bar). Since the exit pressure in a direct gas expansion cycle downstream the post-turbine ($P_{turbine,out}$) has to be greater than 1 bar, the only way to increase the energy recovery potential is to elevate the stream inlet pressure ($P_{turbine,in}$). Taking into account the induced engine pumping power consumption by the elevated exhaust backpressure, the net overall energy conversion efficiency (η_{direct}) for a direct turbine expansion is given as (Xu et al., 2013):

$$\eta_{direct} = \left[1 - \left(\frac{P_{turbine,out}}{P_{turbine,in}}\right)^{\frac{\gamma-1}{\gamma}}\right] - \left[\frac{\gamma-1}{\gamma}\left(1 - \frac{P_{turbine,out}}{P_{turbine,in}}\right)\right] \quad \ldots(4.10)$$

Where, γ (specific heat ratio) =1.4.

Using real quadlateral cycle value for exhaust stream as baseline (Case 5: 296/65°C), Fig. 4.6 shows the results for the parametric study considering the effect of increased exhaust backpressure on the overall conversion efficiency. Ignoring thermodynamic and flow losses, an elevated exhaust backpressure of 5.5 bar (when $P_{turbine,out}$ =1 bar) was

required for equal performance to the real quadlateral cycle. This backpressure value was based on the theoretical maximum of exhaust gas energy conversion. In reality, when including the isentropic efficiency of a turbine, the process will be around 75% efficient. As such, a much higher backpressure of 8 bar was required for equivalent performance. (Note: real quadlateral already includes T_{pp}=20°C and η_{exp}=70%). Hence, indirect WHR concepts are the more efficient technique for energy conversion and yield considerably higher values at near ambient gas stream pressures.

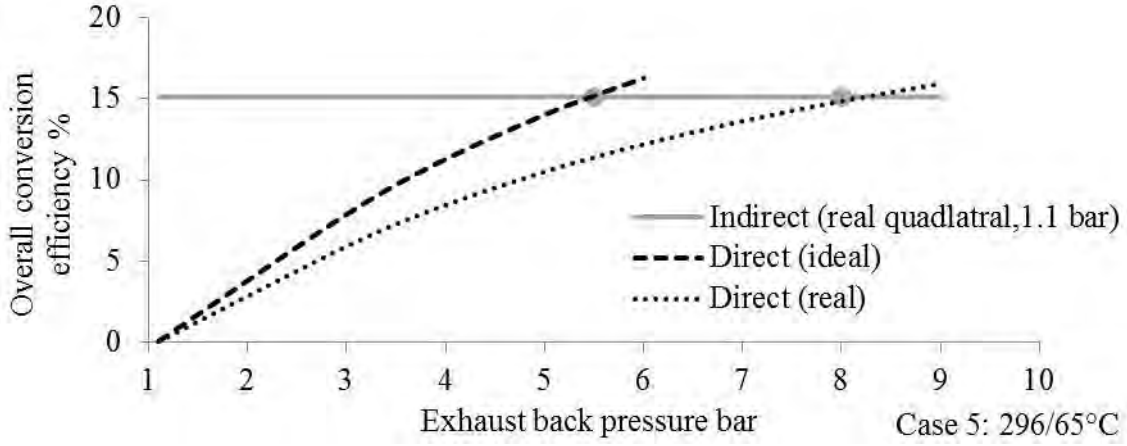

Figure 4.6 Need of high exhaust backpressures in direct WHR methods for increasing overall conversion efficiency

4.3 ORC process and control

This section provides a comprehensive overview of a subcritical ORC process description (Fig. 4.7). Assuming steady-state and steady-flow system, neglecting kinetic and potential energies, the associated energy and exergy balance in the key components are given. Furthermore, the minimum control and flow requirements (Fig. 4.8) to enable the functioning of a unit over start-up and shutdown transients, and the full engine speed and load operating range are discussed. For this, a control unit is required to regulate and monitor pressures, temperatures and mass flow rates so that they are within acceptable ranges for high performance and offer high levels of security for the system components.

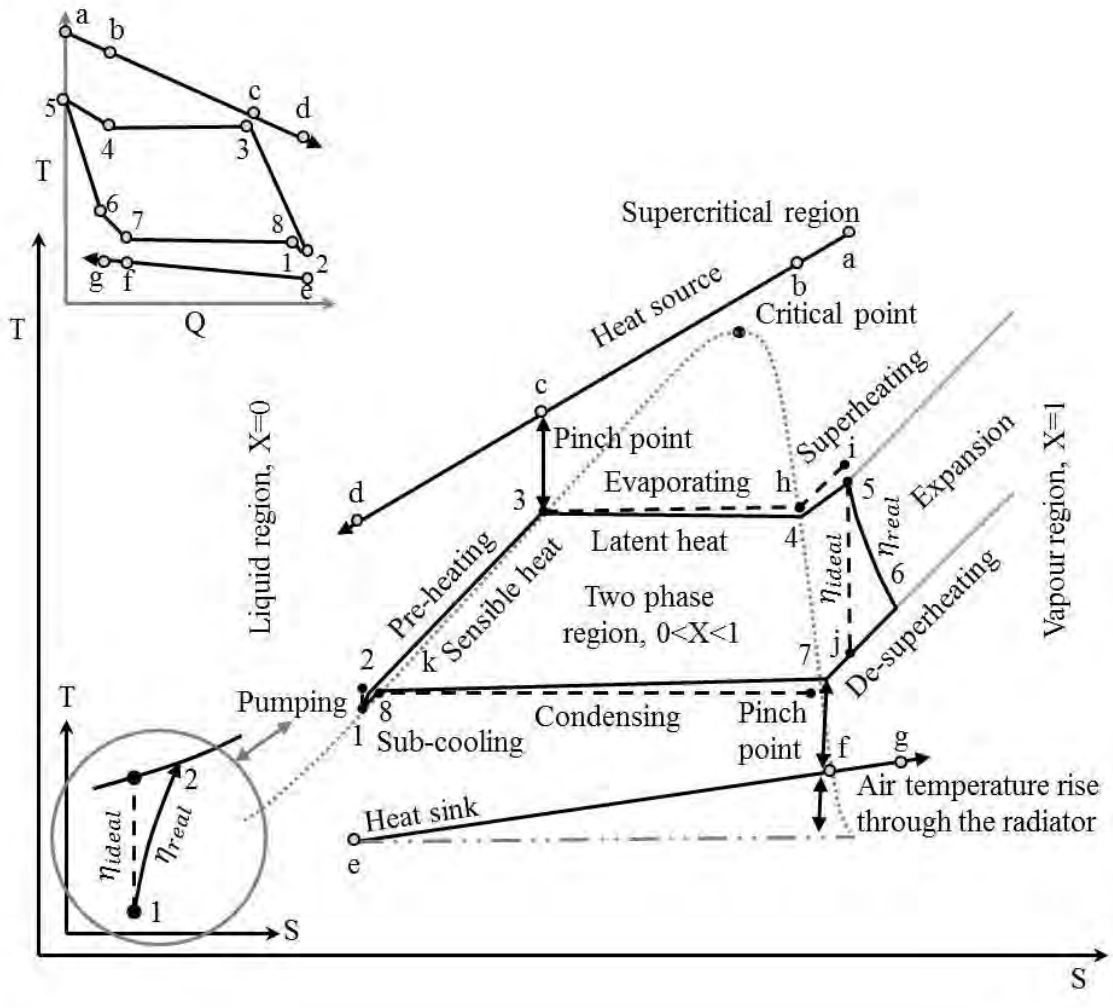

Figure 4.7 Detailed T-S sketch and brief T-Q sketch of a subcritical ORC process description

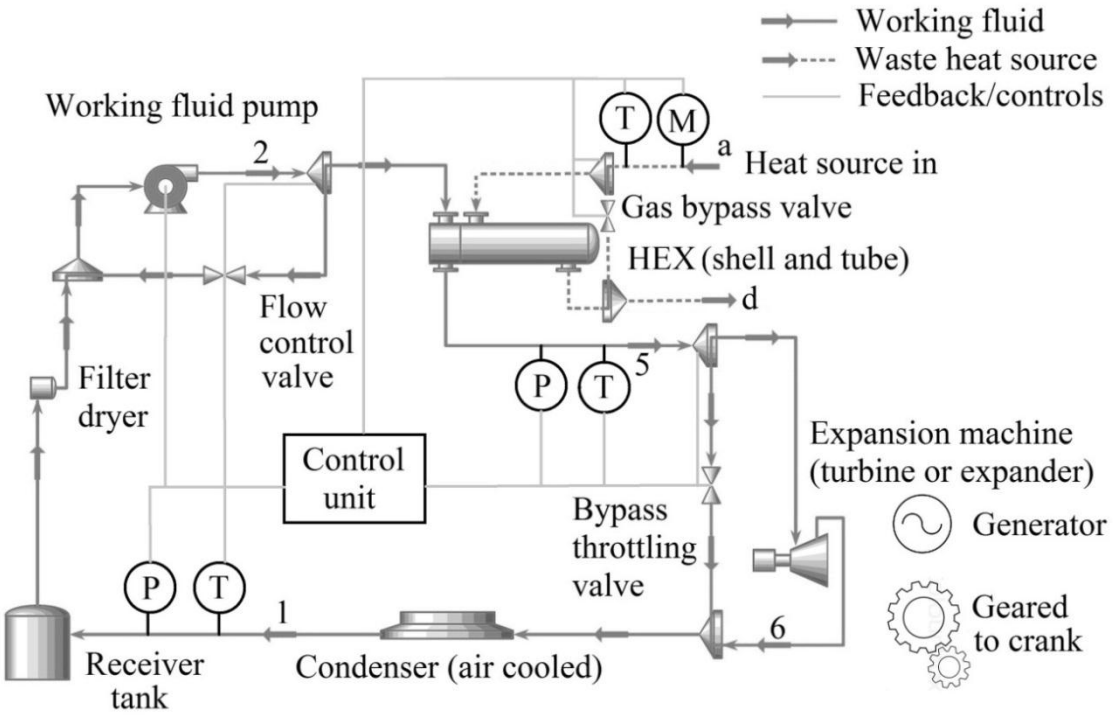

Figure 4.8 A simple ORC layout with instrumentation

The counter current heat exchanger (HEX) in the ORC process generally involves three stages (Fig. 4.7): pre-heating (2-3, heating to the saturation temperature), evaporating (3-4, complete vaporisation) and superheating (4-5) of the working fluid using the waste heat source (a-d). Pt. 2 represents the highest working fluid pressure, which is imposed by the pump and established by the source conditions, the design of HEX and the expansion machine. Whereas, Pt. 5 represents the highest working fluid temperature, which is a function of HEX design, working fluid mass flow rate and source conditions. When recovering exhaust heat an electrically controlled 3-way valve will be required to allow for full flow control over the HEX (Fig. 4.8).

The combination of sensible heat and latent heat of a working fluid results in a single pinch point location (Fig. 4.7), rather than an overall constant pinch point as assumed in Fig. 4.2d. Depending on the heat source, the working fluid and the cycle operating conditions, this point may be located at the preheater inlet (d-2), in the preheater (between 2-3), at the onset of evaporation (c-3) or at expansion inlet (a-5). The selected pinch point value also governs the working fluid mass flow rate, while the pinch point in the condenser (7-f) limits the maximum air flow rate.

Neglecting heat losses in HEXs, the heat balance given in equation 4.11 can be used for preheater, evaporator and superheater.

$$\dot{Q}_{hex} = \dot{m}_{source} c_{p,source} \left(T_{source,hex,in} - T_{source,hex,out} \right) = \dot{m}_{wf} \left(h_{wf,hex,out} - h_{wf,hex,in} \right) \ldots (4.11)$$

Where, wf stands for working fluid, and the total rate of energy transferred to the working fluid is:

$$\dot{Q}_{in} = \dot{Q}_{preheater} + \dot{Q}_{evaporator} + \dot{Q}_{superheater} \ldots (4.12)$$

For each individual component, balance of energy (heat and work) is based on the law of conservation of energy. The equivalent for exergy is the law of degradation caused by irreversibilities ($\dot{I}$) of the real thermodynamic processes. Exergy is shown to be a useful tool for working fluid comparison offering a clearer picture about system losses (Mago et al., 2008). The cause of exergy destruction is attributable to entropy generation during a process inside the system or the components of the system, a control mass for the system or a control volume (as in this work) for each component (Wei et al., 2007). The internal irreversibilities are caused by friction and unconstrained expansion/compression, while heat transfer across a finite temperature difference causes the external irreversibilities. (Note: internal and external irreversibility contributions are calculated in total).

Irreversibilities in the HEX is caused largely by the heat transfer over a finite temperature difference, although the tortuous working fluid path to ensure a good overall heat transfer coefficient also causes pressure drop. This pressure drop is dependent on the HEX design, working fluid and the fluid flow conditions. Mobile ORC analysis is often carried out with overly optimistic assumptions on the minimum temperature difference, e.g. 5°C in cascade HEX (Wang et al., 2012), while neglecting HEX pressure drop. In this thesis, a more practical fixed ΔP of 0.5 bar per HEX and a pinch point value of either 20 or 30°C were employed. The non-isobaric heating process and the pressure drop in the superheater exit to expansion inlet connecting pipe result in the working fluid pressure at Pt. 5 to be lower than Pt. 2 and the cycle maximum temperature reduce from Pt. i to Pt. 5 (Fig. 4.7). The irreversibilities in HEX ($\dot{I}_{hex}$) is calculated using the specific enthalpy and entropy of the working fluid at the inlet and exit conditions, and the source inlet temperature.

$$\dot{I}_{hex} = T_{sink}\dot{m}_{wf}\left[\left(s_{hex,out} - s_{hex,in}\right) - \left(\frac{h_{hex,out} - h_{hex,in}}{T_{source}}\right)\right] \ldots(4.13)$$

The temperature differences along a-d and 2-5 (Fig. 4.7) can be seen as a direct measure of irreversibilities and a properly selected working fluid should minimise this.

The superheated high pressure working fluid (Pt. 5) is then passed through an expansion machine where it releases energy to create mechanical work and exits to the pressure maintained by the condenser (Pt. 6). Depending on the working fluid and the expansion machine (dynamic or positive displacement) the mechanical work can be transferred electrically (generator) or mechanically (gear). The expansion and compression processes are non-isentropic and entropy is increased during the two processes. Real expansion efficiency as a result of friction, leakage, heat loss, pressure drop and other losses are given by:

$$\eta_{exp} = \left(h_{exp,in} - h_{exp,out,real}\right) \Big/ \left(h_{exp,in} - h_{exp,out,ideal}\right) \ldots(4.14)$$

The power output of a real expansion process ($\dot{W}_{exp}$) is then given as:

$$\dot{W}_{exp} = \eta_{exp}\dot{W}_{exp,ideal} = \eta_{exp}\dot{m}_{wf}\left(h_{exp,in} - h_{exp,out,ideal}\right) \ldots(4.15)$$

The expansion irreversibilities ($\dot{I}_{exp}$) expressed using inlet ($s_{exp,in,real}$) and exit ($s_{exp,out,real}$) working fluid conditions for the real expansion is written as:

$$\dot{I}_{exp} = \dot{E}_{exp,in} - \dot{E}_{exp,out} - \dot{W}_{exp} = T_{sink}\dot{m}_{wf}\left(s_{exp,out,real} - s_{exp,in,real}\right) \ldots(4.16)$$

Higher values of entropy at expansion exit correspond to lower isentropic efficiency, and thereby higher irreversibilities.

As shown in Fig. 4.8, a bypass throttling expansion valve (pressure reducing valve) provides a parallel loop to enable the fluid to be circulated with the expansion stage bypassed. This can be used for setting up the required pressure, temperature and flow conditions, bypass when waste heat level is too low or when two-phase flow is experienced at Pt. 5, and as a safety feature in the event of expansion machine failure (reduces to a coolant loop).

In the cross-current air-cooled condenser (Fig. 4.7), the working fluid loses heat by de-superheating (6-7), condensing (7-8) and sub-cooling to saturated liquid (8-1) to the flowing air (e-f-g). In a typical design, the de-superheating and sub-cooling zones occupy 5-10% each of the condensing surface area and the condensing zone occupies 80-90% of the coil area (Ravindra, 2001). The aim is to limit the sub-cooling to a small value. For a fixed heat into the cycle, excessive cooling will only marginally reduce the performance, but will greatly influence the size of the total condenser. Pt. 1 then represents the lowest pressure and temperature in the cycle.

The de-superheating load is a function of the working fluid and the expansion exit conditions (imposed by the expansion losses), while the sub-cooling level is a function of condenser design, heat sink conditions and the working fluid charge in the system. As vapour conditions at the expansion inlet are essential for conventional machines, so is the sub-cooled liquid state entering the pump to prevent the onset of cavitation. Saturated vapour conditions at the expansion inlet and saturated liquid conditions at the pump inlet are possible in simulations but are impractical in real operation. Hence, a slight overdesign ensuring a minimum of 5°C superheating and sub-cooling was considered in this chapter. The expansion inlet conditions are monitored using the P,T sensors at Pt. 5 (Fig. 4.8). Whereas, the condensing temperature and the level of sub-cooling needed are monitored using the P,T sensors shown at Pt. 1 (Fig. 4.8), and regulate the fan air flow.

The condensing temperature (and corresponding saturation pressure) is a function of the condenser size, air mass flow rate and air temperature. The condensing temperature as given in equation 4.17 is calculated using the air temperature at the face of the condenser ($T_{air,face}$, Pt. e), imposing a fixed air temperature rise through the condenser ($T_{air,rise}$, e-f) and using a fixed pinch point value (T_{pp}, 7-f).

$$T_{cond} = T_{air,face} + T_{air,rise} + T_{pp} \ldots (4.17)$$

Reduced air flow and hotter ambient conditions reduce the condenser cooling capacity. As a result, for a fixed expansion inlet condition, the FBC power will fluctuate with driving profile and seasonal changes.

The heat balance given in equation 4.11 can also be used here to give the total heat rejected as:

$$\dot{Q}_{out} = \dot{Q}_{de-superheating} + \dot{Q}_{condensing} + \dot{Q}_{sub-cooling} \quad \ldots(4.18)$$

The working fluid pressure drop in 6-7-8-1 are around 1/3rd that in 2-3-4-5 but cannot be neglected. A fixed ΔP of 0.2 bar per condenser was used in the simulations. The condensing irreversibilities ($\dot{I}_{cond}$) can be determined from the specific enthalpy and entropy of the working fluid at the inlet and exit of the condenser, and the temperature of the sink.

$$\dot{I}_{cond} = T_{sink}\dot{m}_{wf}\left[\left(s_{cond,out} - s_{cond,in}\right) - \left(\frac{h_{cond,out} - h_{cond,in}}{T_{sink}}\right)\right] \ldots(4.19)$$

The temperature differences along e-g and 1-6 (Fig. 4.7) can be seen as a direct measure of irreversibilities. However, the potential of reducing the condensing irreversibilities, with a simple cycle using pure fluids under predefined boundary conditions is rather limited in relation to the heat exchanger irreversibilities (Further details in Section 4.9.3).

Depending on the selected working fluid, a pressurised cylinder or a liquid storage tank with 20% free capacity to allow for expansion will have to be fitted after the condenser (Fig. 4.8). This also provides a reservoir during varying working fluid mass flow rates with engine operating conditions (start-up, transients etc.). Ignoring the static hydraulic pressure and the flow resistance, the receiver tank was considered isenthalpic and isentropic. A filter-drier to remove any moisture, acid and particles is needed prior to the pump inlet.

The sub-cooled liquid at the pump inlet (Pt. 1) is then pressurised to the pre-heater inlet (Pt. 2). The connecting line from the bottom of the working fluid reservoir also offers a slight safety margin in preventing uncondensed vapour at the pump inlet. Furthermore, the receiver tank should be placed higher than the pump to provide as much gravity head as possible. In order to ensure good transient performance, the expansion machine and pump should have independent shafts rather than a hermetic high speed turbine-generator-pump unit. An independent electrically motored variable-speed pump will have a key role in the control of the whole system, and has to provide the desired pressure and varying mass flow rate. To impose the desired pressure and mass flow rate, tuning of the pump control using

instrumentations shown at Pt. a and Pt. 5 are needed (Fig. 4.8). It may also be possible to use pump recirculation (also shown in Fig. 4.8) to control the mass flow rate.

Pump (60%) and expansion (70%) efficiencies are assumed to be constant in this thesis and not a function of the working fluid, mass flow rate and pressure ratio. These values will be lower under off-design conditions. Nonetheless as a first approximation, the considered values provide an insight into the achievable performance. The electromechanical losses and internal leakage lead to irreversibilities in the pump that transforms a part of the useful work into heat. The organic working fluid temperature increases by 3-5°C during this isentropic compression due to a slight decrease in the specific volume of the fluid. A magnified view of the pumping process showing increased entropy and a slight increased temperature is shown in Fig. 4.7.

To maximise the varying heat recovery, the pump exit pressure has to be varied. It may in fact be more convenient to operate the pump with 3 to 4 fixed stepping pressures, e.g. 120, 100, 80, 60% of the design point. The power consumed by the pump ($\dot{W}_{pump}$) and the pumping irreversibilities ($\dot{I}_{pump}$) are calculated as:

$$\dot{W}_{pump} = \frac{\dot{W}_{pump,ideal}}{\eta_{pump}} = \frac{\dot{m}_{wf}\left(h_{pump,out,ideal} - h_{pump,in}\right)}{\eta_{pump}} \ldots(4.20)$$

$$\dot{I}_{pump} = \dot{E}_{pump,in} - \dot{E}_{pump,out} + \dot{W}_{pump} = T_{sink}\dot{m}_{wf}\left(s_{pump,out} - s_{pump,in}\right) \ldots(4.21)$$

The total irreversibilities in the system ($\dot{I}_{cycle}$) based on steady state condition is then obtained using equation 4.22.

$$\dot{I}_{cycle} = \Sigma\dot{I}_x = T_{sink}\dot{m}_{wf}\left[-\left(\frac{h_{hex,out} - h_{hex,in}}{T_{source}}\right) - \left(\frac{h_{cond,out} - h_{cond,in}}{T_{\text{sink}}}\right)\right] \ldots(4.22)$$

The exergy destroyed in the connecting line subsystem were neglected in this chapter. The electric power required for the control of the system will introduce a ≈0.3 kW reduction in the net ORC power in the present application. In this thesis, net ($\dot{W}_{net}$) and system ($\dot{W}_{system}$) power are described as below:

$$\dot{W}_{net} = \dot{W}_{exp} - \dot{W}_{pump} \ldots(4.23)$$

$$\dot{W}_{system} = \eta_{exp,trans}\dot{W}_{exp} - \eta_{pump,trans}\dot{W}_{pump} - \dot{W}_{backpressure} - \dot{W}_{fan} \ldots(4.24)$$

For performance comparison, thermal efficiency (η_I) and external second law efficiency ($\eta_{II,external}$) as defined in equation 4.25 and 4.26 do not completely quantify how well a cycle performs if the energy or exergy of the source stream is discarded or unused.

$$\eta_I = \frac{\dot{W}_{net}}{\dot{Q}_{in}} \quad \ldots(4.25)$$

$$\eta_{II,external} = \frac{\dot{W}_{net}}{\dot{E}_{source,used}} = \frac{\dot{W}_{net}}{\dot{m}_{source}\left[\left(h_{source,in} - h_{source,out}\right) - T_{sink}\left(s_{source,in} - s_{source,out}\right)\right]} \quad \ldots(4.26)$$

These equations only consider how effective the cycle is with respect to power production from a given amount of energy or exergy absorbed. Therefore, recovering only the high quality portion of a heat stream will then result in high η_I and $\eta_{II,external}$ values but will also produce lower net power. Similarly, net power output per unit working fluid mass flow rate is also an unsuitable indicator in the present case.

The more appropriate performance parameters are overall conversion efficiency ($\eta_{conversion}$) and exergy of power production (ξ_P). For applications where the source energy is not used downstream of the HEX, the primary objective is to simultaneously maximise the heat recovery efficiency ($\eta_{recovery}$) and the thermal efficiency of the process (η_I). The overall conversion efficiency is then the product of these two terms and is given as:

$$\eta_{conversion} = \eta_I \eta_{recovery} = \frac{\dot{W}_{net}}{\dot{Q}_{in}} \frac{\dot{Q}_{in}}{\dot{Q}_{max}} = \frac{\dot{W}_{net}}{\dot{Q}_{max}} \ldots(4.27)$$

Where $\dot{Q}_{max}$ is the total heat available in the HEXs as given in Table 3.3. The equivalent of overall conversion efficiency in the second law is the ratio of the net power output to the incoming exergy flow of the source, termed exergy of power production (ξ_P) and is given as equation 4.28.

$$\xi_p = \frac{\dot{W}_{net}}{\dot{m}_{source} c_{p,source}\left[\left(T_{source} - T_{sink}\right) - T_{sink} \ln \frac{T_{source}}{T_{sink}}\right]} \ldots(4.28)$$

This thesis employed $\eta_{conversion}$ as the first primary objective function for the quantitative analysis of FBCs.

4.4 Fluid selection and evaluation methodology

The working fluid directly influences the selection, design and layout of the cycle components; environmental and safety characteristics; size, performance, operating strategy and cost-effectiveness of the system. The literature review (Chapter 2) showed that there were four approaches for the selection of the working fluid:

1. Considering the thermodynamic aspects only (Vaja and Gambarotta, 2010)

2. Selecting working fluids that are commonly used in other applications (Nelson et al., 2009)
3. Using small datasets containing the usual fluids mentioned for an application (Espinosa et al., 2010)
4. Simulating ORCs using a large list of available fluids in more conventional databases like Equation Evaluation Solution and then down selecting optimal fluids based on the objective function (Tian et al., 2012)

Such approaches, although useful, are either time consuming due to the large number of simulations performed or limited in view of the vast list of possible fluids which are usually not included in conventional databases. Therefore, efforts are continuing for formulating the best strategies for selecting the optimal working fluid.

To address this, the novel fluid selection and evaluation methodology summarised by Fig. 4.9 was developed. In this systematic approach, 5 themes combining 25 fluid screening criteria were implemented to narrow down the vast list of potential fluids (Phase 1). Particular attention was paid to the thermo-physical and molecular make-up trends and rules, which highlighted the complexity in choosing a working fluid but also revealed useful trade-offs. Fluids that met the screening requirements were simulated using the same boundary conditions and assumptions about the equipment performance (Phase 2, Table 4.2). Once optimised for maximum power recovery with minimum superheat (Phase 3), the cycles were then assessed according to the 16 performance, size, safety and environmental ranking parameters (Phase 4). For a comprehensive view, the simulation model and the performance aspect of the fluid ranking criteria were based on the energy and exergy equations in all specific points of the cycle. Finally, a Performance and System Index (PSI) was developed using multiple fluid ranking criteria for the comparison of the influence of different working fluids. The PSI benchmarks selected performance and property value of a particular fluid against the optimal fluid. The equation takes the form shown below.

$$PSI_{wf} = \left[\begin{array}{l} PSI_{wt.factor} \dfrac{Parameter_{1(wf)}}{Max.Parameter_{1(optimal,wf)}} + \ldots \\ + PSI_{wt.factor} \dfrac{Min.Parameter_{2(optimal,wf)}}{Parameter_{2(wf)}} + \ldots . \end{array} \right] \quad \ldots (4.29)$$

This helped in the rapid identification of the working fluids of interest, highlighting their favourable process properties and the formative impact on the practicality of the system.

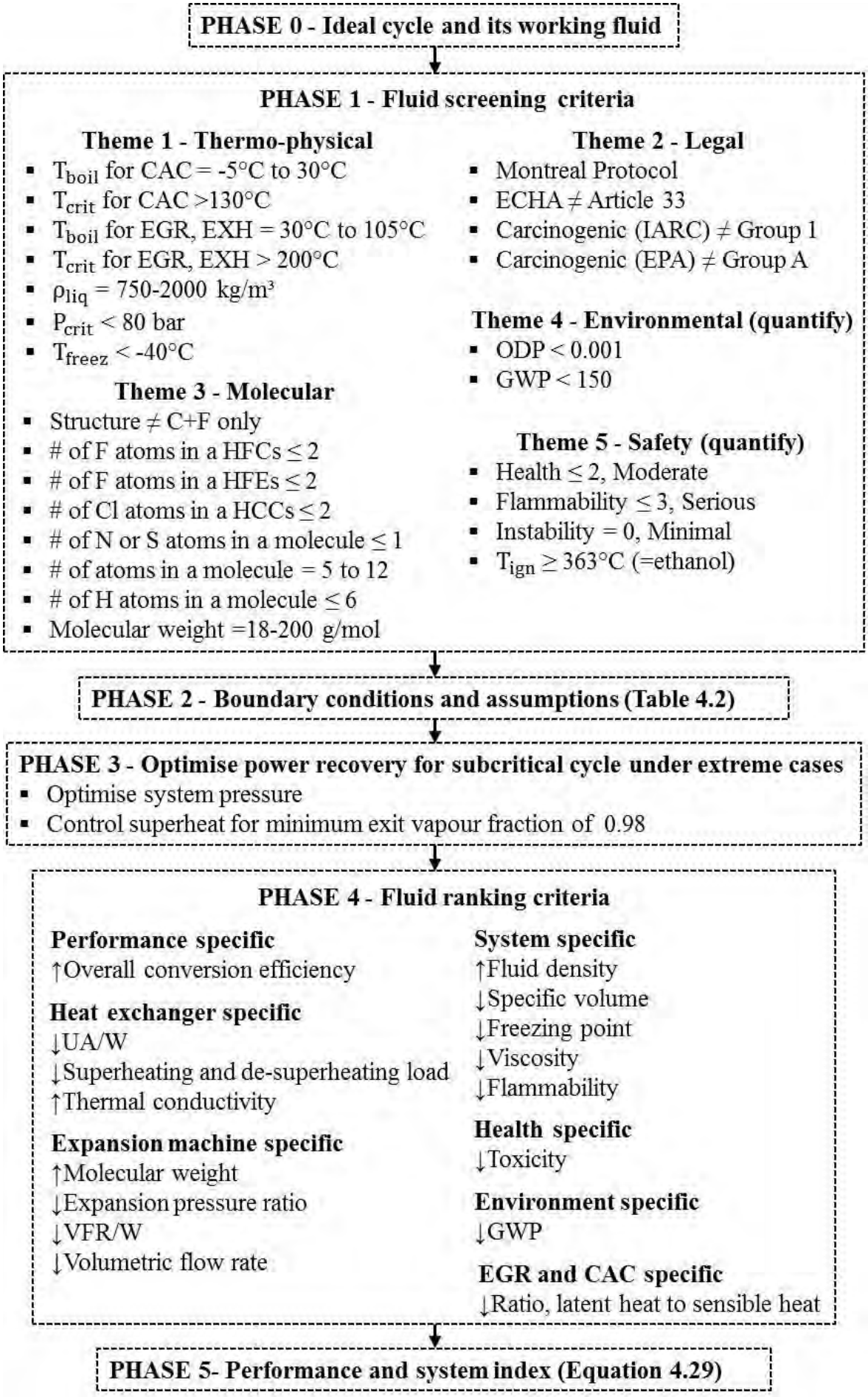

Figure 4.9 Overview of the novel fluid selection and evaluation methodology

Table 4.2 Phase 2 boundary conditions (left) and performance assumptions (right) used in the simulations

▪ T_{post}, EGR ≥ 95°C ▪ T_{post}, EXH ≥ 125°C ▪ T_{post}, CAC ≥ 85°C ▪ T_{max}, organic fluid ≤ 250°C and T_{crit} P_{max}, working fluid ≤ 35 bar and 0.9 P_{crit} ▪ T_{cond}, working fluid = 65°C or 105°C	▪ T_{pp}, EGR = 30°C ▪ T_{pp}, EXH and CAC = 20°C ▪ Air temp. rise through cond. = 15°C ▪ Δ P_{max}, gas side = 0.1 bar/HEX ▪ ΔP, fluid side (HEX) = 0.5 bar/HEX ▪ ΔP, fluid side (cond.) = 0.2 bar/cond. ▪ Sub-cooling and superheating ≥ 5°C ▪ η_{exp} = 70% ▪ η_{pump} = 60%

4.5 Fluid screening (Phase 1)

The selected software package used in this study (HYSYS 7.3) has ≈1800 substances in its database, compared to ≈85 in the REFPROP 8 (Lemmon et al., 2007). Therefore, the earlier mentioned approach number 4 was impractical. Previous sections have identified the available source and sink temperature levels in a HDDE (Section 3.7, 3.8), and some key thermodynamic properties for the ideal fluid for a finite source (Section 4.2). Using this information as a starting point, the following subsections detail the 5 themes of the fluid screening criteria for an effective screening process.

4.5.1 Thermo-physical properties

The thermodynamic and thermo-physical properties of a fluid are interrelated and largely depend on the normal boiling point (T_{boil}), critical temperature (T_{crit}), molecular makeup and structure. The first key thermo-physical property of a working fluid, which is an indicator of the potential temperature level of application, is the normal boiling point. Some stationary ORCs use highly thermal stable fluids e.g. Dowtherm's (A, G and Q), Siloxanes (D4, D5 and D6) and Xylenes (m, o and p-Xylene) (Fernández et al., 2011, Dimian and Bildea, 2008). These fluids can operate up to 300-400°C but were omitted, as they require vacuum condensers and highly pressurised fluid storage tanks (T_{boil} = 138-288°C) incurring additional cost and complexity in preventing in-leakage of ambient air. With 105°C selected as the highest condensing temperature (Fig. 3.15), fluids with higher normal boiling point values than this were excluded in Phase 1.

Next to be considered was the lowest gaseous heat source temperature level of interest, i.e. CAC. As detailed in Fig. 4.4b, the critical temperature of the working fluid should be below the maximum CAC temperature. At low-speed mid-load conditions, the CAC

temperature was ≈160°C (e.g. EGR only A50, Appendix 3.4). Assuming fixed overall 20°C pinch point in the CAC, the critical temperature of the fluid should be ≈140°C. It is observed that for most of the organic fluids the reduced temperature i.e., the ratio of normal boiling point to critical temperature is in the range of 0.6-0.7. Hence, the normal boiling point is a good indicator of the critical temperature of organic fluids as indicated by equation 4.30.

$$T_{boil} = 0.65 T_{crit} \quad \ldots(4.30)$$

Therefore, for a critical temperature of 413 K, the fluid boiling point is 268 K. Hence, considering the upper and lower normal boiling points of 105 and −5°C the fluids of interest reduced to ≈330 (for comparison in REFPROP 8 ≈30).

Furthermore, the majority of organic fluids have critical pressures between 25-65 bar. Fluids with lower critical temperatures demonstrate higher critical pressures. In other words, lower boiling point fluids (i.e. simple organic molecules) have higher critical pressures and vice versa.

In the thermo-physical screening, the liquid fluid density (ρ_{liq}) at normal boiling point was also included. With ethanol showing a liquid density of 792 kg/m^3, a low cut off value of 750 kg/m^3 was set. Consider 1,3-Butadine and E152a (Difluoromethyl-Methyl-Ether) to highlight the significance of this property. These two fluids give nearly equivalent normal boiling point (−4, −5°C), critical temperature (152, 149°C) and critical pressure (43.2, 43.3 bar). As a result, both fluids will then give similar thermodynamic performance. However, due to the much higher density of E152a (1128 vs. 626 kg/m^3) the condensing specific volume and expansion exit volumetric flow rate will be smaller (for the same condensing temperature), resulting in a more compact system. High vapour density in ORCs is of key importance and identifying this property at an earlier stage is vital. Alternative to density, the molecular weight (M_{wt}) can also be used as an approximate comparative screening tool. This is since higher density fluids (e.g. E152a vs. 1,3-Butadine) also have higher molecular weights (82 vs. 54.1 g/mol). The two additional thermo-physical properties used in the screening were a maximum critical pressure (P_{crit}) less than 80 bar (to explore supercritical cycles) and a freezing point (T_{freez}) below −40°C (for frost protection).

4.5.2 Legal criteria

The three environmental factors applicable to fluid selection and comparison are atmospheric lifetime (ATM), ODP and GWP. ATM is the duration a molecule will remain in the atmosphere based on its decay rate and its likeliness to bond with other gases. ATM then influences both ODP and GWP, which are the weight normalised potential for a single molecule to destroy the Ozone layer relative to CFC-11 (trichlorofluoromethane) and warm the planet relative to CO_2 (direct effect, for an integration time horizon of 100 years), respectively. Environmental concerns require ODP and GWP to be as low as possible.

The legal criteria, i.e. Montreal Protocol (US EPA, 2014b) discounted the Chlorofluorocarbons (CFC) and Hydrochlorofluorocarbons (HCFC) as they have high ODP and are either banned or being phased out worldwide. The legal criteria also excluded any substances listed under the candidate list of substances of very high concern, i.e. Article 33 of European Chemicals Agency (ECHA, 2014), and substances classified as carcinogenic to humans according to International Agency for Research on Cancer (for classification rating refer Appendix 4.1) (IARC, 2014). This negated the use of many technically suitable fluids like CFC-113, HCFC-141b and benzene mentioned in Chapter 2 (Tian et al., 2012, Srinivasan et al., 2010, Vaja and Gambarotta, 2010). Fig. 4.10 shows the timeline using commonly preferred fluid classes in vapour compression and expansion cycles. As can be seen, with the enforcement of Montreal Protocol, hydrofluorocarbons (HFC) were introduced that offered zero ODP values.

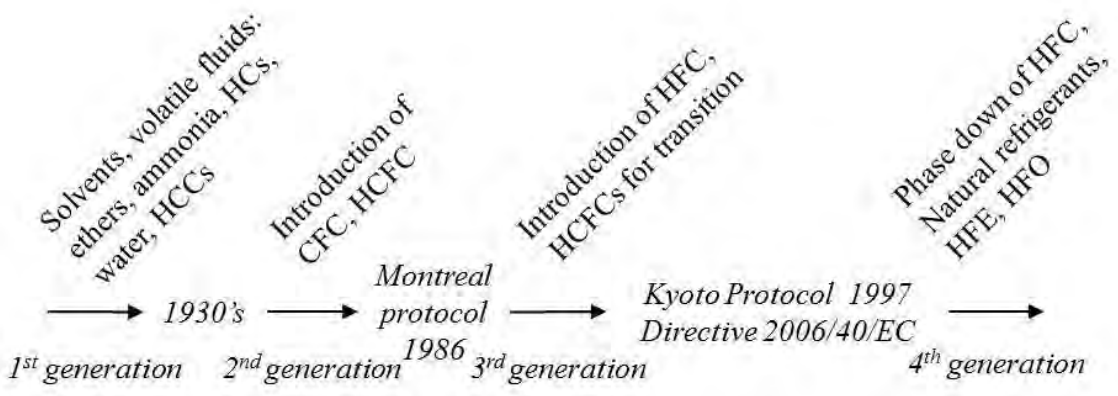

Figure 4.10 Working fluid evolution with international protocols

4.5.3 Molecular properties

The remaining fluids were then assessed based on guidelines derived from the impact of particular chemical groups and atoms (Calm and Hourahan, 2011, Calm and Hourahan, 2007, McQuay International, 2002, Calm and Didion, 1998). As such, molecular properties

were used for assessing environmental aspects, safety characteristics and layout of the cycle component.

Increasing the chlorine (Cl) content in a molecule generally increases the ODP and toxicity (Fig. 4.11a). This also increases the normal boiling point and lubricant miscibility. CFCs that contained chlorine were largely non-flammable and non-corrosive of ordinary metals.

With the implementation of Kyoto Protocol (Fig. 4.10), attention is now focused towards reducing GHG emissions (Peixoto, 2010). Increasing the fluorine content (by displacement of chlorine) generally increases the ATM and GWP (Fig. 4.11a). However, displacement of fluorine (F) with hydrogen (H) generally decreases the ATM and therefore ODP (when containing chlorine) and GWP (when containing fluorine).

This can be best examined using Fig. 4.11b. HFC-134a has 2 hydrogen atoms and 4 fluorine atoms and gives a high GWP of 1370, whereas for the same number of carbon atoms by displacing one fluorine atom with hydrogen then reduces the GWP to 352 in 1,1,2-Trifluoroethane (HFC-143). This is because increasing hydrogen atoms results in the molecule being largely destroyed in the lower atmosphere by naturally occurring hydroxyl radical, ensuring that little of the fluid survives to enter the stratosphere (Chen et al., 2010).

The fluorine content in HFCs has the advantage of reducing toxicity and flammability (by displacement of hydrogen), but molecules with high fluorine contents are being targeted as potent GHGs. Perfluorocarbons also have no ODP, but are chemically very stable, resulting in very long ATM (GWP > 5000) due to the high numbers of carbon-fluorine bonds. Implementation of MAC Directive 2006/40/EC led to the banning of HFC-134a, and such regulations in the future may also apply to ORC systems requiring the use of fluids with GWP less than 150 (European Parliament, 2006).

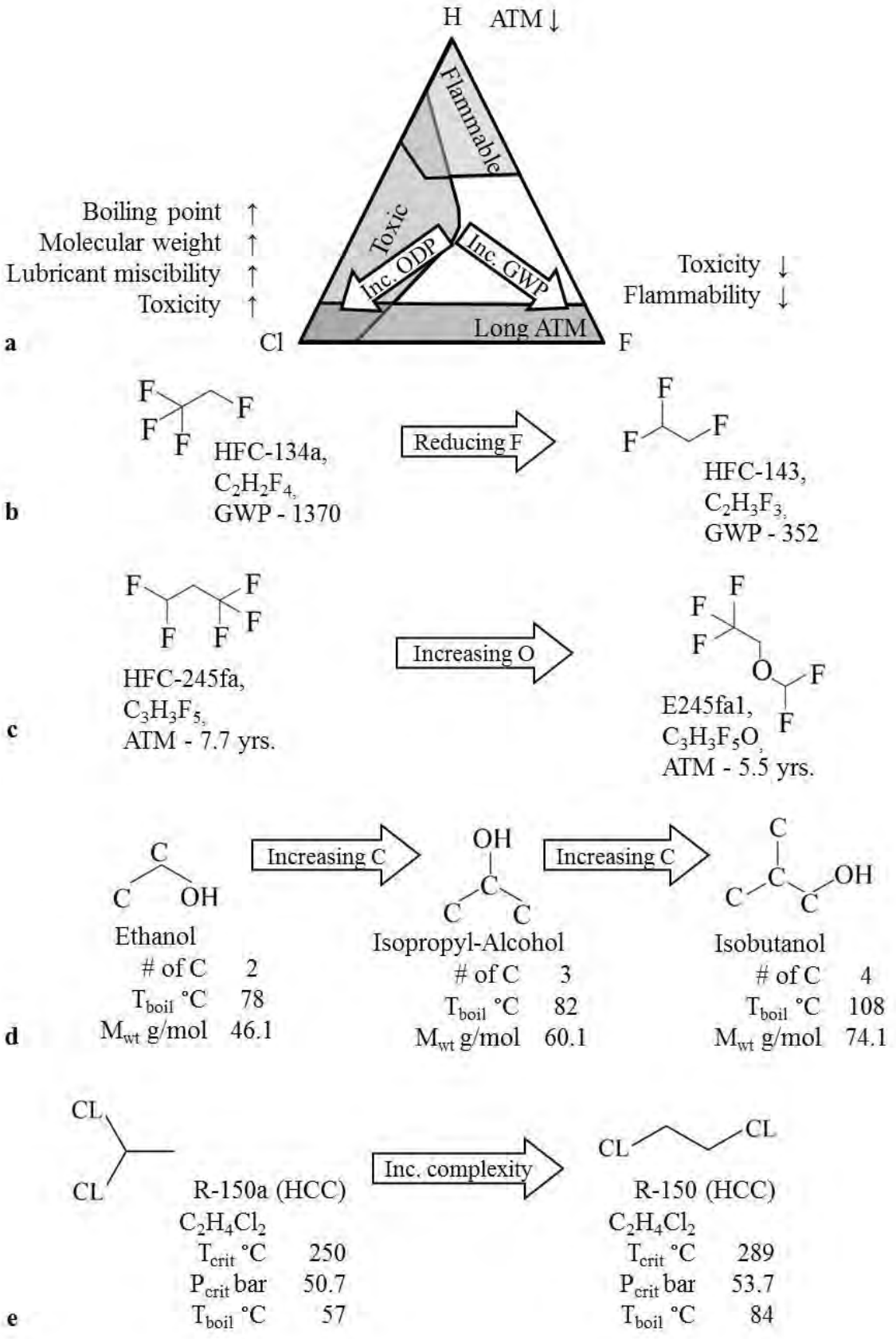

Figure 4.11 Molecular and structural trade-offs with (a) chlorine, fluorine and hydrogen content (b) fluorine content (c) oxygen content (d) carbon content (e) complexity between isomers

Whilst conventional synthetic HFCs are saturated, a small number of unsaturated HFCs, known as Hydrofluoroolefin (HFO) have been developed as 4th generation refrigerants (Fig. 4.10). Two unsaturated double bonded compounds receiving most interest in MAC industry are HFO-1234yf and 1,3,3,3-tetrafluoropropene (HFO-1234ze). They offer GWP values ≤ 6, but also have normal boiling points not suited to the present ORC application (≤ −19°C). Furthermore, HFO-1234yf has a thermal stability limit of only 137°C, and both fluids result in high condensing pressures (≥ 17 bar) at the lowest condensing limit (65°C) considered (Latz et al., 2012).

Apart from reducing the fluorine content in saturated HFCs as a means to screen fluids with lower GWP, which by the substantial decrease in the GWP value in Fig 4.11b was assumed to be ≤ 2 fluorine atoms, other molecular trends were also explored. Consider HFC-245fa (Fig. 4.11c) that shows an ATM of 7.7 years. Retaining the number of carbon, hydrogen and fluorine atoms but adding an oxygen atom in 2-Difluoromethoxy-1,1,1-Trifluroethane (E245fa1) then reduces the atmospheric stability to 5.5 years. Therefore, reduction of fluorine and addition of either (or both) hydrogen and oxygen will then result in lower GWP fluids. In fact, HCFCs, although containing chlorine, have relatively short ATM as its hydrogen content ensures decomposition primarily in the lower atmosphere and thus give much lower ODP than CFCs. Furthermore, when considering the banned chlorine containing molecules, it was noted that in the absence of fluorine atom, there were no combinations of Hydrochlorocarbons (HCC) with ≤ 2 chlorine atoms that were banned. Therefore, HCC molecules with a maximum chlorine content of 2 atoms were not rejected and were considered for further screening.

Hydrogen and oxygen content due present disadvantages due to increased flammability. With ethanol containing 6 hydrogen atoms, molecules with ≤ 6 hydrogen atoms were only considered. However, when hydrogen atoms constitute half of the total atoms connected to a carbon, molecules have shown to demonstrate only marginal flammability. Hydrocarbons and its derivatives exhibit cardiac sensitization potential and anaesthetic effects, however, they generally decompose quickly enough, thus reducing their overall toxicity risks. New selection criteria of low GWP and improved technologies to reduce flammability risks have also led to a revived interest in using hydrocarbons (Underwriters Laboratories, 2011).

A further trend within a functional group of organic fluids is the effect of increasing carbon atoms. With increasing carbon content from 2 in ethanol to 4 in isobutanol (Fig. 4.11d), the

normal boiling point and molecular weight increase. This indicates that, for a class of fluid the ORCs cold weather performance can be improved by using a simpler molecule that will allow super atmospheric condensing at lower temperatures. This tendency is also noticeable within the isomers of some fluids (Fig. 4.11e). 1,1-Dichloroethane (R150a) and 1,2-Dichloroethane (R150) both have the same molecular weight (99 g/mol), but R150 behaves more like a complex molecule. As a result, it has a higher normal boiling point temperature (84 vs. 57°C) and shows that screening isomers is more evolved.

Inclusion of only 1 Nitrogen (N) or Sulphur (S) atom in a molecule was allowed as both increases toxicity and reactivity. To quantify a fluids toxicity and flammability, ASHRAE 34 standard was initially used (ASHRAE, 2012). The classification is divided into two groups according to toxicity and four groups according to flammability (Appendix 4.2). Unfortunately, most of the fluids under consideration were not classified by this standard. Hence, the US National Fire Protection Association (NFPA) 704 standard on health (i.e. toxicity), flammability and reactivity (i.e. instability) was employed as the primary screening tool (NFPA, 2012). This classification was chosen because it covered greater than 75% of the fluids with relative simplicity of the annotations of the hazard level. For each of the three hazards, the fluids are classified from 0 to 4, 0 corresponding to minimal, while 4 corresponds to severe hazard (Appendix 4.3). The maximum NFPA health limit of 2 (moderate), flammability limit of 3 (serious) and reactivity limit of 0 was used for quantified screening (all maximum limits were equivalent to ethanol). In the absence of fluid decomposition temperature for most of the fluids, a 0 instability level then ensured the least hazard with elevated temperatures and pressures.

A major disadvantage in the use of hydrocarbons and some of its derivatives in high temperature application is not only the decomposition temperatures but also their low autoignition temperatures. Although exhaust has a lower oxygen content than air, sufficient self-heating by chemical reactions can still take place to accelerate the rates of reactions to produce full-scale combustion. Autoignition is a particular problem for alkanes, and with increasing complexity of a molecule (i.e. number of atoms in the molecule and chain length) the autoignition temperature (T_{ign}) decreases (Butane 288°C > Pentane 260°C > Hexane 234°C). The low autoignition temperature of some hydrocarbons precludes their use in direct high temperature exhaust heat recovery. The screening criteria disregarded fluids with autoignition lower than that of ethanol i.e. 363°C, and excluded pentane as a potential candidate, contrary to a study reviewed in Chapter 2 (Sprouse III and Depcik, 2013a).

4.5.3.1 Saturation vapour curve

A significant fluid property that affects its applicability, expansion characteristics and the arrangement of associated equipment is its saturation vapour curve. The slope of the saturation vapour curve has been mentioned regularly in the literature, however the reasoning behind this is rarely cited, nor has it been included as a screening tool. The saturated vapour curve is in fact shown to be somewhat dependent on the molecular complexity of the substance (Tabor, 1962). With increase in the number of bonded atoms, the molar heat capacity, and consequently the slope of the saturation boundary has been shown to increase (Calm and Didion, 1998). With pressures slightly below critical pressure, the working fluids can be divided according to the slope of their vapour saturation curve (dT/dS) when expansion begins at this line.

Fluids like water for which the entropy of the saturated vapour decreases with increasing temperatures are called wet fluids ($dT/dS<0$, Fig. 4.12a). Wet fluids require superheating in order to avoid the formation of liquid droplets which may cause blade erosion at the turbine exit. Although it is possible to expand dry saturated vapour (using special materials for leading edges) to allow some vapour fraction at exit (≈10%), this sacrifices the turbine efficiency (Smith et al., 2011). Furthermore, with low quality heat sources it may not be always possible to achieve the necessary level of superheating. In order to limit turbine damage, wet fluids were superheated to ensure a turbine exit vapour fraction of ≈0.98 in this chapter.

Fluids like R245fa (Fig. 4.12c), where the entropy of the saturated vapour increases with increasing temperatures are called dry fluids ($dT/dS>0$). During expansion, they do not condense since the degree of superheat increases as expansion takes place. However, if the fluid is too dry (Fig. 4.12d), the expanded vapour will exit with substantial superheat, increasing the vapour condenser load. Therefore, for dry fluids, superheating was limited to 5°C in this chapter.

An ideal fluid would be the one that requires the least superheating or de-superheating (i.e. Pt. 4 to 5 ≈ Pt. 6 to 7 ≈ 0 kW, Fig. 4.7), as relatively larger heat exchanger surface area are required for vapour heat transfer. The third classification of organic molecules with ≈8-10 atoms are called isentropic fluids, with near quasi-vertical saturated vapour curves ($dT/dS\approx\infty$), they include fluids like ethyl iodide and acetone. For an isentropic fluid, the ideal expansion follows the saturated vapour line. However, with a real expansion, slight superheating at the expansion exit will be experienced. This also points that the real

expansion of a slightly wet fluid, like ethanol, may then avoid the two-phase zone (Fig. 4.12b). Hence, marginally wet fluids will in fact be more suited for use with real expansion machines than dry fluids. For extremely dry fluids like toluene (Fig. 4.12d) a large IHE is necessary, this may have a negative impact on the packaging and control of the system.

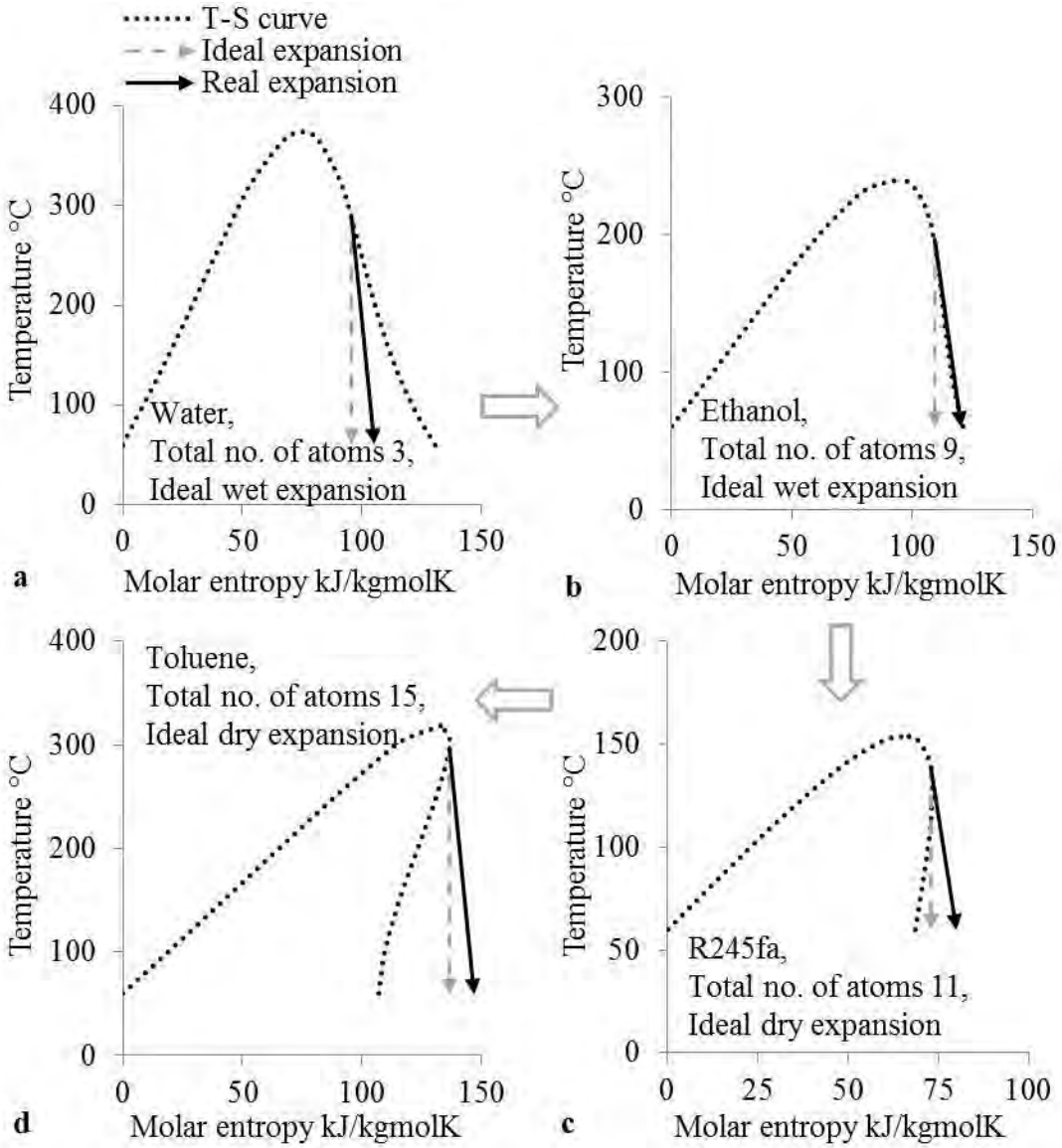

Figure 4.12 Shape of the saturated vapour curve (a) extremely wet fluid (b) marginally wet fluid (c) marginally dry fluid (d) extremely dry fluid, as a function of number of atoms in a molecule

Fluids with strong wet or dry characteristic are less suitable and isentropic or slightly wet fluids were of particular interest in the present application. Observing Fig. 4.12, it can be seen that increasing the number of atoms in a molecule from 3 in water → to 9 in ethanol → to 11 in R245fa → and to 15 in toluene changes the saturation vapour curve from

extremely wet to extremely dry. Therefore, only molecules with 5-12 atoms were selected, resulting in fluids with low superheating and de-superheating loads.

4.5.4 Fluid screening result

The 9 fluids and their chemical classes which met the screening criteria and were used for modelling the ORC are shown in Fig. 4.13. The chemical identification, thermodynamic/thermo-physical and environmental/safety properties of the fluids are given in Appendix 4.4. Furthermore, the screening results of the more commonly known ≈330 pure fluids are documented in Appendix 4.5.

Normal boiling point ranges of −5 to 30°C and 30 to 105°C were considered for low temperature (i.e. CAC) and high temperature (i.e. EGR and exhaust) heat recovery, respectively. Three exceptions to the GWP criteria of less than 150 in Appendix 4.4 include R143 (1,1,2-Trifluoroethane), E245cb1 (Pentafluoroethyl-Methyl-Ether) and E245fa1 for CAC heat recovery. Although they show high GWP (328-740), this is still relatively lower than R245fa (1030). Appendix 4.4 also includes the literature fluids: R245fa, ethanol and water.

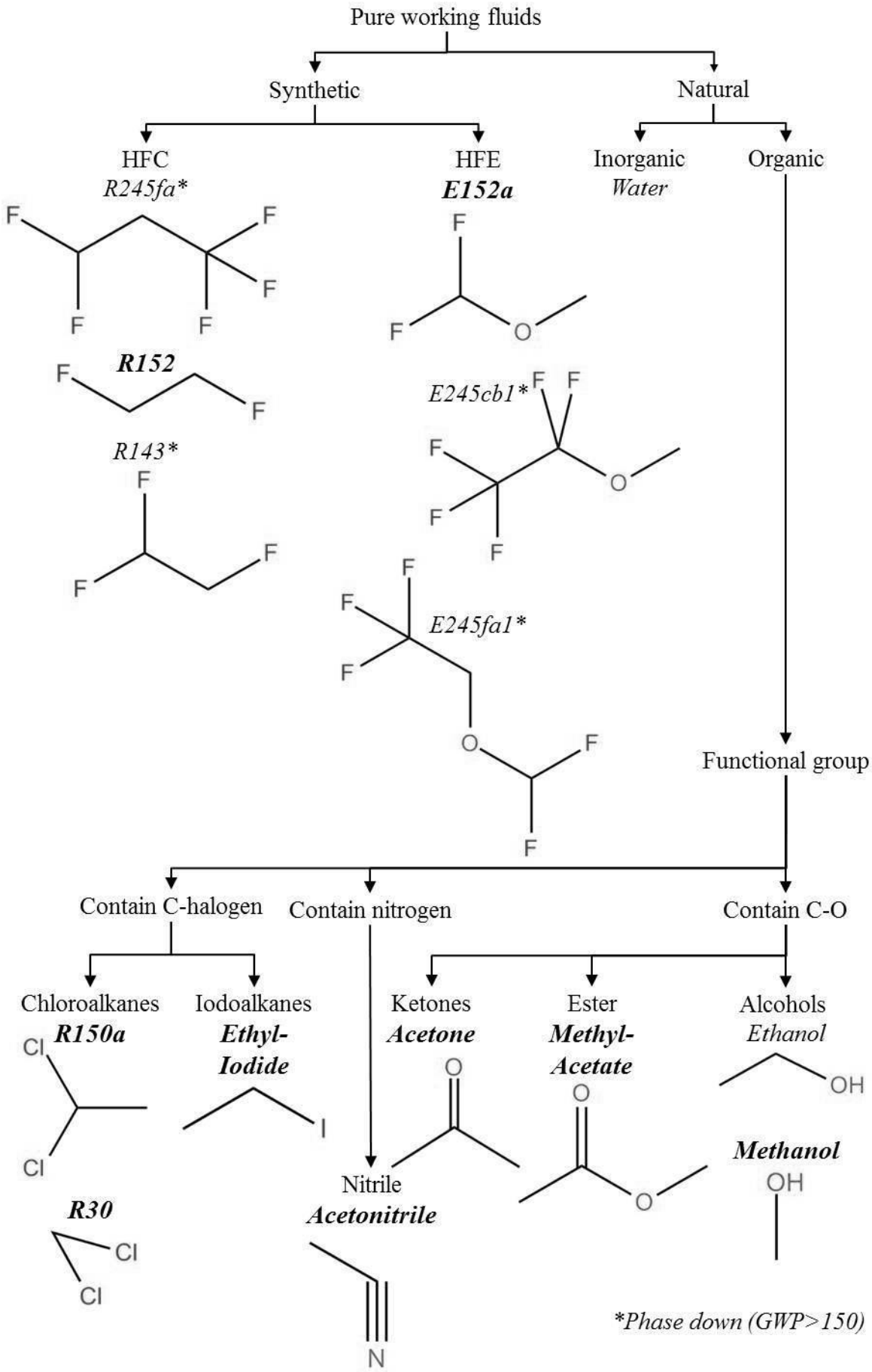

Figure 4.13 Shortlisted fluids under consideration in this study and their chemical classes (shown in bold)

4.6 Optimised power recovery under extreme cases (Phase 3)

For high temperature heat recovery in this chapter, EGR at 427°C with a condensing temperature of 65°C (referred as Case 1: 427/65°C) and exhaust at 296°C with a condensing temperature of 105°C (referred as Case 2: 296/105°C) was chosen from Table 4.1. This is not to propose EGR for a condensing temperature of 65°C only and exhaust for 105°C only, but is to be considered as a fluid selection study with sensitivity analysis. The fluids that will perform well under Cases 1 and 2 will then show less sensitivity to an increasing condensing temperature and decreasing source temperature, and furthermore will also be better suited to combined EGR and exhaust heat recovery. Whereas, for low temperature heat recovery, CAC at 176°C, the lowest condensing temperature of 65°C (referred as Case 3: 176/65°C) was selected.

The simplest configuration of the FBC as shown in Fig. 4.8 was analysed. The simplicity of the cycle arrangement is expected to result in low heat transfer area per net system power output, which is an important factor in the final sizing of FBCs for automotive application. This is due to the higher density/thermal conductivity associated with liquid and two-phases in HEXs, and hence, lower volume/area compared to large superheated or recuperated cycles.

This thesis utilises the idea of local optimisation that is constrained by a set of boundary conditions. In this chapter, this involved determining the subcritical expansion inlet pressures and temperatures corresponding to overall conversion efficiency, given the initial source/sink conditions. This resulted in four distinctive unconstrained/constrained power optimisation cases, explained using examples in Fig. 4.14a-d. The implementation of global optimisation routines remains the focus of future works.

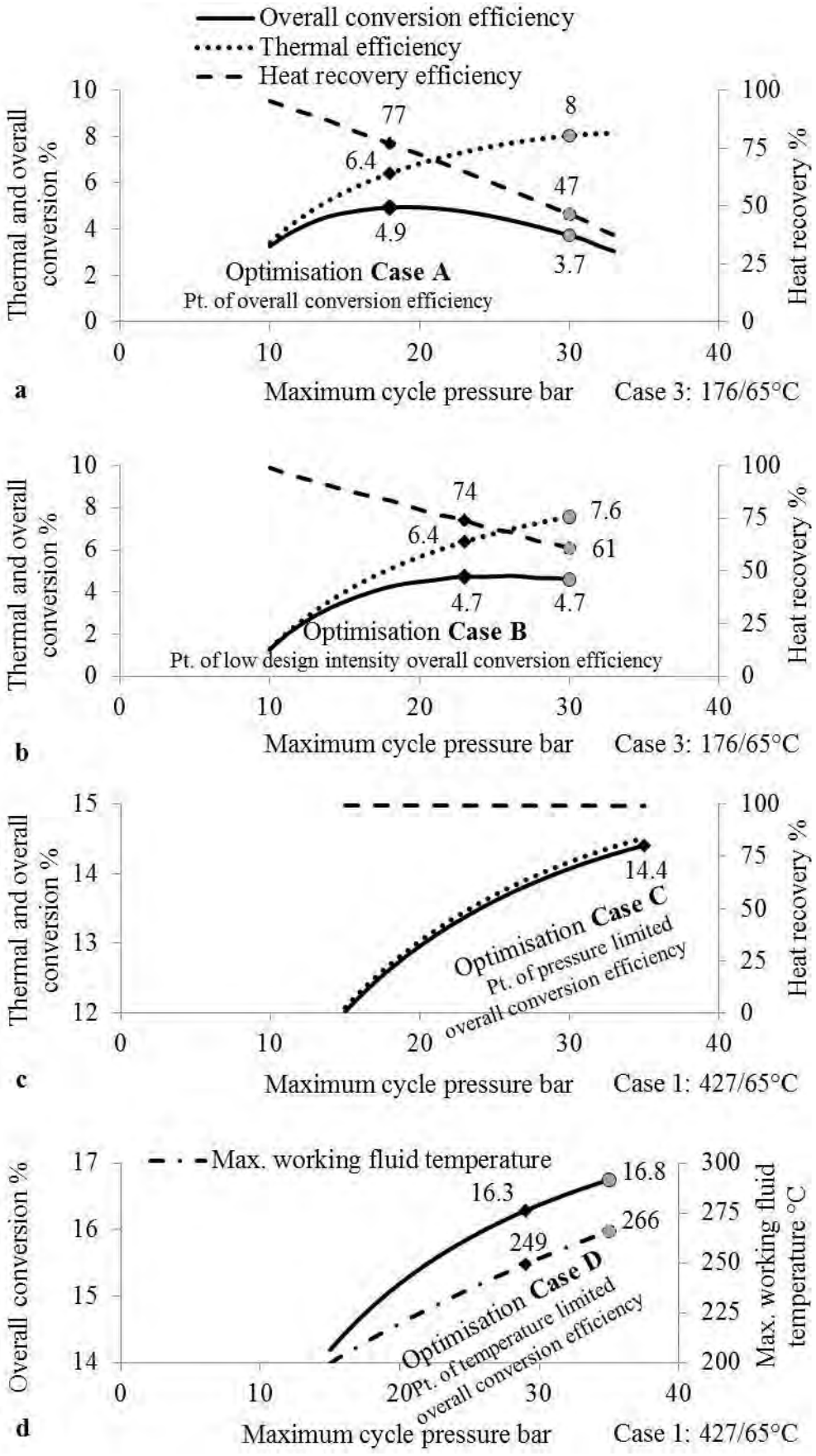

Figure 4.14 Optimisation cases, point of (a) overall conversion efficiency with R245fa in Case 3 (b) low design intensity overall conversion efficiency with R143 in Case 3 (c) pressure limited overall conversion efficiency with ethanol in Case 1 (d) temperature limited overall conversion efficiency with acetonitrile in Case 1

4.6.1 Optimisation Case A

Point of overall conversion efficiency: Fig. 4.14a shows the results of R245fa recovering CAC heat with a pinch point of 20°C (Case 3: 176/65°C). It can be seen that with increasing cycle pressure from 18 to 30 bar the thermal efficiency increased from 6.4 to 8%. However, at the same time the heat recovery efficiency decreased from 77 to 44%, increasing the CAC exit air temperature. With increasing pressure, less quantity but high quality heat was being exchanged. As a consequence, the overall conversion efficiency was reduced from 4.9 to 3.7%. Using the optimisation criteria set out, i.e. overall conversion efficiency (assuming there is no other potential use for the heat source), a maximum working pressure of 18 bar was considered optimal.

4.6.2 Optimisation Case B

Point of low design intensity overall conversion efficiency: Rather than essentially a specific pressure value where the overall conversion efficiency was optimised (Fig. 4.14a), ORCs could also demonstrate a range of pressures over which this was valid. Fig. 4.14b shows CAC heat recovery results using R143 (Case 3: 176/65°C). An equal overall conversion efficiency of 4.7% was calculated with maximum cycle pressures of 23 and 30 bar. The higher pressure cycle resulted in a more thermally efficient system (7.6 vs. 6.4%). However, with increasing maximum cycle pressure, the cost of the HEX and the size of the expansion machine also increase. Furthermore, due to lower heat recovery efficiency (61 vs. 74%), the load on the low temperature air-to-air CAC increased (Fig. 3.14). Hence, the lower pressure cycle, despite the lower thermal efficiency, remained a good option where cycles demonstrated a range of pressures over which the overall conversion efficiency was roughly constant.

4.6.3 Optimisation Case C

Point of pressure limited overall conversion efficiency: Contrary to Fig. 4.14a and b where the critical temperatures of the working fluids were marginally lower than the heat source temperature (Δ ≈20°C), Fig. 4.14c presents the case when the critical temperature was far below the source temperature (Δ ≈185°C). Fig. 4.14c shows ethanol recovering EGR heat with a pinch point of 30°C (Case 1: 427/65°C). With increasing pressure, the heat recovery efficiency remained constant. However, the thermal efficiency increased due to the higher working fluid heat addition temperature. Considering the boundary conditions given in Table 4.2, the maximum system pressure in all cases was then restricted to 35 bar or $0.9P_{crit}$ (which ever was lower) due to economic reasons in this chapter. (Note:

optimisation Case C was also valid for cycles constrained by a given expansion pressure ratio).

4.6.4 Optimisation Case D

Point of temperature limited overall conversion efficiency: Finally, Fig. 4.14d presents the fourth case using acetonitrile to recover EGR heat (Case 1: 427/65°C). At a maximum cycle pressure of 35 bar, acetonitrile gave an overall conversion efficiency of 16.8%. However, acetonitrile is a wet fluid and thus required superheating to 266°C. In the absence of thermal stability data for the majority of the fluids, the maximum fluid temperature was restricted to 250°C for all organic fluids in this chapter. Hence, the maximum cycle pressure was reduced to 29 bar, with the required level of superheating the maximum working fluid temperature was then within the constraints of Table 4.2. This also implies that for each working fluid the vapour fraction or superheat at expansion exit is a function of the maximum cycle pressure and temperature, minimum cycle pressure, expansion efficiency and the shape of the T-S curve. The above four cases also highlight the importance of optimal cycle pressure as it greatly affects the process conditions and performance.

4.7 Results and discussion (Phase 4)

Appendices 4.6 and 4.7 detail the performance and property values of the ORC using the 7 high temperature alternative fluids for Cases 1 and 2, respectively. In Case 1, the ORC minimum pressure (P_{min}) that was determined according to the fixed minimum condensing temperature of 65°C varied with different fluids, leading to sub-atmospheric and super-atmospheric condensation pressures. Also in Case 1, the heat input ($\dot{Q}_{in}$) into all the ORCs was approximately the same (69 kW) as the EGR was cooled ($T_{source\,out}$) down to 97-106°C using a pinch point of 30°C in the EGR cooler. As per equation 4.31, the 30°C pinch point then ensured the cooled EGR temperature was ≥ 95°C.

$$T_{source,out} \geq T_{wf,cond} + T_{pp} \quad \ldots (4.31)$$

For exhaust heat recovery, a 20°C pinch point was considered, resulting in a cooled exhaust temperature of ≥ 125°C.

As detailed earlier, the molecular makeup of the working fluids fundamentally precluded the possibility of an ideal fluid. The next stage, the fluid ranking criteria (Phase 4) as shown in Fig. 4.9, involved the setting up of maximum and minimum working fluid

performance and property guidelines. An extensive trade-off among the simulated fluids was therefore undertaken. The trade-offs between the pure fluids showed ethyl iodide, methanol, dichloromethane (R30) and acetone, as possible suitable alternatives to water, ethanol and R245fa in both Cases 1 and 2. The following subsections discusses the results of the analysis and the trade-offs that influence fluid selection for HDDEs.

4.7.1 Ethyl iodide and methanol compared to water

Emphasis on differentiating between properties of organic fluids and water: Boiler grade water is non-toxic, non-flammable, environmentally friendly, inexpensive, and has the highest thermal conductivity (0.68 W/mK, Appendix 4.4) of any known FBC fluid. High working fluid temperatures are possible with water, as it has no thermal degradation problem for any practical temperature. In comparison, organic and synthetic fluids decompose when the temperature exceeds a certain limiting value.

Detrimental changes in the chemical makeup of organic and synthetic fluids are not limited to the decomposition temperature. In the case of water, moisture will cause corrosion after a period. However, moisture mixed with fluorine or chlorine content present in the working fluid catalyses degradation reactions and will slowly hydrolyse into hydrofluoric and hydrochloric acids (Peixoto, 2010). These acids greatly accelerate metal corrosion and the filter drier has to be changed frequently to provide a moisture free system.

Despite these advantages, water presents challenges for output capacity less than 100 kW and heat source quality less than 450°C. These challenges can be linked to a low molecular weight (18 g/mol) and the extremely wet expansion characteristic (3 atoms in a molecule) amongst any known FBC fluid. To examine and highlight the unique properties of organic fluids where conventional steam conversion technology falters, the following subsections compare two very contrasting ends of organic fluids with water.

4.7.1.1 Case 1 (Appendix 4.6 for tabulated results)

According to Trouton's rule, Fig. 4.15a shows that lower molecular weight fluids have higher latent heat of vaporisation (Arora, 2010). Since, water and organic fluids differ noticeably when comparing molecular weights, it is important to consider the associated implications. Fig. 4.15b shows the entropy change at the saturated vapour line between the evaporating and condensing temperatures in Case 1. Near zero values, represent isentropic fluids, whereas high positive or negative values represent extremely dry and wet fluids, respectively. With increasing molecular weight, the selected organic fluids showed

increasing molecular complexity (i.e. wet to isentropic behaviour). The contrasting end of alternative organic fluids in Cases 1 and 2 included, ethyl iodide which is an isentropic fluid (8 atoms in a molecule) with a high molecular weight (156 g/mol), and methanol which is a wet fluid (6 atoms in a molecule) with a low molecular weight (32 g/mol).

Water with a low molecular weight has large latent heat of vaporisation, and hence, high specific enthalpy in the vapour state. Due to the high specific enthalpy of steam, the pump power consumed was roughly 6-16 times lower than organic fluids (Fig. 4.15c). As a consequence, the expansion of steam showed 2-11 times larger specific enthalpy drop (Fig. 4.15d). That is, the volume of steam produced per unit mass at the expansion inlet is very large compared to that of the water entering the evaporator. Hence, the Rankine cycle pumping work usually accounts for only 1-2% of the expansion work. This indicates that organic pumps should be carefully selected to offer acceptable efficiencies since they also show ≈10% point lower pumping efficiencies (Valentino et al., 2013). The large enthalpy drop with steam results in higher velocities during expansion. This translated to around 1.5-3 times the turbine speed seen with organic fluids, indicated by the speed of sound (Fig. 4.15e). Hence, under the same evaporator and condenser temperature limits, ethyl iodide turbine/alternator will have the lowest speed while water will have the highest.

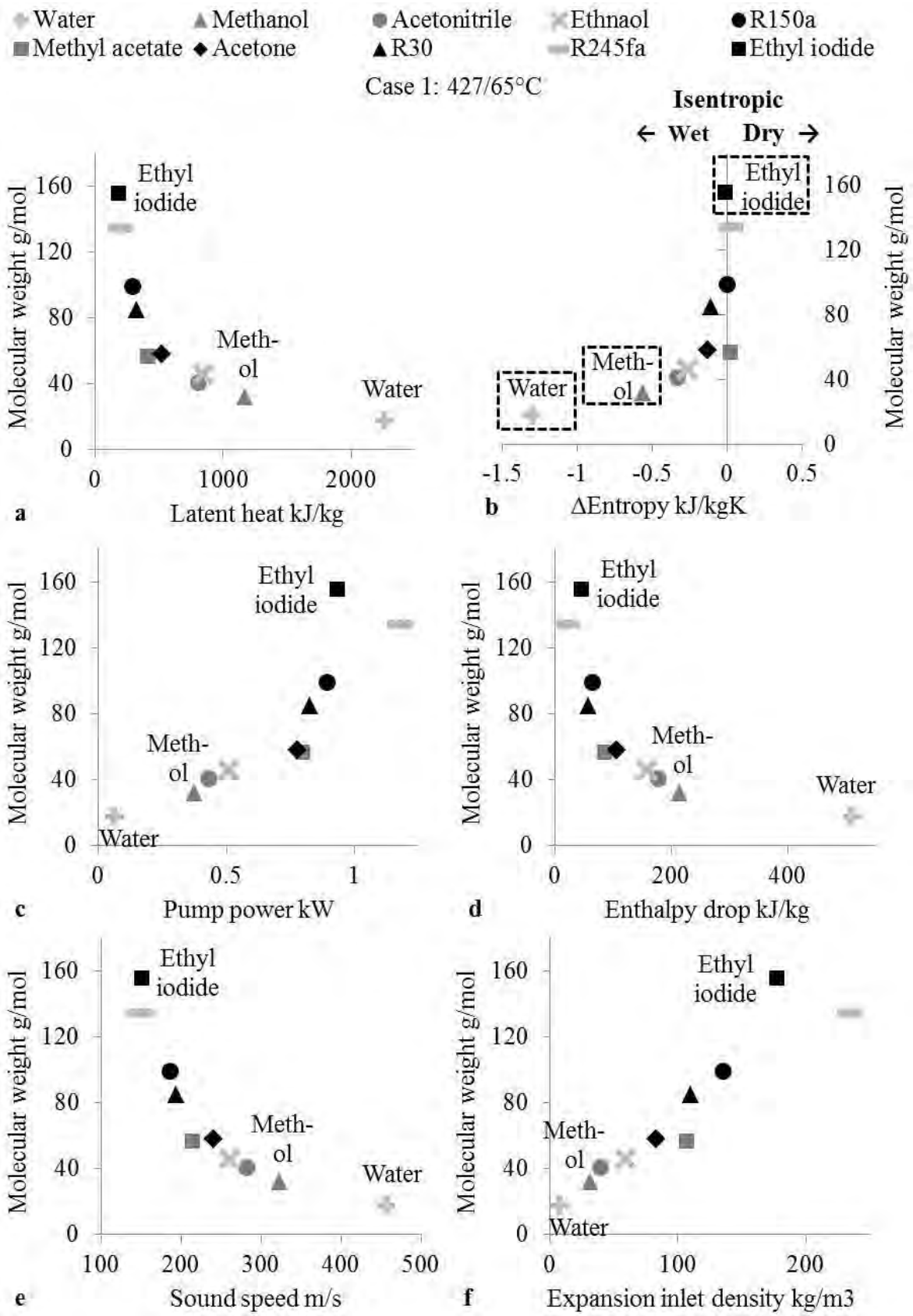

Figure 4.15 Molecular weight correlation to (a) latent heat (b) entropy change (c) pumping power consumption (d) expansion enthalpy drop (e) speed of sound (f) expansion inlet density, in Case 4

Water provided the highest thermal efficiency of 17.7%. This was due to water's large latent heat of vaporisation (H_{vap}) and its influence is illustrated in Fig. 4.16, which shows water and ethyl iodide. Under similar temperature limits in the evaporator and the condenser, water will produce higher net power per unit heat absorbed as the area formed by the cycle will be larger. This understanding can also be gained by using the theoretical expression (i.e. under the assumption of ideal gas with constant c_p) for the enthalpy drop through the expansion stage (Chen et al., 2010):

$$\Delta h_{isentropic} = c_p T_{exp,in}\left[1 - e^{H_{vap}\left(1/T_{evaporator,in} - 1/T_{condenser,out}\right)/c_p}\right] \quad \ldots(4.32)$$

Therefore, equation 4.32 also shows that fluids with higher latent heat give higher unit work output when the temperatures and other parameters are fixed.

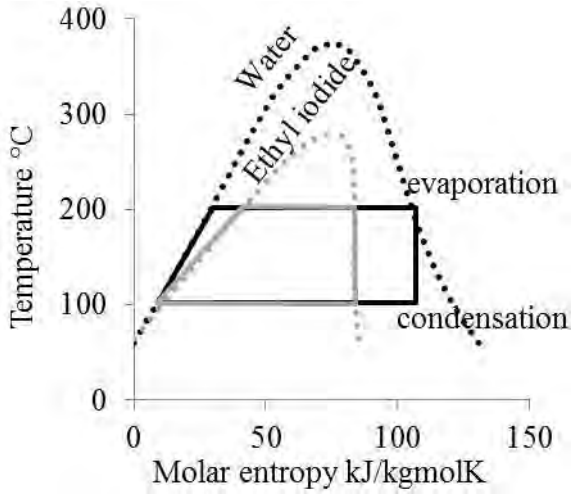

Figure 4.16 Influence of latent heat on the area formed by the cycle

Fig. 4.17a shows water cooling the EGR stream from 427 to 192°C, and recovering 50 kW of heat with contributions of 12, 32 and 6 kW in the preheater, evaporator and superheater, respectively. The major part of the heat transfer takes place in the evaporator at near constant temperature. As a consequence, 30% of the potential heat recovery remained unused. This resulted in reduced overall conversion efficiency and exergy of power production efficiency of 12.6% and 26.7%, respectively. Additionally, if the entire 6 kW of superheat was eliminated (which reduced the exit vapour fraction from 0.98 to 0.88), the heat recovery increased only marginally (from 50 to 51 kW).

In contrast, ethyl iodide has a much lower latent heat and cooled the EGR temperature down to 102°C (Fig. 4.17b) with contributions of 43 and 24 kW in the preheater and evaporator, and a fixed 5°C superheating of 1.3 kW. Hence, irrespective of around 1% point lower thermal efficiency (16.6 vs. 17.7%), it had a higher overall conversion

efficiency and exergy of power production efficiency of 16.2% and 34.5%, respectively. The thermal efficiency was lower due to the additional power being derived from a stream of steadily decreasing source temperature.

For an output capacity less than 100 kW, steam turbines show isentropic efficiencies ≈10% point lower than those for higher molecular weight fluids due to design considerations (Seher et al., 2012, Stine and Geyer, 2001). The higher molecular weight of ethyl iodide enabled a higher mass flow rate (13 times than water), which results in a better match between fluid velocity at the turbine nozzle and rotor tip speed (reduces leakage). Additionally, due to the much lower enthalpy drop (45 vs. 510 kJ/kg), a turbine for ethyl iodide is less complex and only requires a single stage to realise efficiency potential.

As a working fluid, steam attained 4-22 times lower expansion inlet densities compared to the organic fluids (Fig. 4.15f) and a low condensing pressure at 65°C. Water's sub-atmospheric condensing pressure (0.3 bar) was below ethyl iodide's sub-atmospheric (0.8 bar) and methanol's super-atmospheric pressure (1.1 bar). Water had the disadvantage of higher condensing specific volume (3.52 m^3/kg), in contrast to much lower volumes of ethyl iodide and methanol (0.19, 0.69 m^3/kg), resulting in larger condensers. The high volumes implied that the volume flows (0.062 vs. 0.052 and 0.034 m^3/s) in the expansion were high resulting in larger machines. Furthermore, both these organic fluids have lower freezing temperatures, thus eliminating freeze up concerns or equipment expansion issues. Another interesting observation is that high net power was achieved by ORCs with around 100°C lower temperature drop during expansion. This will lower thermal stresses and could reduce manufacturing cost by employing lower cost materials.

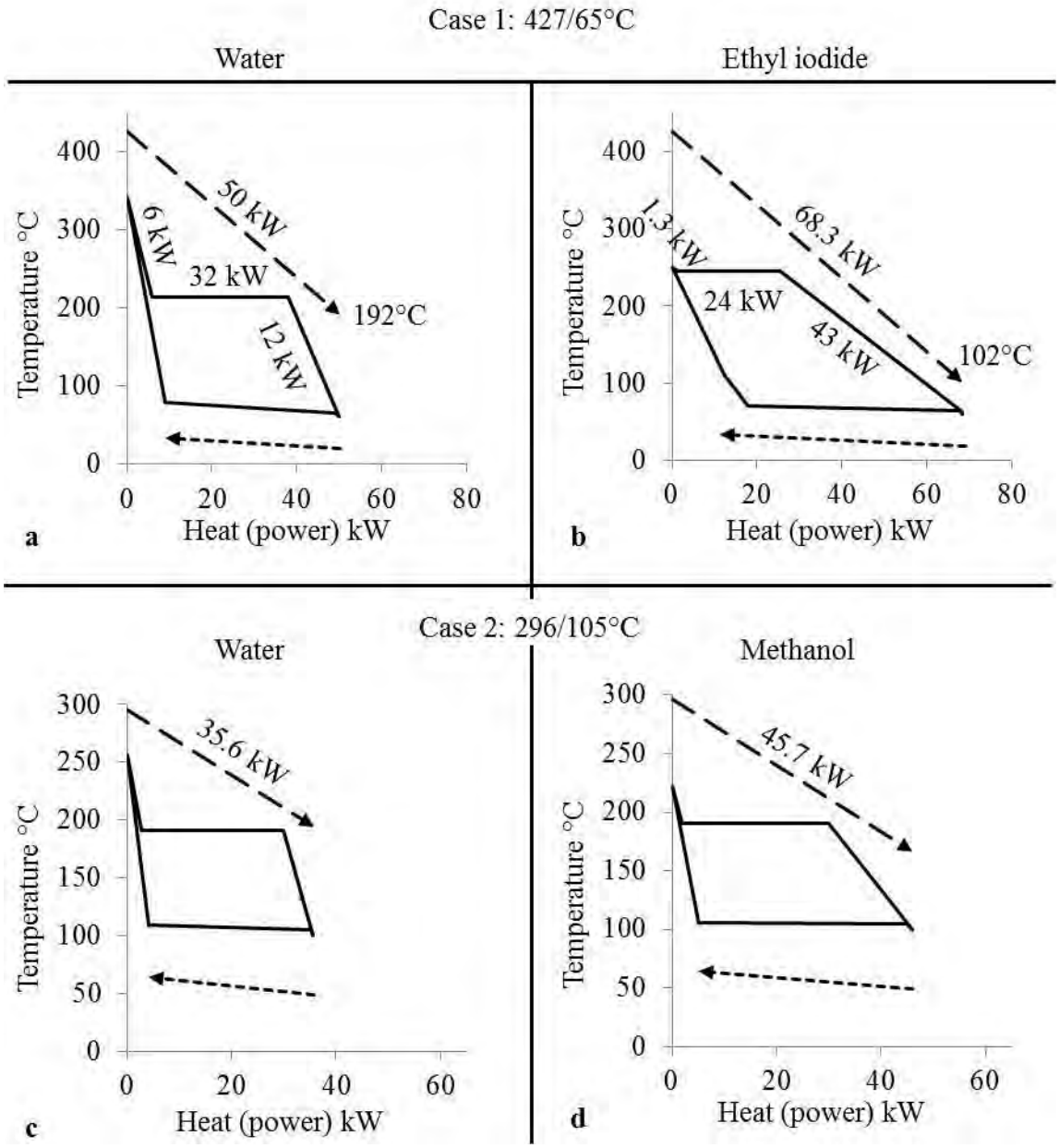

Figure 4.17 T-Q diagram for (a) water Case 1(b) ethyl iodide Case 1 (c) water Case 2 (d) methanol Case 2

4.7.1.2 Case 2 (Appendix 4.7 for tabulated results)

The higher condensing temperature in Case 2 was more suited to water, however with the reduced source temperature the heat recovery efficiency also decreased. In Case 1, the heat recovery efficiency by water was 25% lower than the highest performing organic fluid (water vs. acetonitrile), and increased to 35% in Case 2 (water vs. methyl acetate). Even when compared to the largest latent heat organic fluid, i.e. methanol (Fig. 4.17c vs. d), water recovered 25% less heat (35.6 vs. 45.7 kW) and despite the 1% point higher thermal efficiency (11.4 vs. 10.5%), it showed a 1% point lower overall conversion efficiency (5.8 vs. 6.9%).

The thermodynamic importance of low latent heat was highlighted in Fig. 4.4 for a finite source heat recovery. However, low latent heat also offered a system size advantage. The

system temperatures, corresponding operating pressures and latent heat of vaporisation are related by the Clausius-Clapeyron equation (Moore et al., 2009):

$$\ln \frac{P_1}{P_2} = \frac{H_{vap}}{R}\left(\frac{1}{T_2} - \frac{1}{T_1}\right) \ldots (4.33)$$

Where, R = 8.314 J/molK

Consider acetonitrile, methanol and water. These fluids have a similar evaporation (191°C) and condensation (105°C) temperatures. Then, as the latent heat of vaporisation increased (acetonitrile 805 < methanol 1172 < water 2258 kJ/kg), so did the required pressure ratio (acetonitrile 6.1:1 < methanol 7.7:1 < water 8.9:1), as per equation 4.33. Therefore, for a given evaporator and condenser temperature, as the latent heat of vaporisation increases, the size of the expansion machine also increases.

4.7.1.3 Suitable source temperatures for organic fluids and water

To evaluate water's suitability with increasing heat source temperature, a sensitivity analysis was conducted for Case 1. Fig. 4.18 presents the results using acetonitrile and methyl acetate which gave the upper and lower performance boundaries of the alternative high temperature organic fluids. At source temperatures above 575°C, water outperformed all the organic fluids. This was because the temperature difference between the organic fluids and the heat stream increased, resulting in larger heat transfer irreversibilities. Whereas when the source temperature dropped below 450°C, water was no longer thermodynamically efficient as the organic fluids. For source temperatures between 450-575°C, organic fluids and water resulted in comparable performance. At these temperatures, the fluid selection was more evolved due to fluid decomposition and design considerations, and may in fact favour water. Fig. 4.18 thermodynamically support Rankine cycle application for gasoline engines that offer exhaust temperatures typically greater than 450°C at cruise conditions (preferably with condensing temperature >100°C). For HDDEs, in which the source qualities are lower, higher net power can be achieved using appropriate organic fluids and cycle operating conditions. Hence, the high latent heat characteristic of water is a major limitation in low quality heat recovery. This also stresses investigations of alternative heat recovery architectures or expansion concepts using water that can ensure higher levels of heat recovery from the EGR stream and avoid the need of an additional low temperature EGR cooler.

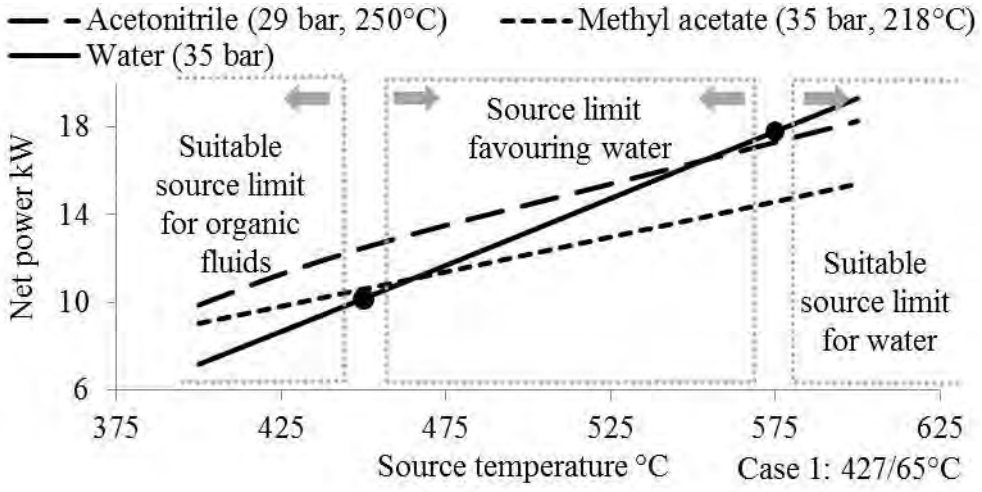

Figure 4.18 Source temperature sensitivity analysis for organic fluids and water

4.7.2 R30 compared to ethanol

Emphasis on safety, volume flow ratio and condensing pressure: Fig. 4.13 includes two chloroalkanes, R150a and R30. They contain chlorine molecules, addition of which leads to ODP. However, the selected two fluids are categorised as Very Short Lived Substances (VSLS). With ATM less than 0.5 years, near zero ODP (<0.001) have been calculated for the chloroalkanes (Calm, 1999). These values show that chlorine from the selected VSLSs are unlikely to affect ozone at quantities likely to be emitted to the atmosphere. Since majority of the ozone loss due to these VSLSs take place in the troposphere, most emissions will decompose before reaching the stratosphere. As their atmospheric persistence will be comparatively short, they will have low GWP values (<20).

With increasing chlorine content, the carcinogenic potential of the fluid also increases. Due to a much lower chlorine content (2 atoms), R30 is not classified in IARC group 1 (i.e. carcinogenic to humans). The third alternative fluid identified for Cases 1 and 2 was R30. R30 is a recommended alternative chlorinated solvent, it is not listed in the Montreal Protocol, and is expected to have no significant impact on stratospheric ozone depletion (US EPA, 2014c). R30's contribution to acid rain and smog formation is negligible (ECSA, 2007). In fact, R30 has a low photochemical ozone creation potential in the troposphere (0.9) when compared with ethanol (27) (WHO, 1996).

With an equal NFPA toxicity classification of moderate hazard (2), R30 is considered as only a slight flammability hazard (1) compared to ethanol's serious flammability hazard (3). Furthermore, due to the highest autoignition temperature (556°C) of R30 within the alternative organic fluids, the risk of leak, leading to mixing of EGR stream and R30, and causing an explosion is greatly reduced. The EGR cooler surface temperatures stayed

below the ignition temperature of R30 by a margin of 90°C over any of the engine conditions considered. This added safety was absent when using ethanol whose autoignition temperature is only 363°C. The other high temperature alternative organic fluids considered also display relatively higher autoignition temperatures (>460°C). Besides ethanol's flammability and autoignition shortcomings, it also has a near ambient flash point (18.5°C), compared to R30 which has no flash point as per the standard test method. The chlorine content of R30 also gives it lubricity and improved miscibility.

4.7.2.1 Case 1 (Appendix 4.6 for tabulated results)

Ethanol and R30 have similar critical temperature (241, 237°C) and pressure (61.4, 60.8 bar). Comparing the T-Q diagrams (Fig. 4.19a and b), it is seen that both fluids showed high levels of similarity with a nearly equal percentage of heat distribution in preheater, evaporator and superheater. For a maximum cycle pressure of 35 bar, the overall conversion efficiency for both cycles was ≈14.4%. For nearly equal average heat addition temperature, the pump power for ethanol was slightly lower (0.5 kW) compared to R30 (0.8 kW), due to its lower density (792 vs. 1318 kg/m^3) and higher latent heat of vaporisation (847 vs. 324 kJ/kg).

The maximum and minimum cycle pressures must be maintained at low levels, yet super-atmospheric, in order to prevent air or moisture ingress into the system, which reduces system efficiency. The reduced system performance is mainly due to poor heat transfer performance and loss of expansion ratio as a result of non-condensable partial pressure (Doty and Shevgoor, 2009). The higher boiling point of ethanol (78°C) compared to R30 (40°C), leads to lower condensing pressures. For the selected 65°C condensing temperature, ethanol showed a sub-atmospheric pressure (0.6 bar) involving the use of expensive equipment, compared to a super-atmospheric pressure by R30 (2.3 bar). Increasing the condensing pressure to 1 bar, to avoid the sub-atmospheric pressure reduced ethanol's operational performance by around 10%. Super-atmospheric operational pressures have the further advantage of avoiding oil leakage in the expansion machine, especially if the selected oil is incompatible with the chosen working fluid. R30 can also offer improved cold weather performance by reducing the condensing temperatures while remaining at super-atmospheric pressures.

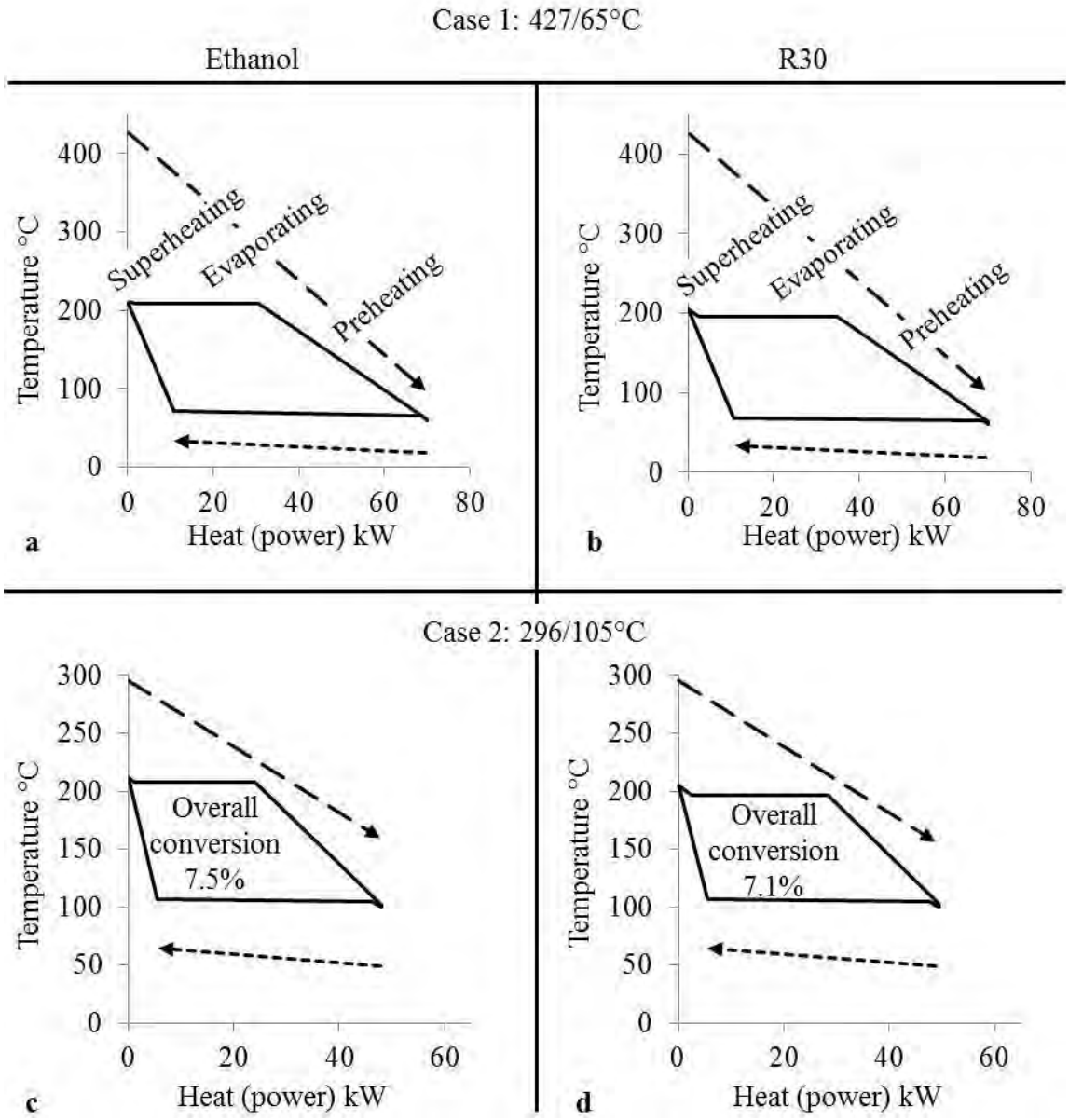

Figure 4.19 T-Q diagram for (a) ethanol Case 1 (b) R30 Case 1 (c) ethanol Case 2 (d) R30 Case 2

When considering HEX and condenser size, the heat transfer coefficients depends on the thermo-physical properties and hydrodynamic regime of the fluid, predominantly, thermal conductivity, viscosity (μ, cP) and heat capacity. Prior to a detailed heat transfer equipment calculation and design for organic fluids, the following was considered for the relative size comparison. It was assumed that the overall heat transfer coefficient (U, W/m^2°C) was similar for all the organic fluids. Therefore, UA (W/°C), i.e. overall heat transfer coefficient multiplied by the heat transfer area (A, m^2), was considered as an indicator for the absolute heat transfer size comparison. However, since heat recovery and thermal efficiency varied among different working fluids, for a relative heat transfer size comparison, UA/W i.e. UA divided by the net power produced by the system, was considered as a suitable indicator. Hence, as a first approximation, for equal heat recovery,

a lower UA/W value was desirable, and a noticeable variation in UA/W value (i.e. > 20%) was used as a screening tool. When ethanol and R30 were compared, the calculated UA/W values were similar (0.42, 0.45). The UA/W value was the second primary objective function employed in this work. (Note: The UA value accounted for the variable slope of the working fluid saturated liquid curve. Refer Appendix 4.8 for further information).

The use of efficient and compact dynamic and positive displacement expansion machines depends on small expansion Volume Flow Ratios (VFR) and low volumetric flow rates. Volume flow ratio, which integrates the density of the fluid, is defined as the ratio between the volumetric flow rates at the expansion outlet to inlet (i.e. also an indicator of the energy density of the system). For relative expansion machine size comparison, VFR/W was the third primary objective function considered. A low VFR/W value was desirable, and a small variation in VFR/W value (i.e. > 5%) was used as a screening tool. R30 compared to ethanol has higher molecular weight (84.9 vs. 46.1 g/mol) and lower condensing saturation volume (0.13 vs. 0.73 m^3/kg). Hence, R30 resulted in 1/3rd VFR/W value (1.3 vs. 4.3), and half the expansion exit flow rates (0.024 vs. 0.049 m^3/s). The noticeable expansion machine size reduction and smaller system volume of R30 then contributes to the choice of this fluid for applications where minimising size and complexity is a priority.

4.7.2.2 Case 2 (Appendix 4.7 for tabulated results)

In Case 2 (Fig 4.19c and d), both fluids once again showed similar overall conversion efficiency (7.5, 7.1%). A higher condensing temperature (105°C) was essential for ethanol, resulting in a super-atmospheric condensing pressure (2.8 bar). However, the VFR/W values for R30 were still less than half that of ethanol (1.1 vs. 2.4). A positive feature of both ethanol and R30 is the slightly negative saturation vapour curve. With real isentropic expansion and control during transient conditions, low levels of superheat are required. In both Cases 1 and 2, this amounted to only 2% of the total heat transferred in the heat exchanger. Such low levels of superheating are manageable within the evaporator, thus preventing the use of a dedicated superheater.

4.7.3 Acetone compared to R245fa

Emphasis on GWP, heat transfer irreversibilities and condensing sensitivity: The fluorine content in R245fa results in low toxicity and flammability, it is classified by NFPA as moderate hazard (2) and minimal hazard (0), respectively. However, the high number of fluorine atoms (5) are also responsible for the increase in ATM (7.7 years), resulting in a high GWP of 1030. This has resulted in consideration of R245fa as a

potential GHG and its phase down is being considered. The fourth alternative fluid identified for Cases 1 and 2 is acetone which is the simplest ketone (i.e. hydrocarbon derivative). When compared to R245fa, acetone has a reduced toxicity classification by NFPA, slight hazard (1), due to its hydrogen content. Hydrocarbons also have short ATMs (acetone's half-life is 22 days) and their GWP is usually around 20 (Calm and Didion, 1998). The disadvantage of the hydrogen content is the increased flammability. NFPA classifies acetone's flammability as a serious hazard (3). Nevertheless, this is still lower than the classification of n-pentane, which is a preferred hydrocarbon in stationary ORCs.

4.7.3.1 Case 1 (Appendix 4.6 for tabulated results)

Compared to acetone, R245fa has a relatively lower boiling point (15 vs. 56°C) and hence, operates at higher super-atmospheric condensing pressures (5.3 vs. 1.3 bar). This implies denser vapours with lower condensing specific volumes (0.04 vs. 0.34 m^3/kg). As a result, the VFR/W values for R245fa were nearly half of acetone (1.5 vs. 2.8). Due to the much higher molecular weight of R245fa (134 vs. 58.1 g/mol), the specific enthalpy drop during expansion is relatively small (22 vs. 106 kJ/kg). Hence, by default, the feed pump work needs to be relatively large. For a maximum cycle pressure of 33 bar, R245fa gave a low thermal and overall conversion efficiency of ≈8.3%, while the pumping power accounted for 17% of the total expansion power. The efficiency of a FBC depends largely on the losses from irreversible heat transfer, best represented by the magnitude difference in matching of the working fluid T-Q curves to the source and sink (Fig. 4.20a vs. b). The lower average heat addition temperature, because of the lower critical temperature of R245fa (154 vs. 235°C), then led to large irreversibilities in the EGR heat exchanger (22.7 vs. 17.4 kW). Also note, when heat recovery is similar, HEX irreversibilities are directly proportional to the heat exchanger Logarithmic Mean Temperature Difference (LMTD) (Fig. 4.21).

Conversely, acetone with a higher critical pressure and temperature is better suited to EGR temperature level. For a cycle pressure of 35 bar, it produced a thermal and overall conversion efficiency of ≈14.5%. Under such conditions, the pump work was relatively low, only 7% of the total expansion power. Acetone will have a larger absolute heat transfer area due to the reduced heat transfer irreversibilities. However, due to the nearly equivalent heat recovery by R245fa and acetone (69.3 kW), and the higher net power produced by acetone, the UA/W value of acetone was 2/3rd of R245fa (0.22 vs. 0.35). Furthermore, acetone offered nearly twice the values of average thermal conductivity when compared to R245fa (0.09 vs. 0.05 W/mK).

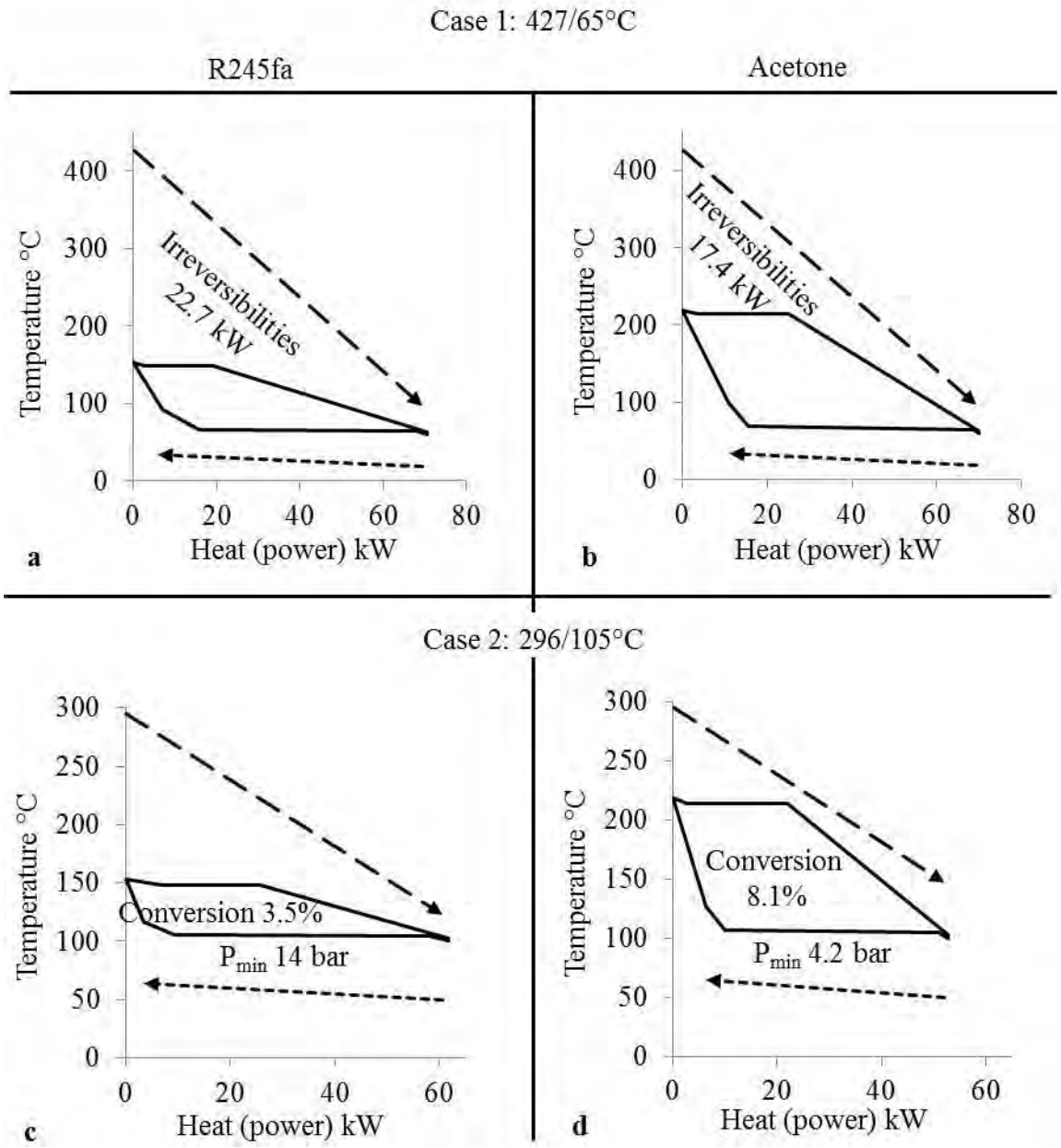

Figure 4.20 T-Q diagram for (a) R245fa Case 1(b) Acetone Case 1 (c) R245fa Case 2 (d) Acetone Case 2

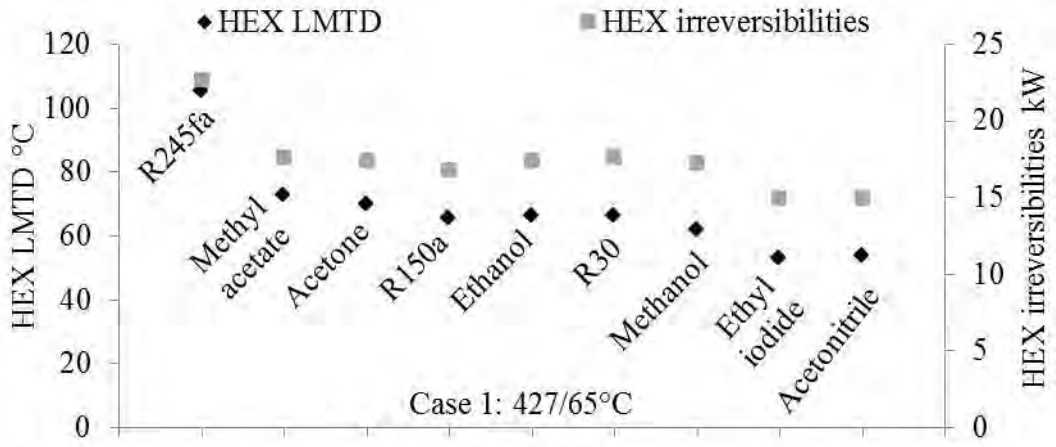

Figure 4.21 Proportionality in exergy destruction in the heat exchanger and the LMTD for equal heat input in Case 1

4.7.3.2 Case 2 (Appendix 4.7 for tabulated results)

In Case 2, despite a more favourable lower source temperature (296°C), R245fa was an unattractive working fluid with a low overall conversion efficiency of 3.5% (Fig. 4.20c vs. d). R245fa in Case 2 recovered similar quantities of heat as in Case 1 (69.2, 60.5 kW), but over a smaller LMTD (105 vs. 54°C). As a result, the working fluid mass flow rate increased from 0.31 to 0.38 kg/s and the pumping power accounted for 30% of the expansion power. Under this condition, VFR/W value increased from nearly half of acetone in Case 1 to 2/3rd in Case 2. R245fa also resulted in heavier air condenser due to the much higher condensing pressure (14 vs. 4.2 bar).

R245fa that is usually marketed for stationary ORCs played a key role in the initial resurgence of mobile ORCs. This was primarily due to a positive stationary ORC experience, and the possibility of using and/or modifying the existing hardware that were available in HDDE and MAC sectors (e.g. Cummins Turbo Technologies developing turbine expanders). However, it was clear that R245fa would be better suited for heat recovery between 150-250°C, where better temperature matching between the heat stream and the working fluid is possible. Furthermore, R245fa performance showed high sensitivity to increased condensing temperature, making it more attractive to condensing temperatures around 30-40°C. However, acetone retained its suitability in Case 2 and provided the highest overall conversion efficiency of 8.1% (along with methyl-acetate). (Note: Due to the change in the gradient of the saturated vapour line, higher levels of superheating were also considered for R245fa. Refer Appendix 4.9 for further information).

4.7.3.4 Rationality of fluid pairing

It is important to point out that the rational for the chosen pairings of working fluids in Sections 4.7.1-4.7.3 for discussion was threefold. Firstly, related to highlighting the contrasting range of potential organic fluid options (Ethyl iodide, methanol). Secondly, related to the T-S curves (ethanol and R30 require marginal superheating, whereas R245fa and acetone do not require superheating). Finally, related to highlighting also the unfavourable process properties of the four alternative fluids. This can be best understood by considering Appendix 4.10, which shows possible alternative parings and some key items of discussion.

The thermodynamic properties of air, exhaust and working fluids were calculated using the Peng-Robinson property package (Aspen HYSYS V 7.3, 2011a, AEA Technology, 2000).

The difference in net power was compared against REFPROP property package. A low discrepancy of 1.4, 0.5, 1.6, 0.7 and 1.8% was calculated in Case 1 for water, ethanol, methanol, acetone and R245fa, respectively.

4.7.4 R152 and E152a compared to R245fa

Emphasis on GWP: This section discusses the possible alternative working fluids for Case 3, i.e. CAC heat recovery using a pinch point of 20°C. The trade-offs were conducted using the simulation results presented in Appendix 4.11, along with emphasis on the environmental impact from Appendix 4.4. For high heat recovery, working fluids with critical temperatures below the CAC temperature were only considered.

4.7.4.1 Case 3 (Appendix 4.11 for tabulated results)

Due to a relatively higher condensing temperature (65°C) for the low quality heat (176°C) in Case 3, the thermal efficiencies for all the fluids were extremely low (5.9-6.6%). As a contrast, 2.5 times more heat was rejected per unit of power output for equivalent condensing temperatures when comparing CAC to EGR (Case 3 vs. 1). The best performing working fluid was E245cb1 with an overall conversion efficiency of 3.2%. The remaining fluids, 1,2-Difluoroethane (R152), R143, E152a, R245fa and R245fa1 all gave similar overall conversion efficiency (2.6-2.8%).

A GWP value less than 150 was a primary consideration preventing the selection of E245fa1, R143, R245fa and E245cb1. However, R152 and E152a with only 2 fluorine atoms gave ATM values ≤ 2 years, resulting in GWP values ≤ 110. When these two fluids were compared with R245fa, they also gave nearly equivalent UA/W value (0.8-0.81 vs. 0.82) and VFR/W value (1.5-1.6 vs. 1.8). The addition of one hydrogen atom and the reduction of three fluorine atoms in these two fluids have the drawback of increased flammability rating by one hazard level compared to R245fa.

These two fluids are not to be confused with R152a (1,1-Difluoroethane, CAS no. 75-37-6), which is being considered for MAC systems (EAA, 2011). R152a has a boiling point of −25°C, much lower than −5°C limit justified in this work. R152a is a HFC like R152, however E152a is a Hydrofluoroether (HFE).

4.7.4.2 Additional possible working fluids

The lack of adequate refrigerants with low GWP and flammability has led to intense R&D efforts by the chemical companies in designing new working fluids with improved molecular makeup. Hence, apart from the 330 pure fluids considered in this work, additional fluids relatively new or currently in the process of being introduced to the market were also screened. Three fluids showing suitability based on the limited available information were HFO-1261zf, DR-2 and Novec 649 (Calm and Hourahan, 2011, Kontomaris, 2011, 3M, 2009).

- HFO-1261zf has a suitable boiling point of −3°C, however the ATM value is extremely low 0.002, creating challenges in handling.
- DR-2 (an HFO) is a non-flammable drying fluid with a critical temperature of 171°C and a GWP value of 9.4. The drawback of using DR-2 is that it required 1.5 times the expansion machine size compared to R245fa (Datla and Brasz, 2012).
- Novec 649 is non-flammable fluid with GWP of 1 and has shown thermal stability up to 300°C. However, containing a total of 19 atoms in the molecule (extremely drying fluid) it will necessitate the use of an IHE.

These three fluids further highlight the extremely low possibility of an ideal working fluid to be synthesised as per the fluid ranking criteria (Fig. 4.9). Also, these new fluids despite their low ATMs have critical temperatures unsuitable for EGR and exhaust streams.

4.8 Performance and system index (Phase 5)

For the final phase of fluid evaluation, a PSI developed using equation 4.29 was used to benchmark 6 selected parameters of any working fluid against the obtained optimal values. The first parameter of equation 4.34 considers the system performance, and the rest indirectly assess the compactness and the cost effectiveness of the overall system.

$$PSI_{wf} = \left[\begin{array}{l} PSI_{0.33} \dfrac{\eta_{conversion,wf}}{\eta_{conversion,optimal}} + PSI_{0.33} \dfrac{VFR / \dot{W}_{net,optimal}}{VFR / \dot{W}_{net,wf}} \\ + PSI_{0.165} \dfrac{\left[\left(UA_{tot} / \dot{W}_{net} \right) / \eta_{recovery} \right]_{optimal,wf}}{\left[\left(UA_{tot} / \dot{W}_{net} \right) / \eta_{recovery} \right]_{wf}} \\ + PSI_{0.055} \dfrac{\lambda_{wf}}{\lambda_{optimal,wf}} + PSI_{0.055} \dfrac{\mu_{optimal,wf}}{\mu_{wf}} + PSI_{0.055} \dfrac{\left(\dot{Q}_{vap} / \dot{Q}_{tot} \right)_{optimal,wf}}{\left(\dot{Q}_{vap} / \dot{Q}_{tot} \right)_{wf}} \end{array} \right] \quad \ldots(4.34)$$

Table 4.3 presents the justification and influence of the 6 parameters used in calculating the PSI values. The 6 selected parameters helped in the rapid identification of working fluids of interest and highlighted their favourable process properties. The most suitable

working fluid was defined as that which has a high overall conversion efficiency, a compact expansion machine, and a low HEX and condenser size for a given net power output (i.e. the three primary objective functions). Fluids with favourable performance and process properties result in high PSI values and vice versa.

Table 4.3 Justification and influence of the 6 parameters used in calculating the PSI value

Parameter 1 ($PSI_{0.33}$=**0.33**) : $\frac{\eta_{conversion,wf}}{\eta_{conversion,optimal}}$ Indicates the conversion efficiency of the available heat to net power. The three design objectives (Parameter 1, 2 and 3) were equally weighed with a PSI weight factor of 0.33.
Parameter 2 ($PSI_{0.33}$=**0.33**) : $\frac{VFR/\dot{W}_{net,optimal}}{VFR/\dot{W}_{net,wf}}$ Indicates the expansion machine size per net power produced. The largest percentage of the FBC component costs (and variations) will be due to the expansion machine, HEX and condenser. (Assumption: piping, storage tank, valves, pump, transmission, controls and fluid costs are the same). In addition, the absolute size of the system, an important design factor in mobile application, as a first approximation is directly proportional to VFR and UA values. Hence, having a compact turbine or expander, and low HEX and condenser areas per net cycle power output is vital.
Parameter 3 ($PSI_{0.165}$=**0.165**) : $\frac{[(UA_{tot}/\dot{W}_{net})/\eta_{recovery}]_{optimal,wf}}{[(UA_{tot}/\dot{W}_{net})/\eta_{recovery}]_{wf}}$ Indicates the overall HEX and condenser footprint (UA_{tot}) of the FBC per net cycle power output. By normalising with the heat recovery efficiency ($\eta_{recovery}$), this parameter will then not be biased towards fluids with higher temperature, lower heat recovery. To account for the heat transfer coefficient differences among the working fluids, Parameters 4, 5 and 6 (sub-set of Parameter 3) were also included. The PSI weight factor of 0.33 was equally divided between Parameter 3 (0.165) and Parameter 4, 5 and 6 (0.055 each).
Parameter 4 ($PSI_{0.055}$=**0.055**) : $\frac{\lambda_{wf}}{\lambda_{optimal,wf}}$ Indicates the average thermal conductivity of the working fluid.
Parameter 5 ($PSI_{0.055}$=**0.055**) : $\frac{\mu_{optimal,wf}}{\mu_{wf}}$ Indicates the average viscosity of the working fluid. Average values in Parameter 4 and 5 are necessary due to the profoundly different liquid and vapour thermal conductivities, and the general trend of decreasing viscosity as temperature increases.
Parameter 6 ($PSI_{0.055}$=**0.055**) : $\frac{(\dot{Q}_{vap}/\dot{Q}_{tot})_{optimal,wf}}{(\dot{Q}_{vap}/\dot{Q}_{tot})_{wf}}$ $\dot{Q}_{vap}$ is the total heat transferred in vapour form by the cycle, i.e. summation of the total superheating and de-superheating load, whereas $\dot{Q}_{tot}$ is the total HEX and condenser duty. As the volume will be high and thermal conductivity will be low for a working fluid in vapour state compared to liquid and two-phase, this parameter will point towards the use of fluids with isentropic expansion (i.e. low vapour heat transfer).

4.8.1 Case 1 and 2

In clockwise direction for decreasing PSI values, Fig. 4.22 shows the normalised values of the selected 6 parameters for all the simulated fluids. In Case 1 (Fig. 4.22a), PSI values could be easily distinguished into 3 groups: high (0.85), medium (0.71-0.68) and low (<0.65) values. R30 demonstrated the highest PSI value (0.85). Ethyl iodide, methanol and acetone were medium performing fluids (0.71-0.7). The three fluids currently in the literature, i.e. R245fa, ethanol and water gave low values (<0.65).

In Case 2 (Fig. 4.22b), PSI values were divided into 4 groups: high (0.87), medium (0.82-0.76), acceptable (0.71) and low (0.59). Once again, R30 showed the highest PSI value (0.87). Ethyl iodide, methanol and acetone remained in the medium performing group (0.81-0.76). Ethanol and water showed acceptable PSI results (0.71), whereas R245fa was clearly least suited in Case 2 (0.59). The improvement of ethanol and water was largely attributed to the higher condensing temperature resulting in lower VFR/W values compared to Case 1. Hence, the overall performance and system suitability of R30, ethyl iodide, methanol and acetone were also reflected in their higher PSI values compared to water, ethanol and R245fa in both Cases 1 and 2.

The relatively narrow window of the PSI values for 6 out of the 7 alternative high temperature fluids presented in this work in Case 1 (0.71-0.68) and Case 2 (0.82-0.76) was due to the screening criteria employed. By classifying fluids into comparable thermo-physical and/or molecular groups, the fluids then exhibited similar thermodynamic characteristics and trends.

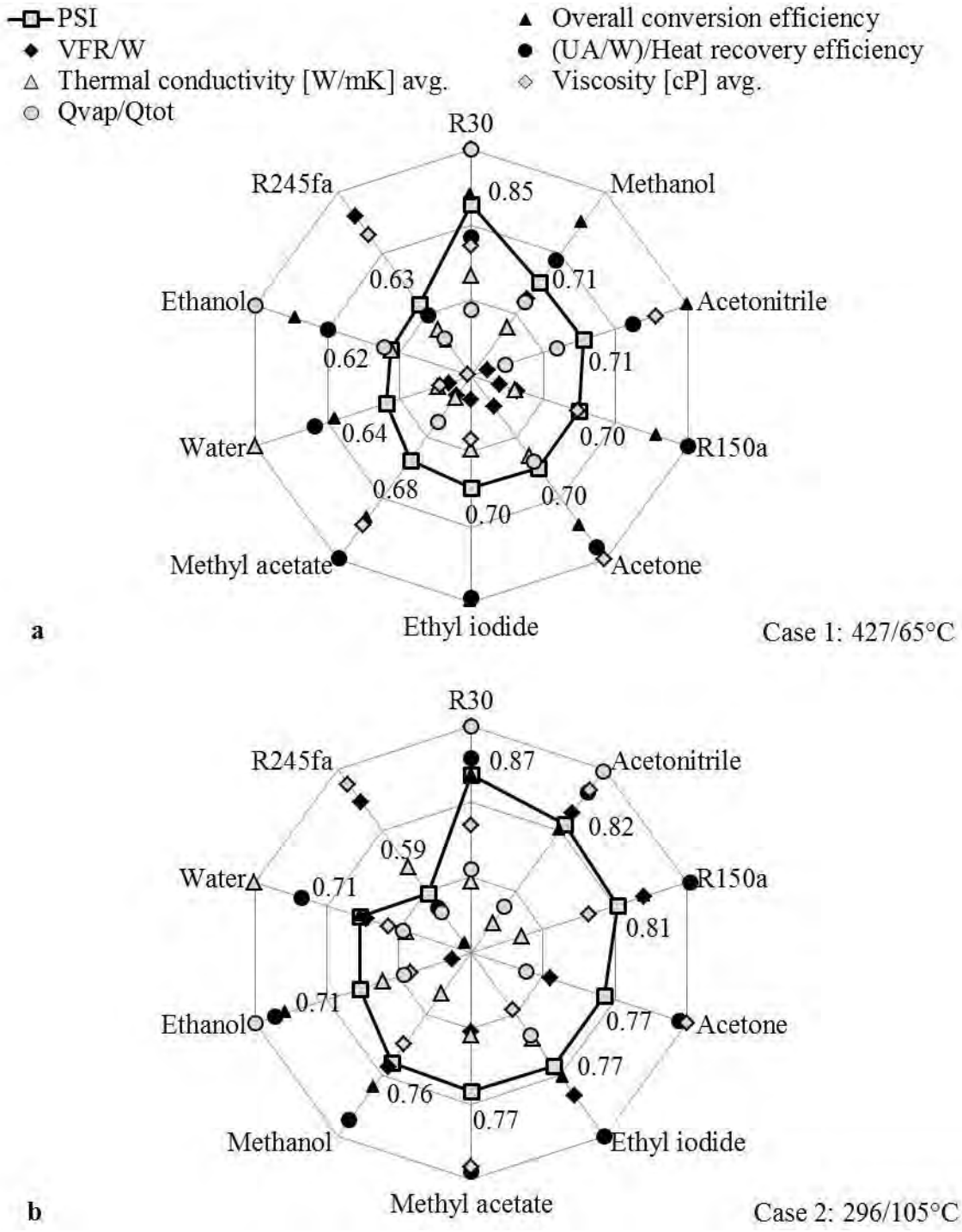

Figure 4.22 Performance and System Index values for (a) Case 1 (b) Case 2, showing suitability of R30, ethyl iodide, methanol and acetone

4.8.2 Case 3

In Case 3 (Fig. 4.23), PSI value distinction was between two groups of high (0.91-0.85) and low (0.79-0.78) values. The two alternative low temperature fluids presented in this work, i.e. R152 and E152a fell under the high PSI value group, with R152 being superior over E152a (0.91 vs. 0.85). Note that R143, another high PSI value fluid (0.88), in fact has the lowest GWP value (352) among the rejected fluids.

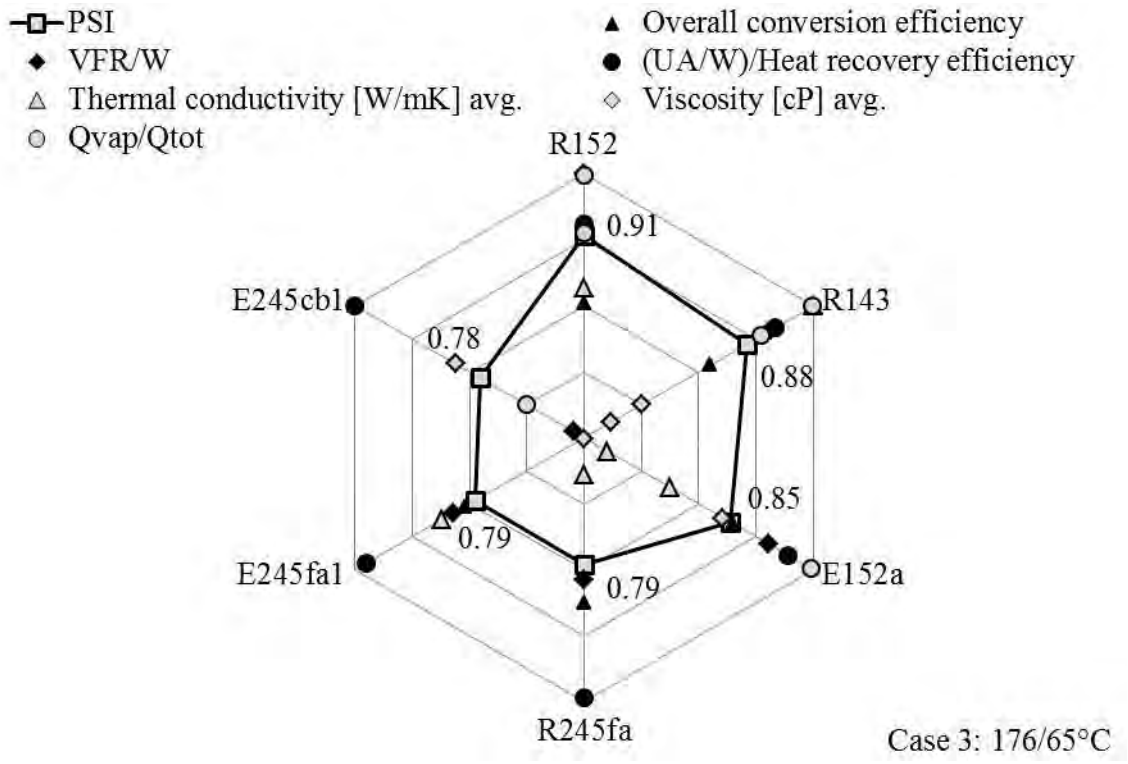

Figure 4.23 Performance and System Index values for Case 3 showing suitability of R152 and E152a

4.8.3 Importance of appropriate performance and system index

It is important to point out the influence on the PSI value by either ignoring component size per unit net power or by a partial selection of the 6 PSI parameters. For this, consider the two modified PSI results for Case 1 given in Fig. 4.24a and b.

Fig. 4.24a replaces the normalised per unit power output values of Parameter 2 (i.e. VFR/W) and Parameter 3 (i.e. UA/W), with VFR and UA. This set of parameters will then be biased towards a compact expansion machine (despite the lower net power output), and low HEX and condenser footprint (despite the lower heat recovery efficiency) reasoning. Therefore, R245fa which gave the lowest volume flow ratio (8.7:1) and lowest net power (5.8 kW), resulted in the second highest PSI value of 0.69. Furthermore, water which only recovered higher source temperatures (from 427 to 192°C), offered low UA value and the third highest PSI value of 0.62, without taking into account that the remaining EGR stream still required additional cooling.

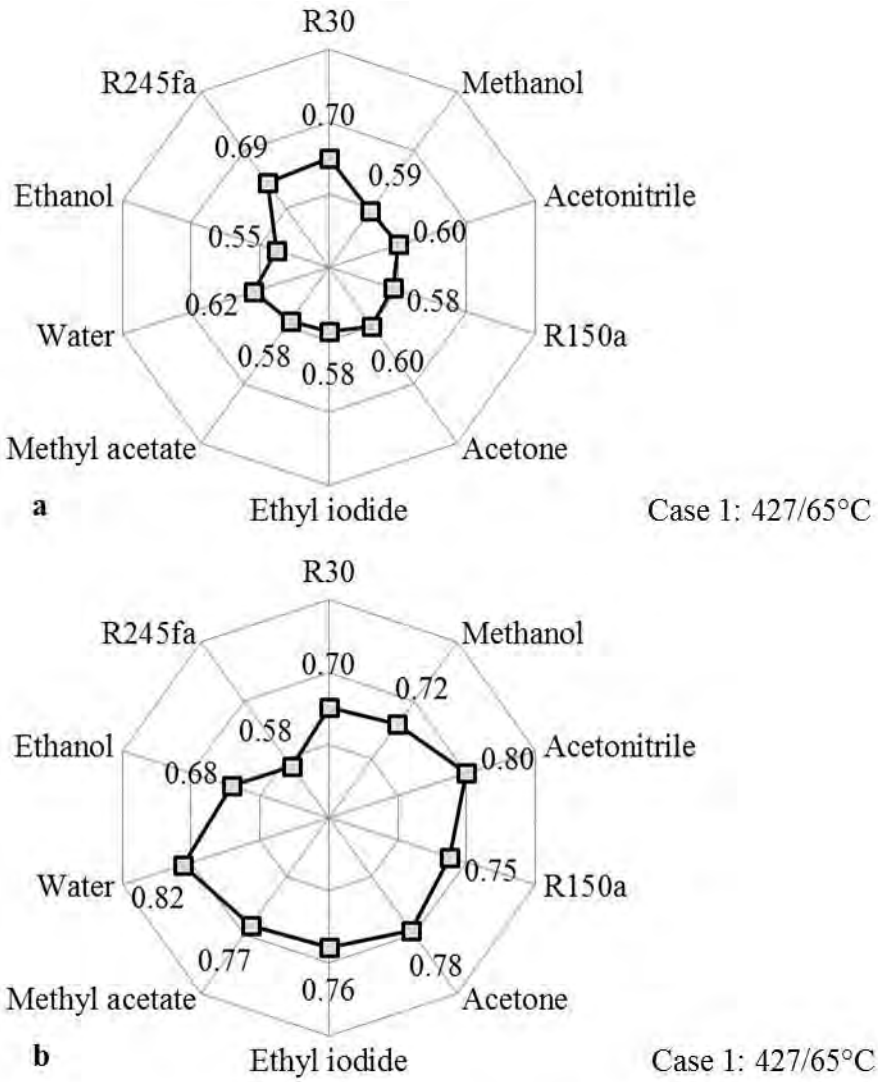

Figure 4.24 Influence on the PSI value in Case 1 by (a) ignoring component size per unit net power (b) partial selection of the PSI parameters

Now consider Fig. 4.24b using the same modifications of Fig. 4.24a, but excluding Parameter 2. This will then favour the suitability of higher critical temperature fluids. As a result, water and acetonitrile gave the highest PSI values (0.82, 0.8). Furthermore, R245fa, which was one of the best fluids in Fig. 4.24a, turned out to be the worst in Fig. 4.24b.

FBC parameters present a multi-dimensional surface on which an optimum condition can be found within prescribed constraints. Inclusion of all the 6 PSI parameters, as shown in equation 4.34 and considered in this chapter attempts to be least biased towards any of the fluids usually considered. The main objective of the 6 parameters was to identify working fluids that could show an improved performance and system (size and cost) trade-off to achieve a better integration within a HDDE.

4.8.4 Sensitivity to the developed performance and system index

To further assess the suitability of the alternative fluids presented in this chapter, a detailed sensitivity study to the assigned PSI weight factors was also considered. Appendices 4.12, 4.13 and 4.14 correspond to Cases 1, 2 and 3, respectively. A ±30% variation in each of the PSI weight factors was considered for all the 6 considered parameters.

Considering Cases 1 and 2, in none of the 12 variations presented, R245fa, ethanol or water outperformed any of the alternative high temperature fluids. Furthermore, R30 offered the best PSI values under all 12 variations, while ethyl iodide, methanol and acetone remained closely grouped. When considering Case 3, the alternative low temperature fluids R152 and E152a also retained higher PSI values compared to R245fa for the 6 variations presented.

Few additional items to point out amongst the high temperature fluids are:

- Ethyl iodide and acetonitrile were suitable for both EGR and exhaust temperature levels. However, due to a normal boiling point of 72 and 82°C, respectively, they will only be used in further analysis with condensing temperatures at typical engine radiator level or higher. Ethyl iodide is recently being included into specialist refrigerant databases and offers a high flash point of 53°C (Calm and Hourahan, 2011).
- Acetone and methyl acetate offer highly similar thermodynamic/thermo-physical and environmental/safety properties. Among the two, only acetone will be used in further analysis, this is since it was marginally superior at EGR temperature level (i.e. Case 1).
- R150a and R30 both belong to the same class of fluids (i.e. HCC). Among the two, only R30 will be used in further analysis due to its noticeably higher PSI value.

4.9 Heat exchanger implications

Finally, this section details some implications related to the minimum approach temperature difference, sub-cooling level and system irreversibilities. As such, some equipment performance assumptions are validated, a statement made earlier is quantified and the direction for the second research avenue is provided.

4.9.1 Minimum approach temperature difference

In this chapter, a minimum pinch point of 20°C and the lowest condensing temperature of 65°C was employed in Cases 2, 3 and 1, 3 respectively. Fig. 4.25 shows the impact of the pinch point on heat exchanger UA/W value for CAC (Case 3, R245fa) and exhaust HEX

(Case 2, ethanol). Also shown is the influence of condensing temperature (Case 1, ethanol) on the condenser UA/W value for a fixed heat input of 70 kW.

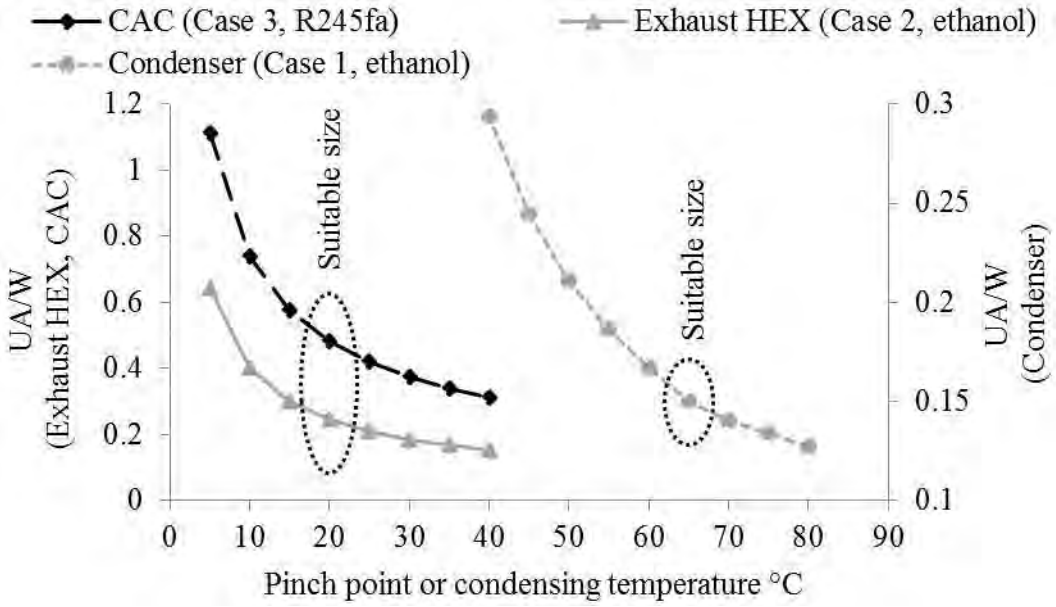

Figure 4.25 Impact of pinch point and condensing temperature on heat exchanger and condenser UA/W value

As can be seen, there is an inflection point at pinch point value of ≈20°C and condensing temperature of ≈65°C where the UA/W values increased dramatically. Lower pinch point values and condensing temperatures lower the irreversibilities, but have a negative impact on packaging and cost. The resultant excessively large surface areas will further increase the working fluid and heat stream pressure losses. Hence, the smallest pinch point value (i.e. 20°C) and the lowest condensing temperature (i.e. 65°C) selected in the simulations made a viable case for ORCs offering a suitable techno-economical trade-off.

4.9.2 Sub-cooling level

It was stated in Section 4.3 that for a fixed heat into the cycle, excessive sub-cooling will only marginally reduce the cycle performance, but will greatly influence the size of the total condenser. This statement can now be quantified. Consider Fig. 4.26a and b, which shows the percentage change in net power and the UA value of the condenser in Case 1 (ethanol) and Case 3 (R245fa) with an increasing sub-cooling level.

In Fig. 4.26a, increasing the sub-cooling to 5°C from the saturated liquid condition at 65°C increased the total condenser size by 8% with a reduction in net power of 2%. However, when the sub-cooling was increased to 15°C, the total condenser size required increased to

28% with a reduction in net power of only 4%. The same trend was also seen in Case 3, however due to the lower quality and the proximity of the working fluid critical temperature to the source inlet temperature, the impact on the net power was higher (9 vs. 4%).

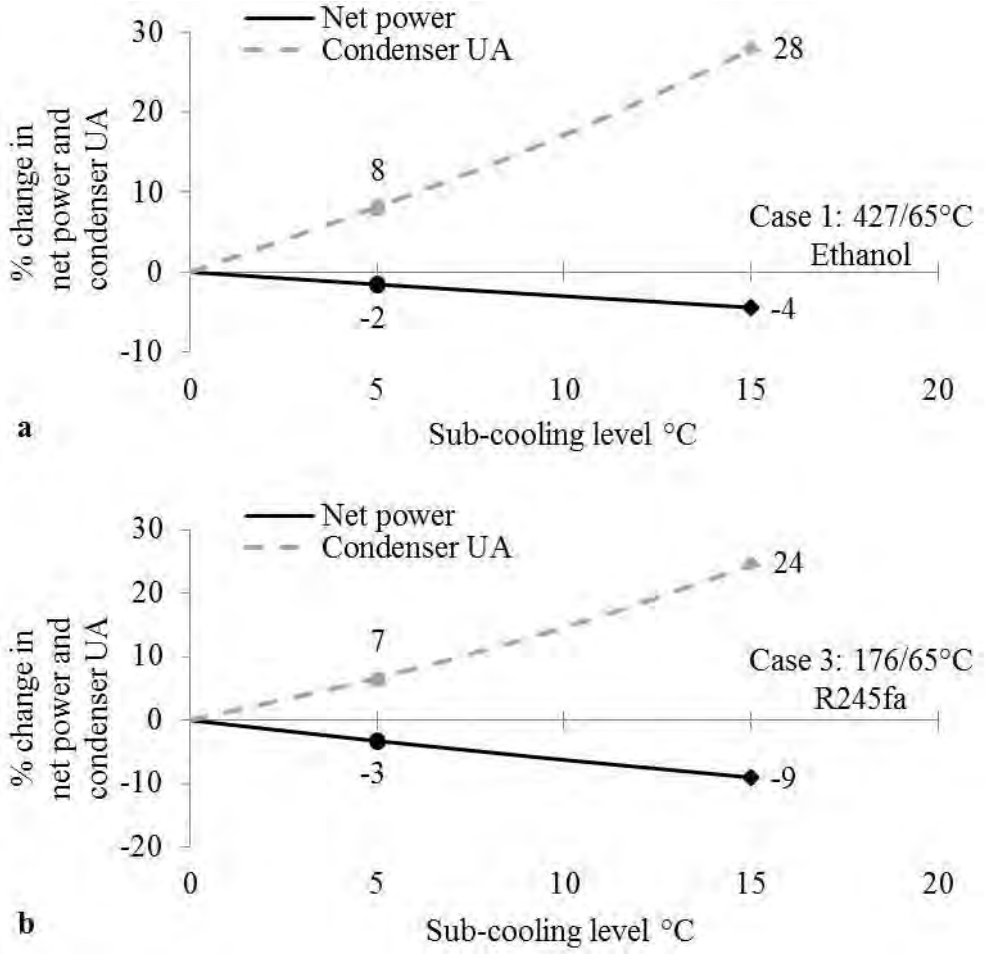

Figure 4.26 Percentage change in net power and condenser UA value due to increased sub-cooling (a) Case 1 with ethanol (b) Case 3 with R245fa

With increasing sub-cooling, the heating of the working fluid to the saturated vapour state requires additional heat. For a fixed enthalpy difference across the expansion, the mass flow rate of the working fluid decreases with increasing sub-cooling. Hence, according to equation 4.15 the expansion power reduces.

4.9.3 Heat exchanger irreversibilities

The importance of exergy destruction analysis resides in its ability to provide directions for performance improvement. Fig. 4.27 presents the averaged relative component irreversibilities in the three cases using the 7 high temperature and the 2 low temperature alternative organic fluids. In all the 3 cases, HEX made the biggest contribution followed

by the condenser. In Case 2, the condenser also showed relatively higher irreversibilities due to a higher condensing temperature (105 vs. 65°C) governed by the hotter inlet cooling air stream (55 vs. 20°C). While in Case 3, although the condensing and the inlet cooling air stream temperatures were same as in Case 1 (65 and 20°C), due to the low temperature heat recovery (176 vs. 427°C), the condenser irreversibilities were equivalent to those of the HEX. The expansion and pumping irreversibilities, which are related to the isentropic efficiencies, were relatively low and insignificant, respectively.

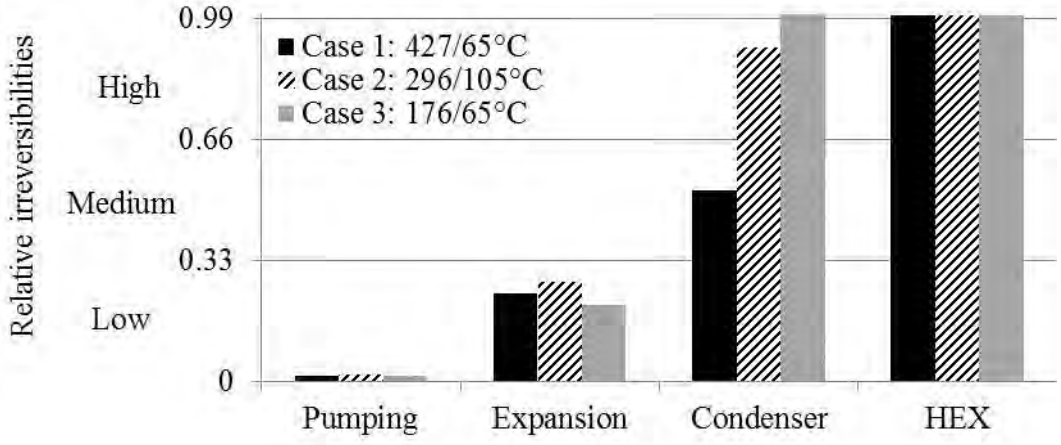

Figure 4.27 Averaged relative component irreversibilities using the alternative organic fluids

4.9.3.1 Condensing irreversibilities

Cases 1 and 2 temperature limits were selected to perform a fluid selection study with sensitivity analysis. Condenser irreversibilities for exhaust (i.e. Case 2) will in fact noticeably decrease when the condensing temperature will be reduced from 105 to 65°C. Nonetheless, for EGR and exhaust temperature level heat recovery, firstly, the condenser irreversibilities will remain the second biggest contributor to the total cycle irreversibilities, and secondly, condenser irreversibilities for different organic fluids will be relatively similar. Furthermore, the opportunity of reducing the condensing irreversibilities with a simple cycle using pure fluids was rather limited.

For this, consider methanol and R245fa in Case 1. The condensing process involved a fixed condensing temperature of 65°C, sub-cooling level of 5°C and air temperature rise through the condenser of 15°C. R245fa simulations gave marginally higher condenser irreversibilities compared to methanol (8.9 vs. 8.4 kW). As shown in Fig. 4.28, R245fa entered the condenser at 93°C with a total of 7.6 kW of de-superheating load, whereas methanol entered with a vapour quality ≈0.98 at 69°C. The grey shaded triangle in

Fig. 4.28 then shows the main cause of the marginally increased condenser irreversibilities in R245fa. Hence, for every case considered in this thesis, the irreversibilities in the condenser for pure fluids were only a function of the de-superheating load and the pressure loss in the condenser.

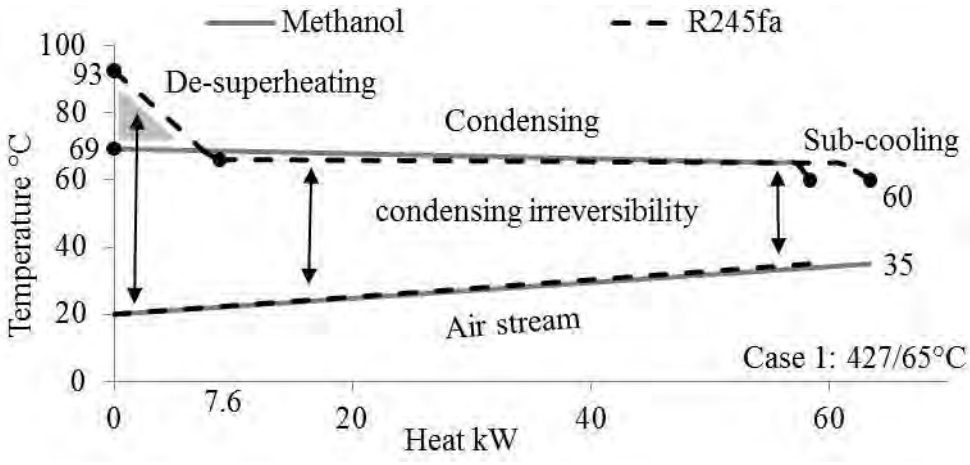

Figure 4.28 Irreversibilities in the condenser as a function of the de-superheating load and the pressure loss in Case 1

4.10 Chapter 4: Summary

The alternative working fluids presented in this chapter were the end result of a detailed pure fluid selection and evaluation methodology. The method developed for ORCs applied to automotive HDDEs considered 1800 fluids in total and examined 330 fluids in detail. Using fundamental fluid chemistry trends and rules, trade-offs among desired properties to identify optimal solutions were conducted. The employed 25 fluid screening criteria gave a screening efficiency of 99.5%, filtering out the near optimum working fluids at an early stage. With 16 maximised and minimised fluid ranking indices for a subcritical cycle with minimum vapour heat transfer, the study identified ethyl iodide, methanol, R30, acetone, R152 and E152a as the most suitable alternatives.

The developed PSI which was based on the primary objective functions ($\eta_{conversion}$, VFR/W and UA/W) validated the suitability of the alternative fluids, with the practicality of a fluid being directly proportional to this index value. The alternative fluids also retained higher PSI values under ±30% variation in the PSI weight factors. This consistency in the results was an important finding as it established the fact that the alternative fluids simultaneously maximised the overall conversion efficiency and minimised the system size and cost. Furthermore, considering extreme cases (e.g. Cases 1 and 2) was an integral part

of the method, highlighting the working fluid sensitivity to varying source and condensing temperatures.

Understanding the fundamental thermo-physical and molecular distinctions between water and organic fluids, and using molecular screening as conducted in this work then presented with suitable alternatives. The three relevant comparisons to fluids in the published literature can be summarised as:

- Compared to water; ethyl iodide and methanol aided in an efficient system and simpler design for Cases 1 and 2. The source characteristics was better matched, resulting in higher overall conversion efficiencies, along with the advantages of compact equipment.
- Elimination of a fluid traditionally based on chlorine content, without distinction between open and closed systems, and excluding ATM is rather simplistic. With nearly equal net power in Cases 1 and 2, R30 was preferred over ethanol due to its lower flammability, higher autoignition temperature and lower VFR/W value.
- Retaining the thermodynamic performance and system size of R245fa in Case 3, but avoiding the adverse environmental impact was addressed using R152 and E152a which contain only 2 fluorine atoms.

Finally, cycle component irreversibilities showed that reducing the extent of losses could be focused primarily on the heat transfer between the high temperature source and the working fluid. Achieving this by varying the expansion inlet parameters and increasing the net power output is a focus for the next chapter.

5 Cycle Operation

5.1 Introduction

A major source of irreversibility in ORCs shown in Chapter 4 was attributable to the temperature difference between the high temperature heat sources and the working fluid (Fig. 4.27). For the studies reviewed in Chapter 2, minimising this irreversibility and increasing overall conversion efficiency was typically addressed using a highly superheated expansion inlet state. However, studies of comparison and trade-offs to the wide range of other expansion inlet states are rarely published. This may ignore the advantages that can be gained by exploring different cycle operating modes with more appropriate working fluids.

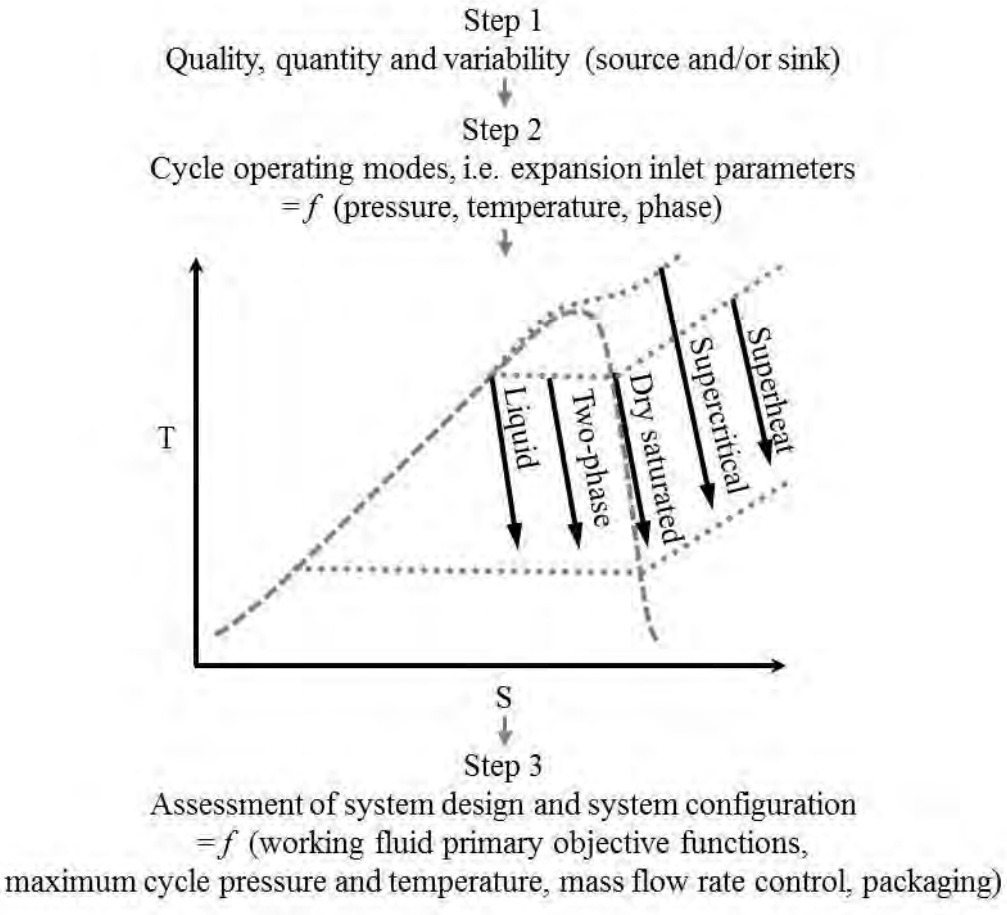

Figure 5.1 Method overview for the assessment of cycle operating modes

In this chapter, expansion machines in the context of existing, as well as developing technologies that are less common within the automotive sector were initially reviewed. Owing to the quality, quantity and variability, associated with the source and/or sink in the selected application (Step 1, Fig. 5.1), selection of the optimal cycle operating mode was explored. By varying expansion inlet pressure, temperature and phase, this chapter presents simulation results for numerous conventional and variations of the conventional closed

loop cycles using pure fluids (Step 2, Fig. 5.1). The numerous parametric studies detail theoretical conclusions, with the results providing directions for practical implementation. For the assessment of system design and system configuration, special attention was paid to the working fluid primary objective functions, maximum cycle pressure and temperature, mass flow rate control, packaging etc. (Step 3, Fig. 5.1). Since, the output capacity of the system is application specific, and the size of a single stage expansion machine is limited:

- Net power output was considered instead of overall conversion efficiency
- Absolute expansion volume flow ratio (and pressure ratio) was considered instead of VFR/W value
- As heat exchanger sizes are relatively scalable, UA/W value remained as the third primary objective function

5.2 Expansion machines

After the selection of a suitable working fluid, the selection of an appropriate expansion machine is the next most important step as this device converts the thermal energy stored in the working fluid into useful work. The performance of the FBC strongly correlates with that of the expansion and power generation unit. The choice of this critical component depends on the:

- Attainable inlet and outlet conditions
- Capacity of the system
- Chosen working fluid
- Way in which power is delivered
- Combined efficiency of the unit
- Influence with varying process conditions
- Cost, size, weight, complexity and durability of the combined hardware

This section briefly reviews the selection of a suitable expansion machine and describes the associated constraints.

The preferred options for expansion machines in automotive applications are mentioned in bold in Fig. 5.2 and can be divided into positive displacement (volumetric expanders) and dynamic machines (Kenneth and Nichols, 2014). Positive Displacement Expanders (PDE) are usually characterised by lower flow rates, less sensitivity to changes in gas composition and density, and speeds roughly one order of magnitude lower than dynamic machines. Fig. 5.2 also shows a typical range of rotational speeds of these machines for power output less than 30 kW. For PDEs, the rotational speeds increase with increasing capacity, scroll and piston expanders demonstrate ≈25% lower speeds than screw expanders. In contrast to PDEs, the inverse of speed and capacity relationship is true for dynamic machines, with radial inflow turbines usually operating with ≈25% lower speeds than axial turbines.

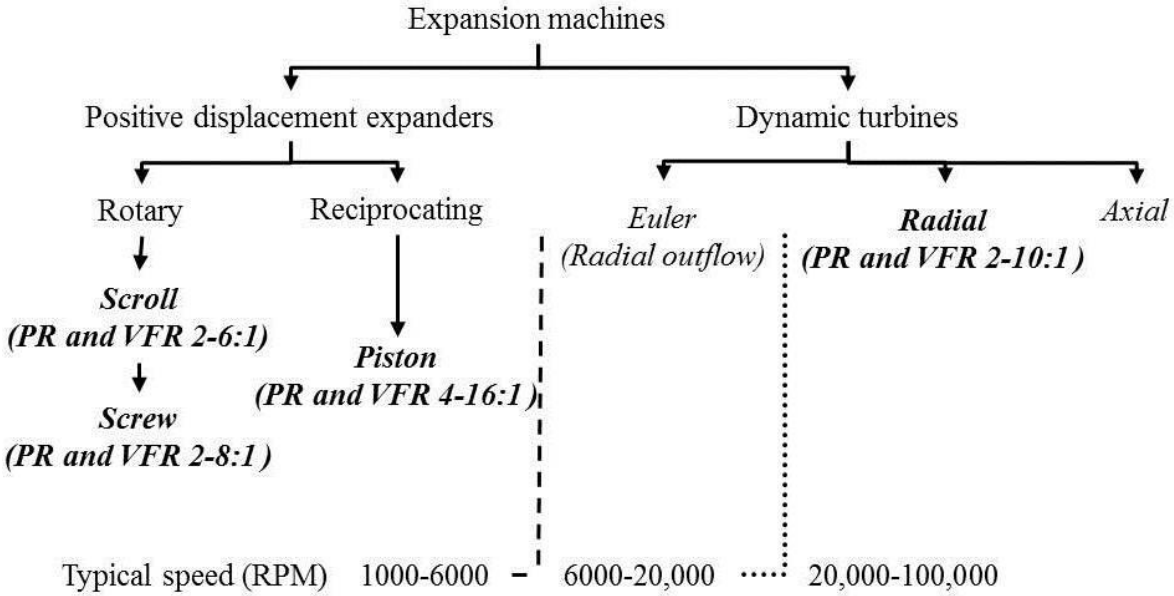

Figure 5.2 Positive displacement and dynamic machine options (<30 kW) preferred in automotive application (mentioned in bold) with typical single stage pressure ratios, volume flow ratios and rotational speeds

Neither a single suitable working fluid nor a single expansion and power generation concept have been identified yet by the HDDE sector. The commonly proposed solutions on how the mechanical energy generated by the expansion machine is used include:

- For high speed turbine: A direct connected generator in axial extension for electrical output or a speed reduction gear box for mechanical output. The lack of a fixed direct relationship between speeds in the turbine-generator unit compared to the mechanical linkage is clearly attractive for turbo-machine design.
- For PDEs: The use of a gearbox or belt compounding directly coupled to the engine crankshaft for mechanical output. When a separate loop of working fluid is used to lubricate the expansion machines (both PDEs and dynamic) and cool the generator and power electronics (high speed turbine-generator unit), then the condenser load is expected to increase marginally.

5.2.1 Positive displacement expanders

Scroll and screw expanders are typically used where the inlet temperature and pressure are below 230°C and 30 bar. Scroll and screw expanders are also characterised by a fixed built-in volume ratio. To optimise their performance, the built-in volume ratio should match the operating condition in order to limit under and over-expansion losses. Fig. 5.2

also includes the typical range of single stage expansion pressure ratios and volume flow ratios achievable for the machines (Vincent and Sylvain, 2012).

Scroll expanders are finding their places primarily in the low capacity range. Scroll expanders used in small scale ORCs (<10 kW) have shown efficiencies greater than 70% with pressure ratios up to 5.5:1 and maximum cycle temperature ≈190°C (Braccoa et al., 2012, Wang et al., 2011b). With higher pressures, leakage was by far the phenomenon most affecting the performance of scroll expanders.

Screw expanders have some advantages over piston expanders (no valves, fewer moving parts, more compact) but also some drawbacks (lower off-design efficiency, higher manufacturing cost due to 3D geometry). With improvements in rotor profile (reduced internal leakage, low contact stresses between the rotors), twin screw expanders have demonstrated efficiencies greater than 70% during low speed (1500-1800 rpm) operation at output capacity under 25 kW (Leibowitz et al., 2006). Furthermore, twin-screw expanders were the only expansion machines also proposed for pure liquid and two-phase expansion (Smith et al., 2011, Smith et al., 2001). The two-phase twin-screw expanders have shown equivalent efficiencies to that of the dry vapour twin-screw expanders. Single dry vapour screw expander with a rated power of 10 kW for recovering vehicles waste heat has also been proposed (Wang et al., 2011a).

Recent experimental results by Bosch on a piston expander using water have demonstrated a mechanical efficiency of 85% at 1500 rpm with inlet temperature and pressure conditions of 380°C and 32 bar (Seher et al., 2012). With parallel EGR and exhaust heat recovery, this amounted to 4.3% (14 kW) of the HDDE power at the chosen operating point. Volvo and Behr's experimental setups also used piston expanders (Christoffel, 2012). For higher steam temperatures and pressures (400-500°C, 70-90 bar), Honda tested a swash-plate axial piston expander, which was more compact than common piston expanders (Endo et al., 2007).

5.2.2 Dynamic turbines

For high-speed turbines, various technologies including, radial inflow, radial outflow and variable phase turbines can be used or adapted. For automotive ORCs, turbine-generator units have already been demonstrated by ORNL and Cummins. ORNL initially used an off-the-shelf modified scroll expander, but this was unable to meet performance expectation due to sealing issues (Wagner et al., 2008). ORNL then demonstrated a radial

inflow turbine-generator unit developed by Barber-Nichols for use with R245fa (Briggs et al., 2010b). The shaft was supported by refrigerant lubricated ball bearings and there were hermetic seals at each end of the shaft. The main characteristics of the unit for LD vehicle were, combined efficiency: 65%, length and diameter: 38 and 15 cm, and peak speed: 80,000 rpm.

Cummins 1st generation system included a fixed-nozzle, 50,000 rpm, axial inflow turbine-generator with a 77% turbine efficiency at the design point with maximum working fluid temperature of 260°C (Barnhart et al., 2005, Millikin, 2005). More recently, Cummins Turbo Technologies designed an ORC turbine by utilising the synergy with current turbocharger architecture. The operating envelope for the R245fa turbine was, maximum inlet pressure and temperature: 27 bar and 230°C, expansion pressure ratio: 10.8:1, and maximum speed 70,000 rpm (Halliwell, 2012). However, the 2nd generation system replaced the high-speed electric generator, power conditioning electronics and flywheel-integrated motor-generator with a speed reduction gearbox. Power transmission parasitic losses through this arrangement were stated to be less than those experienced with the electrically based system (Nelson et al., 2009).

AVL also demonstrated a radial inflow turbine (modified GT-25 turbocharger) with adjustable turbine nozzle ring using ethanol (Park et al., 2011). The turbocharger shaft and bearings were lubricated with ethanol supplied by a separate circulation pump. The series EGR then exhaust arrangement at C100 generated 9.1 kW, resulting in a HDDE fuel consumption improvement of only 3%. This was due to a low pressure ratio of 2:1 and a low EGR flow rate of 10%.

UTRC modelled a supercritical (inlet conditions 260°C, 28 bar) ORC radial inflow turbine with 15 primary vanes and 15 splitter vanes (Cogswell et al., 2011). Primary vanes begin at the radial tip and proceed to the axial exit. Splitter vanes start at the radial stop approximately halfway through the flow passage. A peak efficiency of over 80% was shown near the designed expansion pressure ratio of 12:1 for a power output of 10 kW (78,000 rpm). However in reality, the development of suitable supercritical turbine for organic fluids is lacking that of the subcritical turbine due to the dual nature of the supercritical fluid condition (Ho et al., 2012).

Bosch also simulated a two-stage constant pressure turbine using water, delivering 10 kW with an efficiency of 65% and speed of 150,000 rpm (Seher et al., 2012). For Rankine

cycle applied to automotive HDDEs, the Green Turbine could also be considered (Green Turbine, 2013). The main characteristics of the turbine were, maximum pressure and temperature: 12 bar and 220°C, power: 15 kW, weight: 25 kg, length and diameter: 37 and 26 cm, and design speed: 26,000 rpm.

ORC turbine-generator units with power output as low as 25 kW have also been developed as hermetic systems (Stine and Geyer, 2001). Here the turbine, generator and feed pump are directly coupled on the same shaft, having a high rotational speed, and using working fluid lubricated bearings.

The radial outflow turbine called Euler turbine, which is at an experimental stage (for a 90 kW output capacity) could also be adapted for HDDEs (Welch and Boyle, 2009). Due to the geometry, the optimum speed of a radial outflow turbine is about half that of a comparably sized radial inflow turbine. Steam enters the turbine axially and is turned radially outward before the nozzle row. In the nozzles, the steam accelerates as the pressure is reduced to an intermediate pressure. When steam is typically saturated at the inlet, moisture forms during the expansion. At the nozzle-rotor interface, the pressure gradient forces moisture droplets and particulate through the rotor and out of the turbine. The flow path advantage over radial outflow turbine and the use of titanium alloy makes the Euler turbine extremely erosion resistant.

Finally, the variable phase turbine which uses a proprietary two-phase nozzle can expand hot pressurized liquid or two-phases with high kinetic energy (Welch and Boyle, 2009). As the pressure is reduced in the two-phase nozzle, the liquid begins to flash, forming vapour. Because of the low surface tension and high vapour density of typical organic fluids, the droplets are very small, resulting in a close-coupling of the vapour and liquid phases. Thus, the stream is efficiently accelerated into a high velocity two-phase jet. The kinetic energy is transformed to power by axial impulse turbine blades, directly driving a generator which is cooled by the working fluid. The combined two-phase nozzle and axial impulse turbine efficiencies of 72-82% were demonstrated in a 10 kW pilot plant tested with R245fa and 1,1,1,2,3,3,3-Heptafluoropropane (R227ea).

5.2.3 Expansion machine: Summary

Radial inflow turbines with variable inlet guide vanes maintain high efficiencies over a wide operating range. Dedicated ORC turbines usually offer up to 5% point higher isentropic efficiency than PDEs ($\eta_{turbine}$≈75% vs. $\eta_{expander}$≈70%) but the technological

advancements are narrowing this efficiency disparity. However, the electrical conversion is also associated with up to 5% point lower efficiency ($\eta_{generator}$≈88% vs. η_{gear}≈93%). As a result, the combined expansion and power generation efficiency of the two concepts are similar (66 vs. 65%). Due to higher friction losses, the speed reduction gearbox shows efficiencies between those of the generator and gearbox.

The expansion pressure ratios and built-in volume ratios required in higher temperature ORC systems are typically larger than those achieved in refrigeration systems. Hence, the past 5 years have seen a gradual increase in designs of dedicated PDEs rather than adapting existing compressors (Eneftech Innovation, 2014). PDEs are less cost intensive than turbines but are usually bulkier and heavier, particularly the piston expanders. For example, a turbine with transmission weighs ≈25 kg, whereas a piston expander weighs ≈40 kg for a 25 kW capacity (Seher et al., 2012). However, when costs are considered, radial turbines are ≈15% more expensive to manufacture than piston expanders for capacity under 100 kW (Peters et al., 2003). For high pressure ratio two-stage expansion, the preferred machines are piston expanders (double acting) and radial inflow turbines (common shaft).

Compared to conventional dynamic machines, PDEs offer better off-design performance, permit some condensation during the expansion and show rotational speeds similar to HDDEs. Furthermore, volumetric expanders are more penalised by over expansion than by under expansion phenomena, a situation that will favour the present high pressure application (Braccoa et al., 2012). For EGR and exhaust heat recovery piston expanders are being considered as a valid alternative as they work even at high pressure ratios (20:1) and allow higher inlet pressures and temperatures (50 bar, 300°C) (Wenzhi et al., 2013, Fu et al., 2012, Seher et al., 2012, Badami et al., 2008). With piston expanders the expansion ratio can be adjusted using the valve timing or employing VVT. The flexible operation of piston expanders provides a more practical system which outweighs the efficiency factor and the drawback of driving situations where there is no need for the recovered energy. Furthermore, developing technologies like the novel linear generator free piston expander, that converts mechanical energy directly into electrical energy, leads to a practical solution for HEVs, trucks with increased electrification and long-haul refrigeration trucks (Libertine FPE, 2014).

5.3 Cycle operating modes

The wide variety of turbines and PDEs discussed above has enabled it to consider the start of the working fluid expansion from dry saturated vapour, superheated vapour, supercritical phase, and even saturated liquid or two-phases. When considering expansion inlet conditions and the type of working fluids, at least 12 noticeably different operating modes exist as detailed in Fig. 5.3. The characteristics that distinguish the cycles from each other are the:

- Operating pressures (i.e. subcritical or supercritical)
- Expansion inlet vapour fraction (X_{in}: liquid, two-phase, dry saturated, superheated)
- Expansion exit vapour fraction (X_{out}: two-phase, dry saturated, superheated)
- Phase transition during the expansion (e.g. bi-phase expansion) and
- The slope of the saturated vapour line (i.e. dry, wet or isentropic fluids)

The different operating modes combined with the three heat sources (EGR, exhaust and CAC) then allowed exploring improvements in the overall conversion efficiency. This was achieved by a combination of, increasing the average heat addition temperature, increasing expansion enthalpy drop and increasing the heat recovery efficiency. The variation of the three expansion inlet parameters also detailed the sensitivity of each parameter on the thermodynamic performance and design of the system.

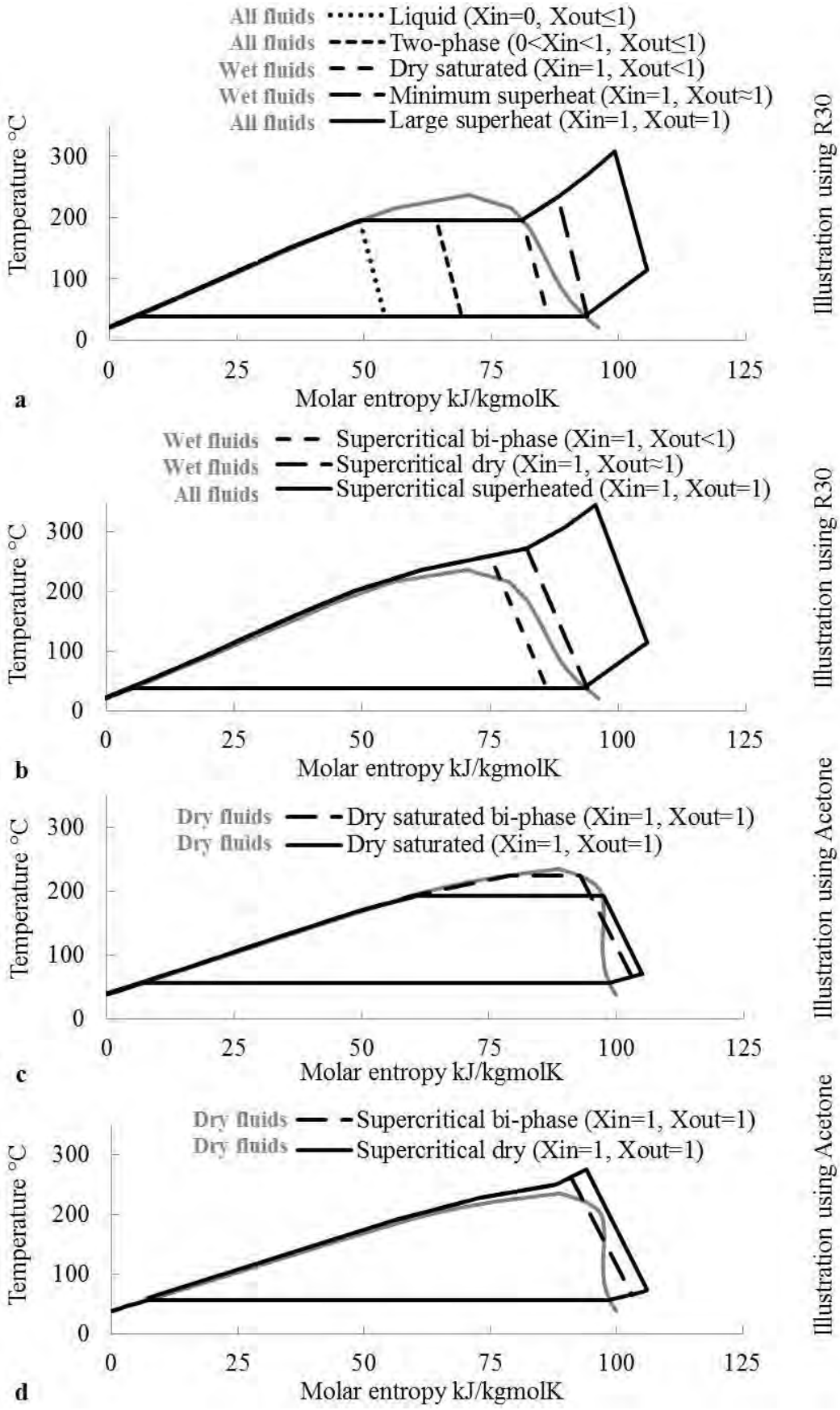

Figure 5.3 12 cycle operating modes using pure fluids for single stage expansion (a) subcritical operating modes (b) supercritical operating modes (c) subcritical operating modes specific to dry and isentropic fluids (d) supercritical operating modes specific to dry and isentropic fluids

5.3.1 Cycle boundary conditions

The fluid selection study with sensitivity analysis in Chapter 4 highlighted that:

- Ethanol and water were better suited to a combination of higher source temperatures and higher super-atmospheric condensers, while
- R245fa was better adapted to lower source temperatures with the lowest super-atmospheric condensing available

Therefore, Case 4: 427/105°C (Table 4.1), i.e. EGR at 427°C with condensation in the high temperature condenser at 105°C will be better matched to ethanol and water. Consequently, Case 5: 296/65°C (Table 4.1), i.e. exhaust at 296°C with condensation in the low temperature condenser at 65°C will be better suited to R245fa. Considering Cases 4 and 5 can then quantify whether the possible alternative fluids identified in Chapter 4 are not only less sensitive to varying source/sink conditions (i.e. Cases 1 and 2), but also whether they can show higher performance under boundary conditions suited to fluids in the published literature (i.e. Cases 4 and 5).

A pinch point of 20°C and 30°C was considered in the EGR (Case 4) and exhaust heat exchanger (Case 5), cooling the stream to ≥ 125°C and ≥ 95°C, respectively. The maximum working fluid boundary conditions that were used in this chapter are given in Table 5.1. The temperature, pressure and pressure ratio boundary conditions were the maximum extreme combinations that could be achieved by the reviewed expansion machines. An 80 bar maximum pressure limit was chosen since this is generally the maximum design pressure of cast iron cylinder materials used in the gas industry (GSAP, 2004). Furthermore, limits reaching a maximum expansion pressure ratio of 16:1 are also detailed, which may be attained using a large single stage piston expander. Pressure ratios higher than 16:1 may result in either reduced expansion efficiency or require a two-stage expansion machine. These values differ from those considered in Chapter 4 (also shown in Table 5.1). This was since, Chapter 4 temperature and pressure boundary conditions were based on typical and not extreme combinations.

Table 5.1 Maximum working fluid pressure and temperature boundary conditions

	Chapter 4	Chapter 5
▪ T_{max}, organic fluid	≤ T_{crit} and 250°C	≤ T_{crit}+50°C and 300°C
▪ P_{max}, working fluid	≤ 35 bar and 0.9 P_{crit}	≤ 80 bar and 1.25 P_{crit}
▪ PR_{max}, expansion		≤ 16:1

5.4 Limited superheat expansion (Cases 4 and 5)

5.4.1 Simulation overview

In the following subsections results for the subcritical cycle with minimum superheat expansion for wet fluids (Fig. 5.3a), and dry saturated expansion for isentropic and dry fluids (Fig. 5.3c) are detailed. Since these two expansion modes limit the superheat need for all three types of fluids, they were collectively referred to as limited superheat expansion. The net power optimisation was conducted up to a maximum pressure of $0.95P_{crit}$, limited by the boundary conditions given in Table 5.1. The performance and system results in this section, especially those using the alternative fluids identified in Chapter 4, will act as a reference for comparison with the other cycle operating modes.

5.4.2 Case 4

Fig. 5.4a demonstrates that the thermal efficiency increased with the increment in cycle pressure. Fluids grouped according to similar critical temperature showed similar thermal efficiency, with higher critical temperature fluids being more thermally efficient. The improvement in thermal efficiency can be best understood with reference to Fig. 5.4b, which refers to ethyl iodide. By increasing the evaporator pressure from 20 to 36 bar, the temperature at which heat is added to the working fluid increases. This results in greater cycle area and hence improved efficiency. Due to the large temperature difference between the organic working fluid critical temperatures (235-281°C) and the EGR inlet temperature (427°C), all fluids provided nearly equal heat recovery (63 kW, Fig. 5.4c) and cooled the EGR stream to ≈130°C. For nearly fixed heat into the cycle, the LMTD in the EGR heat exchanger (i.e. heat transfer irreversibilities) reduced as a function of increasing cycle pressure (Fig. 5.4d). With increasing pressure difference across the expansion stage, the enthalpy drop (i.e. expansion work) also increased (Fig. 5.5e). As a result, maximum power was produced using acetonitrile (9.1 kW) for a 36 bar evaporator pressure (Fig. 5.4f). With the exception of ethyl iodide (8.5 kW, 36 bar), all other organic fluids at 40 bar region provided similar net power (7.1 kW±3%). This power region was also equal to the Rankine cycle optimal performance at 23 bar.

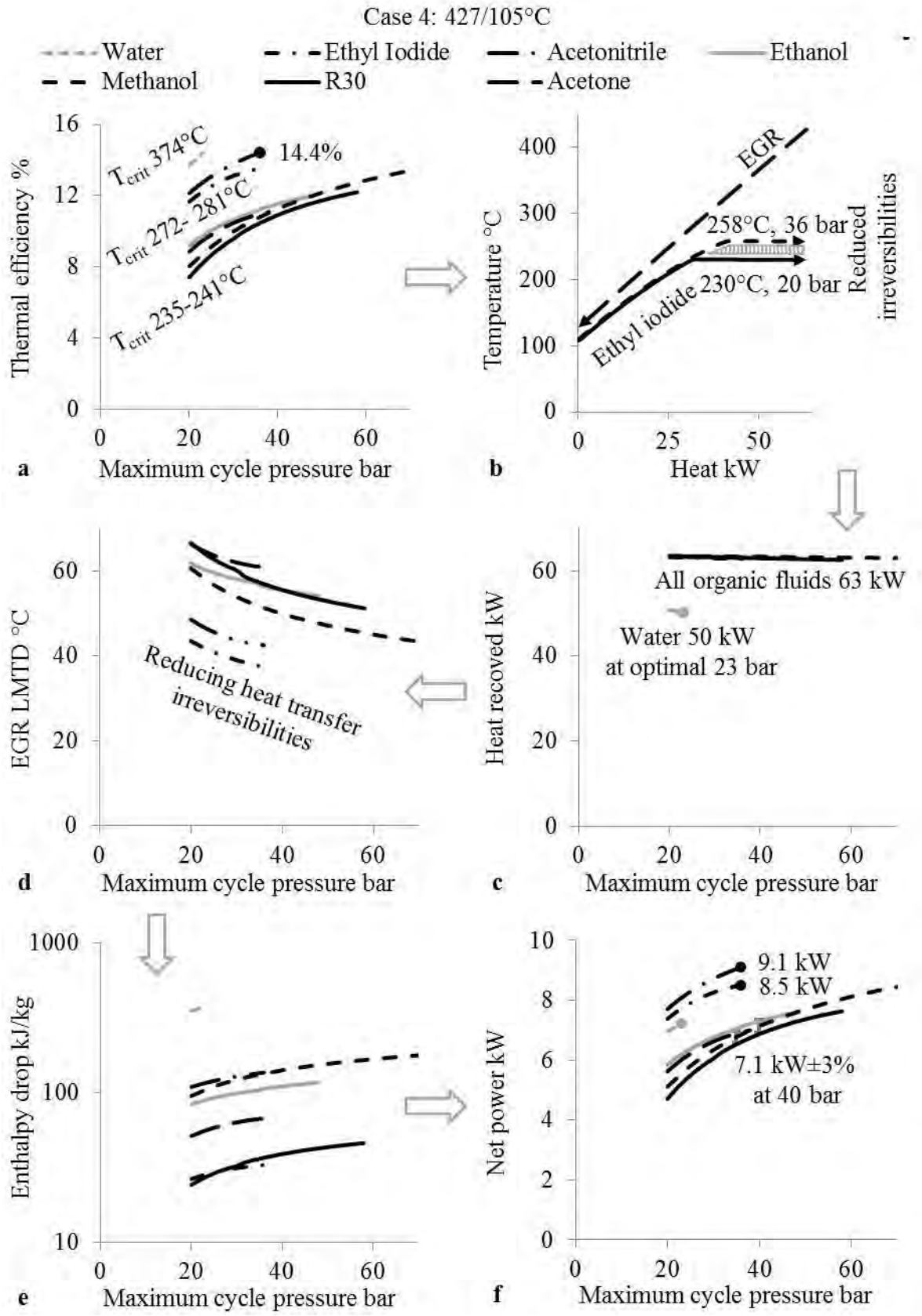

Figure 5.4 Effect of increasing cycle pressure on (a) thermal efficiency (b) heat transfer irreversibilities for organic fluids (c) heat recovery (d) heat exchanger LMTD for organic fluids (e) expansion enthalpy drop (f) net power, in Case 4 for limited superheat expansion

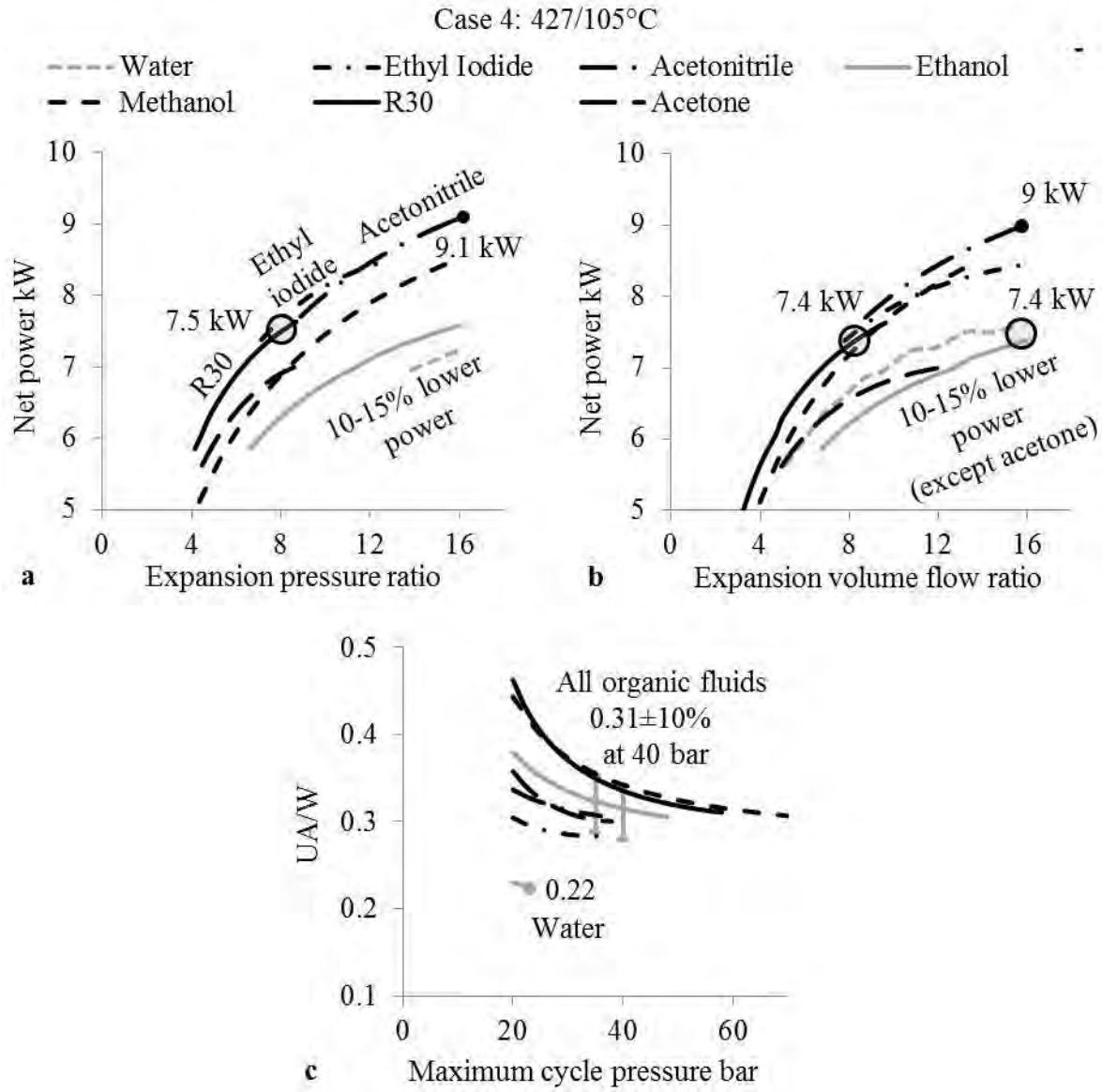

Figure 5.5 Effect of (a) pressure ratio on net power (b) volume flow ratio on net power (c) cycle pressure on UA/W value, in Case 4 for limited superheat expansion

The above performance analysis was also completed with preliminary considerations regarding the relative size and cost of the FBC units. The two criteria used for such evaluations were, volume flow ratio (and pressure ratio) and UA/W value. Fig. 5.5a shows that the alternative fluids delivered 10-15% higher net power under the same pressure ratio compared to ethanol and water. Of particular significance was: R30 under low, ethyl iodide under medium, and acetonitrile under high pressure ratios. The alternative organic fluids (except acetone) also retained the same 10-15% advantage when considering volume flow ratios (Fig. 5.5b). The low volume flow ratio for the same net power advantage was evident for ethyl-iodide, acetonitrile, methanol and R30. For equivalent performance (7.4 kW) to ethanol and water they required half the expansion machine size (VFR 8:1 vs. 16:1). Finally, for equivalent heat recovery, a lower UA/W value meant that a smaller heat transfer area would be needed to achieve the same net power output. For a maximum cycle

pressure of 40 bar all fluids showed similar UA/W value (0.31±10%), with the exception of water, which showed a better value (0.22) due to efficient high temperature heat recovery only (Fig. 5.5c).

5.4.3 Case 5

As can also be expected in Case 5, the thermal efficiency increased with cycle pressure and higher critical temperature fluids remained thermally more efficient (Fig. 5.6a). Due to a reduced temperature difference between methanol, R30 and acetones critical temperature (235-239°C) and the exhaust inlet temperature (296°C), the optimisation trend was that of Case A (Fig. 4.14a). These three alternative fluids recovered 75-80% of the available exhaust heat (Fig. 5.6b) and showed peak power of 7.2±7% kW at 20 bar (Fig. 5.6d).

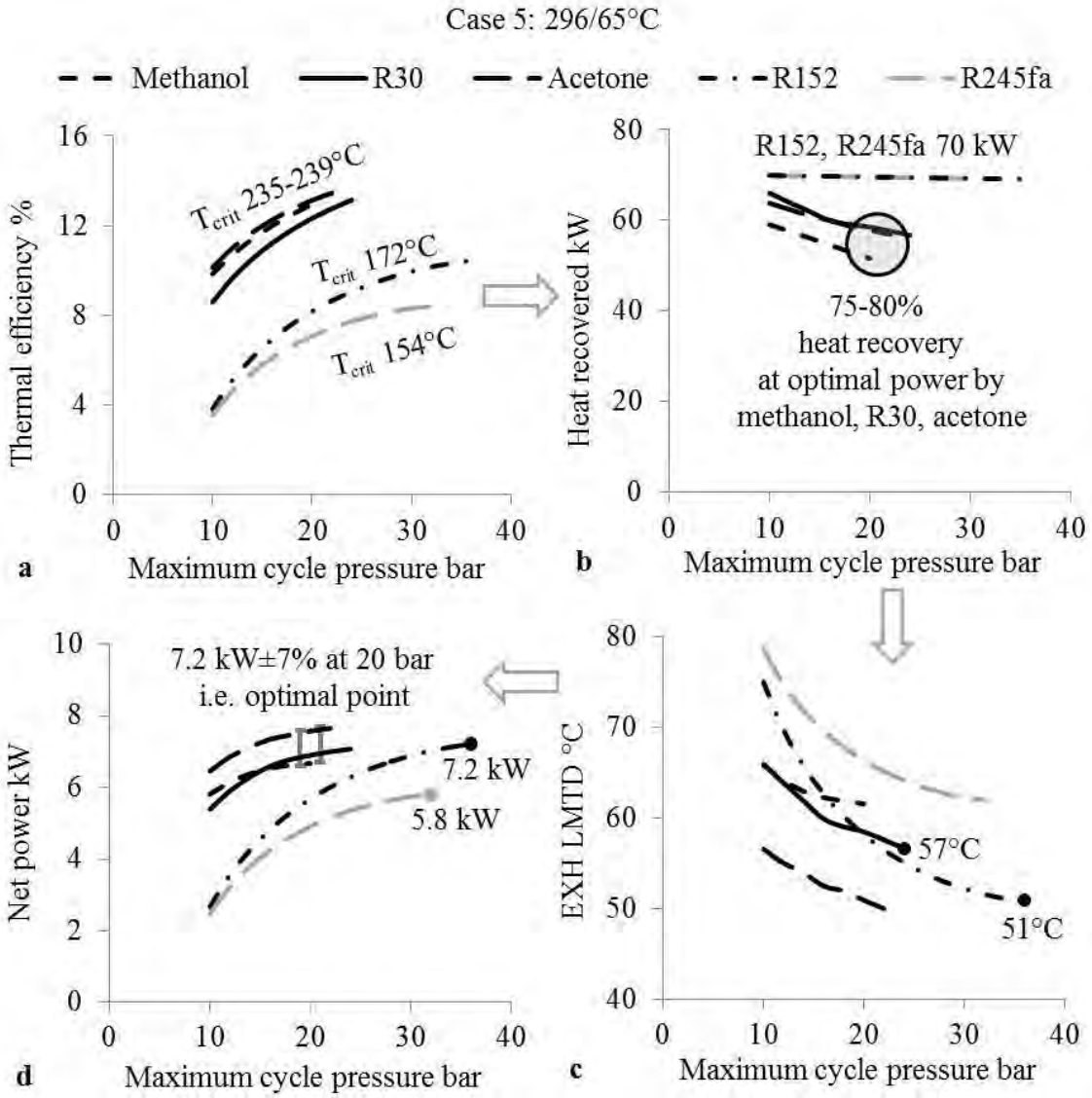

Figure 5.6 Effect of increasing cycle pressure on (a) thermal efficiency (b) heat recovery (c) heat transfer irreversibilities (d) net power, in Case 5 for limited superheat expansion

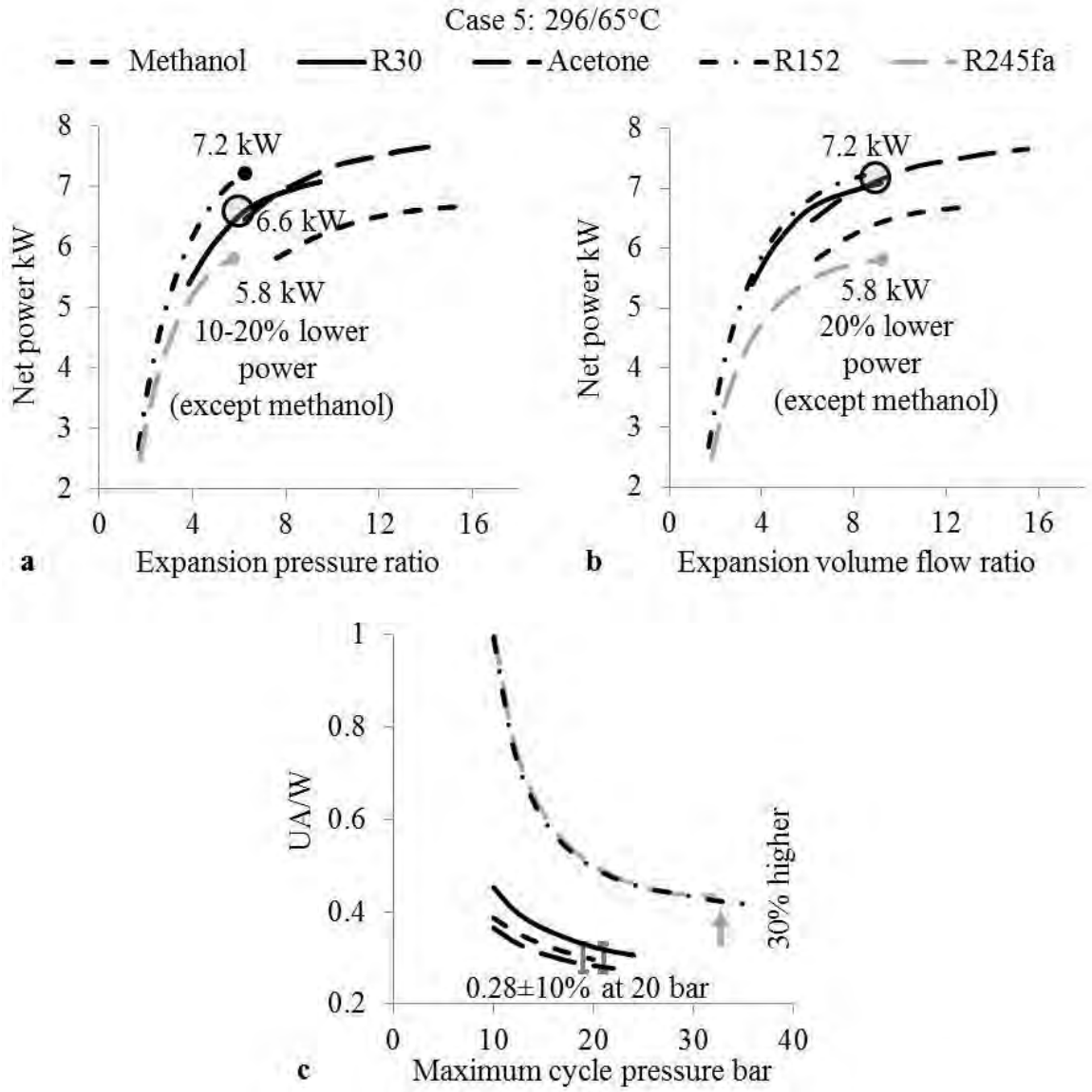

Figure 5.7 Effect of (a) pressure ratio on net power (b) volume flow ratio on net power (c) cycle pressure on UA/W value, in Case 5 for limited superheat expansion

An alternative low temperature fluid shown in Chapter 4 for CAC heat recovery was R152. R152 was also used in this subsection to highlight its high net power output advantage for equivalent pressure ratios and volume flow ratios over R245fa. When R30, acetone and R152 were compared to R245fa, they delivered 10-20% higher net power for similar pressure ratio (Fig. 5.7a) and volume flow ratio (Fig. 5.7b). Furthermore, higher critical temperature fluids optimised at lower evaporator pressures (Fig. 5.6d). As a result, R30 and acetone achieved the 8:1 volume flow ratio with maximum pressures around 10 bar lower than R245fa. Finally, methanol, R30 and acetone showed similar UA/W value (0.28±10%) near the optimal region of 20 bar, this was over 30% lower for equivalent power output to that of R245fa. Since, R152 offered similar expansion machine size when compared to R30 and acetone (Fig. 5.7b), but resulted in an unfavourable UA/W value (Fig. 5.7c) it was only reconsidered when the pressure differential in the cycle were higher.

In summary, the above results for Cases 4 and 5 highlights the advantages of the alternative fluids even when operated under boundary conditions that are more suited to water, ethanol and R245fa. The dry saturated expansion for wet fluids (Fig. 5.3a) and dry saturated bi-phase expansion for dry fluids (Fig. 5.3c) were not simulated in this section. This was done to provide a baseline performance comparison that could be achieved by the reviewed conventional expansion machines. Furthermore, since the EGR and exhaust temperatures were relatively higher than organic fluid critical temperatures, performance of these expansion modes will be similar to the limited superheat expansion.

5.4.4 Process control: Organic fluids vs. water

To reduce the average time required to stabilise the FBC under transient conditions, the working fluid should have a low variation in point-to-point optimisation of mass flow and have a flow rate that can be controlled precisely. The mass flow control is necessary to avoid two-phase or large superheat prior to the expansion inlet. The working fluid mass flow rate ($\dot{m}_{wf}$) is related to the latent heat of a working fluid (H_{vap}), which in turn is related to the molecular weight (M_{wt}) i.e. $M_{wt} \propto 1/H_{vap}{}^{2} \propto \dot{m}_{wf}$.

For latent heat there are different opinions in the present literature (Yamaguchi et al., 2013, Sprouse III and Depcik, 2013b, Arunachalam et al., 2012, Saidur et al., 2012, Bae et al., 2011, Wang et al., 2011c, Cha et al., 2010). The majority of the literature cites the need of a large latent heat, and favoured water due to higher thermal efficiency, reduced pump power consumption and reduced mass flow rate. Analysis conducted in this thesis so far suggests the use of low latent heat fluids to be advantageous in the present application. Low latent heat fluids include isentropic and marginally wet organic fluids, recover higher quantities of heat, and as a result, can give higher expansion power negating the increased pump power consumption.

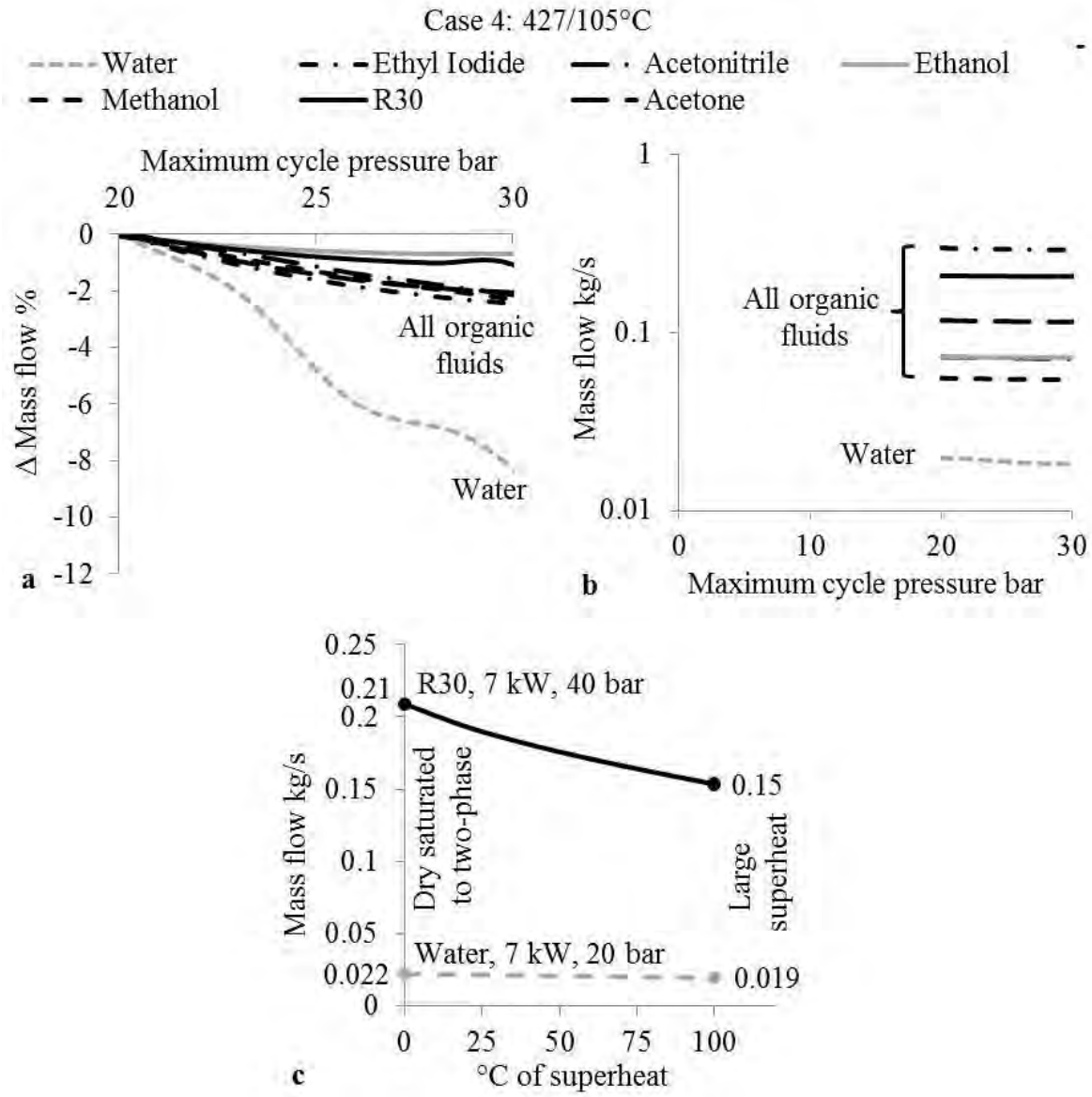

Figure 5.8 (a) working fluid mass flow rate variation (b) working fluid absolute mass flow rate (c) application specific mass flow control challenge for water, in Case 4 for limited superheat expansion

Fig. 5.8a shows the point-by-point optimised mass flow rate variation for an evaporator pressure between 20-30 bar in Case 4. Organic fluids showed a mass flow variation of around 2%, whereas water resulted in over 8% reduction in mass flow rate with increasing pressure. The most significant variable was the value of mass flow rate itself. The mass flow rates of the organic fluids were approximately one order of magnitude higher than water (Fig. 5.8b). A lower mass flow rate offers several advantages for water. The amount of water required for a system will be approximately 3-15 times less than organic fluids. The reduced mass flow rate of water also suggests that the pressure drop in the heat exchanger and condenser will be lower. However, assuming a pressure drop that was only 25% of that assumed for organic fluids (0.5→0.125 bar in evaporator, 0.2→0.05 bar in condenser), the power generated by the Rankine cycle at the optimal 23 bar pressure

identified in Fig. 5.4f increased only by ≈4% (from 7.2 to 7.5 kW). It is important to point out that the increase in the net power was largely attributed to a reduction in the average heat rejection temperature. When the evaporator pressure drop was reduced, the change in net power was negligible (0.05 kW). However, when the condenser pressure drop was reduced, the average condenser heat rejection temperature dropped from 107.3 to 105.6°C, increasing the net power by 0.25 kW. This was not without its drawback, since the required expansion pressure ratio also increased from 16:1 to 18:1.

Water at 20 bar and R30 at 40 bar gave nearly equal net power of 7 kW. Fig. 5.8c shows the effect of reduced mass flow rate of these two fluids. As can be seen, reducing water's mass flow rate by 0.003 kg/s resulted in an added superheat of 100°C over the dry saturated to two-phase expansion mode. Such small changes in mass flow rate with water will be relatively difficult to control, hence the heat exchanger exit conditions will fluctuate rapidly between that related to two-phase and large superheated conditions. For better process control additional instrumentation in the form of the on-line steam quality sensor may be needed (Jelacic, 2007). Whereas, the equivalent superheat for an ORC using R30 was experienced over a relatively broad range of flow rate (Δ 0.06 kg/s).

Mass flow control (Fig. 5.8c), along with turbine design consideration (Section 4.7.1), helps in concluding that conventional Rankine cycle may be better suited to source quantities higher by one magnitude (>500 kW). Hence, organic fluids like ethyl iodide, R30 and acetone with higher mass flow rates are more interesting for small capacity mobile systems due to better response analysis during changed process conditions and turbine design considerations.

5.5 Large superheat expansion (Cases 4 and 5)

5.5.1 Rational and simulation overview

The cycle operating mode in the previous section involved limited levels of superheat. However, due to the critical temperature of the considered organic fluids being lower than the typical EGR and exhaust temperatures, the superheat level can be further raised. Superheating as shown in Fig. 5.9 (using ethanol) can increase the average temperature at which heat is added, reducing irreversibilities at nominal evaporator pressures and expansion pressure ratios.

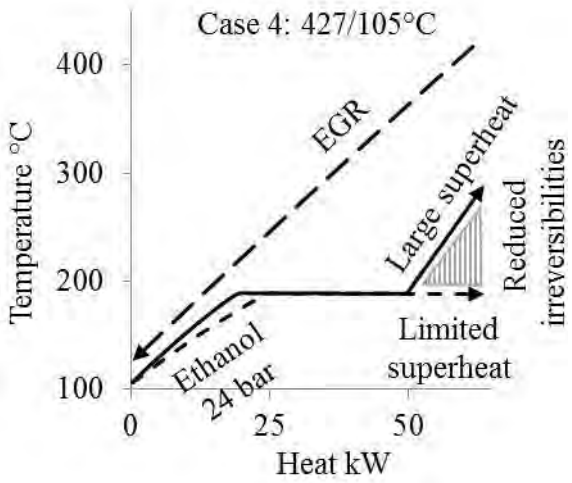

Figure 5.9 Effect of large superheat on reduced EGR cooler irreversibilities in Case 4 for ethanol

In the following subsections, results for the subcritical cycle with large superheat expansion (Fig. 5.3a) for wet, isentropic and dry fluids are detailed. The expansion pressure ratio was fixed at 8:1 in Case 4 and 6:1 in Case 5 for all fluids. The superheat, controlled by the reduction in the working fluid flow rate over limited superheat expansion, was limited to a combination of 50°C over the critical temperature and 300°C for organic fluids (Table 5.1).

5.5.2 Performance: Wet vs. dry fluids

Fig. 5.10a and b shows the variation in the thermal efficiency with a fixed evaporator pressure and increasing superheat in Cases 4 and 5, respectively. Two distinct trends were observed when comparing ethanol (a wet fluid) and R245fa (a dry fluid). The thermal efficiency of ethanol increased with superheat (Fig. 5.10a), whereas for R245fa, after an initial small increase it remained nearly constant (Fig. 5.10b).

This can be understood with reference to Fig. 5.11a and b, where the rate at which the constant isobar lines diverge determines the impact of superheating on thermal efficiency and expansion power. For wet fluids like ethanol, the pressure lines diverge or remain parallel in the superheating zone (Fig. 5.11a), contrary to dry fluids like R245fa which converge (Fig. 5.11b). Large superheated cycles for dry fluids resulted in increased higher temperature de-superheating at the end of expansion (i.e. increased average heat rejection temperature). This negated the thermal efficiency gains obtained from better temperature matching with the heat stream. As a result, when considering the net power change, expansion and net power increased with superheat for ethanol (Fig. 5.11c), whereas expansion power did not improve with superheat for R245fa (Fig. 5.11d). The net power

for R245fa was approximately retained only due to significantly reduced pump power consumption. Hence, an expansion inlet temperature just slightly above the dry saturated vapour temperature is preferred for dry fluids, since thermal efficiency and net power remains relatively constant under superheated conditions.

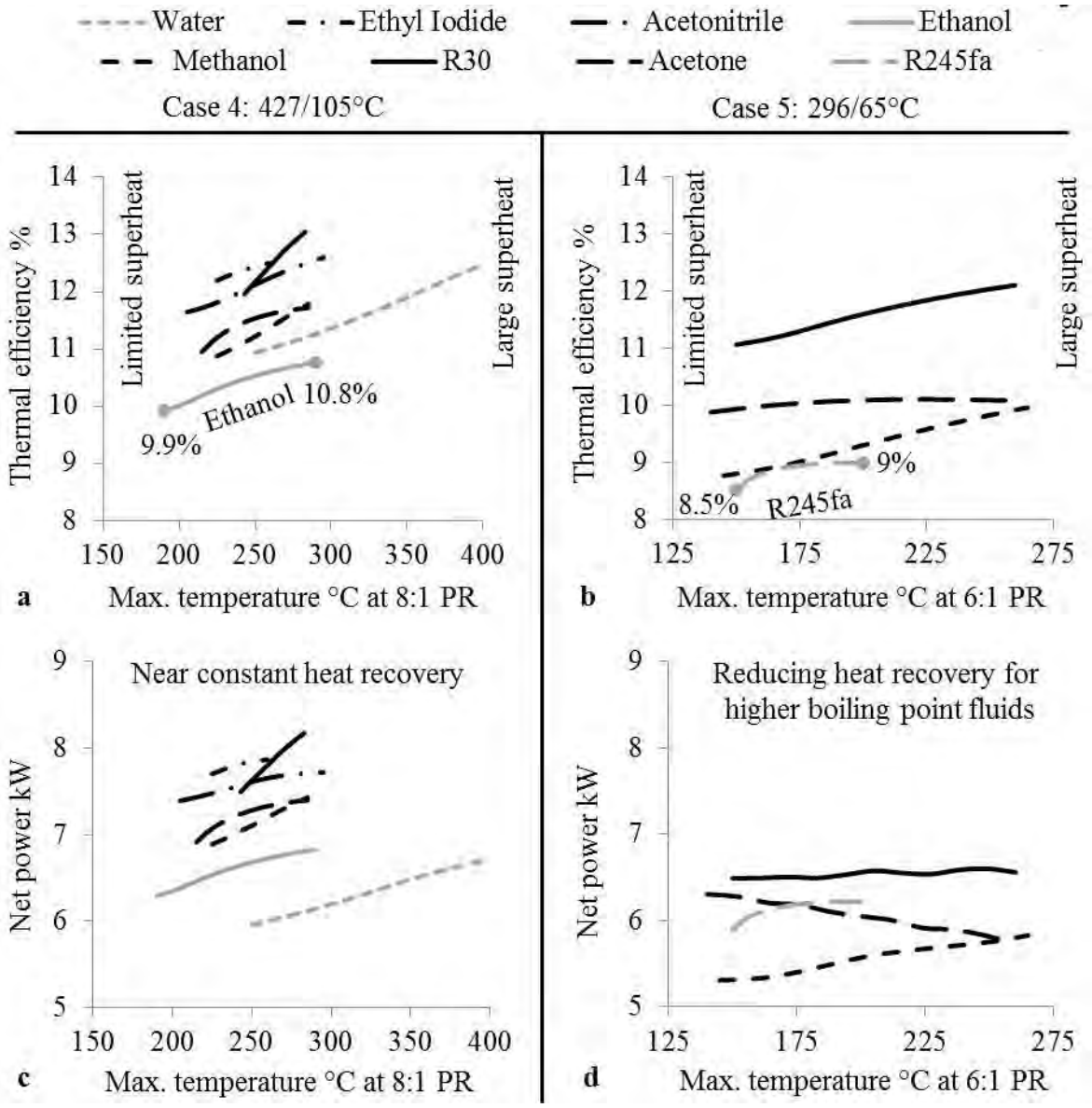

Figure 5.10 Effect of superheating at fixed evaporator pressure on (a,b) thermal efficiency (c,d) net power, in Case 4 (left side) and Case 5(right side)

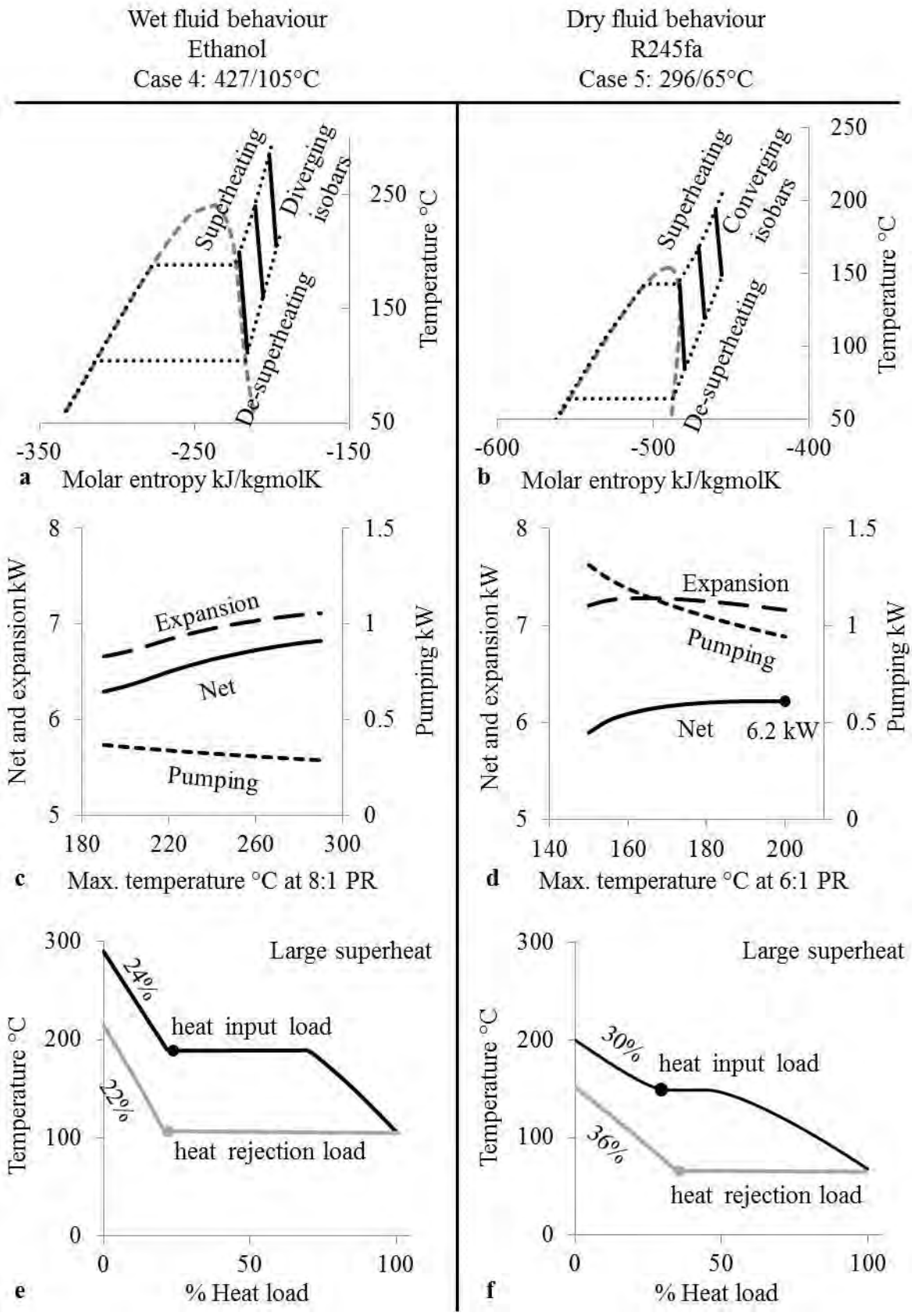

Figure 5.11 Wet vs. dry fluids (a,b) isobars in superheated region (c,d) expansion and pumping power change (e,f) heat transfer percentage load in vapour form, in Case 4 (left side using ethanol) and Case 5 (right side using R245fa)

For optimum performance, increasing superheat increased the net power for all the fluids in Case 4 (Fig. 5.10c). However, in Case 5, with the exception of R245fa, the heat recovery also decreased because of superheating. As a result, no significant performance benefit was achieved by superheating the alternative fluids in Case 5 (Fig. 5.10d). This indicates that when recovering a heat source at Case 5 temperature level, large superheat should be avoided with higher boiling point fluids (>50°C).

5.5.3 Large superheat: Discussion and findings

Fig. 5.12a benchmarks the performance improvement potential using large superheat expansion in Case 4 over limited superheat expansion as reference (i.e. axis 0,0). The average range of increase in net power was 4-9% up to 100°C of superheat among all fluids. R30 showed the best rate of improvement. For an equivalent improvement (9%) to R30, water and ethanol required around twice the superheat (100 vs. 40°C). Hence, for equal pressure ratios, even a 100°C of superheat with ethanol and water will not outperform the alternative fluids with limited superheat (Fig. 5.12a, 5.5a).

A system size advantage that superheating offered under fixed evaporator and condensing pressure was the reduction in expansion volume flow ratio for organic fluids. In Fig. 5.12b this factor is clearly evident with ethanol, R30 and acetone. However, the above two advantages do not justify neglecting the large superheating and de-superheating drawbacks.

With increasing superheat, the density of the fluid in the superheater and the de-superheater also decreases, increasing the volume of the system. For a 50°C superheat, this reduction corresponded to 15% lower densities from the reference limited superheat expansion (i.e. axis 0,0) for organic fluids in the de-superheater (Fig. 5.12c).

For ethanol the total superheating and de-superheating load amounted to 22-24% of the heat transfer load in the heat exchanger and condenser (Fig. 5.11d), and even higher 30-36% for R245fa (Fig. 5.11e). Evaporators and condensers are typically designed to handle less than 10% of the total load in vapour form. For the maximum superheating levels simulated, the vapour load at heat absorption and heat rejection exceeded this limit (Fig. 5.12d), requiring dedicated vapour heat transfer components.

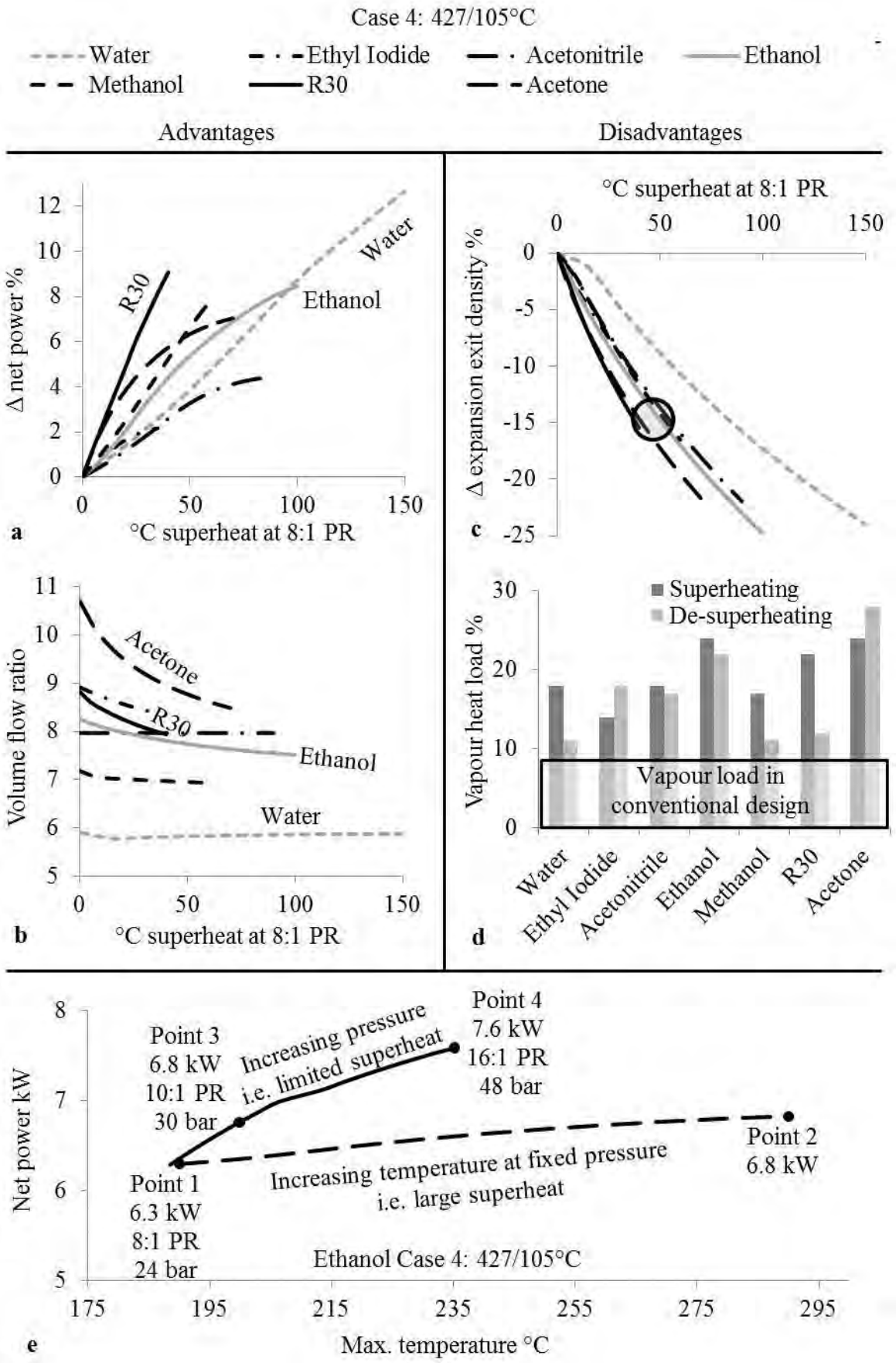

Figure 5.12 Advantages of superheating (a) performance (b) volume flow ratio; Disadvantages of superheating (c) de-superheater inlet densities (d) heat transfer load in vapour form; (e) paths to achieve similar net power by comparing limited superheat using higher pressures and large superheat using lower pressures, in Case 4

Furthermore, when compared to the liquid state, the thermal conductivity of a fluid in the vapour phase decreases (e.g. ethanol at 24 bar: $\lambda_{preheated\ liquid}$ = 0.13 W/mK, λ_{vapour} = 0.033 W/mK), exhibiting almost half the overall heat transfer coefficient values (Siddiqi and Atakan, 2012). Hence, the system will require larger heat transfer surface and volume than a limited superheat cycle.

From a systems trade-off, the ability to operate with limited superheat at the expansion inlet with a reduction of only 4-9% in performance clearly improves the economic viability of the system. Therefore, large superheated cycles, as shown by Teng and Regner (2009), and Arias et al. (2006), may be impractical in real automotive applications. System architectures that may retain the improved performance or reduced volume flow ratio advantages, but provide a partial solution for the vapour load drawbacks may offer a compromise, and remain a theme of investigation in the process integration phase in Chapter 6.

Finally, to assess the relative sensitivity of increasing cycle temperature vs. increasing cycle pressure on performance, consider the results for ethanol in Case 4 (Fig. 5.12e). Pt. 1 represents a limited superheat cycle at 24 bar producing 6.3 kW. The net power benefit that was achieved using 100°C of superheating (Pt. 2), could in fact also be achieved by increasing the evaporator pressure of the limited superheat cycle by only 6 bar (Pt. 3). This however raised the required expansion pressure ratio marginally from 8:1 to 10:1. This shows that the net power is extremely sensitive to subcritical cycle pressure but relatively insensitive to superheat. As a result, increasing the cycle pressure within the constraints of the 16:1 pressure ratio is a more suited method than opting for lower pressure ratio cycles with large superheat.

5.6 Cycles with internal heat exchange (Cases 4 and 5)

5.6.1 Rational and simulation overview

A means to reduce the de-superheat load drawback on the condenser in the large superheat cycle as discussed in the previous section is by the use of a full-flow recuperator, an IHE usually of the counter-flow shell and tube type. The purpose of using an IHE is to internally utilise the considerable exergy exiting the expansion machine, and hence avoid the potential loss in the condenser. As shown in Fig. 5.13a and b, for a superheated cycle with an IHE, the vapour side (low pressure side) of the IHE reduces the high-temperature low-pressure vapour exiting the expansion machine (Pt. 1) to a low-temperature low-pressure vapour prior to the condenser inlet (Pt. 2). In doing so, the high-pressure

low-temperature liquid exiting the pump (Pt. 3, high pressure side) recovers the enthalpy difference and is raised to a higher temperature (Pt. 4).

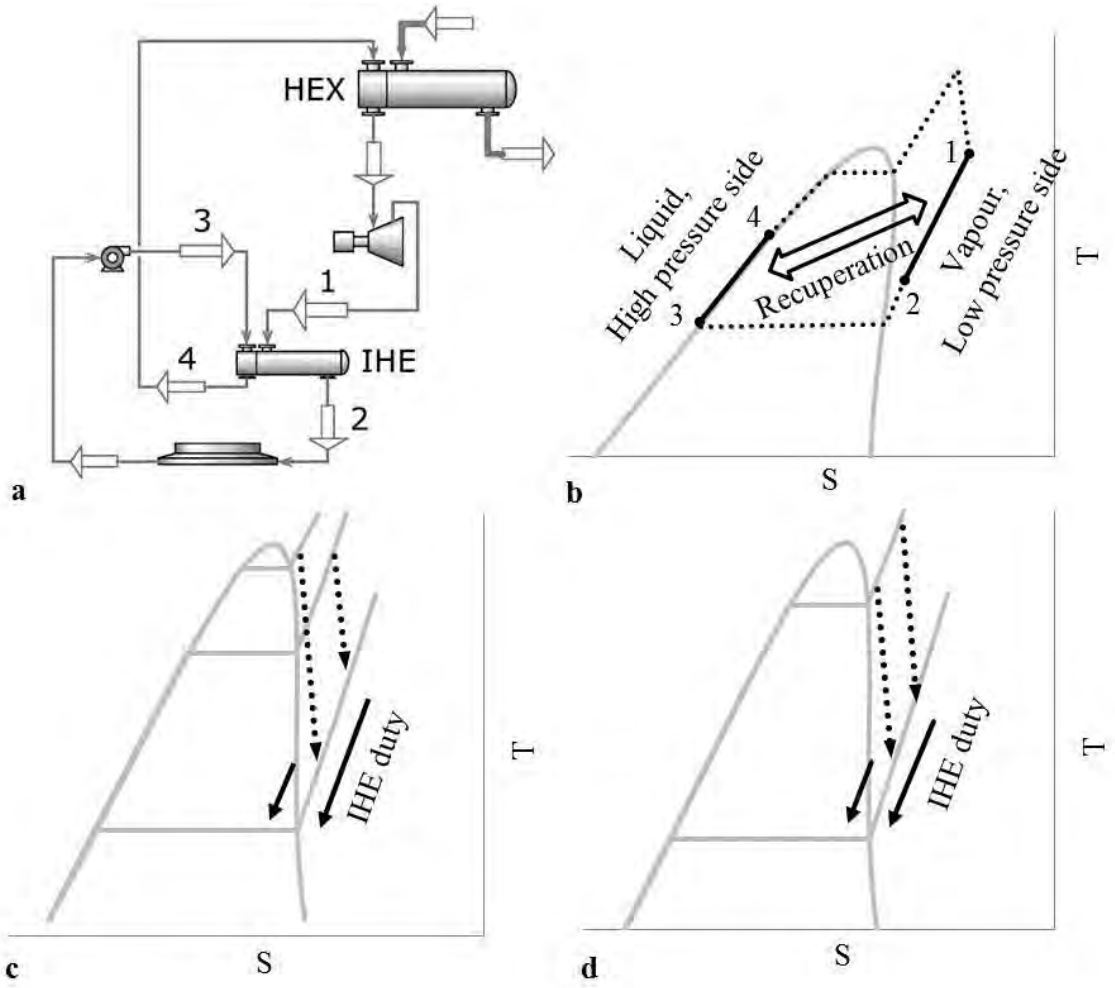

Figure 5.13 Superheated recuperated cycle (a) configuration (b) T-S sketch (c) T-S sketch as a function of cycle pressure for a fixed maximum temperature (d) T-S sketch as a function of cycle temperature for a fixed maximum pressure

Ethanol and R245fa with an IHE were simulated in Case 4 and Case 5, respectively, to quantify the improvement potential. A fixed pressure drop of 0.2 bar was considered at both the liquid and vapour sides of the IHE. This reduces the expansion inlet pressure and raises the expansion exit pressure slightly (i.e. reduces the expansion enthalpy drop). Furthermore, a 20°C pinch point was used in the IHE based on a similar trade-off approach to Fig. 4.26. This implies that, in an ideal case with no pressure loss, an IHE can only be utilised when the working fluid exiting the expansion machine is at least over 20°C higher than the condenser inlet temperature. Ethanol and R245fa were considered up till the combined extreme subcritical boundary conditions (Table 5.1), they being:

- Maximum expansion pressure ratio of 16:1 and maximum temperature of T_{crit}+50°C (≈290°C) for ethanol

- Maximum cycle pressure of $0.95P_{crit}$ (≈35 bar) and maximum temperature of T_{crit}+50°C (≈200°C) for R245fa

5.6.2 Performance

To understand the thermodynamic influence of an IHE, two themes of investigations were conducted to reach the combined extreme pressure and temperature conditions of ethanol and R245fa. Firstly, the effect of increasing the cycle pressure (i.e. pressure ratio) for a fixed maximum cycle temperature (Fig. 5.14a and b), and secondly, the effect of increasing the maximum cycle temperature for a fixed maximum cycle pressure (Fig. 5.14c and d).

As shown in the T-S sketch in Fig. 5.13c, as the cycle pressure increases at a fixed expansion inlet temperature, the expansion exit enthalpy decreases. As a result, Fig. 5.14a and b shows the duty of the IHE decreasing with increasing cycle pressure. At higher pressures the amount of internal heat exchange decreases while the amount of recoverable heat in the HEX increases. For R245fa the thermal efficiency increased with higher cycle pressures to a maximum value of 11.7% at a pressure ratio of 6:1 (Fig. 5.14b). With ethanol the thermal efficiency increased and stabilised to 14.1% at pressure ratios of 14:1 to 16:1 (Fig. 5.14a). The relationship between maximum cycle pressure and thermal efficiency is more complicated for cycles with an IHE and can alter the trend as seen with the simple cycle. If a higher boiling point fluid (dry or isentropic) than ethanol is used in Case 4, then the thermal efficiency will pass through a very clear maximum. The possible different maximum cycle pressure corresponding to maximum thermal and net power with an IHE is an important result, demanding independent optimisation for cycles with an IHE. This difference due to an IHE also points to the importance of identifying the context with which the ORC is to be operated, so that the appropriate efficiency parameter (i.e. thermal or overall conversion) is used in the design and analysis of the system.

Next, consider the T-S sketch in Fig. 5.13d, as the degree of superheat increases, the amount of available energy at the expansion exit also increases. As a result, Fig. 5.14c and d shows that the duty of the IHE increases with increasing superheat. As the IHE partially preheats the working fluid, the average heat addition temperature and thus the thermal efficiency increases.

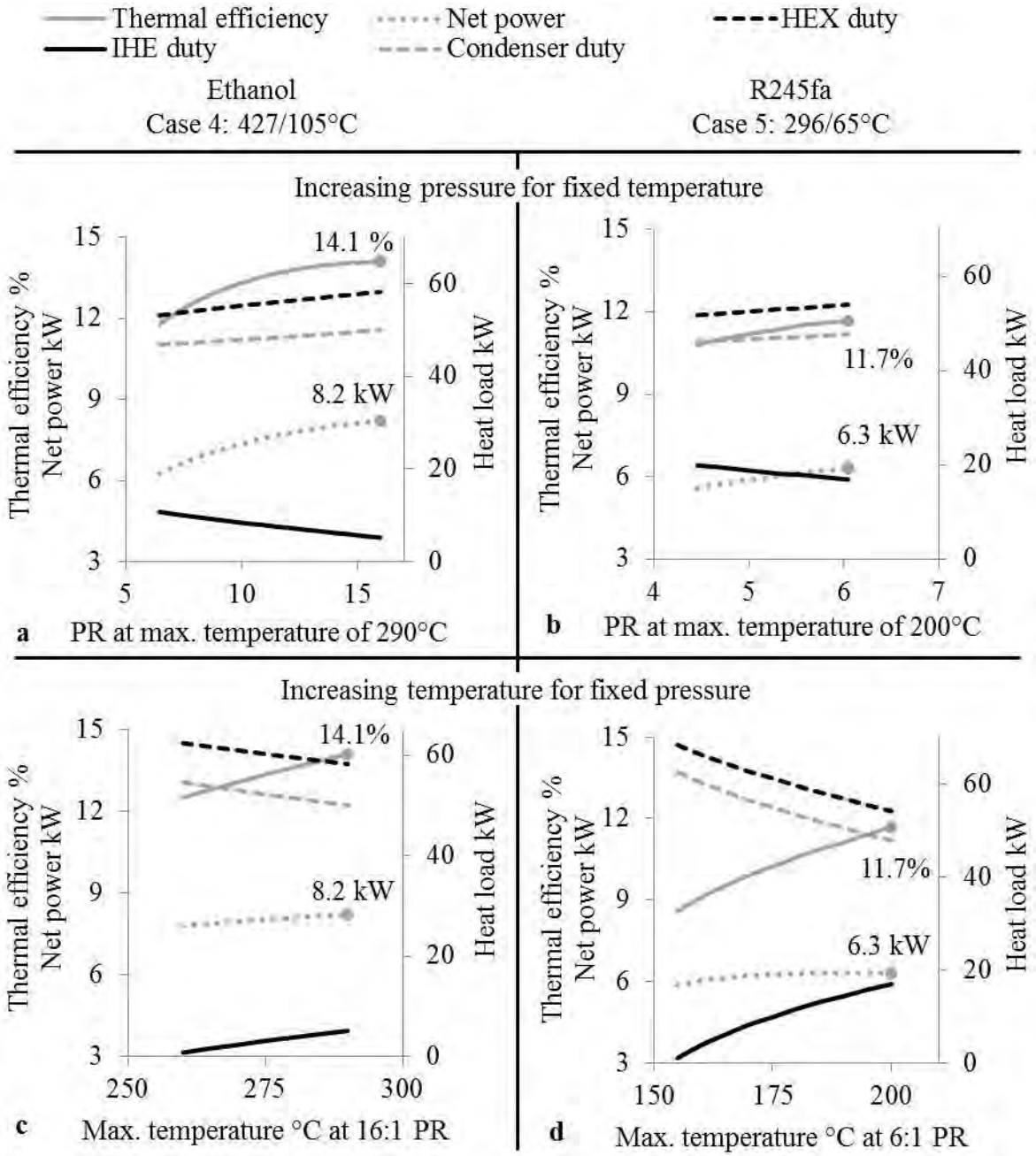

Figure 5.14 (a,b) effect of pressure on fixed superheat cycle with an IHE (c,d) effect of superheat on fixed pressure cycle with an IHE, in Case 4 (left side using ethanol) and Case 5 (right side using R245fa)

5.6.3 Internal heat exchange: Wet vs. dry fluids

Fig. 5.15a and b shows the T-Q diagram for the optimal superheated recuperated cycles. The IHE duty for R245fa amounted to ≈1/3rd of the total heat into the cycle, whereas for ethanol this accounted for less than 10%. As a result, R245fa showed a higher 3 vs. 1% point thermal efficiency improvement over the superheated non-recuperated cycle. The IHE duty is a function of the level of superheat, the shape of the saturated vapour curve and the expansion efficiency. Hence, wet fluids will require larger superheat than dry fluids for an equal level of thermal efficiency improvement. This suggests the use of

limited superheat level and exclusion of the IHE for relatively higher boiling point (>50°C) wet fluids in the present case.

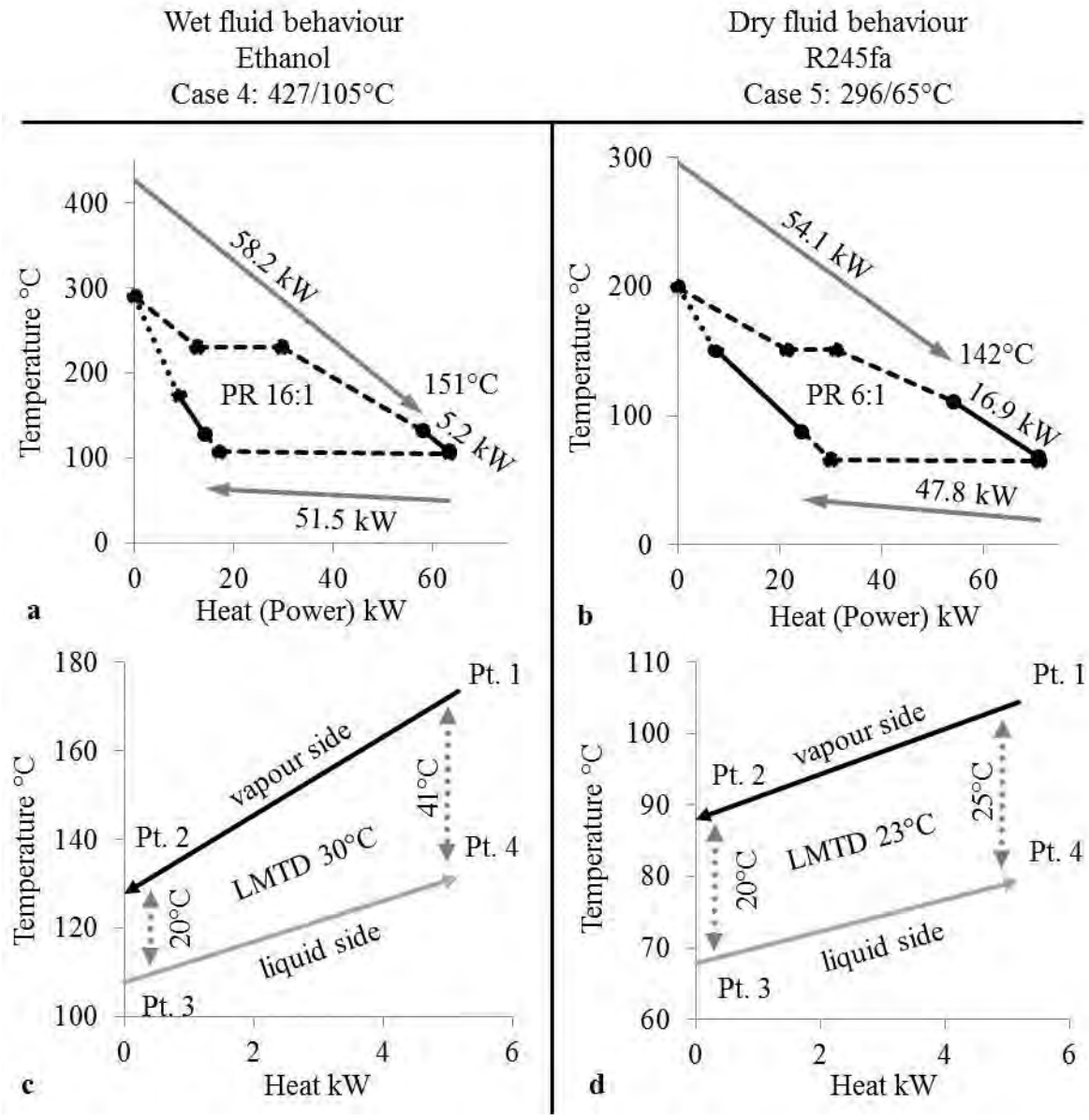

Figure 5.15 Wet vs. dry fluids (a,b) T-Q diagram for the optimised superheated cycle with an IHE (c,d) irreversibilities in the internal heat exchange process for equal load, in Case 4 (left side using ethanol) and Case 5 (right side using R245fa)

Wet fluids also provide a less efficient internal heat exchange compared to dry fluids. Despite the different process conditions, for this illustration, consider the internal heat exchange process for ethanol and R245fa for an equal IHE duty of 5.2 kW (Fig. 5.15c vs. d). For the selected counter-flow IHE the pinch point for both fluids occurred between the low-temperature low-pressure vapour side and the high-pressure low-temperature liquid side (Pt. 2-3). It was found that R245fa offered lower losses in the IHE (LMTD 23 vs. 30°C). This is due to a relatively parallel nature of the saturated liquid curve and the

de-superheating vapour curve for dry and isentropic fluids (T2−T3 ≈ T1−T4, Fig. 5.15d). Relative to R245fa, internal heat exchange can be said to be limited for ethanol (T2−T3 << T1−T4, Fig. 5.15c), furthering the case for exclusion of an IHE for wet fluids. Therefore, for the same heat load and pinch point in the IHE, dry and isentropic fluids obtain higher improvements in thermal efficiency. Hence, the measure of how well the available post expansion vapour is utilised, is defined by the selected value of the IHE pinch point and the associated working fluid internal heat exchange irreversibilities.

5.6.4 Superheated recuperated vs. superheated non-recuperated cycles

In order to understand how the IHE interaction affected the thermal efficiency and net power, the superheated recuperated R245fa (Fig. 5.15) was compared to the superheated non-recuperated counterpart (Fig. 5.10). The superheated recuperated R245fa cycle used a smaller heat input (54.1 vs. 69.1 kW) for obtaining the same net power output (6.3, 6.2 kW), hence it had a better thermal efficiency (11.7 vs. 8.9%) and reduced the load on the condenser (47.8 vs. 62.9 kW). The combined heat ($\dot{Q}_{HEX} + \dot{Q}_{IHE}$) used by the superheated recuperated cycle was roughly constant to the net heat ($\dot{Q}_{HEX}$) into the superheated non-recuperated cycle. This was because the presence of the IHE roughly compensated for the change in heat addition as a function of pressure and temperature. Note that the net power was unchanged either with varying cycle pressure or with varying cycle temperature. This is because the specific work is only a function of pressure difference across the expansion. In summary, large superheated cycles with an IHE increased the cycle thermal efficiency, decreased the heat recovery efficiency and had no impact on the net power.

5.6.5 Cycles with internal heat exchange: Discussion and findings

Fig. 5.16 quantifies the performance changes using superheated recuperated ethanol and R245fa over the simple cycle using the alternative fluids (ethyl iodide and R30) and operating with limited superheat (from Section 5.4). For a 16:1 pressure ratio, ethanol failed to provide higher net power than ethyl iodide and only gave insignificant (4%) improvement in thermal efficiency (Fig. 5.16a). The same was also true for R245fa compared to R30 for a 6:1 pressure ratio (Fig. 5.16b). Since nearly equivalent thermal efficiency can be delivered using a simpler cycle with the alternative fluids suggested avoiding the use of both superheated recuperated ethanol and R245fa cycles in the present application.

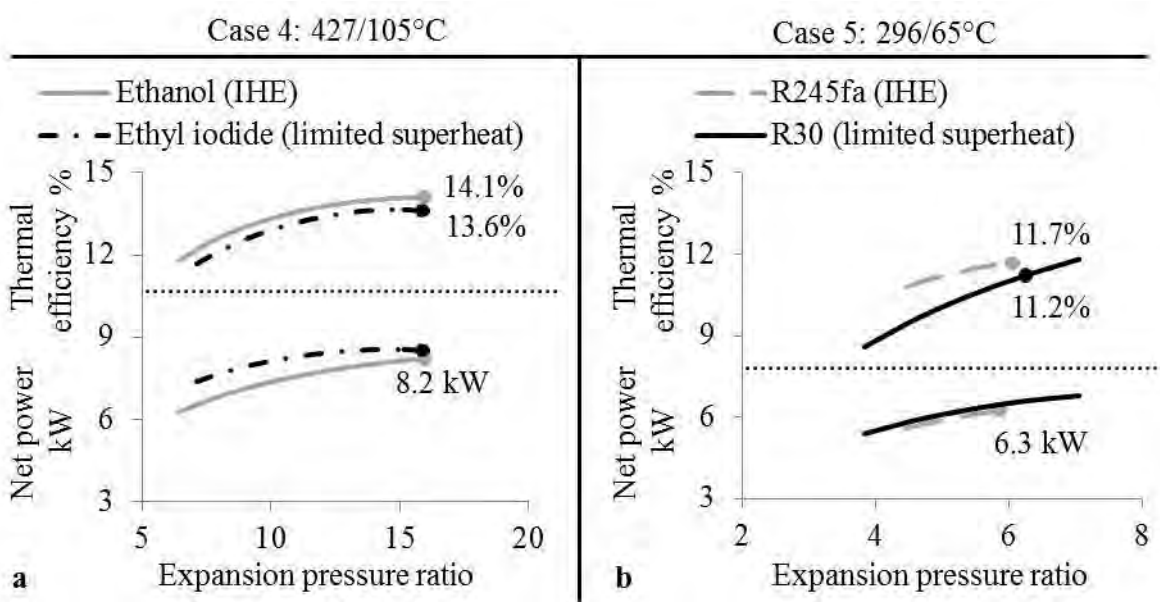

Figure 5.16 Performance change benchmark using superheated recuperated cycle in (a) Case 4 ethanol (b) Case 5 R245fa

Few additional items to point out regarding the IHE are that:

- The IHE also increases the exit heat source temperature, resulting in source enthalpy loss. This, although an advantage for exhaust heat recovery (Fig. 5.15b), is a drawback for EGR heat recovery (Fig. 5.15a) requiring the use of an additional low temperature EGR cooler.
- The addition of an IHE with a 20°C pinch point will not noticeably change the UA/W value. This is since the additional UA of the IHE is compensated by the reduction of the evaporator UA. Note that UA/W value is a useful indicator for relative size and cost considerations, but this parameter is better suited for similar class of fluids under similar cycle operating conditions. In reality, due to the nature of the liquid-vapour heat exchange in the IHE, heat transfer areas increase by 10-20% (Siddiqi and Atakan, 2011).
- The IHE also increases controls, complexity (additional HEX, piping, by-pass loop) and cost (especially if all HEXs are manufactured from the same materials) of the system.

Despite the above three challenges, the concept of internal heat exchange is particularly useful for reducing the size of the air cooled condenser. Hence, other alternative fluids and system architectures using an IHE, which are noticeably superior over ethanol remain a theme of investigation, and will be examined in the process integration phase in Chapter 6.

Other means to improve the cycle thermal efficiency include reheat, turbine bleeding and combinations of internal heat exchange, reheat and turbine bleeding (Ibrahim et al., 2011, Boyce, 2010, Desai and Bandyopadhyay, 2009, Mago et al., 2008). Since the control, complexity, size and cost of the system will increase dramatically due to the integration of these modifications for the same or lower net power, they are inappropriate for the present application.

5.7 Supercritical cycles (Cases 4 and 5)

5.7.1 Rational and simulation overview

A common limitation in the cycle operating modes discussed so far in this chapter using pure working fluids is the irreversibility in the evaporator due to the near isothermal boiling. To reduce this loss, supercritical organic cycles where liquid is directly compressed and heated beyond the critical point conditions can be considered. Fig. 5.17a shows the reduction in EGR heat exchanger irreversibilities with different thermal matches for ethanol at subcritical pressure in a large superheat cycle and supercritical pressure in a supercritical dry cycle (Fig 5.3b). With an appropriate fluid, a supercritical cycle can then approximate the heat addition process of a trilateral cycle.

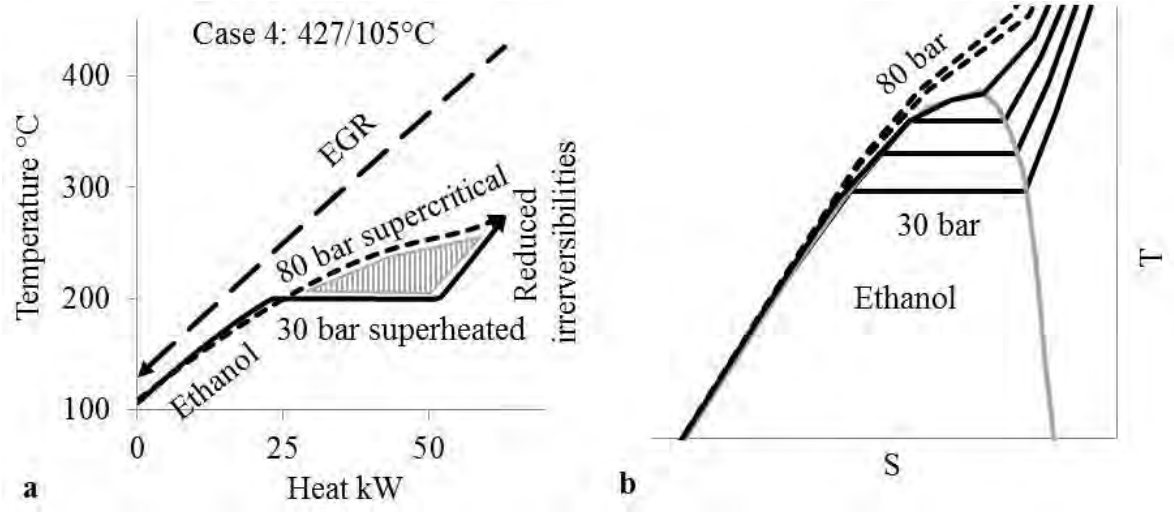

Figure 5.17 (a) heat transfer irreversibilities when comparing supercritical and subcritical operating modes (b) densely packed isobars near and above critical point conditions

The following subsections investigates supercritical fluid parameters for ethanol (Case 4) and R245fa (Case 5) to determine whether it may lead to a more suitable cycle operating mode as suggested in some studies (Teng and Regner, 2009). The range of supercritical pressures was chosen as $1.05\text{-}1.25P_{crit}$.

The selected operating mode of the supercritical cycle influences the turbine performance and cycle arrangement. In a supercritical bi-phase expansion for wet fluids (Fig. 5.3b) the fluid first sub-cools and then nucleates to become a two-phase mixture. The formation and behaviour of the liquid in the turbine create problems that would lower the performance of the turbine. Hence, ethanol was simulated using supercritical dry expansion (Fig. 5.3b).

In a supercritical bi-phase expansion for dry fluids (Fig. 5.3d), it was observed that only extremely fine droplets will form in the two-phase region and without any liquid that may damage the turbine before it starts drying during the expansion (Chen et al., 2010). However, since extremely drying fluids were not considered, supercritical bi-phase (Fig. 5.3d) and supercritical dry expansion (Fig. 5.3d) will give similar performance. Hence, R245fa was simulated with supercritical dry expansion to marginally avoid the two-phase region (i.e. with limited de-superheating load). Furthermore, the supercritical dry expansion mode for both wet and dry fluids also offer higher average heat addition temperatures than the respective supercritical bi-phase expansion.

5.7.2 Performance

Fig. 5.18a and b shows the thermal efficiency and net power results for the supercritical ethanol cycle in Case 4 and supercritical R245fa cycle in Case 5, respectively. With increasing supercritical pressures from 1.05 to $1.25P_{crit}$, insignificant improvements (≈3%) in the thermal efficiency and net power were observed in both cases. This can be better understood considering the subcritical and supercritical isobars for ethanol in Fig. 5.17b. For all working fluids the temperature difference between isobars in the T-S dome reduces faster when approaching the critical point conditions. Above the critical point, due to the densely packed isobars, relatively large changes in pressure only correspond to small changes in temperature. Hence, the enthalpy increase in the expansion stage is relatively lower, while the feed pump power consumption accounts for a greater percentage of the expansion power.

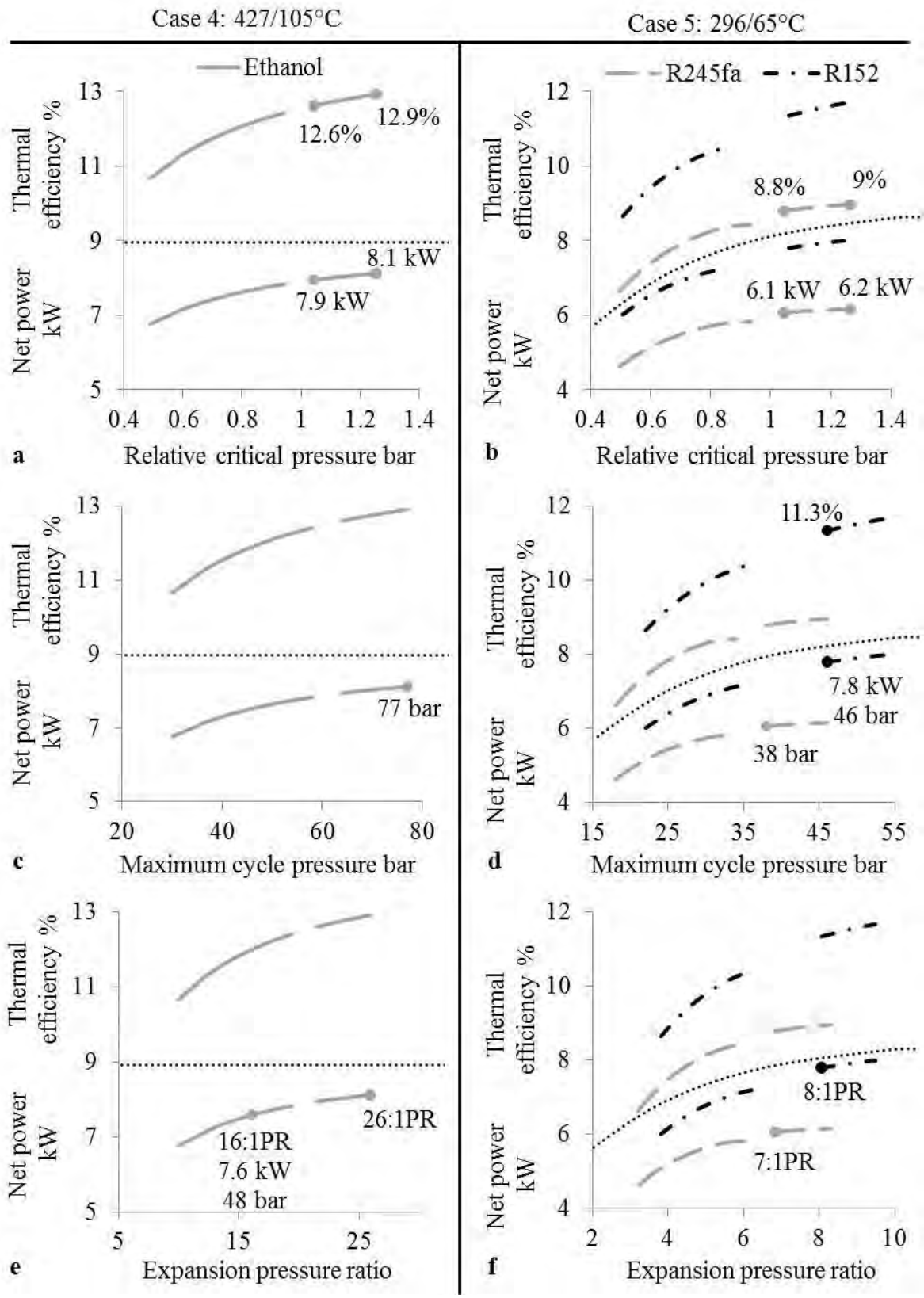

Figure 5.18 Thermal efficiency and net power variation with reference to (a,b) relative critical pressure (c,d) absolute cycle pressure (e,f) expansion pressure ratio, in Case 4 (left side) and Case 5 (right side)

5.7.3 Supercritical cycle: Discussion and findings (Case 4)

An economic review conducted for small scale (<30 kW) ORC units and its associated components resulted in the cost distribution shown in Fig. 5.19a and the heat exchanger pressure vs. cost relationship given in Fig. 5.19b (Matches, 2014, Edwards et al., 2012, Roos, 2009, Quoilin and Lemort, 2009, Thekdi, 2007, Peters et al., 2003). Two relevant points in the present case were that:

- 60% of the total cycle cost (i.e. heat exchanger + expander + pump) was dependent on the maximum system pressure and system pressure differential, and
- In the region of absolute pressures of interest for ethanol, a 20 bar pressure difference resulted in a 15% higher heat exchanger cost. Furthermore, high pressure heat exchangers require thicker walls/tubes, which in turn will increase heat transfer resistance and weight.

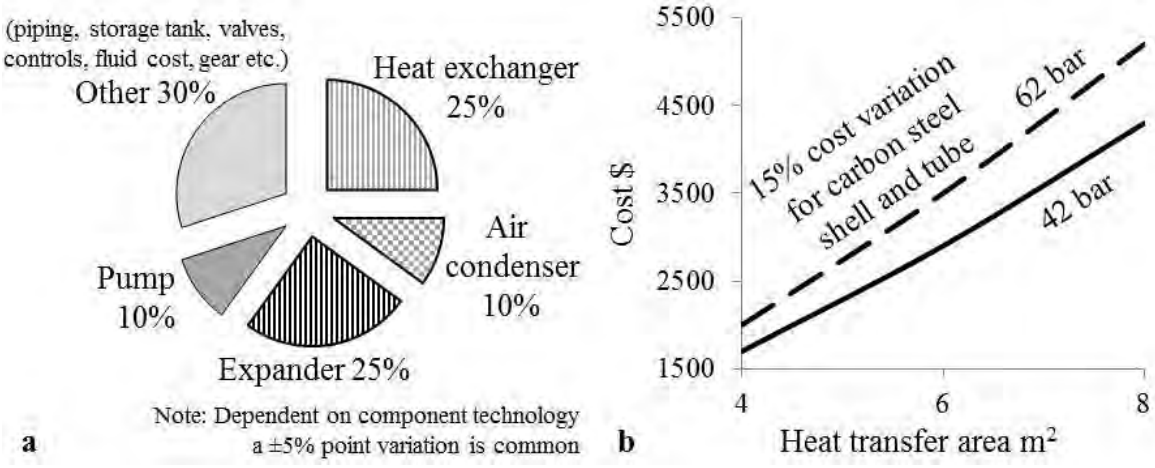

Figure 5.19 (a) small scale ORC component cost distribution (b) shell and tube heat exchanger pressure vs. cost relationship

In case of supercritical ethanol, the resulting implications of the high cycle pressures cannot be ignored. Fig. 5.18c and e replaces the x-axis with the absolute cycle pressures and expansion pressure ratios. The maximum net power of 8.1 kW was related to a 77 bar cycle high pressure (Fig. 5.18c) and a 26:1 expansion pressure ratio (Fig. 5.18e). For comparison, Case 5 also includes the subcritical limited superheat ethanol cycle.

To estimate a techno-economical trade-off between the subcritical 48 bar (PR 16:1) and the supercritical 77 bar (PR 26:1) ethanol cycles, the following was considered. It was assumed that the ratio of cost/kW of the 48 bar ethanol cycle was 1. Therefore, if a 15% increase in the cost of the heat exchanger was considered, then the cost/kW value of the 77 bar ethanol cycle remained ≈1. Such sensitivity analysis is a key element that can help to identify maximum cycle pressures corresponding to viable system configurations. Also

note that the 26:1 expansion pressure ratio was in violation of the boundary condition in Table 5.1 and is unlikely to be achieved by the discussed single stage expansion machines with comparable efficiencies. Supercritical modes due to the highest pressure ratios also have the largest expansion and pumping irreversibilities compared to the previous operating modes.

Considering the $1.25P_{crit}$ ethanol as a reference, the percentage reduction in net power was ≈7% for a $0.9P_{crit}$ cycle. The same was also true for R30 and acetone in Case 4. From a techno-economic analysis, this allows the conclusion that high subcritical pressures and limited superheat cycles to be a suitable solution. In absolute terms, this corresponded to 42-55 bar pressure region. Such pressures are then closer to the higher end values of the piston expanders reviewed. Supercritical superheated cycles (Fig. 5.3b) were not considered. Although they can offer higher thermal efficiencies, they will require a robust IHE, and will not demonstrate any noticeable change in net power.

5.7.4 Supercritical cycle: Discussion and findings (Case 5)

For Case 5, supercritical dry R152 was also simulated (Fig. 5.18b). Although this also showed negligible improvements with increasing supercritical pressures, it may be the only supercritical cycle exception that can be considered suitable in Case 5. This was since R152 at $1.05P_{crit}$ resulted in a relatively low maximum cycle pressure and temperature of 46 bar and 185°C. This pressure was only 8 bar higher than R245fa at $1.05P_{crit}$, but resulted in a cycle with 25% higher thermal efficiency and net power (Fig. 5.18d) for relatively low and similar pressure ratio (Fig. 5.18f).

Supercritical R152 cycle may be particularly advantageous at low exhaust temperature levels (250-300°C), where it becomes increasingly difficult to fully recover the waste heat with higher boiling point fluids (Fig. 5.6c). The maximum heat recovery and high thermal efficiency of supercritical R152 also allows correlating the working fluid critical temperature and the heat source temperature for an optimal fluid as: $T_{crit} \approx T_{source} - 3T_{PP}$ for a cycle pressure of $1.05P_{crit}$. Note that the discontinuity in the curves in Fig 5.18 is to represent the instability region due to near critical pressures. In practice the region of 0.95 to $1.05P_{crit}$ should be avoided (Shengjun et al., 2011).

5.8 Two-phase expansion (Case 4)

5.8.1 Rational and simulation overview

As shown in Case 4, limited superheat ORC net power results surpassed those of the conventional Rankine cycle (Fig. 5.5a). Due to the large heat required to vaporise water and further heat needed to superheat steam, the EGR heat recovery was limited (Fig. 5.4c). Fig. 5.20a and b shows this case, where the heat stream was only cooled to 191°C with an optimised evaporator pressure of 23 bar (optimisation Case C, Fig. 4.14c). However, due to the recent developments in variable phase turbine and twin-screw expander technology, the complete isothermal evaporation, which reduces heat recovery, can now be avoided. These two expansion machines presently appear to be the only viable solutions for the admission of liquid or two-phase mixtures.

To determine the effect of the two-phase cycle operating mode on heat recovery and hence the net power, simulations were conducted with varying expansion inlet vapour fraction with water at a fixed cycle pressure of 30 bar in Case 4. The 30 bar pressure was selected because it corresponds to an evaporator temperature of 233°C, and temperatures much higher than this may lead to thermal distortion of casing and rotors when using screw machines (Smith et al., 2011). To highlight the contrasting behaviour of water and organic fluids under the two-phase cycle operating mode, ethyl iodide at 30 bar was also considered which has an evaporator temperature of 243°C.

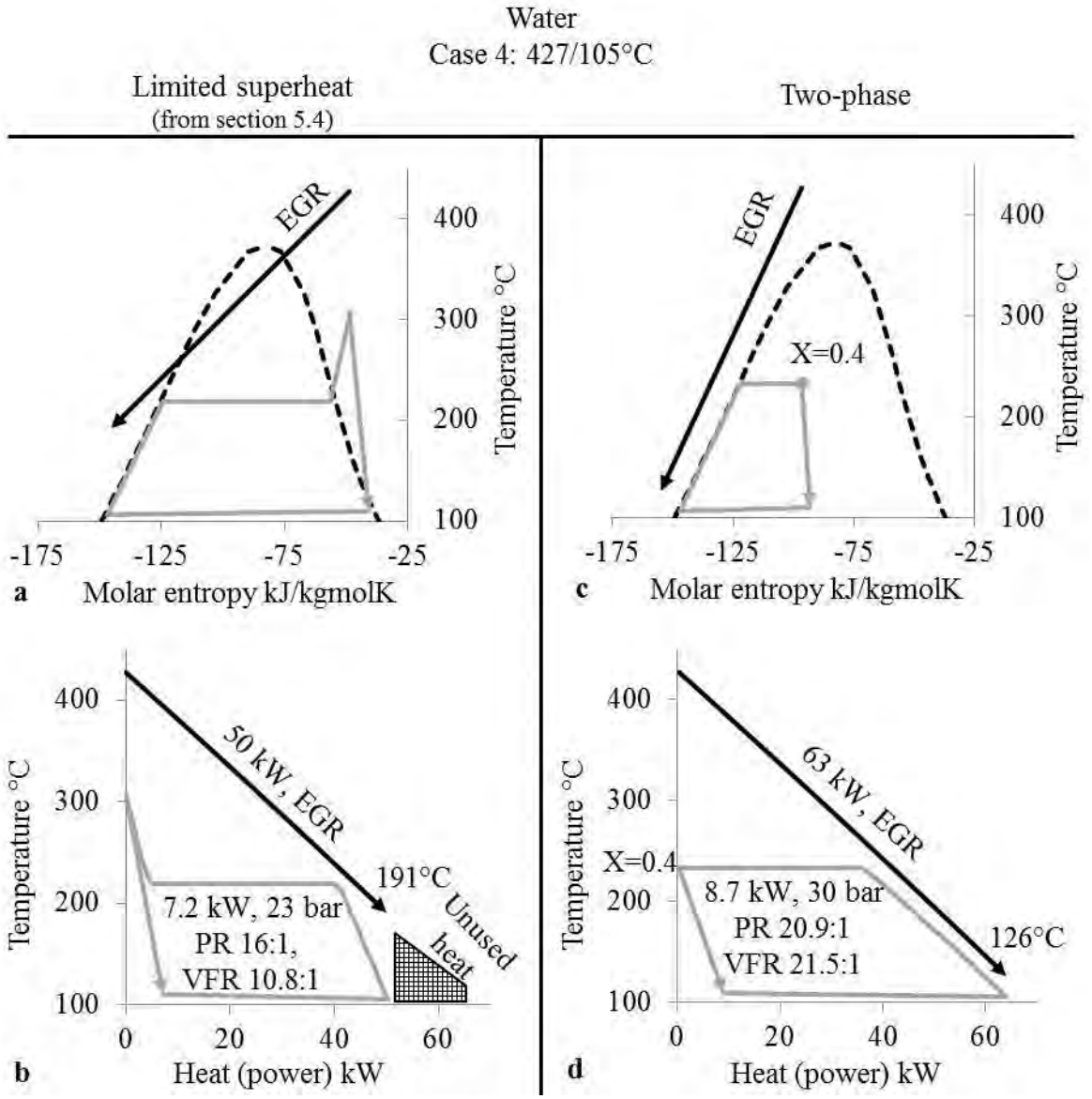

Figure 5.20 23 bar limited superheat water expansion (a) T-S (b) T-Q diagram; 30 bar two-phase water expansion (c) T-S (d) T-Q diagram, in Case 4

5.8.2 Performance

As can be expected, Fig. 5.21a and b shows that with reducing vapour fraction the thermal efficiency decreased. However, for water (Fig 5.21a) the heat recovery also increased. At an expander inlet vapour fraction of 0.4, complete heat recovery (63 kW), combined with the highest thermal efficiency for complete heat recovery (13.6%), resulted in the highest power (8.7 kW). This optimised two-phase water expansion cycle is shown in Fig. 5.20c and d, and when compared to the 23 bar limited superheat cycle, it delivered 20% higher net power. Organic fluids in high temperature application, as in Case 4, were better suited to limited superheat expansion since heat recovery remained constant and the thermal efficiency decreased with decreasing vapour fraction (Fig. 5.21b). Note that given the same heat input and maximum cycle pressure among dry saturated vapour, two-phase and liquid

expansion, the mass flow rate of the working fluid increases, the expansion specific enthalpy drop decreases and the pumping specific enthalpy change increases as the vapour quality at the expansion inlet decreases.

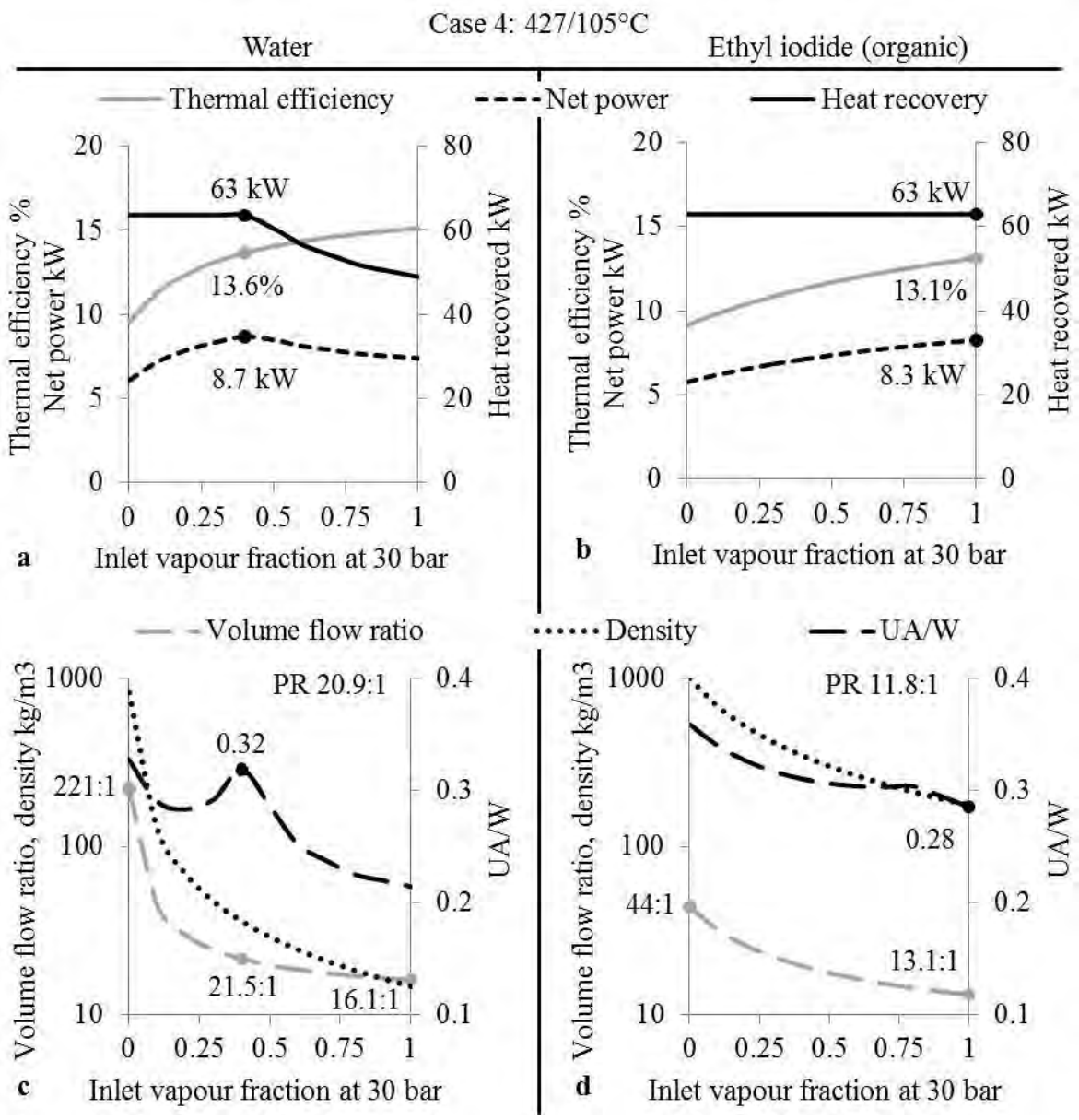

Figure 5.21 Effect of expansion vapour inlet fraction for 30 bar cycle pressure on (a,b) thermal efficiency, heat recovery and net power (c,d) expansion volume flow ratio, UA/W value and density, in Case 4 for water (left side) and ethyl iodide (right side)

With lower temperature heat recovery the UA/W value for the two-phase water expansion cycle was higher (0.32 vs. 0.22) than the limited superheat water expansion (Fig. 5.21c vs. Fig. 5.5c). Furthermore, this value was then similar (0.32 vs. 0.28) to the limited superheat results using the alternative organic fluids (Fig. 5.21c vs. d). The higher heat transfer coefficients associated with water may in fact result in a slightly smaller total heat exchanger surface area per unit power.

5.8.3 Two-phase expansion: Discussion and findings

Two-phase expansion cycles do face some particular challenges:

- Two-phase expansion machines are slightly inefficient than the conventional dry vapour turbines and expanders (Smith et al., 2011). When the two-phase expansion machine was assumed to be 3% point less efficient (67 vs. 70%), then the two-phase water performance was equal to that of the dry saturated vapour ethyl iodide (8.3 kW).
- The 30 bar two-phase water also resulted in nearly twice the expansion pressure ratios and volume flow ratios (Fig. 5.21c vs. d). Such high pressure ratios (20.9:1) are unlikely to be achieved by single stage twin-screw expanders and were in violation of the boundary condition in Table 5.1. Hence, for equivalent performance, two stages of screw expansion will be required, resulting in larger footprint of screw expanders.
- Two-phase expansion cycles will be relatively challenging to control in practice since the information about the enthalpy would be required to exactly define the quality at expansion inlet.

Two-phase water expansion cycles are then mainly recommended for stationary CHP plants or in the upper stage of cascade systems which offer higher values of condensing pressures and relatively non-transient heat flows. Despite the above challenges, since water is the safest fluid for high temperature heat recovery, architectures that may provide a partial solution remain a theme of investigation, and will be examined in the process integration phase in Chapter 6.

Furthermore, an application specific observation was the relatively lower change in volume flow ratios for fluids at higher vapour fraction (especially between 0.5-1, Fig. 5.21c and d). This indicates that despite the decreasing net power with reducing vapour fraction for organic fluids, power can be produced more frequently in a drive cycle using machines that can expand two-phase as well as dry vapour. The increased availability to generate power may then be one of the key significant contributions in improving the case for FBCs for automotive application.

Isentropic (e.g. ethyl iodide) and dry fluids can further simplify the control for a high vapour fraction cycle and provide an estimate of quality at expansion inlet. This can be done using P,T measurements downstream of the bypass throttling expansion valve (Fig. 4.8). When superheated conditions are achieved, a signal can be generated to divert the flow into the expansion machine. Cycles where fluid exits as dry vapour also allow the possibility of mixing oil in the working fluid inventory (≈5% by mass). The oil can be used

for lubrication as the working fluid evaporates during the expansion process. For screw expanders, the presence of liquid also seals the gaps between the rotors and the casing, maintaining efficiency (Smith et al., 2005b). The ability to operate with high vapour quality (between 0.5-0.9) inside a tube also has the advantage of relatively higher boiling heat transfer coefficients (Perry and Green, 2007).

5.9 Liquid expansion (Case 3)

5.9.1 Rational

Consider the heat recovery and volume flow ratio variation between water and ethyl iodide (Fig. 5.21) for expansion inlet condition of dry saturated vapour ($X_{in} = 1$) to liquid ($X_{in} = 0$).

- Firstly, the heat recovery was also maximum at liquid expansion for both fluids.
- Secondly, volume flow ratios of expansion from the liquid phase were significantly higher than those associated with the expansion of dry saturated vapour.
- Thirdly, the volume flow ratio increase in water was by a factor of 14, compared to a factor of 3 for ethyl iodide. The large volume flow ratio with water was due to the low vapour pressure (1.2 vs. 2.5 bar) at the selected condensing temperature (105°C).

When using twin-screw machines for liquid expansion, the overall expansion volume flow ratio of the fluid was shown to be many times greater than the machine built-in volume flow ratio (Smith et al., 2001). This is attributable to the density of the working fluid being higher at liquid state compared to dry saturated vapour state (also shown in Fig. 5.21c and d). The suction (high pressure port) process is accompanied by a comparatively large pressure drop which contributes significantly to the overall expansion. However, irrespective of this advantage over dry saturated vapour expansion, the volume flow ratios seen in liquid expansion in Case 4 (and also in Case 5) for high net power were impractical for single stage machines.

The liquid and two-phase expansion efficiency further decreases as the difference between the source and sink increases. This is due to the need for higher built in volume flow ratios to permit complete expansion across increasing pressure differences, and associated with this, reduced fluid throughput and higher leakage losses (Smith et al., 2005a). The above discussion then indicates that single stage liquid expansion may be only suited to Case 3 (i.e. CAC heat recovery), where the conventional cycle cannot fully recover the available waste heat (e.g. $\eta_{recovery} \approx 77\%$, Appendix 4.11), and a lower boiling point fluid under low temperature differential can be employed.

5.9.2 Simulation overview

Appropriate supercritical cycles can approximate the heat addition curve of the trilateral cycle. However, according to the earlier correlation ($T_{crit} \approx T_{source} - 3T_{PP}$) for supercritical cycles ($1.05P_{crit}$), the desired working fluid boiling point ($T_{boil} \approx 0.65T_{crit}$) in Case 3 should be around −20°C. Fluids with such low boiling points will translate to high pressures (≈20 bar) in the condenser (65°C).

The following subsection explores an alternative approach using E152a liquid expansion with subcritical pressures and temperatures. E152a was an alternative low temperature fluid identified in Chapter 4 for CAC heat recovery. Under liquid expansion mode, the working fluid enters the screw expander as high pressure saturated or slightly sub-cooled liquid and is then flashed to the condensing pressure (Fig. 5.3a). Note that in liquid and two-phase expansion cycles, the exit vapour fraction can be from two-phase to superheated vapour. This is since the exit vapour fraction is a function of the shape of the T-S curve, the proximity of the expansion inlet temperature to the critical temperature, expansion efficiency and quality at the expansion inlet.

As a reference, the limited superheat E152a T-Q diagram (Fig. 5.22a) and performance results (Fig. 5.22b) were considered from Appendix 4.11. The cycle recovered around 30 kW of CAC heat, produced a net power of 2 kW, and showed an optimisation Case A trend (Fig. 4.14a).

5.9.3 Performance

For the liquid expansion cycle (Fig. 5.22d), with increasing cycle pressure the heat recovery was nearly constant (38 kW). However, as a consequence of increasing expansion enthalpy drop, the net power increased linearly. Compared to the dry saturated vapour expansion cycle, the net power eventually surpassed at higher pressures for liquid expansion (Fig. 5.22c vs. d). Liquid E152a expansion was able to deliver 20% higher net power (2.4 vs. 2 kW). Nevertheless, this also required nearly twice the cycle pressures (40 vs. 24 bar).

Fig. 5.22b shows the optimised E152a liquid expansion cycle with almost constant temperature difference in CAC heat exchanger (LMTD 23 vs. 34°C). Due to the close similarity to trilateral cycle, the liquid expansion cycle is also termed as trilateral flash cycle. Therefore, like the two-phase expansion using water in Case 5, liquid expansion using E152a in Case 3 offered higher overall conversion efficiencies.

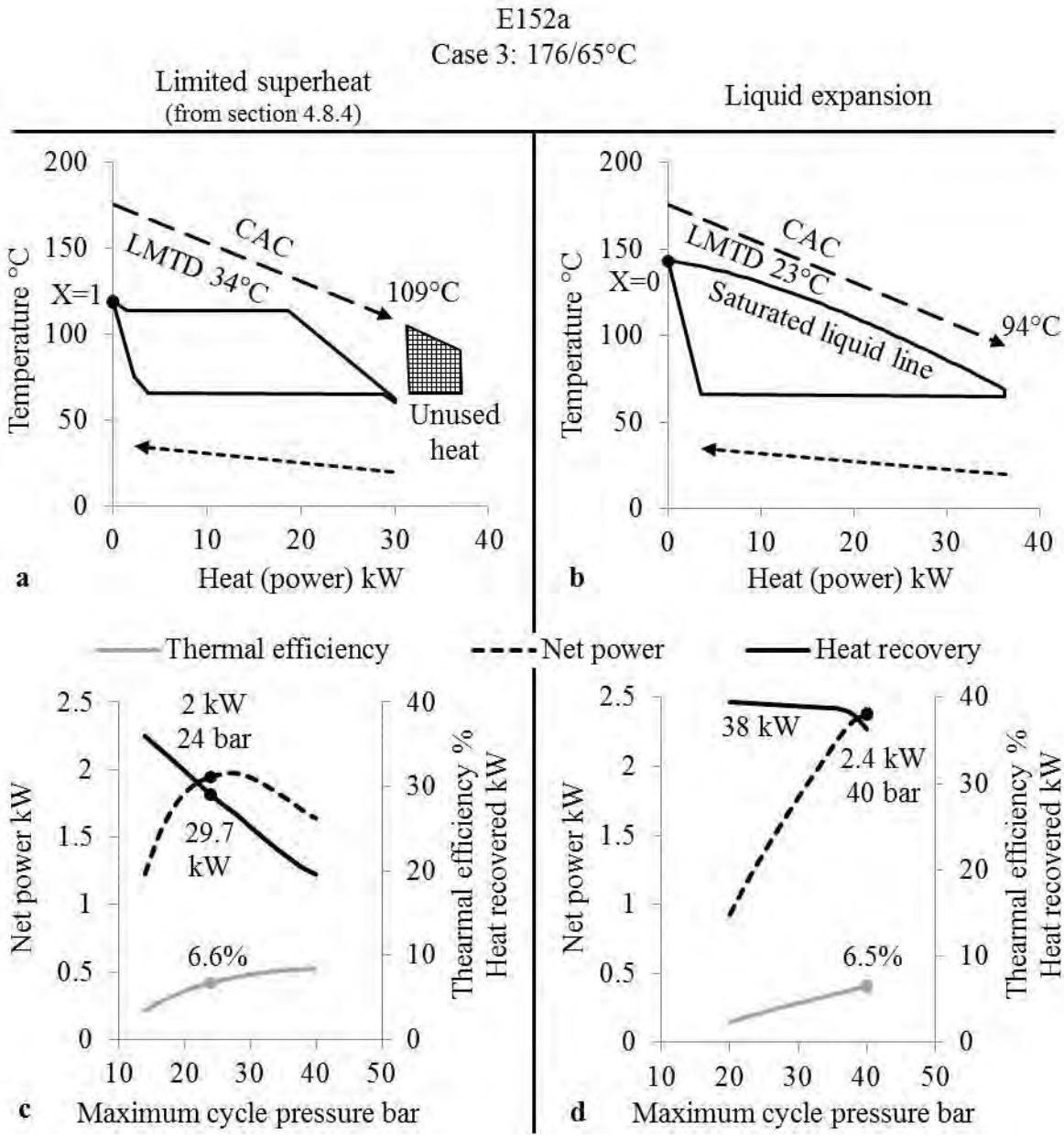

Figure 5.22 (a,b) T-Q diagram for the optimised cycle (c,d) thermal efficiency, heat recovery and net power variation with cycle pressure, for limited superheat (left side) and liquid expansion (right side) in Case 3 for E152a

The sudden drop in heat recovery approaching the 40 bar pressure limit (Fig. 5.22d) was due to a combination of the strong curvature of the saturated liquid line in organic fluids above $0.9P_{crit}$ and the proximity of the maximum cycle temperature (143°C) to the hot CAC temperature (176°C). For the near constant temperature difference across the greater segment of the CAC heat exchanger and higher net power, the critical temperature of the optimal fluid can be correlated as: $T_{crit} \approx T_{source} - 2T_{PP}$. Furthermore, considering near critical pressure ($0.95P_{crit}$) for liquid expansion, the relative reduction in expansion enthalpy drop will be lower when compared to the dry saturated vapour expansion.

For liquid expansion, the net power results only depend on the cycle operating condition rather than both the cycle operating condition and the thermodynamic properties of the selected working fluid. Hence, under similar maximum cycle temperature (with pressures $\leq 0.9P_{crit}$), liquid expansion using different working fluids will provide similar performance. A small variation will only occur due to the different pump power consumption.

5.3.4 Liquid expansion: Discussion and findings

Fig. 5.23 contrasts the primary objective function results between the limited superheat and the liquid expansion cycles. Furthermore, results for R245fa are also included to highlight the advantage of E152a. The practicality of a fluid for liquid expansion cycle is mainly dependent on a lower T_{boil}/T_{crit} value and higher density. Fig. 5.23b shows similar expansion pressure ratio (5:1) for optimised E152a and R245fa for liquid expansion. However, for a similar critical temperature (149, 154°C), E152a offers a much lower boiling point (−5 vs. 15°C). As a result, E152a offered noticeably lower volume flow ratio (14.9:1 vs. 21.4:1). Furthermore, it has already been demonstrated that in order to achieve a volume flow ratio of 12.3:1 using R113 which has a standard liquid density of 1564 kg/m^3, the required build-in volume ratio for the twin-screw expander was 2.85:1 (Smith et al., 1999). E152a at 40 bar showed similar volume flow ratio (14.9:1, 12.3:1) and a standard liquid density only 25% lower (1564 vs. 1128 kg/m^3). As such, liquid E152a expansion may offer a more practical solution over R245fa.

The liquid expansion cycles resulted in a 30% increased UA/W value (Fig. 5.23c vs. d) due to increased lower quality heat recovery. Nonetheless, high heat recovery on heat streams that already require cooling will partially compensate the negative effect of the increased heat transfer areas and the associated costs. Hence, the higher UA/W value does not therefore necessarily imply that the overall system cost/kW will be higher to make the system impractical. Hence, architectures that can recover low temperature heat using liquid expansion will be examined in the process integration phase in Chapter 6. However, this does stress the importance of efficient liquid expanders along with efficient organic pumps, since the pump power is a greater percentage of the recoverable expansion power compared to any other cycle operating mode.

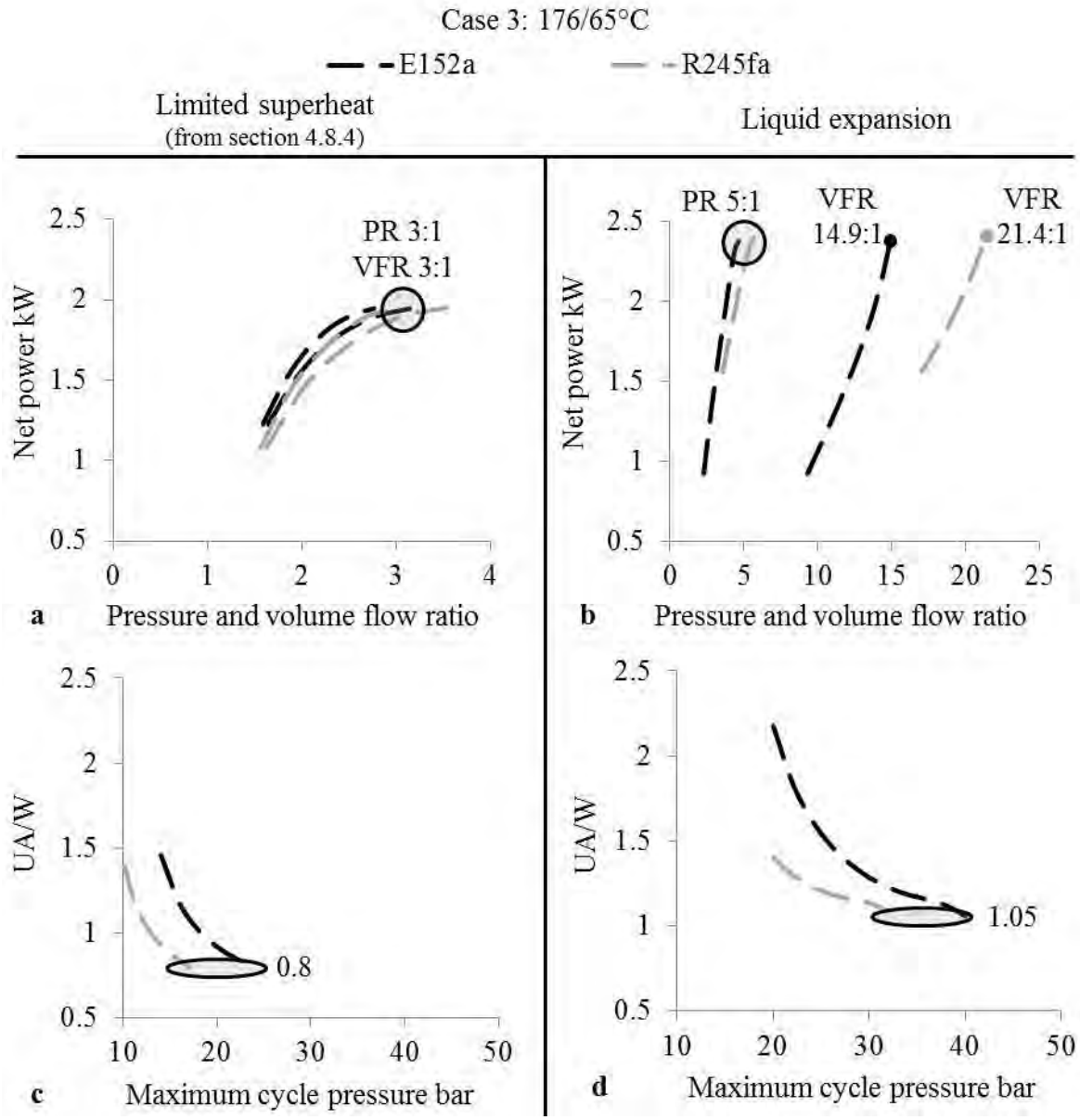

Figure 5.23 (a,b) effect of pressure ratio and volume flow ratio on net power (c,d) effect of cycle pressure on UA/W value, for limited superheat (left side) and liquid expansion (right side) in Case 3 for E152a and R245fa

5.10 Additional inorganic cycles

Apart from the conventional steam cycle which was best suited to high temperature heat recovery (>450°C, Fig. 4.18), there were three other inorganic cycles commonly proposed for lower temperatures. These included supercritical CO_2, ammonia and Kalina cycles (Tian et al., 2013, He et al., 2011). This section assesses the suitability of these additional inorganic cycles for the present application and benchmarks their performance to relevant previous results of conventional ORCs from this chapter.

5.10.1 Carbon dioxide

CO_2 is a natural working fluid and was often cited for offering better thermal match in supercritical cycles. CO_2 was additionally suggested due to its low environmental impact, low cost, non-flammability, stability, good heat transfer properties, compatibility with standard construction materials and lubricants, and high density. However, CO_2 has a relatively low critical temperature and high critical pressure of 31°C and 73.8 bar (Fig. 5.24a).

The CO_2 condensation process requires a sink temperature usually less than 15°C to perform condensation below the critical point, preferably below 20°C. Such low condensing temperature limits are challenging to achieve in stationary air cooled condensers let alone in an engine cooling module. Hence, the reliable low temperature CO_2 condensation and the packaging needs of the corresponding large air cooled condenser is a formidable challenge. Furthermore, the 20°C condensing temperature corresponded to a high condensing pressure of 57.3 bar, and a $1.05P_{crit}$ was already near the 80 bar limit considered in this chapter. Such high pressures then require robust heat exchangers and condensers, adding to safety concerns.

Recent efforts made by the MAC sector led to the development of a compact CO_2 co-axial heat exchanger design with high burst pressure and a low pressure drop which may provide a solution (EAA, 2011). Another obstacle for the supercritical CO_2 cycle, which is the design of a suitable expansion machine, has also seen progress. Published works include adapting gas turbines, development of rolling piston expander, using free piston expander, vane expander (modified vane type oil pump) and scroll expander (modified semi-hermetic R134a scroll compressor) (Facão and Oliveira, 2009). More recently, supercritical CO_2 experimental test platforms less than 10 kW are now also commercially available (Infinity Turbine, 2014). Despite the technical progress in the past 5 years, the requirement of a low condensing temperature makes the supercritical CO_2 inappropriate for the current application.

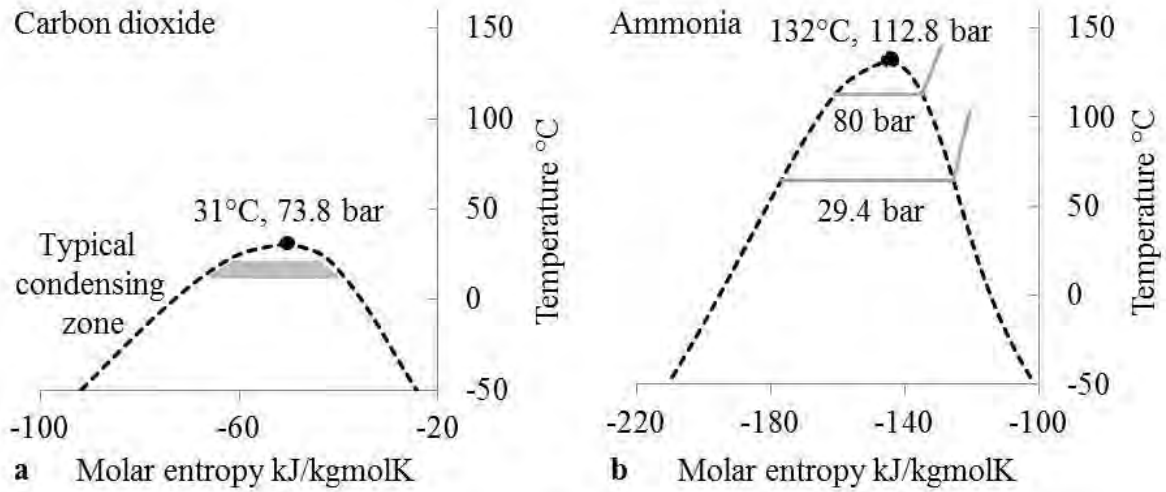

Figure 5.24 T-S diagram (a) carbon dioxide (b) ammonia

5.10.2 Ammonia

Ammonia with a relatively higher critical temperature (132°C, Fig. 5.24b) compared to CO_2 can be considered for heat recovery at the CAC temperature level. Like CO_2, ammonia was also suggested as a working fluid as it offers lower pressure ratios. Fig. 5.25 compares the ammonia cycle performance with the E152a ORC. Ammonia being an extremely wetting fluid was simulated using limited superheat expansion.

The ammonia cycle delivered equivalent performance for equivalent pressure ratios to the limited superheat E152a cycle (Fig. 5.25a). However, the ammonia cycle required an evaporator and condenser pressure around 3.5 times higher (Fig. 5.25b). Furthermore, ammonia's NFPA health rating is higher than that considered in the fluid screening (Fig. 4.9). Ammonia was not considered in supercritical mode since its critical pressure is extremely high (112.8 bar) due to the strong polar forces within its molecule (Smith, 2009). In summary, the ammonia cycle is not recommended in Case 3 since neither performance nor system benefit is experienced over E152a despite the much higher pressures.

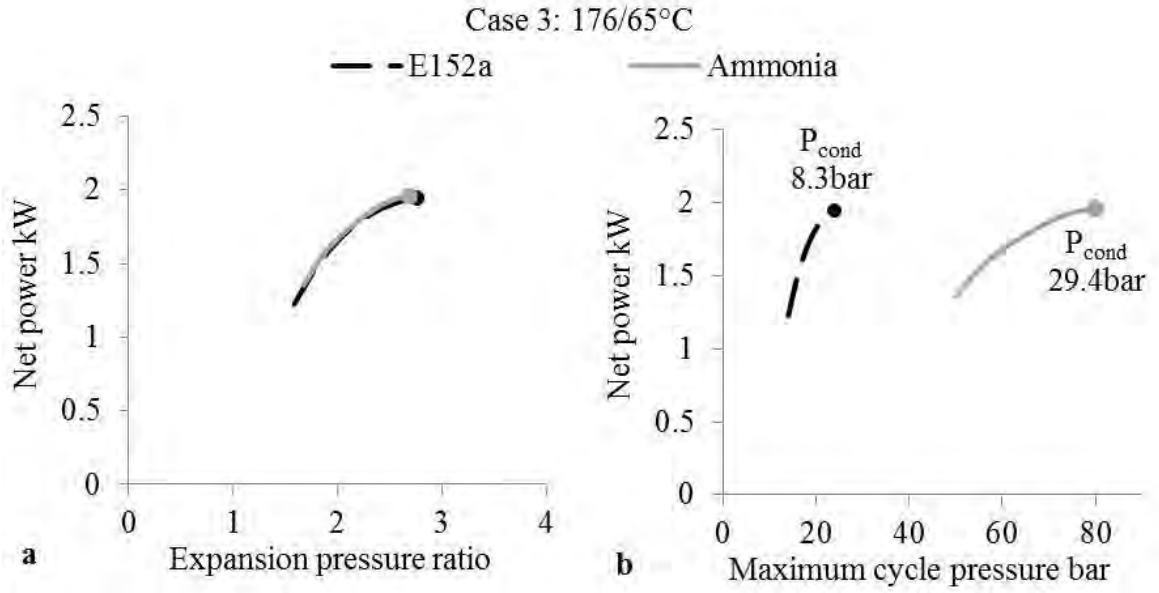

Figure 5.25 Net power comparison for E152a and ammonia with reference to (a) expansion pressure ratio (b) maximum cycle pressure, in Case 3 for limited superheat expansion

5.10.3 Ammonia-water

5.10.3.1 Rational and simulation overview

A popular binary inorganic cycle is the Kalina cycle that offers a good temperature match using an ammonia-water mixture and varies the composition of the mixture in the cycle. Depending on the heat stream conditions, there are several different possible configurations of the Kalina cycle. Fig. 5.26 shows the simplest Kalina cycle arrangement in which the basic ammonia-water liquid mixture is pumped to high pressure (9-1) to be first heated in the IHE (1-2) and then the HEX (2-3). The basic mixture (3) is then split into vapour (4, rich ammonia mixture) and liquid (5, weak ammonia mixture) parts using a separator. The strong ammonia vapour solution is expanded to produce work (4-6) and is then mixed with the weak ammonia liquid solution (5+6→7). Finally, the reconstituted basic mixture is first cooled in the IHE (7-8) and then condensed (8-9). The commonly used weight composition is Ammonia 80% and Water 20% (referred as AW 80/20). A Kalina cycle can offer the possibility of more frequent power generation as vapour at the HEX exit is not necessary. The ammonia-water mixture composition at the expansion inlet can hence be changed during operation in order to adapt the cycle to possible fluctuating heat source and/or sink temperatures.

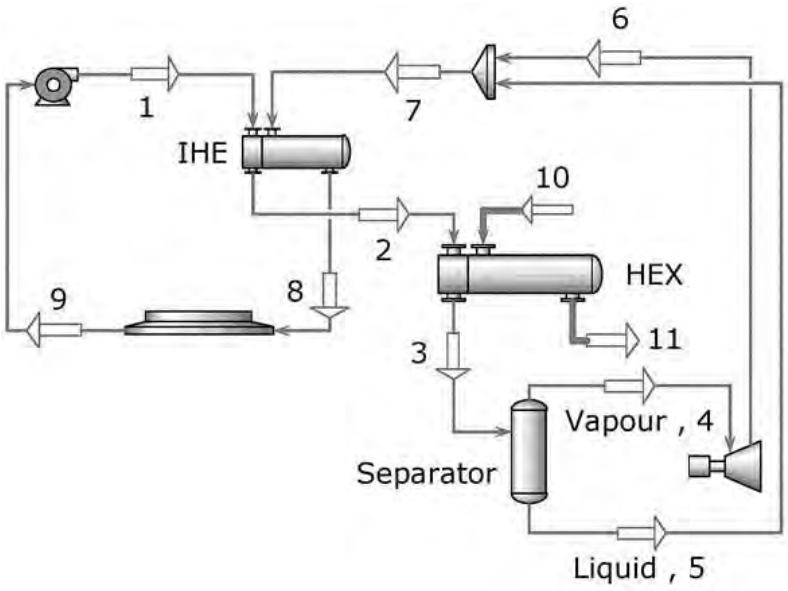

Figure 5.26 Basic Kalina cycle configuration

The following subsections discuss the simulation results of the simplest Kalina cycle configuration for Cases 3 and 5. A fixed pressure drop of 0.2 bar was assumed in the separator and the maximum ammonia-water temperature in both cases was fixed at $T_{source} - T_{pp}$. The use of a mixture adds one degree of freedom, which allows varying the system pressures and temperature glide during evaporation to optimise the cycle. Hence, a parametric study was also conducted by varying the mixture composition.

5.10.3.2 Performance

Fig. 5.27a and b shows the performance results of the parametric study on ammonia-water concentration and cycle pressure in Case 3 and Case 5, respectively. An optimal performance of 1.6 kW in Case 3 (Fig. 5.27a) was achieved using an ammonia-water concentration of 90% and 10% at a cycle pressure of 50 bar. Whereas in Case 5 (Fig. 5.27b), a peak performance of 5.7 kW was attained as 65 bar using the same mixture concentration. The maximum cycle pressure at the optimal point and the condensing pressure (26.1 bar) were rather high, this was due to the higher ammonia concentration. This also means that the IHE has to withstand high pressures on both sides (26.3 bar shell side and 50, 65 bar tube side).

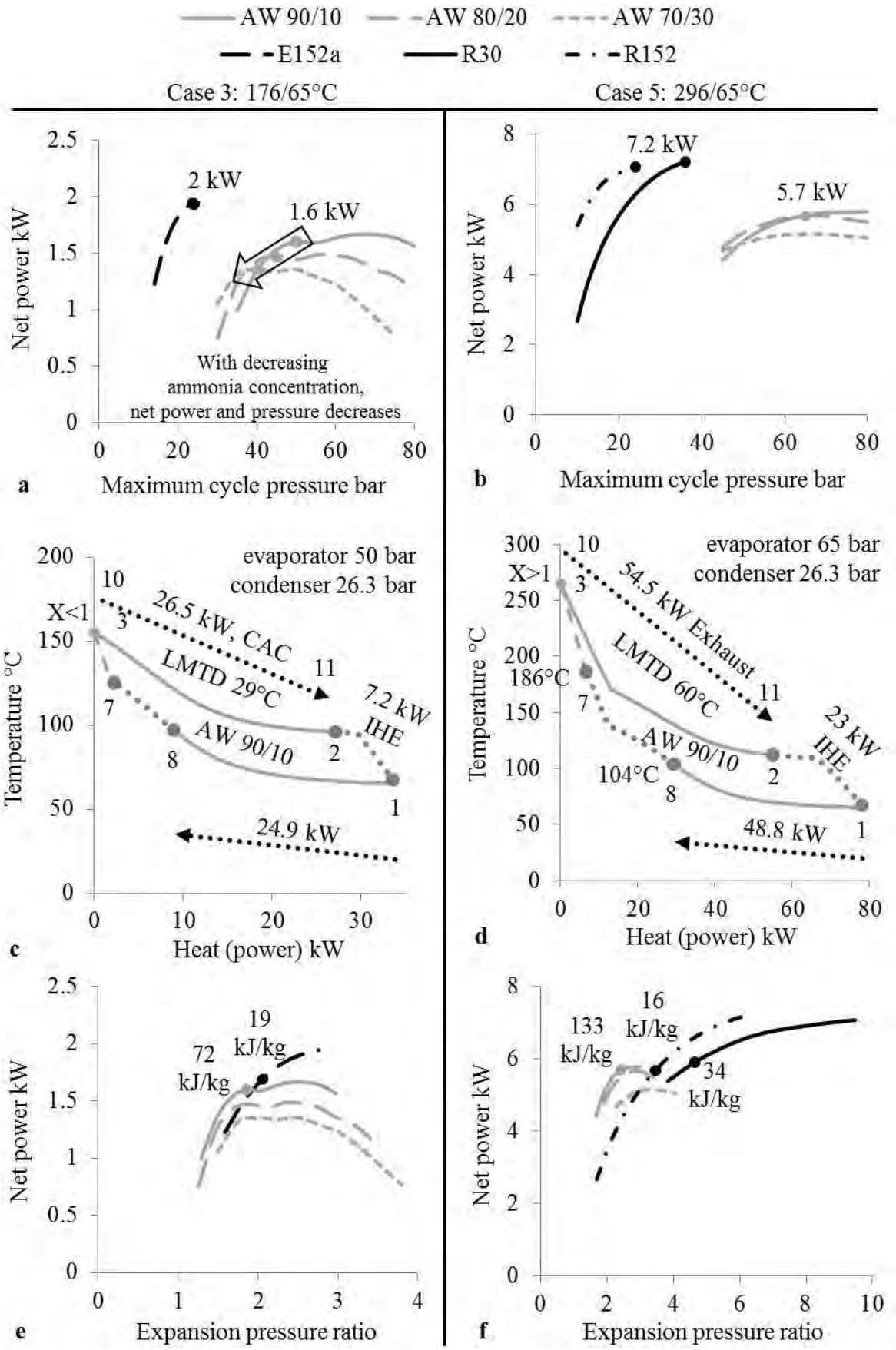

Figure 5.27 (a,b) effect of cycle pressure on net power (c,d) T-Q diagram of the optimised ammonia-water cycle (e,f) effect of pressure ratio on net power, in Case 3 (left side) and Case 5 (right side) for ammonia-water cycle and ORCs

Fig. 5.27c and d depict the T-Q diagram of the selected optimal ammonia-water cycle in the two cases. The mixture exiting the HEX (Pt. 3, Fig 5.27c) was only partially vaporised in Case 3. Often a second high temperature IHE is used to exchange heat between states Pt. 5 and Pt. 2 (Fig. 5.26), but in Case 3 this IHE was omitted. This was because at the 50 bar optimal pressure the mass flow rate of the liquid stream (Pt. 5) consisted of only ≈5% of the total mass flow rate. The ammonia mass fractions for the rich, basic and weak mixtures for the 50 bar optimal cycle were 0.92, 0.9 and 0.44, respectively.

In Case 5, the mixture exiting the HEX was highly superheated (Pt. 3, Fig. 5.27d). As a result it did neither require a separator nor a second IHE. The resultant ammonia-water cycle in Case 5 was not a conventional Kalina cycle (i.e. does not vary the composition of ammonia), but rather an inorganic Rankine cycle with an IHE. The significantly higher temperature at expansion exit (186°C) and the temperature glide during condensation allowed for strong internal heat recuperation from point 7-8 to 1-2.

For Cases 3 and 5 inclusion of the IHE was necessary in the ammonia-water cycle as it represented 30-50% of the condenser load at the optimal operating point. However in Case 3, the separator was also necessary contrary to Case 5, where it could be omitted. These contradicting architectures using ammonia-water may complicate the process integration if different streams are exploited simultaneously. Note that in an ammonia-water mixture the pinch point is located at the terminal end conditions of the HEX (2-11 and 3-10) rather than at an intermediate location as in the case of pure organic fluids (Fig. 5.22a).

5.10.3.3 Ammonia-water cycle: Discussion and findings

Although the Kalina cycle was often stated to be superior to the ORC, simulation results in Cases 3 and 5 showed that a simple ORC operation resulting in equal or higher performance than the Kalina cycle. Fig. 5.27a and b shows that the limited superheat E152a cycle, and limited superheat R152 and R30 cycles produced 25% higher net power, respectively.

Furthermore, the variable evaporation temperature (2-3) did not make a noticeable change. In Case 3, the LMTD improvements (Fig. 5.27b vs. 5.22a) were low (29 vs. 34°C). While in Case 5, this was within the organic fluids range (Fig. 5.27d vs. 5.6c).

Ammonia-water cycles were also proposed due to their low expansion pressure ratios. However, for equivalent net power the expansion pressure ratios were nearly similar in Case 3 (Fig. 5.27e). While in Case 5, the expansion pressure ratios for organic fluids although slightly higher were within the reach of all single stage expansion machines discussed (Fig. 5.27f). In fact, a turbine design may favour the ORC, as the enthalpy drop for equal net power was 4 times higher for the ammonia-water expansion than organic working fluids in both cases (Fig. 5.27e and f).

The simple ORC design also poses less technical, size and cost challenges than the ammonia-water cycle due to half the system pressures (Fig. 5.27a and b) and absence of additional equipment (IHE, separator). The ammonia-water solution is also corrosive to copper and zinc, and air or CO_2 in liquid ammonia may cause stress corrosion cracking of mild steel (Chen et al., 2010).

Kalina cycles are then better suited to applications like geothermal where there is:

- Lower source temperatures (<200°C)
- Lower condensing temperatures (<40°C)
- Lower source temperature differential (ΔT <100°C, slope of line 10-11, Fig. 5.27c)
- Higher source quantities (>500 kW, to allow the use of a second IHE)

In large scale application, conventional axial flow steam turbines can then be used in the Kalina cycle. This is possible because the molecular weights of ammonia (17 g/mol) and water (18 g/mol) are similar. As such, the Kalina cycle has only reached commercial acceptance in larger output capacity (>100 kW) than needed in the present application.

5.11 Chapter 5: Summary

The combination of a suitable working fluid and its associated cycle operating mode for a particular source and sink temperature limit is the key in optimising performance. The investigations conducted in this chapter showed that detailed system design and system configuration analysis is necessary to ensure a techno-economical FBC. Results presented using 10 pure, dry, isentropic and wet working fluids (synthetic, organic and inorganic) operating with expansion starting from the saturated vapour, superheated vapour, supercritical phase, two-phase and saturated liquid, suggests optimal combinations of working fluids and cycle operating modes as:

1. Liquid E152a expansion for CAC temperature limit (Case 3), i.e. under low source temperature (176°C) and low source-to-sink temperature differential (Δ111°C).
2. Limited superheat expansion using methanol, R30 and acetone with optimisation Case A, or $1.05P_{crit}$ R152 dry expansion for exhaust temperature limit (Case 5), i.e.

under medium source temperature (296°C) and medium source-to-sink temperature differential (Δ231°C).

3. Limited superheat expansion using the 5 alternative high temperature organic fluids with maximum $0.9P_{crit}$ pressures for EGR temperature limit (Case 4), i.e. under high source temperature (427°C) and high source-to-sink temperature differential (Δ322°C).

The 5 alternative high temperature organic fluids will also be better suited to an integrated EGR and exhaust heat recovery system. For an integrated exhaust and CAC heat recovery system, methanol, R30, acetone and R152 will be better matched. Additionally, higher molecular weight fluids, like Ethyl iodide and R30, offered a more interesting solution for small capacity mobile systems due to better system response during changed process conditions and turbine design considerations.

Table 5.2 Comparing practical performance results with the real quadlateral cycle

Case		T_{source}/T_{cond} °C	T_{pp} °C	$\dot{W}_{real,quad}$ kW	Results in Chapter 5
3	CAC	176/65	20	3.3	2.4 kW (73% of $\dot{W}_{real,quad}$) Liquid expansion, E152a, VFR 14.9:1, Fig. 5.23b
4	EGR	427/105	20	11.8	9.1 kW (77% of $\dot{W}_{real,quad}$) Limited superheat, acetonitrile, PR 16:1, Fig. 5.5a 7.7 kW (65% of $\dot{W}_{real,quad}$) Limited superheat, R30, PR 9:1, Fig. 5.5a
5	Exhaust	296/65	30	10.8	7.8 kW (72% of $\dot{W}_{real,quad}$) Supercritical dry, R152, PR 8:1, Fig. 5.18f 7 kW (65% of $\dot{W}_{real,quad}$) Limited superheat, R30 and acetone, PR 8:1, Fig. 5.7a

Table 5.2 compares the theoretical results assuming an ideal fluid and cycle operating mode (i.e. real quadlateral cycle) with the above mentioned real working fluids and practical cycle operating modes. The different working fluids and cycle operating modes were 65-77% as efficient as the real quadlateral cycle. This highlights the difficulty for real systems in even approximating to the real quadlateral cycle limit. Nonetheless, the 65-77% limit serves as a baseline for other WHR technologies.

Furthermore the items selected for further investigations were:

4. Improving the performance of wet and isentropic fluids by superheating, but providing a partial solution to the vapour load drawbacks.
5. Using an IHE with other alternative fluids and system architectures that are more superior over ethanol.
6. Employing two-phase water expansion with lower pressure ratios.

The next chapter will focus on process integrations using items 1-6 and their possible combinations.

Fig. 5.28 summarises the most significant sensitivity, performance and system results (referenced to limited superheat expansion). Note that the liquid and two-phase expanders both have undergone demonstrations but are technically the most challenging expansion machines. However, when operated with conditions limited to those given in Fig. 5.28, they can attain adiabatic efficiencies in the region of 70%, improving their case. Possible improvements by any other working fluid or cycle operating mode not summarised above in items 1-6 are insignificant or accompanied with unfavourable systems trade-off. In particular:

7. Techno-economical assessment of supercritical dry ethanol cycle under high source temperature and high source-to-sink temperature differential did not offer any favourable results.
8. Wet fluids (e.g. ethanol) are preferred without an IHE, contrary to dry fluids (e.g. R245fa). Nonetheless, a simple R30 cycle can match the performance of a superheated recuperated R245fa cycle under medium source temperature and medium source-to-sink temperature differential.

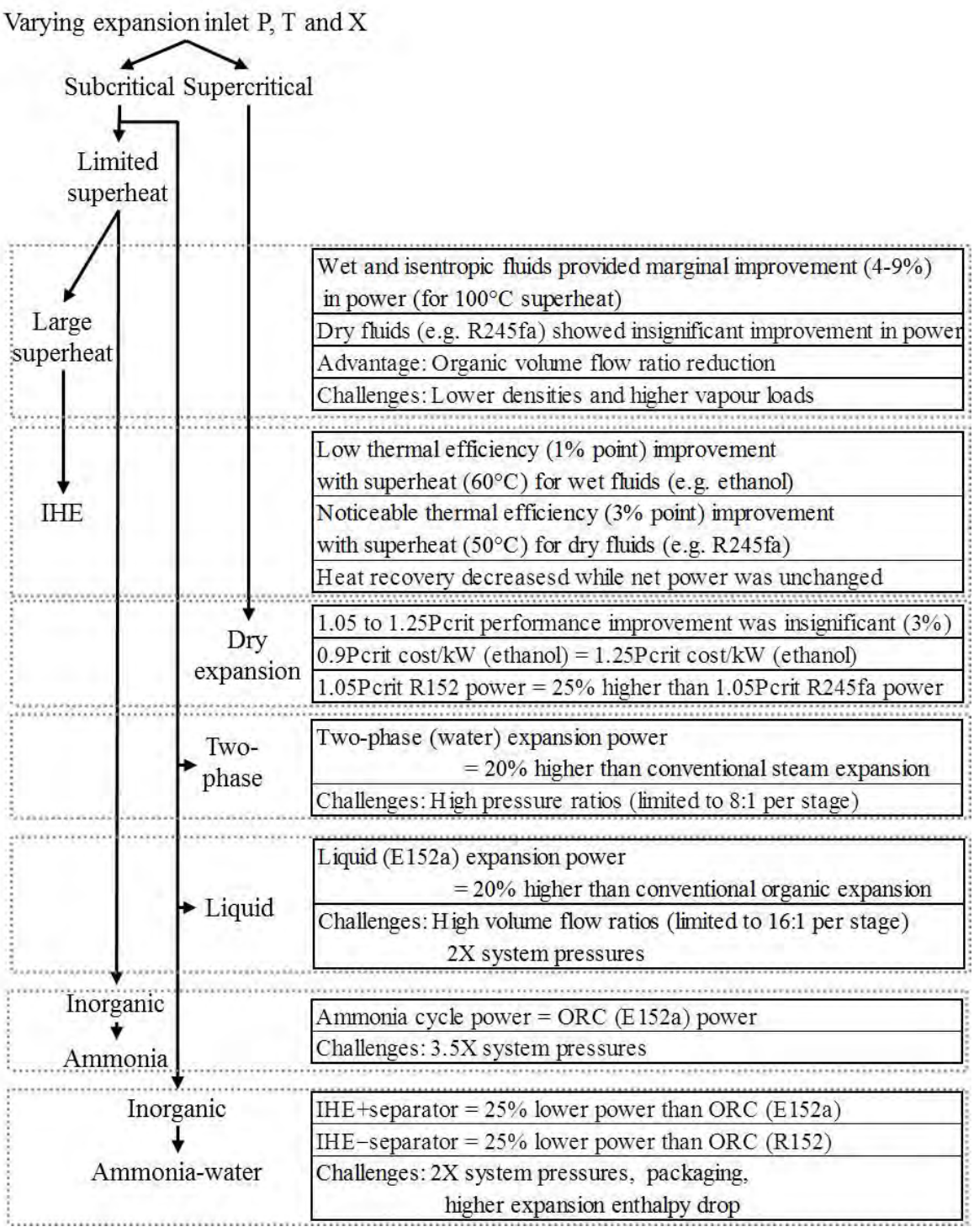

Figure 5.28 Key results and sensitivity of the different cycle operating modes by varying the three expansion inlet parameters

6 Process Integration

6.1 Introduction

Process integration is defined as a system oriented approach for optimal energy conversion by plant optimisation. The plant optimisation embraces at least five overlapping fields, these include:

- Selection of a suitable working fluid
- Optimisation of the cycle operating mode
- Plant thermal architecture
- Plant subsystem architecture, and
- Effects on interconnected processes/utilities

Utilising the findings of working fluids (Chapter 4) and cycle operations (Chapter 5), this chapter explores numerous process integrations with the principal objective of sustainable development for automotive HDDEs.

As a simplified example, for architecture analysis, consider the combined heat recovery from two different quality levels. Under such a case, heat can be recovered at least in series, parallel, cascade, dual pressure and dual cycle arrangements. Therefore, in order to recover the combinations of EGR, post-turbine exhaust (EXH), CAC and engine block heat, multiple series and parallel thermal architectures were considered. Thermal architectures that transfer heat internally, as is the case with cascade condensers and IHEs were also included. Whereas the subsystem architectures considered were limited to 2 expansion stages (with/without reheat stage), 2 pressure levels and 2 fluid loops. Due to the large number of possible architectures, the simple architectures were initially evaluated (e.g. series, parallel). Guidelines derived from their analysis provided the directions for the design of efficient complex architectures (e.g. dual pressure, dual cycle). As a result, 13 most noticeably different arrangements as a function of the above thermal and subsystem architectures, with different working fluids and cycle operations were explored.

These 13 arrangements are presented under 2 different approaches with increasing complexity level (Fig. 6.1). Approach ‘A’ was constrained by the use of a single expansion stage (Fig. 6.1a). In approach ‘A’, compared to theme 1, theme 2 demonstrated higher system power due to increased heat recovery from the thermal loads on the engine cooling module. Whereas approach ‘B’ was primarily focused on high temperature thermally stable solutions (Fig. 6.1b). In approach ‘B’, improved thermal stability water-organic and organic-organic blends were also investigated. Compared to theme 3, theme 4 and 5 demonstrated higher system power and thermal efficiency.

The purpose of considering such large number of process integrations was fourfold:

- Firstly, to quantify for comparable design intensity, the benefits of the process integrations proposed in this thesis to those in the published literature.
- Secondly, to emphasise the benefits/limitations of particular process integration for an engine platform or engine speed/load.
- Thirdly, to recommend a set of universal application guidelines for the different themes of process integrations.
- Finally, to select process integrations that ensure optimal system performance among various engine platforms and engine speeds/loads.

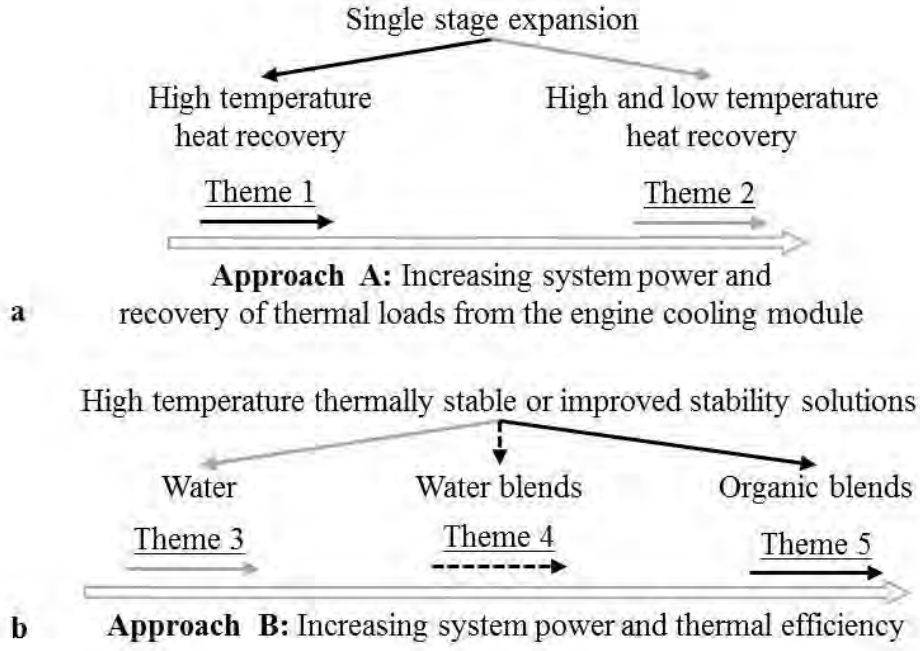

Figure 6.1 Division of process integrations based on 5 themes of approach

Since successful process integration requires considerations of not only the FBC parameters but also the FBCs effects on the engine performance and vehicle, the different process integrations were quantitatively evaluated with considerations given to:

1. Maximum working fluid temperature (T_{max}) and pressure (P_{max})
2. Thermal efficiency (η_I)
3. Net power ($\dot{W}_{net}$)
4. Indicative size of the expansion machine per unit power output (VFR/W value)
5. Indicative total heat transfer equipment footprint per unit power output (UA/W value)
6. Increased load on the engine cooling module ($\dot{Q}_{inc.\ LOAD}$)
7. HDDE platform power loss due to exhaust backpressure and increased fan power requirement ($\dot{W}_{BP+fan}$)
8. System power ($\dot{W}_{system}$ as defined in equation 4.24)

9. Optimal use of exhaust heat recovery (β value as defined in equation 6.1)
10. System complexity

The discussions will also highlight that considerations of at least items 4, 5, 8, 9 and 10 are crucial for identifying successful process integrations. Furthermore, operational methodology, major controlling parameters and challenges unique to process integration are qualitatively described.

6.2 Base engine cooling module

A critical issue for the FBCs coupled with an automotive HDDE is the amount of heat rejection capacity available within the engine cooling module. Fig. 6.2 shows the selected heat loads on the engine cooling module common across both EGR only (E6) and EGR focused (E5) engine platforms, namely EGR, CAC and engine coolant that were used in the different process integrations. Table 6.1 details the breakdown of the heat loads in High-Temperature EGR (HT EGR), Low-Temperature EGR (LT EGR) and CAC from Appendix 3.5 for the B50 and C100 points. Fig. 6.3a and b gives the total maximum heat rejected from the low-temperature and medium-temperature radiators corresponding to the HDDEs (i.e. without a FBC at C100). The low-temperature radiators of both engines were of equal relative dimension/capacity of HDDE power (21-22%), while the E6 medium-temperature radiator was around 1/3rd larger than the E5 medium-temperature radiator (151.6 vs. 112.2 kW).

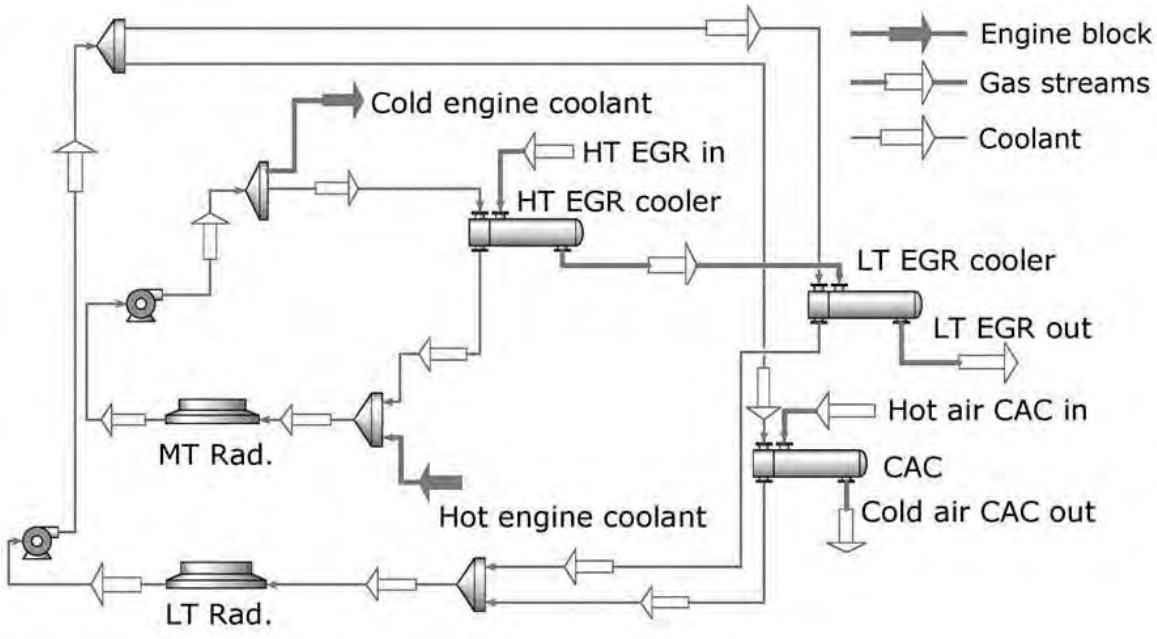

Figure 6.2 Common heat loads on the engine cooling module across all EGR engine platforms

Table 6.1 Maximum available heat loads at mid-speed mid-load and high-speed full-load used in the simulations

	Low Temperature Radiator (LT Rad.)		Medium Temperature Radiator (MT Rad.)		
EGR focused platform (E5) (Fuel flow, BTE, Brake Power)	CAC (air-to-liq.) kW [°C-°C]	LT EGR kW [°C-°C]	HT EGR kW [°C-°C]	Coolant kW [°C-°C]	EXH kW [°C-°C]
B50 (39.9kg/hr, 41.8%, 150kW)	13.8 [147-85]	3.1 [120-96]	28.7 [357-120]	35.3 [97-90]	41.3 [272-110]
C100 (56.2kg/hr, 42.5%, 284kW)	37.2 [169-85]	4 [120-97]	52.2 [436-120]	45.1 [97-90]	94.1 [300-110]
EGR only platform (E6)					
B50 (41.1kg/hr, 40.8%, 151kW)	12.6 [151-85]	4 [120-95]	41.6 [389-120]	38 [97-90]	38.8 [290-110]
C100 (62kg/hr, 40.2%, 296kW)	49.5 [200-85]	6.1 [120-96]	88.8 [466-120]	52.6 [97-90]	92.1 [302-110]

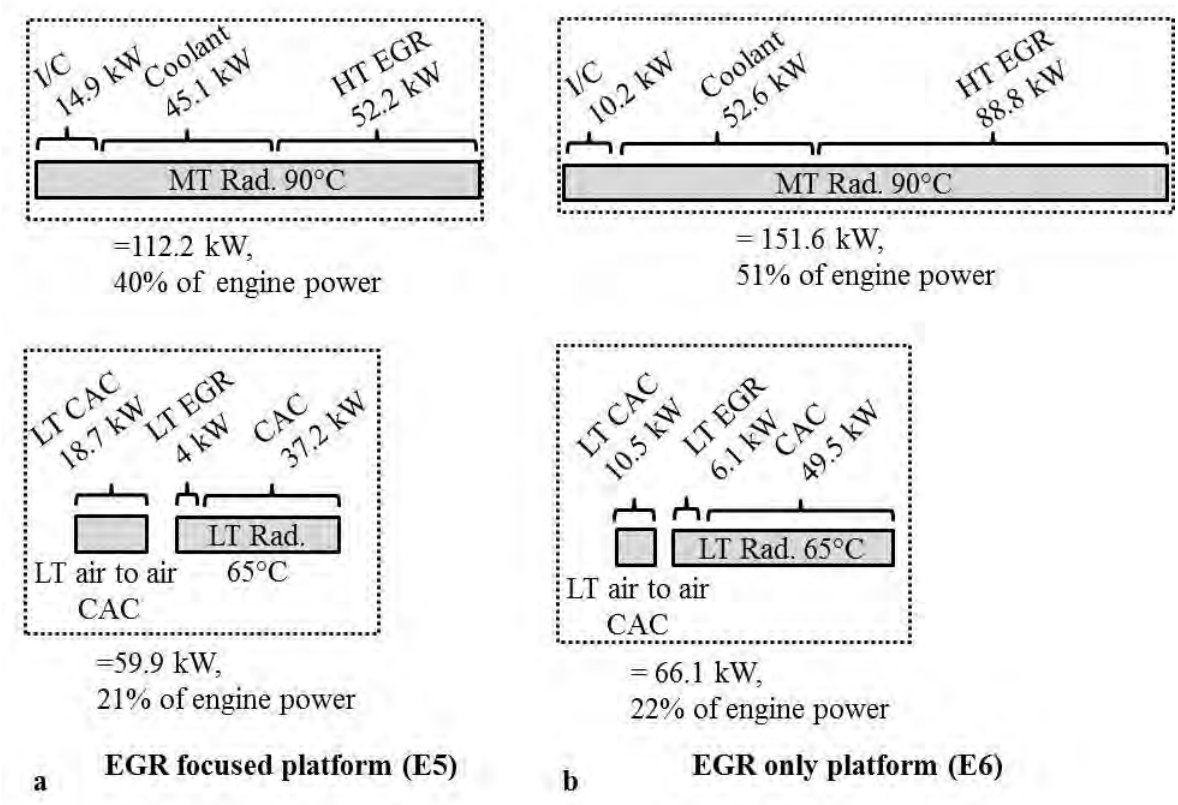

Figure 6.3 Maximum heat rejection capacity of the low and medium-temperature radiators for (a) EGR focused engine (b) EGR only engine

6.2.1 Impact of exhaust heat recovery and modified engine cooling module

The dimension/capacity of the engine cooling module and the required cooling fan power increases either if a medium-temperature radiator load is transferred to the low-temperature radiator load or if EXH heat recovery ($\dot{Q}_{EXH}$) is greater than the FBC net power produced ($\dot{W}_{net}$). To retain the practicality of the FBC, the process integrations proposed in this chapter excluded increasing the low-temperature radiator capacity, and since all the process integrations detailed included EXH heat recovery, the cooling capacity at the medium-temperature radiator level was increased. Furthermore, to represent nearly equivalent total engine cooling module dimension/capacity, the increased medium-temperature radiator heat rejection level was limited to 60% of the HDDE power for both the engines. This meant that at C100, only around 26 kW of the 92.1 kW of heat available in the EXH stream in the E6 engine could be utilised (Fig. 6.4b), whereas the possible EXH heat recovery was much higher at 58.2 kW for the E5 engine (Fig. 6.4a).

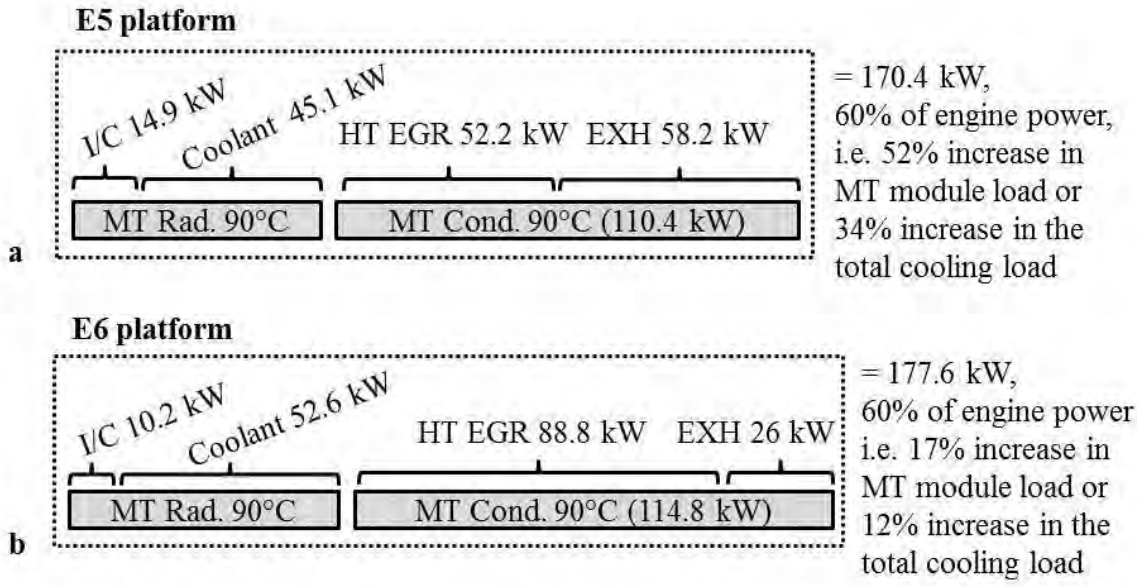

Figure 6.4 Modified cooling capacity at the medium-temperature radiator level for (a) EGR focused engine (b) EGR only engine, used in the simulations

Such a design compromise will limit the maximum FBC power, but is required for successful process integration. Therefore, heat addition of around 30 and 60 kW at C100 were assumed to be the limit which defined the dimensions/capacity of the modified engine cooling modules. This represented a 12% and 34% increases in the engine cooling module capacity compared to the base modules. This additional cooling capacity also meant that up to 75% engine load, the exhaust stream cooling was possible down to 110°C. When considering combined HT EGR and EXH process integrations, Fig. 6.4 shows the

use of the independent medium-temperature condenser (T_{cond} = 90°C) for the FBC at the medium-temperature radiator level.

To assess the impact of EXH heat recovery on the engine and the cooling module, so that the interactions between the two interconnected processes could be analysed, a new term beta (β) was defined.

Where, $\beta = \dot{W}_{net} / \dot{Q}_{EXH}$ …(6.1)

A value of β then provides an assessment and sensitivity of EXH heat recovery on the net power for different heat recovery architectures and with different working fluids. A high β value will represent more favourable process integration, as it will demonstrate efficient and/or low quantity and/or high quality EXH heat recovery. A high β value does not necessarily correspond to lower EXH irreversibilities, but allows identifying more successful process integration from a systems approach.

Furthermore, since high quantity EXH heat recovery also results in greater engine backpressure and increased fan power requirement, a higher β value will also correspond to a lower performance loss of the base engine platform ($\dot{W}_{BP+fan}$). For the maximum EXH cooling at C100 for the E5 engine platform (given in Table 6.1) with an exhaust heat exchanger inducing 0.1 bar backpressure, the performance loss was ≈ 4 kW (Section 3.7.1). For other speed/load points, the performance loss was within ±10% of the correlation below:

$\dot{W}_{BP+fan} = 0.005 \dot{Q}_{EXH}^{1.46}$ …(6.2)

Hence, equation 6.2 was used to estimate the performance loss due to the combined backpressure and increased fan power depending on the duty of the EXH heat exchanger.

6.3 Justification for the use of cruise and full load conditions

Evaluating particular process integration with various heat qualities, different heat quantities and high heat variability is one of the most important steps in predicting the overall system power, level of process integration adaptability/sensitivity, control of the process parameters and estimating the system size. This aspect, which is relatively less crucial for stationary FBC applications, is now becoming more important with the HDDE automotive sector expanding into new WHR markets.

Extensive steady state simulations were carried out at B50 and C100 for the two engine platforms to select suitable process integrations. Over the E5 and E6 engines, CAC, EGR

and EXH showed a high quality and quantity variation of 53, 109, 30°C and 37, 63, 56 kW, respectively (Table 6.1). A further important parameter was the high variation in the percentage of available heat quantity in relation to the engine power since the AFR and EGR fraction varied between 22.1-28.1 and 25-42%, respectively (Table 3.2). As such, the E5-B50 and E6-C100 points represented two contrasting ends for heat quality, quantity and variability. Hence, conclusions also on process integrations suited to either high or low: EGR rates, heat qualities, heat quantities, engine loads etc. could be drawn. For each process integration, relevant parametric studies were conducted to optimise the system power and investigate variations in the process parameters. The process integrations were compared at a high integration level using the boundary conditions and equipment performance assumptions detailed in Table 6.2.

Table 6.2 Boundary conditions (left) and performance assumptions (right) used in simulations

▪ T_{post}, HT EGR ≥ 120°C ▪ T_{post}, EXH ≥ 110°C ▪ T_{post}, LT EGR ≥ 95°C ▪ T_{post}, CAC ≥ 85°C ▪ T_{max}, organic fluid ≤ 250°C and T_{crit} ▪ P_{max}, working fluid ≤ 50 bar ▪ T_{cond}, working fluid = 90°C (MT) ▪ T_{cond}, working fluid = 65°C (LT) ▪ PR_{max}, expansion ≤ 16:1 (single stage) ▪ PR_{max}, expansion ≤ 8:1 (each two stage) ▪ P_{max}, two-phase water expansion ≤ 30 bar ▪ VFR, liquid E152a expansion ≤ 16:1	▪ T_{pp}, EGR (HT and LT) = 30°C ▪ T_{pp}, EXH and CAC = 20°C ▪ T_{pp}, IHE = 20°C ▪ T_{pp}, cascade cond = 15°C ▪ ΔP_{max}, gas side = 0.1 bar/HEX ▪ ΔP, fluid side (HEX) = 0.5 bar/HEX ▪ ΔP, flow distribution valve = 0.5 bar ▪ ΔP, fluid side (cond.) = 0.2 bar/cond. ▪ ΔP, each side (IHE) = 0.2 bar ▪ Ambient air temp. = 20°C ▪ Air temp. rise through cond. = 15°C ▪ η_{exp} = 70% ▪ η_{pump} = 60% ▪ η_{trans} = 93%

6.4 Theme 1 - High temperature heat recovery with single stage expansion

As heat sources, the combination of exhaust flow downstream of the after-treatment devices and EGR were most promising due to their relatively higher energy and exergy contributions (Fig. 3.13). Theme 1 discusses process integrations coupling these two heat sources (Fig. 6.5). For each theme, relevant process integrations reviewed or conceptually similar to those in Chapter 2 were firstly evaluated. These also provided a baseline for comparison with the proposed process integrations in this thesis.

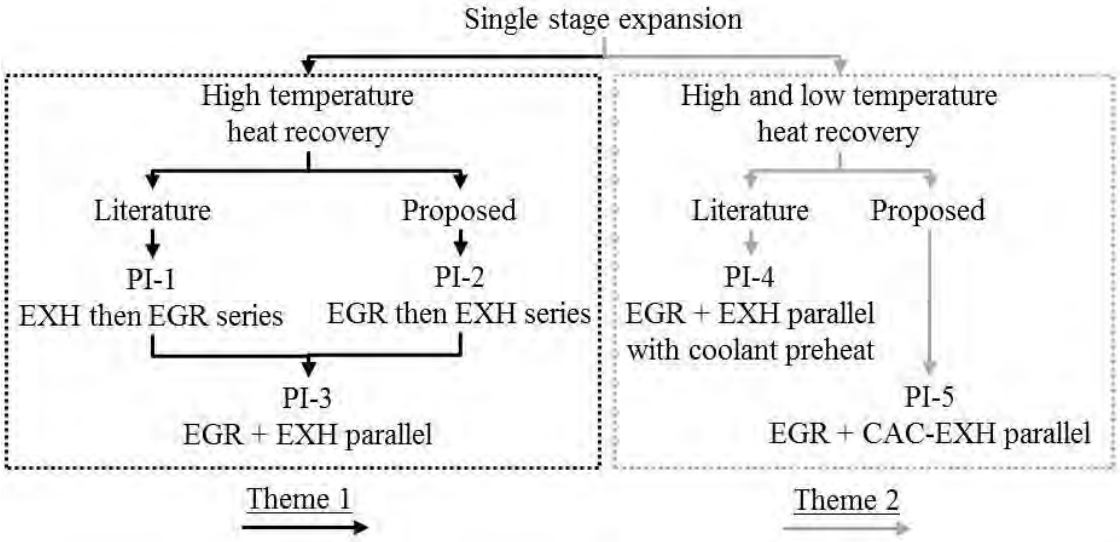

Figure 6.5 Two themes of approach using single stage expansion

6.4.1 Process integration 1: EXH then EGR series (baseline)

6.4.1.1 System architecture, cycle operation and process optimisation

Heat recovery in series, firstly from the EXH and then from the EGR in a counter-current flow was widely reported in the literature using water and R245fa (Katsanos et al., 2010, Edwards et al., 2010). Hence, Process Integration 1 (PI-1) as shown in Fig. 6.6a, termed 'EXH then EGR series' based on its heat recovery architecture was simulated in order to act as a reference for theme 1. It was assumed that each heat recovery element introduced a 0.5 bar fixed working fluid pressure drop (Table 6.2). Common bypass loops and the associated valves for EXH and expansion machine (as shown in Fig. 4.8) amongst all the process integrations were excluded for simplicity.

The T-S diagram for optimal cycle operation with water and R245fa at E5-B50 are given in Fig. 6.6b and c, respectively. The subcritical cycle operating mode used was limited superheat expansion. Complete preheating by all the three fluids was covered using the EXH heat. For relatively higher critical temperature and larger latent heat fluids (i.e. water vs. R245fa), the EXH stream also provided partial evaporation (Pt. 1, Fig. 6.6b vs. c). Complete evaporation for R245fa (Pt. 2, Fig. 6.6c) and further superheating in the case of water (Pt. 2, Fig. 6.6b) was covered by the HT EGR stream. The EXH was modelled with a pinch point of 20°C, hence the exhaust stream cooling was possible to 110°C (Table 6.2). Whereas the HT EGR was modelled with a pinch point of 30°C (Table 6.2), with the pinch point occurring during evaporation (Pt. 1), the EGR stream exiting the HT EGR was always 30°C higher than the working fluid evaporation temperature. For all fluids, the maximum cycle pressure and the corresponding evaporation temperature limited the HT EGR heat recovery.

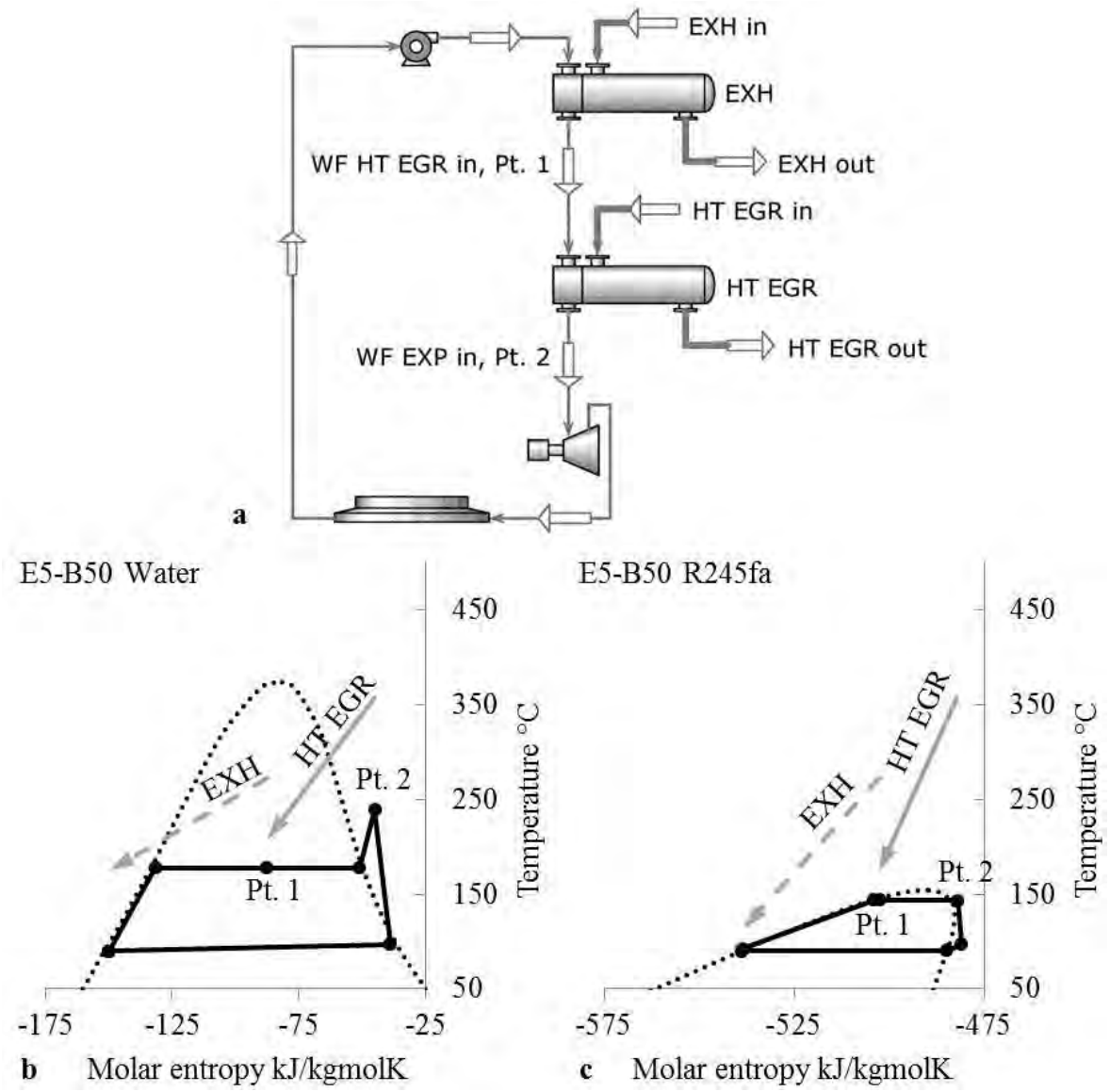

Figure 6.6 EXH then EGR series (a) system architecture (b) T-S diagram using water (c) T-S diagram using R245fa

Fig. 6.7a and b shows the change in heat recovery loads and thermal efficiency for PI-1 with varying maximum cycle pressure for water and R245fa at E5-B50, respectively. Compared to water, R245fa recovered nearly constant and maximum heat from the EXH with increasing cycle pressure. Furthermore, HT EGR heat recovery also showed less variation. Nonetheless, due to the much lower thermal efficiency, R245fa on average produced net power around 40% lower and was only reconsidered in process integrations with low temperature heat recovery. Fig. 6.7c and d also shows the β value with varying cycle pressure. Water was favoured as it offered higher β value and rate of improvement compared to R245fa.

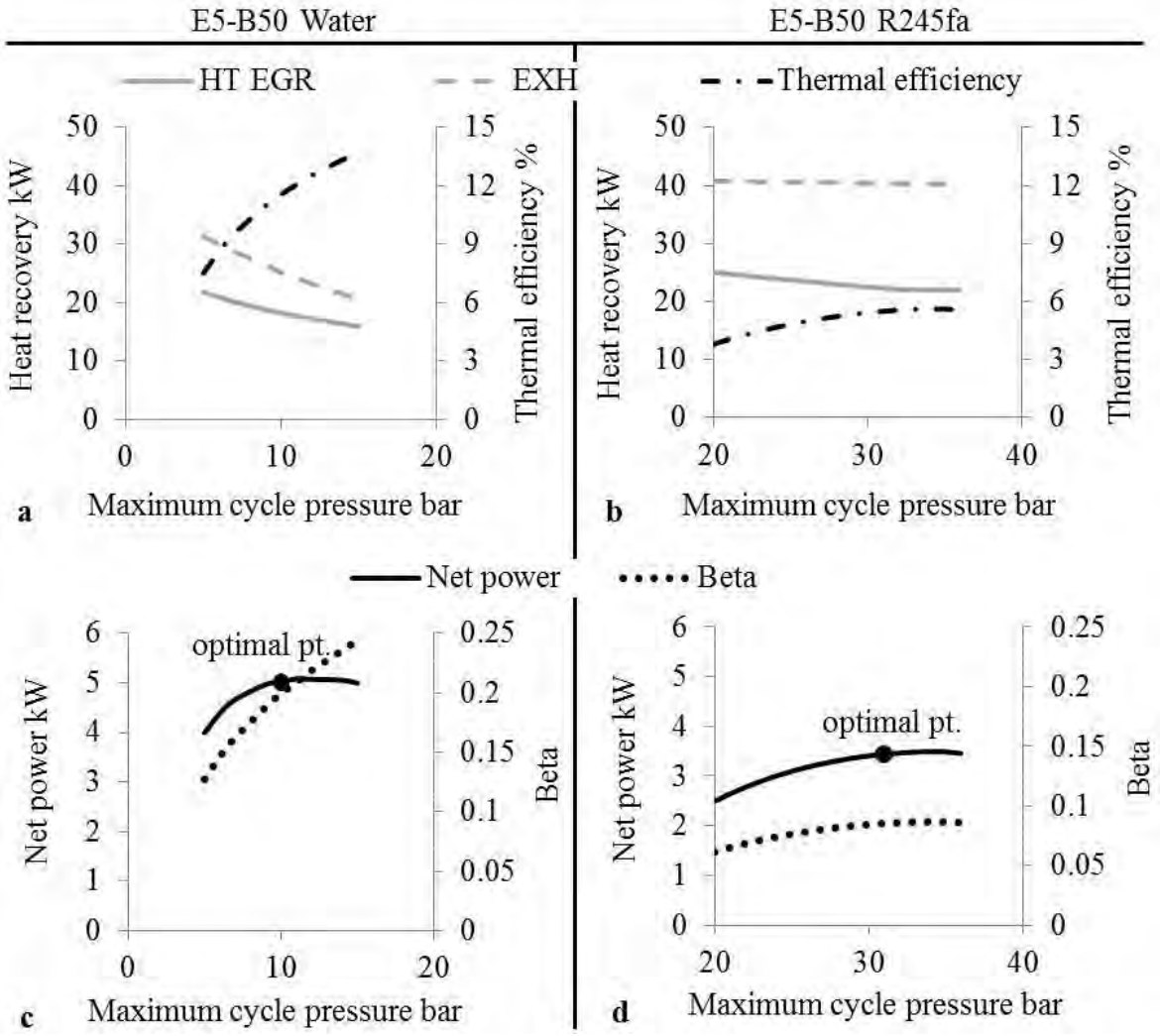

Figure 6.7 PI-1 maximum cycle pressure effect on (a,b) heat recovery and thermal efficiency (c,d) net power and beta value, for water (left side) and R245fa (right side) at E5-B50

6.4.1.2 Results and discussion

Appendix 6.1 details the optimal PI-1 results using water, ethanol and R245fa at the 4 test points. The maximum cycle pressure was limited to a maximum expansion pressure ratio of 16:1 for all process integrations with single stage expansion (Table 6.2). This resulted in a possible maximum cycle pressure of 15.4 bar for water and 30.6 bar for ethanol. PI-1 using ethanol provided the highest net power. However, due to almost complete EXH heat recovery (given in Table 6.1) by ethanol, compared to an average of 65% by water, the exhaust backpressure and increased fan power requirement were 1 kW higher. As backpressure and fan power has to be taken into consideration in a systems approach, it has to be size constrained and stay efficient. As a result, the system power, which included such effects, was nearly equal for ethanol and water. The system power also included a 93% efficiency for the pump and expander transmissions, on top of the 60% pumping and 70% expansion isentropic efficiencies (Table 6.2). Hence, PI-1 was better suited to water

since it provided nearly equal system power to ethanol with higher β and lower UA/W values. Furthermore, PI-1 also offered high temperatures for superheating of high wetting fluids.

The drawback of PI-1 using water was that, on average it also recovered only 65% of the HT EGR stream heat (given in Table 6.1). This resulted in the HT EGR exit temperatures of 208-228°C and in turn increased the load on the LT EGR (and the cooling load on the low-temperature radiator). Process integrations that provide less than 90% cooling for the EGR may require additional cooling elements rather than a possible rebalancing of the engine cooling module, and were termed as 'insufficient EGR cooling PIs'. PI-1 was also better suited to lower EGR rate engines (E5 vs. E6) since at C100 for the E5 engine the increased load on the engine cooling module was 15 kW lower than the maximum defined in Fig. 6.4a. Conversely, for the E6 engine this was around 15 kW higher. At conditions where heat rejection by the engine cooling module is not possible, a partial EXH flow bypass needs to be provided.

6.4.2 Process integration 2: EGR then EXH series

6.4.2.1 Problem definition, system architecture, cycle operation and process optimisation

PI-1 was shown to be better suited when using water for lower EGR rate engines (E5 vs. E6), however, this also resulted in insufficient EGR cooling. Since EGR is a high quality heat source and a load on the engine cooling module, it must be exploited further to obtain maximum process integration benefits. For EGR and EXH heat recovery with the least negative impact on the engine cooling module for both E5 and E6 platforms, the heat recovery architecture as shown in Fig. 6.8a is proposed. The only difference in PI-2 over PI-1 was the change in the order of series heat recovery to HT EGR followed by EXH.

As the EXH stream was typically 100°C cooler than the EGR stream, PI-2 reduced the achievable maximum superheating temperature compared to PI-1. Hence, water was excluded from the analysis in PI-2. However, for organic fluids, including methanol, which is the wettest fluid and has the largest latent heat, the EXH temperatures were sufficient to provide the desired superheating for the limited superheat expansion. Fig. 6.8b shows the T-S diagram for optimal cycle operation at E6-B50 using methanol, where HT EGR was used for preheating and partial evaporation (Pt. 1), and EXH was used for complete evaporation and superheating (Pt. 2).

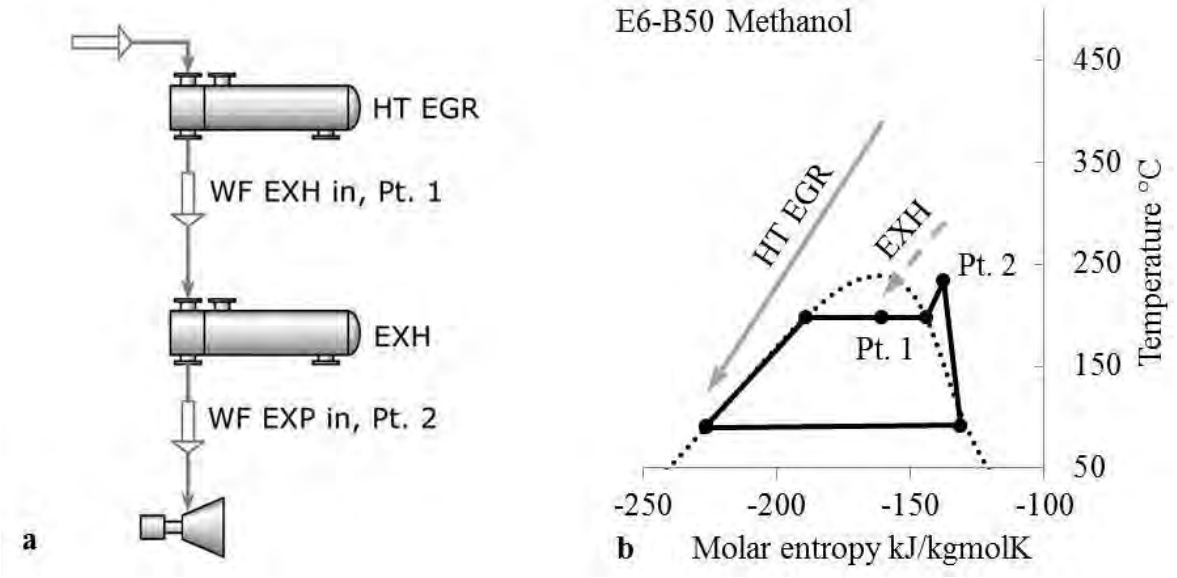

Figure 6.8 EGR then EXH series (a) heat recovery architecture (b) T-S diagram using methanol

Fig. 6.9a shows the change in heat recovery loads and thermal efficiency for PI-2 with varying maximum cycle pressure for methanol at E6-B50. With increasing pressure, the HT EGR heat recovery remained nearly constant and maximum, while EXH heat recovery decreased. The rate of improvement in the thermal efficiency was sufficient to counteract the reducing EXH heat recovery, and hence, the net power continuously improved (Fig. 6.9b). The maximum cycle pressure was limited to 42 bar since this corresponded to the boundary condition defined in Table 6.2, i.e. the maximum working fluid temperature to be lower than the critical temperature after limited superheat.

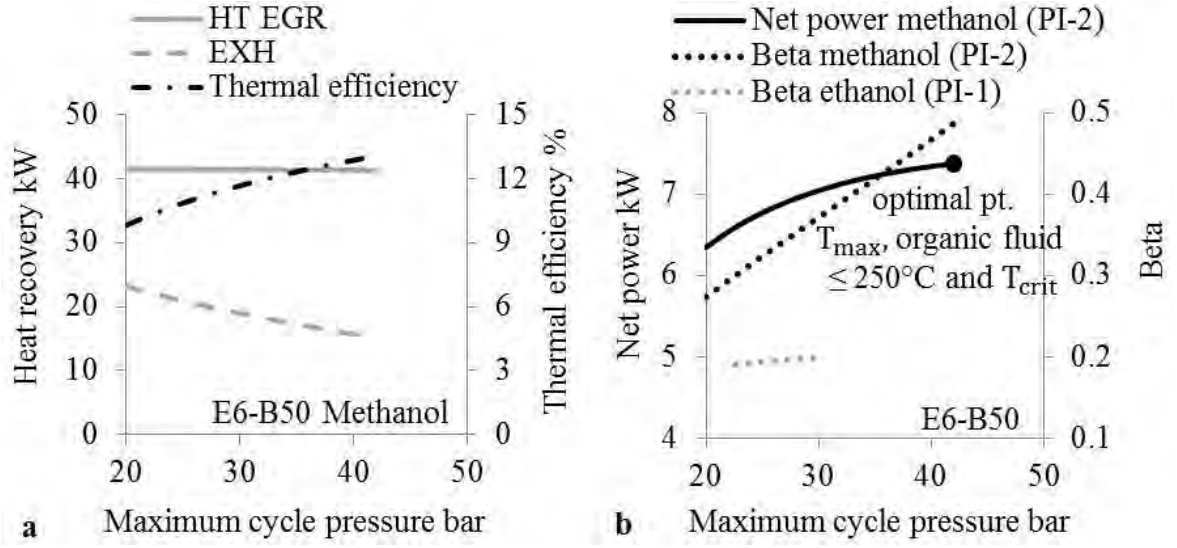

Figure 6.9 PI-2 maximum cycle pressure effect on (a) heat recovery and thermal efficiency (b) net power and beta value, for methanol at E6-B50

6.4.2.2 Results and discussion

Appendix 6.2 details the optimal PI-2 results using ethanol and the 5 alternative high temperature organic fluids at the 4 test points. For all the organic fluids, the system power and UA/W values of PI-2 were within ±10%. Nonetheless, the advantage of the alternative fluids for equal net power over ethanol (e.g. 6.1 kW, E6-B50) was either in the lower pressure ratios (ethanol vs. R30, 14.6:1 vs. 7.5:1), or in higher thermal efficiencies and hence higher values of β (ethanol vs. methanol, 0.43 vs. 0.49).

For a relatively higher boiling point fluid (e.g. ethanol), PI-2 optimised at slightly lower pressures than PI-1. Hence, PI-2 resulted in a marginally lower average thermal efficiency (11.5 vs. 12%). Nonetheless, PI-2 using the alternative organic fluids was an improvement over PI-1 using water. This was due to equivalent system power (Fig. 6.10), despite lower EXH heat recovery (40 vs. 65% of the available load), resulting in simplification of the process integration, smaller EXH heat exchanger and lower impact on the engine/cooling module. As a result, the high β values, which showed an average improvement of 1/3rd from PI-1, provided a new measure for comparison (Fig. 6.10).

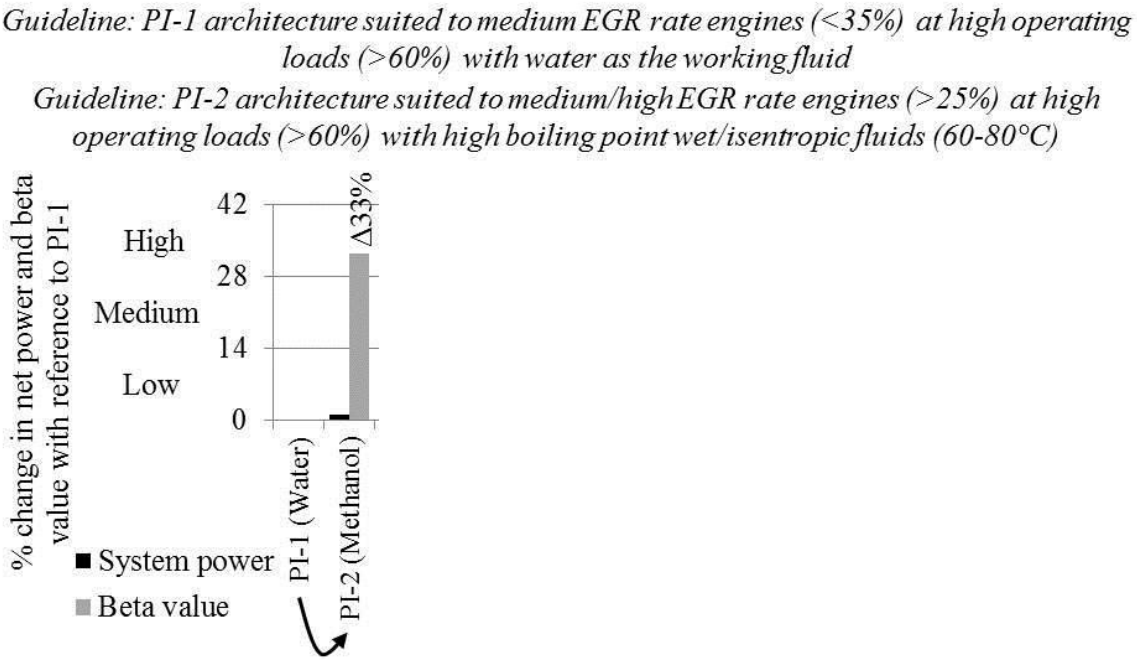

Figure 6.10 PI-2 guideline and system power/beta value change over PI-1

Furthermore, for similar class of fluid (i.e. alcohols), Fig. 6.9b also shows the sensitivity of β value for ethanol from PI-1 at E6-B50. The high β value for PI-2 and its superior rate of improvement (principally due to the changed heat recovery architecture) was evident over alcohols in PI-1. The advantage of this efficient high temperature EXH heat recovery was that, the increased cooling load at E6-C100 was within the upper limit defined in Fig. 6.4b.

6.4.3 Process integration 3: EGR + EXH parallel

6.4.3.1 Problem definition, system architecture, cycle operation and process optimisation

The advantages of PI-2 over PI-1 resulted in its suitability for both E5 and E6 engine platforms. However, PI-2 also comes with its deficiencies. Firstly, for engines with reduced EGR rates (e.g. SCR focused platform, E4) higher EXH heat recovery needs to be targeted for higher system power. If EGR is used for partial preheating in an E4 platform, the optimal cycle pressures will result in larger irreversibilities in the EGR heat exchanger. Secondly, despite the fact that the lower EXH heat recovery at E6-C100 and E5-C100 was advantageous in reducing the size of the medium-temperature condenser, PI-2 also resulted in the underutilisation of the available cooling capacity at E6-B50 and E5-B50 points. Hence, PI-2 was more suited to higher EGR rate engines (i.e. E5 and E6) usually operated at relatively high loads (>60%).

To address the possibility of higher EXH heat recovery at cruise loads and complete HT EGR heat recovery over a drive cycle, PI-3 as shown in Fig. 6.11a is proposed. Such integrations have also recently been proposed by other authors (Latz et al., 2013, Seher et al., 2012, Edwards et al., 2012, Tai et al., 2010, 2009), however, conclusions on PI-3 being a suitable integration for high temperature heat recovery for HDDEs was independently reached in this work (refer Appendix 1.1, publication 4). PI-3 involved simultaneous heat recovery from both HT EGR and EXH at one level of increased complexity compared to PI-2. The pressurised working fluid (Pt. 1, Fig. 6.11a) was conveyed through a 3-way flow distribution valve into the two heat exchangers. Since the distributed working fluid streams were preheated, evaporated and superheated in the two parallel arranged heat exchangers, PI-3 was termed ‘EGR + EXH parallel’. The flow distribution valves were modelled with a fixed 0.5 bar pressure drop for control (Table 6.2). Thermo-physically the only difference among the product streams was the flow rate (flow ratio) which in turn was established by the heat loads of the two heat exchangers and the desired working fluid temperatures exiting the heat exchangers. Working fluid exiting the HT EGR (Pt. 2) and EXH (Pt. 3) were then mixed to form the single outlet stream (Pt. 4).

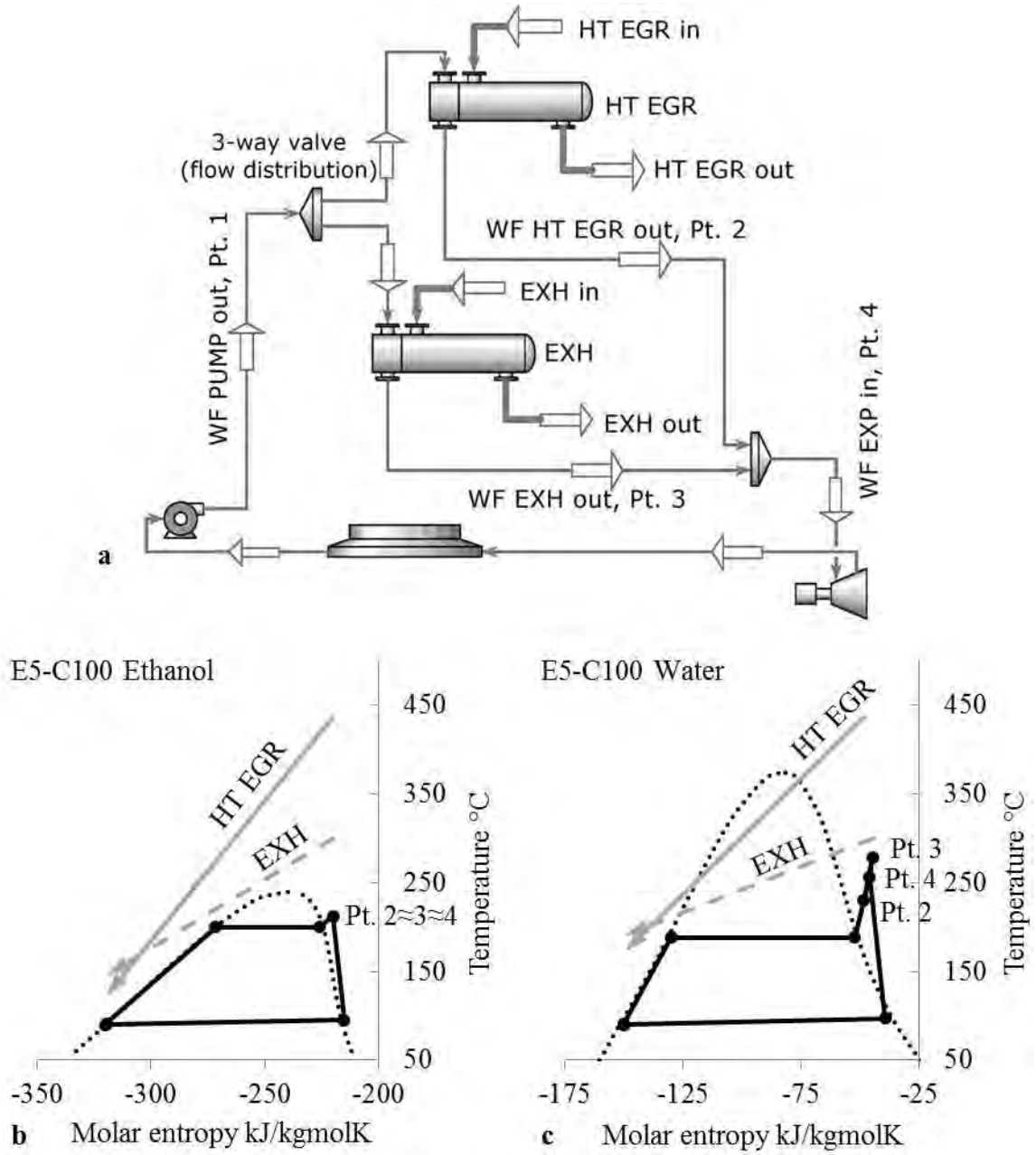

Figure 6.11 EGR + EXH parallel (a) system architecture (b) T-S diagram using ethanol (c) T-S diagram using water

Fig. 6.11b and c shows the T-S diagram for optimal cycle operation with ethanol and water at E5-C100, respectively. As water is the wettest known fluid, the control strategy to reduce moisture at the expansion exit was different from that of organic fluids. When using ethanol, a slight superheating in the two heat exchangers was sufficient to reduce moisture. Hence, the working fluid profiles overlapped for the HT EGR and EXH (i.e. Pt. 2≈3≈4, Fig. 6.11b). However, for water, maximum superheating took place in the EXH (limited by the pinch point occurring at Pt. 3) and the residual superheating was imposed in the HT EGR (Pt. 2). As such, sufficient superheat was generated while marginally higher EGR cooling and β value, compared to residual superheating being imposed in the EXH. The stream temperatures exiting the HT EGR and EXH varied up to 50°C. These two streams

mixed to form a superheated vapour at Pt. 4 (256°C, Fig. 6.11c) before entering the expansion stage.

Fig. 6.12a shows the change in heat recovery loads and thermal efficiency for PI-3 with varying maximum cycle pressure for ethanol at E5-C100. In PI-2 and PI-3, heat recovery from HT EGR was relatively constant and maximum (cooling the EGR stream to 120°C) with increasing cycle pressures for all organic fluids within the defined boundary condition of maximum cycle pressure of 50 bar (Table 6.2). These two process integrations can then provide complete HT EGR cooling by replacement of the standard HT EGR cooler to a high pressure (25-50 bar depending on the working fluid) HT EGR heat exchanger. In case of ethanol, the optimal cycle pressure was limited due to the 16:1 expansion pressure ratio for 3 out of the 4 test points (Fig. 6.12b), resulting in relatively lower β values.

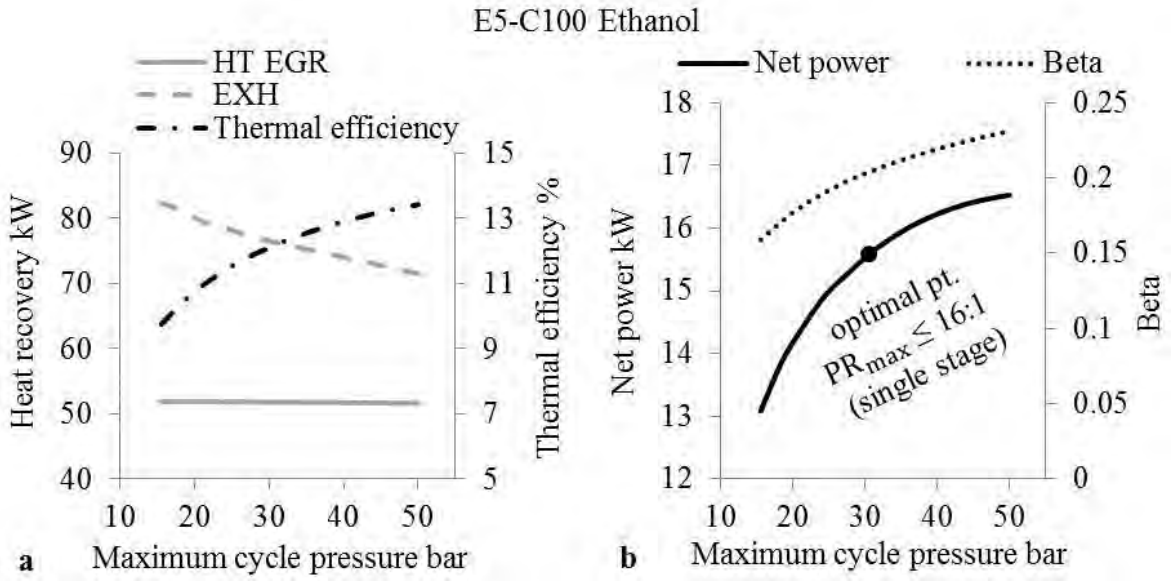

Figure 6.12 PI-3 maximum cycle pressure effect on (a) heat recovery and thermal efficiency (b) net power and beta value, for ethanol at E5-C100

6.4.3.2 Results and discussion

Appendix 6.3 presents the optimal PI-3 results for water, ethanol and the 5 alternative organic fluids at the 4 test points. The average optimal cycle pressures were lowest for water (13 bar), followed by ethyl iodide and acetonitrile (20 bar), then by ethanol (30 bar), and highest for acetone, R30 and methanol (40 bar). When comparing maximum cycle pressures, PI-3 optimised at an average of 5 bar higher pressures than PI-2. Owing to the higher pressure differential, R30 that showed the lowest VFR/W value was best suited. As a consequence of the increased evaporation temperature of organic fluids, PI-3 showed thermal efficiencies higher by 1% point over PI-2. The thermal efficiencies were attractive

at around 11-14%, despite the maximum organic working fluid temperatures being relatively low between 185-240°C.

Despite the 16:1 limitation for ethanol (Fig. 6.12b), the net heat input in PI-3 on average was 20% higher than PI-2, hence the average system power was also around 20% higher for ethanol as well as the other organic fluids (e.g. R30, Fig. 6.13). When water and organic fluids were compared in PI-3, water delivered on average 15% lower system power due to a lower heat recovery for similar thermal efficiency.

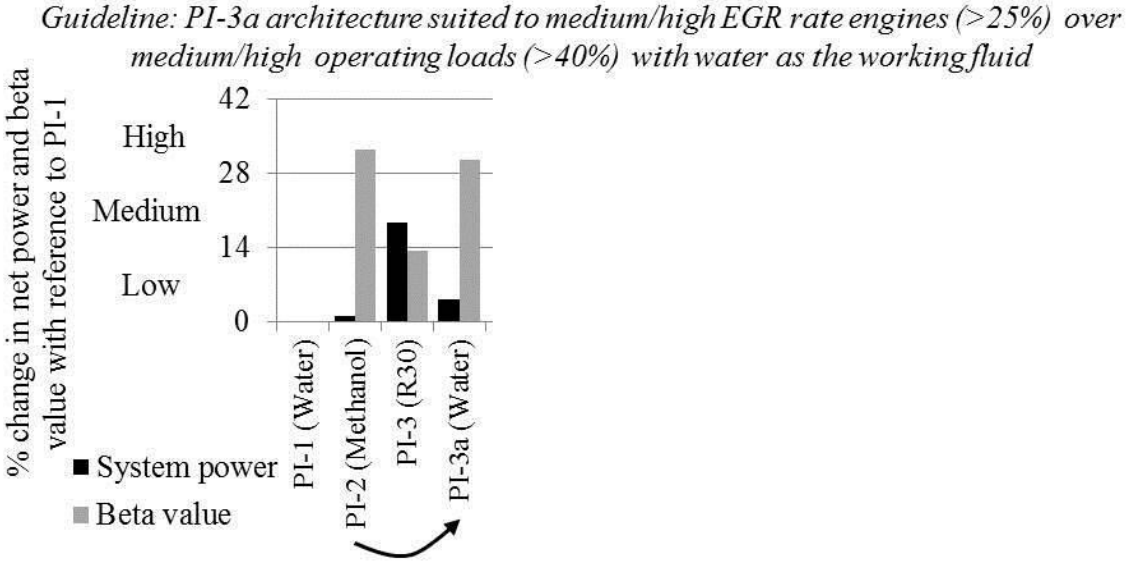

Figure 6.13 PI-3 guideline and system power/beta value change over PI-2

6.4.3.3 High load challenges and solutions

Compared to PI-1 and PI-2, PI-3 offered higher system power and showed the best potential at cruise loads. However at E6-C100, the increased load on the engine cooling module not only by ethanol but also by methanol, R30 and acetone were around twice the limit defined in Fig. 6.4b. The literature approach for this was to provide an EXH flow distribution or bypass loop to limit heat recovery, and avoid backpressures when the heat recovery system was not running. With such a system, the same EXH quality but lower quantity heat was delivered to the process integration. An alternative to this approach for E6 platform, which can also reduce the EXH quantity but retain higher quality, is proposed with the modified heat recovery loop given in Fig. 6.14.

During cruise loads, the process integration behaves as PI-3, i.e. 'EGR + EXH parallel' where the available cooling capacity in the medium-temperature condenser is utilised by recovering higher percentage of EXH heat. While at high loads, the process integration

operates as PI-2, i.e. 'EGR then EXH series' where high quality and low percentage of EXH heat is recovered. The thick dash line in Fig. 6.14 shows the working fluid flow loop operation under PI-2 mode. The integration was termed 'EGR and EXH (series+parallel)', based on the ability to operate either in series or in parallel mode. When considering the change in hardware (excluding piping), Fig. 6.14 only requires the addition of one simple 3-way flow diverting valve over PI-3. In this manner, lower average backpressure losses and high overall system power can be achieved over a drive cycle with the addition of only ≈10% increase in the total engine cooling module capacity for the E6 platform.

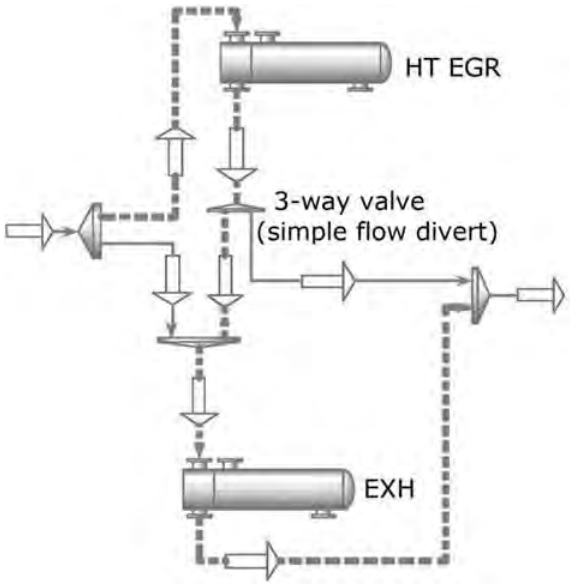

Figure 6.14 EGR and EXH (series+parallel) heat recovery loop as exhaust heat limitation and high power generation strategy

6.4.4 Process integration 3a: High latent heat solution

6.4.4.1 Problem definition, system architecture and cycle operation

When comparing water in PI-3 and PI-1, the two process integrations gave nearly equal system power. However, due to the changed heat recovery architecture and the control strategy mentioned (Fig. 6.11c), PI-3 showed higher HT EGR heat recovery (80 vs. 65% of available load) and lower EXH heat recovery (55 vs. 65% of available load). As a result, water was better suited to PI-3. Nevertheless, the EGR heat recovery was still sub-optimal compared to the desired 90% heat recovery limit.

PI-3a (Fig. 6.15a) combined with its specific control operation (Fig. 6.15b) is proposed as a solution to address the underutilisation of EGR heat when water is the working fluid using conventional expansion machines. The pressurised water firstly recovered heat from the LT EGR, which was modelled using a pinch point of 30°C (Table 6.2). The high pressure

preheated water exiting the LT EGR (Pt. 1) was then divided into two streams to recover heat from the HT EGR and EXH heat exchanger in a parallel thermal architecture. The same flow distribution strategy mentioned in Fig. 6.11c was used to dictate the superheat at Pt. 4.

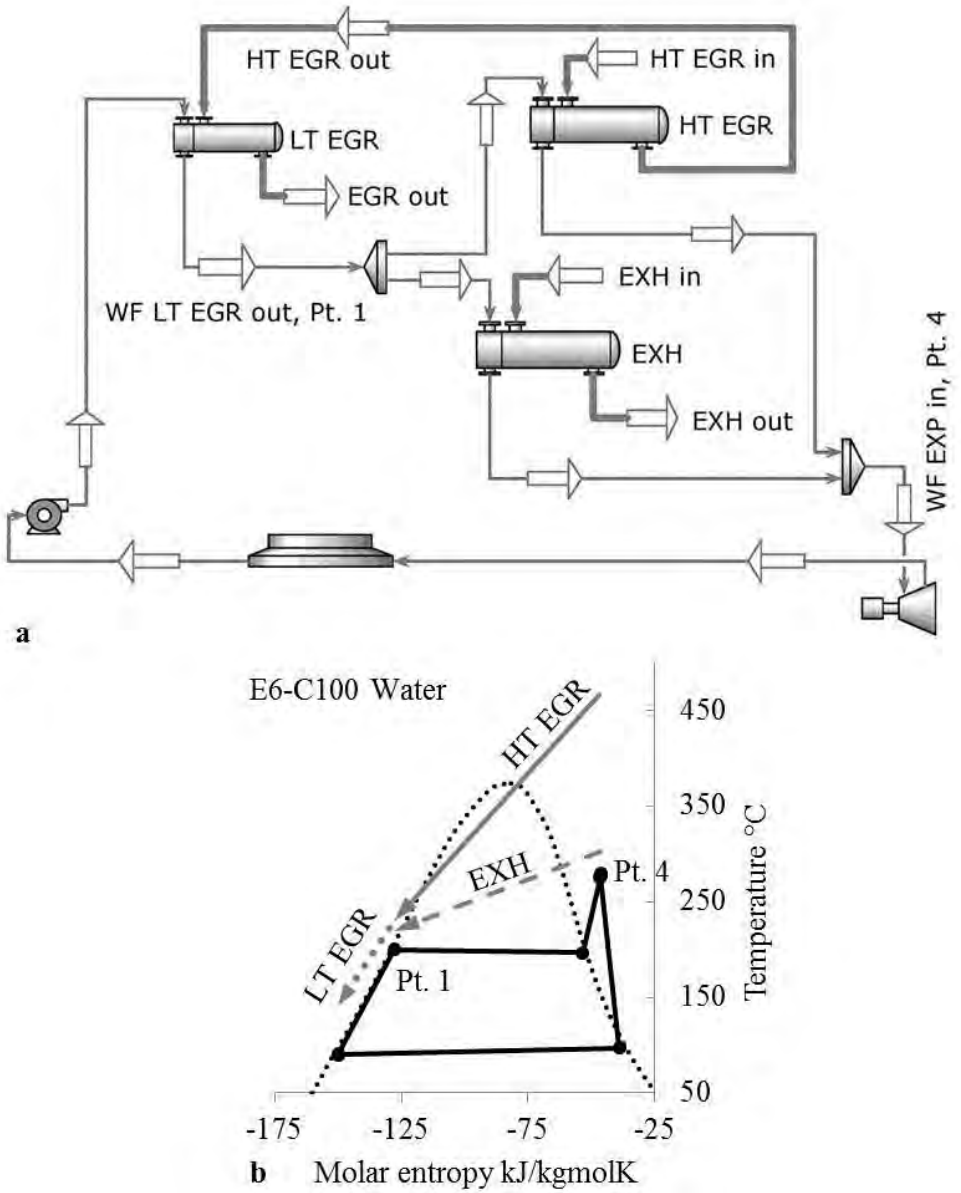

Figure 6.15 High latent heat solution (a) system architecture (b) T-S diagram using water

6.4.4.2 Results and discussion

Fig. 6.16 highlights the change in heat recovery loads and net power for PI-1, PI-3 and PI-3a using water at E6-C100. As can be seen, the EGR heat recovery increased, while EXH heat recovery decreased from PI-1 to PI-3 and finally to PI-3a. By limiting Pt. 1 to a preheated state, and using exhaust heat for evaporation and superheating only, the EGR heat recovery increased in PI-3a. The constant slope of the EGR cooling curve (Fig. 6.11c) was in effect broken into two EGR cooling curves with varying slope, giving a superior temperature match in the LT EGR (Fig. 6.15b).

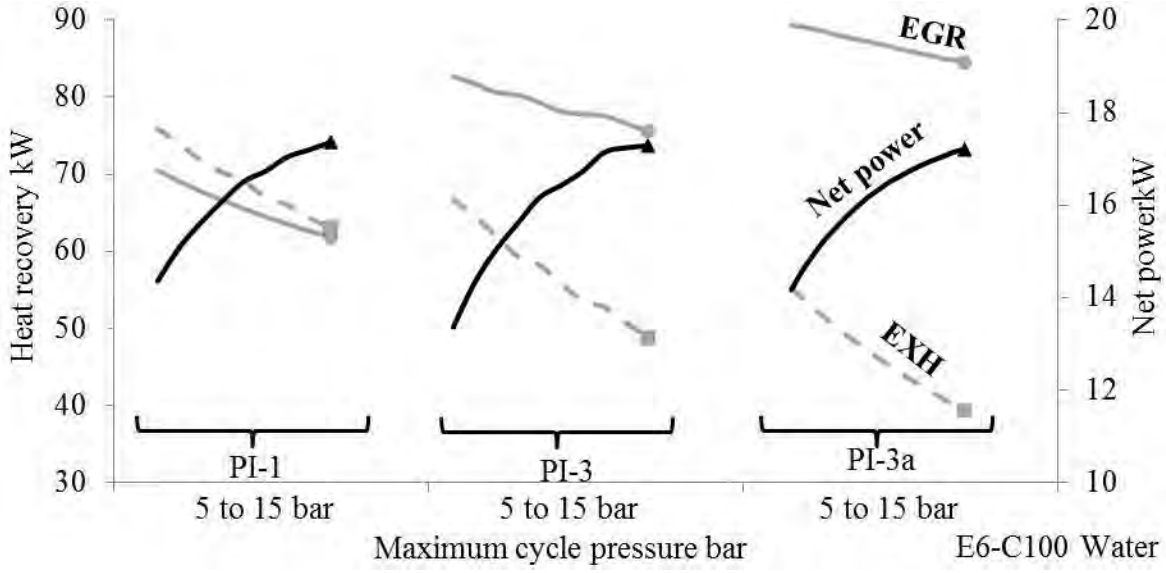

Figure 6.16 Comparison of heat recovery and net power for single-stage expansion process integrations using water with varying maximum cycle pressure at E6-C100

Appendix 6.4 details the optimal PI-3a results using water at the 4 test points. PI-3a also offered nearly equal system power to PI-1. This can also be noticed in Fig. 6.16, where all three process integrations demonstrated nearly equal net power. However, PI-3a attained this with highest HT EGR heat recovery (90% of available load) and lowest EXH heat recovery (45% of available load). As a result, the high β values were nearly equivalent to organics in PI-2 (Fig. 6.17). Hence, by taking advantage of the selected HDDE platforms and using unconventional heat recovery architecture, high levels of EGR cooling was provided even using water. Since the proposed process integration was effectively tailored to address the water's large latent heat drawback to cool EGR, it was termed as 'high latent heat solution'.

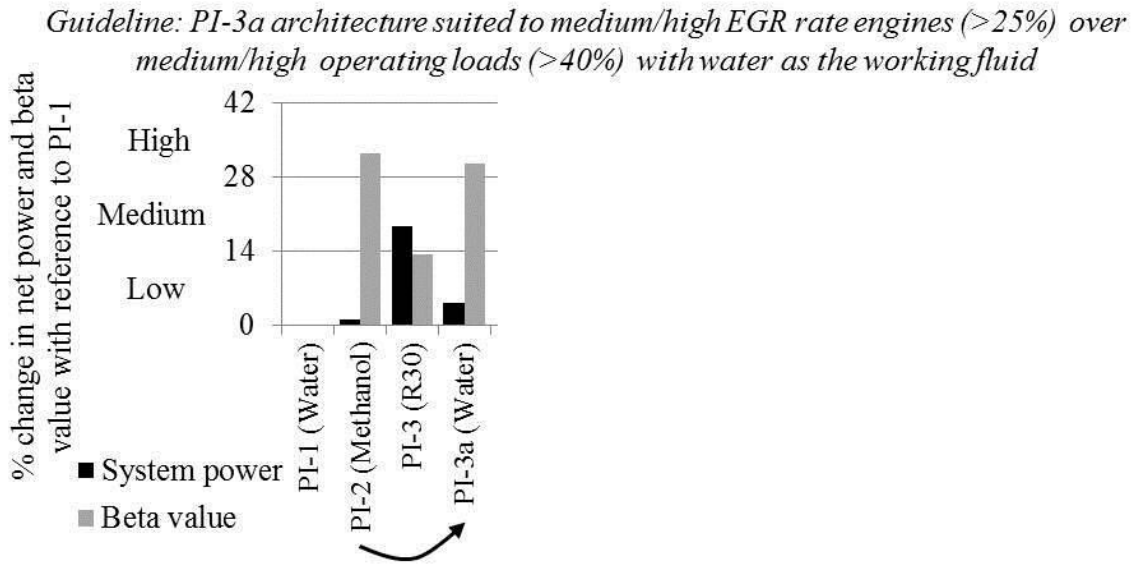

Figure 6.17 PI-3a guideline and system power/beta value change over PI-2

6.4.5 Summary: High temperature heat recovery with single expansion stage

For theme 1, PI-1 resulted in an 'insufficient HT EGR cooling PI', a disadvantage especially for higher EGR rate engines, whereas, at mid-speed mid-load, PI-2 resulted in the underutilisation of the available cooling capacity. As a result, PI-3 using the organic fluids, especially R30, provided a solution to these problems for engines with varying EGR rates.

As the two heat exchangers are in a parallel flow circuit in PI-3, they work effectively as one large heat source. Hence, with decreasing EGR rates from E6>E5>E4 the net system power will decrease and the results for the E4 platform will correspond closely to EXH heat recovery from an SCR only platform. In fact, due to the reduced heat quality and quantity of combined heat source from E6 to E5 platform, PI-3 coupled to E5 platform on average gave 25% lower system power. Therefore, the increased PI-3 system power for E6 compared to E5 platform narrowed the combined BSFC difference from Δ7g/kWh to Δ3g/kWh at cruise loads. Furthermore, Fig. 6.14 provided a possible exhaust heat recovery limitation strategy at high loads for high EGR rate engines.

When water was considered, PI-3a was favoured due to higher EGR cooling for equal system power to PI-1 and PI-3. Nonetheless, this system power was 15% lower than organic fluids in PI-3 (Fig. 6.17).

6.5 Theme 2 - High and low temperature heat recovery with single expansion stage

To date the automotive HDDE sector has predominantly focused on the utilisation of EGR and EXH heat, but less attention has been given to low temperature sources like engine coolant and CAC. This is primarily due to relatively lower thermal efficiencies, increased complexity and higher investment costs associated with conventional energy conversion approaches for low grade heat in transport applications. During the energy and exergy assessment of heat sources, it also became apparent that low temperature sources that were already a load on the engine cooling module should also be targeted. However, these low temperature sources will require innovative approaches in heat recovery and/or power generation. The following subsections detail process integrations which offer combined high and low temperature heat recovery (theme 2, Fig. 6.5), and address the peculiar considerations that arise with such integrations due to the irregularity of the process parameters (i.e. the required working fluid mass flow rate).

6.5.1 Process integration 4: EGR + EXH parallel with coolant preheat (baseline)

6.5.1.1 System architecture and cycle operation

The coolant exergy in the medium-temperature radiator was relatively low (Fig. 3.13) and recovering this heat to generate power would require a relatively large low-temperature condenser. A means to avoid the use of a large low-temperature condenser and retaining the higher quality heat was proposed in the literature by process integrations similar to Fig. 6.18a (Ringler et al., 2009, Endo et al., 2007). PI-4 replaced the engine coolant with the working fluid of the heat recovery system. The engine block heat was used for preheating or partial evaporation prior to the 'EGR + EXH parallel' thermal architecture. As such, PI-4 was termed 'EGR + EXH parallel with coolant preheat'.

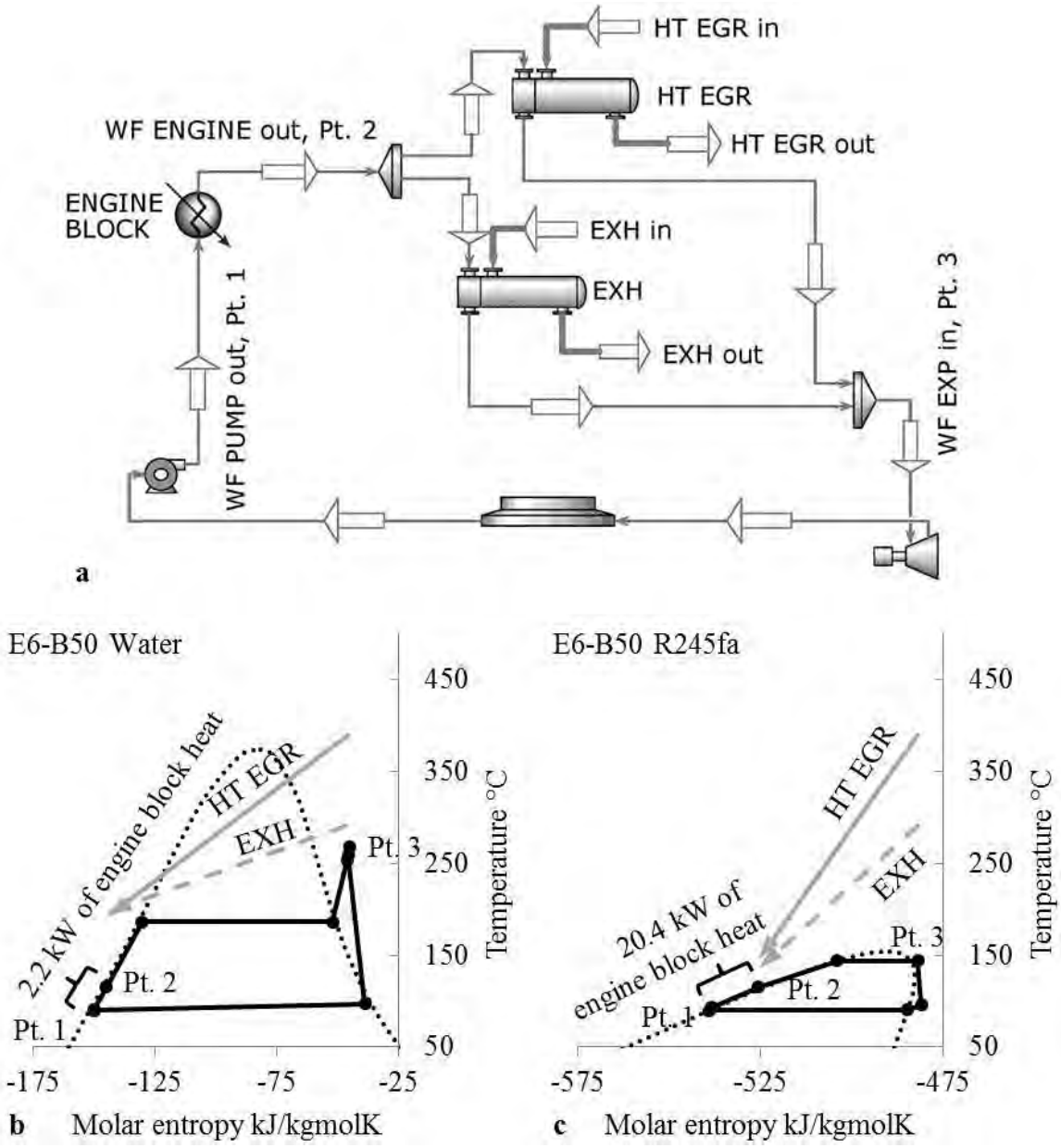

Figure 6.18 EGR + EXH parallel with coolant preheat (a) system architecture (b) T-S diagram using water (c) T-S diagram using R245fa

Fig. 6.18b and c shows the T-S diagram for the optimal cycle operation with water and R245fa at E6-B50. Engines are typically designed to operate within a coolant temperature range of 95-105°C. However, raising the coolant temperature level to a value of 115°C had demonstrated no negative effect on the engine efficiency (Ringler et al., 2009). Therefore, the highest working fluid temperature exiting the engine block (Pt. 2) was fixed at 115°C in order to increase the exergy content.

6.5.1.2 Results and discussion

Appendix 6.5 details the PI-4 results using water and ethanol at the 4 test points for performance comparison change over PI-3. Furthermore, to investigate the effects of lower boiling point and lower latent heat working fluid, results of R245fa in PI-4 were compared with the results of R245fa in PI-3 (given in Appendix 6.6). The optimal maximum cycle temperature, maximum pressure and thermal efficiency corresponding to a particular fluid were nearly equal (±2 bar, ±4°C, ±0.1% point) across both PI-4 and PI-3.

Despite raising the engine coolant temperature by 10°C, the exergy content of the 'engine block heat' and the 'EGR + EXH parallel' thermal architecture were significantly different. Because of this, the working fluid mass flow rate limitation occurred in PI-4, and as a result, underutilisation of the engine block heat was experienced (for further explanation, refer Appendix 6.5). PI-4 on average recovered around 10, 20, and 70% of the available engine block heat (given in Table 6.1) for preheating using water, ethanol and R245fa, respectively. That is to say, the engine block heat recovery increased with decreasing boiling point and latent heat among the working fluids.

In the case of R245fa, the average heat input increased by 15% over PI-3. Higher amounts of 'EGR + EXH parallel' heat recovery went into evaporation, increasing the average mass flow rate and system power by 15% and 35% over PI-3, respectively. Nevertheless, despite the increased heat input in PI-4 for R245fa, due to a much lower thermal efficiency, the average system power was still almost half of ethanol in PI-3. In the case of water and ethanol, the heat recovery from the 'EGR + EXH parallel' thermal architecture reduced approximately by equal amounts to the heat gained from the engine block. Since, the net heat input into PI-4 was nearly equal to PI-3, the working fluid mass flow rate and system power did not change noticeably. Hence, even the highest PI-4 system power fluid i.e. ethanol, was considered inferior over PI-3, since it increased system complexity without any noticeable improvement in system power (Fig. 6.19).

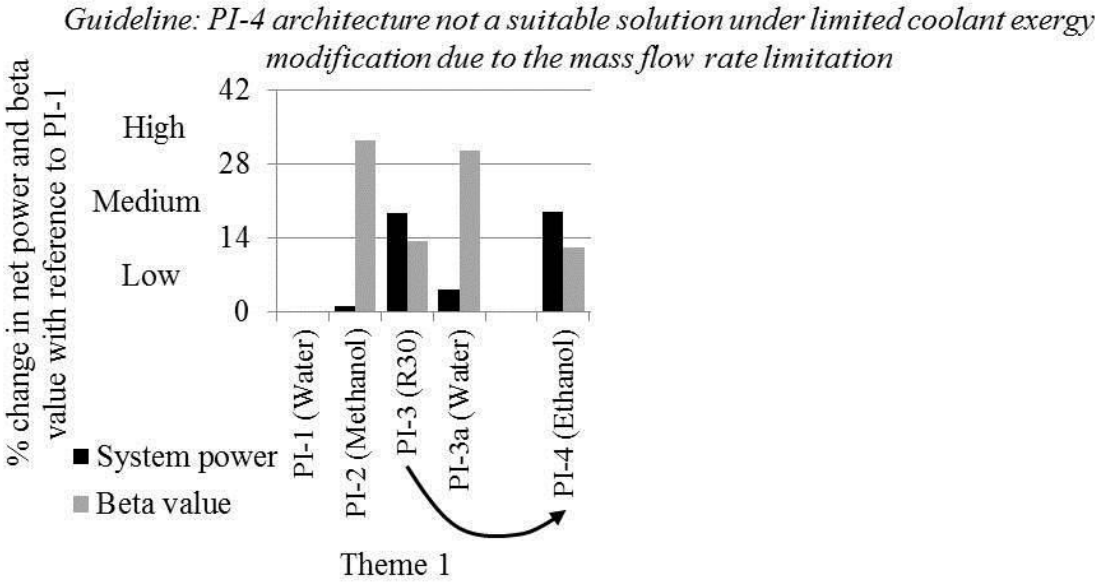

Figure 6.19 PI-4 guideline and system power/beta value change over PI-3

As process integrations with underutilisation of EGR heat were termed 'insufficient EGR cooling PI', similarly PI-4 resulted in an 'insufficient engine cooling PI'. Thus, the engine coolant system and radiator cannot be completely replaced, and the conventional engine cooling system is still needed. Note that, for process integrations with engine block heat recovery, the UA/W value excluded UA value considerations for the engine block. This is because the engine block surface area is fixed and independent of the heat recovery by the process integrations. As a result, the UA/W value for PI-4, especially with R245fa, improved over the value in PI-3.

6.5.2 Process integration 4a: Modified coolant exergy (baseline)

6.5.2.1 Problem definition and process optimisation

The reason for a negligible system power improvement in PI-4 with water and ethanol was due to the 115°C temperature constraint imposed on the maximum coolant temperature. A further process parameter modification to such process integrations, similar to what had also been proposed in the literature (Endo et al., 2007, Arias et al., 2006), is examined in this section. This being, raising the coolant exergy levels to complete engine block heat recovery. To determine this temperature level, a case study was performed using the three literature fluids at E6-B50.

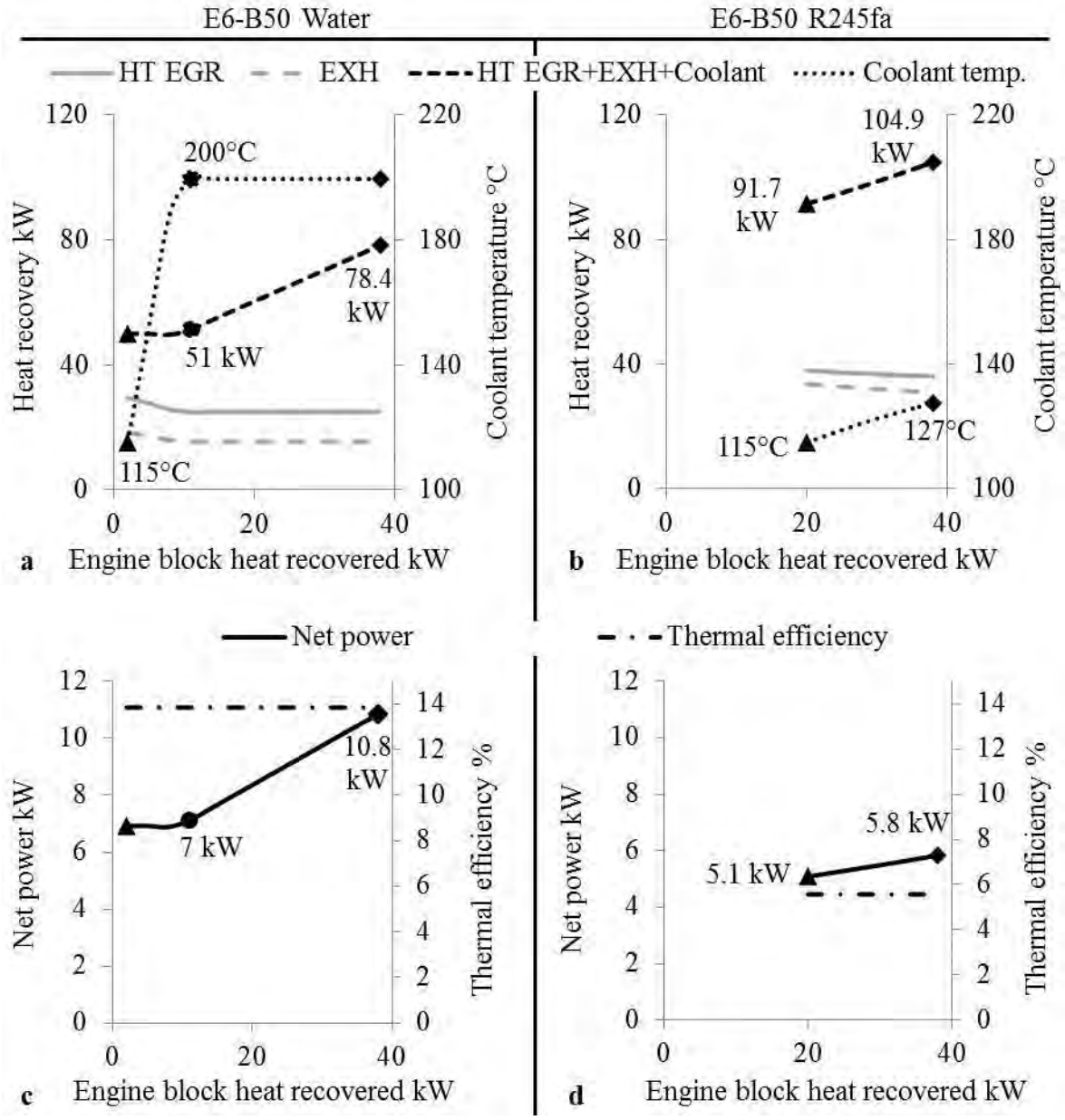

Figure 6.20 Effect of engine block heat recovery on (a,b) EGR, EXH heat recovery and coolant temperature (c,d) net power and thermal efficiency, using water (left side) and R245fa (right side) at E6-B50

For an optimal cycle pressure of 15.9 and 33 bar, Fig. 6.20a and b shows the variation in heat loads and coolant temperature with increasing engine block heat recovery for water and R245fa, respectively. Considering Fig. 6.20a, it was noticed that for the coolant temperature raised to 115°C, only 2.2 kW of engine block heat was recovered using water (also shown in Fig. 6.18b). Increasing this temperature to 200°C, which corresponded to the evaporation temperature of water at the selected pressure, 11 kW of heat was recovered. Finally, for the entire 38 kW of engine block heat recovery, the engine block heat was largely used for partial evaporation as shown in Fig. 6.21a. When considering the variation in heat loads, it was noticed that until the engine block was used for preheating, the net heat input into the cycle (i.e. HT EGR+EXH+Coolant) remained constant at 51 kW.

For the engine block heat used for evaporation, the net heat into the cycle increased to a maximum value of 78.4 kW. Since the thermal efficiency of the cycle remained constant, the net power increased from 7 to 10.8 kW (Fig. 6.20c).

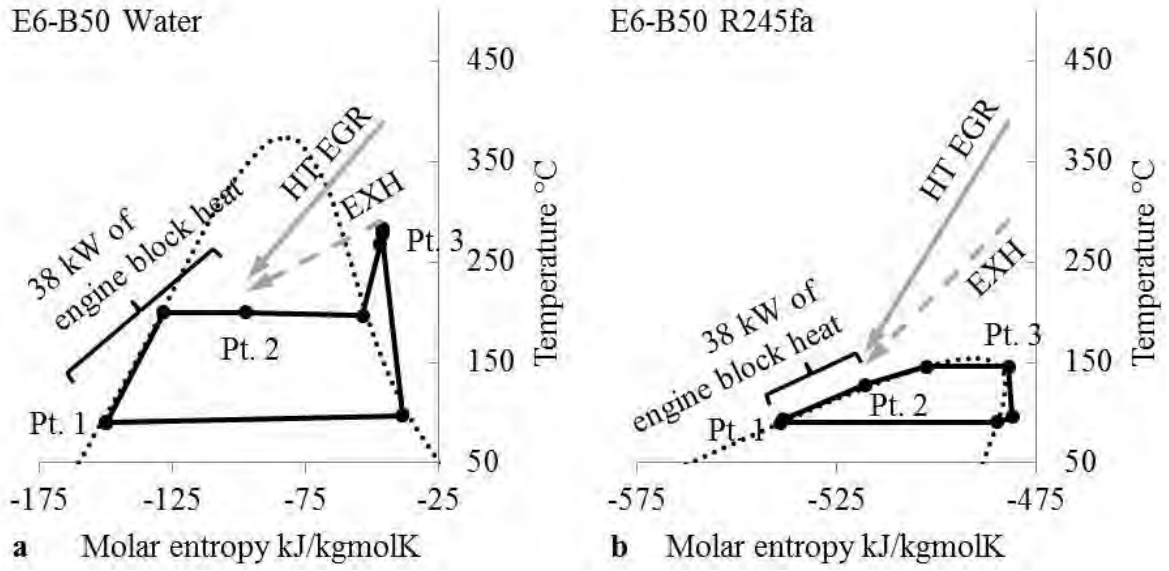

Figure 6.21 T-S diagram for modified coolant exergy corresponding complete engine block heat recovery using (a) water (b) R245fa, at E6-B50

The vastly dissimilar properties of R245fa resulted in a different trend compared to water. By increasing the coolant temperature from 115 to 127°C, the engine block heat recovery increased from 20.4 (also shown in Fig. 6.18c) to a complete 38 kW (Fig. 6.20b). The 127°C temperature was below the evaporation temperature for the corresponding pressure (Fig. 6.21b), and the net heat into the system increased from 91.7 to 104.9 kW (Fig. 6.20b). As a result, for a constant thermal efficiency, the net power increased from 5.1 to 5.8 kW (Fig. 6.20d).

6.5.2.2 Results and discussion

The case study results corresponding to complete engine block heat recovery are presented in Appendix 6.7. Water and R245fa provided the extreme ends of changed exergy content of the engine coolant. Water gave the highest system power of 9.8 kW, but required the coolant temperature to be raised to a much higher value of 200°C. The negative effects arising from this on engine performance cannot be neglected. On the other hand, R245fa achieved the complete 38 kW engine block heat recovery with a raised coolant temperature of only 127°C. Nonetheless, the system power was still 1/3rd lower than PI-3 using ethanol. Hence, neither the modified exergy content of the coolant using water as mentioned by Arias et al. (2006) (similar to Fig. 6.21a), nor the use of a coolant preheat strategy using

R245fa as shown by Ford (Hussain and Brigham, 2010) (similar to Fig. 6.18c) resulted in a more suitable process integration over PI-3. The modified exergy content of the coolant using water also resulted in an 'insufficient EGR cooling PI'.

6.5.3 Process integration 5: EGR + CAC-EXH parallel

6.5.3.1 Problem definition, system architecture, cycle operation and process optimisation

The engine block heat recovery coupled with the 'EGR + EXH parallel' thermal architecture as analysed in PI-4 resulted in an unfavourable system due to the mass flow rate limitation. Contrary to the use of engine block heat for preheating, CAC may be a more suited heat source since it offers relatively lower quantity but higher quality heat. Furthermore, rather than preheating prior to the 'EGR + EXH parallel' thermal architecture, which also reduces EGR heat recovery, preheating by CAC prior to only EXH will result in a more favourable process integration with higher β value.

With a single pressure level and a single stage expansion, PI-5 (Fig. 6.22a) is proposed for the simultaneous heat recovery of EGR, EXH and CAC. The pressurised liquid working fluid was distributed into two streams. One stream was preheated, evaporated and superheated in the HT EGR heat exchanger. The other stream was firstly, preheated in CAC (Pt. 1) under the system evaporation pressure. This stream then underwent residual preheating, followed by evaporation and superheating in the EXH heat exchanger. Since PI-5 was an evolution over PI-3 with the addition of CAC heat prior to EXH heat, it was termed as 'EGR + CAC-EXH parallel'.

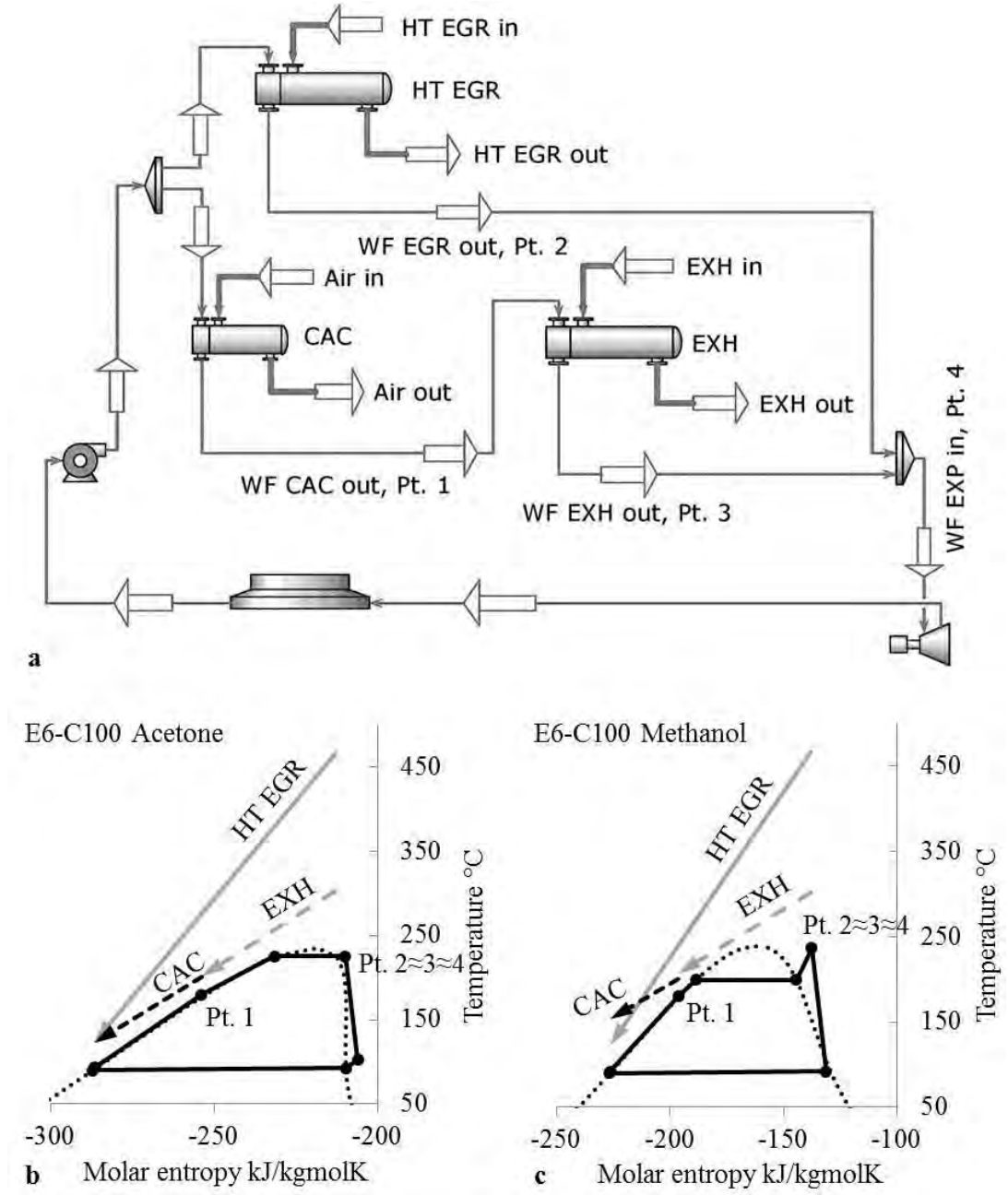

Figure 6.22 EGR + CAC-EXH parallel (a) system architecture (b) T-S diagram using acetone (c) T-S diagram using methanol

Fig. 6.22b and c describe the T-S diagram for optimal cycle operation using acetone and methanol at E6-C100. The CAC was modelled with a 20°C pinch point, this occurred at the saturated liquid curve, and hence the working fluid temperature at Pt. 1 was 20°C below the hot charge air temperature (given in Table 6.1). It is important to highlight that only the air-to-liquid CAC (Fig. 6.2) offering higher quality heat was integrated into PI-5 by moving it from the low-temperature radiator level to the medium-temperature condensing level. While the low-temperature air-to-air CAC was still a part of the engine cooling module providing the desired residual charge air cooling.

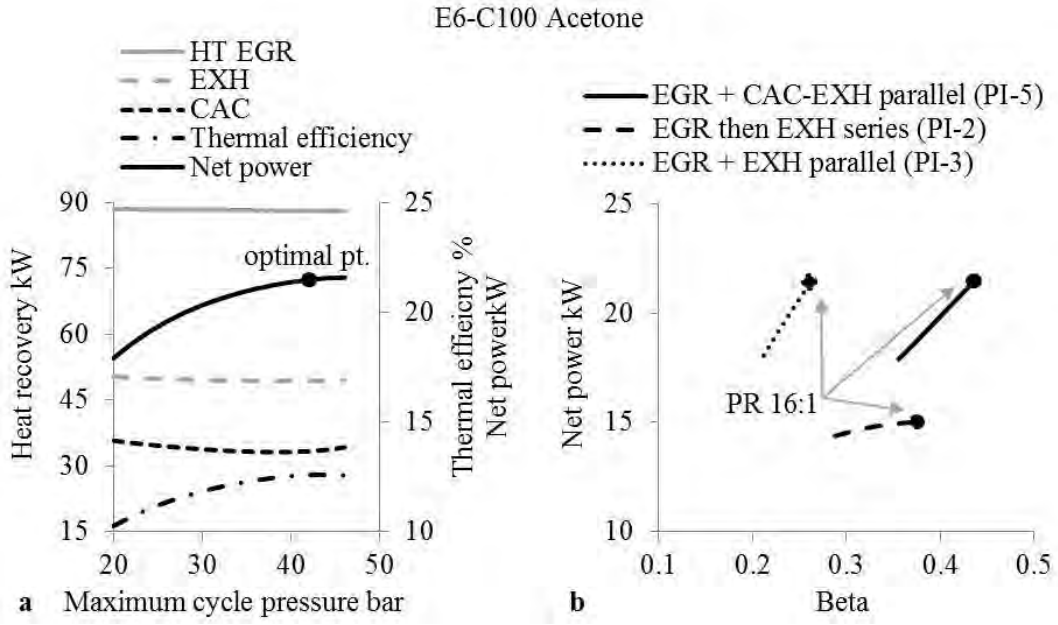

Figure 6.23 (a) PI-5 maximum cycle pressure effect on heat recovery, thermal efficiency and net power (b) baseline net power and beta value comparison

Fig. 6.23a shows the change in heat recovery loads, thermal efficiency and net power for PI-5 with varying maximum cycle pressure with acetone at E6-C100. At high loads, the heat recovery in the different heat exchangers was relatively constant and the cycle optimised with a cycle pressure of 42 bar, i.e. $0.9P_{crit}$.

6.5.3.2 Results and discussion

Appendix 6.8 presents the optimal PI-5 results for ethanol, methanol, R30 and acetone at the 4 test points. As expected, PI-5 and PI-3 optimised under similar pressure (±2 bar) and temperature (±6°C) for a particular fluid. Since the thermal efficiency (±0.3% point) and net heat input was also alike (±1 kW), the system power was similar (±5%). However, due to the 'CAC-EXH' thermal architecture, PI-5 required lower EXH heat recovery (60 vs. 75% of available load), and gave 0.5 kW lower backpressure losses compared to PI-3.

The PI-5 average system power marginally (5%) favoured acetone. This is due a relatively higher sensible heat to latent heat ratio of acetone, resulting in higher CAC heat recovery (Fig. 6.22b vs. c). It was noticed that, PI-5 offered the advantages of high β value nearly equal to PI-2 as well as a high system power nearly equal to PI-3 (Fig. 6.23b). Hence, CAC as a preheat strategy was favoured since using an appropriate fluid it demonstrated noticeable improvements in system power (5%) and beta value (15%) over coolant as preheat (Fig. 6.24). Furthermore, by taking advantage of the significant amounts of heat rejected by the CAC at high loads, the increased load on the E6 engine cooling module with PI-5 were reduced to limits defined in Fig. 6.4b.

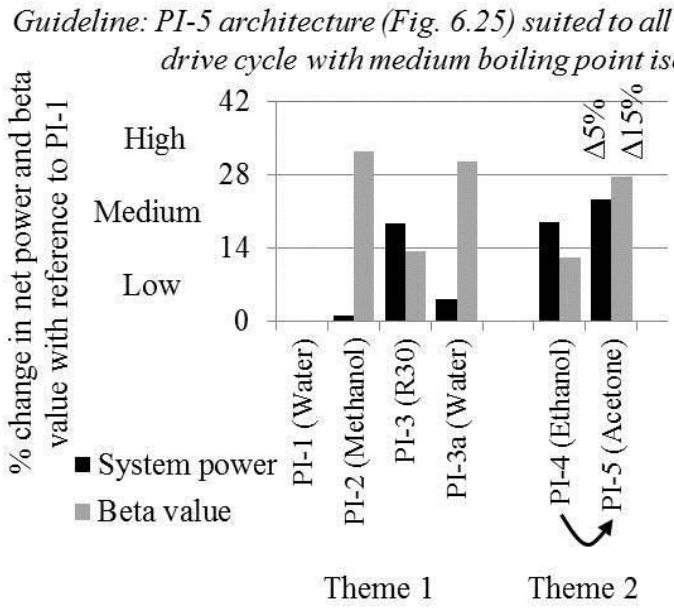

Figure 6.24 PI-5 guideline and system power/beta value change over PI-4

6.5.3.3 Low load challenges and solutions: option 1

The ability of PI-5 to recover CAC heat instead of the lower grade EXH heat was a clear benefit, resulting in a higher system power and β value. However, PI-5 with the 4 fluids considered were more suited to higher engine loads (>60%). This was because at relatively lower loads (<50%) the CAC heat recuperation was fairly low, firstly due to the low CAC quality, and secondly since CAC was moved from the low-temperature radiator level to the medium-temperature condensing level. Since, acetone recovered the highest CAC heat, PI-5 with acetone was best suited to engines usually operating at greater than 60% loads.

When engines are also frequently operated at less than 50% loads, the modified heat recovery loop proposed in Fig. 6.25 can be applied. During low loads (<50%), the CAC is bypassed and the process integration behaves as PI-3, i.e. 'EGR + EXH parallel' (thick dash line). The integration was termed 'EGR + EXH parallel (optional CAC)'. In this manner, the advantages of PI-5 under high engine loads and the advantages of PI-3 under low engine loads can be retained. Fig. 6.25 therefore provides a strategy in EXH heat limitation, while generating highest overall system power over a wider engine operating map.

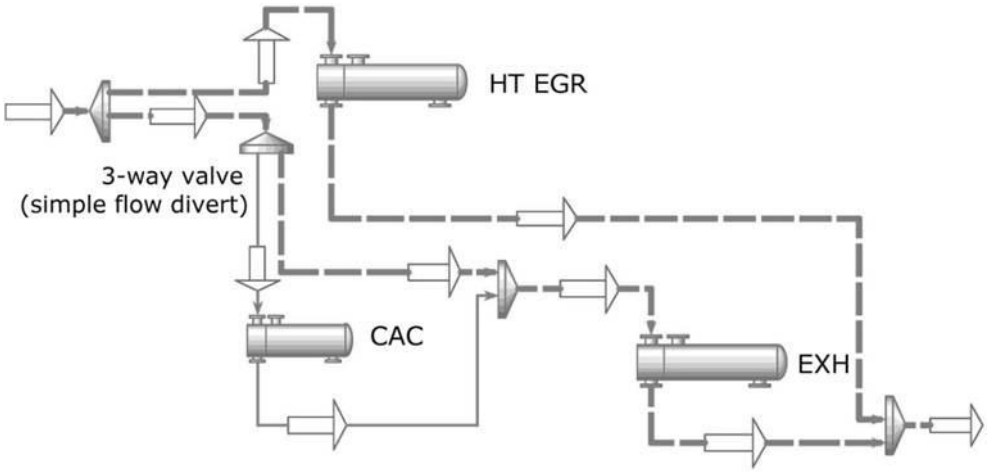

Figure 6.25 EGR + EXH parallel (optional CAC) heat recovery loop as exhaust heat limitation with highest power generation strategy

6.5.3.4 Low load challenges and solutions: option 2

For engines that are predominantly operated at relatively lower loads (<50%), offer lower quality CAC heat (<150°C) and peak heat source temperatures (<350°C), PI-5a is proposed. PI-5a (Fig. 6.26) is a derivative of PI-5 operating under supercritical cycle mode using R152, an isentropic low GWP (43 years) refrigerant. R152 was pressurised to $1.1P_{crit}$ (i.e. <50 bar boundary condition given in Table 6.2) before being distributed for supercritical heating into two streams. Appendix 6.9 presents the B50 results with supercritical R152. Comparing Appendix 6.8 and 6.9, it was noticed that the extracted heat amounts from the CAC by R152 at cruise loads were 50% higher than acetone. This is due to a relatively lower critical temperature (172 vs. 235°C) of R152.

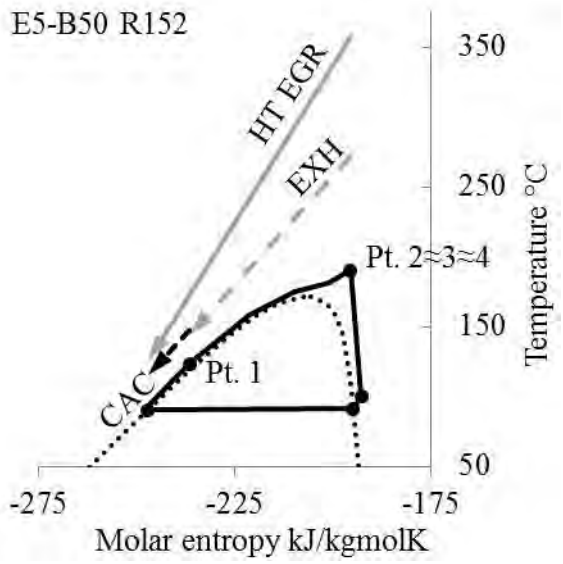

Figure 6.26 EGR + CAC-EXH parallel operating under supercritical mode with R152 as an alternative process integration for relatively lower source quality

Section 5.7.4 detailed a 25% performance advantage of supercritical R152 over supercritical R245fa. With the added PI-5a advantages (e.g. lower backpressure and fan power) over PI-3, PI-5a using R152 gave an average cruise system power which was twice that of PI-3 using R245fa (Appendix 6.6) for a relatively low and comparable expansion pressure ratio (4.6:1 vs. 3:1). PI-5a using R152 also had the advantage of pressure ratios around 3 times lower than ethanol for low EGR rate engine at low loads (E5-B50, Appendix 6.9 vs. 6.3) for a reduction of only 10% in system power.

6.5.4 Summary: High and low temperature heat recovery with single expansion stage

Theme 2 highlighted that integrating different subsystem thermal architectures resulted in at least three process integration challenges. These being:

- Choice of the appropriate energy and exergy content of the subsystem thermal architecture (PI-4 vs. PI-5)
- Influence of working fluid on the heat recovery and maximum system power (PI-5, methanol vs. acetone)
- Consideration of the typical operating speed/load experienced by the engine (PI-5 using acetone vs. PI-5a using R152a)

If the system architecture and its working fluid are properly selected, then integrating CAC leads to fundamentally more successful process integration. PI-5 (preferred using acetone) offered potentiality for complete HT EGR cooling and considerable CAC heat recovery, with the advantages of high β value (similar to PI-2) and high system power (similar to PI-3). Furthermore, Fig. 6.25 provided an effective means to limit EXH heat recovery at high loads while generating maximum system power over varying engine speeds/loads.

6.6 Theme 3 - High temperature thermally stable solutions using water

Optimum system architecture for theme 1 and 2 was possible by PI-3 and PI-5, respectively (Fig. 6.24). However, PI-3 and PI-5 were better suited to organic fluids, namely R30 and acetone, respectively. Organic fluids have a major drawback that they undergo chemical decomposition when fluid conditions exceed certain limiting temperature and pressure combination values. Additional influencing variables include but are not limited to: interaction with plant materials, impurities, lubricant additives and temperature distribution/thermal cycling. The decomposition products can have safety implications and usually include non-condensables, high/low boiling components and

gummy or coke type residue (Guillen et al., 2011, ASTM, 2011, Spurlin M et al., 2000). These products are essentially deleterious to the system components and their performance.

Furthermore, there exists contradictory thermal stability claims for organic fluids. For this consider the thermal stability values reported for R245fa and ethanol (Zyhowski, 2013, Halliwell, 2012, Absalam-Gadzhievich and Ramazanovich, 2012, Arunachalam et al., 2012, Teng and Regner, 2009, Chacartegui et al., 2009, Abdurashidova et al., 2007, Angelino and Invernizzi, 2003). The cited values for R245fa and ethanol each gave a maximum thermal stability temperature variation of Δ125°C and Δ150°C, respectively. Nonetheless, most frequently cited absolute limits included 250°C for R245fa, whereas ethanol showed a more suitable higher value of 350°C.

Reliable thermal decomposition data of the alternative organic fluids used in this work was essentially missing in the published literature. This decomposition limit will vary among the organic fluids, and will influence the final process parameters. However, for other 30-105°C boiling point organic fluids, the instability temperature was typically encountered above 250°C (Latz et al., 2012, Shu et al., 2012a, Ginosar et al., 2011, Chacartegui et al., 2009, Prabhu, 2006). Hence, all the high temperature organic simulation results presented in this chapter were limited to a maximum of 250°C. In practice, for all organic working fluids the flow rate has to be controlled precisely to prevent extreme temperature excursions (e.g. large superheating) and exposure lengths (e.g. heat build-up during impaired flow conditions).

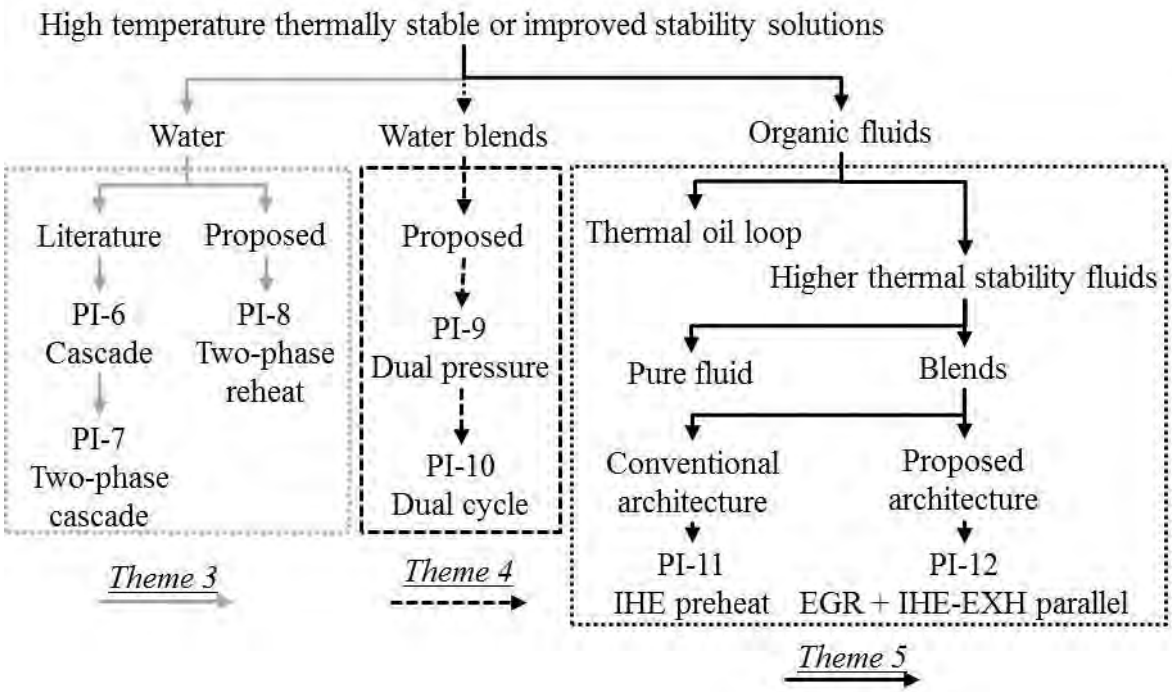

Figure 6.27 Three additional themes of approach coupling fluid selection and system architecture to offer thermally stable or improved stability process integrations

To provide high temperature thermally stable or improved stability solutions (i.e. approach B), three additional themes of process integrations were investigated (Fig. 6.27). Categorised based on the type of working fluid, they were distinguished as: theme 3 using water, theme 4 using water blends and theme 5 using organic fluids. The primary screening criterion for both types of blends included improved thermal stability. The key secondary screening criterion included, potential engine coolant loop replacement by water blends, and improved applicability to cycles with an IHE by organic blends. The following process integrations use water as a working fluid for high temperature heat recovery. Firstly, two cascade process integrations similar to those in the published literature were simulated to act as a baseline (Bae et al., 2013, Wang et al., 2012, Bae et al., 2011, Kim and Yu, 2011, Smith et al., 2011).

6.6.1 Process integration 6: Cascade (baseline)

6.6.1.1 System architecture, cycle operation and process optimisation

Cascade systems are utilised when there exists a large temperature differential (typically >300°C) between the source and sink. A cascade system consists of two different temperature level FBCs. The two closed loop cycles, the high-temperature and the low-temperature cycles are interconnected at least by a common heat exchanger. The common heat exchanger termed ‘cascade condenser’ is effectively an internal heat exchanger for the system. The cascade condenser acts as a condenser for the high-temperature cycle and as an evaporator for the low-temperature cycle. Only the

condenser of the low-temperature cycle plays a role in dissipating heat out of the cascade system. Due to the high temperature differential across the system, need to limit exergy destruction in the cascade condenser and design considerations, two distinct working fluids are used. A higher boiling point fluid is used in the high-temperature cycle, while the low-temperature cycle utilises a relatively lower boiling point fluid.

The first high temperature cascade process integration that recovered large amounts of waste heat and with a low impact on the engine cooling module was investigated using PI-6 (Fig. 6.28a). The high-temperature cycle recovered HT EGR and EXH heat in a parallel thermal architecture. Whereas the low-temperature cycle recovered the residual EGR heat (i.e. LT EGR) and the engine block heat also in a parallel thermal architecture prior to being mixed for recovering the cascade heat load. Cascade process integrations considered in this chapter utilised water for the high-temperature cycle, and both R245fa and ethanol for the low-temperature cycle.

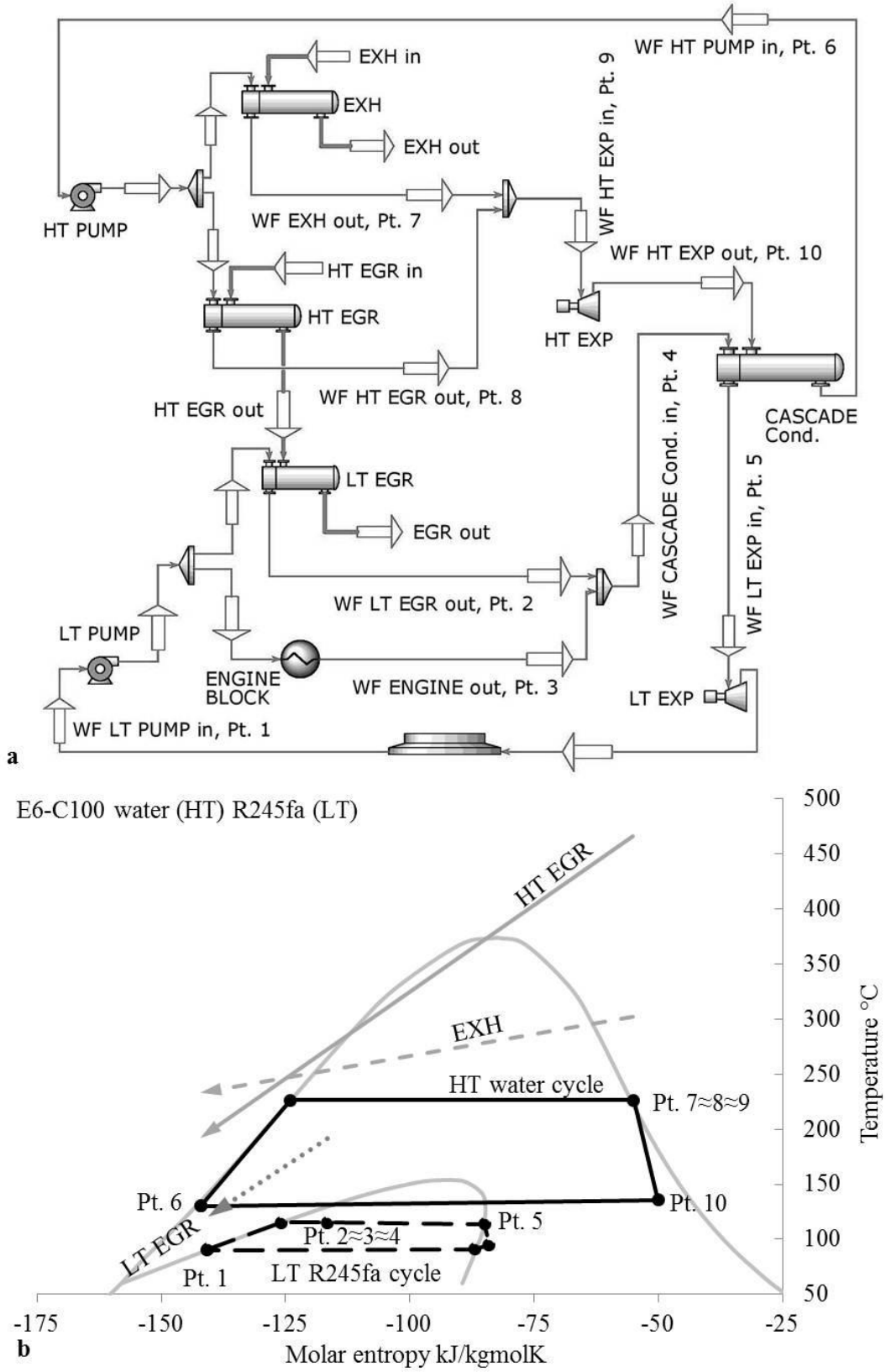

Figure 6.28 Cascade system (a) system architecture (b) T-S diagram using water-R245fa combination

Fig. 6.28b describes the T-S diagram for the optimal cascade system operation using water-R245fa combination at E6-C100. The process integration was simulated with a 90°C condensing temperature (Pt. 1) in the low-temperature cycle. The working fluid

temperature exiting the LT EGR (Pt. 2) and the engine block (Pt. 3) was fixed at 115°C. This governed the maximum pressure in the low-temperature cycle as 18.5 and 4.8 bar for R245fa and ethanol, respectively. The cascade condenser was modelled with a pinch point of 15°C, hence the condensing temperature for the high-temperature cycle (Pt. 6) was also fixed at 130°C. The low-temperature cycle recovered the condensing load (Pt. 10 to 6) of the high-temperature cycle to fully evaporate the low-temperature cycle working fluid (Pt. 4 to 5), which underwent a dry saturated vapour expansion. Owing to a much similar heat quality and quantity between the engine block heat and the cascade condenser, mass flow rate limitation as demonstrated in PI-4 was not experienced in PI-6. As a result, complete engine block heat recovery was possible with working fluid exiting partially evaporated from the engine block. This presented the opportunity of replacing the conventional engine cooling loop with the working fluid of the low-temperature cycle. Due to the increased condensing pressure, the high-temperature cycle was operated without superheat (Pt. 9) since a dryness fraction of ≈0.95 was maintained (Pt. 10). The water temperature exiting the EXH (Pt. 7) and HT EGR (Pt. 8) was also maintained equal. Therefore, the system optimisation was governed by optimisation of the pressure in the high-temperature cycle.

Fig. 6.29a shows the change in the heat recovery loads and net combined power for PI-6 with varying maximum high-temperature cycle pressure for water-R245fa combination at E6-C100. With increasing high-temperature cycle pressure, lower heat (e.g. EXH) was recovered by the high-temperature cycle. In fact, the HT EGR duty also reduced, however since the residual heat was recovered in the low-temperature cycle the duty of the LT EGR increased. As a result, the net EGR heat recovery remained constant. Since the maximum pressure in the low-temperature cycle was fixed, the thermal efficiency of the low-temperature cycle was constant (Fig. 6.29b). Whereas, with increasing high-temperature cycle pressure the thermal efficiency of the high-temperature cycle improved. As a result of combined thermal efficiency improvement and reducing heat recovery, the process optimised at a high-temperature cycle pressure of 27 bar.

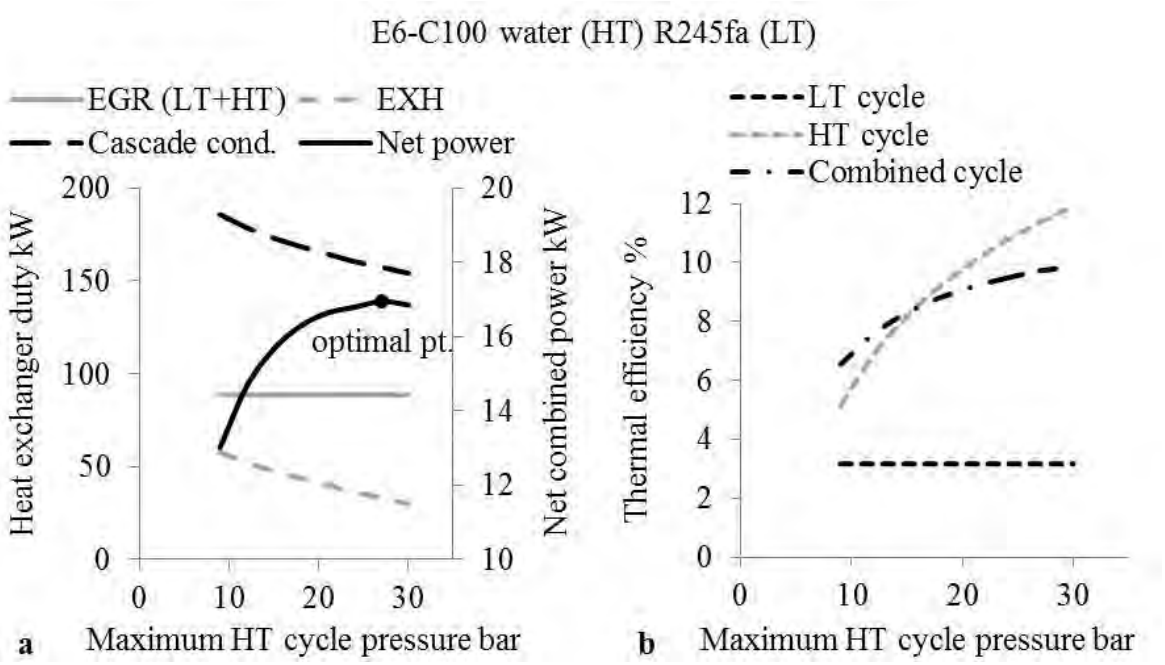

Figure 6.29 PI-6 maximum high-temperature cycle pressure effect on (a) heat recovery and net power (b) thermal efficiency

6.6.1.2 Results and discussion

Appendix 6.10 presents the optimal PI-6 results for water in combination with R245fa and ethanol at the 4 test points. The cascade system offered relatively lower maximum cycle pressures (<28 bar) and relatively higher super atmospheric condensing pressures (>2.5 bar) for both the temperature cycles. This resulted in lower expansion enthalpy drop and expansion pressure ratio. The maximum pressure ratios seen in the high and low-temperature cycles were favourable at 8:1 and 2:1, respectively. This 8:1 pressure ratio also acted as an absolute upper limit per expansion machine when using two separate machines, or per expansion stage when using a two-stage machine in the remaining process integrations. The heat input into the low-temperature cycle on average was 1.7 times higher than the high-temperature cycle, while the thermal efficiency was only 1/3rd. This was primarily due to the entire engine block heat recovery and a high cascade heat load, which was 1-1.8 times that of the engine block heat.

The average system power marginally (5%) favoured water-R245fa over water-ethanol combination owing to a slightly higher net heat recovery for similar combined thermal efficiency. For process integrations discussed in theme 1, water was better suited to PI-3a, despite demonstrating on average a 15% lower system power compared to organic fluids in PI-3. When PI-6 (water-R245fa) was compared to PI-3a, the average system power improvement was insignificant (Fig. 6.30). This was because the average heat recovery was 60% higher, however, the average thermal efficiency was 5% point lower. Hence, for

a fixed low thermal efficiency of the low-temperature cycle, as was in this case, it is vital to maintain high thermal and heat recovery efficiencies in the high-temperature cycle. In fact, over a drive cycle PI-6 may result in lower system power, since insuring dry vapours prior to both the expansion machines, liquid prior to both the pumps and high heat recovery will be a control challenge.

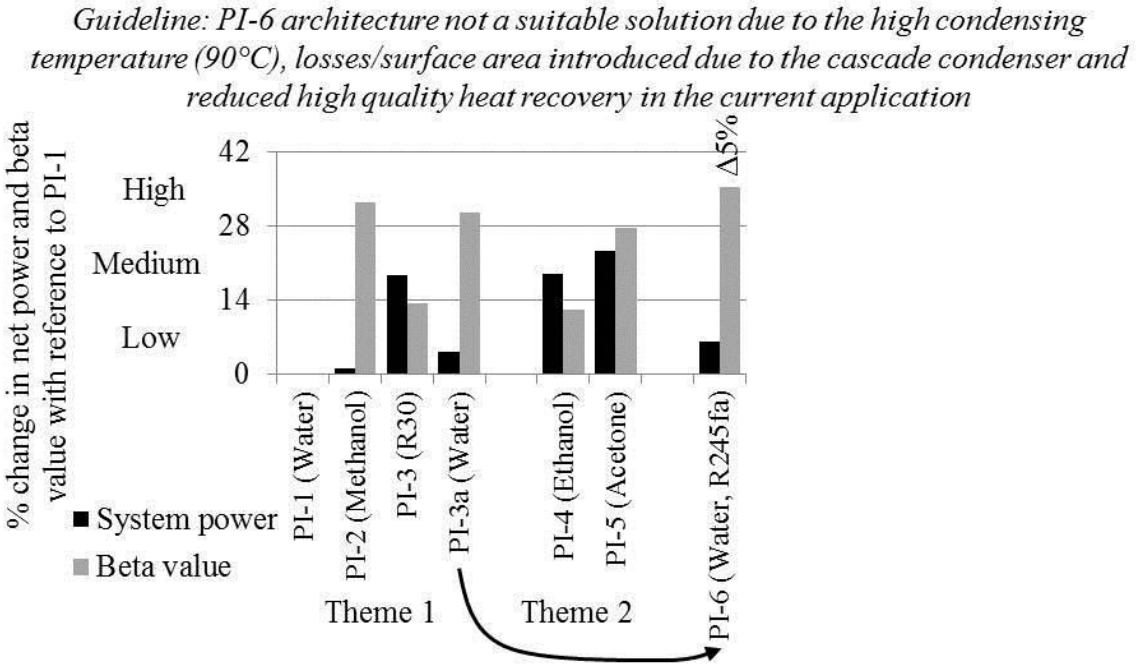

Figure 6.30 PI-6 guideline and system power/beta value change over PI-3a

Since the cascade condenser internally transfers heat in the system, an additional advantage of cascade systems cited can be interpreted as offering lower negative impact on the engine cooling module. However, since the EXH heat recovery was similar (45% of the available load), the β value in PI-6 was not noticeably higher than the benchmark set by water in PI-3a (Fig. 6.30). Furthermore, due to the absence of the cascade condenser the UA/W value of PI-3a on average were 1/3rd of PI-6. Hence, the cascade system as shown in PI-6 provided no new performance measure or a β value over the relatively simple PI-3a.

6.6.2 Process integration 7: Two-phase cascade (baseline)

6.6.2.1 Problem definition, system architecture and cycle operation

Water-organic cascade systems, like PI-6, provide a thermally stable solution for various levels of heat. However, the reasons for lower system power in PI-6 included, low EXH heat recovery and high heat input into the low thermal efficiency low-temperature cycle. To provide a more favourable cascade system by addressing the above two drawbacks and further simplifying the process integration, PI-7 was considered (Fig. 6.31a).

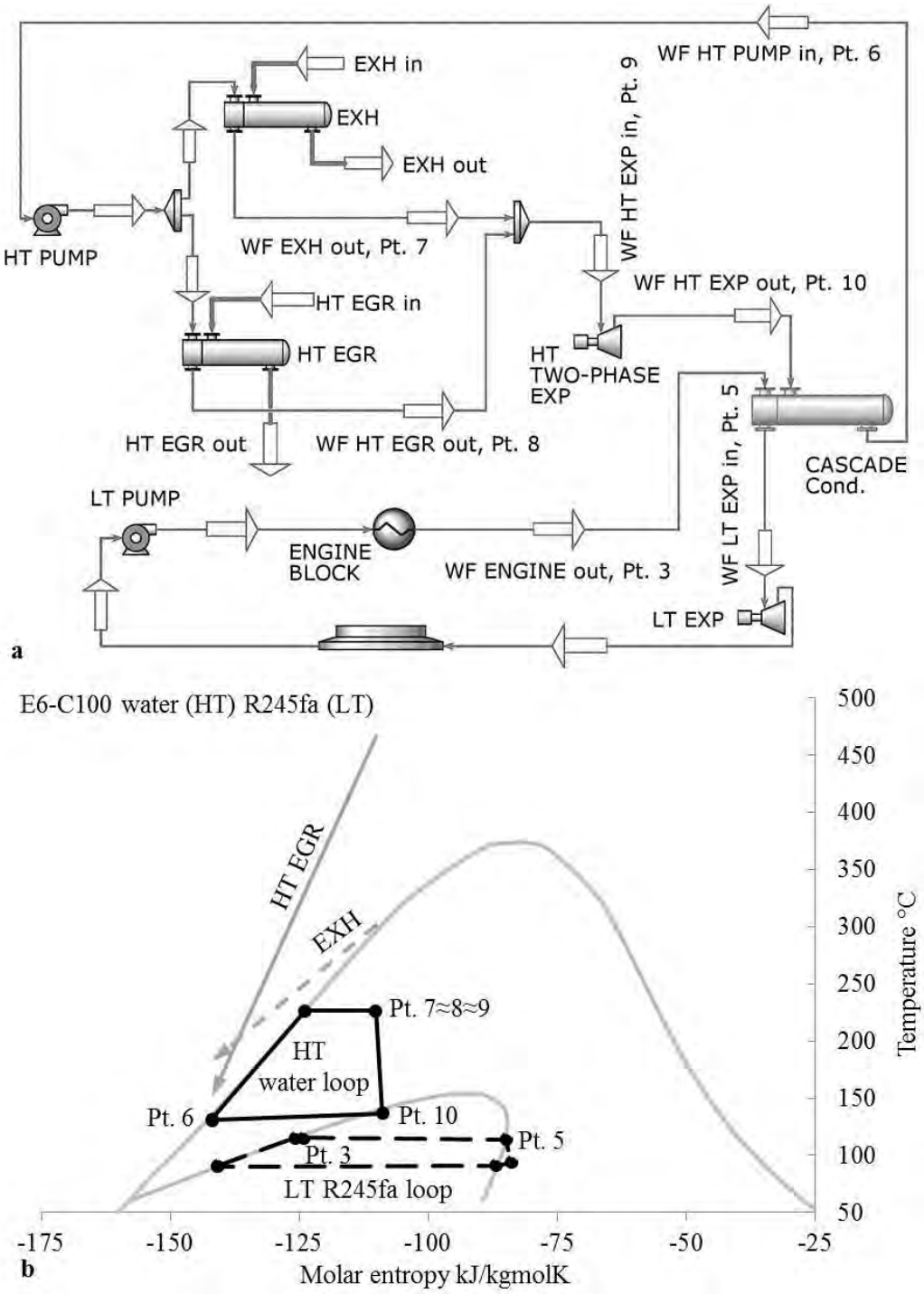

Figure 6.31 Two-phase cascade system (a) system architecture (b) T-S diagram using water-R245fa combination

The fundamental difference in PI-7 over PI-6 was the replacement of the high temperature conventional expansion machine to a two-phase expander. As was shown in Section 5.8.2, two-phase water expansion improved the net power due to increased heat recovery. Since higher heat recovery was possible in the HT EGR, the integration of the LT EGR was excluded from the system, simplifying the process integration (Fig. 6.31a vs. 6.28a).

Fig. 6.31b describes the T-S diagram for this optimised system using water-R245fa combination at E6-C100. The low-temperature cycle pressure and temperature limits were the same as in PI-6, and only the working fluid flow rates and heat loads changed. While the high-temperature cycle underwent a two-phase expansion (Pt. 9 to 10) and the system was termed 'Two-phase cascade'. Section 5.8.2 included only EGR stream heat recovery where the two-phase expansion cycle optimised at an inlet vapour fraction of 0.4. Since the source thermal quality was relatively lower in the 'EGR + EXH parallel' thermal architecture, the high-temperature cycle optimised at a much lower inlet vapour fraction. However, as the volume flow ratio increased substantially for two-phase expansion with inlet vapour fraction below 0.2 (Fig. 5.21c), the vapour fraction at the expander inlet was kept fixed at 0.2. Hence, the high-temperature cycle pressure governed the process optimisation (similar to PI-6).

6.6.2.2 Results and discussion

With similar trends in heat recovery, net combined power and thermal efficiency to PI-6, Appendix 6.11 presents the optimal PI-7 results for water in combination with R245fa and ethanol at the 4 test points. The optimised maximum cycle temperatures and expansion pressure ratios were below the 233°C and 8:1 two-phase screw expander limits, respectively. Furthermore, by condensing at 130°C in PI-7 compared to 105°C in Case 4, the condensing pressure was increased to 2.7 bar and the maximum volume flow ratio was also reduced to 11:1. As such, the problem of large expander footprint to expand two-phase water may be avoided.

The average system power in PI-7 marginally (5%) favoured water-R245fa over water-ethanol combination due to a slightly higher thermal efficiency for similar heat recovery. When PI-7 (water-R245fa) was compared to PI-6 (water-R245fa), the heat input into the low-temperature cycle was lowered to an average of 1.4 from 1.7 times that of the high-temperature cycle. The two-phase expansion also increased the EXH heat recovery (65 vs. 45% of the available load). As a result, PI-7 gave an 8% higher system power (Fig. 6.32). The performance superiority of PI-7 was an advantage over PI-6 and offered a new benchmark of comparison for the following water process integration.

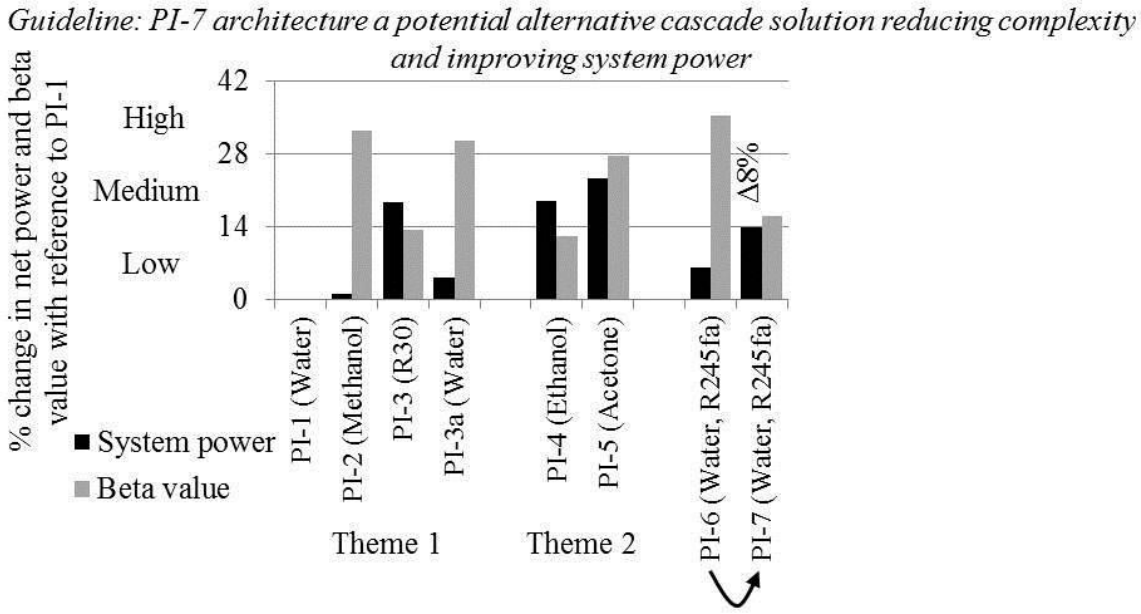

Figure 6.32 PI-7 guideline and system power/beta value change over PI-6

6.6.3 Process integration 8: Two-phase reheat

6.6.3.1 Problem definition, system architecture, cycle operation and process optimisation

PI-7 compared to PI-3a partially addressed the large latent heat drawback of water for EXH heat recovery, and hence provided a higher EXH heat recovery (65 vs. 45% of the available load) which contributed to the 10% higher system power (Fig. 6.32). However, PI-7 also increased the mechanical complexity and the UA/W value over PI-3a. To recommend a more suited solution using water, this section proposes a novel two-phase reheat cycle and its application in the case of engines using EGR. Rather than the reason of increased thermal efficiency, as is the case with conventional reheat cycle, the two-phase reheat concept was approached from a process integration point of view.

Fig. 6.33a depicts the process integration (PI-8) recovering combination of HT EGR and EXH heat in association with a high-pressure two-phase expansion machine and a low-pressure conventional expansion machine. While Fig. 6.33b shows the T-S diagram for the optimal cycle operation at E5-C100. The pressurised water, limited to a maximum pressure of 30 bar, was used to recover the HT EGR heat. The high-temperature high-pressure two-phase stream was expanded in a two-phase expansion machine (Pt. 1 to 2), and exited at an intermediate pressure. Typically, in order to utilise such intermediate pressure two-phase stream, a separator is used (Ho et al., 2012). The separator avoids the use of another large two-phase expansion machine that has to be used to expand the two-phase stream to a low condensing pressure. The vapour stream exiting the separator is used to drive a conventional expansion machine, while the liquid stream is throttled to the

condensing pressure. However, the selected HDDE platforms gave a particular advantage in this case. The expanded two-phase stream with slightly increased vapour fraction was evaporated and superheated (Pt. 2 to 3) using the EXH heat. This intermediate pressure dry stream then underwent a minimum superheat expansion in a conventional machine (Pt. 3 to 4) and exited at the condenser pressure. By using PI-8, the separator was no longer necessary and the irreversibilities during the liquid throttling process were also eliminated.

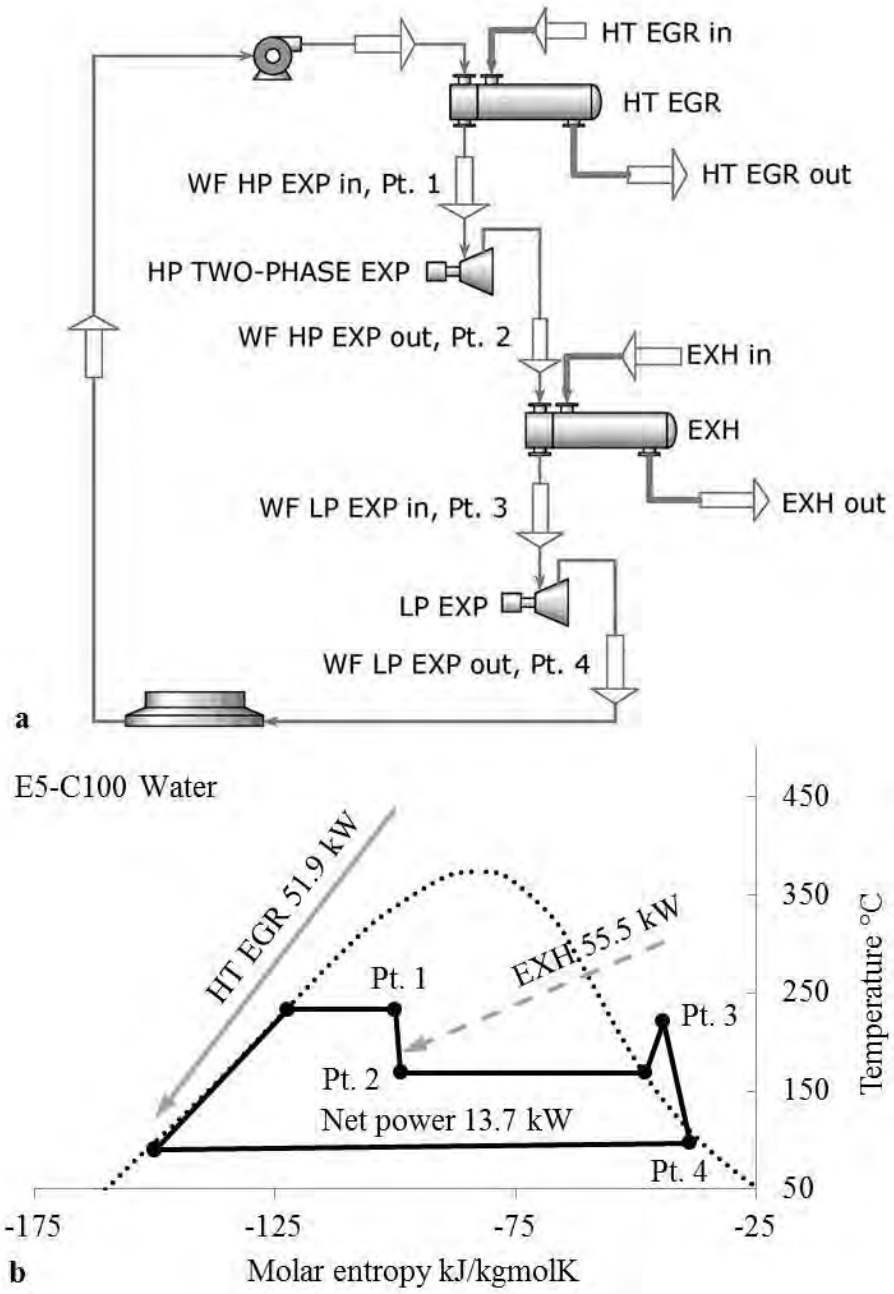

Figure 6.33 Two-phase reheat cycle (a) system architecture (b) T-S diagram using water

Furthermore, to reduce the pressure ratios and volume flow ratios experienced in the two-phase expansion process compared to PI-7, the pressure at Pt. 2 in PI-8 was raised to a fixed value of 8 bar (170°C). This resulted in a pressure ratio of 8:1 (VFR 6:1) for the

conventional expansion machine. Since the condensing temperature was fixed at 90°C, and the vapour fraction at Pt. 4 was maintained at ≈0.98, the maximum temperature at Pt. 3 was also constant at 220°C. Hence, the system optimisation was governed by the cycle high pressure, while ensuring the control of the water mass flow rate to provide the superheated condition at Pt. 3.

Fig. 6.34a shows the change in heat recovery loads, net power and thermal efficiency for PI-8 with increasing maximum cycle pressure at E5-C100. The chosen intermediate pressure at Pt. 2, and the energy and exergy content of the heat streams at high loads were such that the heat recovery was relatively constant. In fact, even under lower source quality (e.g. E5-B50), the EXH heat recovery remained constant, while the HT EGR heat recovery only decreased marginally. With increasing cycle pressure, the thermal efficiency increased to a maximum of 12.8% and the system generated a net power of 13.7 kW. The relatively constant EXH heat recovery was a distinct trend when compared to PI-7 (Fig. 6.34b).

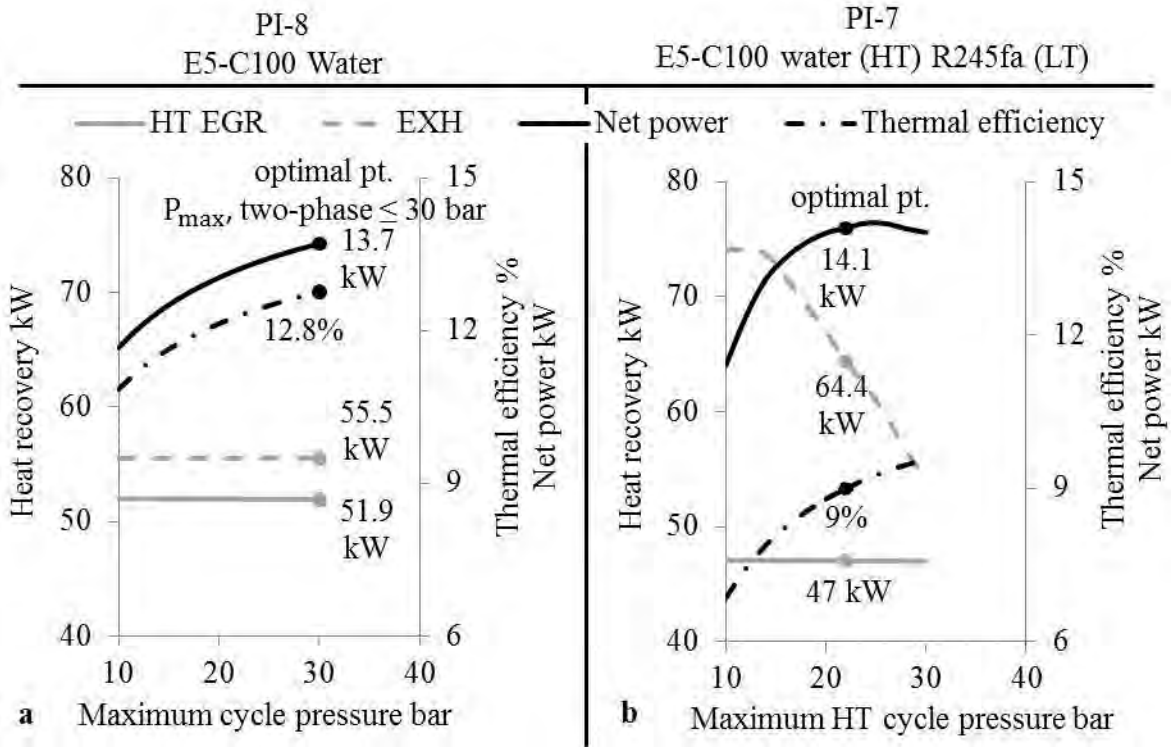

Figure 6.34 Effect on heat recovery, net power and thermal efficiency by varying (a) PI-8 maximum cycle pressure (b) PI-7 maximum high-temperature cycle pressure

6.6.3.2 Results and discussion

Appendix 6.12 presents the optimal PI-8 water results at the 4 test points. PI-8 compared to PI-7 recovered nearly similar quantities of HT EGR heat (90% of the available load, also shown in Fig. 6.34), slightly reduced EXH heat (60 vs. 65% of the available load, also

shown in Fig. 6.34) and no engine block heat. As a result, PI-8 showed a 4% point thermal efficiency improvement (also shown in Fig. 6.34). With noticeably reduced process integration complexity, PI-8 on average gave nearly equal system power and β value to PI-7 (Fig. 6.35). Furthermore, due to the absence of the cascade heat transfer, the UA/W value was around 1/3rd that of PI-7.

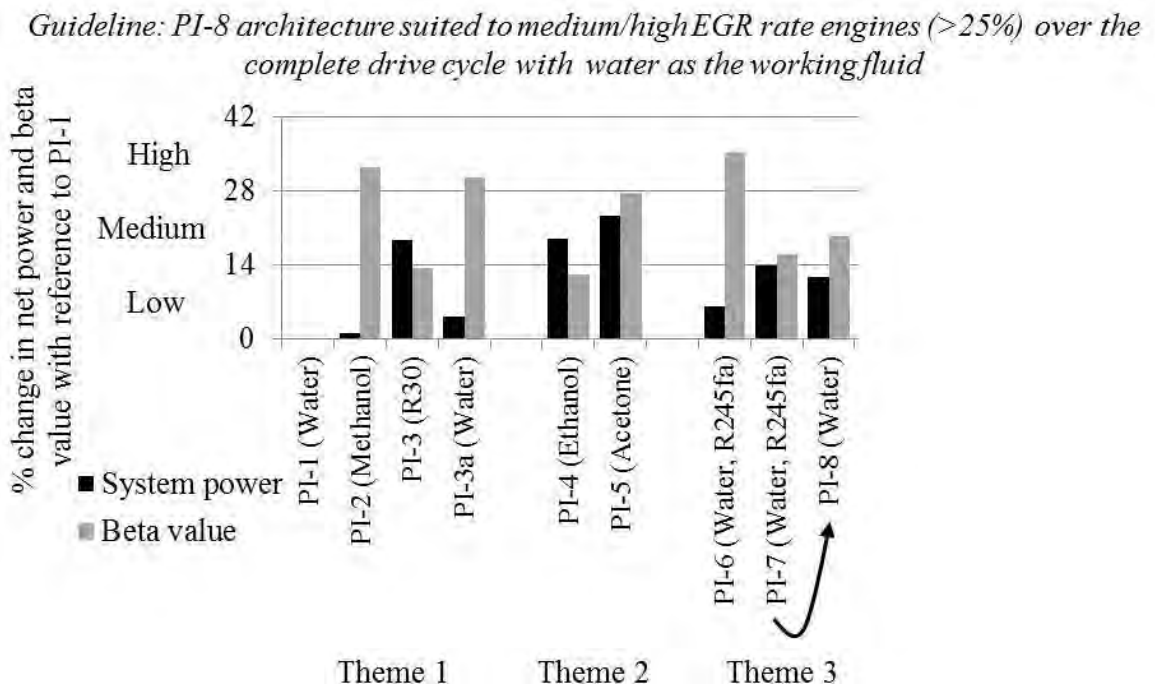

Figure 6.35 PI-8 guideline and system power/beta value change over PI-7

Some of the key advantages and novelty of PI-8 are summarised below:

Reheat concept: Firstly, the advantages of the two-phase reheat cycle over the conventional reheat cycle were quantified. Fig. 6.36 shows the T-S diagram of the conventional reheat cycle having the same thermal architecture as PI-8, and with the same maximum and intermediate pressures as Fig. 6.33b. It can be noticed that the heat recovery by the reheat stage was only 10% of the heat recovery in the first stage (3.7 vs. 38.1 kW) leading to the underutilisation of EXH heat. In the two-phase reheat cycle, the heat recovery in the EXH heat exchanger was a function of the vapour content and pressure at Pt. 2, and at the E5-C100 test point, the heat recovery in both the EGR and EXH heat exchangers were relatively similar (Fig. 6.33b). The two-phase reheat cycle overcame the large latent heat drawback of water, achieving advantageous temperature matching and recovering higher EGR and EXH heat. Despite the 4% point lower thermal efficiency (12.8 vs. 17%) due to higher low temperature heat recovery, the total heat recovery was noticeably higher (2.5 times). As a result, the two-phase reheat cycle produced nearly twice the net power (13.7 vs. 7.1 kW). The principal advantage of the two-phase reheat cycle

over the conventional reheat cycle is that it can recover higher amounts of waste heat and produce higher net power.

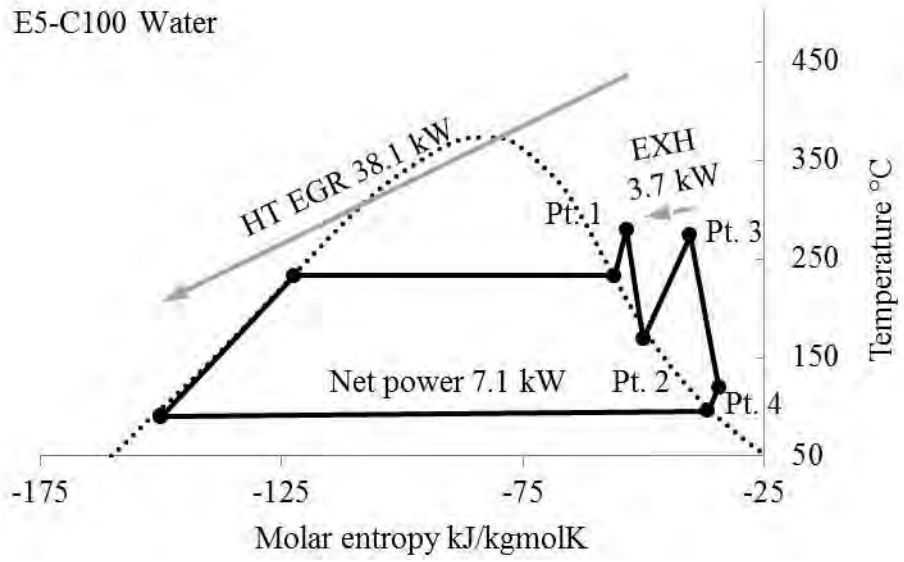

Figure 6.36 Conventional reheat cycle T-S diagram using water

Expander size: Secondly, when compared to PI-7, the maximum pressure ratio in the two-phase expansion stage was reduced from 8:1 to 3.8:1 (VFR from 11:1 to 4.2:1), improving the practicality of the two-phase expanders. This was because of the increased pressure at Pt. 2, and since, PI-8 optimised at higher vapour fraction at the two-phase expansion machine inlet.

Source quality: Finally, since Pt. 2 was already partially vaporised, even the low EXH quality of 300˚C was sufficient to provide the desired superheating level using water for the conventional expansion machine. Hence, even under low loads, water can be employed as a working fluid.

6.7 Theme 4 - Improved thermal stability solutions using water blends

The large latent heat drawback of water, which limited its application to higher source temperatures (>450˚C, Fig. 4.18), was successfully addressed using PI-8 for the selected engine platforms. Despite this, the other drawback of using water is its high freezing temperature of 0°C. Process integrations with water will require freeze protection or drainage capabilities for all the components in the cycle.

To meet the complex requirements for automotive HDDE application, fluid blends may present an alternative avenue. As the resurgence of ORC systems for HDDEs is relatively new, the present research on blends was inadequate to ascertain their suitability for vehicle application. To provide improved thermal stability solutions, theme 4 (Fig. 6.27) was undertaken to investigate the use of binary water blends to provide desired properties and characteristics by varying the water mass fraction.

The justification for the use of a miscible, non-reactive, binary, water and organic blend exists since:

Firstly, compared to pure water, the blend will:

- Provide frost protection when mixed with a lower freezing point organic fluid
- Improve the capability to control working fluid mass flow when mixed with a relatively higher molecular weight organic fluid
- Offer super atmospheric condensing at typical radiator temperature level when mixed with a lower boiling point organic fluid

Secondly, compared to pure organic fluid, the blend will:

- Increase the thermal decomposition temperature and heat transfer coefficient
- Reduce the negative impact of pumping efficiency and power on the net power
- Decrease the flammability, working fluid cost, negative health and environmental impact

Finally, compared to a pure fluid and an azeotropic blend a zeotropic blend will:

- Reduce heat transfer irreversibilities under subcritical cycle operating mode in the heat exchanger by creating a temperature glide
- Provide capability to tailor system pressures by varying the composition

6.7.1 Overview of the water blend study

To screen the list of over 750 documented water blends (DDBST, accessed on 10.10.2014, Ponton, 2007, Lide and Kehiaian, 1994, Horsley, 1973), the developed criteria shown in Fig. 6.37 was used. The environmental, safety and legal criteria used to select the organic fluid as a blend constituent were the same as those used to select the pure organic fluids in Chapter 4. Screening was conducted to identify Homogeneous Positive Azeotropes (HPA) according to three distinct water mass fractions, approximated as low (≈25% water), medium (≈50% water) and high (≈75% water).

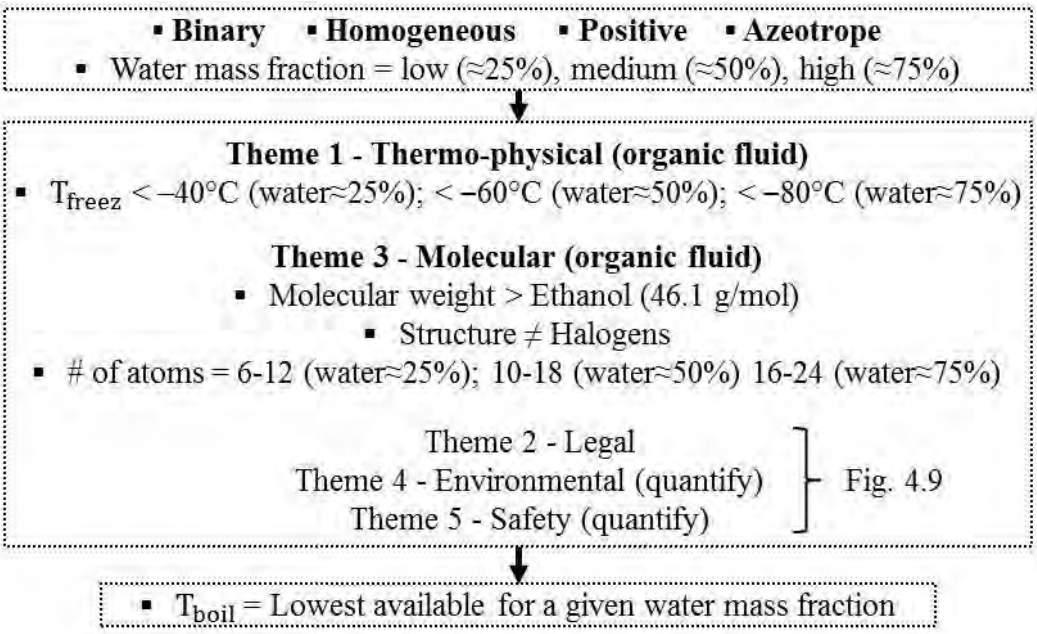

Figure 6.37 Screening method overview of the aqueous blend selection study

The screening results, limited to the selection of just one blend for a given water mass fraction that demonstrated the lowest boiling point resulted in the selection of:

- A blend containing 72% 1-propanol and 28% water forming an azeotrope at 1 bar, referred to as 1-Propanol72% as the low water content HPA.
- A blend containing 53% 3-Methyl-1-Butanol and 47% water forming an azeotrope at 1 bar, referred to as 3M-1B53% as the medium water content HPA.
- Since, no high water content HPA met the requirements set out in Fig. 6.37, 25% 1-propanol and 75% water forming a zeotrope, referred to as 1-Propanol25% was used instead.

For chemical identification, thermodynamic/thermo-physical and environmental/safety properties of the pure organic fluid as blend constituent refer to Appendix 6.13. These three blends were also compared to ethanol and water zeotropes, referred to as Ethanol75%, Ethanol50% and Ethanol25%. The screening results of the more commonly known 230 water blends are documented in Appendix 6.14.

6.7.1.1 Zeotropic and azeotropic blends

The temperature-pressure relationship of zeotropic fluids differs from that of pure and azeotropic fluids during vaporisation. In a zeotropic fluid, the composition (mole fraction) of the vapour and the liquid phases at the vapour-liquid equilibrium state is never the same. Consider an 80% ammonia 20% water mixture at 1 bar (Fig. 6.38a) that was used in Section 5.10.3. The saturated liquid mixture starts to vaporise at Pt. 1 (−28°C). During phase change heating, the blend temperature rises and more of the mixture, mostly

ammonia at first, boils off. At 40°C, the vapour component is shown at Pt. 3 (94% ammonia, 6% water) and the liquid component is shown at Pt. 4 (24% ammonia, 76% water). Vaporisation continues until all of the mixture reaches a dry saturated vapour state at Pt. 5 (62°C). The dissimilar volatilities of the components cause the boiling to span a range between the bubble point and dew point temperature (temperature glide Pt. 1 to Pt. 5). A properly selected temperature glide, which is relative to both the composition and pressure, produces a better temperature match to a finite thermal source, increasing average heat addition temperature and reducing heat exchanger irreversibilities. Furthermore, in the condenser, due to having an increased average heat rejection temperature, the blend has a larger heat transfer driving force to achieve the same condensation exit temperature.

Azeotropic blends on the other hand are those in which both dew point and bubble point curves are touching each other at least at a single point indicating the same composition in the vapour and liquid phases. Fig. 6.38b shows the 3-Methyl-1-Butanol and water HPA at 1 bar with 47% water content. During vaporisation, an azeotropic blend behaves as a pure fluid, the compositions of the vapour and the liquid remain essentially unchanged. Outside of the two-phase region, zeotropic blends, azeotropic blends and pure fluids behave similarly. To distinguish the type of blends in this section, note that multiples of 25% as weight fraction are zeotropes, while other concentrations are azeotropes.

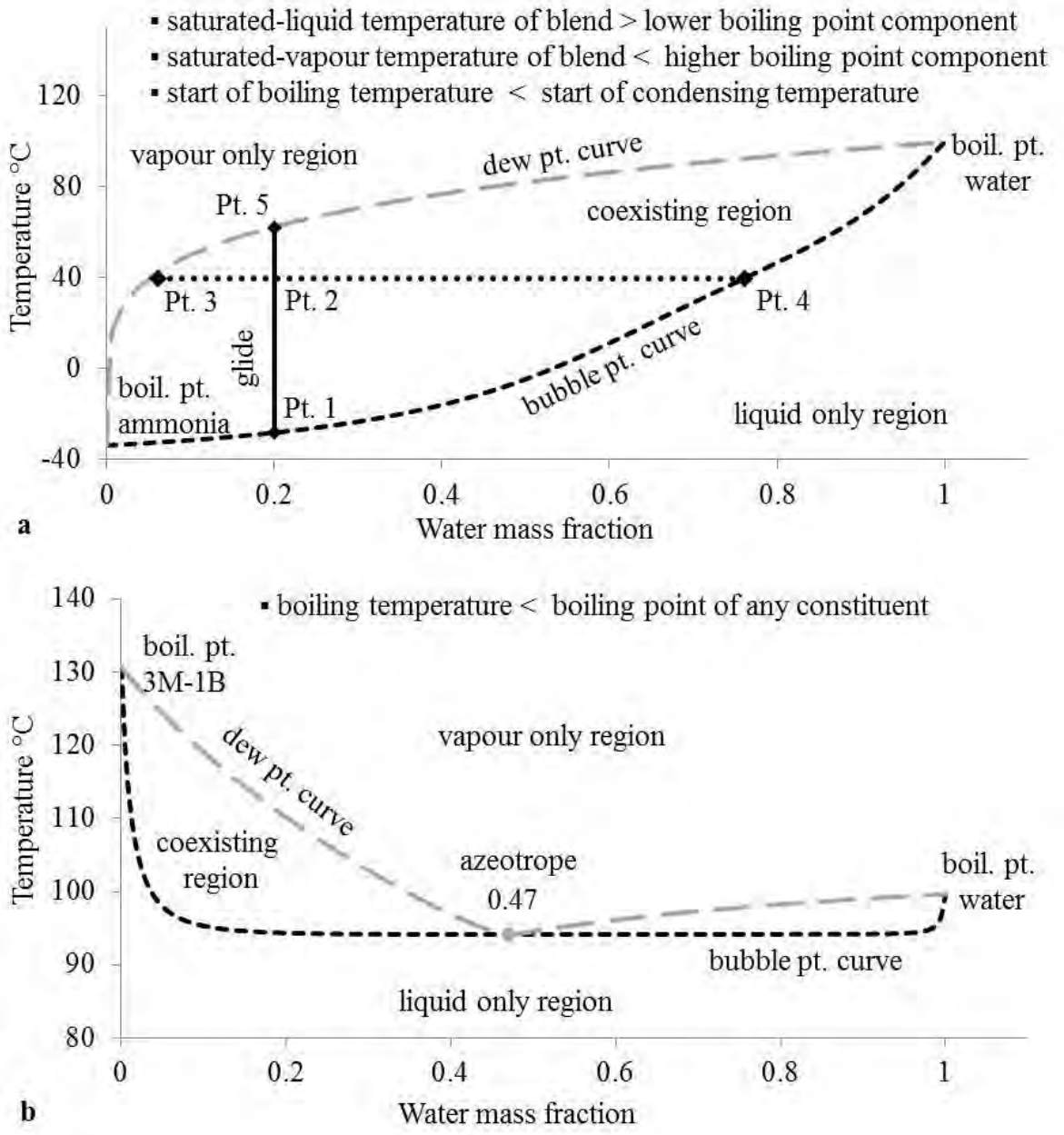

Figure 6.38 Temperature vs. concentration and key attributes of (a) zeotropic ammonia and water blend (b) azeotropic 3Methyl-1Butanol and water blend

6.7.1.2 Performance and sizing results

Fig. 6.39a shows the net power and UA/W value results for the low water content blends in Case 4 using limited superheat expansion up to an expansion pressure ratio of 16:1. Similarly, Fig. 6.39d and g shows the results for medium and high water content blends, respectively. Firstly, for similar water content, the blends gave similar values (within 5%) for both the parameters. Therefore, the selection of a particular blend for the selected water content was more evolved than the simple net power and UA/W value results. Secondly, with increasing water content, the heat recovery, and hence, the net power reduced. The highest net power demonstrated by the low water content blends was marginally below the benchmark set by pure acetonitrile from Fig. 5.5a. While the lowest net power

demonstrated by the high water content blends was just slightly above the results of pure ethanol from Fig. 5.5a. As a result, the net power variation from low to high water content blends was ≈10%, favouring low or medium water content over high water content blends. To assess the suitability of a particular blend for the selected water content, further comparative studies were done concerning heat transfer irreversibilities, enthalpy drop, mass flow control and flash point.

6.7.1.3 Heat transfer irreversibilities

Fig. 6.39b and c compares the T-Q diagram for heat transfer irreversibilities (using LMTD as a measure) for the low water content blends. Similarly, e and f compare the medium, while h and i compare the high water content blends. For the low water content analysis, the heat exchanger LMTD was equal, while the condenser LMTD was higher for 1-Propanol72%. This implied that, for equal net power (Fig. 6.39a), both the ORCs required similar size of heat exchangers, however, 1-Propanol72% required a condenser size 8% smaller than Ethanol75%. The lack of reduction in the heat exchanger LMTD and the increase in condenser LMTD by zeotrope Ethanol75% was due to the small temperature glide of 4°C. For the high water content analysis, both the zeotropes 1-Propanol25% and Ethanol25% exhibited nearly similar heat exchanger and condenser LMTD. This was since the temperature glide difference between the two blends was still relatively small at 7°C.

The limitation of isothermal phase change in pure and azeotropic fluids, leading to relatively higher levels of heat exchanger irreversibilities, was best noticed when comparing the medium water content results. The 15°C glide shown by zeotrope Ethanol50% reduced the condenser size by 8% when compared to azeotrope 3M-1B53%. This also indicated that a temperature glide greater than 10°C was needed in Case 4 to show noticeable LMTD changes. In summary, the heat transfer irreversibility analysis showed that:

- Azeotrope 1-Propanol72% was better suited to low water content
- Zeotrope Ethanol50% was better suited to medium water content
- Either of the zeotropes 1-Propanol25% or Ethanol25% were suited to high water content

Note that, despite the phase change lines drawn linearly for zeotropes in Fig. 6.39 for simplicity, the LMTD values were based on a summation of 15 equal enthalpy intervals to minimise the numerical error.

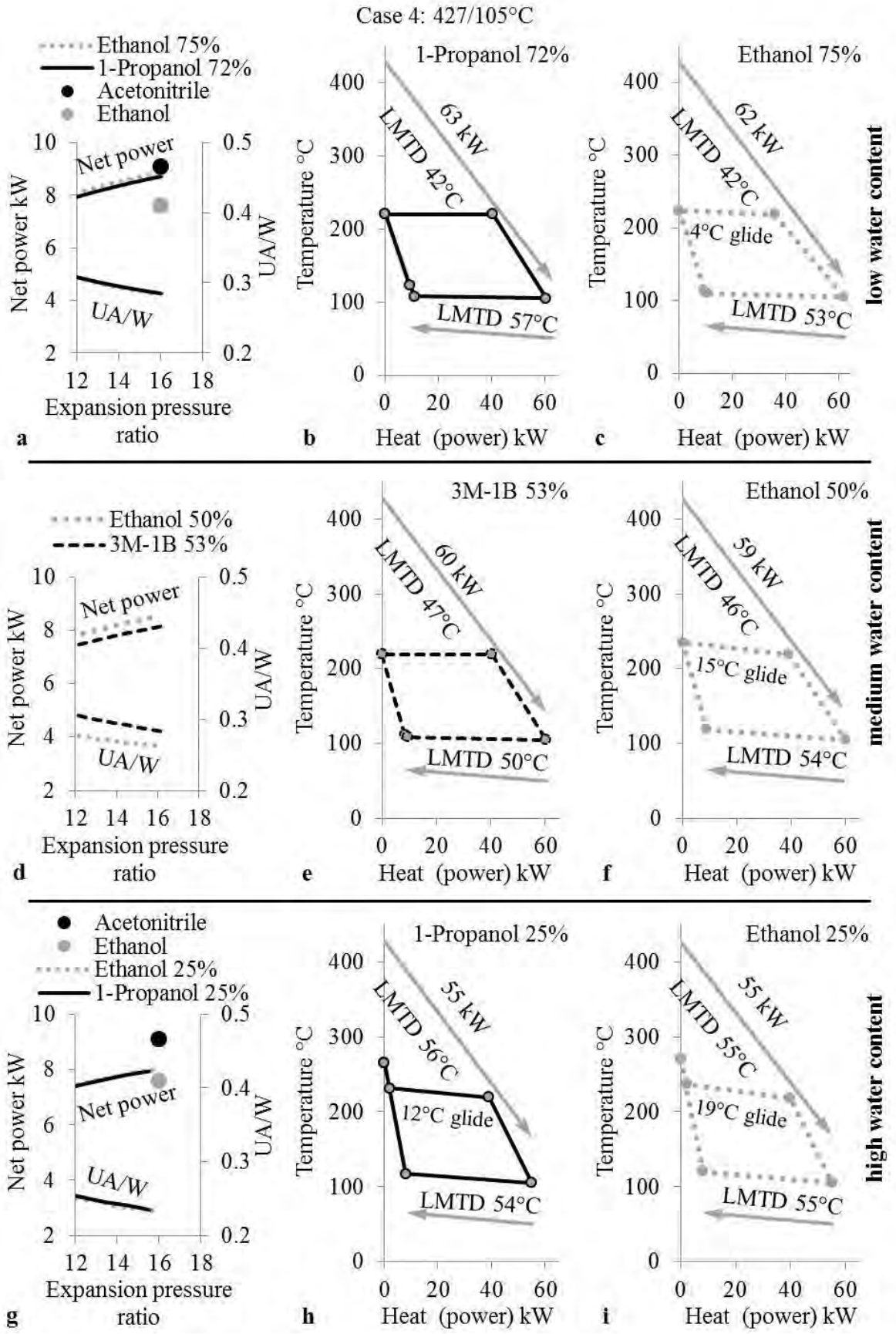

Figure 6.39 Net power, UA/W value and heat transfer irreversibilities in Case 4 for (a,b,c) low (d,e,f) medium (g,h,i) high, water content blends

6.7.1.4 Molecular weight

A new molecular screening criterion for the selection of organic blend constituents in Fig. 6.37 was the molecular weight requirement to be higher than that of ethanol. To highlight the resulting advantages of this, consider Fig. 6.40a which plots the expansion enthalpy drop and mass flow rate at the 16:1 expansion pressure ratio condition for the blends in Fig. 6.39. Also included are the values for pure water and pure ethanol at the same pressure ratio from Section 5.4.2. As can be expected, with increasing water content, the blends expansion enthalpy drop increased, while the mass flow rate decreased. This may result in higher turbine stages (also lower efficiency) and challenges in controlling the mass flow rate relative to pure ethanol. However, for the medium water content analysis, azeotrope 3M-1B53% showed a noticeable reduction in expansion enthalpy drop (Δ45 kJ/kg) over zeotrope Ethanol50%. This is due to nearly twice the molecular weight of pure 3-Methyl-1-Butanol over ethanol (88.1 vs. 46.1 g/mol). Hence, molecular weight considerations favoured azeotrope 3M-1B53%.

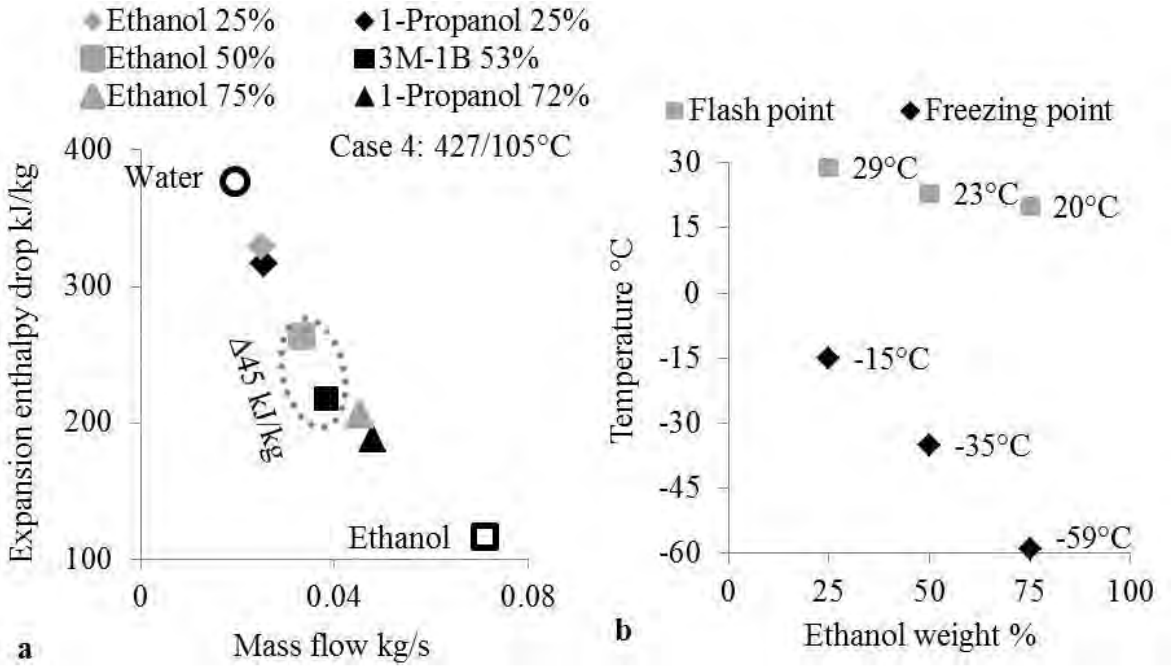

Figure 6.40 (a) effect of water content and molecular weight of the organic fluid on the blend expansion enthalpy drop and mass flow rate in Case 4 (b) freezing and flash point of ethanol-water blend with varying water content

A further new molecular screening criterion for the selection of the organic blend constituent in Fig. 6.37 was the requirement of increasing number of atoms in a molecule when mixed with increased water content. This was done to ensure that the resulting azeotropes retained the near isentropic expansion characteristics for the assumed expander efficiency (Fig. 6.39).

6.7.1.5 Freezing and decomposition

The freezing points for pure 1-Propanol, 3-Methyl-1-Butanol and ethanol are within ±6°C of −120°C. As the freezing point of ethanol-water blends are well documented (Engineering ToolBox, 2014), they were used to approximately assess the freezing point range for the considered azeotropes. Fig. 6.40b shows that medium and low water content ethanol blends are better suited since they can provide freeze protection under extreme North American cold temperatures.

Fig. 6.40b also shows the change in flash point of the water-ethanol blends. Since, ethanol and 1-Propanol have nearly similar flash point (18.5, 15°C), their respective water content blends will have a comparable flash point. Unfortunately, this will be within the warmer Mediterranean temperature limits (<30°C) even for the high water content. However, 3-Methyl-1-Butanol has a much higher flash point of 43.8°C. Assuming a similar increase in temperature from pure ethanol's flash point when mixed with 50% water, the 3M-1B53% will give a flash point of around 48°C, well suited even to hotter equatorial temperatures.

Binary blends with water as a significant component will have an improved thermal stability, as water will repress thermal decomposition. Despite the high water content blends being best suited to this parameter, the reduced net power, lower frost protection, high expansion enthalpy drop and extremely small mass flow rate were its major drawbacks. Hence, freezing point, flash point and decomposition considerations highlighted that azeotrope 3M-1B53% may provide a better trade-off.

6.7.1.6 Zeotrope challenges

The concern with zeotropic blends significant glide in practical application is that under reduced source heat in the evaporator the lower boiling point fluid will boil and float to the top entering the expander first. This may lead to the accumulation of the higher boiling point fluid, bringing challenges such as incomplete phase change (two-phase at expansion inlet) and decreased heat transfer performance. Nevertheless, since blends were formulated to recover high temperature heat, this issue can be addressed by using superheated expansion rather than dry saturated vapour expansion. The higher than usual amounts of superheat in the evaporator will ensure all the constituents are evaporated and the relative mass ratios are maintained.

A similar phenomenon is also seen in the condenser and would require higher levels of sub-cooling. However, as shown in Fig. 4.26, a 5°C increase in sub-cooling increased the condenser size by around 8%. Furthermore in practice, a truck will experience uphill/downhill terrain, and it cannot be assumed that the blend constituents will leak in their design ratio. The high temperature glide experienced in the condenser may then be a key drawback in practice and reduce the thermodynamic advantage.

The selected azeotrope 3M-1B53% or other zeotropes which are less susceptible to fractionation in the condenser and have medium water content can provide a suitable trade-off between the properties of pure water and pure ethanol. Since an azeotropic fluid functions just like a pure fluid, pure fluid design methods can be applied. Furthermore, at 1 bar the two azeotrope blends gave only 1°C temperature glide for a ±4% point variation in composition. This will simplify the servicing procedure (charging and handling) and reduce the loss in performance.

6.7.1.7 Summary: Water blends

Results presented in Fig. 4.18 thermodynamically supported water as a working fluid for source temperatures greater than 575°C. However, it was also mentioned that the working fluid selection is more evolved for source temperatures between 450-575°C due to thermal decomposition and design considerations. Fig. 6.41 evaluates the thermodynamic suitability of 3M-1B53% with increasing heat source temperature in Case 1, limited to the boundary conditions in Table 4.2. It can be noticed that, 3M-1B53% retained the advantage up to a source temperature of 550°C. With a critical temperature greater than 300°C for 3-Methyl-1-Butanol, when mixed with nearly 50% water by mass, the increased thermal stability may present the opportunity to recover heat at EGR and exhaust temperature levels.

In summary, the binary water blend study, conducted to identify azeotropes for high temperature heat recovery, identified a positive homogenous azeotrope 3M-1B53% as a suitable candidate specific to the thermal boundary conditions best matched to water and ethanol (i.e. Case 4). 1-Propanol72% was also considered as a suitable alternative despite the lower water content, since it provided higher net power. In the case of 1-Propanol72%, a stop-flow situation has to be controlled more precisely. Furthermore, for zeotropes, 1-Propanol blends were more suited over ethanol blends. This was since, both blends provided nearly equal performance and LMTD, but as it will be illustrated later, pure 1-Propanol showed a better compatibility and fluid cost compared to pure ethanol.

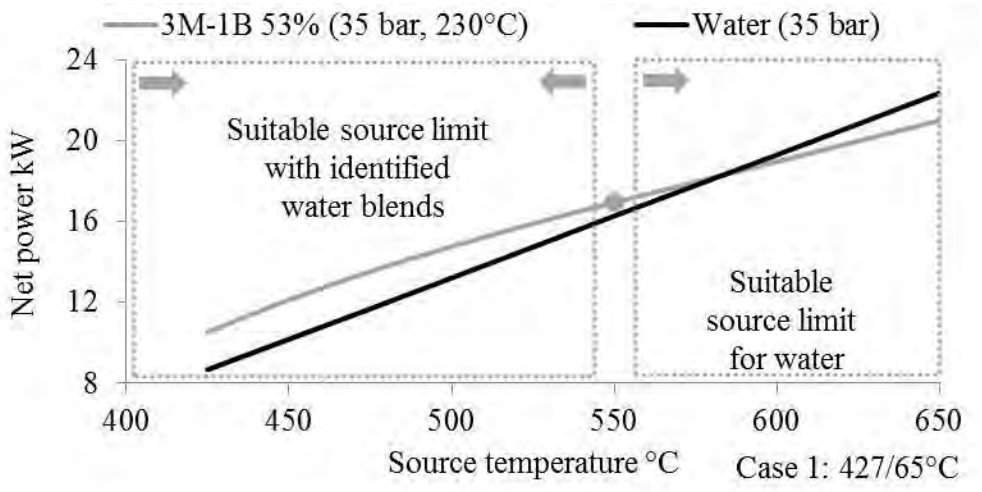

Figure 6.41 Source temperature sensitivity analysis on 3M-1B53% and water

The binary water blend study was simulated using the Wilson property package (Aspen HYSYS V 7.3, 2011a, AEA Technology, 2000). The accuracy at the azeotropic point was checked against the published literature and was within 2% point in mass composition and 1°C in temperature at 1 bar pressure. Using 3M-1B53% and 1-Propanol72% the following two process integrations are proposed as improved thermal stability solutions.

6.7.2 Process integration 9: Dual pressure system

6.7.2.1 Problem definition, system architecture, cycle operation and process optimisation

The availability of waste heat at two vastly different qualities but similar quantity levels is usually a challenge for the application of conventional ORC setups. This issue was highlighted when recovering the 'EGR + EXH parallel' heat and the 'engine block heat' in PI-4. Cascade systems like PI-6 and PI-7, which utilise independent heat recovery systems to match the specific source characteristics, provided a solution to this. The high-temperature cascade cycle allowed higher pressures for the 'EGR + EXH parallel' thermal architecture. On the other hand, the low-temperature cascade cycle provided complete engine block heat exploitation. However, losses due to the cascade condenser indicated that it was not advantageous to build a cascade system for combined heat recovery with maximum system power benefit. The drawback of the cascade condenser will also hold true for any combinations of Rankine, organic Rankine and Kalina cycles. Cascade systems may be better suited to stationary large-scale output capacity units (>100 kW), where near ambient condensing temperatures are possible. This will increase the efficiency of the low-temperature cycle and partially overcome the exergy destruction in the cascade condenser. Furthermore, as a working medium for engine cooling, pure water does not offer any freeze or corrosion protection. While R245fa presents vastly

dissimilar thermodynamic and thermo-physical properties when compared to the conventional engine coolant.

For more suitable process integration than PI-7, while exploiting high grade heat with higher cycle pressures and recovering complete engine block heat, novel PI-9 shown in Fig. 6.42a is proposed using water blends. PI-9 consists of a dual pressure level heat recovery architecture. Two pumps are utilised to generate the different subsystem pressure levels. While the expansion is either performed using two independent expansion machines or a dual pressure expansion machine (i.e. with two different pressure level inlets and one exit). The low-pressure loop was also the low-temperature loop recovering the engine block heat. Similarly, the high-pressure loop was also the high-temperature loop recovering the 'EGR + EXH parallel' heat. Since the maximum system pressure was raised in two steps, the head required per pump was relatively low. The proposed process integration was termed 'Dual pressure system'. Conceptually, PI-9 is an adaptation of the multiple pressure level, heat recovery steam generator concept, used in coal power plants (Boyce, 2010, Zheng and Furimsky, 2003).

Fig. 6.42b describes the T-S diagram for the optimal PI-9 operation using 3M-1B53% at E5-C100. The saturated liquid at 90°C was pumped by the low-pressure pump to a pressure corresponding to evaporation at 115°C and was distributed into two streams. One stream was used to recover the complete engine block heat. The other stream was raised to the highest cycle pressure by the high-pressure pump. The high pressure stream was preheated, evaporated and superheated in the 'EGR + EXH parallel' thermal architecture. The high-pressure high-temperature vapour was then expanded in the high-pressure expander (Pt. 1 to 2). The superheated working fluid stream exiting the high pressure expansion (Pt. 2) was subsequently mixed with the two-phase low pressure stream exiting the engine block (Pt. 3). The mass flow rates in the two loops were controlled to form a slightly superheated vapour after mixing of these two streams (Pt. 4). This stream was then injected into the low-pressure low-temperature expansion stage. Although, the temperature at Pt. 2 was much higher than Pt. 3, the pressure at Pt. 2 was maintained equal to the pressure at Pt. 3. The optimisation of PI-9 was only subjected to the parametric study of the high-pressure loop. This was because the low-pressure expansion inlet pressure was fixed at 2.7 and 3.2 bar for 3M-1B53% and 1-Propanol72% (i.e. corresponding to evaporation pressure at 115°C). This resulted in a low-pressure expansion ratio of 2:1 for both blends.

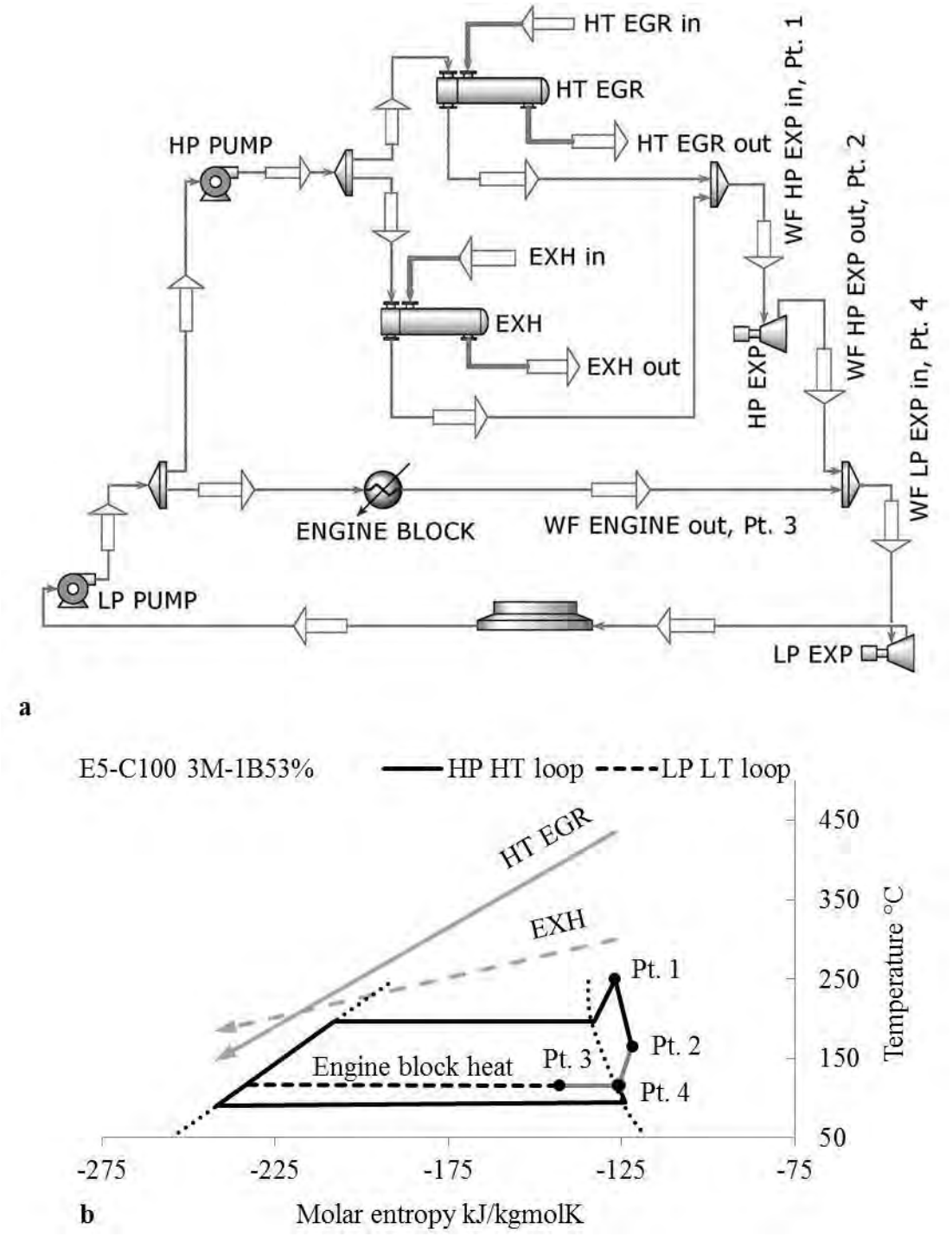

Figure 6.42 Dual pressure system (a) system architecture (b) T-S diagram using 3M-1B53%

Fig. 6.43a shows the change in the heat recovery loads, thermal efficiency and net power for PI-9 with varying high-pressure expansion pressure ratio for 3M-1B53% at E5-C100. Excluded from the graph is the constant and maximum engine block heat recovery (given in Table 6.1). Under high load conditions, the mass flow rate was controlled to maintain a slight superheating at Pt. 1, limited to a maximum working fluid temperature of 250°C. With relatively constant HT EGR heat recovery and noticeably decreasing EXH heat recovery, net power maximisation was observed at 8:1 expansion pressure ratio.

Optimisation of all high expansion pressure ratios were limited to a maximum of 8:1, since this was the limit set by the cascade system in PI-6.

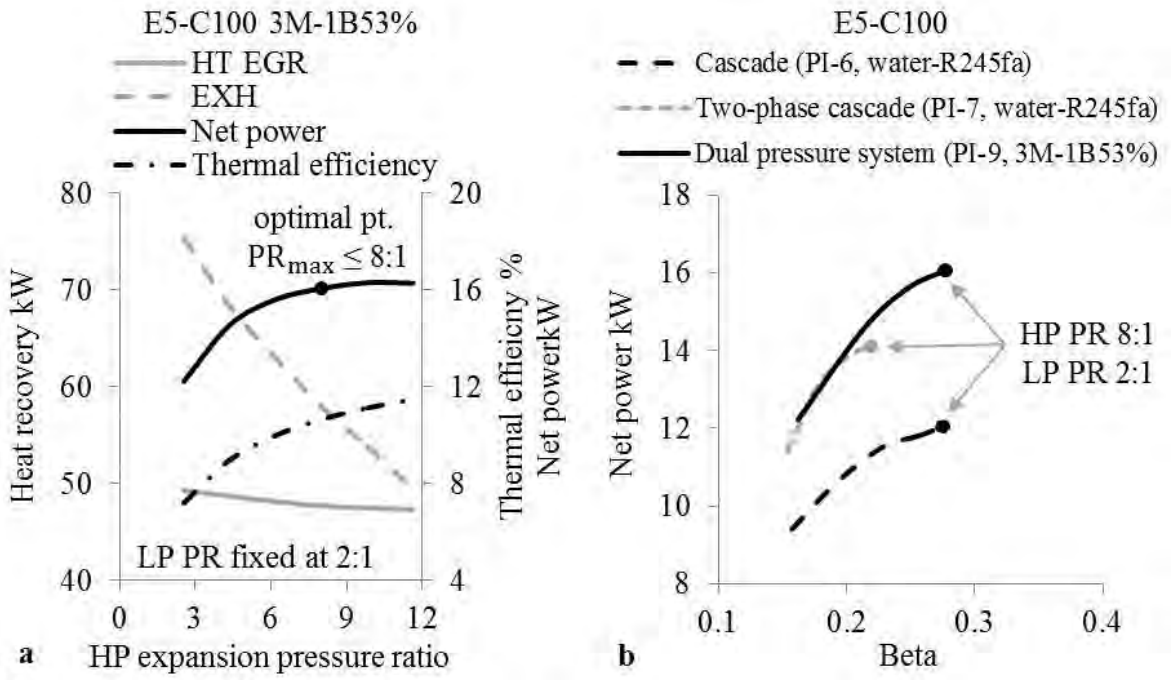

Figure 6.43 (a) PI-9 high-pressure expansion pressure ratio effect on heat recovery thermal efficiency and net power (b) baseline net power and beta value comparison

6.7.2.2 Results and discussion

Appendix 6.15 presents the optimal PI-9 results for 3M-1B53% and 1-Propanol72% at the 4 test points. As shown in Fig. 6.39, higher water content blends reduced the heat recovery and hence the net power, therefore 3M-1B53% demonstrated an average system power around 5% lower than 1-Propanol72%. Nonetheless, 3M-1B53% in PI-9 gave an average system power that was around 15% higher than PI-7 (Fig. 6.43b), i.e. two-phase cascade which was the selected benchmark comparison under high temperature thermally stable solutions. The performance advantage was because PI-9 and PI-7 on average recovered nearly equal amounts of HT EGR (90% of the available load), exhaust (65% of the available load) and engine block heat (100% of the available load). However, PI-9 excluded the losses incurred due to the cascade condenser. Due to the exclusion of the cascade condenser the UA/W value of PI-9 were on average only 40% of PI-7. Furthermore, for equal expansion pressure ratios the high β values of PI-9 were nearly equal to PI-6 (Fig. 6.43b).

Some of the key advantages and novelty of PI-9 are summarised below:

Performance: Compared to the process integrations mentioned in the published literature (i.e. PI-6, PI-7) that recover combinations of high grade heat (i.e. EGR, EXH) and engine block heat, PI-9 showed a significant level (15%) of performance improvement (Fig. 6.44) for comparable process integration complexity. Furthermore, the maximum selected blend temperature of 250°C was over 50°C lower than pure 3-Methyl-1-Butanols critical temperature. PI-9 will also be more suited over the much more complex TEG-ORC and ORC-Kalina systems reviewed in Chapter 2 (Shu et al., 2012a, Shu et al., 2012b, He et al., 2011).

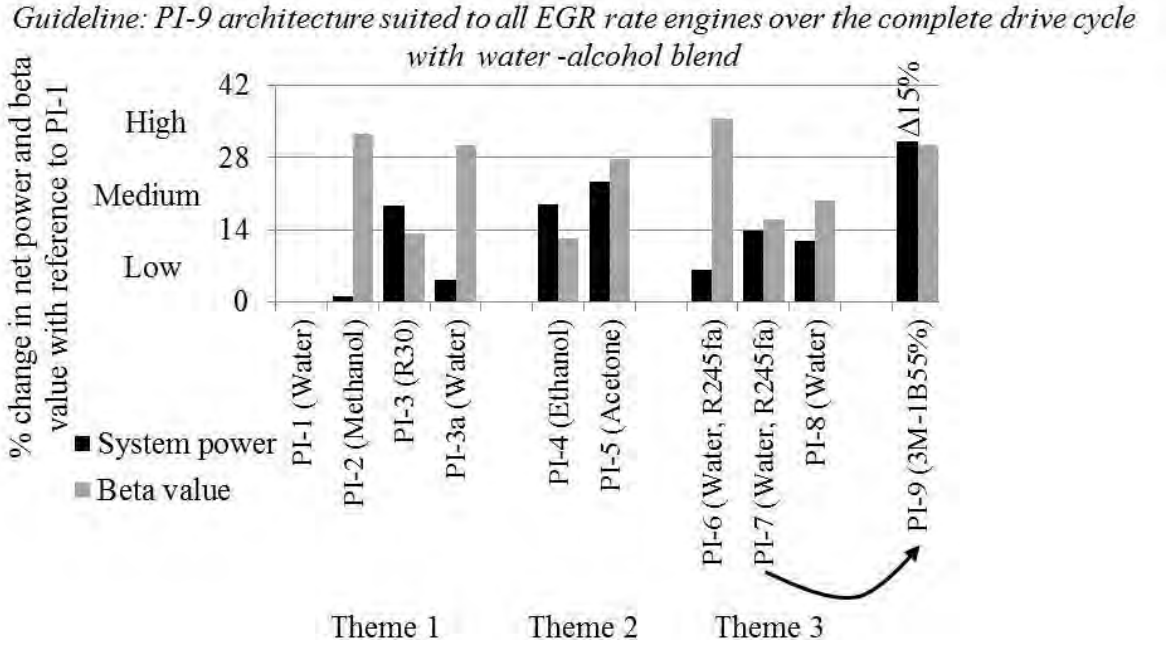

Figure 6.44 PI-9 guideline and system power/beta value change over PI-7

Engine coolant: Table 6.3 compares selected key properties of the conventional engine coolant with 3M-1B53% and fluids proposed for engine block heat recovery in the published literature. Using conventional engine coolant as a reference, it was noticed that 3M-1B53% demonstrated a higher level of suitability when compared to the alternatives. When considering density multiplied by heat capacity, as a first approximation of the fluids heat absorption capacity, 3M-1B53% displayed a higher level of similarity than R245fa or water (0.9 vs. 0.5, 1.3). This presents a favourable case for the opportunity of replacing the conventional engine cooling loop. The freezing point of 3M-1B53% will also be similar (±5°C) to the conventional engine coolant. Furthermore, since the low-pressure low-temperature loop is effectively an independent closed loop, the engine block heat recovery efficiency was 100% with PI-9.

Table 6.3 Relative comparison of key properties for potential replacement of engine coolant

	ethylene-glycol 50% and water 50%	3M-1B53%	R245fa	Water
Molecular weight M_{wt}	1	1.1	4.8	0.6
Liquid density ρ_{liq}	1	0.8	1.1	1.0
Heat capacity c_p	1	1.1	0.5	1.3
Heat of vaporisation H_{vap}	1	0.8	0.1	1.3
Surface tension γ	1	0.9	0.2	0.5
Thermal conductivity λ	1	0.5	0.2	2.0
Viscosity μ	1	0.7	0.4	0.6

Modified coolant exergy: PI-4a using water showed the highest system power of 9.8 kW at E6-B50, but this also required the coolant temperature to be raised to 200˚C. When PI-9 was compared to PI-4a architecturally, PI-9 incurred the additional complexity primarily due to the use of two expansion machines. Nonetheless, for an equal total system pressure ratio of 16:1, the added advantage of PI-9 was in the superior response of the modified coolant exergy on the system power. For this consider 1-Propanol72% at E6-B50, which delivered 8.8 kW with a coolant temperature of only 115˚C (Appendix 6.15). When this coolant temperature was raised to 130˚C, the system power increased from 8.8 to 9.8 kW, i.e. equal to PI-4a using water with a coolant temperature of 200˚C.

Superheating: Section 5.5.3 detailed that performance increased and the expansion machine size decreased using superheated expansion for fluids with diverging isobars when high heat source temperatures were available. However, the drawback included high levels of de-superheating load. PI-9 provides a partial solution to this. Under high heat source temperature level in the 'EGR + EXH parallel' thermal architecture, the superheated temperature at Pt. 1 as shown in Fig. 6.42b can be further increased. Since the liquid fraction exiting the engine block (Pt. 3) can be increased, the de-superheating drawback can be overcome when the streams are mixed (Pt. 4). Hence, PI-9 can benefit from the use of superheating and avoid the large de-superheating load in the condenser. Whereas at low heat source temperature levels, the amount of superheat at Pt. 1 can be reduced so as to retain high heat recovery in the 'EGR + EXH parallel' thermal architecture, while avoiding complete evaporation inside the engine block.

6.7.3 Process integration 10: Dual cycle system

6.7.3.1 Problem definition and baseline solution

When waste heat sources were available at two noticeably different qualities but similar quantity levels (e.g. EGR, EXH vs. engine block), the proposed PI-9, which used a dual pressure setup, was an appropriate solution. Whereas for waste heat sources that were existing at two noticeably different quality and quantity levels (e.g. EGR, EXH vs. CAC), the proposed PI-5 which used CAC for preheating was a suitable solution. In PI-5, the CAC was moved from the low-temperature radiator level (65°C) to the medium-temperature condensing level (90°C). This reduced the heat available in the CAC heat exchanger over the original level in the base engine. The shift to the 90°C condensing temperature was done since, PI-5 included HT EGR and EXH heat recovery, and only increasing the cooling capacity at the medium-temperature radiator level was judged practical. With nearly all the long-haul HDDEs being turbocharged (single or two-stage) and using cooled EGR (from 15-30%), to attain lower engine intake temperatures, higher amounts of heat have to be rejected by the low-temperature engine radiator. Considering E5 and E6 platforms at C100 (Fig. 6.3), it was noticed that CAC heat was a dominant load on the low-temperature engine radiator. Hence, process integrations that can efficiently exploit all the gaseous waste heat sources from a long-haul HDDEs are vital.

The only well documented process integration (using organic fluids) that exploits high levels of gaseous waste heat was proposed by AVL (Arunachalam et al., 2012, Hountalas and Mavropoulos, 2010, Teng et al., 2007). The architecture, reproduced in Fig. 6.45a, used a single working fluid loop with mixing and distribution performed twice. The thermal architecture consisting of two different heat recovery pressure levels was effectively an ‘EGR + EXH parallel’ preheated by a ‘LT EGR + CAC parallel’ and was termed as ‘AVL solution’. As a case study, this process integration was optimised using ethanol at E5-C100. Fig. 6.45b describes the cycle T-S diagram with the maximum thermal and pressure boundary conditions given in Table 6.2 to provide a value for comparison.

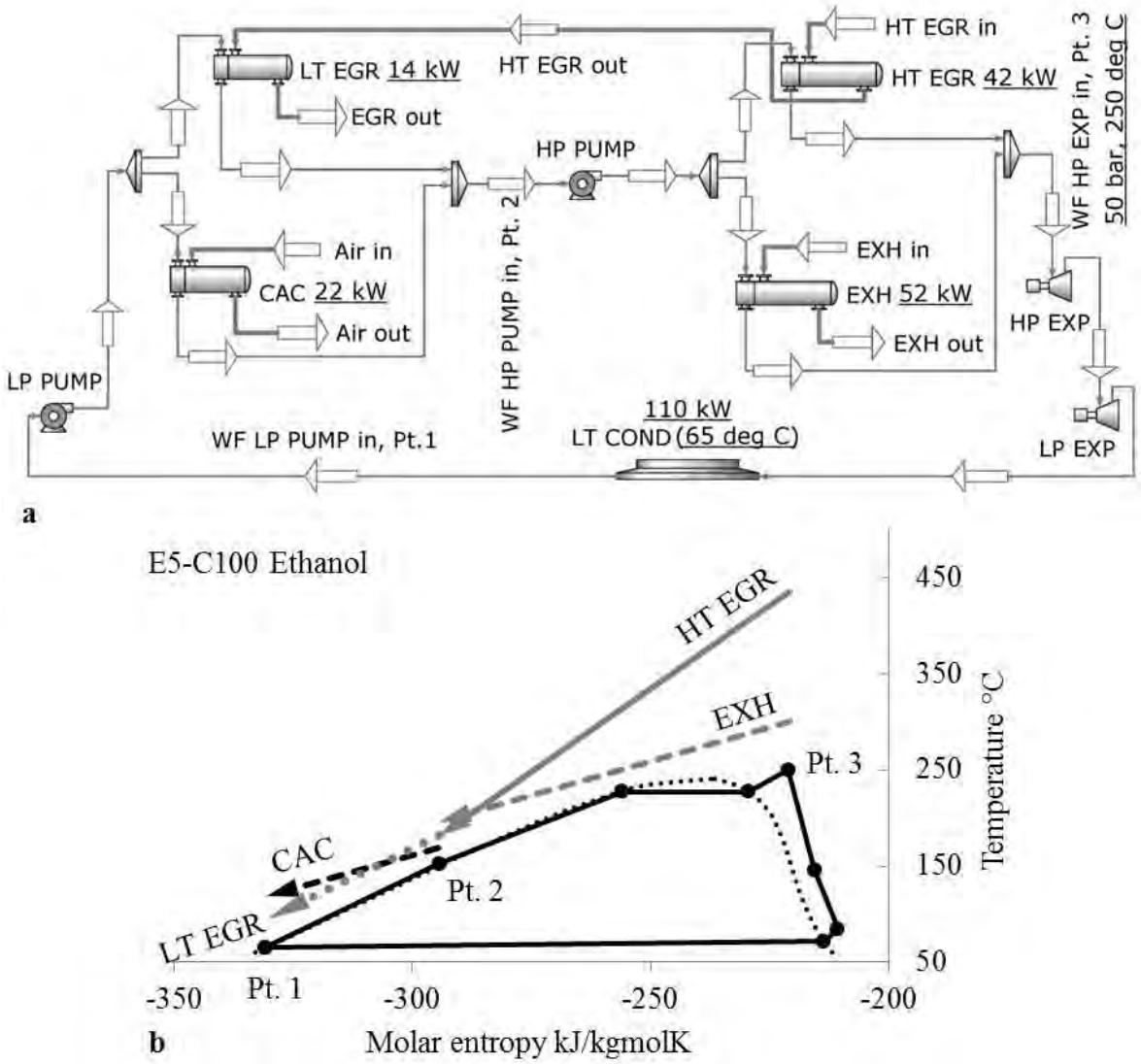

Figure 6.45 AVL solution (a) system architecture (b) T-S diagram using ethanol

Fig. 6.46 shows the change in the heat recovery loads, net power and thermal efficiency with increasing cycle pressure for ethanol at E5-C100. The lowest condensing temperature of 65°C was selected at Pt. 1 (Fig 6.45b). With increasing cycle pressure all the gaseous cooling loads remained relatively constant and maximum, while the EXH heat recovery reduced marginally (Fig 6.46a). The maximum cycle pressure was raised to the 50 bar limit and further superheating was applied to increase the temperature at Pt. 3 to 250°C (Fig. 6.45b). The total expansion pressure ratio at 50 bar was 60:1, requiring two expansion machines or a two-stage expansion machine. The net power produced by the cycle was 20.5 kW (Fig 6.46b).

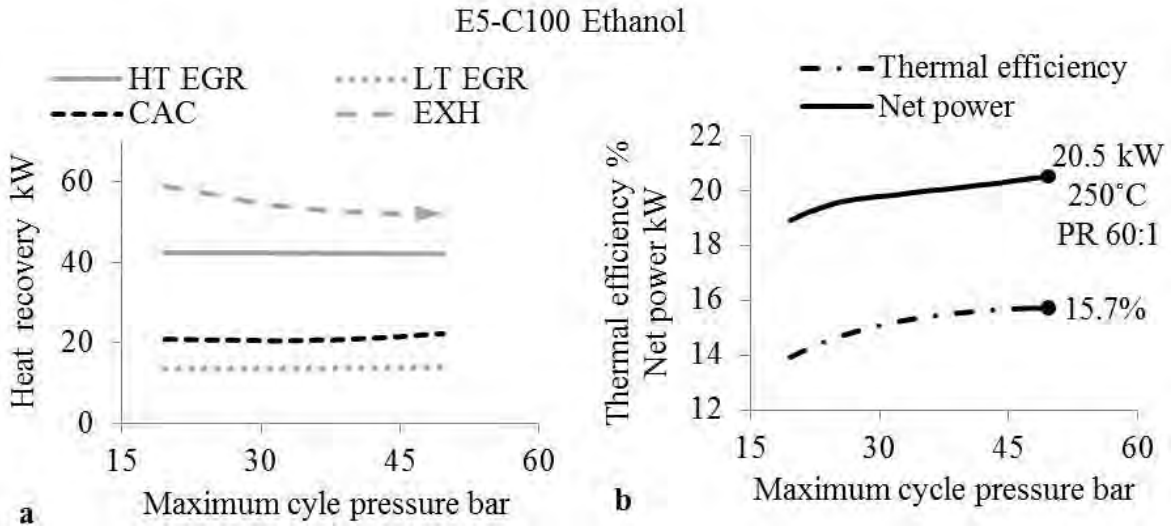

Figure 6.46 AVL solution maximum cycle pressure effect on (a) heat recovery (b) thermal efficiency and net power

The AVL solution overcame the drawbacks of incomplete utilisation of CAC heat and no utilisation of the LT EGR heat over PI-5. This process integration also presented the advantages of using stainless steel tubes only for the LT EGR heat exchanger and using low pressure heat exchangers for the low pressure section. However, in order to increase the low temperature heat recovery, the drawbacks included reducing the cycle condensing temperature to 65˚C. Fig. 6.45a also shows the heat loads at the 50 bar and 250°C operating condition. Since the entire HT EGR heat load and the 52 kW EXH heat load were transferred to the low-temperature condenser, the net load at the low-temperature engine cooling module in Fig. 6.3a increased by 84 kW, i.e. HT EGR (Fig. 6.3a) + EXH (Fig. 6.45a) – Net power (Fig. 6.46b). Therefore the total load on the low-temperature engine cooling module increased from 21 to 51% of the engine shaft power, a 2.4 times increase in the relative cooling module dimension/capacity. The engine cooling modules of current long-haul trucks are already limited on performance/size due to packaging and styling constraints. Hence, a further incremental demand on the engine cooling module due to WHR needs to be managed more effectively. Furthermore, operationally, the AVL solution has the added challenge of ensuring preheated but only liquid entering the high-pressure pump with transient conditions over the entire drive cycle.

6.7.3.2 System architecture, cycle operation and process optimisation

This section proposes a novel process integration (PI-10) using a dual cycle system (Fig. 6.47a). The high-temperature cycle employed the same architecture as PI-3 i.e. ‘EGR + EXH parallel’, whereas the low-temperature cycle employed the ‘LT EGR + CAC parallel’ thermal architecture. The low-temperature cycle was cooled by the 20˚C ambient

air and condensed at 65˚C (Fig. 6.47a). The air temperature increased by 15˚C over that of the low-temperature condenser. The high-temperature cycle was then cooled by this warmer 35˚C air and condensed at 90˚C (Fig. 6.47a). The high-temperature cycle utilised a high boiling point water blend that underwent dry saturated vapour expansion (Pt. 1, Fig. 6.47b), whereas the low-temperature cycle underwent liquid expansion using a low boiling point, low GWP refrigerant (Pt. 3, Fig. 6.47c). The dual cycles were connected by the EGR stream (Pt. 2, Fig. 6.47a). When comparing the total number of hardware, PI-10 required an equal number of heat exchangers (4), pumps (2), expanders (2) and 3-way flow distribution valves (2) to the AVL solution. Although PI-10 required one additional condenser, as it will be detailed, the combined condenser sizing highly favoured PI-10. Therefore, using the proposed integration the HT EGR heat exchanger along with the EXH heat exchanger was condensed in the high-temperature condenser. While the entire low-temperature engine radiator cooling loop (Fig. 6.2) was replaced with the low-temperature cycle along with the addition of a liquid expander.

Process integrations involving dual cycle setups have to operate under the best combined thermodynamic conditions to achieve optimal system integration. The optimisation of the high-temperature cycle was based on the high pressure variation and was similar to PI-3 (Fig. 6.12) limited to the 16:1 pressure ratio. While, Fig. 6.48a, b and c shows the thermal efficiency, net power and change in the heat recovery loads, respectively, for PI-10 with varying low-temperature cycle pressure at E5-C100. The high and low-temperature cycle working fluids used were 3M-1B53% and E152a. As the maximum pressure of the high-temperature cycle was optimised and fixed, the high-temperature cycle thermal efficiency was constant (Fig. 6.48a). With increasing low-temperature cycle pressure, the low-temperature cycle thermal efficiency and the combined cycle thermal efficiency increased (Fig. 6.48a). As the thermal efficiency of the low-temperature cycle increased, the net power produced by the low-temperature cycle and the combined cycle increased (Fig. 6.48b). Since the load on the low-temperature condenser decreased, this allowed an added advantage of transferring higher amounts of heat load to LT EGR from the HT EGR (Fig. 6.48c). By controlling the temperature at Pt. 2 (Fig. 6.47a), the net load on the low-temperature condenser did not change compared to the base low-temperature engine radiator. The liquid expansion volume flow ratio was limited to a maximum of 16:1, corresponding to the maximum low-temperature cycle pressure of 28 bar, and giving a maximum pressure ratio of only 3.3:1

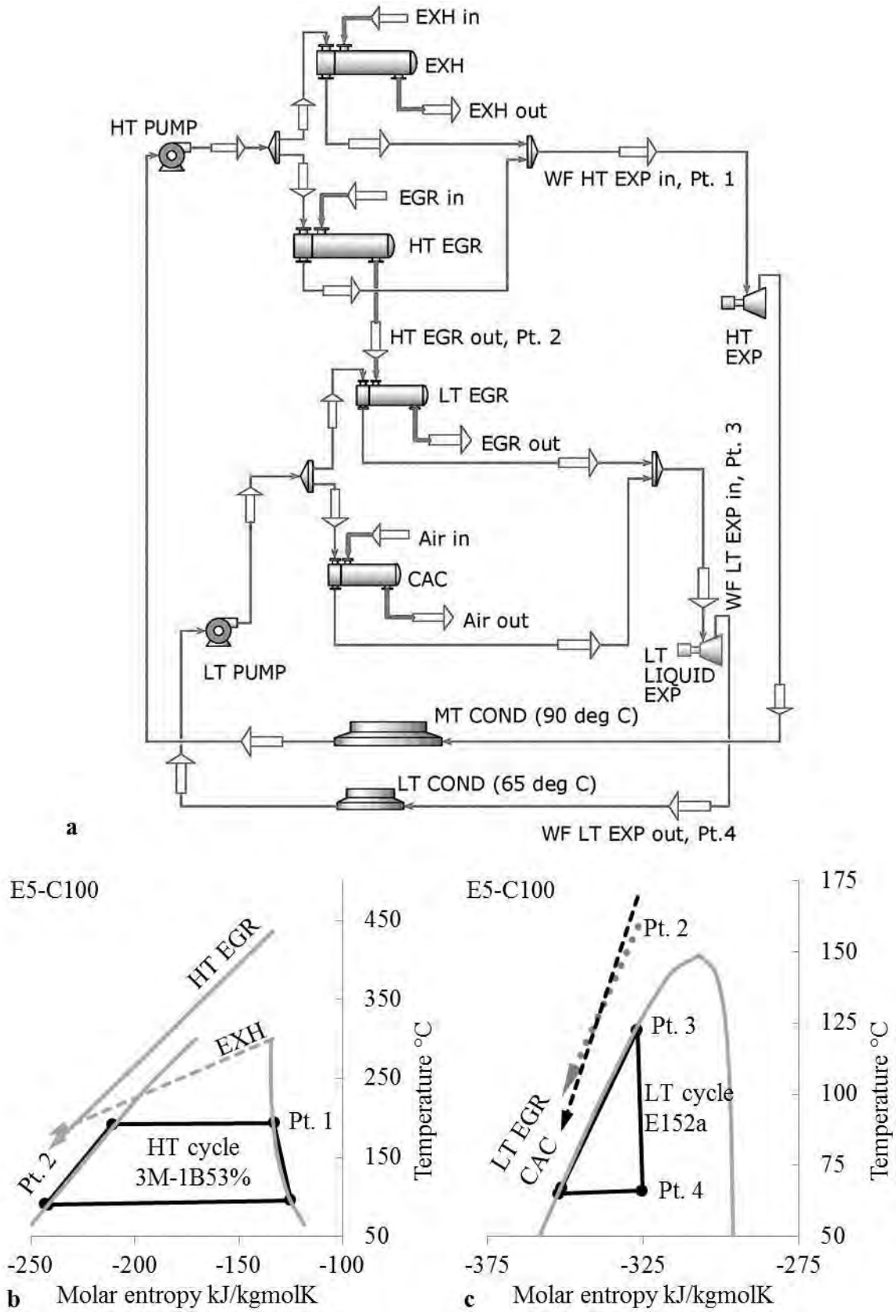

Figure 6.47 Dual cycle system (a) system architecture (b,c) T-S diagram using 3M-1B53%(HT)-E152a(LT)

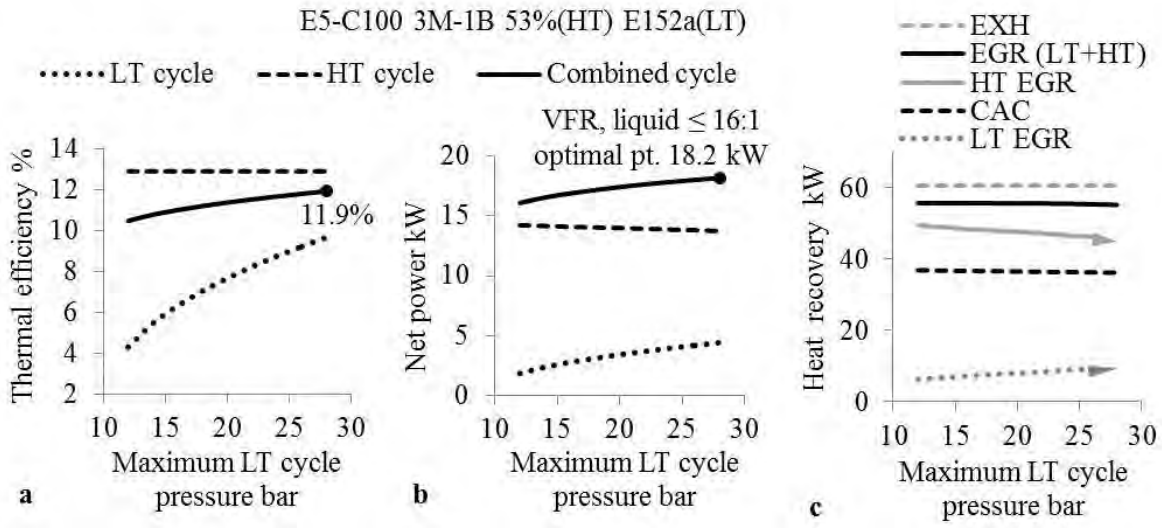

Figure 6.48 PI-10 maximum low-temperature cycle pressure effect on (a) thermal efficiency (b) net power (c) heat recovery

6.7.3.3 Results and discussion

Appendix 6.16 presents the optimal PI-10 results for 3M-1B53% and 1-Propanol72% in combination with E152a at the 4 test points. The dual cycle system recovered nearly 100% of the EGR and CAC heat loads. Both the low-temperature and the high-temperature cycles demonstrated relatively high average thermal efficiencies (≈9, ≈13%) despite the low maximum working fluid temperatures (<125, <200˚C). When comparing the high-temperature cycle in PI-10 to the equal counterpart PI-3, it was noticed that for equal pressure ratios, the average system power of the high-temperature cycle ($\dot{W}_{net}\ HT - \dot{W}_{BP+fan}$) was nearly equal to that of ethanol in PI-3. Hence, when high pressure ratio expansion machines are available PI-3 will perform equally well with the considered water blends. However, the added advantage of the dual cycle system came from the efficient use of the low temperature sources. The low-temperature liquid expansion cycle increased the combined system power by 25% on average over PI-3 using ethanol. Furthermore, the average net power of the low-temperature liquid expansion cycle (3.3 kW) corresponded closely to the on-board electrical demands of a long-haul truck (Espinosa et al., 2010, Cooper et al., 2009).

Some of the key advantages and novelty of PI-10 are summarised below:

Vehicle integration: PI-10 offered high utilisation of the present gaseous thermal loads on the engine cooling module and recovered only high quality EXH heat. This was achieved firstly by, dividing the system into two integrated loops (connected by EGR stream) based on the temperature range of the available heat sources, and secondly, by employing the

series condensing approach. Both these methods mirrored the conventional engine cooling module and provided low temperature at engine intake.

Low grade heat utilisation: PI-10 minimised the heat transfer irreversibilities using appropriate working fluids with suitable cycle operating modes. This was most evident with the low-temperature cycle, which utilised liquid expansion, giving an almost parallel temperature match for higher overall conversion efficiency at low source temperature (Fig. 6.47c). Furthermore, the use of the low GWP (110 years) HFE (E152a) ensures a compact liquid expander (PR 3.3:1, VFR 16:1) without sacrificing the expansion efficiency.

Fluid thermal stability: PI-10 addressed the selection of the working fluid also from a catalysis perspective. The nearly 50% water content in the high-temperature loop boded well for high temperature heat recovery, whereas the pure refrigerant low-temperature loop experienced source temperatures less than 200˚C.

Process optimisation: The temperature at Pt. 2 (Fig. 6.47a) can also be controlled in response to changes in the engine speeds/loads and ambient conditions. Contrary to the zero change in the low-temperature condenser load strategy in Fig. 6.48c, under low-speed high-load engine condition on a hot day, the load on the low-temperature condenser can be reduced from the original level. Inversely, the low-temperature condenser load can also be increased at cruise-speed mid-load with lower ambient temperatures. Hence, the combined waste heat recovery and engine power output can be re-optimised within the possible limits of the engine cooling module capacity.

Benefit vs. impact: Cascade system PI-6 offered the benefit of a high temperature solution with a low negative impact on the engine cooling module, whereas the AVL solution offered the advantage of high net power using a single fluid and one condenser. With a similar complexity level among PI-6, AVL solution and PI-10, Fig. 6.49 compares the net power benefit vs. the increased load impact on the engine cooling module at E5-C100. PI-10 offered a 4 kW higher net power than PI-6 for only 10 kW increase in the heat rejection load. Although the PI-10 net power was 2.3 kW lower than the AVL solution, it was also at a 41 kW lower heat rejection load.

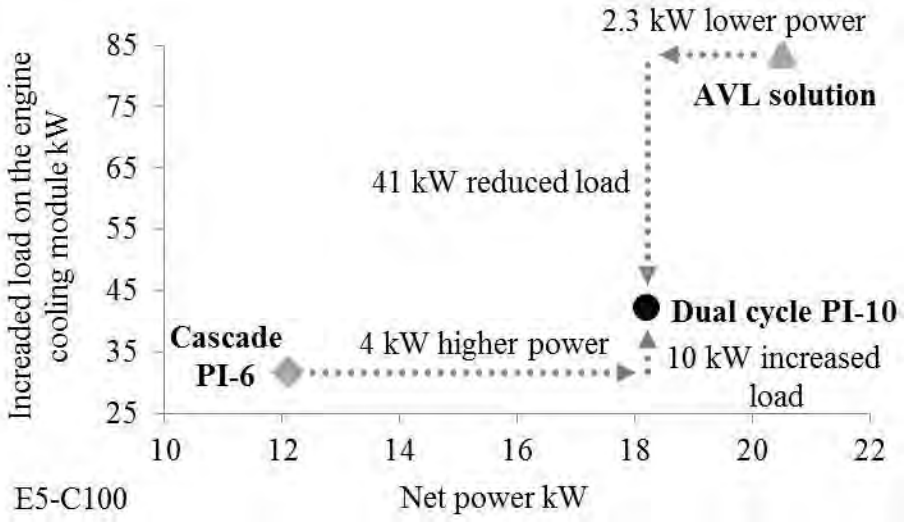

Figure 6.49 Baseline performance benefit and cooling impact comparison

It is important to stress that the increased heat rejection load by PI-6 and PI-10 were at the medium-temperature condensing level (90˚C), whereas the increased heat rejection load for the AVL solution was at the low-temperature condensing level (65˚C). Therefore compared to the 2.4 times increased relative module load at the low-temperature level by the AVL solution, PI-10 increased the relative module load firstly, at the high-temperature level, and secondly, by only 1.4 times. Hence, PI-10 was the only conceivable process integration ensuring efficient heat to power conversion for combined high and low temperature gaseous heat sources. In summary, innovative working fluids, approaches in heat recovery and power generation as offered by PI-9 and PI-10 resulted in the combined highest system power and beta value (Fig. 6.50).

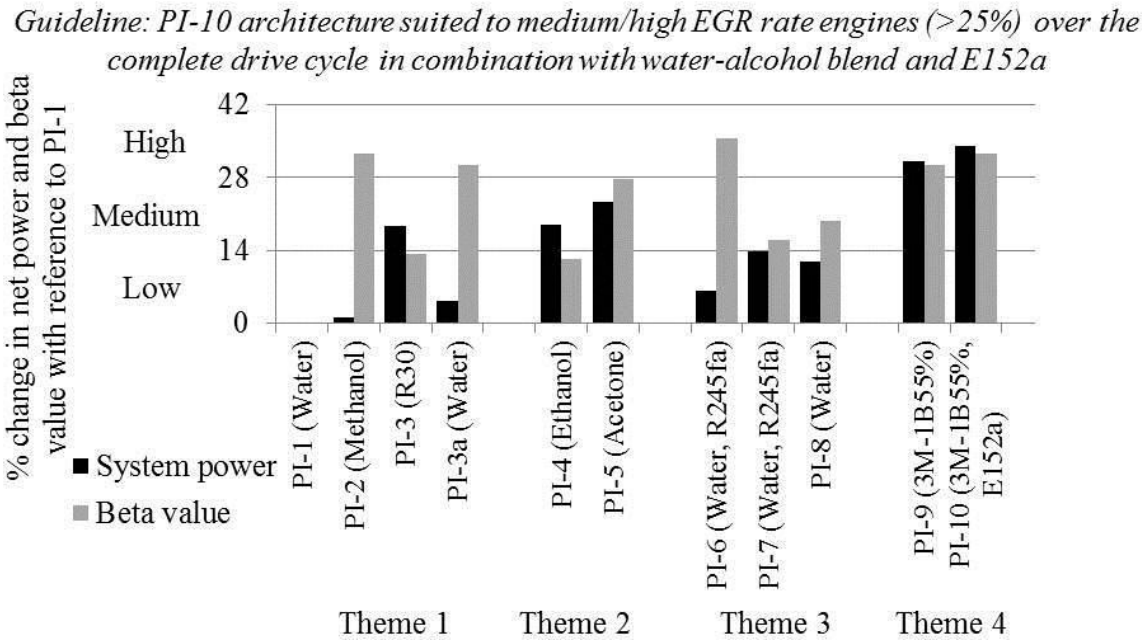

Figure 6.50 PI-10 application guideline and system power/beta value benefits

6.8 Theme 5 - Improved thermal stability solutions using organic fluids

This section considers the final theme of process integration that offer improved thermal stability solutions. This is addressed while retaining organic fluids as the working medium (i.e. theme 5, Fig. 6.27). This approach was discussed in the published literature using two avenues, firstly by using a thermal oil loop (Shu et al., 2013), and secondly by using higher thermal stability fluids. However, due to the thermodynamic, size and cost considerations (refer Appendix 6.17), the thermal oil loop approach was excluded as a potential solution.

6.8.1 Higher thermal stability organic fluids

For the higher thermal stability fluid approach, Appendix 6.18 lists the six well known organic fluids that were associated with a stability range of 300-400˚C (Fernández et al., 2011, Dimian and Bildea, 2008). These fluids failed the screening criteria in Chapter 4 primarily due to their relatively higher boiling points and high number of atoms in a molecule. Fig. 6.51 details the dry saturated expansion net power results for these fluids in Case 4 as a point of reference for further discussion. Since these six fluids are extremely drying, they were simulated using an IHE. The highest net power was recorded by m-Xylene. Fig. 6.51 also includes the results of ethanol using an IHE from Section 5.6.2, this is because ethanol's thermal stability data was within the range considered. When compared to ethanol, m-Xylene failed to provide a favourable case. The use of an IHE has the benefit of reduced condenser size. However, it also introduces additional hardware and associated complexity. The case for the use of a cycle with an IHE will be compelling only when a noticeable level of performance improvement is possible over ethanol.

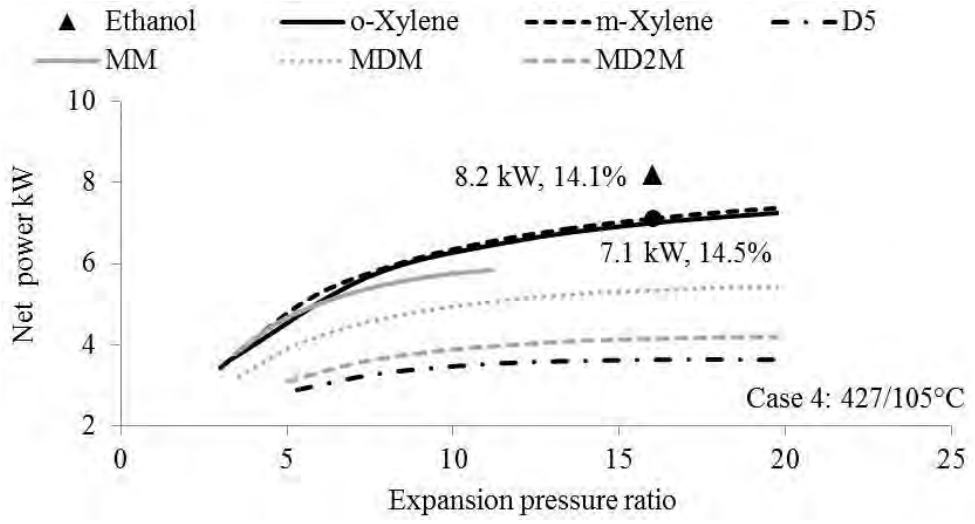

Figure 6.51 Effect of expansion pressure ratio on net power in Case 4 for high thermal stability organic fluids

6.8.2 Overview of the organic blend study

Since both the published approaches to offer a higher thermally stable solution using organic fluids failed to provide a suitable result, a third avenue was explored, i.e. formulating a higher stability binary organic fluid blend. To screen the list of over 700 documented organic blends with known thermally stable fluids as a noticeable blend constituent (DDBST, accessed on 10.10.2014, Ponton, 2007, Lide and Kehiaian, 1994, Horsley, 1973), the developed criteria shown in Fig. 6.52 was used. The primary objective was to ensure firstly, a blend thermal stability greater than 350˚C, and secondly, an HPA pressure swing behaviour.

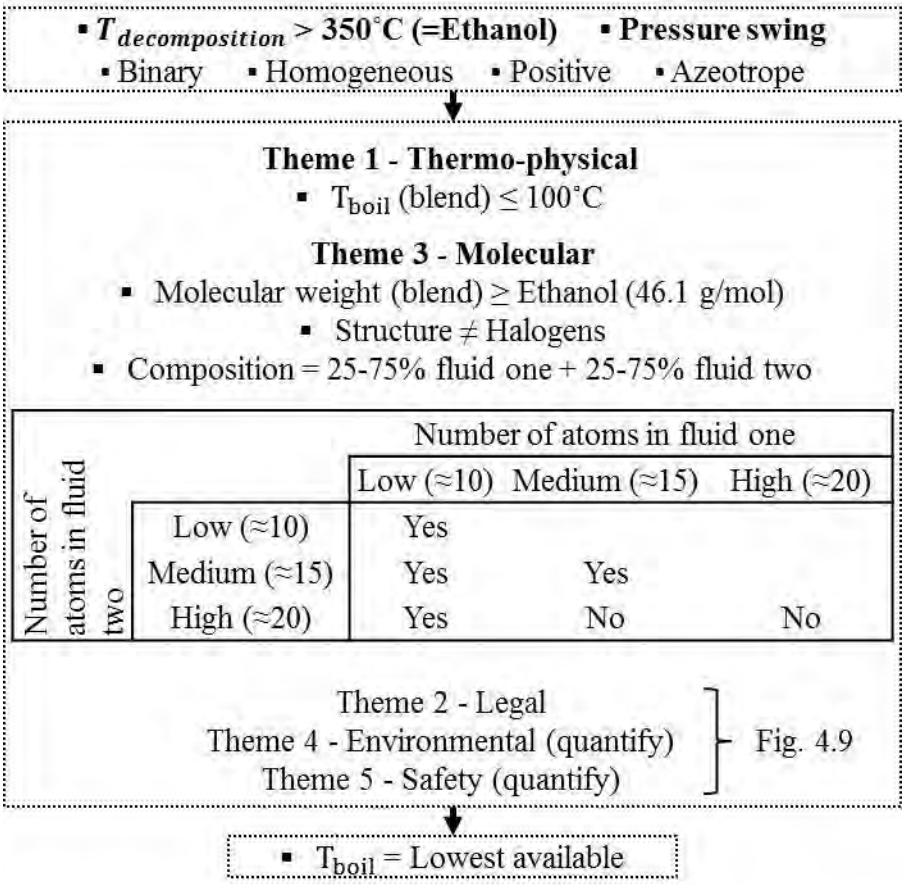

Figure 6.52 Screening method overview of the improved thermal stability organic blend study

A pressure swing azeotrope is one in which the composition at which the azeotrope occurs changes with the pressure chosen for phase change of the blend. For the new criterion of pressure swing azeotrope, consider the three T-S sketches of hypothetical isentropic fluid blends with equal latent heat, evaporator inlet and condenser exit temperatures in Fig. 6.53. As it can be noticed, option 3 representing a pressure swing blend, behaves as azeotrope in the condenser and zeotrope in the evaporator. The temperature glide observed in the evaporator increases the average heat addition temperature. Furthermore, the pure fluid

behaviour in the condenser provides the lowest average condensing temperature. Hence, pressure swing azeotropes give higher thermal efficiency when compared to azeotropic or zeotropic fluid blends.

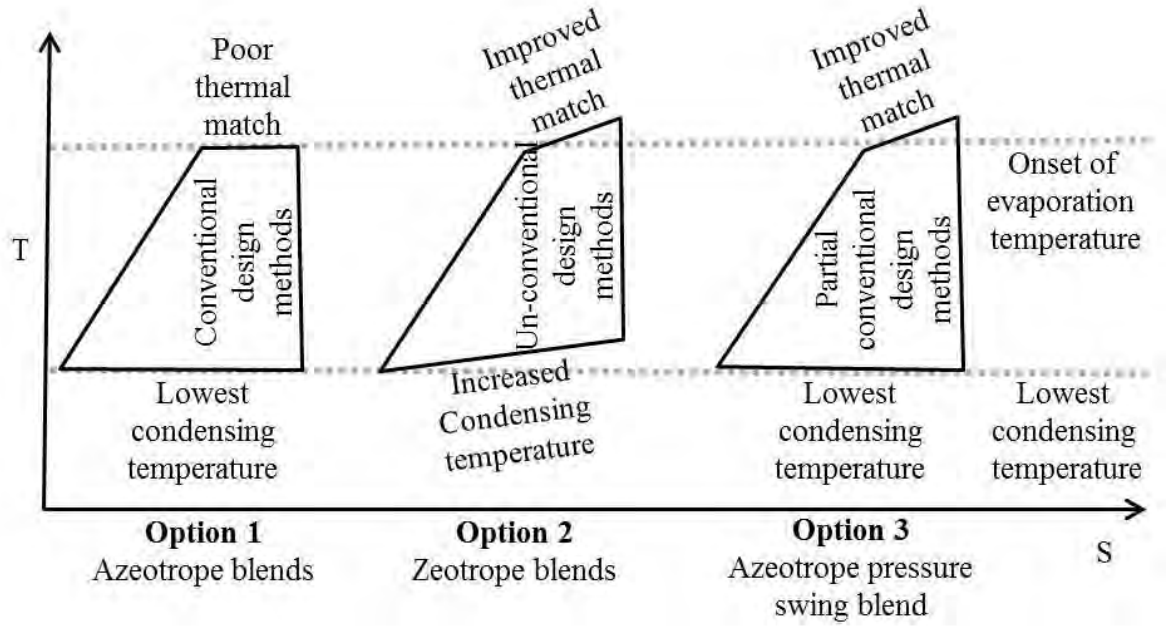

Figure 6.53 Comparative T-S sketches for 3 types of binary blends

The environmental, safety and legal criteria used to select both the organic fluid blend constituents were the same as those used to select the pure organic fluids in Chapter 4. The screening result, limited to the selection of just one blend that demonstrated the lowest boiling point resulted in the formulation of a novel blend with 65% Ethanol and 35% Toluene (referred as ET65/35). For chemical identification, thermodynamic/ thermo-physical and environmental/safety properties of pure toluene, refer to Appendix 6.13. The screening results of the more commonly known 40 improved thermal stability organic blends are documented in Appendix 6.19.

Only limited cited HDDE publications considered toluene, while none recommended it as a suitable working fluid. The thermodynamic reasons for this can be linked to the higher boiling point of 111˚C and the large IHE size due to the extremely drying behaviour (Fig. 4.12d). However, as it will be shown, the drawbacks of pure toluene were successfully addressed with the formulated blend. Furthermore, the formulated blend was favourable over pure ethanol since, pure toluene has a noticeably higher: stability temperature (400 vs. 350˚C) (Buijtenen, 2011, Marciniak et al., 1981), auto-ignition temperature (480 vs. 363˚C) and molecular weight (92.1 vs. 46.1 g/mol).

6.8.2.1 Organic blend results and discussion

Fig. 6.54a compares the net power results for ET65/35, m-Xylene and ethanol in Case 4. ET65/35 provided a combined 10% improvement in net power and thermal efficiency over ethanol at an equal expansion pressure ratio of 16:1. As a result, ET65/35 net power was equal to the benchmark set by acetonitrile (Fig. 5.5a), whose thermal stability limit was unavailable, but was expected to be lower. Note that ethanol's maximum temperature was 290°C, contrary to 250°C for ET65/35. When ET65/35 was superheated to 290°C, the thermal efficiency improvement was 20% (16.9 vs. 14.1%).

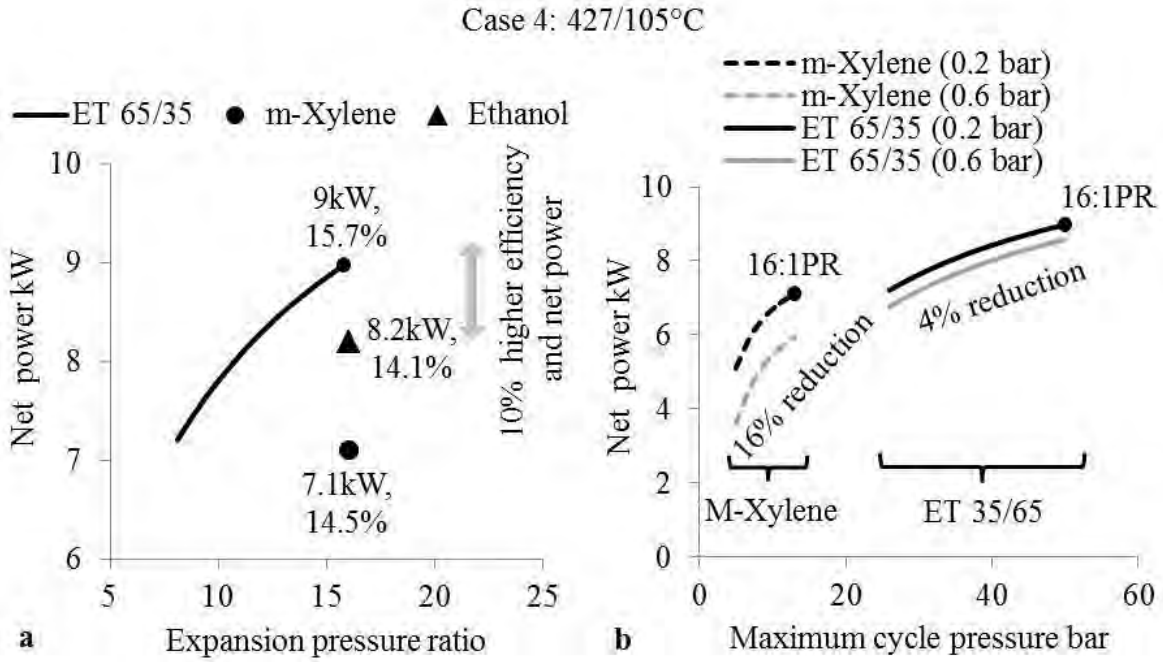

Figure 6.54 (a) performance comparison between ET65/35, m-Xylene and ethanol (b) IHE pressure drop sensitivity comparison between ET65/35 and m-Xylene, in Case 4

Fig. 6.55a and b shows the T-S diagram at the 16:1 pressure ratio condition for m-Xylene and ET65/35, respectively. It is important to highlight that the higher thermal efficiency by ET65/35 was despite recovering higher amounts of lower grade waste heat (156 vs. 206˚C) whilst having a lower IHE duty (6.5 vs. 16 kW). The lower IHE duty, which was only 12% of the total source heat used, was a valuable advantage since it resulted in a compact IHE. Contributing to the improved thermal efficiency was also the temperature glide demonstrated by ET65/35 in the evaporator.

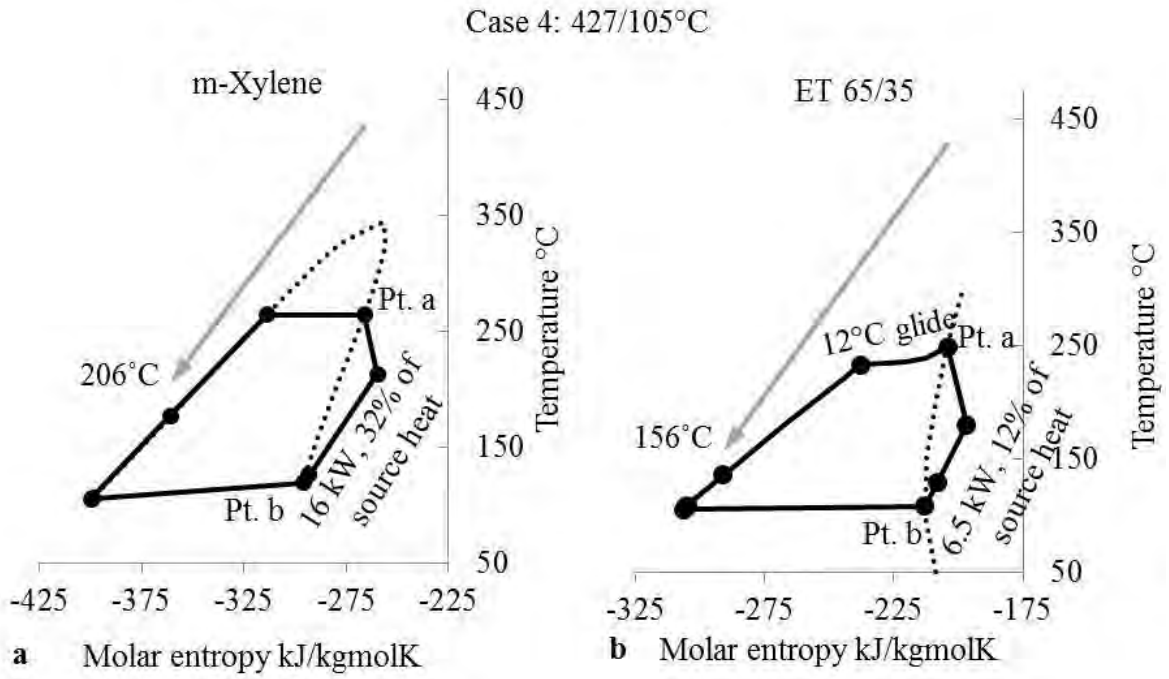

Figure 6.55 T-S diagram comparison between (a) m-Xylene and (b) ET65/35, in Case 4

The reasons for the smaller IHE duty with ET65/35 compared to a fluid like m-Xylene with a total of 18 atoms in the molecule were twofold:

- Firstly, due to the blend being formulated as a mixture of nearly 1/3rd drying (toluene) and 2/3rd slightly wetting (ethanol) fluid. This was since the number of atoms in the molecule for each of the blend constituents were screened in a new molecular screening criterion which restricted the formulation of extremely drying blends (Fig. 6.52).
- Secondly, due to a relatively unconventional saturated vapour curve of the blend (Fig. 6.55). For this, compare the saturated vapour slope of the two fluids (Pt. a to b). In the case of m-Xylene the slope is positive, whereas for ET65/35, at 'Pt. a' it is positive but changes the gradient to negative at 'Pt. b', reducing the vapour load after expansion.

Like the evaporator, sensitivity of the IHE on the performance of the cycle is based on the evaluation of the two main parameters, the pinch point temperature difference and the pressure drop in the IHE. The net power produced is not dependent on the pinch point in the IHE. However, the thermal efficiency and the area required increases monotonically as the pinch point decreases. Regarding the IHE pressure drop, a high pressure drop in the vapour side of the IHE can be used as a means to avoid high expansion pressure ratios. However, this needs to be weighed against the loss in performance. With increasing pressure drop across the IHE, the net power produced reduces as the expansion enthalpy drop decreases for a fixed maximum and minimum cycle pressure. Consider Fig. 6.54b,

which shows the impact of the IHE pressure drop on the net power. All results presented using an IHE were simulated using a 20˚C pinch point and a 0.2 bar pressure drop on each side. When the 0.2 bar pressure drop was increased to 0.6 bar for a higher boiling point fluid like m-Xylene (139˚C), the net power reduced by 16%. Whereas the same increased pressure drop only had a 4% impact with ET65/35. This is since the formulated blend is an HPA and its boiling point of 76˚C is lower than both of its constituents. The IHE sensitivity as given in Fig. 6.54b also corresponds to the condenser sensitivity since the performance loss is largely governed by the change in expansion exit conditions. Hence, the high boiling point of the higher thermal stability fluids given in Appendix 6.18 was a further reason that drove the organic blend study.

The only drawback of ET65/35 over m-Xylene was the higher cycle pressure (50 vs. 15 bar) at 16:1 pressure ratio (Fig. 6.54b). Nonetheless, this pressure was similar to ethanol (50, 51 bar). The noticeably higher net power and thermal efficiency, improved decomposition temperature, compact IHE size, low sensitivity to the IHE pressure drop and super-atmospheric pressure at typical radiator temperatures made ET65/35 the most suited fluid for cycles with an IHE. Hence, the novel blend ET65/35 in conjunction with an IHE was used in the following process integrations to recover high grade heat.

6.8.3 Process integration 11 and 12: High temperature heat recovery with an IHE

6.8.3.1 System architecture, cycle operation and process optimisation

Fig. 6.56a represents PI-11 system architecture, while Fig. 6.56b shows the T-S diagram of the optimal cycle operation at E6-C100 using ET65/35. PI-11 comprises of a conventional heat recovery architecture, where the IHE load was used to preheat the working fluid prior to the ‘EGR + EXH parallel’ thermal architecture. Hence, PI-11 was termed ‘EGR + EXH parallel with IHE preheat’.

For engine cooling modules with severe packaging constraints (e.g. European trucks), an improved heat recovery architecture in the form of PI-12 shown in Fig. 6.56c is proposed. The corresponding T-S diagram of the optimal cycle operation at E6-C100 using ET65/35 is given in Fig. 6.56d. In PI-12, the entire IHE load was used solely for preheating prior to the EXH stream. PI-12 heat recovery architecture in concept is similar to PI-5 by the replacement of the CAC with an IHE. Hence, PI-12 was termed ‘EGR + IHE-EXH parallel’.

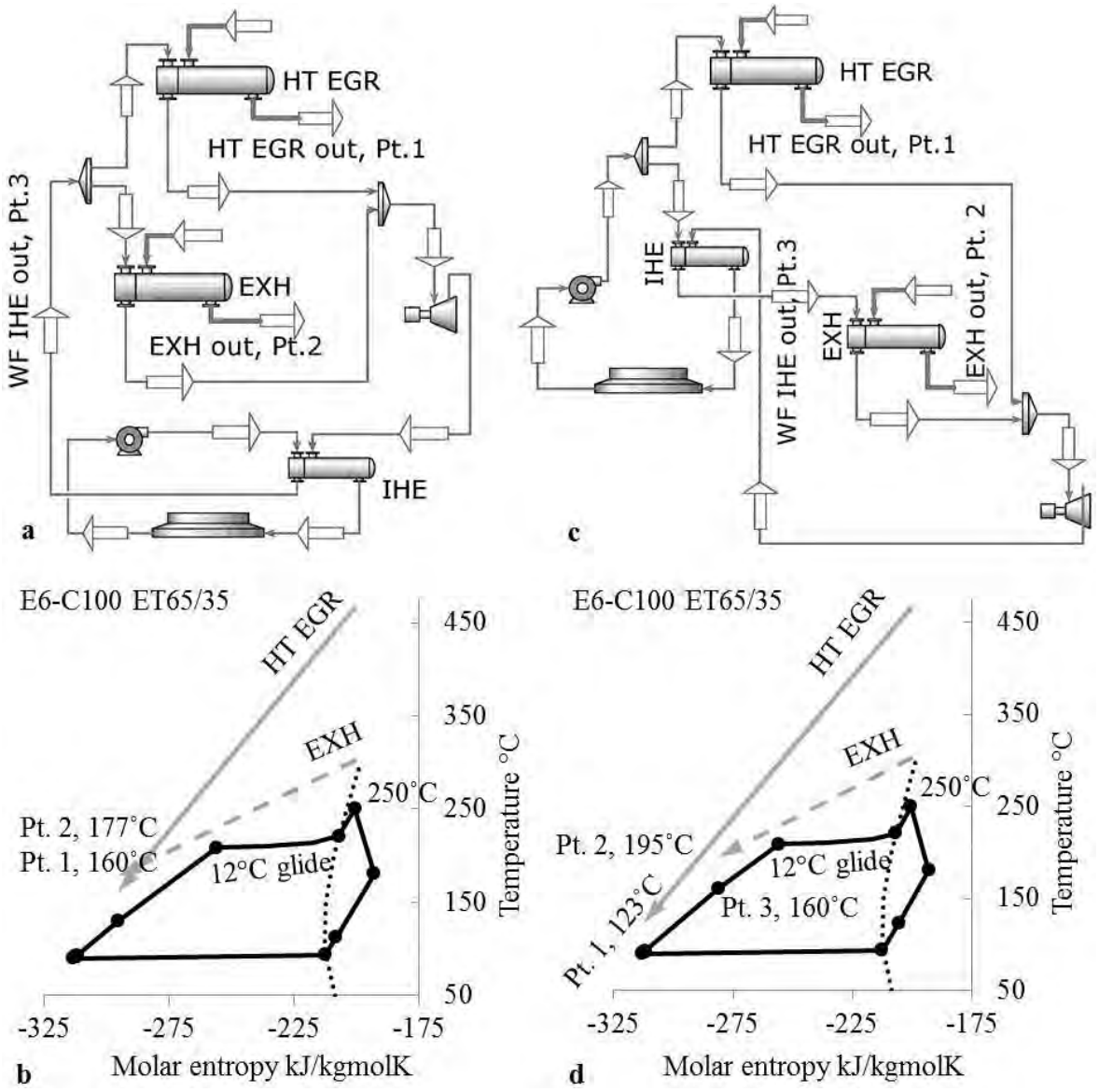

Figure 6.56 System architecture and T-S diagram using ET65/35 (a,b) PI-11, EGR + EXH parallel with IHE preheat (c,d) PI-12, EGR + IHE-EXH parallel

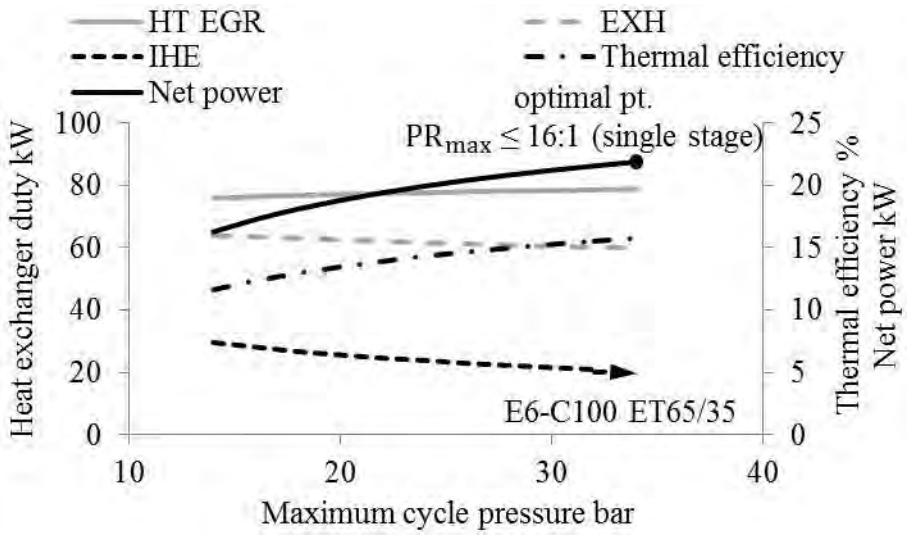

Figure 6.57 PI-11 maximum cycle pressure effect on heat recovery, thermal efficiency and net power

Fig. 6.57 shows the change in heat loads, net power and thermal efficiency for PI-11 with increasing maximum cycle pressure at E6-C100. For both process integrations, ET65/35 was superheated and the maximum fluid temperature was maintained at 250˚C. Increasing the cycle pressure, for a fixed maximum cycle temperature, decreased the IHE duty and increased the thermal efficiency. For a relatively constant HT EGR and EXH heat recovery, the net power increased and the cycle optimised at 34 bar.

6.8.3.2 Results and discussion

Appendix 6.20 presents the optimal PI-11 and PI-12 results with ET65/35 at the 4 test points. As can be expected, the total heat recovery, the optimal cycle pressure, the thermal efficiency and the system power for both the process integrations were nearly equal. Nonetheless, due to the 'IHE-EXH' thermal architecture, PI-12 demonstrated increased HT EGR heat recovery (100 vs. 85% of the available load) and accordingly decreased EXH heat recovery (55 vs. 65% of the available load). This can also be noticed when comparing Fig. 6.56b and d, where PI-12 allowed higher EGR cooling (123 vs. 160˚C) and avoided lower grade EXH heat recovery (195 vs. 177˚C). As a result of the 'IHE-EXH' thermal architecture, the increased cooling load at E6-C100 was within the limit defined in Fig. 6.4b. Furthermore, since the β value will continuously increase with increasing IHE duty, higher levels of superheating, due to higher thermal stability, can be considered for further decreasing the added engine cooling module load due to the EXH heat recovery.

To appreciate the benefits of PI-12 using ET65/35, it was compared to PI-4 using ethanol. This comparison was valid since, both the process integrations targeted the same heat sources in parallel (i.e. EGR and EXH), with some sort of pre-heating load (IHE vs. engine block) and offered a high similarity in the working fluid (65% ethanol vs. pure ethanol). For nearly equal pressure ratios, PI-12 on average gave a combination of 8% higher system power (despite 15% lower heat recovery) and 3% point higher thermal efficiency (i.e. average thermal efficiency of 15%). Hence, under high expansion pressure ratios, PI-12 using ET65/35 was the most superior ORC with the highest beta value (Fig. 6.58).

In the unlikely event of a leak in the EGR heat exchanger, the blend will ignite and burn into H_2O and CO_2 in the combustion cylinder (similar to ethanol). Since pure ethanol and pure toluene have virtually zero electric conductivity, ET65/35 could be used for cooling the electrical components of the ORC system or power electronics in an HEV (Buijtenen, 2009). ET65/35 could also be used for lubricating the turbine bearings. Furthermore, ET65/35 results in a higher molecular weight working fluid over pure ethanol (56 vs.

46 g/mol). This will additionally translate into ≈2% point isentropic efficiency improvement of the turbine due to the increased molecular weight (Stine and Geyer, 2001).

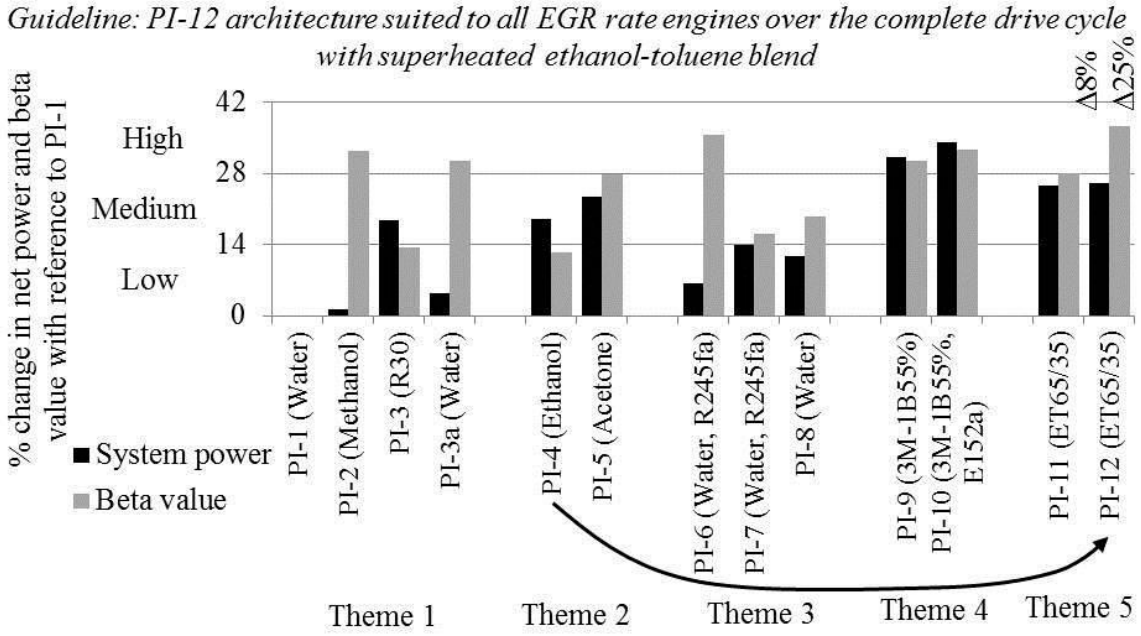

Figure 6.58 PI-12 application guideline and system power/beta value change over PI-4

6.9 Expansion machine type and efficiency

The selected performance assumptions for the heat exchanger and the condenser were validated in Section 4.9.1. However, for another critical component, i.e. the expansion machine, the isentropic efficiency was assumed constant at 70% for all working fluids under varying process conditions. This efficiency assumption, along with the type of expansion machine suitability (for output capacity < 30 kW), was validated using the similarity concept (Kenneth and Nichols, 2014, Badr et al., 1984). This theoretical approach is based on the fact that the number of primary effects describing the characteristics of an expansion machine can be reduced to two dimensionless parameters: the specific speed N_S (equation 6.3) and the specific diameter D_S (equation 6.4). In cases involving compressible flows, these depend on the expansion machine speed (N), the rotor or piston diameter (D), the volume flow at the expansion exit (V_{exp}), and the specific enthalpy drop over the expansion (Δh).

$$N_S = \frac{N.\sqrt{V_{exp}}}{\Delta h^{0.75}} \quad \ldots(6.3)$$

$$D_S = \frac{D.\Delta h^{0.75}}{\sqrt{V_{exp}}} \quad \ldots(6.4)$$

Where,

$N = rpm$

$V_{exp} = ft^3/\mathrm{s}; m^3/\mathrm{s} = 35.3\, ft^3/\mathrm{s}$

$\Delta h = ft.lbf/lb; kJ/kg = 334.5\, ft.lbf/lb$

$D = ft; cm = 0.033\, ft$

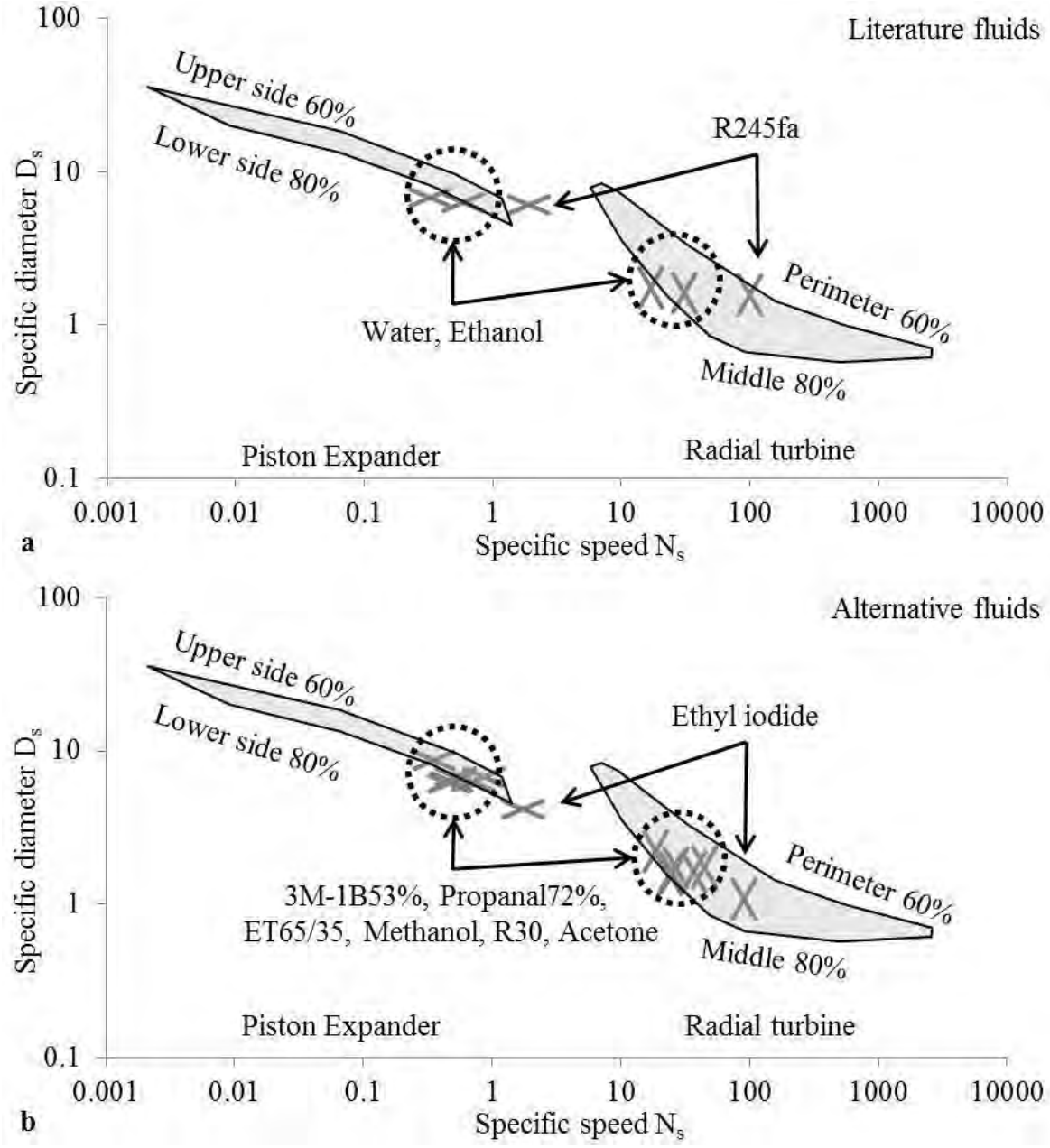

Figure 6.59 Piston expander and radial turbine (selection and efficiency) chart for the application of the similarity concept with (a) literature fluids (b) alternative fluids

For this analysis, the operating parameter for the FBC considered was the mean of B50 and C100 condition, which provided a suitable point for sizing the system components. The architecture considered was "EGR + EXH parallel". The grey shaded efficiency map regions in Fig. 6.59 correspond to 60-80% efficiencies for typical design of piston expanders and radial turbines (Map requires ft, ft^3/s and ft.lbf/lb as input units).

For each fluid, the cross mark in the map corresponds to a 1000-2000 rpm and 14-18 cm diameter for the piston expander, and a 60,000-90,000 rpm and 6-11 cm diameter for the radial turbine. The alternative organic fluids (methanol, R30, acetone), water blends and organic blend, were suited to both piston expanders and radial turbines, whereas

ethyl iodide was preferred only with radial turbines (Fig. 6.59b). Similarly, among the literature fluids, R245fa was preferred only with radial turbines (Fig. 6.59a). Fig. 6.59 confirmed that the preliminary expansion performance assumption was valid and corresponded to a realistic value.

6.10 Chapter 6: Summary

The durability of future long-haul engine platforms will depend not only on the reliability and effectiveness of the regulated emissions control technologies, but also on the WHR system. Furthermore, long-haul trucking sector as well as industrial facilities tends to invest in energy saving technologies only when the payback period is below 2 years. Hence, the implementation of FBCs depends primarily on the economics and perceived technical risks associated with a given benefit. In this section, for a relative trade-off, achievable system power and β value of process integrations are provided in the context of the system complexity and system size, respectively.

6.10.1 System complexity

Table 6.4 presents the complexity rating for all the process integrations. The complexity ratings were based on the below complexity rules:

- Addition of each new component resulted in an increased value by 1 (e.g. EXH heat exchanger)
- Modification or replacement of each component resulted in an increased value by 0.5 (e.g. CAC cooler to CAC heat exchanger)
- Use of water for high temperature heat recovery decreased the value by 1
- Use of ≈50% water content blends for high temperature heat recovery decreased the value by 0.5
- Insufficient cooling of a particular heat recovery element resulted in an increased value by 0.5 (e.g. insufficient EGR cooling PI)

The complexity ratings varied from 0.5 to 5, and were based over the reference complexity rating of a simple EGR only ORC and the engine cooling module given in Fig. 6.2.

Table 6.4 Detailed breakdown of the complexity rating for process integrations discussed in detail in this chapter

	Process integration	EGR heat exchanger (1 or 2 stage)	EXH heat exchanger	CAC heat exchanger	Engine block heat recovery	Medium temperature condenser	Low temperature condenser	Cascade condenser	IHE	Reheat control	# of expansion machines	# of pumps	# of 3-way flow distributor valves	Suitable with water	Suitable with water blends	Insufficient cooling	**Complexity rating**
	EGR only **(Organic)**	0.5				1					1	1					
1	EXH then EGR series **(Water)**	0.5	1			1					1	1		-1		0.5	**0.5**
2	EGR then EXH series **(Methanol)**	0.5	1			1					1	1					**1**
3	EGR + EXH parallel **(R30)**	0.5	1			1					1	1	1				**2**
3a	High latent heat **(Water)**	1	1			1					1	1	1	-1			**1.5**
4	EGR + EXH parallel with coolant preheat **(Ethanol)**	0.5	1		0.5	1					1	1	1			0.5	**3**
5	EGR + CAC-EXH parallel **(Acetone)**	0.5	1	0.5		1					1	1	1			0.5	**3**
6	Cascade **(Water, R245fa)**	1	1		0.5	0.5		1			2	1.5	1.5	-1			**4.5**
7	Two-phase cascade **(Water, R245fa)**	0.5	1		0.5	0.5		1			2	1.5	0.5	-1			**3**
8	Two-phase reheat **(Water)**	0.5	1			1				0.5	2	1		-1			**1.5**
9	Dual pressure **(3M-1B55%)**	0.5	1		0.5	0.5					2	1.5	1.5		-0.5		**3.5**
10	Dual cycle **(3M-1B55%, E152a)**	1	1	0.5		1	0.5				2	1.5	1.5		-0.5		**5**
11	EGR+EXH parallel with IHE preheat **(ET65/35)**	0.5	1			1			1		1	1	1				**3**
12	EGR + IHE-EXH parallel **(ET65/35)**	0.5	1			1			1		1	1	1				**3**

6.10.2 System performance

Fig. 6.60 plots the complexity rating vs. the system power achievable using the combination of the system architectures and working fluids mentioned in Table 6.4 (with heat rejection limited as per Fig. 6.4). The system power is represented as percentage of the engine crankshaft power and was a result of 280 optimised steady state points as a function of:

- 2 engine platforms (E6 and E5)
- 4 engine speed/load points (A50, A70, B50 and C100)
- 13 system architectures (PI-1 to 12 and 3a)
- 12 working fluids (given in Appendix 6.3, 6.6, 6.15 and 6.20)

Baseline process integrations (reproduced from the published literature) are marked in grey, process integrations investigated in this work are marked in black, heat recovery architectures that were also reported by other authors but used fluids from this work are marked in grey-black.

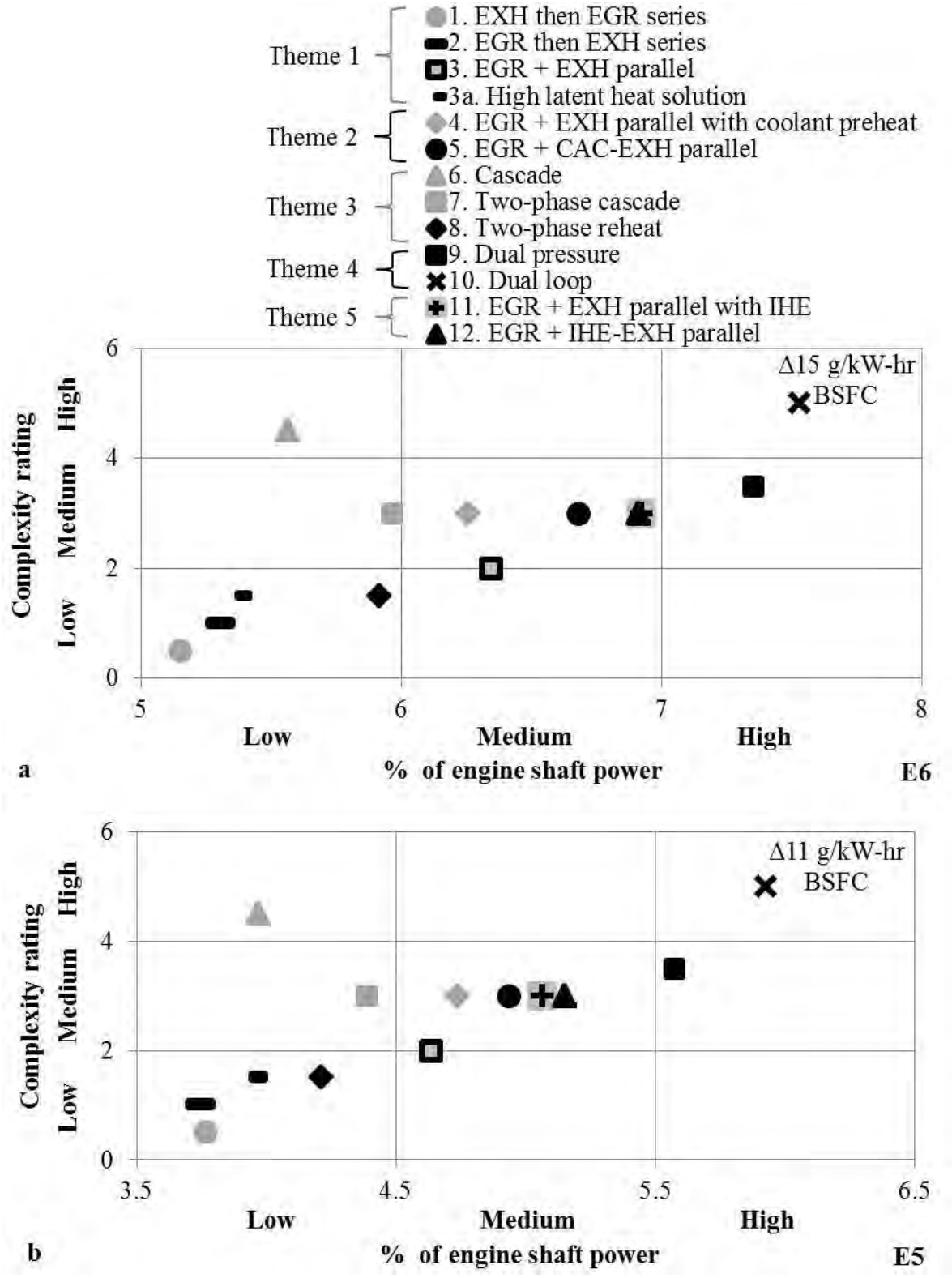

Figure 6.60 Complexity ratings and performance results for different process integrations across (a) EGR only (b) EGR focused platform

Fig. 6.60 shows a much more favourable trend in increased complexity rating and system power by the proposed integrations (black and grey-black markers). The top and bottom graphs correspond to EGR only and EGR focused platforms, respectively. For an average over the 4 speed/load points, PI-10 gave a maximum BSFC reduction of 15 and 11 g/kWh, generating 7.5 and 6% of additional engine crankshaft power. It is important to emphasise

that the simulation results were based on realistic boundary conditions, equipment performance assumptions and parasitic losses. This was done to ensure that potential BSFC reductions can be achieved on a first build and could be translated into an expected fleet CO_2 savings.

The key complexity vs. performance results are summarised below:

- Theme 1: PI-3 (using R30) was preferred over PI-2 (using organics), as well as PI-1 and 3a (using water) due to the highest performance.
- Theme 2: PI-5 (using acetone) was chosen over PI-4 (using ethanol) due to slightly higher performance for equal system complexity.
- Theme 3: When using water for high temperature heat recovery (i.e. PI-6, 7 and 8), PI-8 was better suited since it provided nearly equal system power to the cascade systems with reduced complexity. Architecturally PI-8 is rather simple and requires the addition of a single compact two-phase expander over PI-2.
- Theme 4: Despite the increased complexity, the architectural advantages of PI-9 and 10 can provide an integrated and relatively compact engine and WHR solution for future engine platforms. This is since, PI-9 provided complete cooling of the engine block and replacement of the medium-temperature radiator to a medium-temperature condenser. Whereas, PI-10 mirrored the high and low-temperature cooling loops and replaced the low-temperature loop with the liquid expansion cycle for a net zero impact on cooling. In fact, the complexity rating of PI-9 and 10 were comparable to cascade systems (PI-7 and 6), however the performance was noticeably higher. The engineering challenges that will arise in PI-9 by replacement of the conventional engine coolant to the alternative fluid blends are expected to be low due to the high similarity in fluid properties. Similarly, the engineering challenges associated with the liquid expander in PI-10 are also expected to be low due to the use of a fluid that demonstrated low volume flow ratio and high density. Since heat recovery elements (except EXH) in PI-9 and 10 were the dominant loads on the engine cooling module, these process integrations can also be operated either in cooling only or power generation mode. PI-9 and 10 also produced relatively constant power in relation to the engine crankshaft power for a wide range of thermal quality and quantity inputs (A50 vs. C100).

6.10.3 System size

Since the space available on long-haul trucks is limited, the overall system size has to at least account for the:

- Heat exchanger footprint (quantified using UA/W value)
- Expansion machine size (quantified using VFR/W value)
- Change in the engine cooling module dimension/capacity (quantified using β value)

Direct proportionality to UA/W and VFR/W, and inverse proportionality to β is then not only a relative indicator of the size but also of the systems weight and cost. When comparing UA/W vs. β values, Fig. 6.61 shows that the proposed process integrations outperformed the baseline process integrations.

The key UA/W vs. β value results are summarised below:

- Cascade condenser: Cascade (PI-6) and the dual pressure (PI-9) systems have a common feature of complete engine block heat recovery. However, despite nearly equal or higher β values by PI-6 compared to PI-9, all cascade arrangements were discounted. This was because the cascade condenser increased the cycle irreversibilities and increased the UA/W value by ≈2.5 times over PI-9.
- CAC or IHE as preheat prior to EXH: Since process integrations (except cascade systems) gave a relatively low variation in UA/W value (±10%) for a wide range of heat source quality, more emphasis was placed on achieving higher β values. PI-3 was then better suited to engines typically operated at mid-speed mid-load due to low/medium border line β value. For engines typically operated at high-loads, integrating CAC (PI-5) was better adapted. Similarly, for engines with severe cooling module packaging constraints PI-12 was better suited over PI-11. Since, PI-11 and 12 gave equal complexity and performance, PI-12 was the preferred option. The approach by both PI-5 and 12 was similar, i.e. reducing EXH heat recovery without reducing the net system power.
- Low temperature heat recovery: Conventional low temperature (<200˚C) heat to power conversion approaches usually increases the UA/W value and cost/kW dramatically. However, PI-10 can extend the temperature application range while retaining the economic feasibility of FBCs. For this, consider a comparison between baseline PI-1 and proposed PI-10. PI-1 had high-quality low-quantity heat input, and hence showed the best UA/W value but also the lowest performance. The UA/W of PI-10 increased by 35% over PI-1, however PI-10 also demonstrated a 35% higher performance. Therefore, the negative effect of the increased heat transfer area due to the use of the

alternative ORC is partially compensated by utilising heat streams that already require cooling.

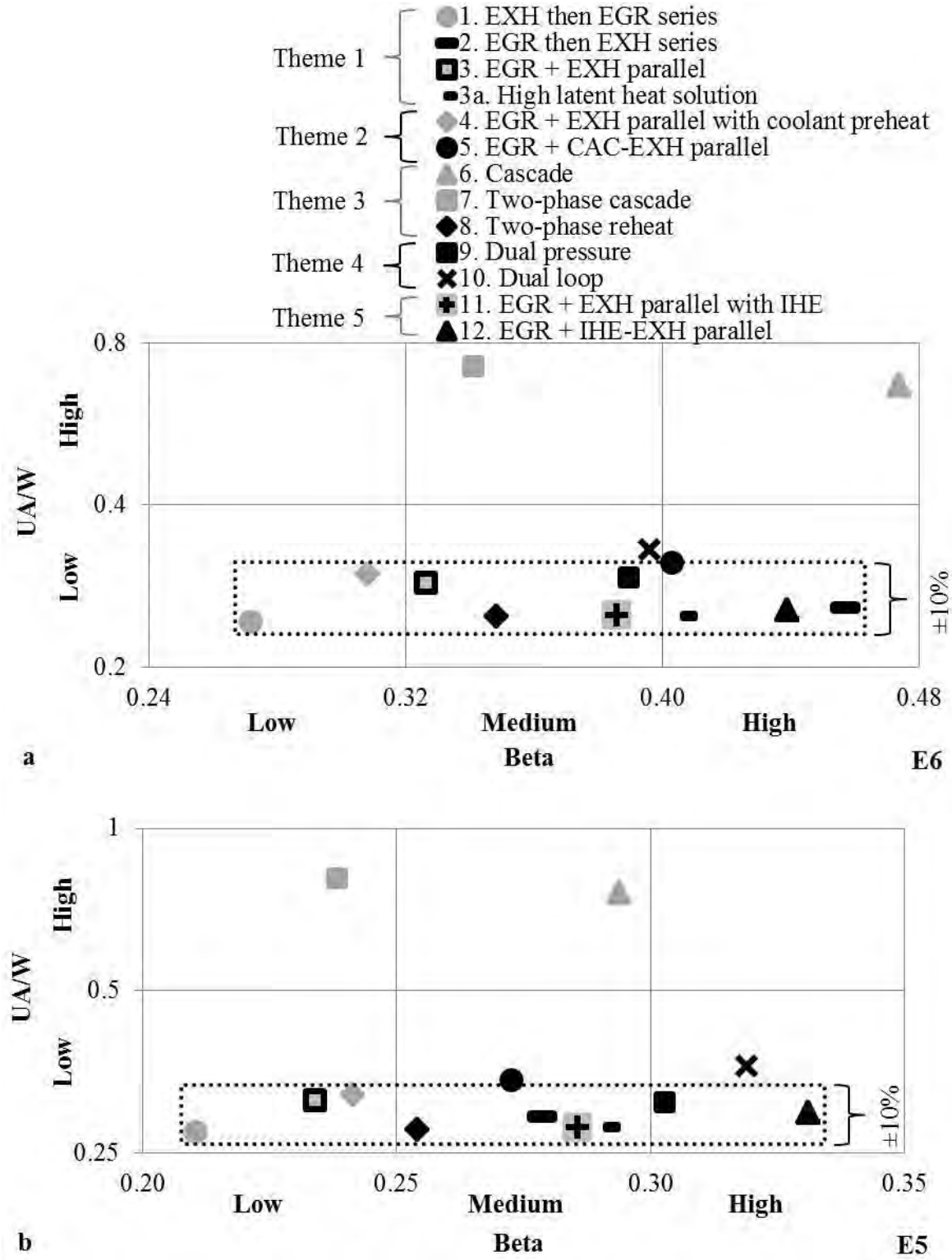

Figure 6.61 UA/W and beta value results for different process integrations across (a) EGR only (b) EGR focused platform

As the parallel EGR and EXH architecture approach was a common feature in the preferred process integrations 3, 5, 9, 10 and 12, the VFR/W values of the alternative fluids can be compared taking ethanol in PI-3 as a reference. Fig. 6.62 shows a VFR/W reduction of: nearly 15% for the water blends, 25% for methanol and ET65/35, and 40% for R30. Hence, all the alternative fluids (except acetone) showed a clear advantage in reduced expansion machine size per unit power output. This will compound the benefit over the relatively low and similar UA/W values of the proposed process integrations. This is since, the average system pressures (also given in Fig. 6.62) experienced by the alternative fluids were comparable to ethanol and will not correspond to a noticeable heat exchanger cost impact.

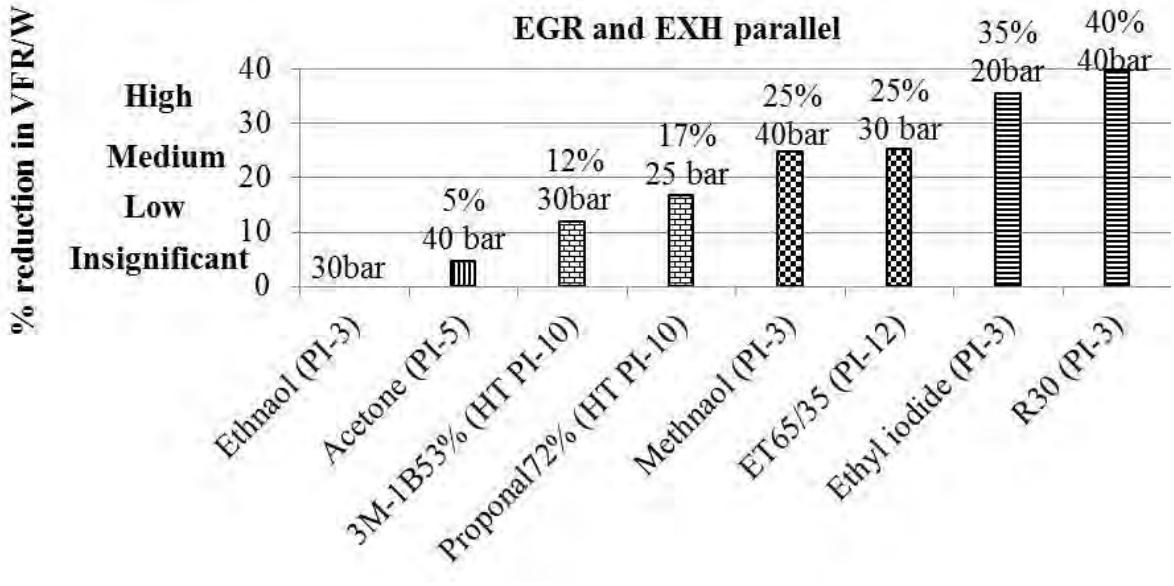

Figure 6.62 Baseline volume flow ratio per unit power output comparison

Finally, since at least exhaust heat and engine block heat are the common heat sources in all stationary and transport ICEs, PI-3, PI-12 and PI-9, without the EGR parallel branch are universal process integrations with relatively low, medium and high complexity, and system power, respectively.

6.10.4 Secondary objective functions

Although the alternative pure fluids, improved stability water blends and high stability organic blend results were compared for primary objective functions ($\eta_{conversion}$, UA/W and VFR/W), they were also screened for additional secondary objective functions like compatibility, cost, availability etc. Appendix 6.21 provides the detailed compatibility of the alternative pure fluids and blend constituents for widely used 10 metals and alloys, 10 O-ring materials and 10 thermoplastics (Cole-Parmer, accessed on 10.10.2014, allorings.com, accessed on 10.10.2014, eFunda, accessed on 10.10.2014, Peixoto, 2010,

Ingersoll Rand, 2008, McQuay International, 2002). Results corresponding dark shaded cells (i.e. 3, 4) have to be avoided to guarantee long system life cycle. Furthermore, Appendix 6.21 also provides the cost and availability for the alternative pure fluids and blend constituents.

Some of the key compatibility, cost and availability guidelines are summarised below:

- High range of compatibility was most important for amyl (3-Methyl-1-Butanol) and propyl (1-Propanol) alcohols used as water blend constituents. This was since water blends were investigated also to recover heat from the engine block, material changes to which will be more challenging. Whereas ET65/35, methanol, R30 and acetone would in any case require replacement to, or installation of, new components. Although amyl alcohol shows a high range of compatibility, propyl alcohol is also a valid alternative since it shows the best compatibility range (including aluminium) among all the fluids used in simulations.
- ET65/35 and acetone have a high range of metal and alloy compatibility, however, they are limited to ChemRaz, Kalrez and Kel-F as O-ring materials.
- Since R30 has a relatively high pressure at typical radiator temperature level (4.5 bar) and poor compatibility with aluminium, the air condenser has to be designed using stainless steel.
- 3-Methyl-1-Butanol and 1-Propanol water blends will cost approximately 10 $/L, this is similar to the cost of the alternative pure fluids. Whereas, ET65/35 will cost over twice, since pure ethanol is the most expensive fluid used in simulations.
- There is a high availability of all the alternative high temperature pure fluids and blend constituents on the market. The relatively low availability of the alternative low temperature fluids is common as only industry specific suppliers (e.g. SynQuest) stock synthetic refrigerants.

7 Conclusion

7.1 Working fluid

For the pure working fluid selection and evaluation, a novel methodology was developed and applied to three different temperature level heat recovery cases: relatively high (EGR, Case 1: 427/65°C), medium (EXH, Case 2: 296/105°C) and low (CAC, Case 3: 176/65°C). Following a theoretical overview of the cycle, 25 fluid screening criteria were employed to narrow down the list of 1800 synthetic, organic and inorganic fluids. The screening phase was a function of the thermo-physical, molecular, environmental and safety characteristics based on fundamental understanding. This resulted in a screening efficiency of 99.5%, filtering out the near optimum working fluids at an early stage. The fluids that met the screening requirements were then simulated using the common boundary conditions and equipment performance assumptions. Each subcritical limited superheat cycle was then optimised for overall conversion efficiency according to one of the four optimisation cases: point specific, low design intensity, pressure limited or temperature limited. The cycles were then assessed according to the 16 maximised and minimised ranking parameters. Finally, a performance and system index was developed to account for key design and operational features of the cycle for an objective assessment, with the value of this index being directly proportional to the performance and practicality of the system.

The application of this methodology led to the identification of ethyl iodide, methanol, R30 and acetone for EGR and exhaust, and R152 and E152a for CAC temperature heat recovery. The developed index which utilised the primary objective functions ($\eta_{conversion}$, VFR/W and UA/W) validated the suitability of these alternative fluids over those in the published literature, namely, water, ethanol and R245fa. The alternative fluids also retained higher PSI values under ±30% variation in the PSI weight factors. Considering extreme thermal boundary cases (e.g. Cases 1 and 2) was an integral part of the method, highlighting the working fluid sensitivity to varying source and condensing temperatures.

7.2 Cycle operation

To best match the cycles to the available heat sources, variations in expansion inlet pressure, temperature and phase were conducted using 10 pure, dry, isentropic and wet working fluids. System design and configuration analysis conducted to ensure a techno-economical unit was considered for three thermal boundary conditions. That is, high, medium and low source temperatures (427, 296, 176°C) and source-to-sink temperature differentials (Δ322, Δ231, Δ111°C), i.e. Cases 4, 5 and 3 (EGR, EXH, CAC).

- **Large superheat expansion:** The thermal efficiency of wet fluids (e.g. ethanol) increased with superheat, whereas for dry fluids (e.g. R245fa), this remained nearly constant. However, the economic viability of the cycle using wet or isentropic fluids can be increased by avoiding large superheat with a marginal reduction in net power.
- **Cycles with internal heat exchange:** Dry fluids (e.g. R245fa) offered higher IHE duty and a more efficient internal heat exchange process compared to wet fluids (e.g. ethanol), hence they showed higher levels of thermal efficiency improvement. Nonetheless, the nearly equivalent thermal efficiency and net power achieved by the simple cycle using the alternative fluids (e.g. R30, ethyl iodide) suggested avoiding the use of both superheated recuperated R245fa and ethanol cycles.
- **Supercritical cycles:** Increasing supercritical pressures from 1.05 to $1.25P_{crit}$ resulted in insignificant improvements in the thermal efficiency and net power. Furthermore, a ≈30 bar increase in the ethanol cycle pressure (from 0.8 to $1.25P_{crit}$) in Case 4 was unable to provide an improved techno-economic trade-off. However, in Case 5, where it became increasingly difficult to fully recover the waste heat with higher boiling point fluids, the $1.05P_{crit}$ R152 cycle was particularly relevant, and superior over R245fa.
- **Limited superheat expansion:** The net power showed the lowest sensitivity to superheat and the highest sensitivity to the subcritical expansion pressure ratios. As a result, the alternative high temperature organic fluids (e.g. R30, acetone) offered the most suitable trade-off using a $0.9P_{crit}$ limited superheat expansion in Case 4.
- **Two-phase expansion:** In Case 4, a two-phase expansion inlet ($X_{in} \approx 0.4$) offered the highest overall conversion efficiency for water as the chosen working fluid, resulting in 20% higher net power compared to the conventional Rankine cycle. Nonetheless, the drawbacks of multiple stages and larger footprint of the expansion machines hinders the application of a complete two-phase water expansion system.
- **Liquid expansion:** An alternative low temperature fluid, E152a, which offered a lower T_{boil}/T_{crit} value and higher density over R245fa, was a more practical solution for the CAC temperature level. Although resulting in nearly twice the system pressures and a 30% increased UA/W value, the liquid E152a expansion cycle offered 20% higher power compared to the dry saturated cycle.

The resulting optimal ORC operating modes over the 3 distinct cases were 65-77% as efficient as the theoretical cycle limit. Furthermore, inorganic cycles like supercritical CO_2, ammonia and Kalina cycles failed to offer performance and system benefits over the selected conventional ORCs.

7.3 Process integration

To provide improved process integration, a methodical analysis, which was a function of the working fluid, cycle operation and thermal/subsystem architecture, was conducted.

- **Series high and low temperature ORCs:** CAC offered a more suited quality and quantity levels compared to the engine block heat for preheating. Over a complete drive cycle, an architecture that allowed optional CAC heat recovery (PI-5) was best suited with acetone at slightly subcritical pressures ($0.9P_{crit}$).
- **Water as the working fluid:** The proposed novel two-phase reheat cycle was the most suitable solution in the case of engines with high EGR. This architecture offered high levels of EGR and exhaust heat recovery in association with a high-pressure two-phase expansion machine and a low-pressure conventional expansion machine.
- **Water-organic and organic-organic blends:** The pure fluid selection method was additionally adapted to screen over 750 binary water blends and 700 binary organic blends. The trade-offs among desired properties, led to the selection of 3-Methyl-1-Butanol as a suitable HPA with water. Additionally, 1-Propanol HPA with water, which also offered properties suitable between those of pure water and pure ethanol, was considered as an alternative due to the highest net power result. Whereas, to capture the combined effect of improved thermal efficiency, firstly due to the use of an IHE, and secondly, due to a temperature glide in the evaporator, a novel organic-organic pressure swing HPA (65% ethanol and 35% toluene) was formulated.
- **High temperature ORCs:** The flexible EGR and exhaust heat recovery architecture (PI-3 using R30) offered high heat exploitation at cruise loads and an exhaust heat limitation strategy at high loads. For engine cooling modules with severe packaging constraints, an improved system architecture (PI-12) which utilises the novel organic-organic blend in conjunction with internal heat recuperation was proposed. Implementation of the above PI-3 and PI-12 corresponded to a 4.6-6.9% additional engine crankshaft power.
- **Combined high and low temperature ORCs:** The proposed novel dual pressure system (PI-9) and the novel dual cycle system (PI-10) can increase the viability of power generation from a combination of heat sources. Both process integrations offer practical application potential with respect to design intensity, utilise water blends in high temperature section, operate efficiently over a wide operating range and provide an integrated cooling loop. As a result, innovative working fluids (e.g. alcohol-water blends, HFE with low GWP), approaches in heat recovery (e.g. direct engine block heat recovery) and power generation (e.g. liquid expansion) offered 5.6-7.5% of additional engine crankshaft power.

7.4 EGR only and EGR focused platforms

The EGR only platform, coupled with an ORC (PI-3), demonstrated an alternative route to meet the Euro 6 NOx limit while reducing the specific fuel consumption of the base engine by 6%. Furthermore, the increased waste heat to power conversion in the E6 platform compared to the E5 platform narrowed the combined BSFC difference to only Δ3g/kWh.

7.5 Recommendations and future works

The deployment of ORC systems for relatively high source temperatures, low output capacity, transient conditions, requires additional investigations in parallel to those recommended for lower source temperatures, larger scale, stationary applications. The crucial recommendations resulting from the works conducted in this thesis and to address its limitations are summarised below:

- **New fluid blends:** To formulate fluid blends that allows improved temperature matching to the source/sink streams and higher thermal efficiency. This is to be achieved firstly by, offering a low glide in the condenser and a relatively high glide in the evaporator, and secondly by, increasing the system temperature differential for a fixed pressure differential. (For a detailed conceptual overview of the idea, refer Appendix. 1.1, publication 6).
- **Thermal decomposition limits:** To construct a bench-top thermal degradation test-rig in order to identify the decomposition limits for the alternative high temperature pure organic fluids (in particular, acetone, R30, ethyl iodide). Furthermore, to quantify the absolute improvement in the decomposition temperature for the water-alcohol blends and organic-organic blend over the pure organic fluid counterparts.
- **Accurate CO_2 reduction potential:** To refine the simulation performance estimates, firstly by, producing a piston expander model to generate an expansion efficiency map in order to replace the fixed expansion isentropic efficiency of 70%, and secondly by, developing transient ORC models operating over real world driving conditions in order to substitute the average steady-state ORC analysis.
- **Holistic optimisation:** To implement global optimisation during process integration, which is at the least a function of the key ORC system parameters (e.g. size/performance of expansion machine and heat exchanger footprint), impact on the connected utilities (e.g. engine cooling load) and system complexity. Such a global optimisation approach being the alternative to the local optimisation considered in this thesis (Section 4.6, Table 6.2).
- **New expansion machine:** To explore modifications in piston machines so as to expand superheated vapour as well as two-phase mixtures for an output capacity of 10-20 kW

in order to increase the ORCs availability to generate power. This is since, organic fluids (in particular, R30, ethyl iodide) offer the advantages of relatively lower pressure ratios, volume flow ratios and variation in volume flow ratio (for $X_{in} \approx 0.5\text{-}1$).

- **Initial hardware layout:** To develop an ORC test-rig based on the PI-9 thermal and sub-system architecture in association with a high pressure ratio expansion machine for initial steady-state testing. This is due to its wide applicability, and since, exhaust heat and engine block heat are the common heat sources on all conventional stationary and transport ICEs.
- **Improved practicality of water:** To identify cost-effective de-freezing capability and precise mass flow control for water, in order to improve the practicality of the two-phase reheat cycle.

Reference

3M 2009. 3M™ Novec™ Fluids, Efficient Stable Sustainable. Environmentally sustainable working fluids for Organic Rankine Cycle (ORC) Systems.

ABDURASHIDOVA, A. A., BAZAEV, A. R., BAZAEV, E. A. & ABDULAGATOV, I. M. 2007. The thermal properties of water-ethanol system in the near-critical and supercritical states. High Temperature, 45, 178-186.

ABSALAM-GADZHIEVICH, D. T. & RAMAZANOVICH, B. A. 2012. Research of Thermal Stability of Water Mixtures of Aliphatic Alcohols. Journal of Materials Science and Engineering A 2 (12) 786-790.

AEA TECHNOLOGY. 2000. Thermodynamics and HYSYS [Online]. Available: http://coursenligne.chimie-paristech.fr/mod/resource/view.php?id=573.

AGARWAL, D., SINGH, S. K. & AGARWAL, A. K. 2011. Effect of Exhaust Gas Recirculation (EGR) on performance, emissions, deposits and durability of a constant speed compression ignition engine. Applied Energy, 88, 2900-2907.

AIXALA, L. RENOTER Project. 2012 Thermoelectric Applications Workshop, March 20-22, Baltimore, USA.

ALLORINGS.COM. accessed on 10.10.2014. O-Ring Fluid Compatibility Guide [Online]. Available: www.allorings.com/compatibility.htm.

AMAR, P., ANDERSSON, A., MCLAUGHLIN, S., GIBBLE, J., LI, J., GRAVEL, R. & NINE, R. 2011. SuperTruck Initiative for Maximum Utilized Loading in the United States. Advanced Combustion Engine Research and Development, Annual Progress Report.

ANEJA, R., SINGH, S., SISKEN, K., DOLD, R. & OELSCHLEGEL, H. Exhaust Heat Driven Rankine Cycle for a Heavy Duty Diesel Engine. Directions in Engine-Efficiency and Emissions Research, October 3-6, Detroit, USA, 2011.

ANGELINO, G. & INVERNIZZI, C. 2003. Experimental investigation on the thermal stability of some new zero ODP refrigerants. International Journal of Refrigeration, 26, 51-58.

ARIAS, D. A., SHEDD, T. A. & JESTER, R. K. 2006. Theoretical Analysis of Waste Heat Recovery from an Internal Combustion Engine in a Hybrid Vehicle. SAE International, 10.4271/2006-01-1605.

ARNEY, G., OLSEN, D. B. & MAYCES, R. 2011. Challenges in Retrofitting Selective Catalytic Reduction (SCR) Systems to Existing Stationary Natural Gas Fired Engines. Gas Machinery Conference, October 5, Nashville, USA.

ARORA, R. C. 2010. Refrigeration and Air Conditioning, PHI Learning, ISBN 9788120339156.

ARUNACHALAM, P. N., SHEN, M., TUNER, M., TUNESTAL, P. & THERN, M. 2012. Waste Heat Recovery from Multiple Heat Sources in a HD Truck Diesel Engine Using a Rankine Cycle - A Theoretical Evaluation. SAE International, 10.4271/2012-01-1602.

ASHLEY, S. 2011. Recovering exhaust heat to generate electricity and boost efficiency [Online]. SAE International. Available: http://articles.sae.org/7916.

ASHRAE 2012. ANSI/ASHRAE 34-2010, Designation and Safety Classification of Refrigerants.

ASPEN HYSYS V 7.3 2011a. Physical Property Methods.

ASPEN HYSYS V 7.3 2011b. Unit Operations Guide.

ASPEN TECHNOLOGY 2011. HYSYS V 7.3.

ASTM 2011. ASTM D6743-11, Standard Test Method for Thermal Stability of Organic Heat Transfer Fluids, 10.1520/D6743-11.

ATKINS, P., CORNWELL, R., TEBBUTT, N. & SCHONAU, N. 2013. Preparing a low CO2 technology roadmap for buses, Final Report, RD.12/409701.5.

BADAMI, M., MURA, M., CAMPANILE, P. & ANZIOSO, F. 2008. Design and performance evaluation of an innovative small scale combined cycle cogeneration system. Energy, 33, 1264-1276.
BADR, O., O'CALLAGHAN, P. W., HUSSEIN, M. & PROBERT, S. D. 1984. Multi-vane expanders as prime movers for low-grade energy organic Rankine-cycle engines. Applied Energy, 16, 129-146.
BAE, S., HEO, H., LEE, H., LEE, D., KIM, T., PARK, J. & KIM, C. 2011. Performance Characteristics of a Rankine Steam Cycle and Boiler for Engine Waste Heat Recovery. The Automotive Research Association of India, 10.4271/2011-28-0055.
BAE, S., HEO, H., PARK, J., LEE, H. Y. & KIM, C. 2013. Performance Design of Low Temperature Condenser for Waste Heat Recovery System. SAE International, 10.4271/2013-01-0046.
BAKER, H., CORNWELL, R., KOEHLER, E., PATTERSON, J. & POWELL, N. 2010. Review of Low Carbon Technologies for Heavy Goods Vehicles, RD.09/182601.7.
BANKS, A., NIVEN, M. & ANDERSSON, P. 2010. Boosting technology for Euro VI and Tier 4 final heavy duty diesel engines without NOx aftertreatment. IMECHE.
BARNHART, B., NELSON, C., GRAVEL, R. & MARONDE, C. 2005. Heavy Truck Engine Project. Advanced Combustion Engine Research and Development, Annual Progress Report.
BCS INCORPORATED 2008. Waste Heat Recovery: Technology and Opportunities in U.S. Industry, Department of Energy, Industrial Technologies Program. US DOE.
BENNION, K., THORNTON, M. & SLEZAK, L. 2008. Integrated Vehicle Thermal Management Systems Analysis/Modeling. Advanced Vehicle Technology Analysis and Evaluation Activities and Heavy Vehicle Systems Optimization Program, Annual Progress Report.
BOYCE, M. P. 2010. Handbook for Cogeneration and Combined Cycle Power Plants, ASME International, ISBN 9780791859537.
BRACCOA, R., CLEMENTEB, S., MICHELIB, D. & REINI, M. 2012. Experimental tests and modelization of a domestic-scale Organic Rankine Cycle. 25th International Conference on Efficiency, Cost, Optimization and Simulation of Energy Conversion Systems and Processes, June 26-29, Perugia, Italy.
BRIGGS, T. E., WAGNER, R., EDWARDS, K. D., CURRAN, S. & NAFZIGER, E. 2010a. A Waste Heat Recovery System for Light Duty Diesel Engines. SAE International, 10.4271/2010-01-2205.
BRIGGS, T. E., WAGNER, R. M., CURRAN, S. J., NAFZIGER, E. J., EDWARDS, K. D. & SCHEFTER, K. 2010b. Achieving and Demonstrating Vehicle Technologies Engine Fuel Efficiency Milestones. Advanced Combustion Engine Research and Development, Annual Progress Report.
BUIJTENEN, J. V. 2009. The Tri-O-Gen Organic Rankine Cycle: development and perspectives. Power Engineer, Volume 13, Issue 1, P567.
BUIJTENEN, J. V. 2011. Design, Development & Operation of the TRI-O-GEN ORC Power Unit. 1st International Seminar on ORC Power Systems, September 22-23, Delft, Netherlands.
CALM, J. M. 1999. Air-Conditioning and Refrigeration Technology Institute Refrigerant Database, Data Summaries Single-compound Refrigerants DOE/CE/23810-105 (JMC/ARTI-9909D - RDB9932), Virginia, U.S.
CALM, J. M. & DIDION, D. A. 1998. Trade-offs in refrigerant selections: past, present, and future. International Journal of Refrigeration, 10.1016/s0140-7007(97)00089-3.
CALM, J. M. & HOURAHAN, G. C. 2007. Refrigerant Data Update. Heating/Piping/Air Conditioning Engineering, 79(1):50-64.
CALM, J. M. & HOURAHAN, G. C. 2011. Physical, Safety, and Environmental Data Summary for Current and Alternative Refrigerants. International Congress of Refrigeration, August 21-26, Prague, Czech Republic.

CHA, W., KIM, K., CHOI, K. & LEE, K. 2010. Optimum Working Fluid Selection for Automotive Cogeneration System. World Academy of Science, Engineering and Technology, 72, 873-7.
CHACARTEGUI, R., SÁNCHEZ, D., MUÑOZ, J. M. & SÁNCHEZ, T. 2009. Alternative ORC bottoming cycles FOR combined cycle power plants. Applied Energy, 86, 2162-2170.
CHEN, H., GOSWAMI, D. Y. & STEFANAKOS, E. K. 2010. A review of thermodynamic cycles and working fluids for the conversion of low-grade heat. Renewable and Sustainable Energy Reviews, 14, 3059-3067, doi:10.1016/j.rser.2010.07.006.
CHEN, S. K. & LIN, R. 1983. A Review of Engine Advanced Cycle and Rankine Bottoming Cycle and Their Loss Evaluations. SAE International, 10.4271/830124.
CHRISTOFFEL, J. 2012. Waste heat recovery by Behr improves fuel economy for long-haul trucks [Online]. SAE International. Available: www.sae.org/mags/tbe/power/11184.
CLOUDT, R., BAERT, R. S. G., WILLEMS, F. P. T. & VERGOUWE, M. 2009a. SCR-only concept for heavy-duty Euro-VI applications. MTZ 09I2009 Vol. 70
CLOUDT, R., WILLEMS, F. & VAN DER HEIJDEN, P. 2009b. Cost and Fuel Efficient SCR-only Solution for Post-2010 HD Emission Standards. SAE Int. J. Fuels Lubr. 2(1):399-406.
COGSWELL, F. J., GERLACH, D. W., WAGNER, T. C. & MULUGETA, J. 2011. Design Of An Organic Rankine Cycle For Waste Heat Recovery From A Portable Diesel Generator. International Mechanical Engineering Congress & Exposition, November 11-17, Denver, USA.
COLE-PARMER. accessed on 10.10.2014. Chemical Compatibility Database [Online]. Available: www.coleparmer.co.uk/Chemical-Resistance.
COOPER, C., KAMAKATE, F., REINHART, T., KROMER, M. & WILSON, R. 2009. Reducing Heavy-Duty Long Haul Combination Truck Fuel Consumption and CO2 Emissions. NESCCAF, ICCT, SwRI, TIAX, LLC.
CPT. 2013. TIGERS [Online]. Available: www.cpowert.com/Products/TIGERS.
CRANE, D. T., LAGRANDEUR, J. & BELL, L. E. Status of Segmented Element Thermoelectrilc Generator for Vehicle Waste Heat Recovery. 2011 Thermoelectric Applications Workshop, January 3-6, San Diego, USA.
CROOK, A. W. 1994. Profiting from Low-grade Heat: Thermodynamic Cycles for Low-temperature Heat Sources, Institution of Electrical Engineers, ISBN 9780852968352.
DATLA, B. V. & BRASZ, J. 2012. Organic Rankine Cycle System Analysis for Low GWP Working Fluids. International Refrigeration and Air Conditioning Conference, July 16-19, Purdue, USA.
DDBST. accessed on 10.10.2014. Online Dortmund Data Bank Search [Online]. ddbonline.ddbst.com/DDBSearch/onlineddboverview.exe. Available: ddbonline.ddbst.com.
DEC, J. E. 2009. Advanced compression-ignition engines-understanding the in-cylinder processes. Proceedings of the Combustion Institute, 32, 2727-2742.
DESAI, N. B. & BANDYOPADHYAY, S. 2009. Process integration of organic Rankine cycle. Energy, 34, 1674-1686.
DIBELLA, F. A., DINANNO, L. R. & KOPLOW, M. D. 1983. Laboratory and On-Highway Testing of Diesel Organic Rankine Compound Long-Haul Vehicle Engine. SAE International, 10.4271/830122.
DICKEY, H. K. Low Temperature Geothermal Power Generation with HVAC Hardware. Geothermal Resource Council, Annual meeting, September 30-October 3, Sparks, USA., 2007.
DIESELNET. 2000a. European Stationary Cycle [Online]. Available: www.dieselnet.com/standards/cycles/esc.php.

DIESELNET. 2000b. European Transient Cycle [Online]. Available: www.dieselnet.com/standards/cycles/etc.php.
DIMIAN, A. C. & BILDEA, C. S. 2008. Chemical Process Design: Computer-Aided Case Studies, WILEY-VCH Verlag GmbH & Co. KGaA, Weinheim, ISBN 9783527314034.
DOMINGUES, A., SANTOS, H. & COSTA, M. 2013. Analysis of vehicle exhaust waste heat recovery potential using a Rankine cycle. Energy, 49, 71-85.
DOTY, F. D. & SHEVGOOR, S. 2009. A Dual-source Organic Rankine Cycle For Improved Efficiency In Conversion Of Dual Low- And Mid-grade Heat Sources. ASME 3rd International Conference of Energy Sustainability, July 19-23, San Francisco, USA.
EAA 2011. Applications - Power train - Heat exchangers. The Aluminium Automotive Manual.
ECHA. 2014. Candidate List of Substances of Very High Concern for Authorisation [Online]. Available: http://echa.europa.eu/candidate-list-table.
ECSA 2007. White Paper: Methylene Chloride.
EDWARDS, K. D., WAGNER, R. & BRIGGS, T. 2010. Investigating Potential Light-duty Efficiency Improvements through Simulation of Turbo-compounding and Waste-heat Recovery Systems. SAE International, 10.4271/2010-01-2209.
EDWARDS, S. 2010. Waste Heat Recovery: The Next Challenge for Truck Engine Development. Thermal management for the reduction of emissions and fuel consumption in trucks. Behr GmbH & Co. KG.
EDWARDS, S., EITEL, J., PANTOW, E., GESKES, P., LUTZ, R. & TEPAS, J. 2012. Waste Heat Recovery: The Next Challenge for Commercial Vehicle Thermomanagement. SAE Int. J. Commer. Veh., 5, 395-406.
EFUNDA. accessed on 10.10.2014. O-Ring Compatibilities [Online]. Available: www.efunda.com/designstandards/oring/oring_chemical.cfm.
EICKELS, B. & MÜLLER, W. 2010. Emissions legislation: EGR systems to meet future standards in off-highway applications. MAHLE Performance.
EL CHAMMAS, R. & CLODIC, D. 2005. Combined Cycle for Hybrid Vehicles. SAE International, 10.4271/2005-01-1171.
ENDO, T., KAWAJIRI, S., KOJIMA, Y., TAKAHASHI, K., BABA, T., IBARAKI, S., TAKAHASHI, T. & SHINOHARA, M. 2007. Study on Maximizing Exergy in Automotive Engines. SAE International, 10.4271/2007-01-0257.
ENEFTECH INNOVATION. 2014. Next generation Scroll turbines [Online]. Available: www.eneftech.com/en/technology.php.
ENGINEERING TOOLBOX. 2014. Freezing and flash points of ethanol based water solutions, [Online]. Available: www.engineeringtoolbox.com/ethanol-water-d_989.html.
ESPINOSA, N., TILMAN, L., LEMORT, V., QUOILIN, S. & LOMBARD, B. 2010. Rankine cycle for waste heat recovery on commercial trucks: approach, constraints and modelling. Diesel International Conference and Exhibition, France.
EUROPEAN COMMISSION. 2014a. Road transport: Reducing CO2 emissions from vehicles [Online]. Available: ec.europa.eu/clima/policies/transport/vehicles/index_en.htm.
EUROPEAN COMMISSION. 2014b. Towards a strategy to address CO2 emissions from Heavy-Duty Vehicles [Online]. Available: ec.europa.eu/clima/policies/transport/vehicles/heavy/index_en.htm.
EUROPEAN PARLIAMENT 2004. Directive 2004/8/EC of the European Parliament and of the Council of 11 February 2004 on the promotion of cogeneration based on a useful heat demand in the internal energy market and amending Directive 92/42/EEC.

EUROPEAN PARLIAMENT 2006. Directive 2006/40/EC of the European Parliament and of the Council of 17 May 2006 relating to emissions from air conditioning systems in motor vehicles and amending Council Directive 70/156/EEC.
EUROPEAN PARLIAMENT 2010. Directive 2010/75/EU of the European Parliament and of the Council of 24 November 2010 on industrial emissions (integrated pollution prevention and control).
FACÃO, J. & OLIVEIRA, A. C. 2009. Analysis Of Energetic, Design And Operational Criteria When Choosing An Adequate Working Fluid For Small ORC Systems. ASME International Mechanical Engineering Congress & Exposition, November 13-19, Lake Buena Vista, USA.
FERNÁNDEZ, F. J., PRIETO, M. M. & SUÁREZ, I. 2011. Thermodynamic analysis of high-temperature regenerative organic Rankine cycles using siloxanes as working fluids. Energy, 36, 5239-5249.
FRÖJD, K., PERLMAN, C., TUNÉR, A. & MAUSS, F. 2011. 1D engine modeling with detailed reaction kinetics. Swedish-Finnish Flames Days.
FU, J., LIU, J., REN, C., WANG, L., DENG, B. & XU, Z. 2012. An open steam power cycle used for IC engine exhaust gas energy recovery. Energy, 44, 544-554.
FU, J., LIU, J., XU, Z., REN, C. & DENG, B. 2013. A combined thermodynamic cycle based on methanol dissociation for IC (internal combustion) engine exhaust heat recovery. Energy, 55, 778-786.
GAIA, M. 2011. 30 Years of Organic Rankine Cycle Development. 1st International Seminar on ORC Power Systems, September 22-23, Delft, Netherlands.
GINOSAR, D. M., PETKOVIC, L. M. & GUILLEN, D. P. 2011. Thermal Stability of Cyclopentane as an Organic Rankine Cycle Working Fluid. Energy & Fuels, 25, 4138-4144.
GREEN TURBINE. 2013. Technical description Green Turbine 15 kW [Online]. Available: www.greenturbine.eu/en/product.php.
GRESZLER, A. 2008. Diesel Turbo-compound Technology. ICCT/NESCCAF Workshop, Improving the Fuel Economy of Heavy-Duty Fleets II.
GUILLEN, D., KLOCKOW, H., LEHAR, M., FREUND, S. & JACKSON, J. Development of a Direct Evaporator for the Organic Rankine Cycle. TMS Annual Meeting, February 27 - March 3, San Diego, USA, 2011.
HABIBZADEH, B., GRAVEL, R. & TAYLOR, S. 2007. Very High Fuel Economy, Heavy Duty, Constant Speed, Truck Engine Optimized via Unique Energy Recovery Turbines and Facilitated by a High Efficiency Continuously Variable Drivetrain. Advanced Combustion Engine Technologies, Annual Progress Report.
HALLIWELL, E. 2012. Testing Waste Heat Expanders for New Generation Diesels. 10th International Conference on Turbochargers and Turbocharging, May 15-16, London, UK.
HE, M., ZHANG, X., ZENG, K. & GAO, K. 2011. A combined thermodynamic cycle used for waste heat recovery of internal combustion engine. Energy, 36, 6821-6829.
HEAT2POWER. 2014. Principle of the technology [Online]. Available: www.heat2power.net/en__principle.php.
HILL, N., FINNEGAN, S., NORRIS, J., BRANNIGAN, C., WYNN, D., BAKER, H. & SKINNER, I. 2011. Reduction and Testing of Greenhouse Gas (GHG) Emissions from Heavy Duty Vehicles – Lot 1: Strategy, Final Report to the European Commission – DG Climate Action Ref: DG ENV. 070307/2009/548572/SER/C3.
HO, T., MAO, S. S. & GREIF, R. 2012. Comparison of the Organic Flash Cycle (OFC) to other advanced vapor cycles for intermediate and high temperature waste heat reclamation and solar thermal energy. Energy, 42, 213-223.
HORSLEY, L. H. 1973. Azeotropic Data-III, Volume 3, American Chemical Society, ISBN 9780841205338.

HOSSAIN, S. N. & BARI, S. 2013. Additional Power Generation from the Exhaust Gas of Diesel Engine by Bottoming Rankine Cycle. SAE International, 10.4271/2013-01-1639.
HOUNSHAM, S., STOBART, R., COOKE, A. & CHILDS, P. 2008a. Energy Recovery Systems for Engines. SAE International, 10.4271/2008-01-0309.
HOUNSHAM, S., WEERASINGHE, R. & STOBART, R. 2008b. Modelling heat recovery systems for hybrid vehicle applications. Vehicle Thermal Management Systems 8. Woodhead Publishing Limited, ISBN 1843343487.
HOUNTALAS, D. T., KATSANOS, C. O. & LAMARIS, V. T. 2007. Recovering Energy from the Diesel Engine Exhaust Using Mechanical and Electrical Turbocompounding. SAE International, 10.4271/2007-01-1563.
HOUNTALAS, D. T. & MAVROPOULOS, G. C. 2010. Potential for Improving HD Diesel Truck Engine Fuel Consumption Using Exhaust Heat Recovery Techniques. New Trends in Technologies: Devices, Computer, Communication and Industrial Systems. ISBN 978-953-307-212-8.
HOWELL, T., GIBBLE, J. & TUN, C. Development of an ORC system to improve HD truck fuel efficiency. Directions in Engine-Efficiency and Emissions Research, October 3-6, Detroit, USA, 2011.
HUSSAIN, Q. E. & BRIGHAM, D. R. Organic Rankine Cycle For Waste Heat Recovery In A Hybrid Vehicle. International Design Engineering Technical Conferences & Computers and Information in Engineering Conference, August 15-18, Montreal, Canada, 2010.
HUSSAIN, Q. E. & BRIGHAM, D. R. Organic Rankine Cycle for Light Duty Passenger Vehicles. Directions in Engine-Efficiency and Emissions Research, October 3-6, Detroit, USA, 2011.
IARC. 2014. Agents Classified by the IARC Monographs, Volumes 1–109 [Online]. Available: http://monographs.iarc.fr/ENG/Classification/index.php.
IBRAHIM, H. G., ELATRASH, M. S. & OKASHA, A. Y. 2011. Steam Power Plant Design Upgrading (Case Study: Khoms Steam Power Plant). Energy and Environment Research ISSN 1927-0577, 1, 202-211.
INFINITY TURBINE. 2014. Waste Heat Turbine and Geothermal [Online]. Available: www.infinityturbine.com.
INGERSOLL RAND 2008. Chemical Compatibility Guide, FORM 8677-P 0508.
JELACIC, A. Geothermal Energy Program. Venture Capital Technology Showcase, August 21, Washington DC, USA, 2007.
JOHNSON, T. 2009. Diesel Emission Control in Review. SAE International Journal of Fuels and Lubricants, 2, 1-12.
JOHNSON, T. 2010. Review of CO2 Emissions and Technologies in the Road Transportation Sector. SAE Int. J. Engines 10.4271/2010-01-1276.
JUNG, D., PARK, S. & MIN, K. 2013. Study on the Application of the Waste Heat Recovery System to Heavy-Duty Series Hybrid Electric Vehicles. SAE International, 10.4271/2013-01-1455.
KADOTA, M. & YAMAMOTO, K. 2008. Advanced Transient Simulation on Hybrid Vehicle Using Rankine Cycle System. SAE Int. J. Engines, 1, 240-247.
KATSANOS, C., HOUNTALAS, D., ZANNIS, T. & YFANTIS, E. 2010. Potentiality for Optimizing Operational Performance and Thermal Management of Diesel Truck Engine Rankine Cycle by Recovering Heat in EGR Cooler. SAE International, 10.4271/2010-01-0315.
KENNETH, E. & NICHOLS, P. E. 2014. How to Select Turbomachinery For Your Application [Online]. Barber-Nichols Inc. Available: www.barber-nichols.com/resources.
KIM, H. J. & YU, J. S. 2011. Design Of A Scroll Expander For An ORC Applicable To A Passenger Car For Fuel Consumption Improvement. 1st International Seminar on ORC Power Systems, September 22-23, Delft, Netherlands.

KONTOMARIS, K. 2011. A Low GWP Replacement for HCFC-123 in Centrifugal Chillers: DR-2.
KRÜGER, U., EDWARDS, S., PANTOW, E., LUTZ, R., DREISBACH, R. & GLENSVIG, M. 2008. High Performance Cooling and EGR Systems as a Contribution to Meeting Future Emission Standards. SAE Int. J. Engines, 1, 756-769.
KRUISWYK, R., FAIRBANKS, J. & MARONDE, C. 2009, 2008. An Engine System Approach to Exhaust Waste Heat Recovery. Advanced Combustion Engine Technologies, Annual Progress Report.
LAGRANDEUR, J., CRANE, D., BELL, L. E., AYERS, S., JOVOVIC, V., MARANVILLE, C., MAZAR, B., HELLER, K., KINNAIRD, E., EDER, A., CHIEW, L., FAIRBANKS, J., MARONDE, C. & YOCUM, A. 2011, 2010, 2009. High-Efficiency Thermoelectric Waste Energy Recovery System for Passenger Vehicle Applications. Advanced Combustion Engine Research and Development, Annual Progress Report.
LAGRANDEUR, J., CRANE, D., MARANVILLE, C., MAZAR, B., EDER, A., FAIRBANKS, J. & MARONDE, C. 2008, 2007. High-Efficiency Thermoelectric Waste Energy Recovery System for Passenger Vehicle Applications. Advanced Combustion Engine Technologies, Annual Progress Report.
LATZ, G., ANDERSSON, S. & MUNCH, K. 2012. Comparison of Working Fluids in Both Subcritical and Supercritical Rankine Cycles for Waste-Heat Recovery Systems in Heavy-Duty Vehicles. SAE International, 10.4271/2012-01-1200.
LATZ, G., ANDERSSON, S. & MUNCH, K. 2013. Selecting an Expansion Machine for Vehicle Waste-Heat Recovery Systems Based on the Rankine Cycle. SAE International, 10.4271/2013-01-0552.
LEIBOWITZ, H., STOSIC, N. & SMITH, I. K. 2006. Cost Effective Small Scale ORC Systems for Power Recovery from Low Grade Heat Sources. ASME International Mechanical Engineering Congress and Exposition, November 5-10, Chicago, USA.
LEISING, C. J., PUROHIT, G. P., DEGREY, S. P. & FINEGOLD, J. G. 1978. Waste Heat Recovery In Truck Engines. SAE International, 10.4271/780686.
LEMMON, E., HUBER, M. & MCLINDEN, M. 2007. NIST Reference Fluid Thermodynamic and Transport Properties Database (REFPROP): V 8. NIST Standard Reference Database, 23.
LIBERTINE FPE. 2014. Available: www.libertine.co.uk.
LIDE, D. R. & KEHIAIAN, H. V. 1994. CRC Handbook of Thermophysical and Thermochemical Data, Volume 1, Taylor & Francis, ISBN 9780849301971.
LOPES, J., DOUGLAS, R., MCCULLOUGH, G., O'SHAUGHNESSY, R., HANNA, A., ROUAUD, C. & SEAMAN, R. 2012. Review of Rankine Cycle Systems Components for Hybrid Engines Waste Heat Recovery. SAE International, 10.4271/2012-01-1942.
MAGO, P. J., CHAMRA, L. M., SRINIVASAN, K. & SOMAYAJI, C. 2008. An examination of regenerative organic Rankine cycles using dry fluids. Applied Thermal Engineering, 28, 998-1007.
MARCINIAK, T. J., KRAZINSKI, J. L., BRATIS, J. C., BUSHBY, H. M. & BUYCO, E. H. 1981. Comparison of Rankine-cycle power systems: effects of seven working fluids. Argonne National Lab, 10.2172/5682289.
MATCHES. 2014. Process Equipment Cost Estimates [Online]. Available: www.matche.com.
MCQUAY INTERNATIONAL. 2002. Application Guide AG 31-007: Refrigerants [Online]. Available: www.daikinmcquay.com.
MECA. 2007. Emission Control Technologies for Diesel-Powered Vehicles [Online]. Available: www.meca.org/resources/reports.

MEISNER, G. P. Thermoelectric Conversion of Exhaust Gas Waste Heat into Usable Electricity. Directions in Engine-Efficiency and Emissions Research, October 3-6, Detroit, USA, 2011.
MILLIKIN, M. 2005. Cummins Targeting 50% Efficiency and 2010 Emissions via Waste Heat Recovery Scheme [Online]. Green Car Congress. Available: www.greencarcongress.com/2005/10/cummins_targeti.html.
MILLIKIN, M. 2007. Daimler Trucks Introduces New Heavy-Duty Engine Platform for North America; DD15 Improves Fuel Economy by 5% [Online]. Green Car Congress. Available: www.greencarcongress.com.
MILLIKIN, M. 2011a. BMW provides an update on waste heat recovery projects; Turbosteamer and the Thermoelectric Generator [Online]. Green Car Congress. Available: www.greencarcongress.com/2011/08/bmwthermal-20110830.html.
MILLIKIN, M. 2011b. Ford study shows Rankine waste heat recovery system on a light-duty vehicle could almost meet full vehicle accessory load on highway cycle [Online]. Green Car Congress. Available: www.greencarcongress.com/2011/10/ford-study-shows-rankine-waste-heat-recovery-system-on-a-light-duty-vehicle-could-almost-meet-full-v.html.
MOORE, J., STANITSKI, C. & JURS, P. 2009. Principles of Chemistry: The Molecular Science, Cengage Learning, ISBN 9780495390794.
MOORE, W. 2003. Living with Cooled-EGR Engines. Construction Equipment.
NELSON, C. 2006. Heavy-Duty Truck Engine Program. Advanced Combustion Engine Research and Development, Annual Progress Report.
NELSON, C., GRAVEL, R. & MARONDE, C. 2009. Exhaust Energy Recovery. Advanced Combustion Engine Research and Development, Annual Progress Report.
NFPA 2012. NFPA 704: Standard System for the Identification of the Hazards of Materials for Emergency Response.
PANTOW, E. 2010. Energy efficient commercial vehicle engine cooling systems for Euro VI. Thermal management for the reduction of emissions and fuel consumption in trucks Behr GmbH & Co. KG.
PARK, T., TENG, H., HUNTER, G. L., VAN DER VELDE, B. & KLAVER, J. 2011. A Rankine Cycle System for Recovering Waste Heat from HD Diesel Engines - Experimental Results. SAE Technical Paper, 10.4271/2011-01-1337.
PATEL, P. S. & DOYLE, E. F. 1976. Compounding the Truck Diesel Engine with an Organic Rankine-Cycle System. SAE International, 10.4271/760343.
PEIXOTO, R. A. 2010. Manual for Refrigeration Servicing Technicians, ISBN: 978-92-807-2911-5, UNEP Job Number: DTI/1040/PA. United Nations Environment Programme.
PERRY, R. H. & GREEN, D. W. 2007. Perry's Chemical Engineers' Handbook, McGraw-Hill, ISBN 0070498415.
PETERS, M., TIMMERHAUS, K. & WEST, R. 2003. Plant Design and Economics for Chemical Engineers, McGraw-Hill Education, ISBN 9780072392661.
PONTON, J. W. 2007. Homogeneous azeotrope databank [Online]. Available: eweb.chemeng.ed.ac.uk.
PRABHU, E. 2006. Solar Trough Organic Rankine Electricity System (STORES). Stage 1. power plant optimization and economics, National Renewable Energy Laboratory.
QUOILIN, S. & LEMORT, V. 2009. Technological and Economical Survey of Organic Rankine Cycle Systems. European Conference on Economics and Management of Energy in Industry, April 14-17, Algarve, Portugal.
RAVINDRA, D. 2001. Air-Cooled Condensers. Indian Society of Heating, Refrigerating and Air Conditioning Engineers.
RICARDO. 2013. Game changing Ricardo concept for high efficiency heavy duty diesel moves forward [Online]. Available: www.ricardo.com/en-GB/News--Media/.
RICARDO SOFTWARE 2008a. WAVE Knowledge Center, WAVE V 8.1.

RICARDO SOFTWARE 2008b. WAVE V 8.1.
RINGLER, J., SEIFERT, M., GUYOTOT, V. & HÜBNER, W. 2009. Rankine Cycle for Waste Heat Recovery of IC Engines. SAE Int. J. Engines, 2, 67-76.
ROOS, C. J. 2009. An Overview of Industrial Waste Heat Recovery Technologies for Moderate Temperatures Less Than 1000F. Northwest Clean Heat and Power Application Center. WSUEEP09-26.
SAIDUR, R., REZAEI, M., MUZAMMIL, W. K., HASSAN, M. H., PARIA, S. & HASANUZZAMAN, M. 2012. Technologies to recover exhaust heat from internal combustion engines. Renewable and Sustainable Energy Reviews, 16, 5649-5659.
SCHNITZLER, J. 2007. Particulate Matter and NOx Exhaust Aftertreatment Systems [Online]. FEV Motorentechnik GmbH. Available: www.fev.com/resource-center/publications/diesel-systems.
SCHOCK, H., CAILLET, T., CASE, E., FLEURIAL, J. P., HOGAN, T., LYLE, M. & MALONEY, R. 2010. Thermoelectric Conversion of Waste Heat to Electricity in an IC Engine Powered Vehicle. Directions in Engine-Efficiency and Emissions Research, September 27-30, Detroit, USA.
SCHOCK, H., CASE, E., HOGAN, T., LYLE, M., MALONEY, R., MORAN, K., RUCKLE, T., SAKAMOTO, J., THOMPSON, T., TIMM, E., ZHANG, L., ZHU, G., FAIRBANKS, J. & TAYLOR, S. 2010, 2009. Thermoelectric Conversion of Waste Heat to Electricity in an Internal Combustion Engine Vehicle. Advanced Combustion Engine Research and Development, Annual Progress Report.
SCHOCK, H., HOGAN, T., CASE, E., PENG, F., REN, F., SAKAMOTO, J., TIMM, E., FAIRBANKS, J. & TAYLOR, S. 2008, 2006, 2005. Thermoelectric Conversion of Waste Heat to Electricity in an Internal Combustion Engine Vehicle. Advanced Combustion Engine Technologies, Annual Progress Report.
SCHREIER, H., WALTER, L., THEISSL, H. & DECKER, M. 2014. Potentials and Challenges For Next Generation HD Diesel Engines. Heavy-Duty Diesel Emissions Control Symposium, September 17-18, Sweden.
SEHER, D., LENGENFELDER, T., GERHARDT, J., EISENMENGER, N., HACKNER, M. & KRINN, I. 2012. Waste Heat Recovery for Commercial Vehicles with a Rankine Process 21st Aachen Colloquium Automobile and Engine Technology, October 8-12, Aachen, Germany.
SHENGJUN, Z., HUAIXIN, W. & TAO, G. 2011. Performance comparison and parametric optimization of subcritical Organic Rankine Cycle (ORC) and transcritical power cycle system for low-temperature geothermal power generation. Applied Energy, 88, 2740-2754.
SHRL. 2010a. GREEN 3, Centre for Automotive Engineering, University of Brighton [Online]. Available: http://www.brighton.ac.uk/shrl/projects/index.php.
SHRL. 2010b. Heavy duty Diesel engine, Centre for Automotive Engineering, University of Brighton [Online]. Available: www.brighton.ac.uk/shrl/laboratories/facilities/green.php.
SHU, G., ZHAO, J., TIAN, H., LIANG, X. & WEI, H. 2012a. Parametric and exergetic analysis of waste heat recovery system based on thermoelectric generator and organic rankine cycle utilizing R123. Energy, 45, 806-816.
SHU, G., ZHAO, J., TIAN, H., WEI, H., LIANG, X., YU, G. & LIU, L. 2012b. Theoretical Analysis of Engine Waste Heat Recovery by the Combined Thermo-Generator and Organic Rankine Cycle System. SAE International, 10.4271/2012-01-0636.
SHU, G. Q., YU, G., TIAN, H., WEI, H. & LIANG, X. 2013. Simulations of a Bottoming Organic Rankine Cycle (ORC) Driven by Waste Heat in a Diesel Engine (DE). SAE International, 10.4271/2013-01-0851.
SIDDIQI, M. A. & ATAKAN, B. 2011. Investigation of the Criteria for Fluid Selection in Rankine Cycles for Waste Heat Recovery. International Journal of Thermodynamics, Vol. 14 (No. 3), pp. 117-123, 10.5541/ijot.323.

SIDDIQI, M. A. & ATAKAN, B. 2012. Binary Alkane Mixtures as Fluids in Rankine Cycles. 25th International Conference on Efficiency, Cost, Optimization and Simulation of Energy Conversion Systems and Processes, June 26-29, Perugia, Italy.
SMITH, I. K. 1992. Matching and Work Ratio in Elementary Thermal Power Plant Theory. Proceedings of the Institution of Mechanical Engineers, Part A: Journal of Power and Energy, 206, 257-262.
SMITH, I. K. 2009. Power Plant Thermodynamics [Monograph]. Positive Displacement Compressor Technology, City University London, UK.
SMITH, I. K., STOSIC, N., ALDIS, C. A. & KOVACEVIC, A. 1999. Twin Screw Two-Phase Expanders in Large Chiller Units. Proceedings of IMechE Conference, Compressors and Their Systems, London, UK.
SMITH, I. K., STOSIC, N. & KOVACEVIC, A. Power Recovery From Low Cost Two-Phase Expanders. Geothermal Research Council Annual Meeting, San Diego, USA, 2001.
SMITH, I. K., STOSIC, N. & KOVACEVIC, A. 2005a. An Improved System for Power Recovery from Higher Enthalpy Liquid-Dominated Fields. Proceedings of World Geothermal Congress. April 24-29, Antalya, Turkey.
SMITH, I. K., STOSIC, N. & KOVACEVIC, A. Screw Expanders Increase Output and Decrease the Cost of Geothermal Binary Power Plant Systems. Geothermal Research Council Annual Meeting, Reno, USA, 2005b.
SMITH, I. K., STOSIC, N., MUJIC, E. & KOVACEVIC, A. 2011. Steam as the working fluid for power recovery from exhaust gases by means of screw expanders. Proceedings of the Institution of Mechanical Engineers, Part E: Journal of Process Mechanical Engineering, 225, 117-125.
SPROUSE III, C. & DEPCIK, C. 2013a. Organic Rankine Cycles with Dry Fluids for Small Engine Exhaust Waste Heat Recovery. SAE Int. J. Alt. Power, 2, 96-104.
SPROUSE III, C. & DEPCIK, C. 2013b. Review of organic Rankine cycles for internal combustion engine exhaust waste heat recovery. Applied Thermal Engineering, 51, 711-722.
SPURLIN M, GAMBLE C & BEAIN A 2000. Defining Thermal Stability. Process Heating Magazine.
SRINIVASAN, K. K., MAGO, P. J. & KRISHNAN, S. R. 2010. Analysis of exhaust waste heat recovery from a dual fuel low temperature combustion engine using an Organic Rankine Cycle. Energy, 35, 2387-2399.
STANTON, D. The Role of Waste Heat Recovery in Meeting Phase 2 US EPA Greenhouse Gas Regulations. Diesel Emissions Conference & AdBlue Forum Europe, 2013.
STINE, W. B. & GEYER, M. 2001. Power Cycles for Electricity Generation. Power From The Sun. www.powerfromthesun.net.
STOBART, R., HOUNSHAM, S. & WEERASINGHE, R. 2007. The Controllability of Vapour Based Thermal Recovery Systems in Vehicles. SAE International, 10.4271/2007-01-0270.
TABOR, H. Solar utilization and development in Israel. 6th World Power Conference, October 20-27, Melbourne, Australia, 1962.
TAI, C., MCLAUGHLIN, S., GIBBLE, J., KANG, H., GRAVEL, R. & TAYLOR, S. 2010, 2009. Very High Fuel Economy, Heavy-Duty, Narrow-Speed Truck Engine Utilizing Biofuels and Hybrid Vehicle Technologies. Advanced Combustion Engine Research and Development, Annual Progress Report.
TCHANCHE, B. F., LAMBRINOS, G., FRANGOUDAKIS, A. & PAPADAKIS, G. 2011. Low-grade heat conversion into power using organic Rankine cycles - A review of various applications. Renewable and Sustainable Energy Reviews, 15, 3963-3979.
TENG, H. 2010. Waste Heat Recovery Concept to Reduce Fuel Consumption and Heat Rejection from a Diesel Engine. SAE Int. J. Commer. Veh., 3, 60-68.

TENG, H., KLAVER, J., PARK, T. & HUNTER, G. 2011. A Rankine Cycle System for Recovering Waste Heat from HD Diesel Engines - WHR System Development. SAE Technical Paper, 10.4271/2011-01-0311.
TENG, H. & REGNER, G. 2009. Improving Fuel Economy for HD Diesel Engines with WHR Rankine Cycle Driven by EGR Cooler Heat Rejection. SAE International, 10.4271/2009-01-2913.
TENG, H., REGNER, G. & COWLAND, C. 2006. Achieving High Engine Efficiency for Heavy-Duty Diesel Engines by Waste Heat Recovery Using Supercritical Organic-Fluid Rankine Cycle. SAE International, 10.4271/2006-01-3522.
TENG, H., REGNER, G. & COWLAND, C. 2007. Waste Heat Recovery of Heavy-Duty Diesel Engines by Organic Rankine Cycle Part I: Hybrid Energy System of Diesel and Rankine Engines. SAE International, 10.4271/2007-01-0537.
THEKDI, A. C. Waste Heat to Power Economic Tradeoffs and Considerations. 3rd Annual Waste Heat to Power Workshop, September 25, Houston, USA, 2007.
TIAN, H., SHU, G.-Q., WEI, H., LIANG, X. & YU, G. 2013. Thermodynamic Analysis of a Novel Combined Power and Cooling Cycle Driven by the Exhaust Heat Form a Diesel Engine. SAE Int. J. Engines, 6, 766-776.
TIAN, H., SHU, G., WEI, H., LIANG, X. & LIU, L. 2012. Fluids and parameters optimization for the organic Rankine cycles (ORCs) used in exhaust heat recovery of Internal Combustion Engine (ICE). Energy, 47, 125-136.
TOOM, R. 2008. The potential of the CO2 emission reduction with a downsized engine and waste heat regeneration system. Engine Expo, May 6, Messe Stuttgart.
UNDERWRITERS LABORATORIES 2011. White Paper: Revisiting Flammable Refrigerants.
US DOE 2008. Advanced Combustion Engine Technologies, Annual Progress Report.
US DOE 2011. Advanced Combustion Engine Research and Development, Annual Progress Report.
US DOT. 2009. Table 3-6. Annual Vehicle Distance Traveled by Highway Category and Vehicle Type: 2009 [Online]. Available: ops.fhwa.dot.gov/freight/freight_analysis/nat_freight_stats/docs/11factsfigures.
US EPA. 2014a. EPA and NHTSA Set Standards to Reduce Greenhouse Gases and Improve Fuel Economy for Model Years 2017-2025 Cars and Light Trucks [Online]. Available: www.epa.gov/otaq/climate/regs-light-duty.htm.
US EPA. 2014b. Ozone Layer Protection [Online]. Available: www.epa.gov.
US EPA. 2014c. Significant New Alternatives Policy (SNAP) Program [Online]. Available: www.epa.gov/ozone/strathome.html.
US NAS 2010. Technologies and Approaches to Reducing the Fuel Consumption of Medium and Heavy Duty Vehicles, ISBN 0309149835.
US NPC 2012. Future Transportation Fuels Study: Heavy-Duty Engines & Vehicles Analysis.
VAJA, I. & GAMBAROTTA, A. 2010. Internal Combustion Engine (ICE) bottoming with Organic Rankine Cycles (ORCs). Energy, 35, 1084-1093.
VALENTINO, R., HALL, M. J. & BRIGGS, T. 2013. Simulation of Organic Rankine Cycle Electric Power Generation from Light-Duty Spark Ignition and Diesel Engine Exhaust Flows. SAE Int. J. Engines, 6, 1299-1310.
VINCENT, L. & SYLVAIN, Q. Advances in ORC expander design. International Symposium On Advanced Waste Heat Valorisation Technologies, September 13-14, Kortrijk, Belgium, 2012.
VUK, C. T., FAIRBANKS, J. & NINE, R. 2007, 2006. Electrically Coupled Exhaust Energy Recovery System Using a Series Power Turbine Approach. Advanced Combustion Engine Research and Development, Annual Progress Report.
WAGNER, R. M., EDWARDS, K. D., BRIGGS, T. E. & SINGH, G. 2008. Achieving and Demonstrating FreedomCAR Engine Efficiency Goals. Advanced Combustion Engine Research and Development, Annual Progress Report.

WANG, E. H., ZHANG, H. G., FAN, B. Y., OUYANG, M. G., ZHAO, Y. & MU, Q. H. 2011a. Study of working fluid selection of organic Rankine cycle (ORC) for engine waste heat recovery. Energy, 36, 3406-3418.
WANG, E. H., ZHANG, H. G., ZHAO, Y., FAN, B. Y., WU, Y. T. & MU, Q. H. 2012. Performance analysis of a novel system combining a dual loop organic Rankine cycle (ORC) with a gasoline engine. Energy, 43, 385-395.
WANG, H., PETERSON, R., HARADA, K., MILLER, E., INGRAM-GOBLE, R., FISHER, L., YIH, J. & WARD, C. 2011b. Performance of a Combined Organic Rankine Cycle and Vapor Compression Cycle for Heat Activated Cooling. Oregon State University.
WANG, T., ZHANG, Y., PENG, Z. & SHU, G. 2011c. A review of researches on thermal exhaust heat recovery with Rankine cycle. Renewable and Sustainable Energy Reviews, 15, 2862-2871.
WEERASINGHE, R., STOBART, R. & HOUNSHAM, S. 2010. Thermal efficiency improvement in high output diesel engines a comparison of a Rankine cycle with turbo-compounding. Applied Thermal Engineering, 30, 2253-2256.
WEI, D., LU, X., LU, Z. & GU, J. 2007. Performance analysis and optimization of organic Rankine cycle (ORC) for waste heat recovery. Energy Conversion and Management, 48, 1113-1119.
WEISSLER, P. 2012. New heavy-duty Ram trucks feature Cummins diesel upgrades [Online]. SAE International. Available: www.sae.org/mags/sve/power/11410.
WELCH, P. & BOYLE, P. New Turbines To Enable Efficient Geothermal Power Plants. Geothermal Resources Council, Annual Meeting, October 4-7, Reno, USA, 2009.
WENZHI, G., JUNMENG, Z., GUANGHUA, L., QIANG, B. & LIMING, F. 2013. Performance evaluation and experiment system for waste heat recovery of diesel engine. Energy, 55, 226-235.
WHO 1996. International Programme On Chemical Safety, Environmental Health Criteria 164, Methylene Chloride. ISBN 9241571640. Geneva, Switzerland.
WILLIGAN, R. R., HAUTMAN, D., KROMMENHOEK, D., MARTIN, P., TAHER, M., KASULE, A., FAIRBANKS, J. & YOCUM, A. 2006, 2005. Cost-Effective Fabrication Routes for the Production of Quantum Well Structures and Recovery of Waste Heat from Heavy Duty Trucks. Advanced Combustion Engine Research and Development, Annual Progress Report.
WILSON, D. E. The design of a low specific fuel consumption turbocompound engine. 1986 Society of Automotive Engineers International Congress and Exposition, February 24, Detroit, USA.
WITCHGER, K. & LAWRENCE, R. 2009. Clean Heat and Power, The Kentucky Aluminum Industry: A Market Analysis for CHP. US DOE Southeast CHP Applications Center.
XU, Z., LIU, J., FU, J. & REN, C. 2013. Analysis and Comparison of Typical Exhaust Gas Energy Recovery Bottoming Cycles. SAE International, 10.4271/2013-01-1648.
YAMADA, N. & MOHAMAD, M. N. A. 2010. Efficiency of hydrogen internal combustion engine combined with open steam Rankine cycle recovering water and waste heat. International Journal of Hydrogen Energy, 35, 1430-1442.
YAMAGUCHI, T., AOYAGI, Y., OSADA, H., SHIMADA, K. & UCHIDA, N. 2013. BSFC Improvement by Diesel-Rankine Combined Cycle in the High EGR Rate and High Boosted Diesel Engine. SAE Int. J. Engines, 6, 1275-1286.
ZHANG, J. 2009. Diesel Emission Technology – Part II of Automotive After-treatment System [Online]. Available: www.bowmannz.com/research.
ZHANG, X., ZENG, K., BAI, S., ZHANG, Y. & HE, M. 2011. Exhaust Recovery of Vehicle Gasoline Engine Based on Organic Rankine Cycle. SAE International, 10.4271/2011-01-1339.
ZHENG, L. & FURIMSKY, E. 2003. ASPEN simulation of cogeneration plants. Energy Conversion and Management, 44, 1845-1851.

ZHENG, M., READER, G. T. & HAWLEY, J. G. 2004. Diesel engine exhaust gas recirculation-a review on advanced and novel concepts. Energy Conversion and Management, 45, 883-900.
ZINK, U. 2011. MD/HD CO2 Reduction by Hybridization & WHR. Technology Impact on Emission Control.
ZYHOWSKI, G. J. 2013. Honeywell Refrigerants Improving the Uptake of Heat Recovery Technologies [Online]. Available: www.honeywell-orc.com.

Chapter 1 Appendix

Appendix 1.1 - List of publications

Published

1. Panesar, A.S., et al., An investigation of bottoming cycle fluid selection on the potential efficiency improvements of a Euro 6 heavy duty Diesel engine, in Vehicle Thermal Management Systems 11, May 15-16, Coventry, UK. 2013.

2. Panesar, A.S., et al., Working fluid selection for a subcritical bottoming cycle applied to a high exhaust gas recirculation engine. Energy, 2013. 60(0): p. 388-400.

3. Panesar, A.S., et al., An Assessment of the Bottoming Cycle Operating Conditions for a High EGR Rate Engine at Euro VI NOx Emissions. SAE Int. J. Engines 6(3):1745-1756, 10.4271/2013-24-0089, 2013.

4. Panesar, A.S., et al., The potential of bottoming cycle applied to a high exhaust gas recirculation engine for maximum fuel consumption improvement, in 2nd International Workshop on Heat Transfer Advances for Energy Conservation and Pollution Control October 18-21, Xi'an, China. 2013.

5. Panesar, A.S., et al., A Novel Organic Rankine Cycle System with Improved Thermal Stability and Low Global Warming Fluids, in 4th International Conference on Production, Energy and Reliability, June 3-5, Kuala Lumpur, Malaysia. 2014.

6. Panesar, A.S., et al., A novel working fluid for Organic Rankine Cycles (ORC), in Vehicle Thermal Management Systems 12, May 10-13, Nottingham, UK. 2015.

7. Panesar, A.S., et al., A novel Organic Rankine Cycle (ORC) for high temperature applications, in 2nd International Conference on Energy & Environment, June 18-19, Guimarães, Portugal. 2015.

8. Panesar, A.S., et al., A novel organic Rankine cycle system for heavy duty Diesel engines, in 3rd Sustainable Thermal Energy Management, July 7-8, Newcastle, UK. 2015.

Under review

9. Panesar, A.S., et al., Integrated Cooling and Heat Recovery Systems Using Organic Rankine Cycles For Diesel Engines, for 1st International ISHMT-ASTFE Heat and Mass Transfer Conference, December 17-20, Thiruvananthapuram, India. 2015.

Chapter 2 Appendices

Appendix 2.1 - Supplement MTC information

Detroit Diesel
Millikin, 2007

The remaining 2% of the benefit on the DD15 engines was due to the electronically optimised fuel delivery that changed the pressure and timing for every injection, to every cylinder, creating effective combustion for each revolution. This improved performance within the cylinders and reduced deposits like soot and carbon, resulting in fewer after-treatment regenerations.

Volvo
Tai et al., 2010, 2009

Greszler, 2008

Habibzadeh et al., 2007

Volvo produced its D12 engine with MTC (2002-2006, European engines only) and is currently working to develop MTC for D13 engine. Fig. 2.1 shows an earlier MTC D12 schematic, the power turbine was directly coupled to the crankshaft via fluid coupling, so it followed the speed of the engine normally operating between 1000-1300 rpm with a maximum allowed speed during engine braking of 1900 rpm. As a result, the turbine was relatively low stressed during the normal operation but highly stressed during engine braking. The MTC included a high efficiency axial turbine (Ø118 mm) with a stator. The duct between the turbocharger and the power turbine was on a common axis which meant that the gas conduit between them was annular with low pressure loss and high pressure recovery. In D13, the fluid coupling used was equal to the D12 except the gears, which were different due to new speeds and slightly changed centre distance.

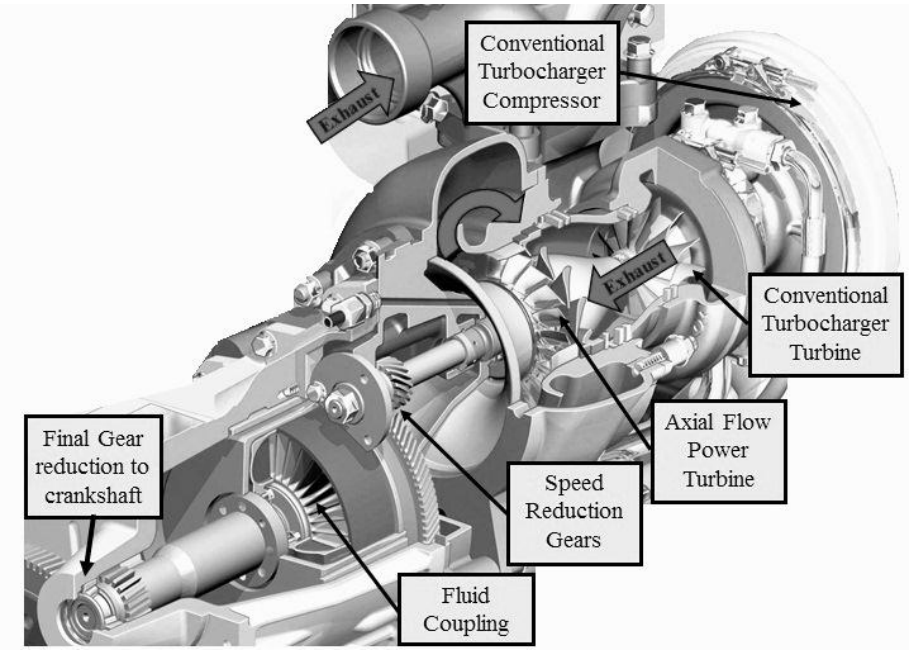

Figure 2.1 Schematic close-up of a Volvo D12 engine showing the turbocharger and turbocompound device

Volvo investigated three different types of transmission for connecting the power turbine and engine crankshaft. The differential fuel consumption results (Fig. 2.2) indicated that a fixed speed ratio fully mechanical system was the most efficient.

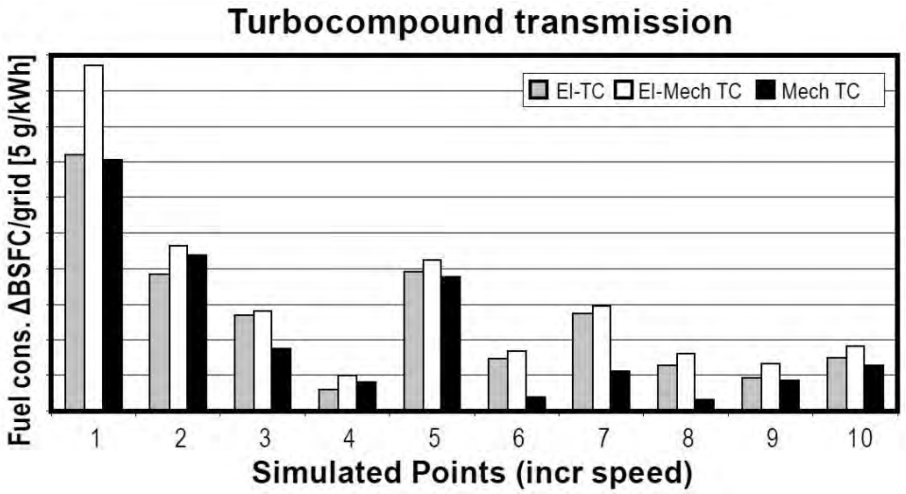

Figure 2.2 Differential fuel consumption of a turbocompound engine system at different engine operating points comparing electrical, electromechanical and mechanical power turbine transmissions

Appendix 2.2 - Supplement ETC information

Caterpillar
Kruiswyk et al., 2009, 2008

Caterpillar intends to deliver a total of 10% improvement in engine thermal efficiency. Remaining benefits are expected from: 3.7% from improving turbocharger efficiencies, 1.3% from intercooling the series turbocharging system, 0.5% from insulating the engine exhaust ports and 0.5% from reducing exhaust piping flow losses.

NTUA
Hountalas and Mavropoulos, 2010

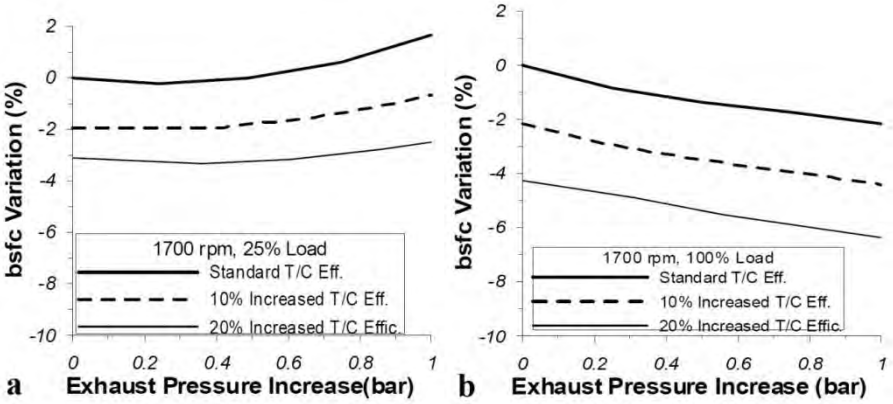

Figure 2.3 BSFC variation vs. exhaust pressure increase for ETC with various turbocharger efficiencies at 1700 rpm (a) 25% (b) 100% load

CPT, 2013

TIGERS included an electronically controlled full flow bypass that ensured the desired proportion of exhaust gas was delivered to the system which was fitted just below the engine exhaust manifold. Disadvantages were that the high temperatures meant the generator had to be water cooled and totally sealed. (Specifications: η generator 70%, weight 11 kg, length 230 mm, engine coolant cooled).

Appendix 2.3 - Supplement TEG information

MSU
Schock et al., 2008, 2006, 2005

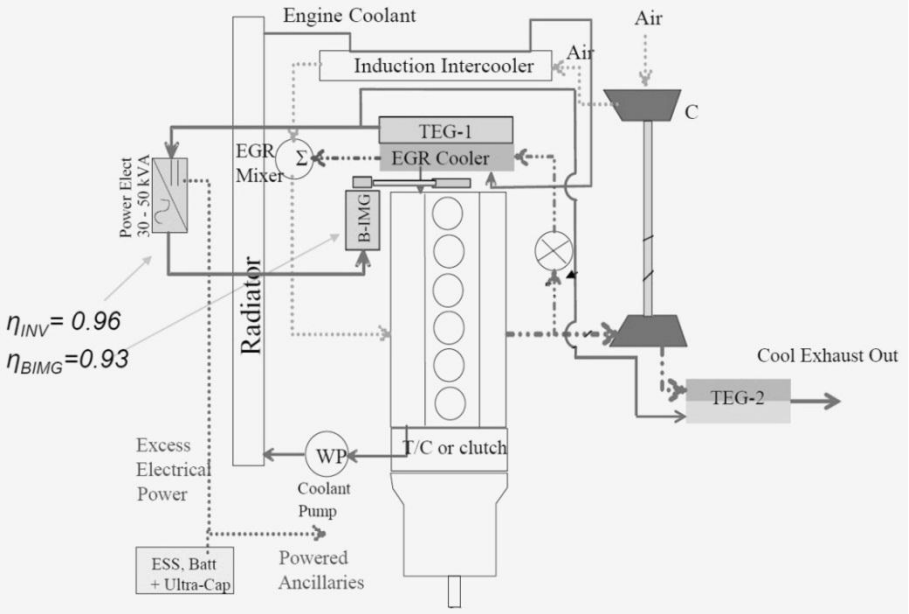

Figure 2.4 Potential dual TEG architecture of the thermal power split system

Appendix 2.4 - Supplement FBC information

Daimler
Aneja et al., 2011

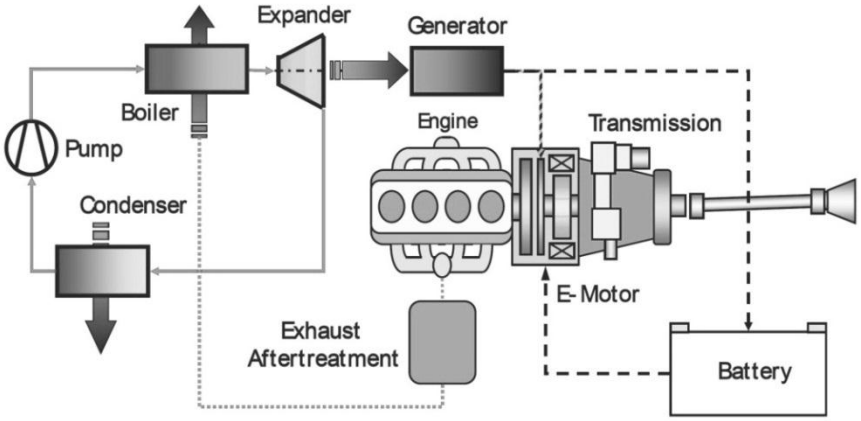

Figure 2.5 Schematic of an FBC integration with a hybrid vehicle

Honda
Endo et al., 2007

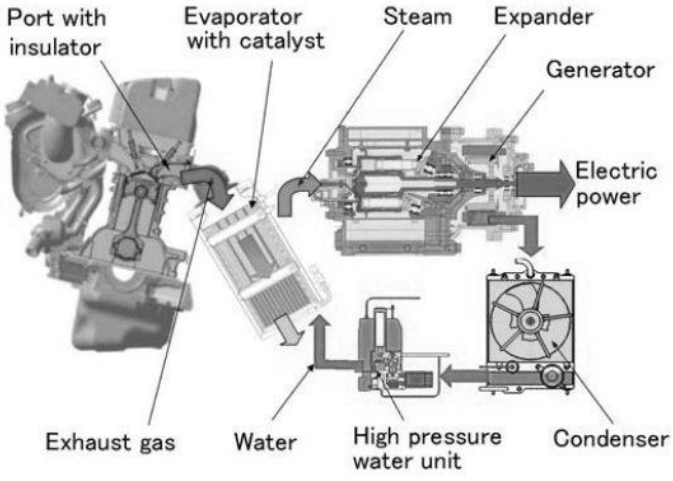

Figure 2.6 Overview of the demonstration Rankine cycle components and exhaust integration

Kim and Yu, 2011

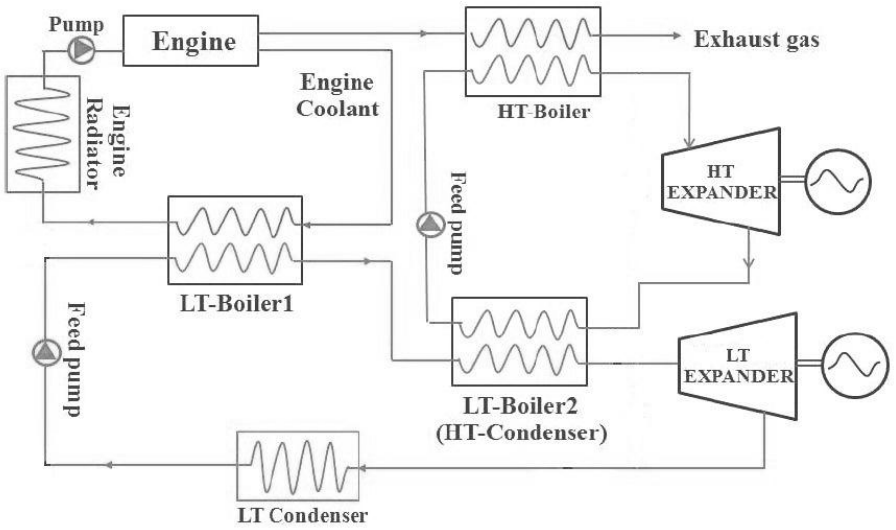

Figure 2.7 Cascade arrangement using water for high temperature heat and organic fluid for low temperature heat

Appendix 2.5 - Supplement open loop Rankine cycle information

Yamada and Mohamad, 2010

Fu et al., 2012

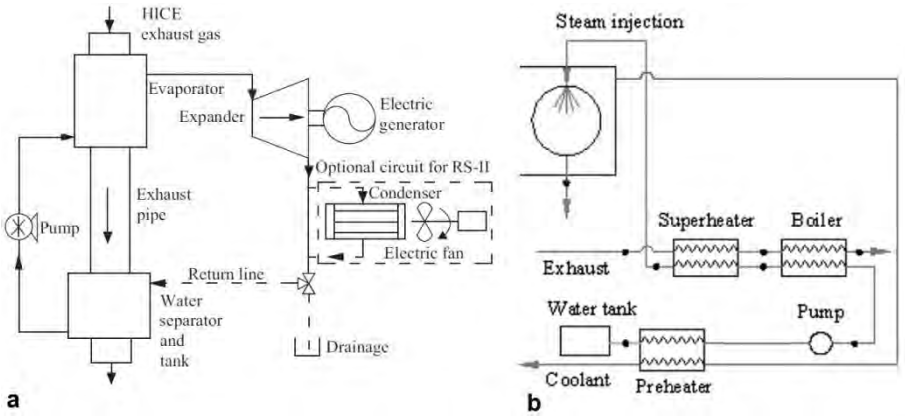

Figure 2.8 Conceptual sketch of open Rankine cycle for (a) hydrogen ICE (b) conventional ICE

Appendix 2.6 - Supplement information on other WHR concepts

heat2power Toom, 2008

Fu et al., 2013

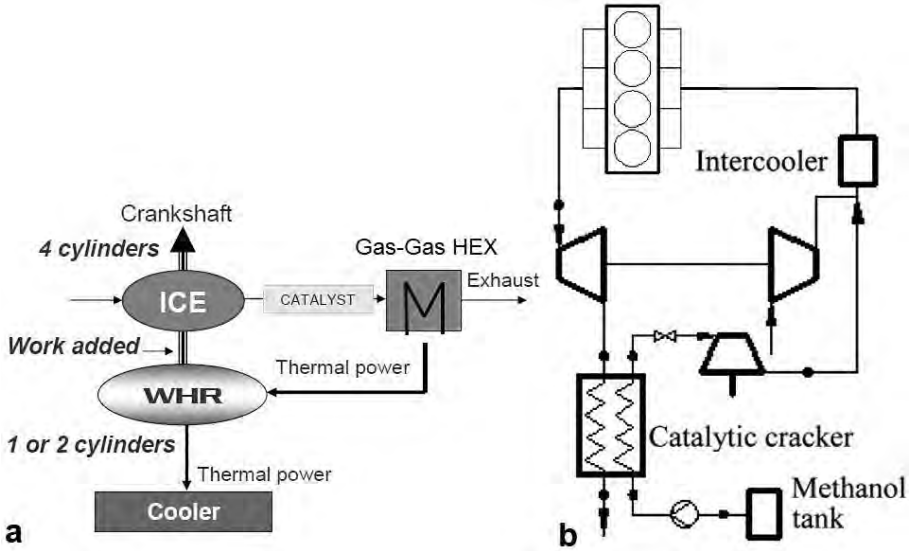

Figure 2.9 Schematic diagram of (a) heat2power concept (b) combined methanol dissociation and ORC system

Appendix 2.7 - Boundary conditions and assumptions in cited literature

<table>
<tr><td colspan="2">Mechanical turbocompounding</td></tr>
<tr><td>Hountalas and Mavropoulos, 2010
Hountalas et al., 2007</td><td>η: gear train 90%, power turbine 80%, mechanical turbine and compressor 95%</td></tr>
<tr><td colspan="2">Electric turbocompounding</td></tr>
<tr><td>Hountalas and Mavropoulos, 2010
Hountalas et al., 2007</td><td>η: electric generator 95%, isentropic turbine and compressor 80%</td></tr>
<tr><td colspan="2">Thermoelectric generator</td></tr>
<tr><td>LaGrandeur et al., 2008, 2007</td><td>Hot side 500°C and cold side 20°C</td></tr>
<tr><td colspan="2">Fluid bottoming cycle</td></tr>
<tr><td>Edwards et al., 2010</td><td>η_{pump}= 90%, $\eta_{turbine}$= 70%, $\varepsilon_{recuperator}$= 80% and $\varepsilon_{evaporator}$= 80%</td></tr>
<tr><td>Wang et al., 2011a</td><td>T_{source}= 327°C, T_{sink}= 27°C, η_{pump}= 80%, $\eta_{expander}$= 55%, $\varepsilon_{recuperator}$= 90% and $PR_{expander}$ = 8:1</td></tr>
<tr><td>Tian et al., 2012</td><td>T_{source}= 519°C, T_{max}= 250°C, T_{min}= 35°C, η_{pump}= 80%, $\eta_{turbine}$= 70% and T_{pp}= 30°C</td></tr>
<tr><td>Wang et al., 2012</td><td>$P_{expander1}$= 24 bar, $T_{condenserR245fa}$= 80°C, $T_{evaporatorR134a}$= 70°C, $T_{condenserR134a}$= 30°C, η_{pump}= 80%, $\eta_{expander}$= 75% and $T_{pp\ cascade}$= 5°C</td></tr>
<tr><td>El Chammas and Clodic 2005</td><td>η_{pump}= 60%, $\eta_{turbine}$= 70% and $\eta_{generator}$= 84%</td></tr>
<tr><td>Hussain and Brigham, 2010</td><td>T_{min}= 50°C, T_{max}= 140°C, $\varepsilon_{coolant\ HEX}$= 50%, $\varepsilon_{preheater}$= 50%, η_{pump}= 50%, $\eta_{turbine}$= 50% and $\eta_{generator}$= 80%</td></tr>
<tr><td>Vaja and Gambarotta 2010</td><td>T_{min}= 35°C, $T_{pp\ coolant}$= 20°C, $T_{pp\ evaporator}$= 30°C, η_{pump}= 80%, $\eta_{turbine}$= 70% and $\eta_{generator}$= 95%</td></tr>
<tr><td>Yamaguchi et al., 2013</td><td>η_{pump}= 95% and $\eta_{expander}$= 90%
<table>
<tr><th>Working fluid</th><th>P_{MAX} MPa</th><th>T_{MAX} C</th><th>P_{MIN} MPa</th><th>T_{MIN} C</th></tr>
<tr><td>Water</td><td>2.5</td><td>340</td><td>0.10</td><td>99.6</td></tr>
<tr><td>Methanol</td><td>4.0</td><td>270</td><td>0.11</td><td>66.6</td></tr>
<tr><td>Toluene</td><td>3.0</td><td>330</td><td>0.12</td><td>113.5</td></tr>
<tr><td>R123</td><td>3.5</td><td>320</td><td>0.21</td><td>49.6</td></tr>
<tr><td>R134a</td><td>4.0</td><td>180</td><td>1.30</td><td>49.5</td></tr>
<tr><td>R245fa</td><td>3.5</td><td>220</td><td>0.40</td><td>54.9</td></tr>
</table></td></tr>
<tr><td>Katsanos et al., 2010</td><td>P_{min}= 0.6 bar, P_{max}= 35 bar and $\eta_{expander}$= 85%</td></tr>
<tr><td>Cooper et al., 2009</td><td>T_{min}= 40°C, P_{max}= 35 bar, T_{pp}= 14°C, η_{pump}= 100%, $\eta_{turbine}$= 70% and $\eta_{generator}$= 90%
The engine model used was that described in Section 2.3 but excluded the VVA.</td></tr>
<tr><td>Arunachalam et al., 2012</td><td>P_{max}= 60 bar, $T_{pp\ evaporator}$= 20°C, η_{pump}= 60% and $\eta_{turbine}$= 78%</td></tr>
<tr><td>Hounsham et al., 2008a</td><td>T_{min}= 25°C, P_{max}= 18 bar and superheating= 300°C</td></tr>
</table>

Stobart et al., 2007	
Weerasinghe et al., 2010 Hounsham et al., 2008b	P_{min}= 1 bar, P_{max}= 18 bar
Ringler et al., 2009	T_{min}= 70°C, $T_{evaporator}$= 110°C and T_{max}= 300°C
Latz et al., 2013	$PR_{expander}$= 10:1, T_{pp}= 20°C, η_{pump}= 70% and $\eta_{expander}$= 70%

Chapter 3 Appendices

Appendix 3.1 - Supplement after-treatment information

- **Diesel Oxidation Catalyst**

DOCs contain palladium or platinum which uses O_2 in the exhaust to convert CO to CO_2 and HC to H_2O and CO_2. These flow-through devices often operate at 90% reduction efficiency. Although originally developed to reduce CO and HC, DOCs have also demonstrated 20-50% reduction in total PM on a mass basis (MECA, 2007). PM consists of carbon compounds (soot) due to incomplete combustion as a result of local low temperatures and fuel rich regions where the fuel is not fully atomised.

- **Diesel Particulate Filter**

DPFs typically consist of a cordierite substrate with a geometry that forces the exhaust gas through the substrate walls, leaving behind trapped soot particles. As the amount of trapped soot increases beyond a predefined limit, so does the ΔP across the DPF which triggers the regeneration. The soot loading is also limited to prevent extreme exotherms from damaging the cordierite substrate during regenerations (Zhang, 2009).

- **Selective Catalytic Reduction**

SCR catalysts are made from various ceramic materials used as a carrier, such as titanium oxide, and active catalytic components are usually oxides of base metals (vanadium, tungsten), zeolites, or various precious metals (Zhang, 2009). Base metal catalysts, such as the vanadium and tungsten, are less expensive but lack high thermal durability (<500°C) and have a high catalysing potential to oxidize SO_2 into SO_3, which can be extremely damaging due to its acidic properties (Cloudt et al., 2009b). Furthermore, high thermal durability is particularly important for SCR downstream an active DPF regeneration system.

Zeolite catalysts have the potential to operate at higher temperatures and can withstand prolonged operation at 630°C with transient conditions of up to 850°C (Zhang, 2009). Zeolites also have a lower potential for potentially damaging SO_2 oxidation. Zeolite catalysts are the mainstay for the EU, US and Japanese applications. Copper (Cu) and Iron (Fe) exchanged zeolites are also being used, both show less sensitivity to NO_2 composition and can be placed downstream of the DPF compared to vanadium catalyst. Cu-zeolite is attractive for its low temperature light-off characteristics whereas Fe-zeolite is better suited to higher temperatures. Cu and Fe zeolites can also be used together for a balanced performance over a broad temperature range (Johnson, 2009).

An SCR system actually comprises multiple catalyst modules (Arney et al., 2011). The first module is an oxidation catalyst, formulated to promote oxidation of NO to NO_2 to obtain a more favourable NO_2/NOx ratio. The second module is a hydrolysis catalyst designed to facilitate decomposition of urea to NH_3. The third module is the SCR catalyst. The final module in the SCR system includes an oxidation catalyst formulated to oxidize NH_3, reducing NH_3 slip that might occur in the SCR. The oxidized NH_3 forms NOx, so this becomes a balance between reducing NOx in the SCR and reducing NH_3 in the oxidation catalyst.

Other main components that make up the SCR system are the urea injection hardware, urea storage tank and a flow mixing device. The control of urea injection rate which is critical in maintaining the required NOx reduction is achieved either by engine mapping or NOx feed-forward control. The urea tank includes level sensor and a freeze expansion allowance. The tank and supply lines also require heating in low temperatures. Furthermore, SCR cannot be positioned really close-coupled to the DPF. There is always a certain length in the exhaust line required for the urea injection and appropriate mixing.

SCR has been deployed for over 6 years in mobile HDDEs and the technology is relatively dynamic. The main challenges facing the system are the reliable urea injection, uniform mixing and distribution of ammonia, NOx neutral SCR catalyst heating-up strategy, minimal ammonia slip, packaging and cost.

- **Other NOx technologies**

There are various other forms of NOx reduction techniques including Lean NOx Traps (LNT or NOx absorbers), combined LNT+SCR and solid SCR. In LNTs, the catalyst stores the NOx until the active sites fill up, this then sets off the regeneration phase, in which Diesel fuel is injected directly into the exhaust gas triggering the conversion of NOx to N_2 and H_2O. LNTs have shown 70-90% NOx reduction efficiency and favourable packaging conditions (MECA, 2007). However, the regeneration phase exacts a fuel penalty in the range of 4-5% of total fuel flow (US DOE, 2011, Schnitzler, 2007). LNTs are also quickly poisoned by sulphur, to drive off accumulated sulphur the absorbers are heated to high temperatures using fuel (desulfation). The regenerations and desulfations have shown to deteriorate the catalyst effectiveness which requires substantial quantities of platinum group metals, and the cost of these materials is high and volatile. While LNTs have a larger fuel penalty than SCR, LD vehicle manufacturers prefer LNTs since the overall fuel efficiency is less of a concern and urea replenishment is more of a challenge compared to HD vehicles. Other drawbacks to LNT use on HDDEs are that they are larger in relation to engine displacement (being over twice as large as those required for LD vehicles) (US DOE, 2011).

For improvements in the temperature range of operation, LNTs can also be placed closer to the engine than SCR systems, which require more distance for urea mixing. Results have shown a 60°C temperature increase, giving a 10% efficiency advantage over an SCR system placed further downstream for a LD vehicle (Johnson, 2009). Another way to potentially extend the operating window of the LNT concept was proposed through a close coupled LNT configuration with two bricks (Schnitzler, 2007). The smaller LNT closer to the engine was used to convert the NOx in the low temperature operating conditions, whereas the under-floor LNT provided the required efficiencies under high temperature operating conditions. An additional development being pursued for LNT technology is to pair them with SCR catalysts for LD vehicles (US DOE, 2011). The advantage was that the SCR catalyst used the NH_3 produced by the LNT so no urea was needed. Results have shown NOx reduction efficiency of 90% from the LNT alone have been increased to 98% from the LNT+SCR combination for equivalent fuel penalty.

For HDDE, Navistar offer a DOC+DPF+EGR only solution for US 2010 NOx limit based on credits obtained from exceeding US 2007 limit. These engines achieve 0.54-0.67 g/kWh, to finally reach the 0.27 g/kWh NOx emission standard, Navistar is exploring the use of solid SCR system (Zhang, 2009). The solid SCR System is a viable alternative to a liquid urea SCR system and the retrofit market is seen as a prime target. With a volume reduction of ≈70%, the solid SCR system is stated to offer equivalent performance to a liquid urea SCR system. It offers packaging advantages and does not require the heated storage tanks as in the liquid urea SCR system.

Appendix 3.2 - Relationship between the selected ESC test points and ETC

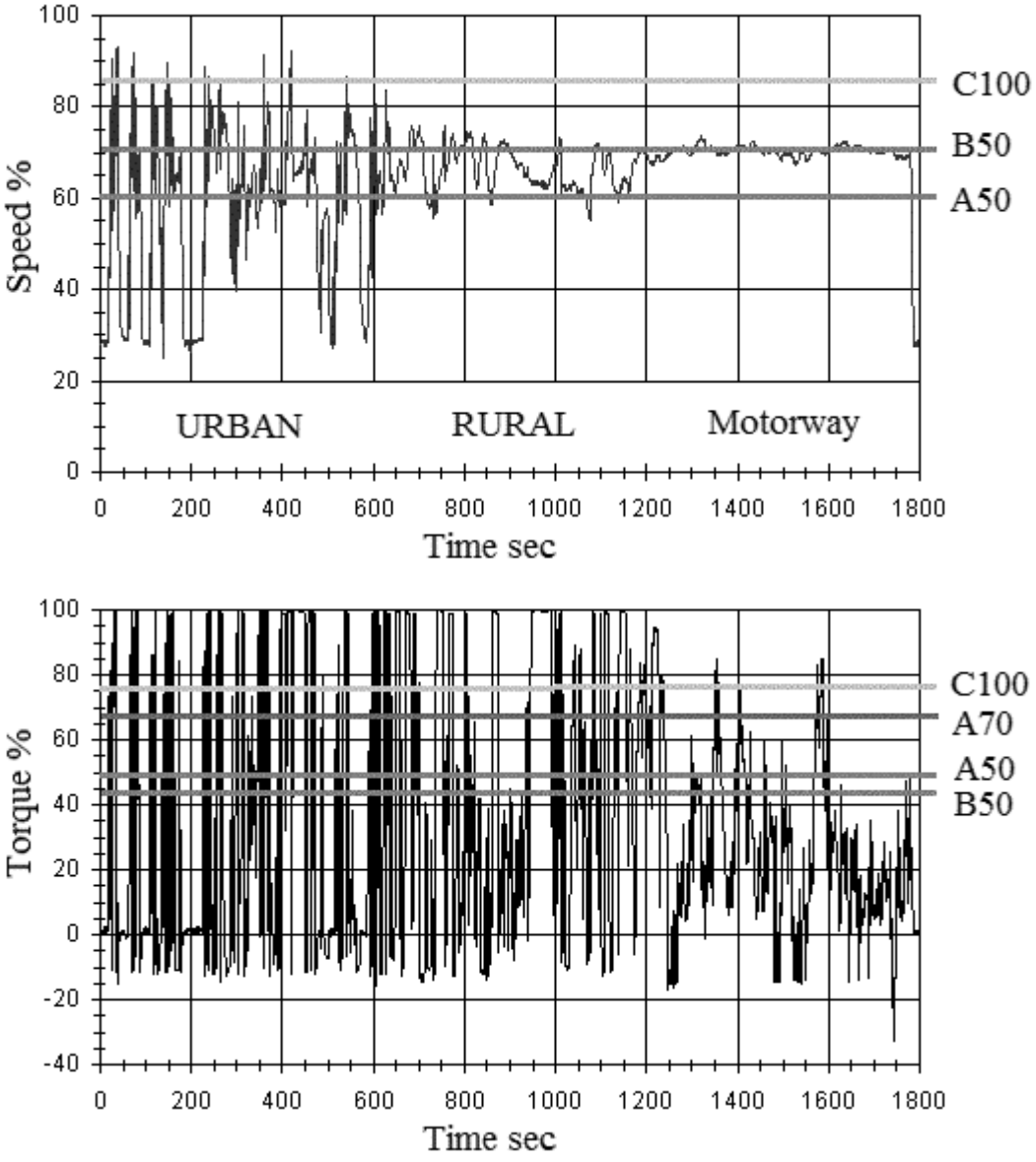

Figure 3.1 Relationship between the 4 selected speed/load ESC test points, and its speed relevance to ETC rural and motorway driving conditions

Appendix 3.3 - Test bed dimension

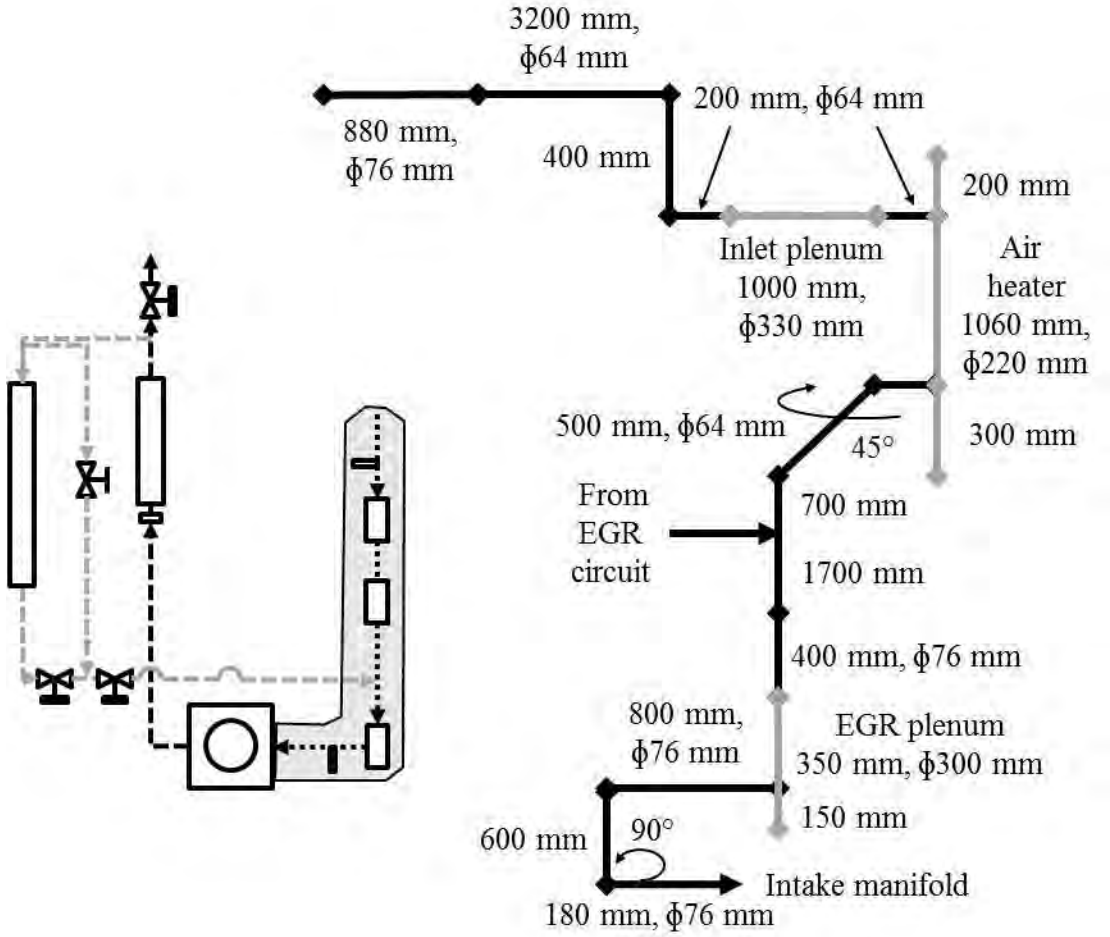

Figure 3.2 Test bed - intake side dimensions (lengths, orientations and cross sections)

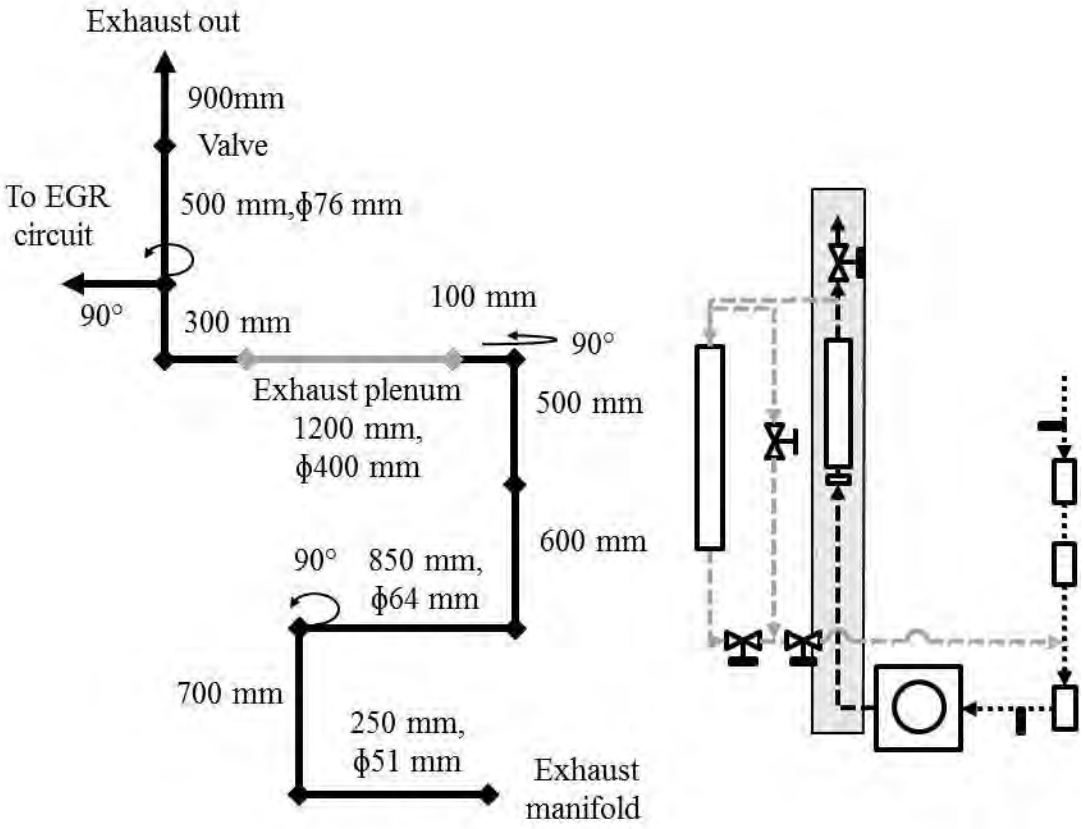

Figure 3.3 Test bed - exhaust side dimensions (lengths, orientations and cross sections)

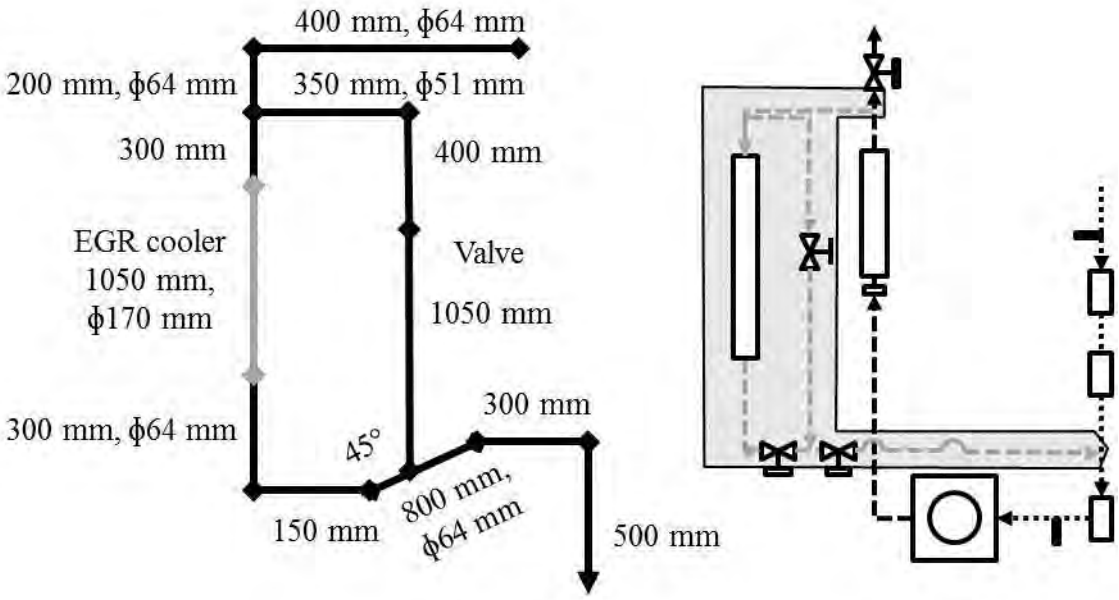

Figure 3.4 Test bed - EGR side dimensions (lengths, orientations and cross sections)

Appendix 3.4 - HDDE energy balance

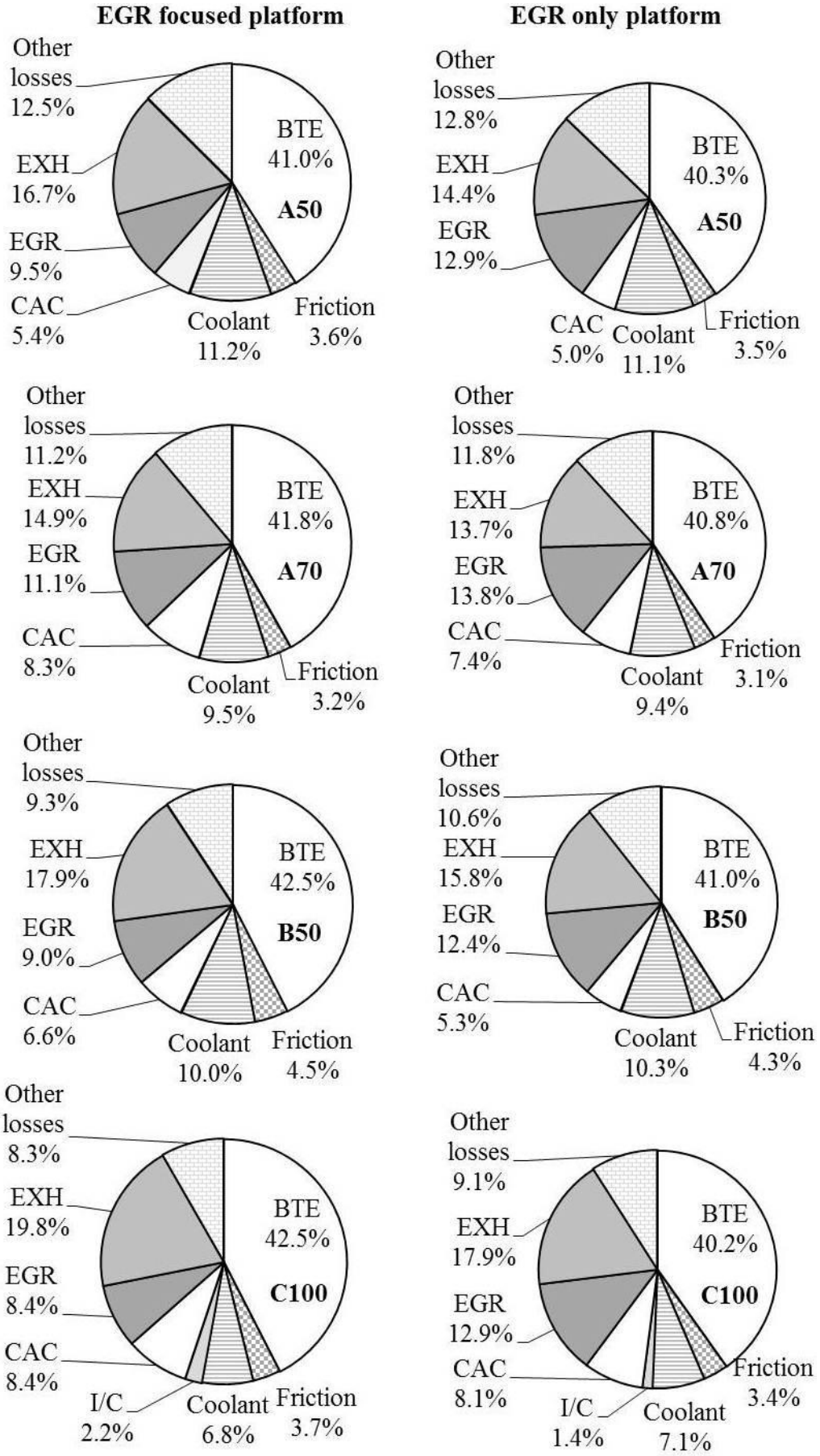

Figure 3.5 Energy balance of the two selected engine platforms at the 4 test points

Note: As the values for EGR, CAC and inter-cooler correspond only to the available heat in the heat exchangers, the miscellaneous heat loss that usually accounts for 3-6% are

slightly higher around 8.3-12.8%. This miscellaneous heat loss also includes lubricant cooling, which was typically 20% of the engine coolant load.

Appendix 3.5 - HDDE heat quality and quantity

Table 3.1 Engine performance, waste heat qualities and quantities in the different heat exchanger streams

EGR focused platform (BSFC, Brake Power, Brake Torque)	Inter-cooler kW [°C-°C]	CAC kW [°C-°C]	EGR kW [°C-°C]	EXH kW [°C-°C]	Coolant kW [°C-°C]
A50 (205g/kWh,145kW,1062Nm)		18.9 [146-45]	33.3 [409-96]	46.6 [321-96]	39.4 [97-90]
A70 (201g/kWh,198kW,1457Nm)		39.2 [203-60]	52.7 [400-96]	51 [262-95]	45 [97-90]
B50 (198g/kWh,150kW,955Nm)		23.4 [147-42]	31.8 [357-96]	44.1 [272-95]	35.3 [97-90]
C100 (198g/kWh,284kW,1505Nm)	14.9 [137-103]	55.9 [169-43]	56.2 [436-97]	99.5 [300-96]	45.1 [97-90]
EGR only platform					
A50 (209g/kWh,150kW,1104Nm)		18.6 [163-49]	48.2 [430-96]	42.5 [325-98]	41.3 [97-90]
A70 (206g/kWh,199kW,1462Nm)		35.9 [204-56]	67.5 [420-95]	48.6 [276-98]	46 [97-90]
B50 (205g/kWh,151kW,960Nm)		19.5 [151-50]	45.6 [389-95]	41.3 [290-97]	38 [97-90]
C100 (209g/kWh,296kW,1571Nm)	10.2 [145-121]	60 [200-61]	94.9 [466-96]	97.8 [302-96]	52.6 [97-90]

Note: The exhaust heat as a percentage of fuel combustion energy is lower in Appendix 3.5 compared to Appendix 3.4, this is because in Appendix 3.5 the exhaust is cooled between 95-100°C, while the energy balance for exhaust in Appendix 3.4 considers cooling to the ambient conditions.

Chapter 4 Appendices

Appendix 4.1 - Carcinogenic risk category

Table 4.1 IARC and EPA hazard identification and carcinogenic risk categories

IARC	
1	Carcinogenic to humans
2A	Probably carcinogenic to humans
2B	Possibly carcinogenic to humans
3	Not classifiable as to its carcinogenicity to humans
4	Probably not carcinogenic to humans

EPA	
A	Human carcinogen
B	Likely to be carcinogenic to humans
C	Possible human carcinogen
D	Not classifiable as to human carcinogenicity
I	Inadequate information to assess carcinogenic potential

Appendix 4.2 - ASHRAE 34 classification

Table 4.2 ASHRAE 34 safety group classification consisting of two alphanumeric characters

Flammability in Air @ 60°C & 1.013 Bar	ASHRAE 34 Safety group	
Higher Flammability, LFL or ETFL60 ≤ 100 g/m^3 or HOC ≥ 19 MJ/kg	A3	B3
Lower Flammability, LFL or ETFL60 > 100 g/m^3 & HOC < 19 MJ/kg	A2	B2
Lower Flammability, LFL or ETFL60 > 100 g/m^3 & HOC < 19 MJ/kg with a maximum burning velocity of ≤ 10 cm/s	A2L	B2L
No flame Propagation	A1	B1
	Lower Toxicity OEL ≥ 400 ppm	Higher Toxicity OEL < 400 ppm
LFL, Lower Flammability Limit ETFL60, Elevated Temperature Flame Limit @ 60°C HOC, Heat Of Combustion OEL, Occupational Exposure Limits		

Appendix 4.3 - NFPA 704 classification

Table 4.3 NFPA 704 standard system for the identification of the hazards of materials for emergency response

Hazard level	Health	Flammability	Instability/Reactivity
0 Minimal	Poses no health hazard, no precautions necessary	Will not burn	Normally stable, even under fire exposure conditions, and is not reactive with water
1 Slight	Exposure would cause irritation with only minor residual injury	Must be heated before ignition can occur. Flash point over 93°C	Normally stable, but can become unstable at elevated temperatures and pressures
2 Moderate	Intense or continued but not chronic, exposure could cause temporary incapacitation or possible residual injury	Must be moderately heated or exposed to relatively high ambient temperature before ignition can occur. Flash point between 38°C and 93°C	Undergoes violent chemical change at elevated temperatures and pressures, reacts violently with water, or may form explosive mixtures with water
3 Serious	Short exposure could cause serious temporary or moderate residual injury	Liquids and solids that can be ignited under almost all ambient temperature conditions. Liquids having a Flash point below 23°C and having a Boiling point at or above 38°C or having a Flash point between 23°C and 38°C	Capable of detonation or explosive decomposition but requires a strong initiating source, must be heated under confinement before initiation, reacts explosively with water, or will detonate if severely shocked
4 Severe	Very short exposure could cause death or major residual injury	Will rapidly or completely vaporize at normal atmospheric pressure and temperature, or is readily dispersed in air and will burn readily. Includes pyrophoric substances. Flash point below 23°C	Readily capable of detonation or explosive decomposition at normal temperatures and pressures

Appendix 4.4 - Fluids under consideration in this study

Table 4.4 Chemical identification of the fluids in the present literature and under consideration in this study

Number	Chemical class	Formula	Name	CAS no.
Fluids in the present literature				
R718	other-inorganic	H2O	Water	7732-18-5
	n-alcohols	C2H6O	Ethanol	64-17-5
R245fa	CHF-compounds	C3H3F5	1,1,1,3,3-Pentafluoropropane	460-73-1
Fluids under consideration for EGR and exhaust heat recovery				
R160I1	CHI-compounds	C2H5I	Ethyl-Iodide	75-03-6
	nitriles	CH3CN	Acetonitrile	75-05-8
R150a	C1/C2-aliphatic-chlorides	C2H4Cl2	1,1-Dichloroethane	75-34-3
	n-alcohols	CH4O	Methanol	67-56-1
R30	C1/C2-aliphatic-chlorides	CH2Cl2	Dichloromethane	75-09-2
	ketones	C3H6O	Acetone	67-64-1
	acetates	C3H6O2	Methyl-Acetate	79-20-9
Fluids under consideration for CAC heat recovery				
R152	CHF-compounds	C2H4F2	1,2-Difluoroethane	624-72-6
E245fa1	polyfunctional-CHO,halide	C3H3F5O	2-Difluoromethoxy-1,1,1-Trifluroethane	1885-48-9
R143	CHF-compounds	C2H3F3	1,1,2-Trifluoroethane	430-66-0
E152a	polyfunctional-CHO,halide	C2H4F2O	Difluoromethyl-Methyl-Ether	359-15-9
E245cb1	polyfunctional-CHO,halide	C3H3F5O	Pentafluoroethyl-Methyl-Ether	22410-44-2

Table 4.5 Thermodynamic and thermo-physical properties of the fluids in the present literature and under consideration in this study

	T_{crit} °C	P_{crit} bar	T_{boil} °C	M_{wt} g/mol	ρ_{liq} kg/m³	T_{freez} °C	λ W/mK at T_{boil}	H_{vap} kJ/kg at T_{boil}
Fluids in the present literature								
Water	374	220.6	100	18	998	0	0.68	2258
Ethanol	241	61.4	78	46.1	792	-114	0.15	847
R245fa	154	36.4	15	134	1364	-107	0.08	196
Fluids under consideration for EGR and exhaust heat recovery								
Ethyl-Iodide	281	47.1	72	156	1923	-111	0.08	183
Acetonitrile	272	48.3	82	41.1	777	-44	0.18	805
1,1-Dichloroethane	250	50.7	57	99	1168	-97	0.1	293
Methanol	239	80.8	65	32	794	-98	0.19	1172
Dichloromethane	237	60.8	40	84.9	1318	-95	0.13	324
Acetone	235	47	56	58.1	785	-95	0.15	519
Methyl-Acetate	233	47.5	57	74.1	928	-98	0.14	410
Fluids under consideration for CAC heat recovery								
R152	172	43.4	11	66.1	1013		0.12	366
E245fa1	171	34.2	29	150	1386	-123	0.11	183
R143	157	52.4	5	84	1216	-84	0.15	308
E152a	149	43.3	-5	82	1128	-71	0.1	284
E245cb1	134	28.9	6	150	1266	-120	0.08	161

Table 4.6 Environmental and safety properties of the fluids in the present literature and under consideration in this study

	ATM years	ODP	GWP	ASHRAE 34	Carcinogen IARC	Carcinogen EPA	NFPA H	NFPA F	NFPA I	T_{ign} °C
Fluids in the present literature										
Water	<0.019		0	A1			0	0	0	
Ethanol					1		2	3	0	363
R245fa	7.7		1030	B1			2	0	1	412
Fluids under consideration for EGR and exhaust heat recovery										
Ethyl-Iodide	0.011						2	2	0	
Acetonitrile						D	2	3	0	524
1,1-Dichloroethane		<0.001				C	2	3	0	458
Methanol							1	3	0	464
Dichloromethane	0.394	<0.001	10	B2	2B	B	2	1	0	556
Acetone						I	1	3	0	465
Methyl-Acetate							1	3	0	502
Fluids under consideration for CAC heat recovery										
R152	0.5		43							
E245fa1	5.5		740							
R143	3.5		352							
E152a	2		110							
E245cb1	4.9		680							

Appendix 4.5 - Pure fluid screening

Table 4.7 Pure fluid screening result
(Phase 1: Thermo-physical, Legal, Molecular, Environmental and Safety)

Name	T_{boil} °C	Formula	Structure	5 ≤ # of atoms ≤ 12	# of H ≤ 6	# of F ≤ 2	T_{crit} > 130 °C	ρ_{liq} 750-200 kg/m^3	T_{freez} < – 40 °C	Health ≤ 2	Flammability ≤ 3	Instability = 0	T_{ign} ≥ 363 °C
Bicyclo-2-2-1-Heptane	105	C7H12		X									
1,3-Dioxane	105	C4H8O2		X									
2,4,4-Trimethyl-2-Pentene	105	C8H16		X									
Bromotrichloromethane	105	CBRCL3	X										
1,1,3-Trimethylcyclopentane	105	C8H16		X									
n-Ethyl-2-Methylallylamine	105	C6H13N		X									
n-Pentylamine	105	C5H13N		X									
Allyl-Acetate	104	C5H8O2		X									
Isobutyronitrile	104	C4H7N								X			
Acetal	104	C6H14O2		X									
Ethylcyclopentane	103	C7H14		X									
Perfluoro-n-Octane	103	C8F18		X									
Valeraldehyde	103	C5H10O		X									
Methyl-Butyrate	103	C5H10O2		X									
Trans-Crotonaldehyde	103	C4H6O								X			
n-Propyl-Iodide	102	C7H7I		X									
Methyl-n-Propyl-Ketone	102	C5H10O		X									
Benzotrifluoride	102	C7H5F3		X									
2-Methyl-2-Butanol	102	C5H12O		X									
Diethyl-Ketone	102	C5H10O		X									
n-Propyl-Acetate	102	C5H10O2		X									
2,4,4-Trimethyl-1-Pentene	101	C8H16		X									
Ethyl-Tert-Pentyl-Ether	101	C7H16O		X									
1,4-Dioxane	101	C4H8O2		X									
1-Bromobutane	101	C4H9BR	X										
Nitromethane	101	CH3NO2							X				
Methylcyclohexane	101	C7H14		X									
Hexamethyldisiloxane	101	C6H18OSI2		X									
Methyl-Methacrylate	100	C5H8O2		X									
Water	100	H2O											
1-Heptyne	100	C7H12		X									
2-Butanol	100	C4H10O		X									
Cis-1,2-Dimethylcyclopentane	100	C7H14		X									
Ethyl-Acrylate	100	C5H8O2		X									
2,2,4-Trimethylpentane	99	C8H18		X									
Ethyl-Propionate	99	C5H10O2		X									
Trimethyl-Silanol	99	C3H10OSI		X									
Methyl-T-Butyl-Sulfide	99	C5H12S		X									
Methyl-n-Pentyl-Ether	99	C6H14O		X									
n-Butyl-Mercaptan	98	C4H10S		X									
n-Heptane	98	C7H16		X									
Cis-2-Heptene	98	C7H14		X									
Isobutyl-Formate	98	C5H10O2		X									
Isopropyl-Isobutyl-Ether	98	C7H16O		X									

Methyl-Isopropenyl-Ketone	98	C5H8O		X									
Trans-2-Heptene	98	C7H14		X									
Ethyltrichlorosilane	98	C2H5SICL3	X										
Trichloroacetaldehyde	98	C2HCL3O	X										
Propionitrile	97	C3H5N								X			
1-Propanol	97	C3H8O		X									
Allyl-Alcohol	97	C3H6O								X			
Dibromomethane	97	CH2BR2	X										
3-Methoxyisopropylamine	97	C4H11NO		X									
1-Methylvinyl-Acetate	97	C5H8O2		X									
1,2-Dichloropropane	96	C3H6CL2								X			
Tert-Butyl-Acetate	96	C2H12O2		X									
Cis-3-Heptene	96	C7H14		X									
Trans-3-Heptene	96	C7H14		X									
Methyl-n-Propyl-Sulfide	96	C4H10S		X									
2-Norbornene	96	C7H10		X									
Vinyl-Propionate	95	C5H8O2		X									
Trimethylene-Sulfide	95	C3H6S									X		
Methyl-Isopropyl-Ketone	94	C5H10O		X									
2-Ethyl-1-Pentene	94	C7H14		X									
N,n-Dimethyl-n-Butylamine	94	C6H15N		X									
Butyl-Vinyl-Ether	94	C6H12O		X									
Methyl-Vinyl-Dichlorosilane	94	C3H6SICL2								X			
1-Heptene	94	C7H14		X									
3-Ethylpentane	93	C7H16		X									
sec-Butyl-Formate	93	C5H10O2		X									
2,3-Dichloropropene	93	C3H4CL2								X			
1,2-Dimethoxypropane	93	C5H12O2		X									
1,1,1-Trichlorofluoroethane	93	C2H2CL3F	X										
Ethyl-Chloroformate	93	C3H5CLO2								X			
3-Methylbutyraldehyde	93	C5H10O		X									
Methyl-Isobutyrate	92	C5H10O2		X									
Ethyl-Butyl-Ether	92	C6H14O		X									
Diethyl-Sulfide	92	C4H10S		X									
Trans-1,2-Dimethylcyclopentane	92	C7H14		X									
3-Methylhexane	92	C7H16		X									
2-Methyl-1-Hexene	92	C7H14		X									
Trans-1,3-Dimethylcyclopentane	92	C7H14		X									
2-Methylbutyraldehyde	92	C5H10O		X									
2-Bromobutane	91	C4H9BR	X										
Cis-1,3-Dimethylcyclopentane	91	C7H14		X									
Vinyltrichlorosilane	91	C2H3SICL3	X										
Methacrylonitrile	90	C4H5N							X				
Dimethyl-Carbonate	90	C3H6O3							X				
Di-n-Propyl-Ether	90	C6H14O		X									
2-Methylhexane	90	C7H16		X									
2,3-Dimethylpentane	90	C7H16		X									
Isopropyl-Iodide*	90	C3H7I											
Dichloroacetaldehyde**	89	C2H2CL2O											
Triethylamine	89	C6H15N		X									
Cis-Crotonaldehyde	89	C4H6O								X			
Isopropyl-Acetate	89	C5H10O2		X									
Isobutyl-Mercaptan	88	C4H10S		X									
1,1-Dichloropropane**	88	C3H6CL2											

1,1-Dimethylcyclopentane	88	C7H14		X									
Ethylal	88	C5H12O2		X									
1,4-Cyclohexadiene	87	C6H8		X									
Trichloroethylene	87	C2HCL3	X										
4-Methyl-1-Hexene	87	C7H14		X									
Pyrrolidine	87	C4H9N		X									
Methyl-Tert-Pentyl-Ether	86	C6H14O		X									
3,3-Dimethylpentane	86	C7H16		X									
5-Methyl-1-Hexene	85	C7H14		X									
sec-Butyl-Mercaptan	85	C4H10S		X									
Chloroacetaldehyde	85	C2H3CLO							X				
Methyl-Isopropyl-Sulfide	85	C4H10S		X									
Fluorobenzene***	85	C6H5F											
1,2-Dimethoxyethane	85	C4H10O2		X									
2-Hexyne	85	C6H10		X									
Trimethoxysilane	84	C3H10SIO3		X									
Thiophene	84	C4H4S							X				
3-Ethyl-1-Pentene	84	C7H14		X									
3-Methyl-1-Hexene	84	C7H14		X									
Diisopropylamine	84	C6H15N		X									
Cis,Trans-2,4-Hexadiene	84	C6H10		X									
1,2-Dichloroethane	83	C2H4CL2							X				
Cyclohexene	83	C6H10		X									
Tert-Butyl-Formate	83	C5H10O2		X									
Tert-Butyl-Alcohol	82	C4H10O		X									
Isopropyl-Alcohol	82	C3H8O			X								
2-Methyldioxolane	82	C4H12SIO2		X									
Trans,Trans-2,4-Hexadiene	82	C6H10		X									
Acetonitrile	82	C2H3N											
Dimethyldimethoxysilane	81	C4H12SIO2		X									
3-Hexyne	81	C6H10		X									
Ethyl-Isobutyl-Ether	81	C6H10O		X									
2,2,3-Trimethylbutane	81	C7H16		X									
n-Propyl-Formate	81	C4H8O2		X									
Cyclohexane	81	C6H12		X									
2,4-Dimethylpentane	80	C7H16		X									
1,3-Cyclohexadiene	80	C6H8		X									
Perfluorobenzene	80	C6F6		X									
Methyl-Acrylate	80	C4H6O2								X			
Benzene	80	C6H6							X				
2-Methyloxolane	80	C5H10O		X									
Methyl-Ethyl-Ketone	80	C4H8O		X									
Methyl-Propionate	79	C4H8O2		X									
2,2-Dimethylpentane	79	C7H17		X									
n-Methylpyrrolidine	79	C5H11N		X									
1-Chlorobutane	78	C4H9CL		X									
Ethanol	78	C2H6O											
2,3,3-Trimethyl-1-Butene	78	C7H14		X									
n-Butyl-Amine	77	C4H11N		X									
Acrylonitrile	77	C3H3N								X			
Ethyl-Acetate	77	C4H8O2		X									
2-Methyl-2-Aminobutane	77	C5H13N		X									
1,2-Hexadiene	76	C6H10		X									
Trans-2-Methyl-1,3-Pentadiene	76	C6H10		X									

1-Methylcyclopentene	75	C6H10		X									
n-Butyraldehyde	75	C4H8O		X									
1,1,1-Trichloroethane	74	C2H3CL3	X										
2,3-Dimethyl-2-Butene	73	C6H12		X									
Methylcyclopentadiene	73	C6H8		X									
Vinyl-Acetate	73	C4H6O2										X	
Trans-1,3-Hexadiene	73	C6H10		X									
Ethyl-Iodide	72	C2H5I											
Tert-Butyl-Ethyl-Ether	72	C6H14O		X									
Methylcyclopentane	72	C6H12		X									
Trifluoroacetic-Acid	72	C2HF3O2							X				
1-Hexyne	71	C6H10		X									
1-Bromopropane	71	C3H7BR	X										
Methyl-Chloroformate	71	C2H3CLO2								X			
3-Methyl-Trans-2-Pentene	70	C6H12		X									
Dimethyldichlorosilane	70	C2H6SICL2								X			
Methyl-n-Butyl-Ether	70	C5H12O		X									
Cis-2-Hexene	69	C6H12		X									
Isobutyl-Chloride	69	C4H9CL		X									
2,3-Dimethyl-1,3-Butadiene	69	C6H10		X									
n-Hexane	69	C6H14		X									
Diisopropyl-Ether	68	C6H14O		X									
2-Chlorobutane	68	C4H9CL		X									
Bromochloromethane	68	CH2BRCL	X										
Methacrolein	68	C4H6O								X			
Trans-2-Hexene	68	C6H12		X									
Isobutyl-Amine	68	C4H11N		X									
n-Propylmercaptan	68	C3H8S			X								
3-Methyl-Cis-2-Pentene	68	C6H12		X									
2-Methyl-2-Pentene	67	C6H12		X									
Trans-3-Hexene	67	C6H12		X									
Methyl-Ethyl-Sulfide	67	C6H8S		X									
Propyleneimine	67	C3H7N								X			
Cis-3-Hexene	66	C6H12		X									
Methyl-Trichlorosilane	66	CH3SICL3	X										
Tetrahydrofuran	66	C4H8O		X									
2,5-Dihydrofuran****	66	C4H6O											
4-Methylcyclopentene	66	C6H10		X									
N,n-Diethylmethylamine	65	C5H13N		X									
1,4-Hexadiene	65	C6H10		X									
3-Methylcyclopentene	65	C6H10		X									
Methanol	65	CH4O											
2-Ethyl-1-Butene	65	C6H12		X									
1,1-Dimethoxyethane	64	C4H10O2		X									
Tert-Butyl-Mercaptan	64	C4H10S		X									
Isobutyraldehyde	64	C4H8O		X									
Ethyl-Propyl-Ether	64	C5H12O		X									
1-Hexene	63	C6H12		X									
1,2-Epoxybutane	63	C4H8O		X									
3-Methyl-Pentane	63	C6H14		X									
sec-Butylamine	63	C4H11N		X									
2-Methyl-1-Pentene	62	C6H12		X									
Chloroform	61	CHCL3	X										
Cis-1,2-Dichloroethylene	61	C2H2CL2										X	

2-Methyl-Pentane	60	C6H14		X									
Chloromethyl-Methyl-Ether	60	C2H5CLO							X				
1,5-Hexadiene	59	C6H10		X									
2-Bromopropane	59	C3H7BR	X										
Chloroprene	59	C4H5CL									X		
Methyl-sec-Butyl-Ether	59	C5H12O		X									
4-Methyl-Trans-2-Pentene	59	C6H12		X									
Methyl-Isobutyl-Ether	59	C5H12O		X									
2,3-Dimethyl-Butane	58	C6H14		X									
Propargyl-Chloride	58	C3H3CL							X				
Trimethylchlorosilane	58	C3H9SICL		X									
1,1-Dichloroethane	57	C2H4CL2											
Methyl-Acetate	57	C3H6O											
4-Methyl-Cis-2-Pentene	56	C6H12		X									
Acetone	56	C3H6O											
2-Pentyne	56	C5H8		X									
Ethylene-Imine	56	C2H5N											X
2,3-Dimethyl-1-Butene	56	C6H12		X									
Diethyl-Amine	55	C4H11N		X									
Methyl-Tert-Butyl-Ether	55	C5H12O		X									
Ethyl-Formate*****	54	C3H6O2											
3-Methyl-1-Pentene	54	C6H12		X									
4-Methyl-1-Pentene	54	C6H12		X									
Allylamine	53	C3H7N			X								
Ethyl-Isopropyl-Ether	53	C5H12O		X									
3-Methyl-1,4-Pentadiene	53	C6H10		X									
Acrolein	53	C3H4O							X				
Isopropyl-Mercaptan	53	C3H8S			X								
1,2-Epoxy-2-Methylpropane	52	C4H8O		X									
Acetyl-Chloride	51	C2H3CLO							X				
Tert-Butyl-Chloride	51	C4H9CL		X									
Glyoxal	50	C2H2O2						X					
Cyclopropylamine	50	C3H7N			X								
2,2-Dimethyl-Butane	50	C6H14		X									
Cyclopentane	49	C5H10		X									
2,3-Pentadiene	48	C5H8		X									
n-Propionaldehyde	48	C3H6O											X
n-Propyl-Amine	48	C3H9N		X									
Trans-1,2-Dichloroethylene	48	C2H2CL2									X		
1,2,2-Trichloro-1,1,2-Trifluoroe	48	C2CL3F3	X										
Vinyl-Formate****	47	C3H4O2											
Propyl-Chloride	47	C3H7CL			X								
1,1,1-Trichlorotrifluoroethane	46	C2CL3F3	X										
Allyl-Chloride	45	C3H5CL							X				
1,2-Pentadiene	45	C5H8		X									
Tert-Butylamine	44	C4H11N		X									
Cyclopentene	44	C5H8		X									
Cis-1,3-Pentadiene	44	C5H8		X									
Methyl-Iodide	42	CH3I					X						
1-Trans-3-Pentadiene	42	C5H8		X									
Methylal	42	C3H8O2		X									
Methyl-Dichlorosilane	42	CH4SICL2							X				
3,3-Dimethyl-1-Butene	41	C6H12		X									
3-Methyl-1,2-Butadiene	41	C5H8		X									

1-Pentyne	40	C5H8		X									
Dichloromethane	40	CH2CL2											
Methyl-n-Propyl-Ether	39	C4H10O		X									
2-Methyl-2-Butene	39	C5H10		X									
Ethyl-Bromide	38	C2H5BR	X										
Dimethyl-Sulfide	37	C2H6S								X			
Cis-2-Pentene	37	C5H10		X									
Trans-2-Pentene	36	C5H10		X									
n-Pentane	36	C5H12		X									
Isopropyl-Chloride	36	C3H7CL			X								
Vinyl-Ethyl-Ether	36	C4H8O		X									
Dimethylchlorosilane	36	C2H7SICL			X								
Ethyl-Mercaptan	35	C2H6S								X			
Propylene-Oxide	35	C3H6O							X				
Diethyl-Ether	34	C4H10O		X									
2-Methyl-1,3-Butadiene	34	C5H8		X									
1,1-Dichloro-1-Fluoroethane	32	C2H3CL2F	X										
Trichlorosilane	32	SIHCL3	X										
Isopropyl-Amine	32	C3H9N		X									
Methyl-Formate	32	C2H4O2								X			
1,1-Dichloroethylene	32	C2H2CL2							X				
Furan	31	C4H4O							X				
2-Methyl-1-Butene	31	C5H10		X									
Methyl-Isopropyl-Ether	31	C4H10O		X									
2,2-Dichloro-1,1,2-Trifluoroetha	30	C2HCL2F3	X										
1-Pentene	30	C5H10		X									
2-Difluoromethoxy-1,1,1-Trifluro	29	C3H3F5O											
3-Methyl-1-Butyne	29	C5H8		X									
Divinyl-Ether	28	C4H6O					X						
1,2-Dichloro-1,1,2-Trifluoroetha	28	C2HCL2F3	X										
1,1-Dichloro-2,2,2-Trifluoroetha	28	C2HCL2F3	X										
2-Methyl-Butane	28	C5H12		X									
2-Butyne	27	C4H6					X						
Tetramethylsilane	27	C4H12SI		X									
1,4-Pentadiene	26	C5H8		X									
1,1,2,2,3-Pentafluoropropane	25	C3H3F5				X							
Trichlorofluoromethane	24	CCL3F	X										
2-Chloropropene	23	C3H5CL								X			
Acetaldehyde	21	C2H4O								X			
3-Methyl-1-Butene	20	C5H10		X									
Ethyl-Amine	17	C2H7N			X								
Vinyl-Bromide	16	C3H3BR	X										
1,1,1,3,3-Pentafluoropropane	15	C3H3F5				X							
Cyclobutane	13	C4H8					X						
Ethyl-Chloride	12	C2H5CL								X			
1,2-Butadiene	11	C4H6					X						
1,2-Difluoroethane	11	C2H4F2											
2,2-Dimethyl-Propane	10	C5H12		X									
Dichloromonofluoromethane	9	CHCL2F	X										
Methyl-Chlorosilane	9	CH5SICL							X				
Dichlorosilane	8	SIH2CL2							X				
Methyl-Ethyl-Ether	7	C3H8O					X						
Dimethylamine	7	C2H7N			X								
Trimethyl-Silane	7	C3H10SI		X									

1,1,1,2,3,3-Hexafluoropropane	6	C3H2F6				X							
2-Chloro-1,1,1-Trifluoroethane	6	C2H2CLF3	X										
Methyl-Mercaptan	6	CH4S								X			
Hexafluoro-1,3-Butadiene	6	C4F6								X			
Pentafluoroethyl-Methyl-Ether	6	C3H3F5O											
Vinyl-Methyl-Ether	6	C3H6O						X					
Vinylacetylene	5	C4H4						X					
1,1,2-Trifluoroethane	5	C2H3F3											
1,2-Dichloro-1,1,2,2-Tetrafluoro	4	C2CL2F4	X										
Cis-2-Butene	4	C4H8						X					
Methyl-Bromide	4	CH3BR	X										
1,1-Dichloro-1,2,2,2-Tetrafluoro	3	C2CL2F4	X										
Trimethyl-Amine	3	C3H9N		X									
Trans-2-Butene	1	C4H8						X					
n-Butane	-1	C4H10		X									
1,1,1,3,3,3-Hexafluoropropane	-1	C3H2F6				X							
Decafluorobutane	-1	C4F10		X									
Octafluoro-2-Butene	-3	C4F8					X						
1,3-Butadiene	-4	C4H6						X					
Difluoromethyl-Methyl-Ether	-5	C2H4F2O											

*Ethyl iodide more suited
**1,1-Dichloroethane more suited
***Driest among shortlisted fluids
****Poor information
*****Methyl-Acetate more suited

Appendix 4.6 - Case 1 simulation results

Table 4.8 Detailed performance and property values of different fluids in Case 1: 427/65°C

	Water	Ethanol	R245fa	Ethyl iodide	Acetonitrile	R150a	Methanol	R30	Acetone	Methyl acetate
$T_{evaporation}$ °C	215	208	148	246	236	221	191	197	214	213
T_{max} °C	340	211	153	250	249	227	237	204	219	218
$T_{post\ expansion}$ °C	79	72	93	110	74	108	69	68	99	110
$T_{source\ out}$ °C	192	97	98	102	106	98	101	98	97	97
m_{wf} kg/s	0.02	0.07	0.31	0.27	0.07	0.18	0.05	0.19	0.1	0.13
Q_{in} kW	50	69.5	69.2	68.4	67.6	69.2	68.6	69.2	69.3	69.3
W_{pump} kW	0.1	0.5	1.2	0.9	0.4	0.9	0.4	0.8	0.8	0.8
W_{exp} kW	8.9	10.6	7	12.3	11.8	11.3	10.6	10.8	10.9	10.7
W_{net} kW	8.9	10.1	5.8	11.4	11.4	10.4	10.3	10	10.2	9.9
$Q_{preheater}$ kW	12.1	39.5	49.1	43	37.1	43.6	27.9	35.2	45	46.4
$Q_{evaporator}$ kW	32	28.6	16.1	24	27.8	22.9	35.3	32.7	22.9	20.2
$Q_{superheater}$ kW	6	1.4	4	1.3	2.6	2.7	5.4	1.4	1.3	2.7
$Q_{de-superheater}$ kW	0	0	7.6	4.6	0	5.9	0	0	3.6	5.9
$HEX, UA\ W/°C$	575	1047	656	1289	1251	1054	1104	1043	988	952
$Cond., UA\ W/°C$	1012	1583	1357	1060	1463	1106	1602	1654	1198	1103
UA_{tot}/W_{net}	0.18	0.26	0.35	0.21	0.24	0.21	0.26	0.27	0.22	0.21
$HEX, LMTD$ °C	87	66	105	53	54	66	62	66	70	73
$Cond., LMTD$ °C	42	38	48	56	39	55	37	36	51	56
P_{min} bar	0.3	0.6	5.3	0.8	0.6	1.3	1.1	2.3	1.3	1.3
P_{max} bar	21	35	33	31	29	35	35	35	35	35
PR_{exp}	45.6	42.1	5.9	29.3	37.8	22.6	27.6	13.9	22.6	22.7
ΔS_{exp} kJ/kg	510	158	22	45	177	64	214	57	106	85
V_{exp} m^3/s	0.062	0.049	0.012	0.052	0.06	0.036	0.034	0.024	0.035	0.035
VFR_{exp}	26.6	43.6	8.7	34	35.4	27.5	21.8	13.9	28.1	29.5
VFR_{exp}/W_{net}	3	4.3	1.5	3	3.1	2.6	2.1	1.4	2.8	3
v_{cond} m^3/kg	3.52	0.73	0.04	0.19	0.9	0.2	0.69	0.13	0.34	0.28
λ_{avg} W/mK	0.35	0.10	0.05	0.05	0.11	0.06	0.11	0.07	0.09	0.08
μ_{avg} cP	0.25	0.29	0.14	0.21	0.13	0.17	0.19	0.16	0.12	0.13
η_I %	17.7	14.6	8.4	16.6	16.9	15.1	15	14.5	14.6	14.3
$\eta_{recovery}$ %	71.5	99.3	98.9	97.7	96.5	98.9	98.1	98.9	99	99
$\eta_{conversion}$ %	12.6	14.5	8.3	16.2	16.3	14.9	14.7	14.3	14.5	14.1
I_{pump} kW	0.1	0.2	0.4	0.4	0.1	0.3	0.1	0.3	0.2	0.3
I_{exp} kW	3.2	3.9	2.4	4.3	4.3	3.9	3.9	4	3.8	3.6
I_{HEX} kW	10.2	17.4	22.7	14.9	14.9	16.8	17.2	17.6	17.4	17.6
I_{cond} kW	6.9	8.9	8.9	8.8	8.7	8.8	8.4	8.3	8.7	8.9
I_{cycle} kW	20.2	30.3	34.5	28.4	27.9	29.8	29.6	30.2	30.2	30.4
ξ_P%	26.7	30.5	17.5	34.3	34.3	31.5	30.9	30.2	30.6	29.8

Appendix 4.7 - Case 2 simulation results

Table 4.9 Detailed performance and property values of different fluids in Case 2: 296/105°C

	Water	Ethanol	R245fa	Ethyl iodide	Acetonitrile	R150a	Methanol	R30	Acetone	Methyl acetate
$T_{evaporation}$ °C	191	208	148	199	191	197	191	197	214	213
T_{max} °C	256	213	153	203	194	201	222	204	219	218
$T_{post\ expansion}$ °C	109	107	117	134	108	134	106	106	127	136
$T_{source\ out}$ °C	195	160	123	171	170	152	166	157	147	140
m_{wf} kg/s	0.01	0.05	0.38	0.21	0.05	0.15	0.04	0.15	0.09	0.12
Q_{in} kW	35.6	47.7	60.5	44	44.3	50.5	45.7	48.8	52.1	54.5
W_{pump} kW	0.1	0.4	1.1	0.3	0.1	0.5	0.3	0.6	0.7	0.7
W_{exp} kW	4.1	5.6	3.6	5	4.7	5.5	5.1	5.6	6.3	6.4
W_{net} kW	4	5.2	2.5	4.6	4.6	5	4.8	5	5.6	5.7
$Q_{preheater}$ kW	5.7	24.2	35.8	16.9	14.3	22.5	15.8	20.8	31.7	34.4
$Q_{evaporator}$ kW	27	22.5	20.1	26.2	29	27	26.2	27	18.4	18.1
$Q_{superheater}$ kW	2.8	0.9	4.7	0.9	0.9	1	3.6	1	2	2.1
$Q_{de-superheater}$ kW	0	0	4.6	2.4	0	3.6	0	0	2.8	3.9
$HEX, UA\ W/°C$	716	1287	1114	1024	974	1320	1045	1252	1666	1837
$Cond., UA\ W/°C$	674	926	1164	685	856	792	898	964	851	838
UA_{tot}/W_{net}	0.34	0.42	0.93	0.37	0.4	0.42	0.4	0.45	0.45	0.47
$HEX, LMTD$ °C	50	37	54	43	45	38	44	39	31	30
$Cond., LMTD$ °C	47	46	51	59	47	59	46	46	56	60
P_{min} bar	1.2	2.8	14	2.5	2	4	4.3	6.4	4.2	4.2
P_{max} bar	13	35	33	16	14	24	35	35	35	35
PR_{exp}	8.9	11.7	2.3	5.7	6.1	5.6	7.7	5.2	7.9	7.9
ΔS_{exp} kJ/kg	289	107	9	24	93	36	133	36	70	56
V_{exp} m^3/s	0.017	0.012	0.005	0.015	0.017	0.012	0.008	0.008	0.011	0.011
VFR_{exp}	6.5	12.8	3	5.9	5.9	6.3	6.9	5.5	10.1	10.4
VFR_{exp}/W_{net}	1.6	2.4	1.2	1.3	1.3	1.3	1.4	1.1	1.8	1.8
v_{cond} m^3/kg	1.21	0.22	0.01	0.07	0.33	0.08	0.2	0.05	0.12	0.1
λ_{avg} W/mK	0.36	0.09	0.04	0.04	0.1	0.06	0.11	0.06	0.08	0.08
μ_{avg} cP	0.15	0.16	0.1	0.16	0.1	0.13	0.13	0.13	0.09	0.1
η_I %	11.4	11	4.1	10.5	10.3	10	10.5	10.2	10.8	10.5
$\eta_{recovery}$ %	50.9	68.1	86.5	62.9	63.2	72.1	65.3	69.7	74.4	77.9
$\eta_{conversion}$ %	5.8	7.5	3.5	6.6	6.5	7.2	6.9	7.1	8.1	8.2
I_{pump} kW	0.1	0.1	0.4	0.1	0.1	0.2	0.1	0.2	0.2	0.2
I_{exp} kW	1.5	2.1	1.3	1.7	1.7	1.9	1.9	2	2.2	2.2
I_{HEX} kW	4.9	6.8	13.5	6.5	6.8	7.8	6.9	7.4	7.4	7.9
I_{cond} kW	4.9	6.4	8.6	6.1	6.1	6.9	6.1	6.5	7	7.5
I_{cycle} kW	11.3	15.4	23.7	14.4	14.6	16.8	14.9	16.1	16.9	17.9
ξ_P%	18	23.3	10.9	20.6	20.3	22.4	21.4	22	25.1	25.4

Appendix 4.8 - Accurate overall UA and LMTD

It is important to highlight that due to the variable slope of the working fluid curve a Logarithmic Mean Temperature Difference (LMTD) between the terminal ends in the counter-current preheater is not an acceptable assumption. Fig. 4.1 shows such a linear preheating curve for ethanol in Case 1. However, the weighted HEX design as employed in this thesis allowed the heat curve for either side of the HEX to be broken into equal enthalpy intervals. All the process conditions were calculated for each of the interval terminal ends. Using each element calculation as given in equation 4.1 the energy transfer was then summed to determine the overall UA.

$$\dot{Q}_{a,a+x} = (UA)_{a,a+x} \frac{\Delta T_a - \Delta T_{a+x}}{\ln\left(\frac{\Delta T_a}{\Delta T_{a+x}}\right)} \quad \ldots(4.1)$$

Where, $\Delta T_a = T_{hot,out} - T_{cold,in}$ and $\Delta T_{a+x} = T_{hot,in} - T_{cold,out}$.

A sensitivity study with increasing interval number (1→5→10→15) was conducted on the LMTD value. A 4% difference was observed in the LMTD value when interval number was increased from 1 to 5. This difference reduced to less than 0.5% between 10 and 15 intervals. Hence, all the heating/cooling curves in each heat transfer process (e.g. preheating, evaporation etc.) in this thesis were at least divided into 15 elements for pure fluids. Fig. 4.1 also includes ethanol's non-linear preheating curve, highlighting this phenomena.

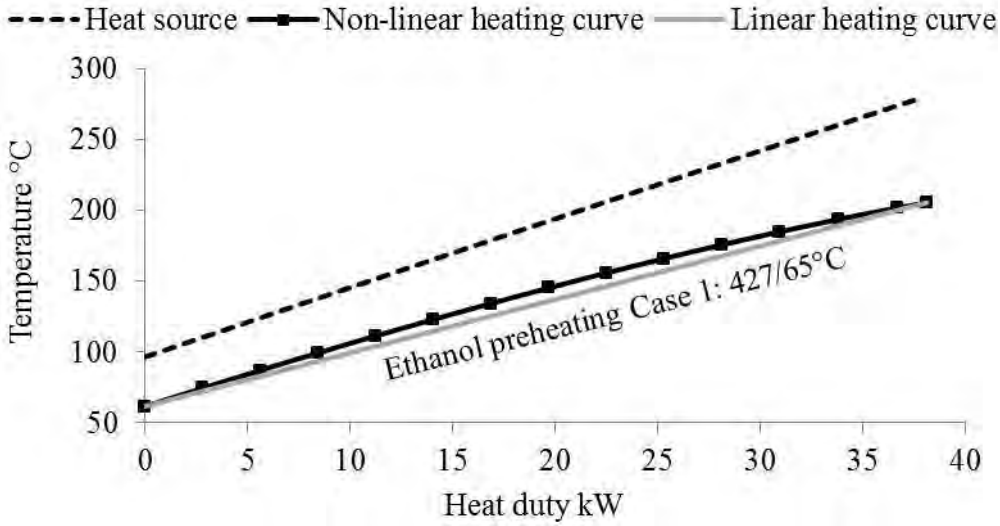

Figure 4.1 Non-linear preheating curve with 15 intervals as a more appropriate assumption for calculating overall UA and LMTD

Appendix 4.9 - Varying dT/dS slope

An often neglected fact about dry and isentropic fluids is the change in the gradient of the saturated vapour line with higher pressures. Consider an ideal dry saturated expansion at 23 bar using R245fa (Fig. 4.2a). It can be viewed that ideal and real expansion at this pressure will then result in a moisture free expansion stage. However, consider the increase in pressure to 35 bar and then the ideal as well as the real expansion stages pass through the two-phase region. This happens due to the change of gradient of the saturated vapour line from positive to negative. Examining the change in molar entropy at the saturated vapour line (Fig. 4.2b) in fact shows this change in gradient to occur at a pressure of 23 bar. Hence, in order to avoid bi-phase during expansion, superheating beyond the minimum 5°C was also considered for dry fluids.

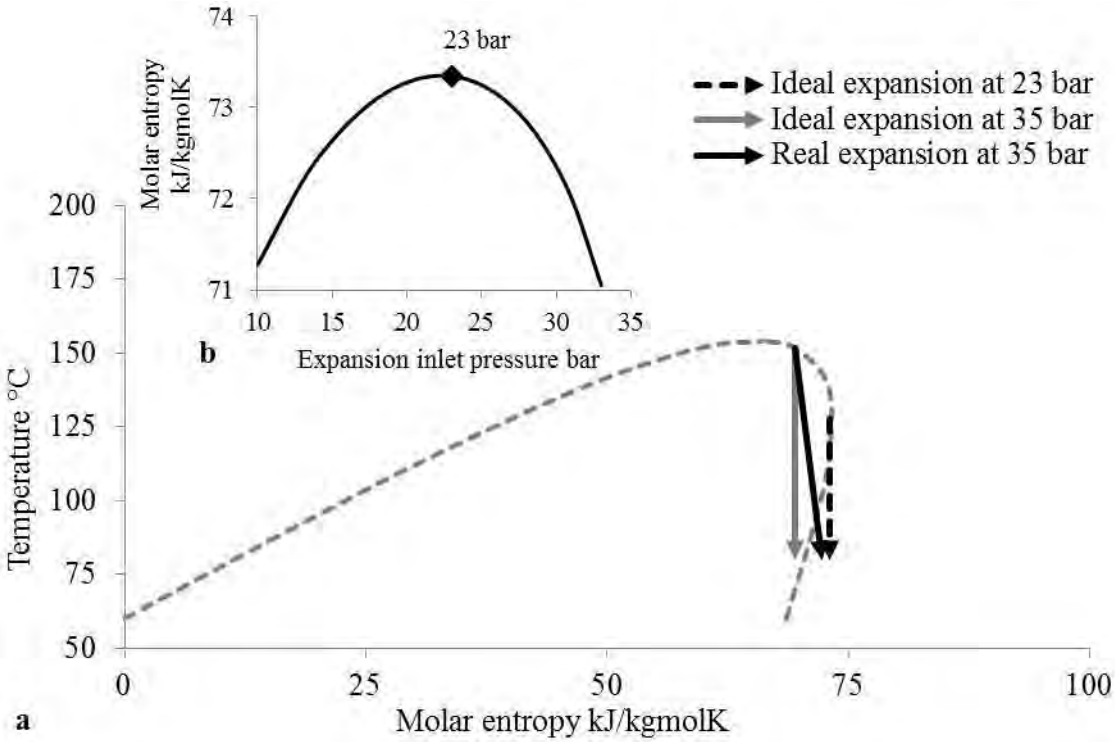

Figure 4.2 Change in the gradient of the saturated vapour line with higher pressures for R245fa by examining (a) T-S curve (b) change in entropy

Appendix 4.10 - Fluid pairing

Table 4.10 Rational for the chosen pairings of working fluids

Current Pairing	Alternative paring
Ethyl iodide and methanol vs. water ▪ Paired to provide the contrasting range of organic fluid options	
R30 vs. ethanol ▪ Can highlight R30's drawback of marginally lower average thermal conductivity (0.07 vs. 0.1 W/mK) ▪ Can highlight R30's drawback of marginally higher feed pump power (8 vs. 5% of expansion power)	**R30 vs. R245fa** ▪ Cannot highlight R30's drawback of lower average thermal conductivity (0.07 vs. 0.05 W/mK) ▪ Cannot highlight R30's drawback of higher feed pump power (8 vs. 17% of expansion power)
Acetone vs. R245fa ▪ Can highlight acetone's drawback of higher flammability due to hydrogen content (3 vs. 1) ▪ Can highlight acetone's drawback of higher VFR/W value in Case 1 (2.8 vs. 1.5).	**Acetone vs. ethanol** ▪ Cannot highlight acetone's drawback of higher flammability due to hydrogen content (3 vs. 3) ▪ Cannot highlight acetone's drawback of higher VFR/W value in Case 1 (2.8 vs. 4.3)

Appendix 4.11 - Case 3 simulation results

Table 4.11 Detailed performance and property values of different fluids in Case 3: 176/65°C

	R245fa	R152	E245fa1	R143	E152a	E245cb1
$T_{evaporation}\ °C$	113	110	111	110	114	127
$T_{max}\ °C$	118	113	115	114	119	132
$T_{post\ expansion}\ °C$	88	75	93	76	76	88
$T_{source\ out}\ °C$	105	111	105	108	109	95
$m_{wf}\ kg/s$	0.15	0.08	0.15	0.1	0.11	0.21
$Q_{in}\ kW$	31.3	28.4	31.1	30	29.7	35.5
$W_{pump}\ kW$	0.2	0.3	0.1	0.2	0.3	0.6
$W_{exp}\ kW$	2.2	2	2	2.1	2.2	2.9
$W_{net}\ kW$	1.9	1.8	1.8	1.9	2	2.3
$Q_{preheater}\ kW$	12.6	8	11.3	9.7	11.5	23.1
$Q_{evaporator}\ kW$	17.4	19.8	19.2	19.7	17.1	10.3
$Q_{superheater}\ kW$	1.2	0.6	0.6	0.6	1.2	2.1
$Q_{de-superheater}\ kW$	2.9	0.5	3.5	0.6	1.1	4.6
$HEX, UA\ W/°C$	932	782	897	844	877	1366
$Cond., UA\ W/°C$	653	684	625	717	707	738
UA_{tot}/W_{net}	0.82	0.8	0.83	0.84	0.81	0.93
$HEX, LMTD\ °C$	34	36	35	36	34	26
$Cond., LMTD\ °C$	46	40	48	40	40	46
$P_{min}\ bar$	5.3	5.4	3.4	7.7	8.3	6.7
$P_{max}\ bar$	17	15	11	22	24	26
PR_{exp}	3	2.6	3	2.7	2.8	3.7
$\Delta S_{exp}\ kJ/kg$	15	25	14	21	20	14
$V_{exp}\ m^3/s$	0.005	0.005	0.008	0.004	0.004	0.005
VFR_{exp}	3.5	2.7	3.2	2.9	3.1	5.4
VFR_{exp}/W_{net}	1.8	1.5	1.8	1.6	1.6	2.4
$v_{cond}\ m^3/kg$	0.04	0.07	0.05	0.04	0.04	0.03
$\lambda_{avg}\ W/mK$	0.05	0.06	0.06	0.07	0.05	0.04
$\mu_{avg}\ cP$	0.14	0.08	0.15	0.12	0.10	0.10
$\eta_I\ \%$	6.2	6.4	5.9	6.2	6.6	6.4
$\eta_{recovery}\ \%$	44.7	40.6	44.4	42.8	42.4	50.7
$\eta_{conversion}\ \%$	2.8	2.6	2.6	2.7	2.8	3.2
$I_{pump}\ kW$	0.08	0.03	0.05	0.08	0.08	0.19
$I_{exp}\ kW$	0.8	0.7	0.7	0.8	0.8	1
$I_{HEX}\ kW$	4	3.7	4.1	3.9	3.7	4.2
$I_{cond}\ kW$	4.1	3.7	4.2	3.8	3.8	4.6
$I_{cycle}\ kW$	8.9	8.1	9	8.6	8.4	10
$\xi_P\%$	14.1	13.3	13.4	13.6	14.3	16.6

Appendix 4.12 - PSI weight factor sensitivity in Case 1

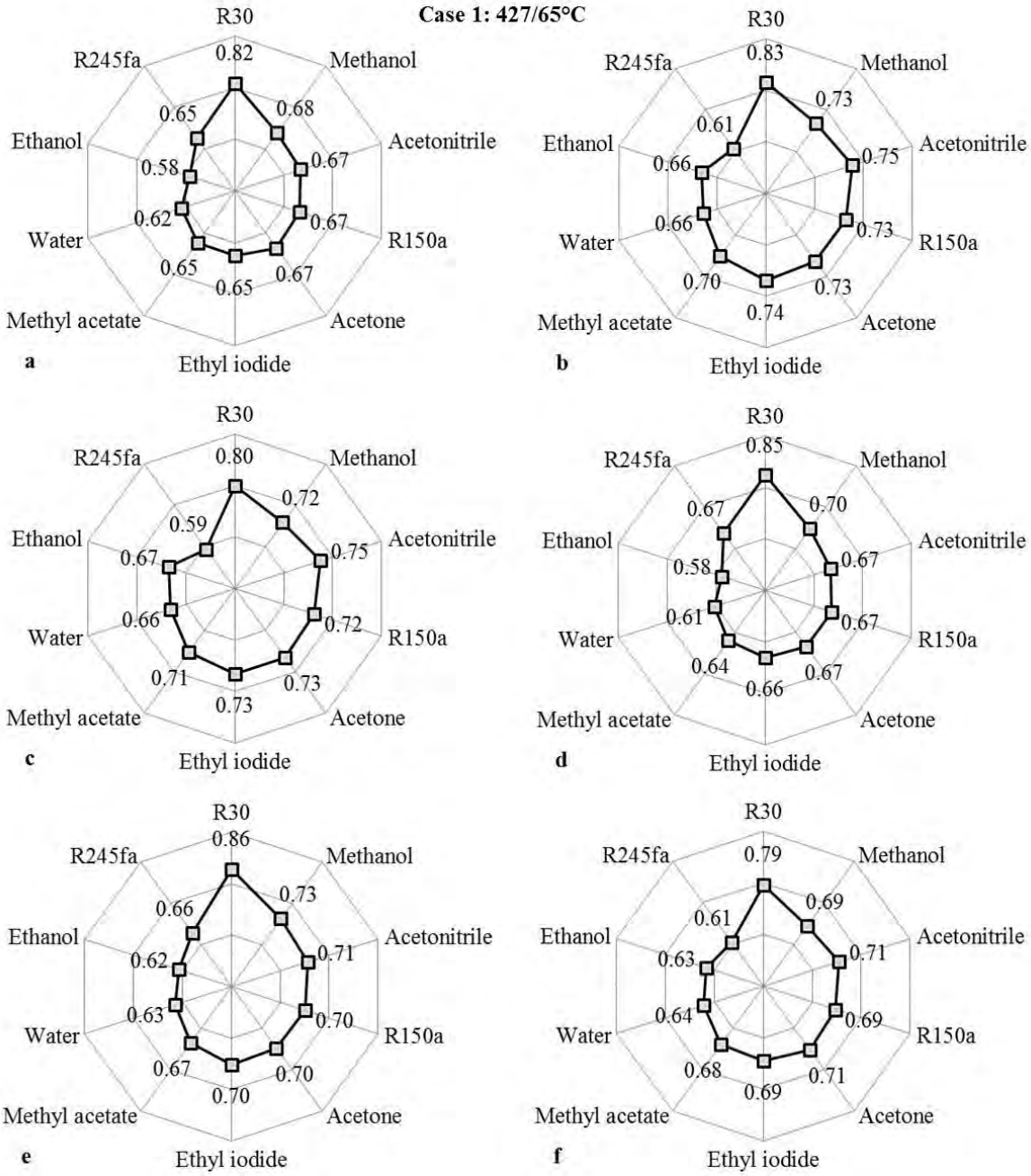

Figure 4.3 Case 1 PSI value sensitivity analysis (a,b) ±30% variation in Parameter 1 (c,d) ±30% variation in Parameter 2 (e,f) ±30% variation in Parameter 3,4,5 and 6

Note in Fig. 4.3 to 4.5: All figures labelled 'a' correspond to a +30% variation in the weight factor (from 0.33 to 0.43) for Parameter 1, and all the figures labelled 'b' corresponds to a −30% variation in the weight factor (from 0.33 to 0.23) for Parameter 1. Similarly, figures labelled 'c' and 'd' are ±30% variation in Parameter 2, and figures labelled 'e' and 'f' are ±30% variation in Parameter 3,4,5 and 6.

Appendix 4.13 - PSI weight factor sensitivity in Case 2

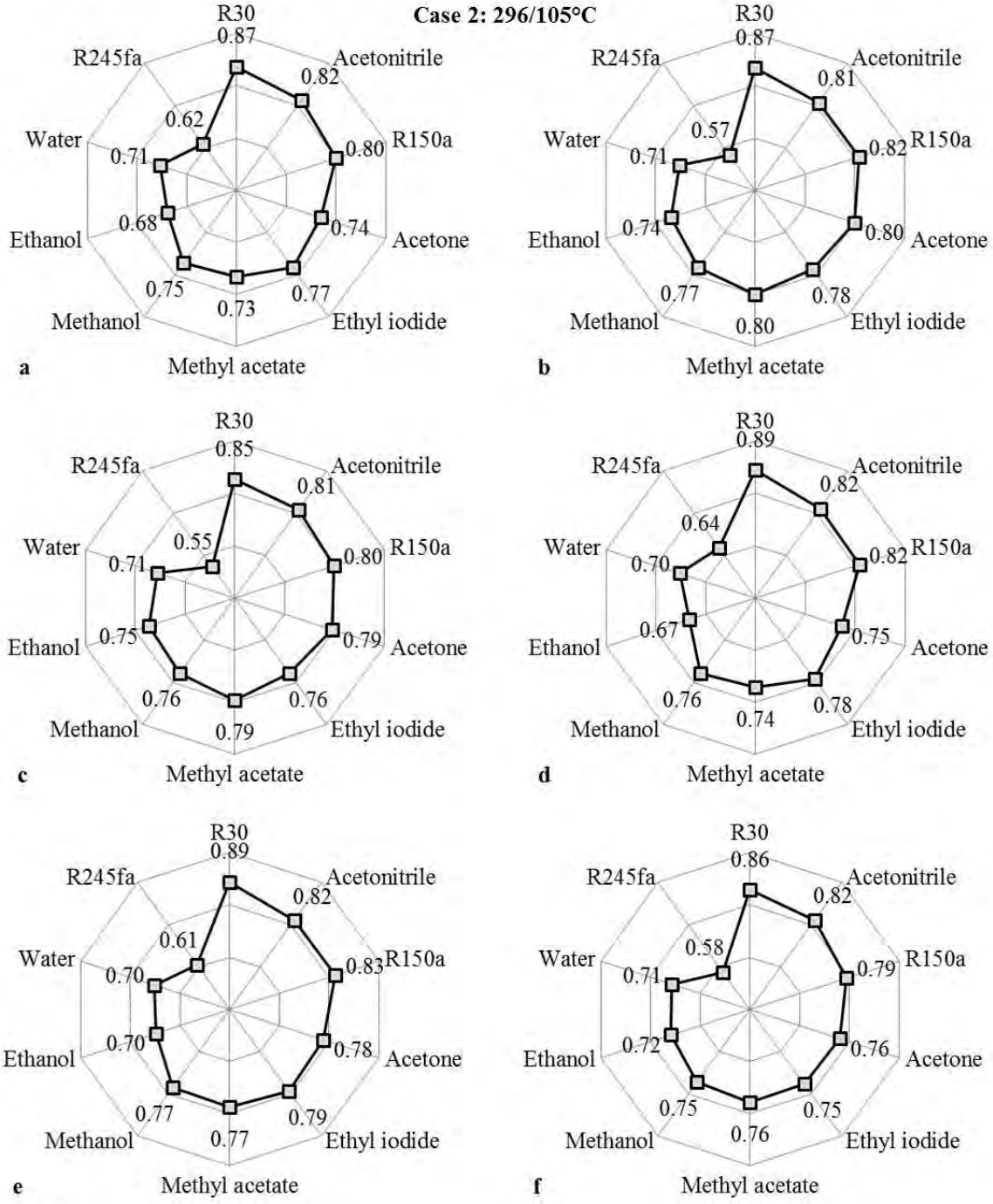

Figure 4.4 Case 2 PSI value sensitivity analysis (a,b) ±30% variation in Parameter 1 (c,d) ±30% variation in Parameter 2 (e,f) ±30% variation in Parameter 3,4,5 and 6

Appendix 4.14 - PSI weight factor sensitivity in Case 3

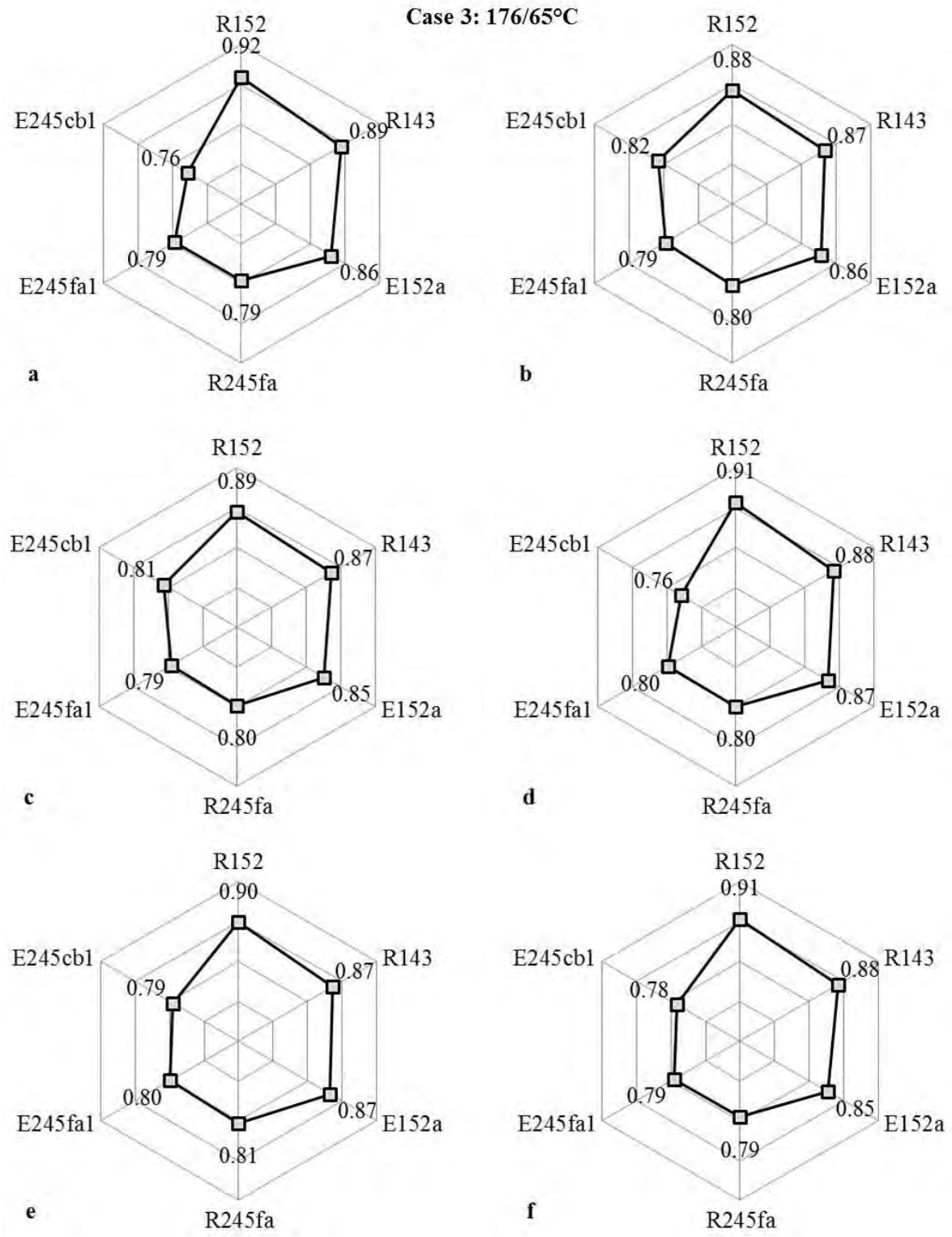

Figure 4.5 Case 3 PSI value sensitivity analysis (a,b) ±30% variation in Parameter 1 (c,d) ±30% variation in Parameter 2 (e,f) ±30% variation in Parameter 3,4,5 and 6

Chapter 6 Appendices

Appendix 6.1 - Results for process integration 1

Table 6.1 Key system and performance parameters for optimised PI-1

PI-1	E6-C100			E5-C100			E6-B50			E5-B50		
	Water	Ethanol	R245fa	Water	Ethanol	R245fa	Water	Ethanol	R245fa	Water	Ethanol	R245fa
$P_{max}\ bar$	15.4	30.6	33	15.4	30.6	34	14	30.6	33	10	25	31
$T_{max}\ °C$	278	200	147	278	200	148	269	200	147	238	190	143
$m_{wf}\ kg/s$	0.05	0.17	1.03	0.04	0.14	0.84	0.02	0.07	0.45	0.02	0.06	0.38
$T_{wf\ Pt.1}\ °C$	198	201	141	198	201	148	193	201	140	178	191	144
$X_{wf\ Pt.1}$	0.44	0.23	0	0.60	0.48	0	0.43	0.24	0	0.54	0.47	0.07
$Q_{EXH}\ kW$	63.1	91.5	90.8	57.8	93.2	92.6	25.6	38.5	38.2	25.1	38.8	40.4
$Q_{HT\ EGR}\ kW$	61.9	61.1	76.3	34.6	34.2	42.7	25.9	24.8	34.1	18.3	16.7	22.3
PR_{exp}	16	16	3.1	16	16	3.2	14.4	16	3.1	10	13	2.9
VFR_{exp}	10.8	17	4.8	10.8	17	5.2	9.9	17	4.8	7.2	13.3	4.3
$\eta_I\ \%$	13.9	12.2	5.6	13.9	12.2	5.6	13.4	12.2	5.6	11.6	11.5	5.5
$W_{net}\ kW$	17.3	18.5	9.3	12.8	15.5	7.6	6.9	7.7	4	5	6.4	3.4
UA_{tot}/W_{net}	0.23	0.31	0.55	0.24	0.37	0.58	0.25	0.33	0.57	0.30	0.41	0.62
β	0.27	0.2	0.1	0.22	0.17	0.08	0.27	0.2	0.11	0.2	0.16	0.09
$Q_{inc.LOAD}\ kW$	45.8	72.9	81.4	45	77.7	85	18.7	30.8	34.1	20.1	32.4	36.9
$W_{BP+fan}\ kW$	2.1	3.7	3.6	1.9	3.8	3.7	0.6	1	1	0.6	1	1.1
$W_{system}\ kW$	14	13.6	5.1	10	10.6	3.3	5.8	6.1	2.7	4.1	4.9	2.1

Appendix 6.2 - Results for process integration 2

Table 6.2 Key system and performance parameters for optimised PI-2

PI-2	E6-C100						E5-C100					
	Ethanol	Ethyl iodide	Acetonitrile	Methanol	R30	Acetone	Ethanol	Ethyl iodide	Acetonitrile	Methanol	R30	Acetone
P_{max} bar	30.6	22	21	42	38	28	25	16	17	36	34	22
T_{max} $°C$	200	218	217	238	208	198	190	196	201	225	198	183
m_{wf} kg/s	0.14	0.53	0.13	0.1	0.39	0.22	0.1	0.43	0.1	0.08	0.29	0.17
$T_{wf\ Pt.1}$ $°C$	201	220	214	201	202	199	191	198	201	192	194	185
$X_{wf\ Pt.1}$	0.4	0.5	0.54	0.56	0.44	0.34	0.19	0.26	0.31	0.31	0.2	0.13
Q_{EXH} kW	39.4	30.2	33	39.5	39	40.1	44.8	41.1	39.5	43.9	43	47.8
$Q_{HT\ EGR}$ kW	88.5	88.2	88.6	88.4	88	88.4	51.8	51.7	51.9	51.8	51.5	51.8
PR_{exp}	16	10.9	13.5	14.4	7.9	9	13	7.8	10.8	12.3	7	7
VFR_{exp}	17	11.9	13	12.4	8.3	10.8	13.3	8.1	10.3	10.6	7.3	7.8
η_I %	12.2	13.4	13.7	13.1	12.2	11.7	11.5	12	12.8	12.4	11.8	10.8
W_{net} kW	15.5	15.9	16.7	16.7	15.5	15	11.1	11.2	11.7	11.9	11.1	10.7
UA_{tot}/W_{net}	0.26	0.22	0.24	0.25	0.26	0.25	0.28	0.25	0.26	0.27	0.28	0.28
β	0.39	0.53	0.5	0.42	0.4	0.37	0.25	0.27	0.3	0.27	0.26	0.22
$Q_{inc.LOAD}$ kW	23.9	14.4	16.4	22.8	23.5	25.1	33.7	29.9	27.8	32	31.9	37
W_{BP+fan} kW	1.1	0.7	0.8	1.1	1.1	1.1	1.3	1.1	1.1	1.2	1.2	1.4
W_{system} kW	13.4	14	14.7	14.5	13.4	12.9	9.1	9.3	9.8	9.8	9.1	8.6
PI-2	E6-B50						E5-B50					
P_{max} bar	28	18	18	42	36	27	19	14	13	30	26	21
T_{max} $°C$	195	204	206	238	203	196	176	187	183	212	177	180
m_{wf} kg/s	0.06	0.25	0.06	0.05	0.17	0.1	0.05	0.21	0.05	0.04	0.15	0.08
$T_{wf\ Pt.1}$ $°C$	196	206	205	201	198	197	177	189	186	183	177	182
$X_{wf\ Pt.1}$	0.48	0.55	0.59	0.64	0.52	0.43	0.37	0.43	0.45	0.47	0.38	0.32
Q_{EXH} kW	16.1	14	14.3	15.1	15.7	15.9	19.1	16.1	17	17.7	19.3	18
$Q_{HT\ EGR}$ kW	41.4	41.3	41.5	41.3	41.1	41.3	28.6	28.5	28.6	28.5	28.4	28.5
PR_{exp}	14.6	8.8	11.5	14.4	7.5	8.7	9.7	6.7	8.1	10.2	5.3	6.7
VFR_{exp}	15.2	9.3	10.9	12.4	7.8	10.3	9.6	6.9	7.6	8.9	5.4	7.4
η_I %	11.9	12.6	13	13.1	12	11.6	10.5	11.4	11.5	11.7	10.5	10.6
W_{net} kW	6.8	7	7.3	7.4	6.8	6.6	5	5.1	5.2	5.4	5	4.9
UA_{tot}/W_{net}	0.29	0.26	0.28	0.28	0.29	0.27	0.34	0.3	0.32	0.32	0.34	0.31
β	0.43	0.5	0.51	0.49	0.43	0.42	0.26	0.32	0.31	0.31	0.26	0.27
$Q_{inc.LOAD}$ kW	9.2	7	7	7.8	8.9	9.3	14.1	11	11.7	12.3	14.2	13.1
W_{BP+fan} kW	0.3	0.2	0.2	0.3	0.3	0.3	0.4	0.3	0.3	0.3	0.4	0.3
W_{system} kW	6.1	6.2	6.5	6.6	6.1	5.9	4.3	4.4	4.6	4.7	4.3	4.2

Note: An additional parameter of interest in PI-2 was the cooled EXH temperatures. Using the 5 alternative organic fluids, the EXH temperatures were kept above 200-240°C. Contrary to PI-1, PI-2 may allow the EXH heat exchanger to be placed post-turbine but pre-DPF. Temperature levels preferably over 240°C may permit uninterrupted DPF operation and reduce the thermal cycling in the EXH heat exchanger. Furthermore, the backpressure losses were further reduced and were negligible (0.3 kW) at cruise loads.

Appendix 6.3 - Results for process integration 3

Table 6.3 Key system and performance parameters for optimised PI-3

PI-3	E6-C100							E5-C100						
	Water	Ethanol	Ethyl iodide	Acetonitrile	Methanol	R30	Acetone	Water	Ethanol	Ethyl iodide	Acetonitrile	Methanol	R30	Acetone
$P_{max}\ bar$	15.4	30.6	24	24	42	48	40	13	30.6	20	20	42	46	40
$T_{wf\ Pt.1}\ °C$	276	200	225	228	238	230	222	230	200	211	214	238	226	222
$T_{wf\ Pt.2}\ °C$	280	200	225	228	238	230	222	278	200	211	214	238	226	222
$m_{wf}\ kg/s$	0.05	0.18	0.64	0.16	0.12	0.48	0.29	0.04	0.14	0.52	0.12	0.1	0.37	0.23
$Q_{EXH}\ kW$	49.2	75.9	55.6	54.2	66.7	70.6	82.3	54.4	76.4	62.4	59.5	67.1	71.5	83
$Q_{HT\ EGR}\ kW$	75.2	88.5	88.2	88.6	88.4	87.8	88.1	43.7	51.8	51.6	51.8	51.7	51.4	51.5
PR_{exp}	16	16	11.9	15.5	14.4	10	13	13.3	16	9.8	12.8	14.4	9.6	13
VFR_{exp}	10.8	17	13.3	15.1	12.4	10.9	18.5	9.3	17	10.6	12.3	12.4	10.3	18.5
$\eta_I\ \%$	13.9	12.2	13.7	14.2	13.1	13.1	12.6	12.9	12.2	13	13.5	13.1	12.9	12.6
$W_{net}\ kW$	17.2	20	19.7	20.3	20.3	20.7	21.4	12.7	15.6	14.9	15	15.5	15.9	16.9
UA_{tot}/W_{net}	0.23	0.3	0.23	0.25	0.28	0.29	0.31	0.26	0.32	0.27	0.28	0.29	0.32	0.34
β	0.35	0.26	0.36	0.37	0.3	0.29	0.26	0.23	0.2	0.24	0.25	0.23	0.22	0.2
$Q_{inc.LOAD}\ kW$	32	55.9	35.8	33.9	46.4	49.9	60.9	41.7	60.8	47.5	44.5	51.6	55.6	66.1
$W_{BP+fan}\ kW$	1.5	2.8	1.8	1.7	2.3	2.5	3.1	1.7	2.8	2.1	2	2.3	2.5	3.2
$W_{system}\ kW$	14.6	15.8	16.6	17.2	16.5	16.7	16.8	10.1	11.7	11.7	12	12.1	12.2	12.6
PI-3	E6-B50							E5-B50						
$P_{max}\ bar$	13	30.6	20	20	42	44	38	10	24	14	15	34	32	26
$T_{wf\ Pt.1}\ °C$	258	200	211	214	238	222	219	227	187	187	193	221	193	194
$T_{wf\ Pt.2}\ °C$	268	200	211	214	238	222	219	250	187	187	193	221	193	194
$m_{wf}\ kg/s$	0.02	0.08	0.29	0.07	0.05	0.2	0.13	0.02	0.06	0.24	0.05	0.04	0.17	0.1
$Q_{EXH}\ kW$	21	29.2	23.2	22.3	25.5	27	31.6	22.2	28.1	25.4	23.1	25.2	27.2	29.5
$Q_{HT\ EGR}\ kW$	32.1	41.4	40.5	39.2	40.1	40.9	41.2	21.5	28.2	26.6	25.1	26.1	27.7	28.5
PR_{exp}	13.3	16	9.8	12.8	14.4	9.2	12.3	10	12.4	6.7	9.4	11.6	6.6	8.3
VFR_{exp}	9.3	17	10.6	12.3	12.4	9.8	16.9	7.2	12.7	6.9	8.9	10	6.8	9.7
$\eta_I\ \%$	13	12.2	13	13.5	13.1	12.8	12.5	11.6	11.4	11.4	12.2	12.2	11.5	11.4
$W_{net}\ kW$	6.9	8.6	8.3	8.3	8.6	8.7	9.1	5.1	6.4	5.9	5.9	6.3	6.3	6.6
UA_{tot}/W_{net}	0.26	0.32	0.28	0.28	0.3	0.32	0.32	0.3	0.36	0.31	0.31	0.32	0.35	0.34
β	0.33	0.29	0.36	0.37	0.34	0.32	0.29	0.23	0.23	0.23	0.25	0.25	0.23	0.22
$Q_{inc.LOAD}\ kW$	14.2	20.6	14.9	14	17	18.3	22.5	17.1	21.7	19.4	17.3	18.9	20.9	22.9
$W_{BP+fan}\ kW$	0.4	0.7	0.5	0.5	0.6	0.6	0.8	0.5	0.7	0.6	0.5	0.6	0.6	0.7
$W_{system}\ kW$	6	7.3	7.2	7.2	7.4	7.5	7.7	4.2	5.3	4.9	5	5.3	5.3	5.5

Appendix 6.4 - Results for process integration 3a

Table 6.4 Key system and performance parameters for optimised PI-3a

PI-3a High latent heat solution Water	E6-C100	E5-C100	E6-B50	E5-B50
$P_{max}\ bar$	15.9	14.5	13	11.5
$T_{wf\ Pt.1}\ °C$	200	195	190	184
$T_{wf\ Pt.4}\ °C$	277	269	259	247
$m_{wf}\ kg/s$	0.05	0.04	0.02	0.02
$Q_{EXH}\ kW$	40	42.5	17.5	17.4
$Q_{HT\ EGR}\ kW$	61.5	35.2	26.5	17.5
$Q_{LT\ EGR}\ kW$	22.3	16.3	8.7	6.5
PR_{exp}	16	14.4	12.8	11.1
VFR_{exp}	10.8	9.9	8.9	7.9
$\eta_I\ \%$	13.8	13.4	12.8	12.1
$W_{net}\ kW$	17.2	12.6	6.7	5
UA_{tot}/W_{net}	0.24	0.27	0.26	0.29
β	0.43	0.3	0.38	0.29
$Q_{inc.LOAD}\ kW$	22.9	30	10.8	12.4
$W_{BP+fan}\ kW$	1.1	1.2	0.3	0.3
$W_{system}\ kW$	14.9	10.5	5.9	4.3

Appendix 6.5 - Results for process integration 4

Table 6.5 Key system and performance parameters for optimised PI-4

PI-4	E6-C100			E5-C100			E6-B50			E5-B50		
	Water	Ethanol	R245fa	Water	Ethanol	R245fa	Water	Ethanol	R245fa	Water	Ethanol	R245fa
$P_{max}\ bar$	15.9	31.1	33	13	31.1	33	13	31.1	32	10	26	32
$T_{max}\ °C$	272	200	146	264	200	146	260	200	144	235	191	144
$m_{wf}\ kg/s$	0.05	0.18	1.29	0.04	0.14	1.02	0.02	0.08	0.56	0.02	0.06	0.48
$Q_{Coolant}\ kW$	5	14.7	46.5	4	11.4	37.0	2.2	6.2	20.4	1.8	5	17.3
$Q_{EXH}\ kW$	48.0	69.1	80.4	52.8	69.6	81.9	20.5	26.5	33.5	21.8	25	34.8
$Q_{HT\ EGR}\ kW$	72.6	82.7	82.7	42	48	48	30.9	37.8	37.8	20.8	25.6	25.7
PR_{exp}	16	16	3.1	12.8	16	3.1	12.8	16	3	9.4	13.2	3
VFR_{exp}	10.9	17	4.7	8.8	17	4.7	8.9	17	4.4	6.9	13.6	4.4
$\eta_I\ \%$	13.8	12.2	5.5	12.8	12.2	5.5	12.8	12.1	5.5	11.3	11.6	5.5
$W_{net}\ kW$	17.4	20.2	11.6	12.6	15.7	9.2	6.8	8.6	5	5	6.4	4.3
UA_{tot}/W_{net}	0.23	0.29	0.52	0.26	0.31	0.54	0.26	0.3	0.54	0.3	0.33	0.57
β	0.36	0.29	0.14	0.24	0.23	0.11	0.33	0.32	0.15	0.23	0.26	0.12
$Q_{inc.LOAD}\ kW$	30.7	48.9	68.8	40.2	53.9	72.7	13.6	17.9	28.5	16.8	18.5	30.5
$W_{BP+fan}\ kW$	1.4	2.4	3	1.6	2.4	3.1	0.4	0.6	0.8	0.4	0.5	0.9
$W_{system}\ kW$	14.7	16.4	7.8	10.1	12.1	5.5	5.9	7.4	3.8	4.2	5.4	3.1

Note: The desired mass flow rate in PI-4 was a function of the energy and exergy contents of the engine block heat and the 'EGR + EXH parallel' thermal architecture, along with the ratio of sensible heat to latent heat of the working fluid. For this explanation, consider water at E6-B50. The mass flow rate of water for complete heat recovery of engine block

heat was noticeably greater than the corresponding value to absorb heat from 'EGR + EXH parallel' thermal architecture (0.51 vs. 0.02 kg/s). If the higher mass flow rate was selected it would recover the entire coolant heat but will also result in two-phase at the expansion inlet. Hence, the mass flow rate of water was considered the minimum of these two. Thus, there was a mass flow rate limitation for complete engine block heat recovery.

Appendix 6.6 - Results for process integration 3 (with R245fa)

Table 6.6 Key system and performance parameters for optimised PI-3 using R245fa

PI-3 R245fa	E6-C100	E5-C100	E6-B50	E5-B50
$P_{max}\ bar$	33	32	31	33
$T_{max}\ °C$	147	145	143	147
$m_{wf}\ kg/s$	1.1	0.88	0.48	0.42
$Q_{EXH}\ kW$	90.8	92.7	38.2	40.3
$Q_{HT\ EGR}\ kW$	88.1	51.6	41.2	28.3
PR_{exp}	3.1	3	2.9	3.1
VFR_{exp}	4.8	4.5	4.3	4.8
$\eta_I\ \%$	5.6	5.6	5.5	5.6
$W_{net}\ kW$	10	8	4.4	3.8
UA_{tot}/W_{net}	0.57	0.6	0.6	0.64
β	0.11	0.09	0.11	0.1
$Q_{inc.LOAD}\ kW$	80.7	84.7	33.9	36.4
$W_{BP+fan}\ kW$	3.6	3.7	1	1.1
$W_{system}\ kW$	5.7	3.7	3	2.5

Appendix 6.7 - Results for process integration 4a (case study)

Table 6.7 Key system and performance parameters for optimised PI-4a case study

PI-4a Modified coolant exergy	E6-B50		
	Water	Ethanol	R245fa
$P_{max}\ bar$	15.9	28	33
$T_{max}\ °C$	277	194	146
$m_{wf}\ kg/s$	0.03	0.09	0.64
$T_{wf\ Pt.2}\ °C$	200	196	127
$X_{wf\ Pt.2}$	0.41	0.04	0
$Q_{EXH}\ kW$	15.4	16.1	30.9
$Q_{HT\ EGR}\ kW$	25	25.5	36
PR_{exp}	16	14.3	3.1
VFR_{exp}	10.8	14.9	4.7
$\eta_I\ \%$	13.8	11.8	5.5
$W_{net}\ kW$	10.8	9.4	5.8
UA_{tot}/W_{net}	0.18	0.22	0.49
β	0.71	0.59	0.19
$Q_{inc.LOAD}\ kW$	4.5	6.7	25.1
$W_{BP+fan}\ kW$	0.3	0.3	0.7
$W_{system}\ kW$	9.8	8.5	4.6

Appendix 6.8 - Results for process integration 5

Table 6.8 Key system and performance parameters for optimised PI-5

PI-5	E6-C100				E5-C100			
	Ethanol	Methanol	R30	Acetone	Ethanol	Methanol	R30	Acetone
$P_{max}\ bar$	31.1	42	50	42	31.1	42	47	42
$T_{max}\ °C$	200	237	233	225	200	237	227	225
$m_{wf}\ kg/s$	0.18	0.12	0.47	0.3	0.14	0.1	0.37	0.23
$Q_{CAC}\ kW$	28.1	20.4	23.6	33.3	17.4	12.5	14.6	20.5
$Q_{EXH}\ kW$	48.1	46.3	46.4	49.3	59.2	54.6	56.7	62.8
$Q_{HT\ EGR}\ kW$	88.5	88.4	87.8	88.1	51.8	51.7	51.3	51.5
PR_{exp}	16	14.2	10.4	13.5	16	14.2	9.7	13.5
VFR_{exp}	17	12.2	11.2	19.8	17	12.2	10.5	19.8
$\eta_I\ \%$	12.1	13	13.1	12.6	12.1	13	12.9	12.6
$W_{net}\ kW$	20	20.2	20.7	21.5	15.6	15.5	15.9	17
UA_{tot}/W_{net}	0.31	0.28	0.3	0.33	0.34	0.31	0.33	0.36
β	0.42	0.44	0.45	0.44	0.26	0.28	0.28	0.27
$Q_{inc.LOAD}\ kW$	28.1	26.1	25.7	27.8	43.7	39.1	40.8	45.8
$W_{BP+fan}\ kW$	1.4	1.4	1.4	1.5	1.9	1.7	1.8	2.1
$W_{system}\ kW$	17.2	17.4	17.9	18.5	12.6	12.7	13	13.7

PI-5	E6-B50				E5-B50			
$P_{max}\ bar$	31.1	42	45	40	25	32	32	28
$T_{max}\ °C$	200	237	223	221	188	215	192	197
$m_{wf}\ kg/s$	0.08	0.05	0.2	0.13	0.06	0.04	0.17	0.1
$Q_{CAC}\ kW$	4.4	3.2	3.6	5.2	3.8	3	3.5	4.3
$Q_{EXH}\ kW$	24.8	22.4	23.2	26.5	24	23.1	23.9	24.7
$Q_{HT\ EGR}\ kW$	41.4	40.1	40.9	41.2	28.1	26.2	27.7	28.4
PR_{exp}	16	14.2	9.3	12.8	12.7	10.7	6.5	8.8
VFR_{exp}	17	12.2	10	18.1	13	9.3	6.7	10.5
$\eta_I\ \%$	12.1	13	12.8	12.5	11.4	11.9	11.4	11.6
$W_{net}\ kW$	8.6	8.6	8.7	9.1	6.4	6.2	6.3	6.7
UA_{tot}/W_{net}	0.33	0.31	0.33	0.33	0.37	0.34	0.37	0.35
β	0.35	0.38	0.37	0.34	0.27	0.27	0.26	0.27
$Q_{inc.LOAD}\ kW$	16.2	13.9	14.6	17.4	17.6	16.9	17.6	18
$W_{BP+fan}\ kW$	0.5	0.5	0.5	0.6	0.5	0.5	0.5	0.5
$W_{system}\ kW$	7.4	7.5						

Appendix 6.9 - Results for process integration 5a

Table 6.9 Key system and performance parameters for optimised PI-5a

PI-5a Supercritical R152	E6-B50	E5-B50
$P_{max}\ bar$	48	48
$T_{max}\ °C$	191	190
$m_{wf}\ kg/s$	0.24	0.21
$Q_{CAC}\ kW$	7	7.3
$Q_{EXH}\ kW$	31.8	32.7
$Q_{HT\ EGR}\ kW$	40.9	28.2
PR_{exp}	4.6	4.6
VFR_{exp}	5.8	5.8
η_I %	9	8.9
$W_{net}\ kW$	7.1	6.1
UA_{tot}/W_{net}	0.42	0.47
β	0.22	0.19
$Q_{inc.LOAD}\ kW$	24.7	26.6
$W_{BP+fan}\ kW$	0.8	0.8
$W_{system}\ kW$	5.9	4.9

Appendix 6.10 - Results for process integration 6

Table 6.10 Key system and performance parameters for optimised PI-6

PI-6	E6-C100		E5-C100		E6-B50		E5-B50	
	R245fa	Ethanol	R245fa	Ethanol	R245fa	Ethanol	R245fa	Ethanol
$P_{max}\ (HT)\ bar$	27	27	18	22	18	18	14	14
$T_{max}\ (HT)\ °C$	226	226	204	215	204	204	192	192
$m_{wf}\ (HT)\ kg/s$	0.05	0.05	0.04	0.04	0.02	0.02	0.02	0.02
$m_{wf}\ (LT)\ kg/s$	1.03	0.19	0.84	0.15	0.58	0.11	0.49	0.09
$X_{wf\ Pt.4}$	0.23	0.35	0.21	0.36	0.37	0.46	0.4	0.49
$Q_{EXH}\ kW$	33.1	33.1	43.8	38.7	16.5	16.5	17.1	17.1
$Q_{HT\ EGR}\ kW$	70.8	70.9	41.3	40.3	30.2	30.3	20.1	20.1
$Q_{LT\ EGR}\ kW$	17.8	14.9	10.5	9.7	11.2	8.9	8.5	6.5
$Q_{Cascade\ Cond}\ kW$	92.1	92.2	77.3	70.9	42.4	42.4	34.3	34.3
$PR_{exp}\ (HT)$	8	8	5.3	6.6	5.3	5.4	4	4.1
$VFR_{exp}\ (HT)$	6.8	6.8	4.6	5.6	4.5	4.6	3.5	3.6
$PR_{exp}\ (LT)$	1.7	1.8	1.7	1.8	1.7	1.8	1.7	1.8
$VFR_{exp}\ (LT)$	1.9	1.7	1.9	1.7	1.9	1.7	1.9	1.7
$\eta_I\ \%\ (HT)$	11.4	11.4	9.2	10.3	9.2	9.3	7.8	7.8
$\eta_I\ \%\ (LT)$	3.2	2.9	3.2	2.9	3.2	2.9	3.2	2.9
$\eta_I\ \%\ (combined)$	9.7	9.6	8.6	8.8	7.5	7.4	6.6	6.5
$W_{net}\ kW$	16.9	16.5	12.1	11.8	7.2	6.9	5.4	5.1
UA_{tot}/W_{net}	0.61	0.61	0.72	0.66	0.72	0.72	0.8	0.81
β	0.51	0.5	0.27	0.3	0.44	0.42	0.31	0.3
$Q_{inc.LOAD}\ kW$	16.2	16.7	31.8	26.9	9.3	9.6	11.8	12
$W_{BP+fan}\ kW$	0.8	0.8	1.2	1	0.3	0.3	0.3	0.3
$W_{system}\ kW$	14.9	14.5	10	9.9	6.4	6.1	4.7	4.4

Appendix 6.11 - Results for process integration 7

Table 6.11 Key system and performance parameters for optimised PI-7

PI-7	E6-C100		E5-C100		E6-B50		E5-B50	
	R245fa	Ethanol	R245fa	Ethanol	R245fa	Ethanol	R245fa	Ethanol
$P_{max}\ (HT)\ bar$	27	28	22	22	24	24	16	18
$T_{max}\ (HT)\ °C$	226	228	215	215	220	220	198	204
$m_{wf}\ (HT)\ kg/s$	0.18	0.18	0.15	0.15	0.08	0.08	0.07	0.07
$m_{wf}\ (LT)\ kg/s$	1.13	0.21	0.93	0.18	0.6	0.11	0.52	0.09
$X_{wf\ Pt.3}$	0.04	0.22	0.06	0.22	0.22	0.34	0.25	0.38
$Q_{EXH}\ kW$	58.4	56.3	64.4	64.8	22.5	22.5	23.8	22.3
$Q_{HT\ EGR}\ kW$	81.1	80.5	47	47.2	36.9	37	25	25.1
$Q_{Cascade\ Cond}\ kW$	126.6	124.3	102	102.4	54.2	54.2	45.3	43.7
$PR_{exp}\ (HT)$	8	7.8	6.4	6.6	7.1	7.1	4.6	5.3
$VFR_{exp}\ (HT)$	11	10.8	8.6	8.8	9.6	9.6	5.8	6.9
$\eta_I\ \%\ (HT)$	9.2	9.2	8.5	8.6	8.8	8.8	7.2	7.8
$\eta_I\ \%\ (combined)$	9.6	9.3	9	8.8	8.3	8.1	7.2	7.2
$W_{net}\ kW$	18.5	17.7	14.1	13.8	8.2	7.9	6.1	6
UA_{tot}/W_{net}	0.7	0.66	0.77	0.77	0.75	0.74	0.85	0.83
β	0.32	0.31	0.22	0.21	0.36	0.35	0.26	0.27
$Q_{inc.LOAD}\ kW$	39.9	38.6	50.3	51	14.3	14.6	17.7	16.4
$W_{BP+fan}\ kW$	1.9	1.8	2.2	2.2	0.5	0.5	0.5	0.5
$W_{system}\ kW$	15.3	14.7	10.9	10.7	7.2	6.9	5.2	5.1

Appendix 6.12 - Results for process integration 8

Table 6.12 Key system and performance parameters for optimised PI-8

PI-8	E6-C100	E5-C100	E6-B50	E5-B50
$P_{max}\ bar$	30	30	28	24
$T_{max}\ °C$	233	233	229	221
$m_{wf}\ kg/s$	0.054	0.042	0.021	0.017
$X_{wf\ Pt.1}$	0.54	0.35	0.53	0.41
$Q_{EXH}\ kW$	54.8	55.5	22	21.2
$Q_{HT\ EGR}\ kW$	86.7	51.9	33.2	22.7
$PR_{exp}\ (two-phase)$	3.8	3.8	3.6	3.1
$VFR_{exp}\ (two-phase)$	3.8	4.2	3.6	3.2
$\eta_I\ \%$	13.8	12.8	13.6	12.6
$W_{net}\ kW$	19.5	13.7	7.5	5.6
UA_{tot}/W_{net}	0.25	0.27	0.25	0.28
β	35.3	41.8	14.5	15.7
$Q_{inc.LOAD}\ kW$	0.36	0.25	0.34	0.26
$W_{BP+fan}\ kW$	1.7	1.8	0.5	0.4
$W_{system}\ kW$	16.4	11	6.5	4.7

Note: An additional parameter of interest in PI-8 was the intermediate pressure (Pt. 2). Since the intermediate pressure was relatively high, the sensitivity to pressure drop was

extremely low. For example (at E5-C100), when the pressure drop in EXH heat exchanger was raised from 0.5 to 1 bar the loss in net power was only 2%.

Appendix 6.13 - Blend constituents under consideration in this study

Table 6.13 Chemical identification of the organic blend constituents under consideration in this study

Number	Chemical class	Formula	Name	CAS no.
	n-alcohols	C5H12O	3-Methyl-1-Butanol	123-51-3
	n-alcohols	C3H8O	1-Propanol	71-23-8
	n-alkylbenzenes	C7H8	Toluene	108-88-3

Table 6.14 Thermodynamic and thermo-physical properties of the organic blend constituents under consideration in this study

Name	T_{crit} °C	P_{crit} bar	T_{boil} °C	M_{wt} g/mol	ρ_{liq} kg/m³	T_{freez} °C
3-Methyl-1-Butanol	304	39.3	131	88.1	812	-117
1-Propanol	264	51.7	97	60.1	806	-126
Toluene	319	41.1	111	92.1	870	-95

Table 6.15 Environmental and safety properties of the organic blend constituents under consideration in this study

Name	ATM years	ODP	GWP	ASHRAE 34	Carcinogen IARC	Carcinogen EPA	NFPA H	NFPA F	NFPA I	T_{ign} °C
3-Methyl-1-Butanol							1	2	0	350
1-Propanol							1	3	0	371
Toluene					3	I	2	3	0	480

Appendix 6.14- Aqueous blend screening

Table 6.16 Aqueous blend fluid screening result
(Phase 1: Thermo-physical, Legal, Molecular, Environmental and Safety)

2nd constituent	T_{boil} °C	Homogenous	PHA	Water 25-75%	Availability	Health ≤ 2	T_{freez} < – 40 °C	T_{ign} ≥ 363 °C
Diethyl phthalate	296	X						
alpha-Methylbenzyl ether	287	X						
Dibutyl fumarate	285	X						
Dimethyl phthalate	283	X						
Dibutyl maleate	281	X						
2-Ethylhexyl ether	270	X						
Butyl salicylate	268	X						
Diethyl pimelate	268	X						
2-Ethylhexyl hexanoate	267	X						
Phenyl ether	259	X						
Diethylene glycol	255	X						
2-Butyl octanol	253	X						
Butyl benzoate	250	X						
Dimethyl pimelate	249	X						
Hexylhexanoate	245	X						
Tridecanol	244	X						
2-Ethylhexyl crotonate	241	X						
n-Butyl aniline	241	X						
Triglycol dichloride	241	X						
Dihexyl amine	240	X						
Hexyl-2-ethyl butyrate	230	X						
Dibutyl ethanolamine	229	X						
Diisopropyl maleate	229	X						
2-Ethylhexanoic acid	228	X						
Diethyl maleate	225	X						
Ethyl octanol	221	X						
Di(2-chloroethyl)formal	218	X						
Diethyl fumarate	218	X						
Diethyl succinate	218	X						
Isophorone	215	X						
Butyl acetoacetate	214	X						
Tributyl amine	214	X						
Benzyl alcohol	205			X				
Hexanoic acid	205	X						
Methylphenyl carbinol	205	X						
n-Ethyl aniline	205	X						
Trimethyltetrahydrobenzal	205	X						
Methylphenyl ketone	202	X						
2-Ethylbutyl butyrate	200	X						
2-Ethylhexyl acetate	199	X						
2-Methylpentanoic acid	196	X						
Tetrahydrobenzonitrile	195	X						
2-Ethylbutyric acid	194	X						
Styrene oxide	194	X						
Glycol diacetate	191			X				

Diisopropylethanol amine	190	X						
Dibutyl acetal	189	X						
alpha-Methylbenzyl amine	187	X						
Chloroisopropyl ether	187	X						
Valeric acid	186	X						
Vinyl-2-ethyl hexanoate	185	X						
2-Ethyl hexanol	185	X						
4-Methyl-2-pentyl butyrat	183	X						
2,3-Dichloropropanol	182	X						
Dibutyl formal	182				X			
2-Chloroethyl ether	179	X						
2,6-Dimethyl-4-heptanol	178	X						
2-Methyl-5-ethyl pyridine	178	X						
Vinyl-2-ethylhexyl ether	178	X						
2-Heptyl acetate	176	X						
3-Heptyl acetate	174	X						
2-Ethylhexyl chloride	173	X						
3-Methoxybutyl acetate	171	X						
Butyl-2-ethoxyethanol	171			X				
1-Butoxy-2-propanol	170	X						
Ethyl-3-ethoxy propionate	170	X						
Dicyclopentadiene	170	X						
Diacetone alcohol	169			X				
Hexyl acetate	169	X						
2-Ethylhexyl amine	169	X						
Diisobutyl ketone	168	X						
Butyl butyrate	166	X						
1,2,3,6-Tetrahydrobenzaldehyde	164	X						
n-Ethylcyclohexyl amine	164	X						
Butyric acid	164			X				
n-Methyldibutyl amine	163	X						
2-Ethylbutyl acetate	162	X						
Diethyl ethanolamine	162					X		
Cyclohexanol	162			X				
Dibutyl amine	160	X						
Hexanol	158	X						
Cyclohexanone	155	X						
Isopropyl benzene	152	X						
Triallyl amine	151	X						
Diallyl acetal	151	X						
Nonane	151	X						
Diethylisopropanol amine	151				X			
Methylamyl ketone	151	X						
1,4-Thioxane	149	X						
2-Hexenal	149	X						
Vinyl-2-methyl pentanoate	149	X						
Ethylbutyl ketone	149	X						
2-Methyl pentanol	148	X						
2,6-Dimethyl morpholine	147				X			
Dipropyl acetal	147	X						
Diethyl butyral	146	X						
4-Methyl-2-pentyl acetate	146	X						
2-Ethyl butanol	146	X						
Styrene	145	X						

Diethylaminoethyl amine	145			X				
Diethylaminoethyl amine	145			X				
gamma-Picoline	145					X		
Dipropyl ketone	144	X						
5-Methyl-2-hexanone	144	X						
Butyl ether	142	X						
Propionic acid	142			X				
Cyclopentanol	141						X	
2,4-Pentanedione	141	X						
m-Xylene	139	X						
Ethyl morpholine	138							X
Ethyl crotonate	138	X						
Ethyl benzene	136	X						
2-Ethoxy ethanol	135							X
Cyclohexylamine	134					X		
Hexyl chloride	134	X						
Vinyl crotonate	134	X						
Hexyl amine	133					X		
1-Ethoxy-2-propanol	132				X			
Chlorobenzene	132					X		
4-Methyl-2-pentanol	131	X						
Cyclopentanone	131	X						
Isoamyl alcohol	131							
Allyl acetone	130	X						
Ethylene chlorohydrin	129					X		
Mesityl oxide	129	X						
Hexaldehyde	129	X						
Propylene chlorohydrin	127				X			
Butyl acetate	127	X						
2-Methoxy ethanol	125			X				
Paraldehyde	125	X						
Ethylidene acetone	124	X						
1-Chloro-2-propanol	119					X		
Allyl cyanide	119	X						
1-Methoxy-2-propanol	119							X
2-Methyl pentanal	118	X						
Butyl acrylate	118	X						
Acetic acid	118			X				
Butyronitrile	118	X						
1-Butanol	118	X						
2-Methylpropyl acetate	117	X						
Epichlorohydrin	117	X						
4-Methyl-2-pentanone	117			X				
2-Ethylbutyraldehyde	117	X						
Vinyl butyrate	117	X						
Ethylene diamine	117		X					
3-Pentanol	116	X						
Pyridine	116					X		
Methylisobutyl ketone	115	X						
n-Methyl morpholine	115			X				
Butylisopropenyl ether	115	X						
Dimethyl butyral	114	X						
Toluene	111	X						
Vinyl-2-Chloroethyl ether	109	X						

1,3-Dimethylbutyl amine	109				X			
Isobutyl alcohol	108	X						
Vinyl isobutyrate	105	X						
Dimethyl isobutyral	105	X						
Allyl Acetate	104	X						
Croton aldehyde	104	X						
Valeraldehyde	103	X						
Diisobutylene	103	X						
Methyl-n-Propyl-Ketone	102	X						
Diethyl acetal	102	X						
Propyl acetate	102			X				
1,4-Dioxane	101			X				
Formic acid	101		X					
2-Butanol *	100							
Ethyl acrylate	100	X						
n-Heptane	98	X						
Chloral	98			X				
Methylisopropenyl ketone	98	X						
Propionitrile	97	X						
Propanol	97							
Allyl alcohol	97					X		
1,2-Dichloropropane	96	X						
Vinyl propionate	95	X						
Butylvinylether	94	X						
2,5-Dimethyl furan	93	X						
Isoveralaldehyde	93			X				
Ethylbutyl ether	92	X						
n-Methylbutyl amine	91			X				
1-Methoxy-1,3-butadiene	91	X						
Triethyl amine	90			X				
Isopropyl acetate	89	X						
Hydrogen nitrate	86		X					
Diisopropyl amine	84			X				
1,2-Dichloroethane	84			X				
Vinylisobutyl ether	83	X						
tert Butanol	83			X				
2-Methyl-2-propanol	83			X				
Isopropyl alcohol	82			X				
Acetonitrile	82			X				
Cyclohexane	81	X						
Benzene	80	X						
Methylvinyl ketone	80			X				
Methylethyl ketone	80			X				
Ethanol	79			X				
1-Chlorobutane	78	X						
Acrylonitrile	77	X						
Ethyl acetate	77	X						
1-Butenylmethylether	77	X						
1,3-Dioxolane	76			X				
Vinyl acetate	73	X						
1-Butenylethyl ether(cis)	72	X						
Isopropyl ether	68	X						
Methacrylaldehyde	68	X						
Vinylallyl ether	67	X						

Vinylpropyl ether	65	X						
Dimethyl acetal	65			X				
Methyl acetate	57			X				
4-Methyl-Cis-2-Pentene	56	X						
Vinylisopropyl ether	56	X						
Ethyl formate	54	X						
Acrolein	53			X				
Propionaldehyde	49			X				
1,1,2-Trichlorotrifluoroethane	48	X						
Propyl chloride	47	X						
Carbon disulfide	46	X						
Allyl chloride	45			X				
Methylal	42			X				
Dichloromethane	40	X						
n-Pentane	36	X						
Isopropyl chloride	36	X						
Vinylethyl ether	36	X						
Ethyl ether	35			X				
Methylvinyl chloride(cis)	33	X						
Hydrogen fluoride	19		X					
Hydrogen iodide	-36		X					
Hydrogen bromide	-67		X					
Hydrogen chloride	-84		X					
*1-Propanol more suited								

Appendix 6.15 - Results for process integration 9

Table 6.17 Key system and performance parameters for optimised PI-9

PI-9	E6-C100		E5-C100		E6-B50		E5-B50	
	3M-1B53%	1-Propanol72%	3M-1B53%	1-Propanol72%	3M-1B53%	1-Propanol72%	3M-1B53%	1-Propanol72%
$P_{max}\ (HP, HT)\ bar$	18.6	22.6	18.6	22.6	18.6	22.6	14	20
$T_{max}\ (HP, HT)\ °C$	250	250	250	250	196	197	183	191
$m_{wf}\ (HP, HT)\ kg/s$	0.08	0.1	0.06	0.08	0.04	0.05	0.03	0.04
$m_{wf}\ (LP, LT)\ kg/s$	0.04	0.06	0.04	0.05	0.03	0.03	0.03	0.03
$X_{wf\ Pt.3}$	0.84	0.79	0.86	0.81	0.99	0.97	0.99	0.97
$Q_{EXH}\ kW$	57.5	61.1	58	61.6	22.8	24.6	24	23.2
$Q_{HT\ EGR}\ kW$	85	88	47.7	50.7	35.8	39.1	23.7	24.9
$PR_{exp}\ (HP, HT)$	8	8	8	8	8	8	5.9	7
$VFR_{exp}\ (HP, HT)$	6.7	6.8	6.7	6.8	6.6	6.8	5	6
$\eta_I\ \%$	10.9	11.2	10.6	11	9.5	9.9	8.4	9.1
$W_{net}\ kW$	21.4	22.6	16.1	17.2	9.2	10	7	7.6
UA_{tot}/W_{net}	0.28	0.28	0.28	0.29	0.3	0.31	0.34	0.33
β	0.37	0.37	0.28	0.28	0.4	0.41	0.29	0.33
$Q_{inc.LOAD}\ kW$	36.2	38.5	41.9	44.3	13.6	14.5	17	15.7
$W_{BP+fan}\ kW$	1.9	2	1.9	2	0.5	0.5	0.5	0.5
$W_{system}\ kW$	18	19	13.1	14	8.1	8.8	6	6.5

Appendix 6.16 - Results for process integration 10

Table 6.18 Key system and performance parameters for optimised PI-10

PI-10	E6-C100		E5-C100		E6-B50		E5-B50	
	3M-1B53%	1-Propanol72%	3M-1B53%	1-Propanol72%	3M-1B53%	1-Propanol72%	3M-1B53%	1-Propanol72%
$P_{max}\ (HT)\ bar$	17.8	21.8	17.8	21.8	17.8	21.8	16	20
$T_{max}\ (HT)\ °C$	194	195	194	195	194	195	188	191
$m_{wf}\ (HT)\ kg/s$	0.09	0.11	0.07	0.08	0.04	0.05	0.03	0.04
$P_{max}\ (LT)\ bar$	24	24	28	28	26	20	28	24
$T_{max}\ (LT)\ °C$	114	114	123	123	119	104	123	114
$m_{wf}\ (LT)\ kg/s$	0.61	0.61	0.37	0.37	0.19	0.24	0.17	0.2
$Q_{EXH}\ kW$	60.1	64.5	60.6	65	23.4	25	22.6	23.2
$Q_{HT\ EGR}\ kW$	81.7	81.7	45.7	45.8	36.2	39.1	23.3	24.9
$Q_{LT\ EGR}\ kW$	12.3	12.3	9.5	9.4	8.7	5.7	8	6.4
$Q_{CAC}\ kW$	48.7	48.7	36.2	36.2	12.2	12.4	12.7	13.5
$PR_{exp}\ (HT)$	16	16	16	16	16	16	14.3	14.6
$VFR_{exp}\ (HT)$	12.5	12.8	12.5	12.8	12.5	12.8	11.3	11.7
$PR_{exp}\ (LT)$	2.8	2.8	3.3	3.3	3	2.3	3.3	2.8
$VFR_{exp}\ (LT)$	13.9	13.9	15.9	15.9	15	11.5	15.9	13.9
$\eta_I\ \%\ (HT)$	12.9	13.2	12.9	13.2	12.9	13.2	12.4	12.8
$\eta_I\ \%\ (LT)$	8.8	8.8	9.7	9.7	9.2	7.7	9.7	8.8
$\eta_I\ \%\ (combined)$	11.7	11.9	11.9	12.2	12	12	11.6	11.7
$W_{net}\ kW(HT)$	18.3	19.3	13.7	14.7	7.7	8.5	5.7	6.2
$W_{net}\ kW\ (combined)$	23.7	24.7	18.2	19.1	9.6	9.9	7.7	7.9
UA_{tot}/W_{net}	0.32	0.31	0.34	0.34	0.35	0.34	0.39	0.38
β	0.39	0.38	0.3	0.29	0.41	0.4	0.34	0.34
$Q_{inc.LOAD}\ kW$	36.5	39.8	42.5	45.9	23.4	15.1	14.9	15.3
$W_{BP+fan}\ kW$	2	2.2	2	2.2	0.5	0.5	0.5	0.5
$W_{system}\ kW$	20	20.8	14.9	15.5	8.5	8.6	6.7	6.9

Appendix 6.17- Thermal oil loop

In the thermal oil loop approach, high temperature thermally stable diathermic oil recovers the high temperature waste heat and transfers it to the ORC working fluid at a lower temperature, avoiding the risk of thermal degradation. Such process integration, reproduced in Fig. 6.1a, was proposed by Shu et al. (2013) for vehicle engine heat recovery using conventional refrigerants like R245fa and isopentane. If the pressure limits of the ORC do not change with the addition of the oil loop, and the maximum available waste heat is transferred to the thermal oil, then the system power of the ORC will not noticeably reduce. This is since the total heat transfer losses in the heat recovery are divided between two heat exchangers (Fig. 6.1b)

Unfortunately, the thermal oil loop also introduces a number of disadvantages. The additional subsystem components include a gas-to-oil heat exchanger, the thermal oil and the oil pump. Hence, for nearly equal power, the system complexity, size, weight and

opportunity for failure increase. The additional sub-system components also increase the system cost by ≈20% (Guillen, 2008). Thermodynamically, the oil loop fails to provide any opportunity to reduce the overall system irreversibility. Fundamentally, such systems cannot take full advantage of the high grade waste heat, and in fact, mimic low grade heat recovery systems. For the above drawbacks, which have a higher impact in transport applications, the thermal oil loop approach was excluded as a potential solution.

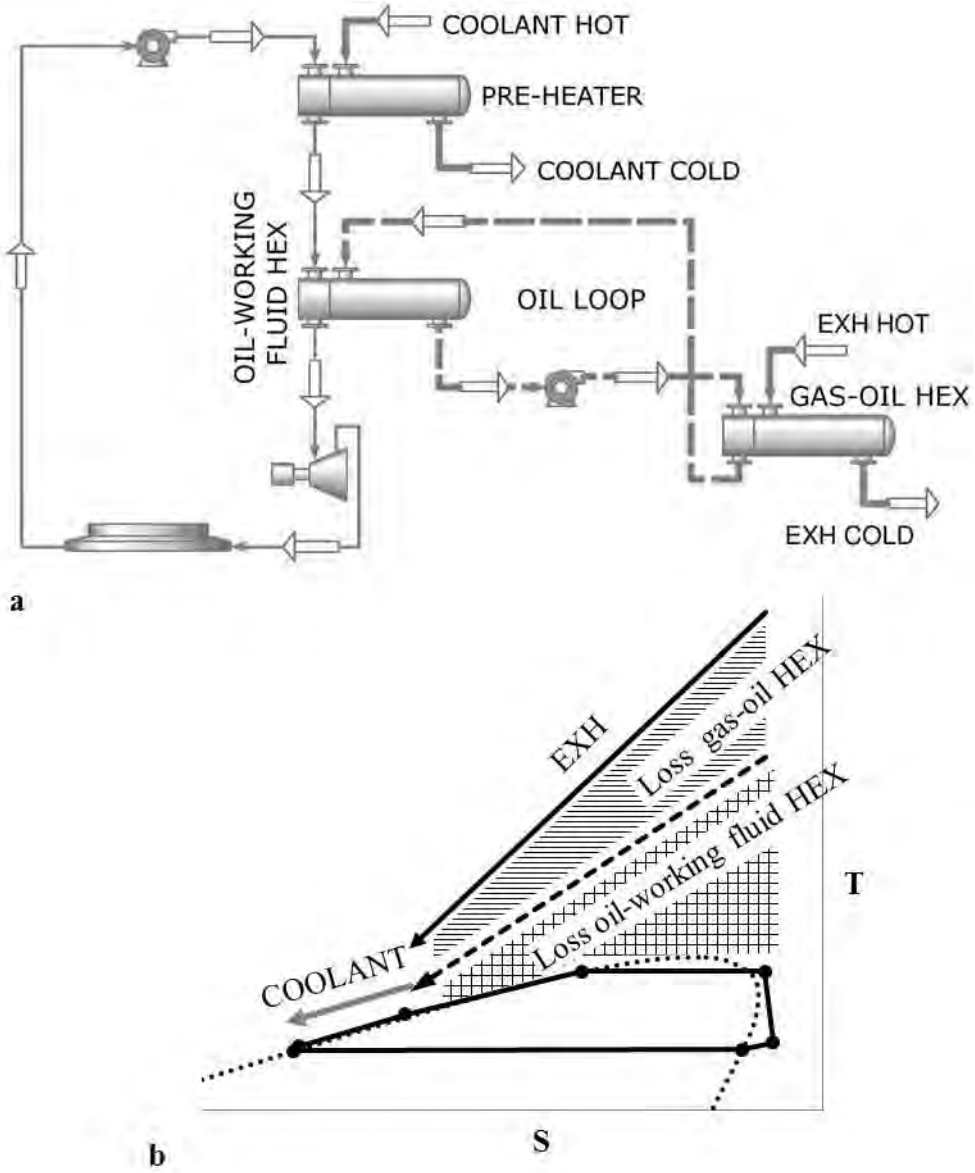

Figure 6.1 Thermal oil loop system (a) system architecture (b) T-S sketch

Appendix 6.18- High temperature stability organic fluids

Table 6.19 Key properties of selected high thermal stability organic fluids usually recommended for stationary applications with an IHE

Formula	Name	CAS no.	T_{crit} °C	P_{crit} bar	T_{boil} °C	M_{wt} g/mol	ρ_{liq} kg/m^3	T_{freez} °C
C8H10	o-Xylene	95-47-6	357	37.3	144	106.2	883	-25
C8H10	m-Xylene	108-38-3	344	35.4	139	106.2	867	-48
C10H30SI5O5	D5	541-02-6	346	11.6	211	370.8	954	-38
C6H18OSI2	MM	107-46-0	246	19.1	101	162.4	760	-68
C8H24SI3O2	MDM	107-51-7	291	14.4	153	236.5	815	-86
C10H30SI4O3	MD2M	141-62-8	326	12.3	194	310.7	848	-68

Appendix 6.19- Organic blend screening

Table 6.20 High temperature organic blend screening result (Phase 1: Thermo-physical, Legal, Molecular, Environmental and Safety)

High temperature stable organic	2nd constituent	T_{boil} °C	Blend $T_{boil} \leq 100$ °C	Pressure swing	Health ≤ 2
o-Xylene	Acetamide	222	X		
o-Xylene	Propionamide	213	X		
Toluene	Glycol	197	X		
o-Xylene	Glycol	197	X		
o-Xylene	Chloroacetic acid	189	X		
o-Xylene	Butyric acid	164	X		
m-Xylene	Butyric acid	164	X		
p-Xylene	Butyric acid	164	X		
o-Xylene	2-Furaldehyde	162	X		
o-Xylene	Cyclohexanol	162	X		
o-Xylene	Propionic acid	142	X		
p-Xylene	Propionic acid	142	X		
m-Xylene	Cyclopentanol	141	X		
Toluene	2-Ethoxy ethanol	135	X		
o-Xylene	2-Ethoxy Bethanol	135	X		
o-Xylene	Isoamyl alcohol	131	X		
Toluene	2-Methoxy ethanol	125	X		
Toluene	Propylene diamine	121	X		
Toluene	1-Chloro-2-propanol	119	X		
Toluene	Acetic acid	118	X		
m-Xylene	Acetic acid	118	X		
Toluene	Butyronitrile	118	X		
Toluene	1-Butanol	118	X		
o-Xylene	1-Butanol	118	X		
Toluene	Epichlorohydrin	117	X		
Toluene	Ethylene diamine	117	X		
Toluene	Pyridine	116	X		
Toluene	Nitroethane	115	X		
Toluene	Isobutyl alcohol	108	X		

Toluene	tert Amy alcohol	102	X		
Toluene	Nitromethane	101		X	
Toluene	Formic acid	101		X	
Toluene	2-Butanol *	100			
Toluene	Propanol	97		X	
m-Xylene	Propanol	97		X	
Toluene	Allyl-alcohol	97			X
Toluene	Isopropyl alcohol *	82			
Toluene	Ethanol	79			
Toluene	Methanol	65		X	
*Ethanol more suited					

Appendix 6.20 - Results for process integration 11 and 12

Table 6.21 Key system and performance parameters for optimised PI-11 (left) and PI-12 (right)

	PI-11					PI-12			
ET 65/35	E6-C100	E5-C100	E6-B50	E5-B50		E6-C100	E5-C100	E6-B50	E5-B50
$P_{max}\ bar$	34	34	34	24		34	34	31	24
$m_{wf}\ kg/s$	0.17	0.13	0.07	0.06		0.17	0.13	0.07	0.06
$Q_{IHE}\ kW$	20.3	15.5	8.5	7.7		17.1	15.4	6.9	7.3
$Q_{EXH}\ kW$	60.1	60.2	22.5	21.8		51.7	53.6	19.5	18.2
$Q_{HT\ EGR}\ kW$	78.8	45.5	35.6	23		88	51.5	40.8	27
PR_{exp}	16	16	16	11.1		16	16	14.6	11.1
VFR_{exp}	13.9	13.9	13.9	9.8		13.9	13.9	12.7	9.8
η_I %	15.8	15.8	15.8	14.3		15.4	15.8	14.9	14.2
$W_{net}\ kW$	21.9	16.7	9.2	6.4		21.6	16.6	9	6.4
UA_{tot}/W_{net}	0.24	0.26	0.26	0.3		0.24	0.27	0.27	0.32
β	0.36	0.28	0.41	0.29		0.42	0.31	0.46	0.35
$Q_{inc.LOAD}\ kW$	38.2	43.5	13.4	15.4		30.1	37	10.5	11.8
$W_{BP+fan}\ kW$	2	2	0.5	0.4		1.6	1.7	0.4	0.3
$W_{system}\ kW$	18.4	13.5	8	5.5		18.5	13.7	8	5.6

Appendix 6.21 - Secondary objective functions

Table 6.22 Detailed relative compatibility of alternative pure and blend fluid constituents

	Typical vehicle compatibility					Water blends			Organic blend		Pure organic		
Excellent 1 / Good 2 / Fair 3 / Severe Effect 4	Antifreez	Hydraulic Oil	Motor oil	Diesel Fuel	Urea	Water	Alcohols:Amyl	Alcohols:Propyl	Toluene	Ethanol	Methanol	Dichloromethane	Acetone
Metals and alloys													
Aluminum	1	1	1	1	2	1	2	1	1	2	1	3	1
Brass	n/a	1	n/a	n/a	n/a	1	1	1	1	1	1	1	1
Bronze	1	1	1	1	2	n/a	1	1	1	1	1	2	1
Carbon Steel	n/a	1	1	1	2	1	2	1	1	2	1	2	2
Carpenter 20	1	1	n/a	1	n/a	n/a	1	1	1	1	1	1	1
Cast iron	1	1	n/a	1	n/a	4	2	1	1	2	1	2	1
Copper	n/a	1	n/a	n/a	n/a	2	1	1	1	1	2	2	1
stainless steel - 304	n/a	1	1	1	2	1	1	1	1	1	1	2	1
stainless steel - 316	1	1	1	1	2	1	1	1	1	1	1	2	1
Titanium	n/a	n/a	1	2	1	1	2	1	1	1	2	2	1
O-Ring materials													
ChemRaz (FFKM)	n/a	1	n/a	1	n/a	4	3	1	1	1	1	1	1
EPDM	1	4	4	4	1	1	1	1	4	1	1	3	1
Hypalon®	n/a	1	n/a	2	n/a	1	1	1	4	1	1	n/a	3
Hytrel®	n/a	n/a	2	1	n/a	n/a	1	n/a	2	n/a	2	4	2
Kalrez	1	1	1	1	n/a	n/a	1	1	1	1	1	1	1
Kel-F®	n/a	n/a	1	1	n/a	1	1	n/a	2	1	1	1	1
Natural rubber	1	4	n/a	4	n/a	1	2	1	4	1	1	2	3
Neoprene	3	1	2	2	2	1	1	1	4	1	1	n/a	3
Silicone	3	2	n/a	4	2	n/a	4	1	4	2	1	n/a	4
Viton®	1	1	n/a	1	1	1	1	1	3	1	3	2	4
Thermoplastics													
Acetal (Delrin®)	4	2	2	4	1	n/a	1	1	3	1	1	2	1
CPVC	1	n/a	1	n/a	1	1	1	1	4	2	1	4	4
LDPE	n/a	3	3	1	1	n/a	2	1	3	2	1	4	2
NORYL®	1	n/a	1	4	1	1	3	1	4	1	1	2	4
PEEK	1	1	1	1	1	n/a	1	1	1	1	1	1	1
Polypropylene	4	4	1	1	1	1	2	1	3	1	1	2	1
PPS (Ryton®)	n/a	4	1	1	1	1	1	1	1	n/a	1	1	1
PTFE	n/a	1	1	1	1	1	1	1	1	1	1	1	1
PVC	1	1	2	2	4	1	1	1	4	3	1	4	4
PVDF (Kynar®)	n/a	1	2	1	1	1	1	1	1	n/a	1	2	4

Table 6.23 Cost and availability of alternative pure and blend fluid constituents (updated Q4, 2013)

	Cost		Availability									
	$/L for 200L	$/L for 200L	Science Lab	Spectrum Chemical	Sigma Aldrich	Fisher Scientific	MP Biomedicals	SynQuest	TCI	Alfa Aesar	Matrix Scientific	Apollo Scientific
High temperature blend constituents												
3-Methyl-1-Butanol	10.7	19.5	Y	Y	Y	Y		Y	Y	Y		
1-Propanol	19	10.3	Y	Y	Y	Y	Y		Y	Y		
Toluene	5.1	6.9	Y	Y	Y	Y	Y		Y	Y		
Ethanol	33.7	38.2	Y	Y	Y	Y	Y			Y		
High temperature pure organic												
Methanol	4.2	7.2	Y	Y	Y	Y	Y		Y	Y		
Dichloromethane	7.8	11.1	Y	Y	Y	Y	Y	Y	Y	Y		
Acetone	5.8	7.4	Y	Y	Y	Y	Y		Y	Y		
Low temperature pure organic												
1,2-Difluoroethane						Y		Y			Y	Y
Difluoromethyl-Methyl-Ether								Y				Y

Note: Costs are tabulated in $/L for 200L quantity quotations from two different suppliers, while availability was assessed by checking the inventory of 10 well-known chemical suppliers.